



UNIVERSITÀ  
DEGLI STUDI  
DI PADOVA

**University of Padua**

Department of Management and Engineering

Ph.D. Course in Mechatronics and Product Innovation Engineering

Cycle 30°

**MASSIVE FATIGUE ASSESSMENT OF WELDED  
MEGASTRUCTURES BY ADVANCED METHODS**

**Coordinator:** Prof. Roberto Caracciolo

**Supervisor:** Prof. Filippo Berto

**Ph.D. student:** Marco Colussi





UNIVERSITÀ  
DEGLI STUDI  
DI PADOVA

**Università degli Studi di Padova**

Dipartimento di Tecnica e Gestione dei Sistemi Industriali

Corso di Dottorato di Ricerca in Ingegneria Meccatronica e  
dell'Innovazione Meccanica del Prodotto

Ciclo 30°

**METODI AVANZATI PER L'ANALISI MASSIVA  
DELLA RESISTENZA A FATICA NELLE  
MEGASTRUTTURE SALDATE**

**Coordinatore:** Ch.mo Prof. Roberto Caracciolo

**Supervisore:** Ch.mo Prof. Filippo Berto

**Dottorando:** Marco Colussi





# Contents

<b>Abstract</b> .....	<b>I</b>
<b>1. Introduction</b> .....	<b>1</b>
1.1 Background and motivations .....	1
1.2 Thesis structure .....	6
References .....	8
<b>2. Local approaches for fatigue assessment of welded joints</b> .....	<b>13</b>
2.1 Introduction .....	15
2.2 Notch stress intensity factor approach .....	16
2.2.1 Local stress fields near pointed V-notches.....	16
2.2.2 Endurable NSIFs of fatigue-loaded welded joints .....	20
2.2.3 Potential and weak points of the NSIF approach .....	21
2.3 Averaged strain energy density approach .....	22
2.3.1 Basic relationships of the SED approach .....	23
2.3.2 Endurable SED of fatigue-loaded welded joints.....	30
2.3.3 Potential and weak points of the SED approach .....	31
2.4 Peak stress method .....	32
2.4.1 Basic relationships of the PSM .....	33
2.4.2 Potential and weak points of the PSM .....	36
2.5 Brief open epistemological discussion on fatigue design .....	36
References .....	38
<b>3. Fatigue characterization of welded cover plates</b> .....	<b>43</b>
3.1 Introduction .....	45
3.2 Literature and normative review .....	47
3.2.1 Fatigue classification according to standards in force .....	48
3.3 Preliminary numerical analyses .....	54
3.3.1 Cover plate with tapered end.....	55
3.3.2 Cover plate with transverse weld .....	57
3.4 Experimental procedure .....	65
3.4.1 Analysis of crack initiation causes .....	69

3.4.2 Discussion on experimental results .....	75
3.4.3 Micrographic analysis .....	76
3.4.4 Workshop drawings of tested specimens .....	80
3.5 Detailed numerical analyses .....	84
3.5.1 Effect of plates thickness ratio .....	85
3.5.2 Effect of the local weld toe slope .....	87
3.5.3 Effect of transverse welds misalignment .....	88
3.6 SED based summary of experimental results.....	91
3.7 Discussion and conclusion .....	93
References .....	96
<b>4. Rapid local Strain Energy Density evaluation through coarse free-generated meshes.....</b>	<b>99</b>
4.1 Introduction .....	101
4.2 Averaged strain energy density numerical calculation .....	106
4.3 Basic theoretical recalls on averaged SED from sharp V-notches.....	107
4.3.1 Sharp V-notches under pure loading modes .....	107
4.3.2 Sharp V-notches under mixed mode loading (1+2) .....	108
4.3.3 Scale effect .....	109
4.4 Averaged SED evaluation by using free-generated mesh patterns .....	110
4.4.1 Plane condition.....	110
4.4.2 Three-dimensional condition.....	113
4.5 Limitation of applicability of the volume-free SED approach.....	114
4.5.1 Pure mode 1 loading.....	114
4.5.2 Pure mode 2 loading.....	117
4.6 Volume-free SED approach applied to 2D and 3D welded joints .....	120
4.6.1 Plane models .....	120
4.6.2 Three-dimensional models .....	126
4.7 Practical applications on cover plates by using different software .....	129
4.7.1 Plane models .....	129
4.7.2 Three-dimensional models .....	132
4.8 Discussion and conclusion .....	137
References .....	139

<b>5. Local parameters and nominal stresses: a sound link for an efficient structural design.....</b>	<b>145</b>
5.1 Introduction.....	147
5.2 Analytical preliminaries.....	149
5.3 Some assumptions on nominal stress evaluation in welded plates.....	152
5.4 Relationship between local SED and nominal stress components.....	154
5.5 Analytical expression of the stress offset.....	157
5.5 Abaci of welded joints stress concentration.....	161
5.5.1 Numerical analyses and data fitting.....	162
5.5.2 Double fillet welded cruciform joint.....	164
5.5.3 Double fillet welded T-joint.....	170
5.5.4 Full penetration welded cruciform joint.....	172
5.5.5 Full penetration welded T-joint.....	175
5.5.6 Double fillet welded longitudinal attachment.....	177
5.6 Practical application.....	182
5.7 Discussion and conclusion.....	184
References.....	186
<b>6. A mathematical definition of modified nominal stress and experimental validation .....</b>	<b>189</b>
6.1 Introduction.....	191
6.2 Literature and normative review on the effect of loading type.....	192
6.3 Local finite element calculation of nominal stress components.....	195
6.4 A loading type dependent modified nominal stress.....	196
6.4.1 Application to fillet-welded non-load-carrying cruciform and T-joints.....	198
6.4.2 Reanalysis of data from the literature.....	199
6.4.3 Results of the investigation.....	203
6.5 Open wide discussion and conclusion.....	204
References.....	208
<b>7. Automatic fatigue assessment of large structures by using a dedicated post-processor .....</b>	<b>211</b>
7.1 Introduction.....	213
7.2 Assessing welds and parent material with PostFatigue.....	213
7.2.1 Graphical user interface.....	214

7.2.2 Workflow of fatigue assessment with PostFatigue .....	216
7.2.3 Results cache management.....	216
7.3 Model and load groups .....	217
7.3.1 Material parameters .....	217
7.3.2 Fatigue load groups .....	217
7.4 Normative reference .....	219
7.5 Fatigue assessment of parent material.....	220
7.5.1 Fatigue details .....	220
7.5.2 Graphical output of stresses and parent material details .....	223
7.5.3 Analysis options .....	223
7.5.4 Fatigue check.....	226
7.6 Fatigue assessment of check lines .....	227
7.6.1 Fatigue details .....	227
7.6.2 Weld geometry design tool .....	235
7.6.3 Assessing welds with shell models .....	236
7.6.4 Fatigue check according to nominal and hot spot stress approaches .....	239
7.6.5 Fatigue check according to local SED approach.....	243
7.7 Global fatigue screening of parent material and welds .....	244
7.8 Report generation .....	245
7.9 Practical applications.....	246
7.9.1 Symmetric non-load-carrying transverse attachment.....	246
7.9.2 Symmetric load-carrying cruciform joint.....	253
7.10 Program specification overview .....	260
7.11 Discussion and conclusion .....	261
References .....	264
<b>8. Fatigue assessment of a New Panama Canal lock gate: comparison of procedures.....</b>	<b>267</b>
8.1 Introduction .....	269
8.2 The case study: a section of a New Panama Canal lock gate.....	270
8.3 “Manual” fatigue assessment procedure .....	273
8.3.1 Method of analysis .....	273
8.3.2 Designation of check lines .....	274
8.3.3 Fatigue assessment .....	278

8.4 Automatic fatigue assessment with PostFatigue .....	280
8.5 Discussion and conclusion .....	285
<b>9. The PSM to rapidly calculate residual notch stress intensity factors in welded joints .....</b>	<b>287</b>
9.1 Introduction .....	289
9.2. The PSM basic relations .....	291
9.3. Calibration of the PSM in Sysweld® environment.....	294
9.4. Discussion on the PSM calibration .....	297
9.5. Rapid R-NSIF estimation by using the PSM .....	300
9.6. Discussion and conclusion .....	306
References .....	308
<b>10. Overall concluding remarks.....</b>	<b>313</b>
<b>Bibliography .....</b>	<b>315</b>
Literature .....	315
Standards .....	328
<b>Acknowledgments .....</b>	<b>331</b>



## Abstract

In steel megastructures welding is a widely used and accepted joining technique. However, welds are geometrical discontinuities, resulting in severe local stress gradients, which strongly affect the fatigue strength of components. Advanced fatigue assessments are usually based on the local stress and strain state in the close neighborhood of such stress raisers. Despite this, current standards are lacking in giving a real guidance on how to perform a reliable fatigue assessment. Still, most of them do not refer to any local concept and lead to the nominal stress method. Even so, no recommendations exist on how to derive the nominal stress from a finite element (FE) model and it is left to the engineering assessment of a designer to establish which nominal stress is the right one.

Within this framework, the present Ph.D. thesis, focused on making the fatigue assessment of large steel structures possible, is divided into ten Chapters. Purposes of this thesis are both giving scientific contributions to advanced local approaches for fatigue assessment and developing a method fully compliant with current standards, in order to be employed in the industrial context.

In the *first Chapter*, a general introduction and the state of the art on fatigue design of welded structures are presented, with the aim to clarify the motivations of the present research work. In the *second Chapter*, the adopted local approaches, namely the notch stress intensity factor (NSIF) based approach, the averaged strain energy density (SED) criterion and the peak stress method (PSM), are briefly introduced and described along with their theoretical frameworks. The *third Chapter* deals with the fatigue behavior of large-scale welded cover plates, for which non uniform fatigue classification is highlighted at standards' level. Through the application of the SED approach and adopting both bi-dimensional and three-dimensional FE models, parameters which mainly affect the fatigue strength are identified and alternatives to those provided by standards are proposed. Experimental data of four geometric variants are successfully summarized into a unique scatter band in terms of SED, regardless of the weld geometry. The suitability of the SED approach and of the related design curve to perform the fatigue assessment of welded cover plates is, therefore, not proven wrong. The *fourth Chapter* is focused on the local SED numerical computation. Its principal drawback, consisting in the need of a specific

control volume centered on a notch tip (i.e. at the weld toe and at the weld root in case of welded joints), within which the strain energy density has to be averaged, is overcome by using coarse meshes completely free-generated. The method and its limitations are formalized. For the sake of generality, some practical applications are given by using both Ansys® and Straus7® FE software. Robustness in terms of insensitivity to mesh pattern, mesh refinement and FE formulation are proven advantages of the method. The *fifth Chapter* establishes a link between local stress fields, near weld toes and roots, and the nominal stress components evaluated at a proper distance from the weld. An analytical relationship between such distance and the loaded plate thickness is provided. A criterion to estimate SED values, both at the weld toe and at the weld root, as well as *a posteriori* the related NSIFs, as an explicit function of the nominal load components (membrane loads, shear loads and bending moments) is also presented. The proposed method is suitable for automation to perform the large number of fatigue assessments that a nowadays complex steel structure requires. However, the current lack of normative compliance of both SED and NSIF approaches can be a possible obstacle in industrial applications. That is why in the *sixth Chapter* a method, scientifically and normatively compliant, to improve the classical nominal stress approach for welded structures, which is still the most widely accepted and recognized in standards, is proposed. The methodological problem of the nominal stress definition is overcome through an original, finite element based approach, which takes into account both membrane and bending effects. An experimental validation is presented and the implications in fatigue design of large steel structures are discussed. The *seventh* and *eighth Chapters* present a finite element post-processor, developed to perform the almost automatic fatigue assessment of a large structure. The post-processor is compatible with Straus7® finite element solver and it is based on shell models to be suitable for large assemblies. Many of the findings of the present research work are automated: local SED and NSIF approaches are implemented, as well as the modified nominal stress and, finally, the classical nominal stress and hot spot stress approaches. A very good agreement between “manually” performed assessments, both through global and local approaches, and those rapidly performed by using the post-processor is found. Further good agreement is found between expected fatigue lives estimated through the local SED approach and those estimated through the modified nominal stress, in



the presence of bending stresses. The *ninth Chapter* deals with the rapid estimation of residual notch stress intensity factors (R-NSIFs), due to the welding process, by using the PSM and Sysweld® FE dedicated software. First, the calibration of the PSM in Sysweld® environment is presented; afterwards, practical applications of the PSM to evaluate the R-NSIFs are illustrated. Finally, the *tenth Chapter* presents some overall concluding remarks, in order to discuss the main obtained results.



# 1. Introduction

## 1.1 Background and motivations

In recent decades, there has been an increasing design and construction of steel structures, such as bridges, skyscrapers and stadia roofs characterized by large sizes and high slenderness. This phenomenon is motivated by ever-larger social and economic needs and is supported by various factors such as the constant increase in computational capacity, the development of software which enable the optimization of many design aspects, the scientific progress and the availability of high resistance materials. Such structures are no longer only susceptible to traditional traffic induced fatigue (e.g. rail bridges) but also to vibrations and to wind induced fatigue (e.g. light stadia roofs) and, in addition, the large size also affects the potential number of imperfections, as shown by Davidenkov et al. [1], Radaj and Sonsino [2] and Bazant [3]. As a consequence, it becomes essential for a designer to have a numerical method to perform a fatigue assessment. To this end, structural engineers need reliable approaches which not only are accurate but also allow the time and costs associated with the design process to be in the range of a budget.

In steel structures welding is a widely used and accepted joining technique. However, a weld line represents a geometrical discontinuity (a notch) and both weld toes and weld roots act as stress concentrators resulting in severe local stress gradients, which strongly affect the fatigue strength of a structure. The fatigue behavior of such joints is further worsened by the welding process, which may introduce defects, distortions and residual stresses that can be harmful for fatigue, as shown by Fricke [4]. In this complex framework, further worsen if multiaxial stress states are considered [5–7], performing the fatigue assessment of welded connections is an issue which must be properly addressed in order to avoid in-service failures.

The criteria, which can be found in current standards and in the literature, vary depending on the parameters to be considered significant for fatigue resistance. These criteria can be divided into different categories depending on the type of stress analysis performed on structural details, as shown by Radaj [8]. It is possible to distinguish criteria based on nominal stress, structural stress, local stress or other well-established methodologies concerning residual life assessments carried out on

the basis of real defects or assumed crack-like defects, according to linear elastic fracture mechanics, as shown by Maddox [9] and Gurney [10]. Basically, according to Radaj et al. [11], it is possible to distinguish between global and local approaches. The former are less time consuming methods, whereas the latter are the most sophisticated methods, which require a large computational effort and a high professional skill.

At present, the fatigue design of welded joints is primarily based on global approaches and in particular on nominal stress or, sometimes, on hot spot stress, with a series of classified structural details and related S-N curves, as discussed by Hobbacher [12,13]. The widely used one is the nominal stress method: this approach has been well accepted by major industries and recommended by numerous national and international codes and standards (IIW recommendations [14,15], Eurocode 3 [16–18] and the related design manual [19]). Despite this, some drawbacks characterize this method. The definition of nominal stress is simple only at first glance [12,13]: it is an average value computed with the classical principles of beam theory and does not exist any longer if stresses are computed with the Finite Element (FE) method, which by nature provides local stresses [20]. Besides, according to current standards, the dominant loading mode (membrane or bending) is not considered, except rare and well-defined cases (e.g. orthotropic decks), which can only lead to a random design in worst cases. When either nominal stress cannot be clearly calculated for excessive gradients or a reference fatigue curve for the assessed detail is not available, then hot spot stress based approaches are recommended to be used in literature (Niemi and Taskanen [21], Niemi et al. [22] Lotsberg and Sigurdsson [23] and Lotsberg [24]). However, these approaches are not as widely accepted as the nominal stress method, nor has generally been proven their reliability, as shown by Tovo and Lazzarin [25]. The complex conditions imposed in mesh generation and the large number of different extrapolation formulations, depending on the field (tubular structures, ship buildings, off-shore structures, pressure vessels, cranes, railways, etc.), introduce uncertainties in the applicability. Furthermore, the extension to the fatigue assessment of weld roots is still unclear.

To overcome these problems, local approaches have been developed in the last two decades. The purpose of these methods is to provide an accurate correlation between local stress fields in proximity of the critical areas (weld toe and weld root) and the

fatigue life. This idea has been widely discussed in the literature and is still subject of theoretical and experimental analyses. The main problem in applying the local criteria to fatigue strength assessment is the degree of arbitrariness caused by the scattering of the actual weld shape and the difficulty in defining an exact value for the geometrical parameters, as noticed by Radaj [26]. Different choices are possible. In the effective notch stress method, as formulated by Radaj [8], a fictitious notch radius is introduced at the weld toe and weld root. Differently, in the notch stress intensity approach, extensively proposed in the literature from the end of '90s (Lazzarin and Tovo [27], Atzori et al. [28], Lazzarin and Livieri [29]), the weld toe is modeled as a sharp V-notch (zero radius). The mode 1 and mode 2 notch stress intensity factors (NSIFs) quantify the magnitude of the asymptotic stress distribution according to Williams' exact solution [30]. In case of weld-like geometries, the NSIFs quantify the intensity of the elastic stress field near the weld toe and the weld root, capturing not only the weld shape effect but also the global size effect and the loading (membrane and bending) condition. As a consequence it has been proven that the fatigue strength of many steel welded joints follows the same design master curve with a reduced scatter band [29]. A closed form relation between the well-established fracture mechanics approach and the criterion based on the stress intensity factors exists and has been demonstrated by Atzori et al. [31]. It has been proved that a fatigue assessment in terms of NSIFs is much easier to perform than, and as accurate as (sometimes better), the one made by using the classic fracture mechanics. However, the main drawback of this method is that the knowledge of the elastic stress field in the surroundings of the weld toe and root requires FE meshes very refined in these regions. The required degree of refinement is generally not easy to obtain in plane cases and very difficult in 3D cases, which represents a strong limit in industrial applications. The problem was considered by Tovo and Lazzarin [25], who provided an explicit link between NSIF values and structural stresses at a well-defined distance from the weld toe. Such a distance (where bending, membrane and shear stresses can be evaluated) was chosen equal to the main plate thickness. Afterwards, Dong [32] defined a structural stress parameter which quantifies the intensity of the structural stress distribution at weld toe by means of thin shell models, or relatively coarse solid models, and also proved its mesh size insensitivity. Thereafter, the strain energy density (SED) approach has been formulated by

Lazzarin and Zambardi [33]. According to this criterion, the total strain energy density, averaged over a control volume surrounding the weld root or weld toe, is the parameter which controls the fatigue resistance of a joint. Failure occurs when the SED reaches a critical value, dependent on the material but independent of the weld geometry, which corresponds to the Beltrami criterion [34]. The underlying approach to which this idea can be related is Neuber's concept of elementary structural volume [35,36]. The critical volume is represented by a portion of a circular sector at weld toe and a full circular sector at weld root. In case of steel welded joints the radius of the control volume is equal to 0.28 mm. Thereafter, many researchers worked on this criterion (Berto et al. [37–39], Gómez et al. [40,41], Torabi and Berto [42]) and proved that it can successfully predict brittle and high cycle fatigue failures of pre-cracked, U- or V-notched specimens made out of several materials, including metals and ceramics, trying to propose SED as an all-around method. This method keeps the robustness of the notch stress intensity approach, as shown by Livieri and Lazzarin [43], because closed form relations between the strain energy density and the relevant NSIFs exist [33], and at the same time it does not require extremely refined meshes, as proved by Lazzarin et al. [44,45]. Another technique to estimate the NSIFs, known as the Peak Stress Method (PSM), has been more recently suggested by Meneghetti and Lazzarin [46,47]. According to this technique, after a proper calibration, it is possible to evaluate the NSIFs basing on the fictitious linear-elastic peak stress components computed at the point of singularity (weld toe and root), through a free-generated mesh pattern. Both SED and PSM approaches have also been mentioned by Fricke for the assessment of weld root fatigue [48].

Finite element meshes with a degree of refinement up to three and four orders of magnitude larger than the ones used in NSIF approach and fracture mechanics are allowed, adopting SED and PSM respectively. The direct application of local approaches on fatigue investigations in large-scale structures (thousands of welds to be checked), whose only possibility of numerical modeling is often based on really coarse and shell based finite elements, is still a difficult challenge, despite the increasing computational capabilities and model reduction techniques (such as the Craig-Bampton method [49]) can be used. Besides, it is important to notice that in mechanical engineering the approach to design, at least for fatigue, is quite different than in civil engineering. The link between mechanical design and scientific

literature is strong, probably because there is almost always an experimental validation, justified by serial production of components [8]. Large civil structures are all different from each other and there is not serial production. So, with rare exceptions, the fatigue design cannot be based on large-scale experimental investigations and certainly not on full-scale testing. As a consequence, in order to prove the safety of a civil structure, compliance with standards must be met, from the design to the inspection and acceptance phases. What is more, the European standards have recently reinforced the request to consider the fatigue phenomenon for the design of large steel structures [16]. The size of the structure is now implicitly part of the concept of Consequence Class and the large size almost automatically leads to fatigue calculations. Moreover, at the end of the process of fabrication it is necessary to perform inspections on the welds in workshop, where the inspection is function, weld by weld, of the designed fatigue utilization factor [50]. The outcome of the inspection may lead to a possible defect to repair or to acceptance actions, as a consequence of a fracture mechanics based calculation, as explained by Jonsson et al. [51]. Despite this new scenario, current standards are lacking in giving a real guidance on how to perform a reliable fatigue assessment. Still, most of them do not refer to any local concept and lead to use the nominal stress method. Even so, no recommendations exist on how to derive the nominal stress from a finite element model, so that it is left to the engineering assessment of a designer to establish which nominal stress is the suitable for performing a fatigue check, as recently pointed out by Hobbacher [13]: *"At this point no clear definition of nominal stress does exist, nor a recommendation, how to derive it from the finite element stress plot. [...] It is more than astonishing that several new design codes do not refer to any local concepts, leaving the designer alone with his modern computational equipment."*

Addressing the theme of this research, focused on the massive fatigue assessment, which means that the fatigue investigation is extended to the entire large-scale structure, could not have ignored the described background. Thus, purposes of this thesis are both giving a scientific contribution to some local approaches for fatigue assessment proposed in the recent literature and developing a method that nowadays could be considered fully complying with standards, in particular with Eurocode 3 and IIW recommendations, in order to be accepted in the industrial context.

## 1.2 Thesis structure

In general, each chapter is introduced by some *Highlights*, which provide a summary of aims, methods and most significant results. Subsequently, an *Introduction* presents the topic and the motivations of the study. At the end of each chapter a *Discussion and conclusion* section is given. For easy reading, *References* are listed for each chapter. The complete *Bibliography* is reported at the end of the thesis.

The topics are structured as follows:

- **Chapter 1** presents a general introduction on fatigue design of welded structures. A brief state of the art on the topic and some comments on the available methods are given. The motivations of the present work and the structure of the thesis are also presented.
- **Chapter 2** introduces the theoretical framework of the local approaches for fatigue assessment considered in this thesis, namely the notch stress intensity factor (NSIF) based approach, the averaged strain energy density (SED) criterion and the peak stress method (PSM). Advantages and drawbacks of the methods are critically highlighted and a short discussion from the historical and epistemological point of view on fatigue design is also given.
- **Chapter 3** presents the fatigue characterization of welded cover plates, through experimental procedure and local approaches. Parameters which significantly affect the fatigue resistance are isolated and optimized solutions are proposed. It is found that some mechanical treatments and geometrical solutions, which are requirements of many standards, have negligible effect on fatigue behavior, while other aspects, which are not even mentioned by norms, could have a crucial role on fatigue strength. It is also found that the SED approach and the related design master curve are suitable to perform the fatigue assessment of welded cover plates.
- **Chapter 4** is focused on the SED approach. The principal drawback of the method, consisting in the need of a specific control volume located at a notch tip (i.e. at the weld toe and at the weld root in case of welded joint), within which the strain energy density has to be averaged, is overcome by using a coarse mesh pattern, simply generated by a free-meshing algorithm, both in plane and three-dimensional cases and with different software. The proposed alternative is shown to be robust in terms of insensitivity to mesh pattern,



mesh refinement and finite element formulation. Practical applications on welded geometries, highlighting pre-processing, solution and post-processing efficiency of the method are also given.

- **Chapter 5** proposes a new link between local approaches and nominal stress method to the fatigue assessment of welded joints. Numerical results obtained through parametric finite element analyses have been properly fitted and a significant set of ready-to-use abaci of welded joints' stress concentration is presented, leading to the rapid calculation of local parameters (NSIFs and SED) once known the nominal stress components. Both membrane and bending load effects are considered. Furthermore, how to derive the nominal stress components from a finite element model is analytically explained.
- **Chapter 6** overcomes the methodological problem of the *modified nominal stress* definition, given by the Eurocode and IIW recommendations, through an original, finite element based approach, which takes into account both membrane and bending effects on the fatigue resistance of welded joints. An experimental validation is also presented.
- **Chapter 7** presents a shell finite element based post-processor, named PostFatigue, developed by Cimolai SpA with the aim to make the rapid fatigue assessment of a large steel structure possible. Many of the findings of the present research are automated in PostFatigue. Some practical applications are also given, showing a good agreement between “manually” performed assessments, both through global and local approaches, and those rapidly performed by using the post-processor.
- **Chapter 8** shows a practical application of PostFatigue on a real large steel structure subjected to fatigue loading. With this purpose, a section of steel gate build by Cimolai SpA for the New Panama Canal is chosen.
- **Chapter 9** deals with the rapid estimation of residual notch stress intensity factors (R-NSIFs), due to the welding process, by using the PSM and Sysweld® finite element code. First, the calibration of the PSM in Sysweld® environment is presented; afterwards, practical applications of the PSM to evaluate the R-NSIFs are illustrated.
- **Chapter 10** presents some concluding remarks on the work.

## References

- [1] N.N. Davidenkov, E. Shevandin, F. Wittmann, The Influence of Size on the Brittle Strength of Steel, *J. Appl. Mech.* 14 (1947) A63–A67.
- [2] D. Radaj, C.M. Sonsino, *Fatigue assessment of welded joints by local approaches*, Woodhead Publishing, 1998.
- [3] Z. Bazant, *Scaling of structural strength*, Elsevier, Oxford, 2005.
- [4] W. Fricke, Fatigue analysis of welded joints: State of development, *Mar. Struct.* 16 (2003) 185–200.
- [5] G. Marquis, Current Trends in Multiaxial Fatigue Research and Assessment, in: *ICMFF9*, 2007.
- [6] A. Fatemi, N. Shamsaei, Multiaxial fatigue modeling and some simple approximations, in: *ICMFF9*, 2010.
- [7] M. Sakane, S. Zhang, T. Kim, Notch effect on multiaxial low cycle fatigue, *Int. J. Fatigue.* 33 (2011) 959–968.
- [8] D. Radaj, *Design and analysis of fatigue resistant welded structures*, Woodhead Publishing, Cambridge, 1990.
- [9] S.J. Maddox, *The Effect of Plate Thickness on the Fatigue Strength of Fillet Welded Joints*, (1987).
- [10] T.R. Gurney, *The fatigue strength of transverse fillet welded joints*, Abington Publishing, Cambridge, 1991.
- [11] D. Radaj, C.M. Sonsino, W. Fricke, *Fatigue assessment of welded joints by local approaches*, Woodhead Publishing, Cambridge, 2006.
- [12] A.F. Hobbacher, The new IIW recommendations for fatigue assessment of welded joints and components - A comprehensive code recently updated, *Int. J. Fatigue.* 31 (2009) 50–58.
- [13] A.F. Hobbacher, New developments at recent update of the IIW recommendations for fatigue of welded joints and components, *Steel Constr.* 3 (2010).
- [14] A.F. Hobbacher, *Recommendations for Fatigue Design of Welded Joints and Components*, International Institute of Welding, 2008.
- [15] A.F. Hobbacher, *Recommendations for Fatigue Design of Welded Joints and Components*, Springer International Publishing, 2016.
- [16] EN 1993-1-1+A1 Eurocode 3: Design of steel structures - Part 1-1: General

- rules and rules for buildings, European Committee for Standardization, Brussels, 2014.
- [17] EN 1993-1-9 Eurocode 3 - Design of steel structures - Part 1-9: Fatigue, European Committee for Standardization, Brussels, 2005.
- [18] EN 1993-2 Eurocode 3 - Design of steel structures - Part 2: Steel bridges, European Committee for Standardization, Brussels, 2006.
- [19] A. Nussbaumer, L. Borges, L. Davaine, Fatigue Design of Steel and Composite Structures: Eurocode 3: Design of Steel Structures, Part 1-9 Fatigue; Eurocode 4: Design of Composite Steel and Concrete Structures, John Wiley & Sons, 2012.
- [20] A. Catanzano, L. Colussi, C. Romaro, G. Romaro, Sollevamento con un'unica manovra a 40 metri di altezza, di una copertura di circa 3 ettari di area e del peso di 8500 tonnellate (in Italian), in: III Settim. Delle Costr. Acciaio, Collegio dei Tecnici dell'Acciaio, 2003.
- [21] E. Niemi, P. Tanskanen, Hot spot stress determination for welded edge gussets, *Weld. World.* 44 (2000) 31–37.
- [22] E. Niemi, W. Fricke, S.J. Maddox, Fatigue analysis of welded components: Designer's guide to the structural hot-spot stress approach, Woodhead Publishing, Cambridge, 2006.
- [23] I. Lotsberg, G. Sigurdsson, Hot Spot Stress S-N Curve for Fatigue Analysis of Plated Structures, *J. Offshore Mech. Arct. Eng.* 128 (2006) 330–336.
- [24] I. Lotsberg, Fatigue design of marine structures, Cambridge University Press, 2016.
- [25] R. Tovo, P. Lazzarin, Relationships between local and structural stress in the evaluation of the weld toe stress distribution, *Int. J. Fatigue.* 21 (1999) 1063–1078.
- [26] D. Radaj, Review of fatigue strength assessment of non-welded and welded structures based on local parameters, *Int. J. Fatigue.* 18 (1996) 153–170.
- [27] P. Lazzarin, R. Tovo, A Notch Intensity Factor Approach To the Stress Analysis of Welds, *Fatigue Fract. Eng. Mater. Struct.* 21 (1998) 1089–1103.
- [28] B. Atzori, P. Lazzarin, R. Tovo, Stress field parameters to predict the fatigue strength of notched components, *J. Strain Anal. Eng. Des.* 34 (1999) 437–453.
- [29] P. Lazzarin, P. Livieri, Notch stress intensity factors and fatigue strength of

- aluminium and steel welded joints, *Int. J. Fatigue*. 23 (2001) 225–232.
- [30] M.L. Williams, Stress singularities resulting from various boundary conditions in angular corners of plates in tension, *J. Appl. Mech.* 19 (1952) 526–528.
- [31] B. Atzori, P. Lazzarin, R. Tovo, From a local stress approach to fracture mechanics: a comprehensive, *Fatigue Fract. Eng. Mater. Struct.* 22 (1999) 369–381.
- [32] P. Dong, A structural stress definition and numerical implementation for fatigue analysis of welded joints, *Int. J. Fatigue*. 23 (2001) 865–876.
- [33] P. Lazzarin, R. Zambardi, A finite-volume-energy based approach to predict the static and fatigue behavior of components with sharp V-shaped notches, *Int. J Fract.* 112 (2001) 275–298.
- [34] E. Beltrami, Sulle condizioni di resistenza dei corpi elastici (in Italian), *Rend. Del Reg. Ist. Lomb.* XVIII (1885) 704–714.
- [35] H. Neuber, *Kerbspannungslehre* (in German), 2nd Edition, Springer Verlag, Berlin, 1958.
- [36] H. Neuber, *Kerbspannungslehre* (in German), 3rd Edition, Springer Verlag, Berlin, 1985.
- [37] F. Berto, P. Lazzarin, A review of the volume-based strain energy density approach applied to V-notches and welded structures, *Theor. Appl. Fract. Mech.* 52 (2009) 183–194.
- [38] P. Berto, F., Lazzarin, Recent developments in brittle and quasi-brittle failure assessment of engineering materials by means of local approaches, *Mater. Sci. Eng.* 75 (2014) 1–48.
- [39] F. Berto, P. Lazzarin, M.R. Ayatollahi, Brittle fracture of sharp and blunt V-notches in isostatic graphite under pure compression loading, *Carbon N. Y.* 63 (2013) 101–116.
- [40] P. Gómez, F.J., Elices, M., Berto, F., Lazzarin, Fracture of U-notched specimens under mixed mode: Experimental results and numerical predictions, *Eng. Fract. Mech.* 76 (2009) 236–249.
- [41] P. Gómez, F.J., Elices, M., Berto, F., Lazzarin, Fracture of V-notched specimens under mixed mode (I + II) loading in brittle materials, *Int. J. Fract.* 159 (2009) 121.
- [42] F. Torabi, A.R., Berto, Fracture Assessment of Blunt V-Notched Graphite

- Specimens by Means of the Strain Energy Density, *Strength Mater.* 45 (2013) 635–647.
- [43] P. Livieri, P. Lazzarin, Fatigue strength of steel and aluminium welded joints based on generalised stress intensity factors and local strain energy values, *Int. J. Fract.* 133 (2005) 247–276.
- [44] P. Lazzarin, F. Berto, F.J. Gomez, M. Zappalorto, Some advantages derived from the use of the strain energy density over a control volume in fatigue strength assessments of welded joints, *Int. J. Fatigue.* 30 (2008) 1345–1357.
- [45] P. Lazzarin, F. Berto, M. Zappalorto, Rapid calculations of notch stress intensity factors based on averaged strain energy density from coarse meshes: theoretical bases and applications, *Int. J. Fatigue.* 32 (2010) 1559–1567.
- [46] G. Meneghetti, P. Lazzarin, Significance of the elastic peak stress evaluated by FE analyses at the point of singularity of sharp V-notched components, *Fatigue Fract. Eng. Mater. Struct.* 30 (2007) 95–106.
- [47] G. Meneghetti, P. Lazzarin, The Peak Stress Method for Fatigue Strength Assessment of welded joints with weld toe or weld root failures, *Weld. World.* 55 (2011) 22–29.
- [48] W. Fricke, IIW guideline for the assessment of weld root fatigue, *Weld. World.* 57 (2013) 753–791.
- [49] M.C.C. Bampton, R.R. Craig, Coupling of substructures for dynamic analyses, *AIAA J.* 6 (1968) 1313–1319.
- [50] prEN 1990-2:2016 Execution of steel structures and aluminium structures - Part 2: Technical requirements for steel structures, European Committee for Standardization, 2016.
- [51] B. Jonsson, G. Dobmann, A. Hobbacher, M.E. Kassner, G. Marquis, International Institute of Welding., IIW guidelines on weld quality in relationship to fatigue strength, 2016.



## **2. Local approaches for fatigue assessment of welded joints**

### **Highlights**

The stress intensity factor approach, which is well known from fracture mechanics, has been extended in the literature in some directions. One extension refers to pointed V-notches (among which there are welded joints), whose singular stress field is described by mode related and angle dependent notch stress intensity factors. The other extension is related to rounded notches, whose non-singular stress field is governed by generalized notch stress intensity factors. The stress intensity factor approaches just mentioned have been further extended into a local energy concept, which is well suited for the assessment of the brittle fracture or fatigue failure limit of sharply notched structural members. The local energy concept is generally more appropriate for strength assessments than the conventional stress concentration concept, because the local average strain energy density, based on stress intensity factors, characterizes the strength-relevant field as opposed to stress concentration factors which are related to strength-irrelevant point stresses. Moreover, what is important for applications is that finite element analyses based on coarse meshes can be used without a major loss in accuracy of the results. Finally, as an application of the notch stress intensity factor approach, the peak stress method, which is based on a special coarse finite element mesh, is also available for welded joints.

In this chapter, the theoretical frameworks of the above mentioned local approaches, namely the notch stress intensity factor (NSIF) approach, the averaged strain energy density (SED) criterion and the peak stress method (PSM), are presented. Advantages and drawbacks of the methods are highlighted with the purpose to guide the reader through the choices made by the author in the present research work.





## 2.1 Introduction

The stress intensity factor (SIF) concept has originally been developed in the context of fracture mechanics. For fracture phenomena, both brittle fracture and fatigue failure, the asymptotic singular stress field at the pointed crack or slit tip is of paramount importance. The local three-dimensional stress singularity at a definite point of the crack or slit front can generally be described by superimposition of three two-dimensional stress singularities corresponding to three independent loading or opening modes of the crack tip: transverse tensile loading (mode 1), in-plane shear loading (mode 2) and out-of-plane shear loading (mode 3). The corresponding SIFs are  $K_I$ ,  $K_{II}$  and  $K_{III}$ . Non-singular crack-parallel stresses (the T-stress) may be further superimposed.

In the literature, the stress intensity factor concept has been extended in two directions. One extension refers to pointed V-notches with stress intensities depending on the notch opening angle. The loading mode related notch stress intensity factors (NSIFs)  $K_1$ ,  $K_2$  and  $K_3$  have been introduced for this purpose. Another extension refers to rounded notches with crack shape or V-notch shape in two variants: parabolic, elliptic or hyperbolic notches (*blunt notches*) on the one hand and root hole notches (*keyholes* when considering crack shapes) on the other hand. Being this the case, the loading mode related generalized notch stress intensity factors  $K_{1\rho}$ ,  $K_{2\rho}$  and  $K_{3\rho}$  have to be used.

The local strain energy density (SED) approach has been elaborated for strength assessments in respect of brittle fracture and high-cycle fatigue. Pointed and rounded V-notches subjected to tensile loading (mode 1) have been primarily considered, but the method has been extended also to multiaxial conditions (mode 3, mixed mode 1 and 2). The application to brittle fracture is related to PMMA, metals and ceramics in the presence of U- and V-notches. The application to high-cycle fatigue comprises fillet-welded joints, weld-like shaped and V-notched base material specimens, as well as round bar specimens with V-notches. Coarse finite element meshes at pointed or rounded notch tips are acceptable for accurate local SED evaluations. The peak stress method (PSM), as an application of the notch stress intensity factor approach, which is based on a special coarse finite element mesh, is also available for the assessment of welded joints.

In this chapter, the above mentioned local approaches, namely the notch stress intensity factor-based approach (NSIF), the averaged strain energy density (SED) criterion and the peak stress method (PSM), are briefly described along with their theoretical frameworks. In the present work such approaches are considered with reference to structural components weakened by sharp V-notches (which include both the toe and the root regions of a welded joint and the general crack case). For a most comprehensive description of the above local approaches, including the application to blunt U- and V-notches, the reader can refer to the recent reviews by Radaj focused on the NSIF approach [1] and on the local SED concept and its relation to the PSM [2]. The SED criterion and its applications to fracture and fatigue problems have been recently reviewed also by Berto and Lazzarin [3,4].

## **2.2 Notch stress intensity factor approach**

The well-known concept of SIFs describing the stress singularity at crack tips or slit tips under linear-elastic material conditions can be transferred to pointed notches (e.g. V-notches, stepped bars and weld toe like notches). The SIF concept has been substantially extended since Williams' basic contribution on stress fields at angular corners [5].

### **2.2.1 Local stress fields near pointed V-notches**

Whereas the asymptotic stress drop from the singularity at the crack tip is described by the inverse square root of the radial distance  $r$  from the crack tip (the exponent is  $-0.5$ ), a smaller, notch-angle-dependent exponent occurs in the case of corner notches, which means that the degree of the singularity is reduced [5]. The stress field close to corner notches (just as the stress field close to crack tips) can be described by stress intensity factors [6]. These are named notch stress intensity factors (NSIFs) as distinguished from the conventional SIFs related to crack tips. The singular in-plane and out-of-plane stress fields at pointed corner notches can be specified by three notch loading modes (in analogy to the crack opening modes) related to the bisector plane of the notch: symmetric in-plane stresses (mode 1), anti-metric in-plane stresses (mode 2) and out-of-plane shear stresses (mode 3). The corresponding notch loading modes are in-plane tensile loading, in-plane shear loading and out-of-plane shear loading. The three basic loading modes with singular

stresses at the notch tip produce the following asymptotic stress distribution (stress tensor  $\sigma_{ij}$  and  $\sigma_{kz}$ ) around the notch tip, restricted to the first-order terms (Figures 2.1 and 2.2) [5,7]:

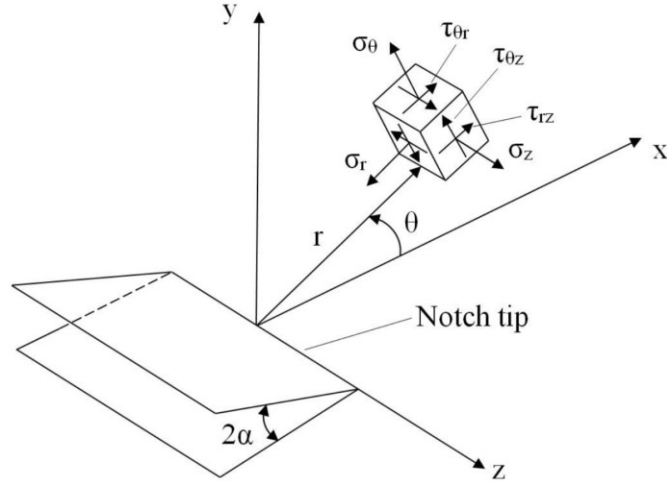


**Figure 2.1.** Sharp V-notch: generic three-dimensional stress field in a polar reference system.

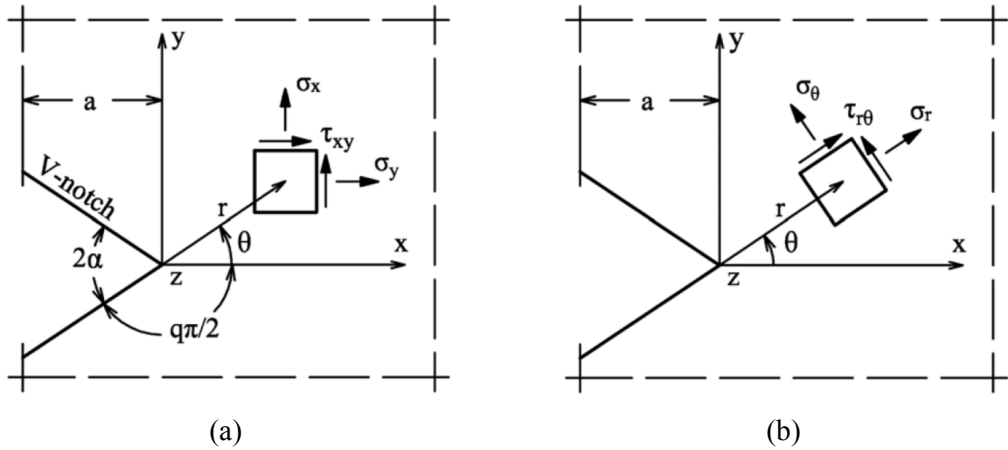


**Figure 2.2.** Sharp V-notch: in-plane stress field in (a) Cartesian and (b) polar reference systems.

$$\sigma_{ij} = \frac{1}{\sqrt{2\pi}} \left[ K_1 \cdot r^{\lambda_1-1} \cdot f_{1,ij}(\theta) + K_2 \cdot r^{\lambda_2-1} \cdot f_{2,ij}(\theta) \right] \quad (2.1)$$

$$\sigma_{kz} = \frac{1}{\sqrt{2\pi}} \left[ K_3 \cdot r^{\lambda_3-1} \cdot f_{3,kz}(\theta) \right] \quad (2.2)$$

In Equation (2.1)  $i, j = x, y$  or  $i, j = r, \theta$ ; in Equation (2.2)  $k = x, y$  or  $k = r, \theta$ .

The NSIFs  $K_1$ ,  $K_2$  and  $K_3$  depend on the magnitude of the load, the notch depth  $a$ , the notch opening angle  $2\alpha$  and further geometric parameters of the considered configuration. The angular functions  $f_{1,ij}$ ,  $f_{2,ij}$  and  $f_{3,kz}$  describe the angular distribution of the stress close to the notch tip. The aforementioned relationship is strictly valid for  $r \rightarrow 0$  and approximately valid for values of  $r$  which are small in relation to the notch depth and other geometrical parameters of the configuration. Just as with the crack problem ( $2\alpha=0$ ), the complete solution comprises additional non-singular higher-order terms. Williams' solution for the in-plane stress field is based on the Airy stress function in polar coordinates in the following form, which comprises a symmetrical component and an anti-metrical component [5]:

$$F(r, \theta) = r^{1+\lambda} \cdot f(\theta) \quad (2.3)$$

where the values of  $\lambda$  have to be determined as part of the solution. The angular functions have to comply with the boundary conditions on the load-free faces of the V-notch. The stress can now be expressed in terms of  $r$ ,  $\lambda$  and  $f(\theta)$ . The application of the boundary conditions produces a system of four simultaneous equations for four unknown constants. This system can be separated into two independent sets of equations related to the symmetrical and anti-metrical stress fields. A non-trivial solution can be obtained only if the determinants of the coefficient matrices are equal to zero each. From this requirement, the condition follows:

$$\sin(\lambda_1 q\pi) \pm \lambda_1 \sin(q\pi) = 0 \quad (2.4)$$

where  $q$  is related to the notch opening angle by the expression  $2\alpha = \pi(2-q)$ .

Since the notch opening angle  $2\alpha$  is a fixed parameter for a specific wedge or notch, Equation (2.4) provides the values  $\lambda_1$  and  $\lambda_2$ , called *eigenvalues*, necessary to ensure a nontrivial solution. Williams' solution has been widely used under the name of *eigenfunction expansion method*. Another more versatile function-analytical approach for solving the problem of the in-plane loaded blunt V-notch comprising the sharp V-notch as a special case has been applied by Lazzarin and Tovo [8,9], Lazzarin et al. [10] and Atzori et al. [11]: the Kolosov–Muskhelishvili complex stress function method. The principal mathematical steps remain the same as in the Airy stress function method. The stress field analysis for the V-notch subjected to out-of-plane shear loading (mode 3) is easier to perform, because the governing equation in terms of the out-of-plane displacements is a potential function

substituting the bi-potential stress function in the case of the in-plane stresses. Performing similar mathematical steps as before, the following eigenvalue equation is found [7]:

$$\sin[\lambda_3(2\pi - 2\alpha)] = 0 \quad (2.5)$$

The smallest positive eigenvalues  $\lambda_1$ ,  $\lambda_2$  and  $\lambda_3$  defining the degree of the stress singularity at the notch tip depend solely on the notch opening angle  $2\alpha$  (Figure 2.3).

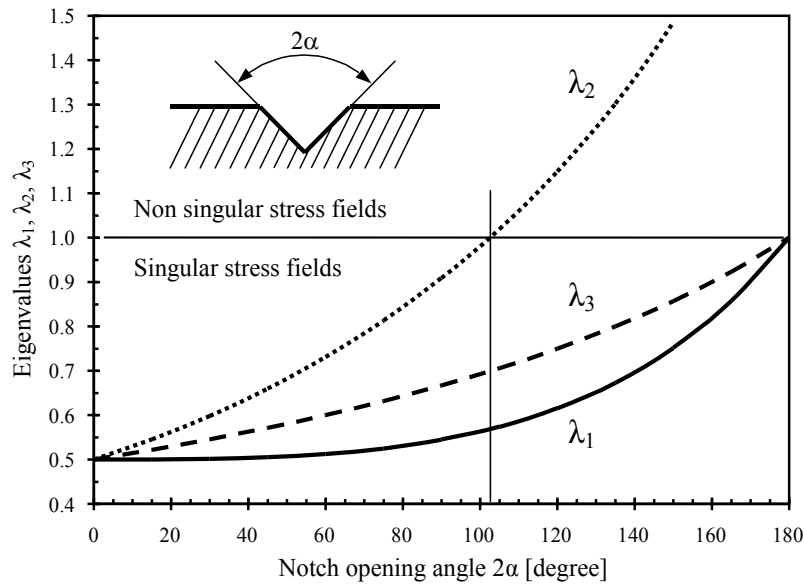


**Figure 2.3.** Eigenvalues  $\lambda_1$ ,  $\lambda_2$  and  $\lambda_3$  defining the degree of stress singularity at sharp V-notches subjected to modes 1, 2 and 3 loading conditions, dependent on notch opening angle  $2\alpha$  (Lazzarin et al. [12]).

The eigenvalue 0.5 is related to crack tips,  $2\alpha=0$ , and the eigenvalue 1.0 (no singularity) to straight edges,  $2\alpha=\pi$  (but only for modes 1 and 3). The eigenvalues for mode 1 loading are slightly smaller than those for mode 3 loading. They are substantially smaller in relation to mode 2 loading, thus designating more severe singularities. The stress singularity in mode 2 loading is weaker and vanishes completely for  $2\alpha \geq 102.6^\circ$  [12]. The characteristic stress components in the bisector plane ( $\theta=0$ ) have the following simple form:

$$\sigma_\theta(r, 0) = \frac{1}{\sqrt{2\pi}} K_1 \cdot r^{\lambda_1 - 1} \quad (2.6)$$

$$\tau_{r\theta}(r, 0) = \frac{1}{\sqrt{2\pi}} K_2 \cdot r^{\lambda_2 - 1} \quad (2.7)$$

$$\tau_{\theta z}(r, 0) = \frac{1}{\sqrt{2\pi}} K_3 \cdot r^{\lambda_3 - 1} \quad (2.8)$$

The NSIFs  $K_1$ ,  $K_2$  and  $K_3$  may be evaluated on the basis of the aforementioned characteristic stress components considering the limit values for  $r \rightarrow 0$  [6]:

$$K_1 = \sqrt{2\pi} \lim_{r \rightarrow 0} \sigma_{\theta}(r, 0) r^{1 - \lambda_1} \quad (2.9)$$

$$K_2 = \sqrt{2\pi} \lim_{r \rightarrow 0} \tau_{r\theta}(r, 0) r^{1 - \lambda_2} \quad (2.10)$$

$$K_3 = \sqrt{2\pi} \lim_{r \rightarrow 0} \tau_{\theta z}(r, 0) r^{1 - \lambda_3} \quad (2.11)$$

The dimensions of  $K_1$ ,  $K_2$  and  $K_3$  are  $\text{MPa} \cdot \text{mm}^{1 - \lambda_1}$ ;  $\text{MPa} \cdot \text{mm}^{1 - \lambda_2}$  and  $\text{MPa} \cdot \text{mm}^{1 - \lambda_3}$ .

It should be noted that the elastic notch stress intensity factors are used to describe the fatigue strength of fillet-welded attachment joints; moreover the fracture toughness of brittle materials may also be evaluated on this basis. The numerical values of  $K_1$ ,  $K_2$  and  $K_3$  can be set into comparison, e.g. as failure criteria, provided their dimensions are identical, i.e. only under the condition of an identical notch angle besides an identical loading mode.

The NSIFs  $K_1$ ,  $K_2$  and  $K_3$  of V-notches or re-entrant corners can be calculated on the basis of the FEM using a very fine mesh near the sharp notch tip. The degree of mesh refinement in the proximity of the notch tip requires finite elements having edge dimension of  $10^{-5}$  mm according to Lazzarin and Tovo [9].

### 2.2.2 Endurable NSIFs of fatigue-loaded welded joints

The fatigue strength of welded joints in the medium-cycle to high-cycle fatigue range ( $N \geq 10^4$ ) can advantageously be described by endurable (elastic) NSIFs [13–15]. In contrast to the endurable nominal stresses, the endurable NSIFs are independent of the plate thickness, i.e. the size effect is already included. Fatigue test data from the literature referring to non-load-carrying fillet welds at tensile loaded transverse attachment joints of steel (mainly cruciform joints) in as-welded conditions have been evaluated to demonstrate this (Figure 2.4) [9]. Large variations in the geometrical data are covered by the fatigue test data: plate thickness  $t = 13\text{--}100$  mm, fillet weld leg length  $h = 5\text{--}16$  mm, attachment length  $L = 3\text{--}220$  mm. Only the NSIF  $K_1$  is used to summarize the fatigue data, whereas the effect of  $K_2$  is considered negligible in this type of joint ( $2\alpha = 135^\circ$ ), because no stress singularity occurs in the

latter case (Figure 2.3). The large scatter range of the original nominal stress S–N curve is substantially reduced to conventional values experienced with geometrically uniform specimens.

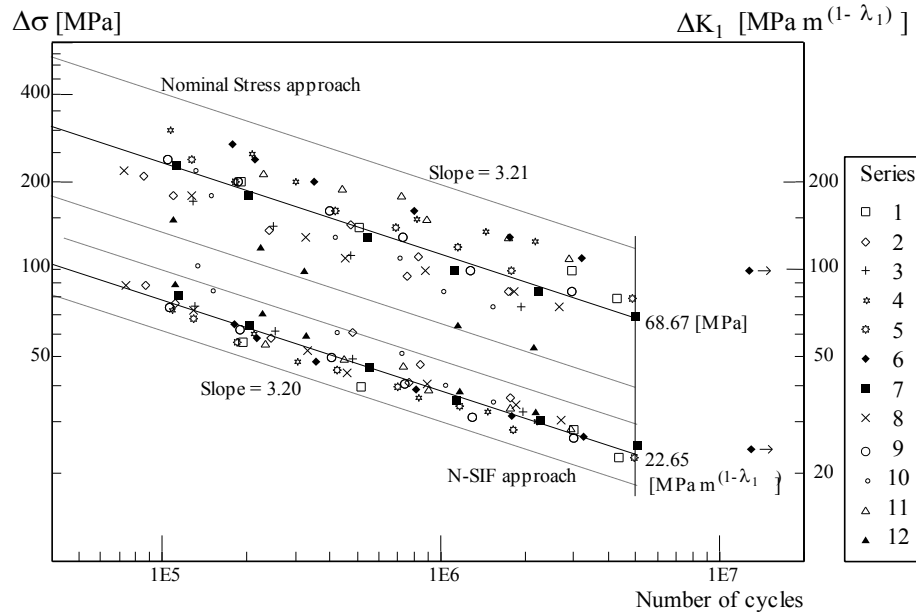


**Figure 2.4.** Fatigue test data (toe failures) for fillet-welded steel joints (transverse attachments) under tensile loading; nominal stress based curves are contrasted with NSIFs based curves; scatter bands are defined with  $P_f = 2.3\%$  [9].

An explanation for the fact that not only the crack initiation life but actually the evaluated total life is correctly described by endurable values of  $\Delta K_I$  is given in the following form [16]: the crack initiation life (initiated crack length  $a_i = 0.3$  mm) and the residual crack propagation life (critical crack length  $a_{cr} = t/3$ ), occurring in the ratio approximately 2:1 in the investigation just quoted, are both controlled by the NSIF  $\Delta K_I$  as the dominant parameter. The SIF  $\Delta K_I$  for a developing crack in the bisector plane is proportional to the NSIF  $\Delta K_I$ .

### 2.2.3 Potential and weak points of the NSIF approach

The potential of the notch stress intensity factors approach is that the NSIFs describe the stress field at sharp notches with different notch opening angles in a uniform and theoretically based manner. Dealing with welded joints, the NSIFs accurately describe stress distributions in the toe and root regions, incorporating the global geometry influence (size effect), the local geometry influence (weld geometry) and

the stress levels (taking into account also the loading condition effect, which can be pure membrane load, pure bending load or a combination of them). As such, they can provide more information than any arbitrary stress concentration factor. A demonstration of this is the careful check performed by Lazzarin and Tovo [9] using the well-documented fatigue test results from Maddox and Gurney [17,18] for transverse non-load-carrying fillet welds: due to large variations of the main plate thickness, bead and attachment sizes, the original nominal stress based data are largely scattered; the scatter band is greatly reduced using NSIF approach (see Figure 2.4).

However, there are some possible weak points associated with the NSIF approach. One of them is that the NSIFs (as well as all NSIFs derived approaches) characterize the condition of crack initiation, but further crack propagation is governed by crack-related parameters to an increasing extent. The assumption that the total fatigue life consists predominantly of crack propagation in the notch-related stress field is not generally applicable. The NSIF approach is primarily a crack initiation concept and should therefore be combined with a crack propagation analysis if the residual life has to be described.

A further important drawback is that the asymptotic nature of the stress field close to the weld toe and root requires very refined finite element meshes, at least locally, to numerically evaluate the NSIFs. The required degree of refinement is generally not easy to obtain in plane cases and very difficult in 3D cases. This is generally a problematic obstacle to overcome in industrial applications.

Finally, being the unit of NSIF values formally dependent on the notch opening angle, the NSIFs can be used for the direct fatigue assessment of a structure only if the available reference data refer to notches having the same opening angle of the ones under evaluation.

### **2.3 Averaged strain energy density approach**

The basic idea behind the local strain energy density (SED) approach corresponds to Neuber's concept of an *elementary material volume* or *microstructural support length* used for stress averaging [19,20]. According to Neuber's idea, it is not the maximum elastic notch stress that controls static, dynamic or cyclic crack initiation at notches of structural members, but rather the notch stresses averaged over a



definite finite volume of the material at the notch root, which is assumed as homogeneous.

Similarly, the average SED in a defined control volume around the pointed or rounded notch (or crack) tip is considered to be the material parameter which describes the initiation of brittle fracture or high-cycle fatigue failure. In the case of sharp notch tips, not only the stresses at the notch tip tend towards infinity but the SED does too. Contrary to this, the averaged SED in a local finite volume around the notch (or crack) tip has a finite value. This value is considered to be the material parameter that describes the initiation of brittle fracture or fatigue failure. The proposal to use the SED as a strength parameter goes back to Beltrami [21]. The approach was originally named *finite volume energy-based approach* or *equivalent strain energy density approach* (Lazzarin and Zambardi [22,23]), and later on *local strain energy density approach* Lazzarin et al. [24]).

The approach has been elaborated for pointed and rounded V-notches (inclusive of U-notches) subjected to tensile loading (mode 1) with extensions to torsional (mode 3) and multiaxial (mixed mode) loading. The static strength properties of V-notched specimens made of brittle material are thus described in a uniform manner, both for pointed notches [22,25] and for blunt notches [26]. Also, the high-cycle fatigue strength of welded joints made of steel or aluminium alloy is given in terms of the cyclic average SED of the pointed weld notch [27,28].

### 2.3.1 Basic relationships of the SED approach

In this section the basic relationships for the local SED are presented, with reference to sharp V-notches. A structural component weakened by a sharp V-notch and subjected to in-plane mixed mode 1+2 is considered. The analytical frame of the local SED approach refers to the stress conditions in the cross-sectional plane, Figure 2.5. The polar coordinate system is brought into line with the notch bisector ( $\theta=0$ ), Figure 2.5(a). The shape and size of the finite volume around the notch tip is conceived as a sector-shaped cylinder of radius  $R$ , named *control volume*. The material is assumed to be isotropic and linear-elastic. The first analysis step consists of defining the stresses  $\sigma_{ij}(r,\theta)$  and strains  $\varepsilon_{ij}(r,\theta)$  in terms of the mode-related notch stress intensity factors  $K_I$  and  $K_2$  [6] and Williams' eigenvalues  $\lambda_1$  and  $\lambda_2$  [5]. Therefore, the SED  $W(r,\theta)$  is derived consisting of the components  $W_1$ ,  $W_2$  and  $W_{12}$

related to the mode 1, mode 2 and mixed mode stress and strain fields. The component  $W_{12}$  is not further needed, because its contribution to the averaged SED vanishes for symmetric sector areas. The component  $W_2$  may be neglected for  $2\alpha \geq 102.6^\circ$ , which produces a non-singular stress field. The second analysis step is to determine the averaged SED within a sector area of radius  $R$  around the notch tip. The radius  $R$  should be small enough, so that the sector area remains within the range of validity of the one-term stress expansion resulting in the NSIF.

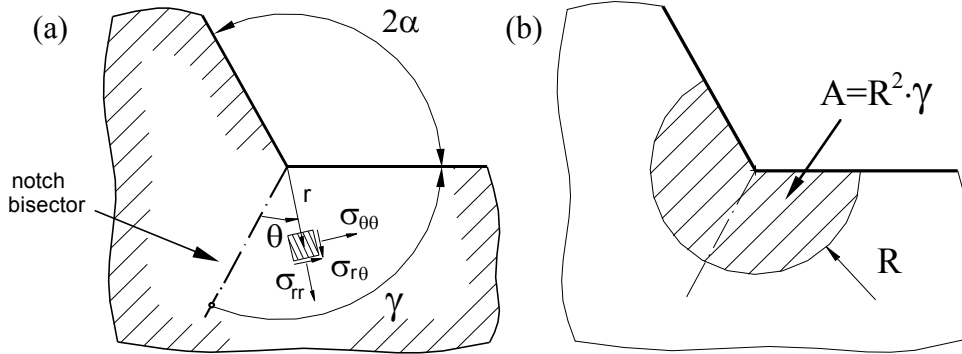


**Figure 2.5.** Polar coordinate system centered at the V-notch tip (a) and control volume (area) of radius  $R$  surrounding the V-notch tip (b) [22].

According to Beltrami [21], the total strain energy density (SED) is equal to the total work done by the system and it is given by Equation (2.12), expressed in terms of the principal stresses in a given reference system.

$$W(r, \theta) = \frac{1}{2E} \left\{ \sigma_{11}^2 + \sigma_{22}^2 + \sigma_{33}^2 - 2\nu(\sigma_{11}\sigma_{22} + \sigma_{11}\sigma_{33} + \sigma_{22}\sigma_{33}) \right\} \quad (2.12)$$

In the case of a V-notch under mixed mode 1+2 loading, when only the contribution of the first singular terms is significant, the SED can be directly linked to the NSIFs,  $K_I$  and  $K_2$ , by substituting into Equation (2.12) the singular stress field given by Equation (2.1). The strain energy density, averaged in a circular sector of radius  $R$  surrounding the notch tip (Figure 2.5(b)), is given by the ratio between the elastic strain energy  $E(R)$  and the area of the circular sector  $A(R)$ . The sector area of radius  $R$ , over which the averaged SED is determined, is given by:

$$A(R) = \int_0^{R+\gamma} \int_{-\gamma}^{\gamma} r dr d\theta = R^2 \gamma \quad (2.13)$$

By integration of  $W(r, \theta)$  over the symmetric sector area and division by  $A(R)$ , the averaged local SED turns out to be:

$$\bar{W}(R) = \frac{E(R)}{A(R)} = \frac{\int_A W dA}{\int_A dA} = \frac{\int_{0-\gamma}^{R+\gamma} \int W(r, \theta) r dr d\theta}{\int_{0-\gamma}^{R+\gamma} r dr d\theta} = \quad (2.14)$$

$$= \frac{1}{E} \cdot e_1 \cdot K_1^2 \cdot R^{2(\lambda_1-1)} + \frac{1}{E} \cdot e_2 \cdot K_2^2 \cdot R^{2(\lambda_2-1)}$$

$$e_1(\gamma) = \frac{I_1(\gamma)}{4\lambda_1\gamma} \quad (2.15)$$

$$e_2(\gamma) = \frac{I_2(\gamma)}{4\lambda_2\gamma} \quad (2.16)$$

$$I_1(\gamma) = \int_{-\gamma}^{+\gamma} f_1(\theta) d\theta \quad (2.17)$$

$$I_2(\gamma) = \int_{-\gamma}^{+\gamma} f_2(\theta) d\theta \quad (2.18)$$

The internal notch angle  $2\gamma$  being linked to the notch opening angle  $2\alpha=2\pi-2\gamma$ , the total SED coefficients  $e_1$  and  $e_2$  can be plotted dependent on the notch opening angle  $2\alpha$ , Figure 2.6 (for plane strain conditions).

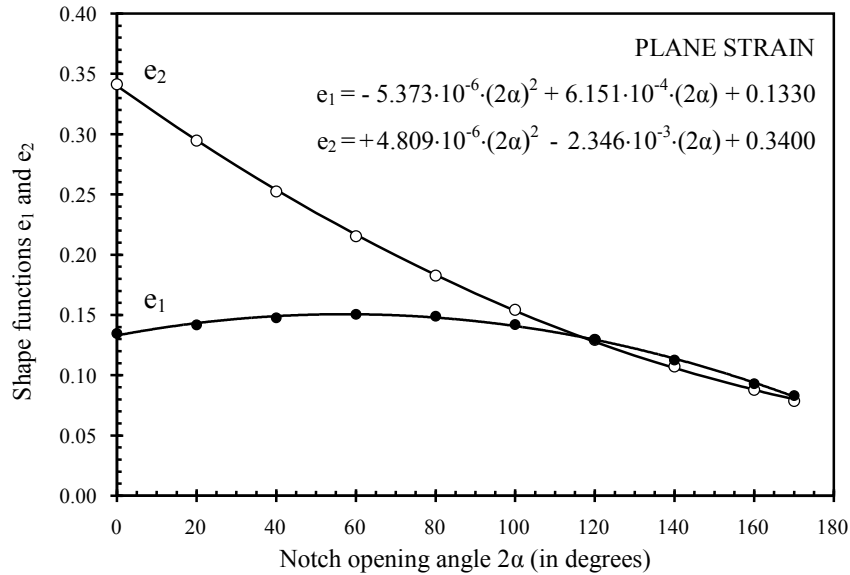


**Figure 2.6.** Total SED coefficients  $e_1$  and  $e_2$  dependent on notch opening angle  $2\alpha$  under plane strain conditions, assumed Poisson's ratio equal to 0.3 [22]. Being  $2\alpha=135^\circ$ ,  $e_1$  and  $e_2$  values are 0.118 and 0.111, respectively.

For sufficiently small values of  $2\alpha$ , the value of  $e_2$  is substantially larger than that of  $e_1$ . Even for  $2\alpha \geq 102.6^\circ$ , where the SED field is non-singular,  $e_1$  and  $e_2$  have approximately the same value. This is not an indication that the SED values are approximately the same. Actually,  $\bar{W}_2 \ll \bar{W}_1$  because of the missing singularity in the stress and strain field of mode 2 loading.

For the sake of brevity, the out-of-plane shear loading (mode 3) is not considered here, but the interested reader can refer to [12].

### 2.3.1.1 Static loading

The characteristic feature of brittle fracture is that it occurs under elastic stress field conditions, either without any plastic deformation (glass and ceramics) or without deformation on a macroscale (brittle technical metals). The SED concept is applicable to sharp V-notches made of brittle materials in the following way [22]. Brittle fracture at sharp V-notches may be assumed to occur when the averaged local SED  $\bar{W}$  within the control volume reaches a critical value  $W_c$  which is independent of the notch opening angle and independent of the loading type (tensile or in-plane shear loading). This corresponds to the Beltrami failure criterion [21]. The material parameter  $W_c$  may be determined from the ultimate tensile strength  $\sigma_c$  of un-notched specimens:

$$\bar{W} \leq W_c = \frac{\sigma_c^2}{2E} \quad (2.19)$$

The radius  $R_0$  of the control volume, where the critical local SED value  $W_c$  occurs, may be determined from the plane strain fracture toughness  $K_{Ic}$ . It is considered to be a material parameter. When the mode 2 SED  $\bar{W}_2$  is zero (symmetric geometry and loading) or negligibly small (large notch opening angle with vanishing mode 2 singularity), the NSIF  $K_I$  can be correlated with the averaged local SED  $\bar{W}_I$  according to Equation (2.14):

$$K_I = \sqrt{\frac{4E\lambda_1\gamma}{I_1(\gamma)} \cdot \bar{W}_I} \cdot R_0^{(1-\lambda_1)} \quad (2.20)$$

The critical condition  $\bar{W}_I = W_c$  is expressed by introducing Equation (2.19) in Equation (2.20), obtaining:

$$K_{Ic} = \sqrt{\frac{2\lambda_1\gamma}{I_1(\gamma)}} \cdot \sigma_c \cdot R_0^{(1-\lambda_1)} = f_1(2\alpha) \cdot \sigma_c \cdot R_0^{(1-\lambda_1)} \quad (2.21)$$

where the intensity coefficient  $f_I(2\alpha)$  should not be confused with  $f_I(\theta)$  in Equation (2.16). When the V-notch becomes a crack ( $2\alpha=0$ ),  $K_{Ic}$  coincides with the fracture toughness  $K_{Ic}$ :

$$K_{Ic}(2\alpha=0) = K_{Ic} = f_1(0) \cdot \sigma_c \cdot \sqrt{R_0} \quad (2.22)$$

Thus, the control volume radius  $R_0$  turns out to be:

$$R_0 = \left( \frac{K_{Ic}}{f_1(0) \cdot \sigma_c} \right)^2 = \frac{I_1(\pi)}{\pi} \left( \frac{K_{Ic}}{\sigma_c} \right)^2 \quad (2.23)$$

or in an explicit form related to plane strain conditions [25]:

$$R_0 = \frac{(1+\nu)(5-8\nu)}{2\pi} \left( \frac{K_{Ic}}{\sigma_c} \right)^2 \quad (2.24)$$

The corresponding expression for plane stress conditions, with  $K_c$  (depending on plate thickness  $t$ ) substituting  $K_{Ic}$ , is [29]:

$$R_0 = \frac{(5-3\nu)}{4\pi} \left( \frac{K_c}{\sigma_c} \right)^2 \quad (2.25)$$

The control volume radius  $R_0$  depends on the material. Its value decreases with rising brittleness. It does not depend on the notch opening angle by definition. The described analytical approach referring to the total SED has been validated on the basis of experimental data reported in the literature [22,30].

### 2.3.1.2 Fatigue loading

In the following, the specific application of the SED approach to welded joints under fatigue loading is described; however the general considerations remain valid for a generic component weakened by a sharp V-notch and subjected to fatigue loading conditions.

The averaged local SED at the notch tip of the weld toe is evaluated for linear-elastic material behavior which is an appropriate approximation in the high-cycle fatigue range ( $N \geq 5 \cdot 10^5$  cycles). It is also used in the medium-cycle fatigue range ( $10^4 \leq N \leq 5 \cdot 10^5$  cycles) where plastic deformations occur. The plastic zone may even be larger than the control volume, whose radius is  $R_0 \approx 0.3$  mm for steels. The justification to use the linear-elastic strain energy under small-scale yielding conditions is provided by the *equivalent strain energy density approach* according to Glinka [31]. Following this approach, which works well under plane strain

conditions, the elastic-plastic SED at the root of a rounded notch is set equal to the SED determined under purely elastic conditions. This concept is not directly applicable to sharp V-notches because the SED at the notch tip tends towards infinity both for linear-elastic and power law elastic-plastic material behavior. If applied to the averaged SED in the control volume at the notch tip, this problem is removed [23]. The elastic SED concept is thus applicable over the whole medium-cycle and high-cycle fatigue range. The first step in the local SED approach is the determination of the control volume radius  $R_0$  for the specimens under investigation. It depends on the material and on the multiaxial failure criterion. This task is more complicated for welded joints under cyclic loading producing fatigue failure than for specimens under static loading producing brittle fracture. In the former case, the material is locally inhomogeneous in the as-welded condition and the cracking phenomena change to some extent with the cyclic load level or the endured load cycles. The control volume radius  $R_0$  is determined for fillet-welded joints ( $2\alpha=135^\circ$ ) with experimental data gained in the high-cycle fatigue range. Only the mode 1 averaged local SED  $\bar{W}_1$  is evaluated whereas the mode 2 component  $\bar{W}_2$  remains negligibly small. Plane strain conditions are assumed together with the Beltrami total strain energy criterion [21]. In analogy to Equation (2.23), the control volume radius  $R_0$  is given by the following expression [22]:

$$R_0 = \left( \frac{\Delta K_{1,A}}{f_l(2\alpha) \cdot \Delta \sigma_A} \right)^{\frac{1}{(1-\lambda_l)}} = \left( \frac{\sqrt{2e_1} \Delta K_{1,A}}{\Delta \sigma_A} \right)^{\frac{1}{(1-\lambda_l)}} \quad (2.26)$$

where  $\lambda_l$  and  $f_l$  depend on the notch opening angle  $2\alpha$ , while  $\Delta K_{1,A}$  is the reference value of the endurable NSIF range for the fillet-welded joints and  $\Delta \sigma_A$  is the reference value of the endurable stress range at a flush ground butt weld, which simulates the material behavior at the weld toe or root. The reference values  $\Delta K_{1,A}$  and  $\Delta \sigma_A$  are mean values ( $P_S=50\%$ ) at  $N_A=2 \cdot 10^6$  cycles (according to Eurocode 3 [32] and IIW recommendations [33]) or  $5 \cdot 10^6$  cycles (other authors) with load ratio  $R=0$ . With the usual inverse slope exponent  $k=3$  for welded joints of steel, the factor 1.36 occurs between the fatigue strength at  $2 \cdot 10^6$  cycles compared with the fatigue strength at  $5 \cdot 10^6$  cycles. With the common scatter range index, the factor 1.37 occurs between the data for  $P_S=50\%$  compared with those for  $P_S=2.3\%$ . For  $2\alpha=135^\circ$ , the parameters in Equation (2.26) are  $f_l=2.065$  and  $\lambda_l=0.674$ , whereas for  $2\alpha=0^\circ$ ,

$f_I=1.936$  and  $\lambda_I=0.5$ . Recommended parameter values for welded joints of carbon steels with toe failure ( $2\alpha=135^\circ$ ) are [28]:

$$R_0=0.28 \text{ mm}, \Delta K_{I,A}=211 \text{ MPa}\cdot\text{mm}^{0.326}, \Delta\sigma_A=155 \text{ MPa} (P_S=50\%, N=5\cdot 10^6 \text{ cycles})$$

Different parameter values are recommended for aluminium alloys [28] and different values of  $R_0$  may be appropriate under mode 1 and mode 3 loading conditions.

A uniform material-dependent value of  $R_0$  is used for evaluating test data not only in the high-cycle fatigue range but also in the medium-cycle and low-cycle fatigue range [22,28,34,35]. This is a simplification appropriate for engineers, considering that under small-scale yielding conditions the elastic-plastic SED matches the elastic SED under plane strain conditions.

It should be noted that the local SED concept for sharp V-notches (which include also welded joints) can be applied also to generic multiaxial loading conditions (modes 1, 2, 3 superimposed). The relevant expression (see [12] for details) for the averaged total SED range  $\Delta\bar{W}$  is:

$$\Delta\bar{W} = \frac{e_1}{E} \cdot \left( \frac{\Delta K_1}{R_0^{(1-\lambda_1)}} \right)^2 + \frac{e_2}{E} \cdot \left( \frac{\Delta K_2}{R_0^{(1-\lambda_2)}} \right)^2 + \frac{e_3}{E} \cdot \left( \frac{\Delta K_3}{R_0^{(1-\lambda_3)}} \right)^2 \quad (2.27)$$

When evaluating welded joint fatigue test results in terms of the averaged SED, the SED range  $\Delta\bar{W}$  depends on the nominal stress ratio  $R=\sigma_{min}/\sigma_{max}$  (not to be confused with the radius  $R$  of the control volume), where  $\sigma_{min}$  and  $\sigma_{max}$  are the lower and upper nominal stresses of the load cycle, through Equation (2.28) (Figure 2.7):

$$\begin{aligned} \Delta\bar{W}(R) &= c_w \cdot \Delta\bar{W}(0) = \frac{1+R^2}{(1-R)^2} \cdot \Delta\bar{W}(0) \quad \text{for } -1 \leq R < 0 \\ \Delta\bar{W}(R) &= c_w \cdot \Delta\bar{W}(0) = \frac{1-R^2}{(1-R)^2} \cdot \Delta\bar{W}(0) \quad \text{for } 0 < R \leq 1 \end{aligned} \quad (2.28)$$

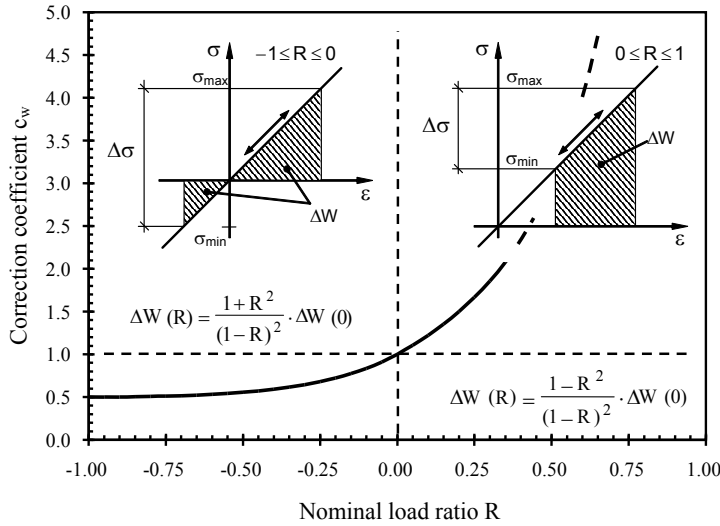


**Figure 2.7.** Coefficient  $c_w$  as a function of the nominal stress ratio  $R$  for cyclic SED with constant  $\Delta\sigma$  [12].

For welded joints under fatigue loading in the as-welded condition, it is appropriate to assume  $c_w$  equal to 1, independently of  $R$ , because of the tensile residual stresses produced by welding. The value  $c_w$  equal to 0.5 should be used for welded joints with a stress relief treatment when tested under  $R = -1$ .

### 2.3.2 Endurable SED of fatigue-loaded welded joints

First, accurate fatigue test data (toe failures) for fillet-welded transverse attachment joints, tensile or bending loaded, made of low and medium carbon steels [17,18,36], have been re-evaluated in terms of  $\Delta\bar{W}$  [22]. A wide range of base plate thicknesses,  $t$  ranging from 6 to 100 mm, has been included. The data base of test results was then broadened with fatigue test data for fillet welded transverse attachment joints with varying gradients of the fillet weld, 30–70° [27]. Also, a test series with  $t=3$  mm was included. Further fatigue test data were added to the scatter band of the  $\Delta\bar{W}$ - $N$  curve, including test results for cruciform fillet-welded joints, load-carrying fillet welds with root failures [28] and for butt joints [37]. In all those cases, the weld toe (or the weld root) was modeled like a sharp notch (zero radius).

The actual  $\Delta\bar{W}$ - $N$  diagram comprises 900 test data and is shown in Figure 2.8. The inverse slope exponent  $k=1.5$  of the  $\Delta\bar{W}$ - $N$  curve corresponds to  $k=3.0$  of the S- $N$  curve, a usual value for welded joints in design codes. The bold solid line denotes the medium line ( $P_s=50\%$ ). The scatter index  $T_w$ , related to probabilities of survival



$P_S=2.3\%$  and  $97.7\%$ , is 3.3. However, it becomes 1.50 if converted into an equivalent local stress range with probabilities of survival  $P_S=10\%$  and  $90\%$ , in agreement with Haibach's normalized  $S-N$  curve [38,39].

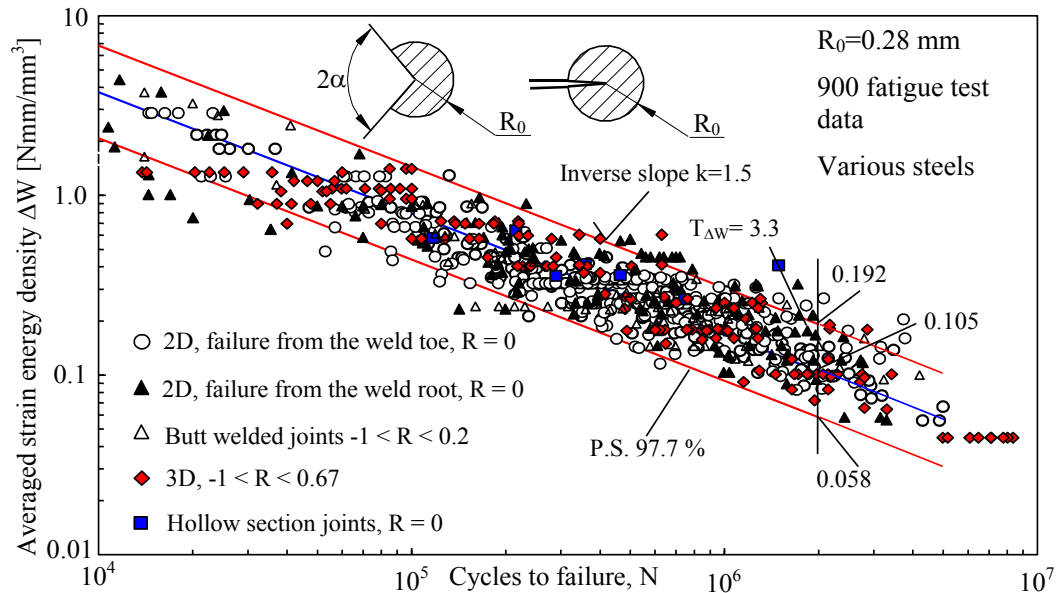


**Figure 2.8.** Fatigue strength of fillet welded joints made of steels as a function of the averaged local strain energy density; scatter band defined by mean value  $\pm 2$  standard deviations; fatigue crack initiation at weld toe or weld root; diagram taken from [40]. More details on materials, geometries and original sources are in [28].

### 2.3.3 Potential and weak points of the SED approach

It has been shown that the NSIF is a useful parameter to control the crack initiation phase in members with sharp notches. However, the NSIF approach requires knowledge of the elastic stress field in the region very close to the notch tip. The degree of refinement necessary is not easy to obtain in plane cases and generally very difficult in three-dimensional cases. As opposed to the direct evaluation of the NSIFs, the averaged local SED can be determined with high accuracy by using coarse meshes. If needed, the NSIFs can be eventually determined *a posteriori*, by means of simple closed-form expressions linking the SED, the NSIFs and the control volume radius. The NSIFs therefrom derived are sufficiently accurate for engineering applications. The reason for the excellent performance of SED evaluations within the widely used displacement method in finite element analysis is the fact that the nodal point displacements of the FE structural system are the primary unknown parameters

that are determined based on a variational formulation of the potential  $\Pi$  leading to the principle of virtual work. Within this approach, the element displacements are fully compatible whereas the stresses are not equilibrated at the element boundaries. Therefore, the evaluation of the strain energy from the nodal point displacements is superior to its evaluation from the element stresses. The procedural steps in terms of FE analysis are readily available [41,42].

A further advantage related to the SED approach is that local SED quantities associated to notches having different opening angles are directly comparable, as opposed to NSIF values, whose unit formally depends on the opening angle itself. That is because the critical value of the averaged SED, at which failure or crack initiation occurs, is a material characteristics, not dependent on the notch opening angle. As a practical consequence, uniform damage maps can be produced in terms of local SED, to know and directly compare, weld by weld and point by point, the fitness of a whole structure, regardless of the weld shape and the bead angle.

However, the need of a control volume centered on a notch tip (i.e. at the weld toe and at the weld root in case of welded joints), within which the SED has to be computed and averaged, is a limitation in plane conditions and a strong limitation in three-dimensional modeling of large structures. Building the control volume requires local modification of the notch geometry before meshing, making the SED method not so suitable for automation, such as in a post-processor.

## 2.4 Peak stress method

The peak stress method (PSM) is a simplified, FE-based method to approximate the NSIFs at sharp V-notches inclusive of slits or cracks. The PSM has its origins in a numerical technique proposed by Nisitani and Teranishi [43] to rapidly estimate by FEM the SIF of a crack initiating from an ellipsoidal cavity. Such a procedure is based on the usefulness of the linear elastic peak stress  $\sigma_{peak}$  calculated at the crack tip by means of FE analyses characterized by a mesh pattern having a constant element size. In particular, Nisitani and Teranishi [43] were able to show that the ratio  $K_I/\sigma_{peak}$  depends only on the element size, such that  $\sigma_{peak}$  can be used to rapidly estimate  $K_I$ , provided that the adopted mesh pattern has previously been calibrated on geometries for which the exact  $K_I$  values are known. A theoretical justification to the PSM has been provided later on and the method has been extended also to sharp and

open V-notches in order to rapidly evaluate the mode 1 NSIFs [44]. Subsequently, the PSM has been formalized to include also cracked components under mode 2 loading conditions [45] and open V-notches subjected to pure mode 3 (anti-plane) stresses [46].

#### 2.4.1 Basic relationships of the PSM

The PSM enables to rapidly estimate the NSIFs  $K_1$ ,  $K_2$  and  $K_3$  from the notch tip singular, linear elastic, opening, sliding and tearing FE peak stresses  $\sigma_{yy,peak}$ ,  $\tau_{xy,peak}$  and  $\tau_{yz,peak}$ , respectively, which are referred to the notch bisector line according to Figure 2.9. The peak stresses are defined as the maximum linear elastic stresses in the considered crack tip or notch tip nodal point of the mesh. Each nodal point stress results as the arithmetic mean of the stress components in the two ( $2\alpha > 90^\circ$ , as described in detail below) or four finite elements ( $2\alpha < 90^\circ$ ) meeting at the nodal point.

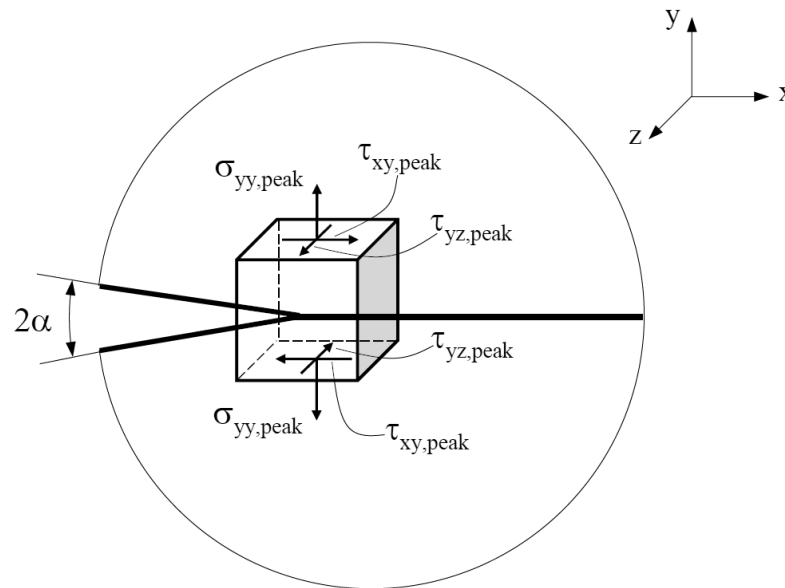


**Figure 2.9.** Definition of the notch tip singular, linear elastic, opening, sliding and tearing FE peak stresses  $\sigma_{yy,peak}$ ,  $\tau_{xy,peak}$  and  $\tau_{yz,peak}$ , respectively, which are referred to the bisector line according to PSM.

More precisely, the following expressions are valid [44–46]:

$$K_{FE}^* = \frac{K_1}{\sigma_{yy,peak} \cdot d^{1-\lambda_1}} \cong 1.38 \quad (2.29)$$

$$K_{FE}^{**} = \frac{K_2}{\tau_{xy,peak} \cdot d^{1-\lambda_2}} \cong 3.38 \quad (2.30)$$

$$K_{FE}^{***} = \frac{K_3}{\tau_{yz,peak} \cdot d^{1-\lambda_3}} \cong 1.93 \quad (2.31)$$

where  $d$  is the so-called *global element size* parameter to input in Ansys® FE software, i.e. the average FE size adopted by the free mesh generation algorithm available in the FE code. It is proven that the above ratios depend mainly on the element size and type, modified solely by the stress singularity exponent which depends on the notch opening angle  $2\alpha$ .

Equations (2.29) to (2.31) have been derived using particular 2D or 3D finite element types and sizes, so that a proper range of applicability exists, which has been presented in detail in previous contributions [44–46].

More precisely, Equations (2.29) to (2.31) are valid under the following conditions:

- i) concerning Equations (2.29) and (2.30) related to mode 1 and mode 2 loadings, respectively, use of 4-node quadrilateral finite elements with linear shape functions, as implemented in Ansys® numerical software (PLANE 42 of the Ansys® element library or alternatively PLANE 182 with K-option 1 set to 3, which corresponds to a simplified enhanced strain formulation of the finite elements). Concerning instead Equation (2.31) related to mode 3 loading, use of two-dimensional, harmonic, 4-node linear quadrilateral elements, as implemented in Ansys® numerical code (PLANE 25 of Ansys® element library). Finally, the use of three-dimensional, eight-node brick elements (SOLID 45 of Ansys® element library or equivalently SOLID 185 with K-option 2 set to 3) is allowed for all loading modes;
- ii) the pattern of finite elements around a notch or crack tip must be the one shown in Figure 2.10 (see also [44–46]); in particular, four elements share the node located at the notch tip if the notch opening angle  $2\alpha$  is lower than  $90^\circ$ , while two elements share the node at the notch tip when the notch opening angle  $2\alpha$  is equal or greater than  $90^\circ$ ;
- iii) concerning Equations (2.29) and (2.31) related to mode 1 and mode 3 loadings, respectively, V-notches are characterized by an opening angle  $2\alpha$  ranging from  $0^\circ$  to  $135^\circ$ ; while it should be remembered that calibration for mode 2 loading is restricted to  $2\alpha=0$  (crack case);

iv) for mode 1 loading (Equations (2.29)) the mesh density ratio  $a/d$  that can be adopted in numerical analyses must be  $a/d \geq 3$  to obtain  $K^*_{FE} = 1.38 \pm 3\%$ ,  $a$  being the notch depth (or crack length); for mode 2 loading (Equations (2.30)) more refined meshes are required, the mesh density ratio  $a/d$  having to satisfy  $a/d \geq 14$  to obtain  $K^{**}_{FE} = 3.38 \pm 3\%$ ; finally, in case of mode 3 loading (Equations (2.31)) the condition  $a/d \geq 3$  must again be satisfied to obtain  $K^{***}_{FE} = 1.93 \pm 3\%$ .

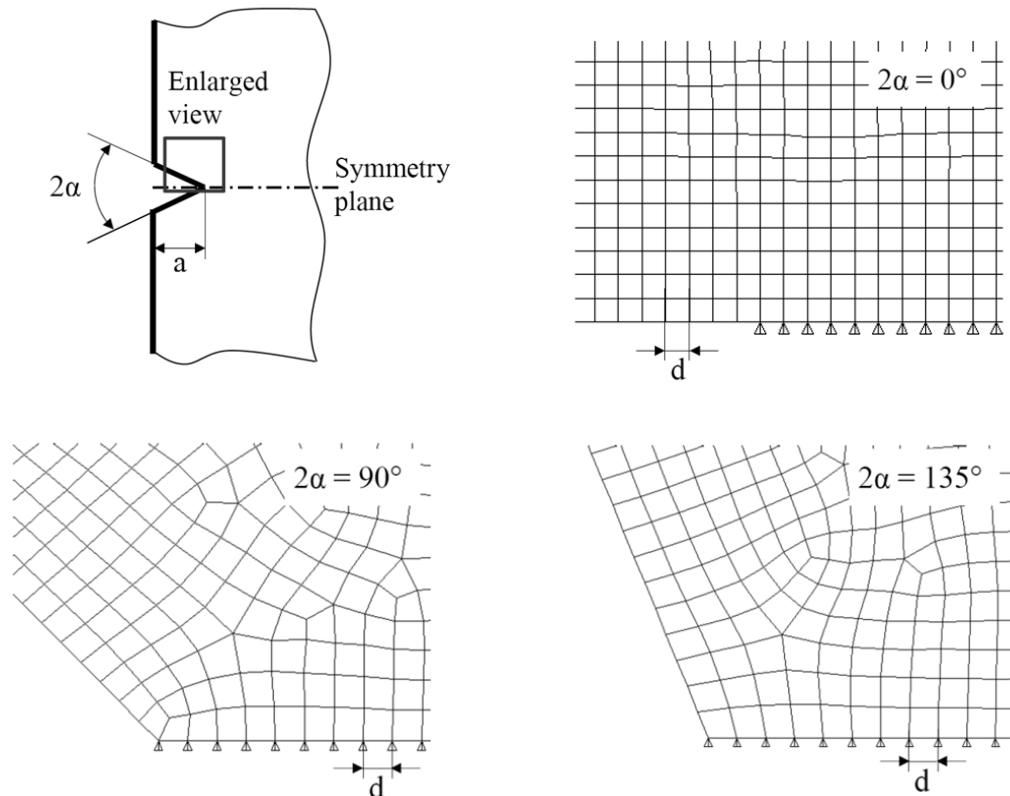


**Figure 2.10.** Mesh patterns according to PSM. The automatic free mesh generator available in Ansys® code was used and the global element size  $d$  was set equal to 1 mm [44].

The method was originally based on two-dimensional FE models. Afterwards, the PSM has also been combined with 3D numerical models and eight-node brick elements to assess the fatigue strength of steel-welded joints having complex geometry and characterized by toe as well as root cracking [47]. Recently, the PSM has been calibrated under plane condition also for other FE software which differ from Ansys® [48].

Finally, being the PSM a simplified method to approximate the NSIFs, both the fatigue failure criterion provided by the NSIF approach (see section 2.2.2) and by the

averaged SED one (see section 2.3.2), the latter being based on the NSIFs, can be used together with the PSM.

### 2.4.2 Potential and weak points of the PSM

The computational effort required to compute the NSIFs implies strong limitations of applicability in practice, due to the very refined meshes needed, especially in three-dimensional numerical models of large structures. The PSM is a design approach which takes care of the industrial needs of rapidity and ease of use.

The most important advantage of using the PSM is that the finite element size required to evaluate  $K_1$ ,  $K_2$  and  $K_3$  from  $\sigma_{yy,peak}$ ,  $\tau_{xy,peak}$  and  $\tau_{yz,peak}$ , respectively, is several orders of magnitude greater than the one required to evaluate the entire local stress field. Further advantage of using  $\sigma_{yy,peak}$ ,  $\tau_{xy,peak}$  and  $\tau_{yz,peak}$  is that a single stress value is sufficient to estimate  $K_1$ ,  $K_2$  and  $K_3$ , respectively, instead of a number of stress FE data, as is usually made by applying definitions provided by Equations (2.9) to (2.11).

However, some drawbacks exist. It should be noted that different stress extrapolation rules from the integration points to the nodal points lead to different values of the peak stresses; moreover finite element analyses performed using higher-order elements or significantly different free generated FE patterns imply that the coefficients of Equations (2.29) to (2.31) should be recalculated. All the mentioned aspects take part in the determination of the mean value of the PSM calibration constant and its scatter band and in principle can differ from code to code. This behavior, which can be considered as a dependence on the adopted FE code, is an intrinsic feature of the PSM and can be a limitation. Furthermore, coefficients of Equations (2.29) to (2.31) are in principle dependent on the notch opening angle, which means that, for example, values provided under loading mode 1 by Equation (2.9) could be not reliable, if angles significantly larger than  $135^\circ$  are considered.

## 2.5 Brief open epistemological discussion on fatigue design

Historically, the problem of fatigue has been addressed through the empirical approach of testing. Much information has been obtained thanks to testing, before mechanisms of fatigue were understood. At the beginning there was no underlying central theme to correlate the data and the relationship among sets of data was not

clear [49]. Numerous theories, some seriously misleading [50], have been developed in attempts to explain experimental results. Fatigue testing of components and structures started in the 1830s. The first known fatigue test results were published in German by Albert in 1837, who tested mine hoist chains under cyclic loads [51]. His testing setup is illustrated, among others, by Timoshenko [52]. Fatigue testing of specially designed laboratory specimens started in the 1850s. It is generally accepted that the first fatigue tests on laboratory specimens were carried out by Wöhler. This enabled him to relate his experimental results to service stresses in railway axles, and hence produce design rules which were incorporated in technical regulations for German railways. Since then, for a long time fatigue has been largely a descriptive subject [53]. This changed in the last four decades. The increasing power of computers has meant an increase in the application of numerical methods, sometimes based on sophisticated mathematics, to metal fatigue research and development. One of the consequences is that approaches to metal fatigue have become much more mathematical than experimental [54]. It is the case of local approaches proposed in the last three decades. Among them, the ones presented in this chapter.

In the author's opinion, from the epistemological point of view, the central role of experiments in understanding the fatigue phenomenon (mentioned also by Gumbel [55]) is still causing within the scientific community the need to use experiments in the role of supporting theories. However, as soon as the epistemological role of experiments is more definite, it can be highlighted a broad spectrum of views ranging from experiments as a basis for simple inductions [56] to experiments used for refuting theories by falsification [57]. Nowadays available local approaches for fatigue assessments are built on theoretical deductions based on mathematics, mechanics and physics and their suitability in fatigue design of welded joints has still not been proven wrong. It is the case, for example, of the local SED approach, whose suitability in fatigue assessment of welded joints has been already evaluated with more than 900 experimental tests (see Figure 2.8). In spite of this, experimental verification of fatigue theoretical based analyses is still thought indispensable, being considered an intrinsic principle of mathematical sciences applied to real-world phenomena [58]. Is it possible that this historical attachment to empiricism is actually limiting the achievement of an all-around and reliable theory on the fatigue design?

## References

- [1] D. Radaj, State-of-the-art review on extended stress intensity factor concepts, *Fatigue Fract. Eng. Mater. Struct.* 37 (2014) 1–28.
- [2] D. Radaj, State-of-the-art review on the local strain energy density concept and its relation to the J-integral and peak stress method, *Fatigue Fract. Eng. Mater. Struct.* 38 (2015) 2–28.
- [3] F. Berto, P. Lazzarin, A review of the volume-based strain energy density approach applied to V-notches and welded structures, *Theor. Appl. Fract. Mech.* 52 (2009) 183–194.
- [4] F. Berto, P. Lazzarin, Recent developments in brittle and quasi-brittle failure assessment of engineering materials by means of local approaches, *Mater. Sci. Eng. R.* 75 (2014) 1–48.
- [5] M.L. Williams, Stress singularities resulting from various boundary conditions in angular corners of plates in tension, *J. Appl. Mech.* 19 (1952) 526–528.
- [6] B. Gross, A. Mendelson, Plane elastostatic analysis of V-notched plates, *Int. J. Fract. Mech.* 8 (1972) 267–276.
- [7] J. Qian, N. Hasebe, Property of eigenvalues and eigenfunctions for an interface V-notch in antiplane elasticity, *Eng. Fract. Mech.* 56 (1997) 729–734.
- [8] P. Lazzarin, R. Tovo, A unified approach to the evaluation of linear elastic stress fields in the neighborhood of cracks and notches, *Int. J. Fract.* 78 (1996) 3–19.
- [9] P. Lazzarin, R. Tovo, A Notch Intensity Factor Approach To the Stress Analysis of Welds, *Fatigue Fract. Eng. Mater. Struct.* 21 (1998) 1089–1103.
- [10] P. Lazzarin, R. Tovo, S. Filippi, Elastic stress distributions in finite size plates with edge notches, *Int. J. Fract.* 91 (1998) 269–282.
- [11] B. Atzori, P. Lazzarin, R. Tovo, Stress distributions for v-shaped notches under tensile and bending loads, *Fatigue Fract. Eng. Mater. Struct.* 20 (1997) 1083–1092.
- [12] P. Lazzarin, C.M. Sonsino, R. Zambardi, A notch stress intensity approach to assess the multiaxial fatigue strength of welded tube-to-flange joints subjected to combined loadings, *Fatigue Fract. Eng. Mater. Struct.* 27 (2004) 127–140.
- [13] T. Boukharouba, T. Tamine, L. Niu, C. Chehimi, G. Pluvinage, The use of



- notch stress intensity factor as a fatigue crack initiation parameter, *Eng. Fract. Mech.* 52 (1995) 503–512.
- [14] Y. Verreman, B. Nie, Early development of fatigue cracking at manual fillet welds, *Fatigue Fract. Eng. Mater. Struct.* 19 (1996) 669–681.
- [15] Y. Verreman, B. Nie, Short crack fatigue propagation at fillet welds, in: *Proc Int Conf Perform. Dyn. Loaded Welded Struct.* New York, WRC, 1997: pp. 240–253.
- [16] B. Atzori, P. Lazzarin, R. Tovo, From a local stress approach to fracture mechanics: a comprehensive, *Fatigue Fract. Eng. Mater. Struct.* 22 (1999) 369–381.
- [17] S.J. Maddox, *The Effect of Plate Thickness on the Fatigue Strength of Fillet Welded Joints*, (1987).
- [18] T.R. Gurney, *The fatigue strength of transverse fillet welded joints*, Abington Publishing, Cambridge, 1991.
- [19] H. Neuber, *Kerbspannungslehre* (in German), 2nd Edition, Springer Verlag, Berlin, 1958.
- [20] H. Neuber, *Kerbspannungslehre* (in German), 3rd Edition, Springer Verlag, Berlin, 1985.
- [21] E. Beltrami, *Sulle condizioni di resistenza dei corpi elastici* (in Italian), *Rend. Del Reg. Ist. Lomb. XVIII* (1885) 704–714.
- [22] P. Lazzarin, R. Zambardi, A finite-volume-energy based approach to predict the static and fatigue behavior of components with sharp V-shaped notches, *Int. J Fract.* 112 (2001) 275–298.
- [23] P. Lazzarin, R. Zambardi, The Equivalent Strain Energy Density approach reformulated and applied to sharp V-shaped notches under localized and generalized plasticity, *Fatigue Fract. Eng. Mater. Struct.* 25 (2002) 917–928.
- [24] P. Lazzarin, P. Livieri, F. Berto, M. Zappalorto, Local strain energy density and fatigue strength of welded joints under uniaxial and multiaxial loading, *Eng. Fract. Mech.* 75 (2008) 1875–1889.
- [25] Z. Yosibash, A.R. Bussiba, I. Gilad, Failure criteria for brittle elastic materials, *Int. J. Fract.* 125 (2004) 307–333.
- [26] F. Lazzarin, P., Berto, Some Expressions for the Strain Energy in a Finite Volume Surrounding the Root of Blunt V-notches, *Int. J. Fract.* 135 (2005)

- 161–185.
- [27] P. Lazzarin, T. Lassen, P. Livieri, A notch stress intensity approach applied to fatigue life predictions of welded joints with different local toe geometry, *Fatigue Fract. Eng. Mater. Struct.* 26 (2003) 49–58.
- [28] P. Livieri, P. Lazzarin, Fatigue strength of steel and aluminium welded joints based on generalised stress intensity factors and local strain energy values, *Int. J. Fract.* 133 (2005) 247–276.
- [29] P. Lazzarin, F. Berto, From Neuber's elementary volume to Kitagawa and Atzori's diagrams: an interpretation based on local energy, *Int. J. Fract.* 135 (2005) L33--L38.
- [30] F. Berto, P. Lazzarin, Recent developments in brittle and quasi-brittle failure assessment of engineering materials by means of local approaches, *Mater. Sci. Eng. R.* 75 (2014) 1–48.
- [31] G. Glinka, Energy density approach to calculation of inelastic strain-stress near notches and cracks, *Eng. Fract. Mech.* 22 (1985) 485–508.
- [32] EN 1993-1-9 Eurocode 3 - Design of steel structures - Part 1-9: Fatigue, European Committee for Standardization, Brussels, 2005.
- [33] A.F. Hobbacher, Recommendations for Fatigue Design of Welded Joints and Components, International Institute of Welding, 2008.
- [34] P. Berto, F., Lazzarin, A review of the volume-based strain energy density approach applied to V-notches and welded structures, *Theor. Appl. Fract. Mech.* 52 (2009) 183–194.
- [35] P. Berto, F., Lazzarin, Recent developments in brittle and quasi-brittle failure assessment of engineering materials by means of local approaches, *Mater. Sci. Eng.* 75 (2014) 1–48.
- [36] D.P. Kihl, S. Sarkani, Thickness effects on the fatigue strength of welded steel cruciforms, *Int. J. Fatigue.* 19 (1997) 311–316.
- [37] P. Lazzarin, F. Berto, D. Radaj, Uniform fatigue strength of butt and fillet welded joints in terms of the local strain energy density, in: *Proc. Fatigue*, 2006.
- [38] E. Haibach, C. Matschke, The concept of uniform scatter bands for analyzing SN curves of unnotched and notched specimens in structural steel, in: *Low-Cycle Fatigue Life Predict.*, ASTM International, 1982.

- [39] E. Haibach, Service fatigue strength-methods and data for structural analysis, Springer Verlag, Berlin. (2002).
- [40] F. Berto, P. Lazzarin, The volume-based Strain Energy Density approach applied to static and fatigue strength assessments of notched and welded structures, *Procedia Eng.* 1 (2009) 155–158.
- [41] P. Lazzarin, F. Berto, F.J. Gomez, M. Zappalorto, Some advantages derived from the use of the strain energy density over a control volume in fatigue strength assessments of welded joints, *Int. J. Fatigue.* 30 (2008) 1345–1357.
- [42] P. Lazzarin, F. Berto, M. Zappalorto, Rapid calculations of notch stress intensity factors based on averaged strain energy density from coarse meshes: theoretical bases and applications, *Int. J. Fatigue.* 32 (2010) 1559–1567.
- [43] H. Nisitani, T. Teranishi, KI of a circumferential crack emanating from an ellipsoidal cavity obtained by the crack tip stress method in FEM, *Eng. Fract. Mech.* 71 (2004) 579–585.
- [44] G. Meneghetti, P. Lazzarin, Significance of the elastic peak stress evaluated by FE analyses at the point of singularity of sharp V-notched components, *Fatigue Fract. Eng. Mater. Struct.* 30 (2007) 95–106.
- [45] G. Meneghetti, The use of peak stresses for fatigue strength assessments of welded lap joints and cover plates with toe and root failures, *Eng. Fract. Mech.* 89 (2012) 40–51.
- [46] G. Meneghetti, The peak stress method for fatigue strength assessment of tube-to-flange welded joints under torsion loading, *Weld. World.* 57 (2013) 265–275.
- [47] G. Meneghetti, C. Guzzella, The peak stress method to estimate the mode I notch stress intensity factor in welded joints using three-dimensional finite element models, *Eng. Fract. Mech.* 115 (2014) 154–171.
- [48] G. Meneghetti, A. et al. Campagnolo, Rapid Evaluation of notch stress intensity factors in welded joints using the peak stress method: comparison of commercial finite element codes for a range of mesh patterns, IIW-Document XIII-2696-17. (2017).
- [49] N.E. Frost, K.J. Marsh, L.P. Pook, Metal fatigue, Courier Corporation, 1974.
- [50] W. Schütz, A history of fatigue, *Eng. Fract. Mech.* 54 (1996) 263–300.
- [51] N.E. Dowling, Mechanical behavior of materials: engineering methods for

- deformation, fracture, and fatigue, Pearson, 2012.
- [52] S. Timoshenko, History of strength of materials: with a brief account of the history of theory of elasticity and theory of structures, Courier Corporation, 1953.
- [53] L.P. Pook, The role of crack growth in metal fatigue, Met. Soc. 1 Carl. House Terrace, London SW 1 Y 5 DB, England, 1983. (1983).
- [54] R.I. Stephens, A. Fatemi, R.R. Stephens, H.O. Fuchs, Metal fatigue in engineering, John Wiley & Sons, 2000.
- [55] E.J. Gumbel, Statistics of extremes. 1958, Columbia Univ. Press. New York. (1958).
- [56] S. Weinberg, Dreams of a final theory, Vintage, 1992.
- [57] K. Popper, The logic of scientific discovery, Routledge, 2005.
- [58] D. Radaj, C.M. Sonsino, W. Fricke, Fatigue assessment of welded joints by local approaches, Woodhead Publishing, Cambridge, 2006.

# 3. Fatigue characterization of welded cover plates

## Highlights

In the present chapter the fatigue behavior of large-scale welded cover plates, which are usually adopted to locally increase bridge girders static resistance, has been investigated both numerically and experimentally. Non-uniform fatigue classification of cover plates has been highlighted at standards level. Thus, such joint has been chosen as a good candidate to be investigated through local approaches. By the application of the SED approach and adopting both bi-dimensional and three-dimensional FE models, it has been possible to isolate the parameters which mainly affect the fatigue strength of the joint and to propose alternatives to those provided by codes currently in force. Four geometric variants have been selected as eligible to be experimentally tested against fatigue and the related fatigue classes at 2 million cycles and 97.7% probability of survival have been obtained. Numerical calculations have been compared with test results and it has been found that all experimental data can successfully be summarized in a unique scatter band in terms of SED, regardless of the specimen geometry. The scatter index related to the two curves with probabilities of survival  $P_S=2.3\%$  and  $97.7\%$ , has been found equal to 2.50, which returns a scatter index  $T_\sigma=1.58$  when reconverted to an equivalent local stress range. Then, it has been also found that all experimental data fit well inside the SED based master scatter band proposed by Lazzarin and coworkers. The suitability of the SED approach and of the related design curve to perform the fatigue assessment of welded cover plates has, therefore, not been proven wrong.



### 3.1 Introduction

Cover plates (also called doubler plates) are typically used to strengthen the cross section of the chords of trusses, or of the flanges of I section girders, if the standard section available is not adequate, or if reinforcement is only necessary for some length of the girder. Cover plates are often welded to the flanges of steel bridge girders in order to increase the moment capacity and consequently the allowable traffic load and span of the bridge. The cover plate can be narrower or wider than the flanges. According to Radaj [1], although the reinforcing effect of the narrower plate is considerably less than that of the wider one, the former is preferable in the presence of fatigue loading because the notch effect of the ends of the plate can only be reduced adequately in this version by design and manufacturing measures, as shown in Figure 3.1. In Figure 3.1 different cover plate design solutions are compared in terms of fatigue strength reduction factor  $\gamma$ , according to Neumann [2], defined as the ratio between the tensile fatigue strength of the mill finished sheet of parent material without a weld and the same sheet with a weld. The cover plate end without transverse weld (a) is not generally permissible because of the risk of crevice corrosion. The version with transverse weld (b) without any other measures gives a severe notch effect and a corresponding reduction of fatigue strength. This version is used when the end of the plate can be placed in an area with a low bending moment. Adequate strength at the plate end is achieved by giving the corners a rounded shape, beveling the plate and grinding the weld toe (c). Making the plate ends pointed (d) is not advantageous. The end of the wider plate (e) gives particularly low fatigue strength, to which reference has already been made.

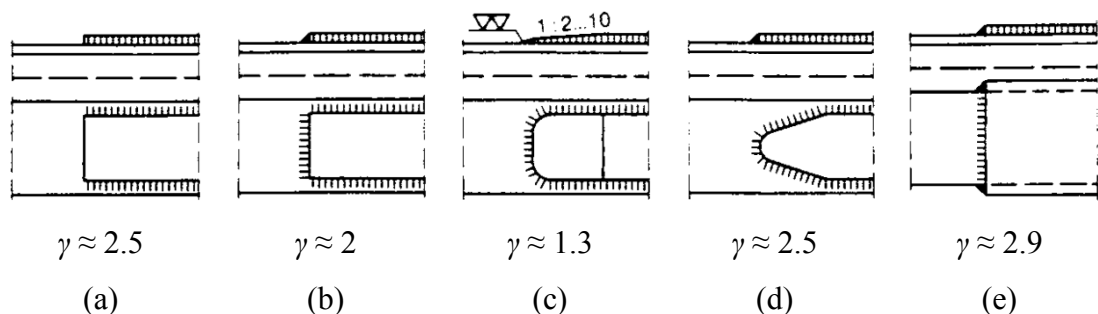


**Figure 3.1.** Cover plate end design variants after Radaj [1] and corresponding fatigue strength reduction factors  $\gamma$  after Neumann [2].

Among all, version (d), representing a cover plate having the pointed end, is one of the most frequently adopted solution in design practice. This is probably because making the end pointed gives the idea of improving the detail fatigue resistance, by reducing the stress concentration effect at the weld toe and so inducing a gradual stress transferring from the main plate to the attached plate (Figure 3.2). Moreover, according to this solution, possible machining operations are localized at the pointed end, which is small as compared to the transverse weld of cover plate version (b), so leading to a cheaper design in terms of time-working. However, such a solution is not taken into account in any of the standards in force dealing with fatigue design.



**Figure 3.2.** Example of practical design solution of a cover plate with pointed end.

Furthermore, if a survey of current standards from different fields (civil, railway, crane, off-shore, pressure vessels, and so on) is made, a lot of uncertainty about the real fatigue strength of all cover plate versions can be found, as discussed in detail in the next section. Such lack of unambiguous classification makes the detail under investigation a good candidate to be characterized through the local SED approach, whose theoretical framework has been introduced in Chapter 2.

In the present chapter, after reporting a review of the literature and standards related to welded cover plates fatigue behavior, a numerical and experimental investigation is presented. Different geometrical solutions have been analyzed and compared with those proposed by standards and in particular with those suggested by the Eurocode 3 [3] and by the IIW recommendations [4,5]. The purposes of the present study are the identification of the parameters which mainly affect the fatigue strength of cover



plates and the proposal of some alternative solutions, as compared to those provided by standards. Particular attention has been given to the SED approach, also investigating its accuracy and mesh sensitivity in both 2D plane strain condition and 3D condition. Finally, experimental results have been summarized in terms of local SED, adopting a unique scatter band regardless of the weld geometry.

### **3.2 Literature and normative review**

Numerous studies [6–8] have shown that the cover plate ends have a very low fatigue resistance. The main reason is the stress concentrating effect due to the local increase of stiffness introduced by the transverse weld. Munse and Stallmeyer [9] performed a series of fatigue tests to investigate the effect of the geometry on the fatigue behavior of flexural welded members such as cover plates. With respect to beams with partial length cover plates, the authors concluded the followings: i) tapered partial length cover plates have insignificantly greater life than square-ended cover plates; ii) omitting transverse end welds increases the fatigue life by a small percentage; iii) a gradual transition in thickness or width of flanges is the most effective way of increasing the fatigue strength. However, the main finding was that changing the cover plate end shape results in comparable fatigue lives. Fisher et al. [7] tested 193 beams with various square-ended cover plates that were made of three different steel types and subjected to various stress ranges. This study specified the stress range and the detail type as the fatigue strength determining factors. It was also found that the following variations of cover plates do not influence the fatigue life: cover plates with or without transverse end welds; cover plates wider or narrower than the flange; cover plates up to 19 mm thick; single or multiple cover plates. The only exception was the not-welded end cover plates wider than the flange which exhibited a much shorter fatigue life. Such results do not completely agree with those found by Neumann [2] and summarized in Figure 3.1.

Lack of a clear fatigue classification of welded cover plates exists also at normative level: the fatigue strength at 2 million cycles and 2.3% of failure probability of a welded cover plate ranges between 36 MPa and 121 MPa according to investigated standards (see next section).

### 3.2.1 Fatigue classification according to standards in force

According to the most well-known fatigue design codes and guidelines, dealing with civil buildings, mechanics, railways, cranes, off-shore structures, pressure vessels and so on, the cover plate end is one of the most severe details. The normative classifications are usually dependent on the shape of the weld and of the end of the attached plate; moreover the presence of a lateral reinforced weld, close to the cover plate end, is sometimes considered, as well as the ratio between the thickness of the attached plate and the main plate. However, only cover plates having transverse end weld (Figure 3.1(b)) are considered by standards (as far as the author knows).

The following standards have been taken into account:

Civil:

*EN 1993-1-9:2005 - Design of steel structures - Part 1.9: Fatigue.* [3]

*IIW-1823-07:2008 - Recommendations for fatigue design of welded joints and components.* [4]

*BS 7608:2014 - Code of Practice for Fatigue Design and Assessment of Steel Structures.* [10]

Railways:

*DVS-1612:2009 - Design and endurance strength assessment of welded joints with steels in railway applications.* [11]

Cranes:

*EN 13001-3-1:2013 - Cranes - General design - Part 3-1: Limit state and proof competence of steel structure.* [12]

*DIN 15018:1984 - Cranes: Steel structures. Verification and analyses.*[13]

Off-shore:

*DNVGL-RP-C203:2016 - Fatigue design of offshore steel structures.* [14]

Pressure vessels:

*EN 13445-3:2014 - Unfired pressure vessels - Part 3: Design.* [15]

Mechanics:

*FKM Guideline:2012 - Analytical strength assessment of components.* [16]

An excursus of the aforementioned norms is provided below, detailing the proposed fatigue classes and thus the geometric requirements imposed for each of them, for the welded joint here studied. The comparison between fatigue classes is provided at the

same number of cycles ( $N=2 \cdot 10^6$ ) and probability of survival (97.7%). Similarly, when not otherwise indicated, fatigue classes are intended for joints in *as welded* conditions. For the sake of brevity, if analogy between two or more norms has been found, they have been grouped together.

Figure 3.3 and Figure 3.4 show the fatigue classifications of cover plates according to Eurocode 3 and IIW recommendations, respectively. Both design codes categorize the cover plates based on the relative thickness of the involved plates. It is interesting to note that, except for the cover plates wider than the flange, the transverse end welds can be omitted. FKM guideline perfectly agrees with IIW recommendations.

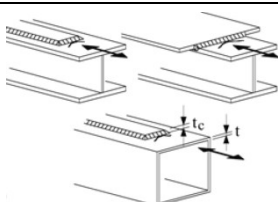
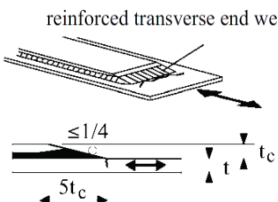
Detail	Description	Requirements		Class [MPa]
		$t_c < t$	$t_c \geq t$	
	Cover plates in beams and plate girders; single or multiple welded cover plates; with or without transverse end weld	$t \leq 20$	-	56
		$20 < t \leq 30$	$t \leq 20$	50
		$30 < t \leq 50$	$20 < t \leq 30$	45
		$t \geq 50$	$30 < t \leq 50$	40
		-	$t > 50$	36
	Cover plates in beams and plate girders; $5 \cdot t_c$ is the minimum length of the reinforcement weld.	-	-	56

Figure 3.3. Fatigue classification according to the Eurocode 3 [3].

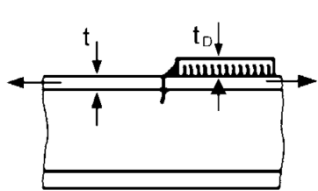
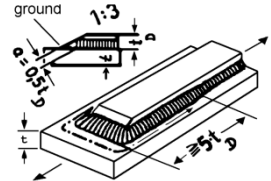
Detail	Description	Requirements	Class [MPa]
	End zones of single or multiple welded cover plates, with or without transverse welds. If the cover plate is wider than the flange, a transverse weld is needed. No undercut at transverse welds.	$t_c/t_m \leq 0.8$	56
		$0.8 < t_c/t_m \leq 1.5$	50
		$t_c/t_m > 1.5$	45
	Grinding parallel to stress direction.	$t_D/t \leq 0.8$	71
		$0.8 < t_D/t \leq 1.5$	63
		$t_D/t > 1.5$	56

Figure 3.4. Fatigue classification according to the IIW recommendations [4] and FKM guideline [16].

The suggested fatigue classes range from a minimum of 36 MPa to a maximum of 71 MPa. The highest class, according to Figure 3.4, is obtainable through a weld reinforcement and grinding the weld parallel to the stress direction. A well-defined weld throat dimension is also required (equal to 0.5 times the attached plate thickness) and the cover plate end has to be machined to obtain a 1:3 slope of the transverse end weld.

Figure 3.5 shows the fatigue classifications according to the crane standard EN 13001-3-1. There are 5 resistance classes ranging from a maximum of 112 MPa to a minimum of 56 MPa. The lower class is assigned to all joints, regardless of their geometric characteristics. While respecting most restrictive constraints on geometry and welding quality, highest ratings are achieved. This classification strongly disagrees with the Eurocode 3.

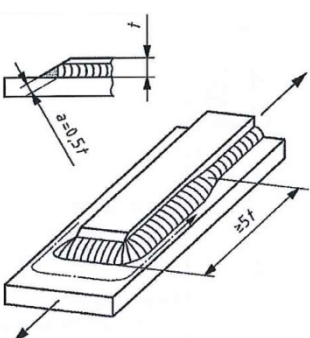
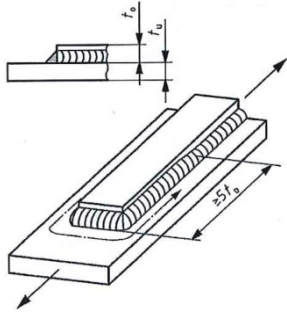
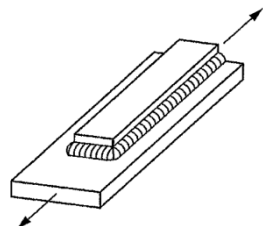
Detail	Description	Requirements	Class [MPa]
	Continuous component with load carrying flange plate, stress in continuous component at end of connection.	End chamfer $\leq 1:3$ ; edge weld and end of flank weld in weld quality B*.	112
		End chamfer $\leq 1:2$ ; edge weld and end of flank weld in weld quality B*.	100
	Continuous component with load carrying flange plate, stress in continuous component at end of connection.	Edge weld and end of flank weld in weld quality B*.	80
	Continuous component with load carrying flange plate, stress in continuous component at end of connection.	Quality level B	63
		Quality level C	56

Figure 3.5. Fatigue classification according to EN 13001-3-1 [12].

Figure 3.6 shows the fatigue classifications according to DVS 1612 for railway bogies. The following resistance classes are indicated: E1, E5 and F1. Such classes, converted in terms of nominal stress, correspond to fatigue classes ranging from a minimum of 76 MPa to a maximum of 121 MPa (further increase is permitted if non-destructive controls are performed).

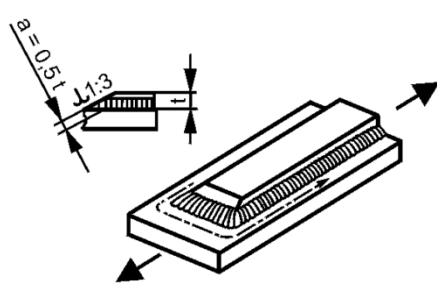
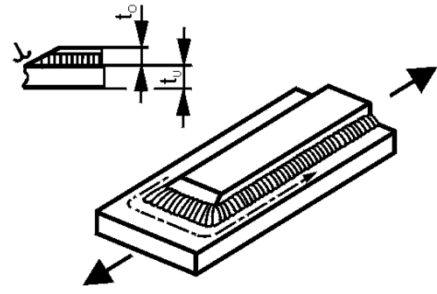
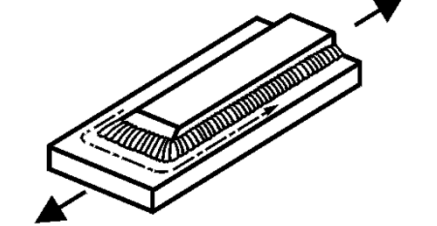
Detail	Description	Requirements	Class [MPa]
	Welded-on flange plate, fillet welds with post-weld treatment and flange plate processed at the front faces. Fillet weld respectively lap seam weld.	End chamfer $\leq 1:3$ ; $a = 0.5t$	E1 [121]
	Welded-on flange plate, fillet welds with post-weld treatment and flange plate processed at the front faces. Fillet weld respectively lap seam weld.	-	E5 [96]
	Welded-on flange plate and fillet welds without post-weld treatment. Fillet weld respectively lap seam weld.	-	F1 [76]

Figure 3.6. Fatigue classification according to DVS 1612 [11].

The lowest class is assigned without needing to meet any requirement, while the highest one requires a specific slope of the transverse weld, as well as a specific weld throat dimension (equal to 0.5 times the attached plate thickness, as for IIW recommendations). It should be specified that, in transposing DVS resistance classes in terms of nominal stress ranges, a choice has to be made for the value of the loading ratio to be adopted. This value has been assumed here equal to 0.5, which is the same value on which the fatigue data of the Eurocode 3 and the IIW

recommendations are based, according to Appendix A of DVS 1612. However, such value for the loading ratio is not explicitly confirmed by the Eurocode 3, nor by the IIW recommendations.

Figure 3.7 reports the fatigue classifications according to the British standard BS 7608. The norm provides a unique resistance class (indicated by the letter G), which corresponds to 50 MPa. In this case, reference is also made to the width of the plate and the relative distance between the weld and the edge of the main plate.

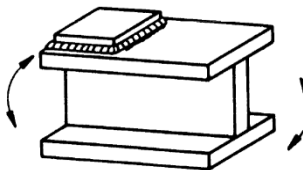
Detail	Description	Requirements	Class [MPa]
	<p>The classification may be deemed to include stress concentrations arising from normal eccentricities in the thickness direction. This type includes parent metal adjacent to the ends of flange cover plates regardless of the shape of the ends.</p>	<p><math>l &gt; 150 \text{ mm}</math> <math>w &gt; 50 \text{ mm}</math></p>	<p>G [50]</p>

Figure 3.7. Fatigue classification according to BS 7608 [10].

Figure 3.8 shows the fatigue classifications according to DNVGL-RP-C203. The detail is classified as G and W3, which corresponds to 50 MPa and 36 MPa, respectively. The distinction between the two classes is only defined by the thickness of the plates: according to the higher class it is required that they are both smaller or equal to 20 mm.

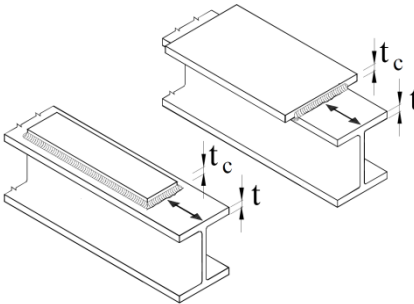
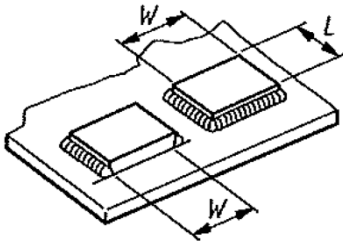
Detail	Description	Requirements	Class [MPa]
	<p>End zones of single or multiple welded cover plates in beams and plate girders. Cover plates with or without frontal weld.</p>	<p><math>t \text{ and } t_c \leq 20 \text{ mm}</math></p>	<p>G [50]</p>
		<p><math>t \text{ and } t_c &gt; 20 \text{ mm}</math></p>	<p>W3 [36]</p>

Figure 3.8. Fatigue classification according to DNVGL-RP-C203 [14].

Finally, Figure 3.9 shows the fatigue classifications according to UNI EN 13445-3 for pressure vessels. This norm stipulates for this detail three classes of resistance, from 45 to 56 MPa, depending only on the size of the attached plate.

Detail	Description	Requirements	Class [MPa]
	Attachment of any shape with surface in contact with stressed member, with welds continuous around or not.	$L \leq 160 \text{ mm}$ $W \leq 55 \text{ mm}$	56
		$L > 160 \text{ mm}$ $W \leq 55 \text{ mm}$	50
		$L > 160 \text{ mm}$ $W > 55 \text{ mm}$	45

**Figure 3.9.** Fatigue classification according to UNI EN 13445-3 [15].

### 3.2.1.1 Summary and observations

It has been shown how often a strong inconsistency between standards exists (for a rapid comparison see Table 3.1). It could be not a source of uncertainty for a designer, who blindly uses the correct standard for the field he deals with. On the other hand, however, it arouses scientific doubts about the real fatigue resistance of the detail under examination, and thus the safety margins related to the defined classes. In particular, assuming that all standards provide values on the safety side, the classification proposed by the Eurocode 3 appears to be very conservative. It is reasonable to ask how far is justified the use of such hypothetical safety margin, which involves obvious weight gains and constructive complications, as well as an increased cost of buildings.

In the light of these premises, investigating the fatigue behavior of welded cover plates appears interesting, looking for the most effective geometric configurations and for solutions other from those proposed by standards in force, which could be simpler and maybe equally resilient.

**Table 3.1.** Comparison of cover plates fatigue classification according to the nominal stress approach after some current standards.

STANDARD	$\Delta\sigma_c$ at $2 \cdot 10^6$ cycles and $P_f=2.3\%$	Conditions
EN 1993-1-9 (2005)	56	End plate chamfer 1:4 End weld reinforcement $a=0.5t_c$ for a length $\geq 5t_c$
IIW-1823-07 (2008) and FKM-Guideline (2012)	71 if $t_c \leq 0.8t$ ; 63 if $0.8t < t_c \leq 1.5t$ ; 56 if $t_c > 1.5t$	End plate chamfer 1:3 End weld reinforcement $a=0.5t_c$ for a length $\geq 5t_c$
	56 if $t_c \leq 0.8t$ ; 50 if $0.8t < t_c \leq 1.5t$ ; 45 if $t_c > 1.5t$	Fillet weld (no chamfer)
EN 13001-3-1 (2013)	112	End plate chamfer 1:3 End weld reinforcement $a=0.5t_c$ for a length $\geq 5t_c$
	100	End plate chamfer 1:2 End weld reinforcement $a=0.5t_c$ for a length $\geq 5t_c$
BS 7608 (2014)	63	Fillet weld (no chamfer)
	50	Fillet weld (no chamfer)
DVS 1612 (2009)	121	End plate chamfer 1:3 End weld reinforcement $a=0.5t_c$ for a length $\geq 5t_c$
	96	End plate chamfer 1:3
	76	Fillet weld (no chamfer)
DNVGL-RP-C203 (2016)	50 if $t$ and $t_c \leq 20$ mm; 36 if $t$ and $t_c > 20$ mm	Fillet weld (no chamfer)
EN 13445-3 (2014)	71 (as welded); 81 (dressed)	Fillet weld (no chamfer)

### 3.3 Preliminary numerical analyses

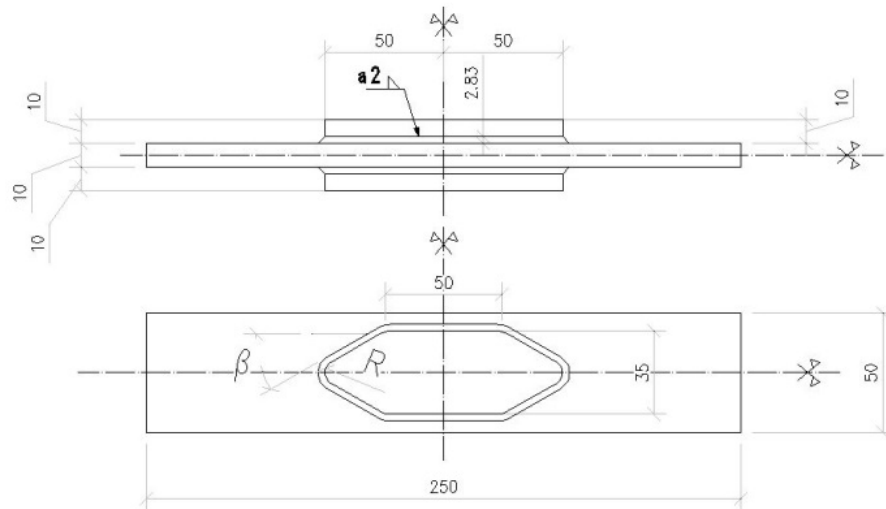
Numerical analyses have been carried out using Ansys® finite element software to investigate the effects of various geometrical solutions and then identify those which most affect the fatigue behavior of welded cover plates. First, the cover plate having tapered ends (Figure 3.1(d)) has been analyzed, which is a widely used solution but without a satisfactory numerical and normative background. Afterwards, the cover



plate having transverse weld (Figure 3.1(b)) has been considered. All the numerical analyses reported in this chapter assume linear elastic material having Young modulus  $E=206000$  MPa and Poisson's ratio  $\nu=0.3$ .

### 3.3.1 Cover plate with tapered end

The two  $R$  and  $\beta$  parameters for the welded plate are defined, which are respectively the radius and the angle of the tapered end (Figure 3.10). Other geometrical dimensions are fixed in accordance to Figure 3.10.



**Figure 3.10.** Cover plate with tapered ends. Investigated parameters  $R$  and  $\beta$  are defined in the figure; other geometrical dimensions are fixed.

Three-dimensional finite element models have been produced. Solid elements, named Solid186 in Ansys® library, which have three degrees of freedom per node and quadratic shape functions, have been adopted. To save computational time and make modeling the geometry easier, three-plane symmetry has been taken advantage of. In doing so, only one eighth of the geometry has been modeled. The averaged strain energy density (SED) approach has been applied, as described in Section 2.3. According to the SED approach, the weld toe has been modeled as a sharp V-notch, with zero radius, while the weld root has been modeled like a crack. Cylindrical control volumes have been placed throughout the weld toe and root lines. Such control volumes are characterized by radius  $R_0$  and height equal both to 0.28 mm. The applied loading condition is a traction, which corresponds to a nominal stress of 56 MPa (which is the fatigue class suggested by the Eurocode 3). The radius  $R$  and

the angle  $\beta$  characterizing the cover plate end have been varied in the following ranges:  $5 \text{ mm} \leq R \leq 25 \text{ mm}$  and  $10^\circ \leq \beta \leq 60^\circ$ . Figure 3.11 provides an example of the realized models and shows the typical three-dimensional SED control volume of radius  $R_0$  at the weld toe. Figure 3.12 qualitatively shows the Von Mises stress contour in one of the studied models.

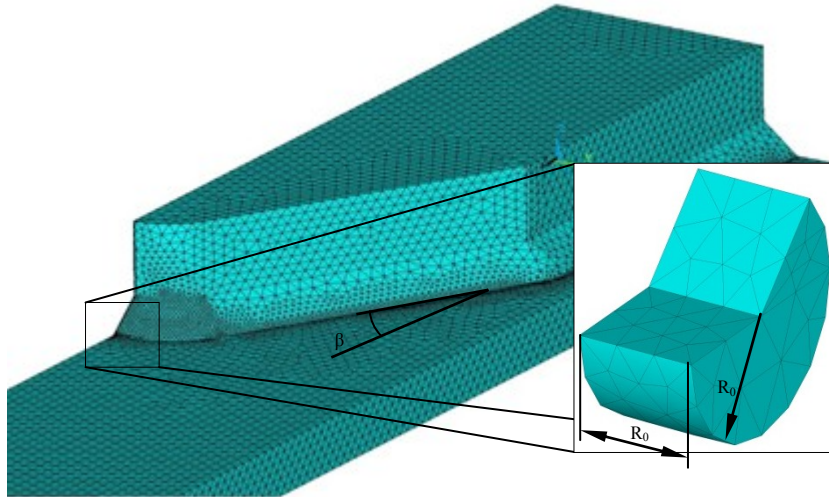


**Figure 3.11.** Example of finite element model used to study the fatigue behavior of tapered cover plates according to the SED approach. Taking advantage of symmetry, only one eighth of geometry has been modeled. Enlarged view of the SED control volume is also given.

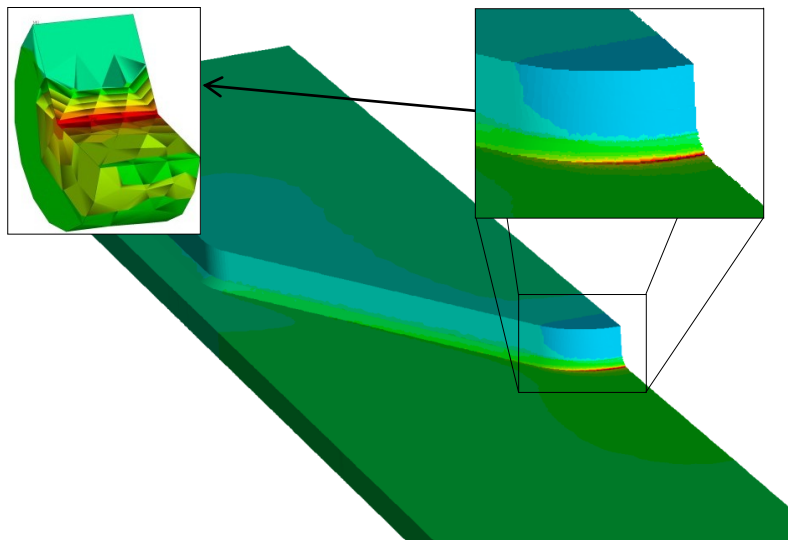


**Figure 3.12.** Von Mises stress contour. In red the highly stressed regions; in blue the lower stressed ones. It is possible to notice the high stress concentration at the weld toe and inside the SED control volume.

Simulations have shown a strong stress concentration at the weld toe. It has also been observed that such stress concentration decreases with the increase of the angle  $\beta$  and the radius  $R$ , indicating that probably a non-tapered geometry has a better fatigue behavior, as reported in the literature [1].

Figure 3.13 summarizes the obtained results in terms of SED at the weld toe, as a function of the angle  $\beta$  and the radius  $R$ . Results in terms of SED at the weld root are not reported here, being considered without interest, as such values are lower (at least one order of magnitude) than the corresponding values at the weld toe for all the studied geometries.

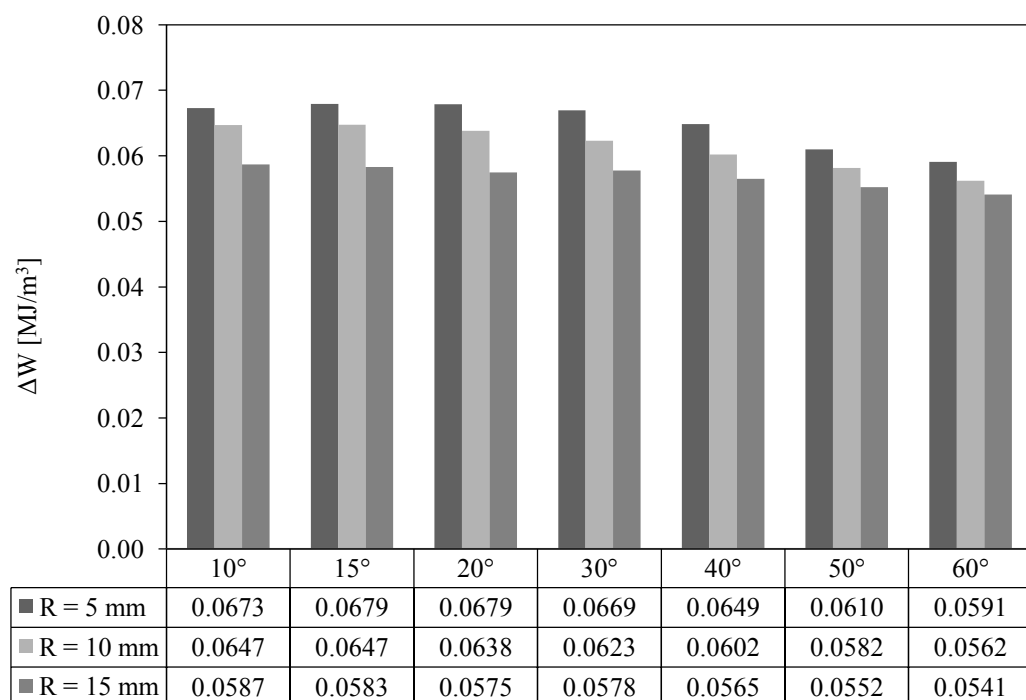


**Figure 3.13.** Trend of SED as a function of the angle  $\beta$  and the radius  $R$ .

### 3.3.2 Cover plate with transverse weld

First, it has been investigated the geometrical configuration which complies with the Eurocode 3. Such geometry is characterized by an end chamfer having slope 1:4 (both for the transverse weld and the attached plate), a weld throat equal to 0.5 times the attached plate thickness and reinforcing lateral weld having length 5 times the attached plate thickness (see Figure 3.3 for reference).

Subsequently, the effect of the length of the lateral reinforcement, the effect of slope of the end chamfer, as well as the effect of the weld throat dimension have been investigated.

### 3.3.2.1 Cover plate geometry suggested by the Eurocode 3

As for the analyses reported in the previous section, three-dimensional finite element models have been produced. Solid elements, named Solid186 in Ansys® library, have been used. Main plate and attached plate dimensions are in accordance with Figure 3.10. Advantage has been taken of the three-plane symmetry, so that only one eighth of the geometry has been modeled. A loading stress equal to 56 MPa has been applied to the main plate nominal section. Non-linear analyses have been performed in order to take into account contact between main plate and attached plates. According to the SED approach, control volumes with radius and height both equal to 0.28 mm have been modeled along the whole weld toe and weld root lines, in order to find the most critical region (Figure 3.14).

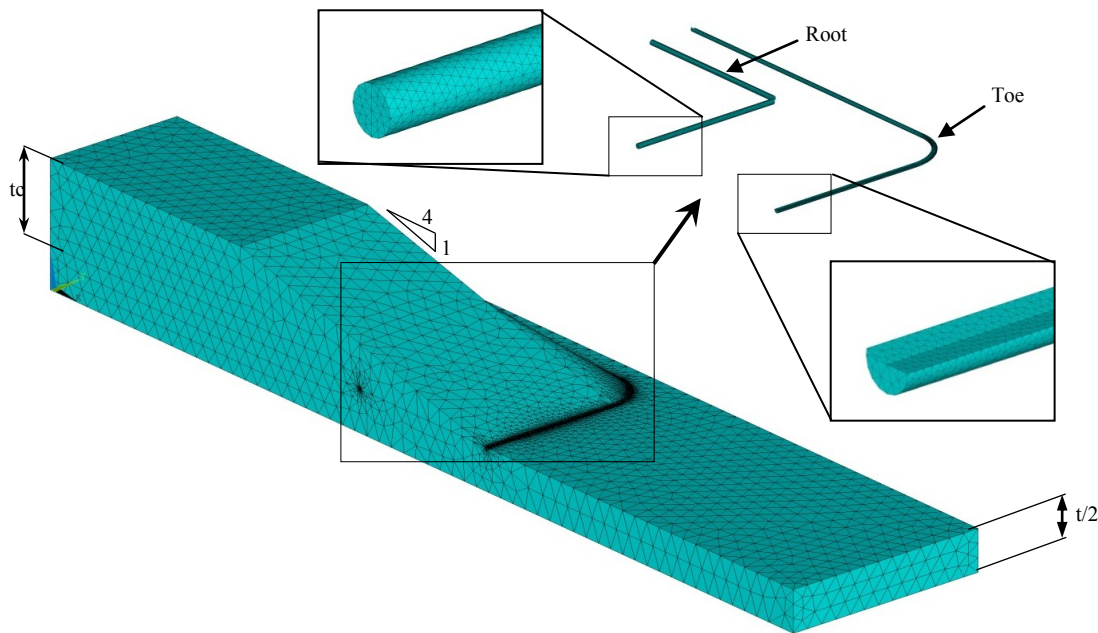


**Figure 3.14.** Example of finite element model used to study the fatigue behavior of transverse cover plates according to the SED approach. Taking advantage of symmetry, only a quarter of geometry has been modeled. Enlarged view of the SED control volumes all along the weld toe and root lines are given.

It has been found that, in terms of SED, the maximum value is reached at the weld toe, in correspondence to the vertical-longitudinal plane of the figure. Moving away from that point, along the weld toe line, the SED keeps first an almost constant value, then declines. Similar behavior can be found at the weld root. However, the weld root is always less critical than the weld toe in terms of SED.

Figure 3.15 shows the trend of SED, as a function of the curvilinear coordinate  $s$ , moving from the central section of the transverse weld, at the weld toe (solid line) and at the weld root (dashed line), respectively.

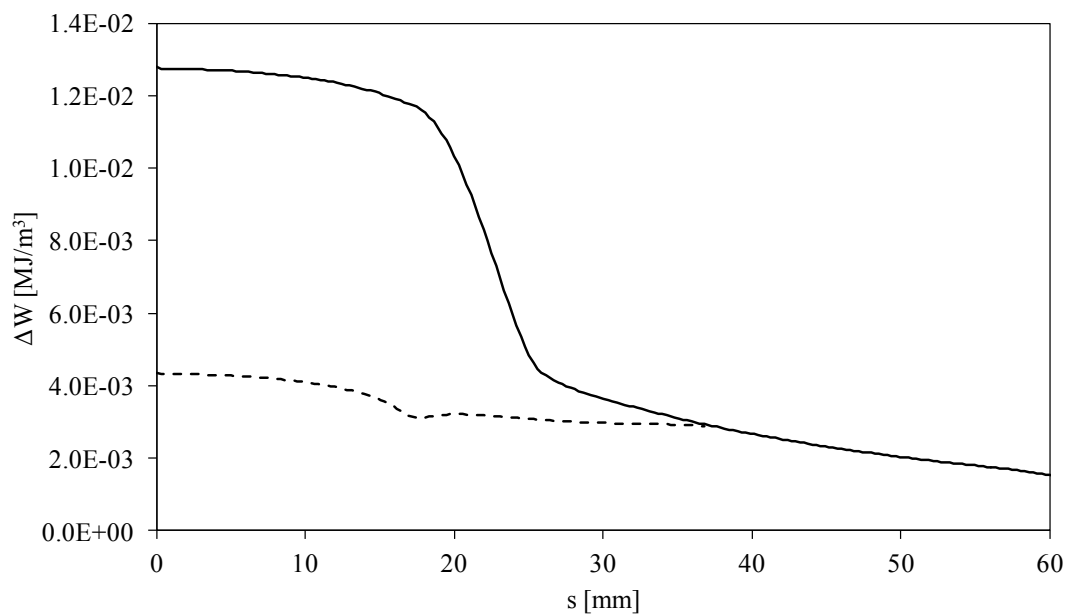


**Figure 3.15.** Trend of SED along the weld toe (solid line) and along the weld root (dashed line).

It can be noticed that the SED at the weld toe is always greater (at least an order of magnitude) than the one calculated at the root, qualifying the toe as the critical point against fatigue for the component. Moreover, the value of SED is almost near the section where it reaches its maximum value, allowing the assumption of plane strain condition if needed (as discussed in Section 3.3.2.7).

By comparing the numerical results of Figure 3.15 with those of Figure 3.13, the worst fatigue behavior of the latter can be deduced, which, probably not casually, is not a suggested solution in the Eurocode 3.

### 3.3.2.2 Effect of the length of the lateral reinforcing weld

It has been found that changing the length of the lateral reinforced weld has no appreciable effect on the stress concentration at the weld toe and root. In particular, its total absence does not increase the value of SED at the weld toe, nor at the weld root.

### 3.3.2.3 Effect of the transverse weld throat dimension

Regarding the transverse weld throat dimension  $a$  (see Figure 3.16), it has been observed that it has a stronger influence on the stress concentration at the weld root, as compared to the weld toe. Small weld throat values (0.1 to 0.2 times the attached plate thickness) show a high stress concentration effect near the root, which can lead to SED values higher than those computed at the toe. This behavior is not desirable and therefore avoided in good design practice because, as opposed to the weld toe, the weld root cannot be controlled by visual inspections. As the size of the throat grows, an opposite trend is observed, claiming that a dimension of 0.5 times the attached plate thickness, as suggested by regulations, is the good compromise to ensure crack initiation at the weld toe.

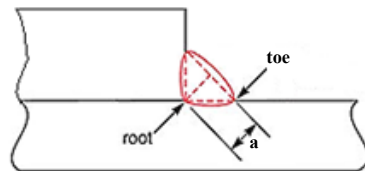


**Figure 3.16.** Definition of weld toe, weld root and weld throat dimension  $a$ .

### 3.3.2.4 Effect of the cover plate chamfer

Similarly to what is observed for the lateral weld reinforcement, the presence of a chamfer on the welded plate does not bring any benefit with regard to the stress state near the weld toe and the weld root. Likewise is for SED values computed at the weld toe and at the weld root.

### 3.3.2.5 Effect of the transverse weld slope

The following slopes ( $1/n$ ), according to Figure 3.17, have been compared to assess the effect of the transverse weld slope on the stress concentration and on SED, both at the weld toe and at the weld root:  $n = 4$  ( $2\alpha = 166^\circ$ );  $n = 2$  ( $2\alpha = 153^\circ$ );  $n = 1$  ( $2\alpha = 135^\circ$ ). Computed SED values are summarized in Table 3.2.

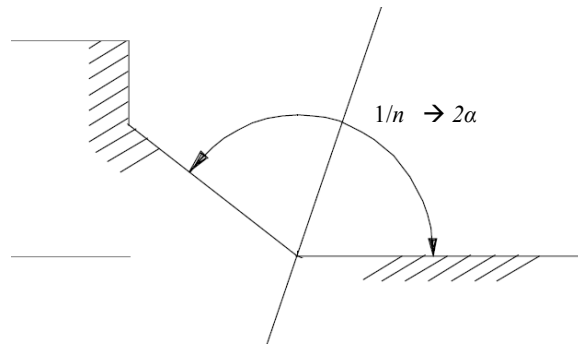


**Figure 3.17.** Definition of weld slope  $1/n$ .

**Table 3.2.** SED values computed at the weld toe and at the weld root as a function of the end weld slope. Values have been computed at the midpoint of the transverse weld.

$n$ [-]	$2\alpha$ [°]	SED [MJ/m <sup>3</sup> ]	
		Toe	Root
4	166	0.01237	0.00434
2	153	0.01873	0.00628
1	135	0.03131	0.01095

The transverse weld slope strongly affects the stress concentration and the SED near the weld toe. The same occurs at the root where the SED value increases with the increase of  $n$ , but never matching the values computed at the toe. This parameter, therefore, has an important role in the joint fatigue classification.

### 3.3.2.6 Evaluation of SED mesh sensitivity under 3D condition

The 3D finite element model above presented has been used here to evaluate the mesh sensitivity of SED. Two highly different levels of mesh refinement have been tested. With reference to the geometry of Figure 3.14, the following Figure 3.18 compares the two mesh refinements in the weld toe regions. The obtained results are summarized in Table 3.3. By comparing results, it can be pointed out that there is a negligible difference on SED value (<1%).

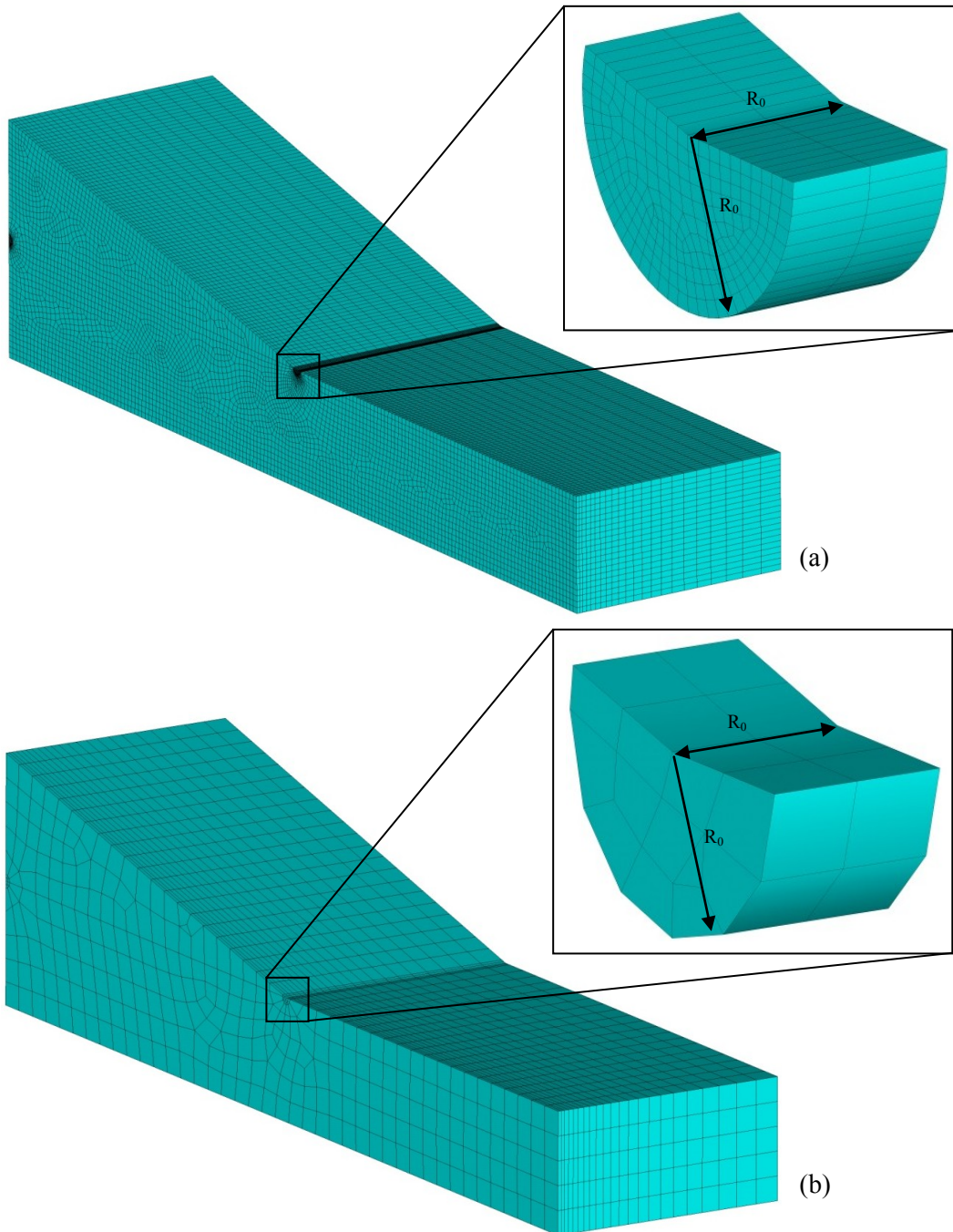


**Figure 3.18.** Detailed views of the weld toe region and corresponding SED control volumes, with reference to the geometry of Figure 3.14. The extremely refined mesh (a) and the coarse one (b) used to evaluate the SED approach mesh sensitivity are shown.

The reduction in computational time provided by the coarse mesh option is remarkable. The SED mesh independence, already mentioned in the literature [17,18], has been here confirmed under 3D conditions.



**Table 3.3.** SED values computed at the weld toe through two different mesh refinements under three-dimensional condition.

Number of FE in the control volume	Number of FE in the whole model	SED [MJ/m <sup>3</sup> ]	$\Delta$ (%)
463	684269	0.0128	//
23	43571	0.0127	-0.78

### 3.3.2.7 Evaluation of the suitability of the 2D plane strain condition

To prove the suitability of the plane strain condition (already mentioned in Section 3.3.2) a 2D finite element model, representing the section of the model shown in Figure 3.14 taken on his longitudinal-vertical plane of symmetry, has been used. Taking advantage of the symmetry, one eighth of the geometry has been modeled. Plane finite elements having quadratic shape functions (named Plane183 in Ansys® library) have been used. A circular control volume having radius 0.28 mm has been placed both at the weld toe and at the weld root (Figure 3.19), according to the SED approach. Contact elements have been introduced inside the plates' gap and a traction stress equal to 56 MPa has been applied to the nominal cross section. It has been observed that the critical point against fatigue is the weld toe and the corresponding computed SED is 0.0124 MJ/m<sup>3</sup>.

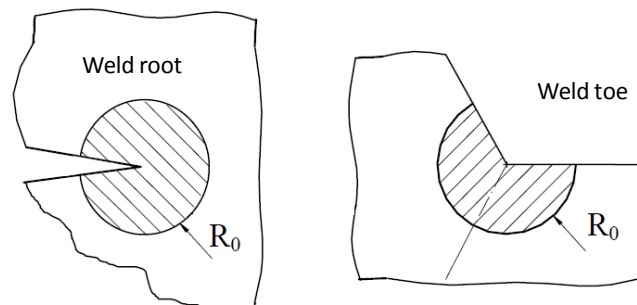


**Figure 3.19.** SED control volumes (areas) at the weld toe and root in plane condition.

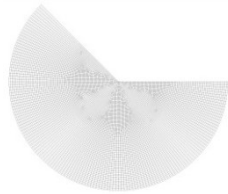
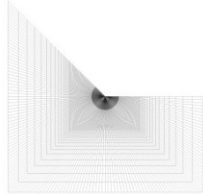
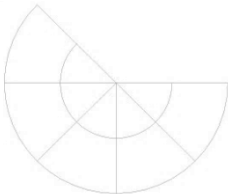
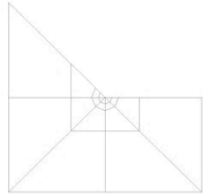
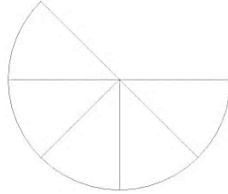
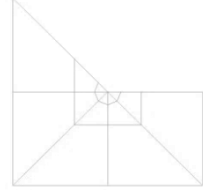
As compared to the SED value computed with the 3D model, the difference is less than 3%, highlighting the suitability of 2D plane strain condition to model the joint under examination. In Section 3.5 further detailed numerical analyses have been reported, assuming plane strain condition.

### 3.3.2.8 Evaluation of SED mesh sensitivity under 2D plane strain condition

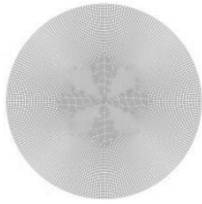
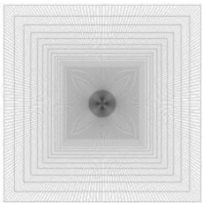
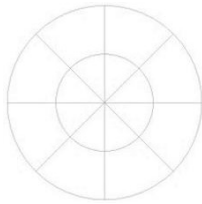
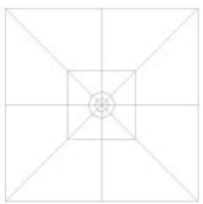
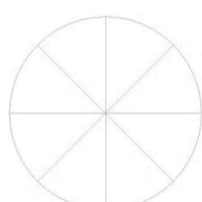
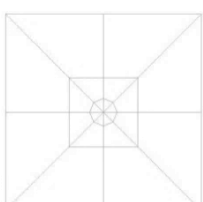
For the sake of completeness, it has been considered of interest to verify the SED mesh independence even under 2D plane strain condition. The bi-dimensional model introduced in the previous section has been here reanalyzed considering three different levels of mesh refinement. Both at the weld root and at the weld toe the SED control volumes have been placed inside two concentric squares, having side equal to 1 mm and 4 mm, respectively. A similar approach to test the SED mesh sensitivity has been adopted by Lazzarin and coworkers [18].

In Tables 3.4 and 3.5 the obtained results are summarized at the weld toe and at the weld root, respectively. The percentages indicate the variation of SED with reference to the values computed with the most refined mesh. The maximum deviations which have been found are 1.51% at the weld toe and 1.12% at the weld root, confirming the substantial mesh independence of the method.

**Table 3.4.** SED values computed at the weld toe through three different mesh refinements under bi-dimensional condition.

Number of FE in the control volume	Weld toe ( $R_0=0.28$ mm)		Number of FE in the model	SED [ $\text{MJ}/\text{m}^3$ ]	$\Delta$ (%)
10543			52304	0.02519	//
10			102	0.02557	1.51
5			87	0.02556	1.47

**Table 3.5.** SED values computed at the weld root through three different mesh refinements under bi-dimensional condition.

Number of FE in the control volume	Weld toe ( $R_0=0.28$ mm)		Number of FE in the model	SED [ $\text{MJ/m}^3$ ]	$\Delta$ (%)
17108			52304	0.00436	//
16			102	0.00440	1.12
8			87	0.00438	0.59

### 3.4 Experimental procedure

On the basis of the preliminary numerical analyses presented in Section 3.3, it has been possible to establish which interesting parameters are to be further investigated through experimental procedure. The following parameters have been selected: the transverse weld slope and the cover plate chamfer. The former has been selected mainly because it strongly affects the fatigue resistance; the latter because, despite not affecting the fatigue strength, it is imposed by standards.

Four series of specimens have been produced and tested. Below the peculiarities of each series are summarized:

*Series 1000:* cover plate geometry according to the Eurocode 3 (class 56 MPa);

*Series 1001:* cover plate having transverse weld slope equal to 1:2 and chamfer;

*Series 1011:* cover plate having transverse weld slope equal to 1:2 and no chamfer;

*Series 1002:* cover plate having transverse weld slope equal to 1:1 (simple fillet weld) and no chamfer.

It should be noted that the specimens of the series 1001 and 1011 differ only in the presence or not of the chamfer, in order to highlight its actual influence. For all four series, a weld throat equal to 0.5 times the thickness of the attached plate has been considered. All the specimens have been made of S355J0 steel and have been manually welded with MIG (Metal Inert Gas) technology. No post weld treatments have been performed. In Section 3.4.4 the workshop drawings of specimens series 1000, 1001, 1011 and 1002 are reported, respectively.

Fatigue tests have been conducted at the Laboratory of Experimental Mechanics of the Department of Engineering and Management (DTG) of the University of Padua, using an MTS 810 250 kN fatigue testing machine. Tests have been performed at room temperature. The loading ratio imposed for all tests is equal to zero. Test results are summarized in Table 3.6.

**Table 3.6.** Fatigue test results obtained on the four series of cover plate specimens.

Specimen	Series 1000		Series 1001		Series 1011		Series 1002	
	$\Delta\sigma$ [-]	$N$ [MPa]	$\Delta\sigma$ [MPa]	$N$ [-]	$\Delta\sigma$ [MPa]	$N$ [-]	$\Delta\sigma$ [MPa]	$N$ [-]
1	200	1.70E+05	130	1.23E+06	200	1,87E+05	200	1,49E+05
2	110	3.00E+06	150	6.73E+05	150	4,13E+05	120	1,02E+06
3	150	4.76E+05	170	6.12E+05	120	1,28E+06	200	1,78E+05
4	120	1.14E+06	200	3.13E+05	110	1,78E+06	150	2,40E+05
5	150	5.86E+05	150	1.04E+06	150	4,93E+05	200	1,57E+05
6	120	1.12E+06	150	1.42E+06	170	2,50E+05	130	4,91E+05
7	110	1.67E+06			200	1,98E+05	150	3,15E+05
8	200	1.71E+05			170	2,86E+05	170	2,25E+05
9	140	6.93E+05			140	5,06E+05	110	7,66E+05
10	200	1.75E+05			120	1,32E+06	110	8,71E+05
11	180	2.65E+05			110	1,99E+06		
12					120	1,27E+06		

The fatigue data were statistically elaborated in accordance with ISO 12107, by using a log-normal distribution and are plotted in Figures 3.20 to 3.23 in a double log scale. All stress ranges are referred to the nominal section. The mean Wöhler curve (probability of survival  $P_s = 50\%$ ) and the Haibach scatter band referred to 10% and 90% of probabilities of survival (for confidence level equal to 95%) are represented through solid lines. The run-out samples, over two million cycles, have not been included in the statistical analysis and are marked with a tilted arrow. The vertical

red line indicates the two million cycles. For the sake of completeness the values of the inverse slope  $k$  and the scatter index  $T_\sigma$  are also shown.

More specifically, Figures 3.20 shows the fatigue data of the 1000 series. The scatter index  $T_\sigma$  is very narrow, being 1.077. The stress range at two million cycles reaches a value of 104.32 MPa and the inverse slope is  $k=3.74$ . Figures 3.21 shows the fatigue data of the 1001 series. The scatter index  $T_\sigma$  is larger, as compared to the previous series, being 1.597. This is probably due to the poor number of tested specimens. The stress range at two million cycles reaches a value of 122.16 MPa and the inverse slope is  $k=3.37$ . Figures 3.22 shows the fatigue data of the 1011 series. The scatter index  $T_\sigma$  is very narrow, being 1.184. The stress range at two million cycles reaches a value of 106.30 MPa and the inverse slope is  $k=3.98$ . Finally, Figures 3.23 shows the fatigue data of the 1002 series. The scatter index  $T_\sigma$  is quite narrow, being 1.39. The stress range at two million cycles reaches a value of 83.33 MPa and the inverse slope is  $k=2.92$ . For all series the inverse slope is inside the range 2~4 as suggested in the literature for welded joints in *as welded* conditions [1]. Moreover, both the Eurocode 3 and the IIW recommendations suggest the use of  $k=3$  for welded cover plates, which is in good agreement with experimental results here reported.

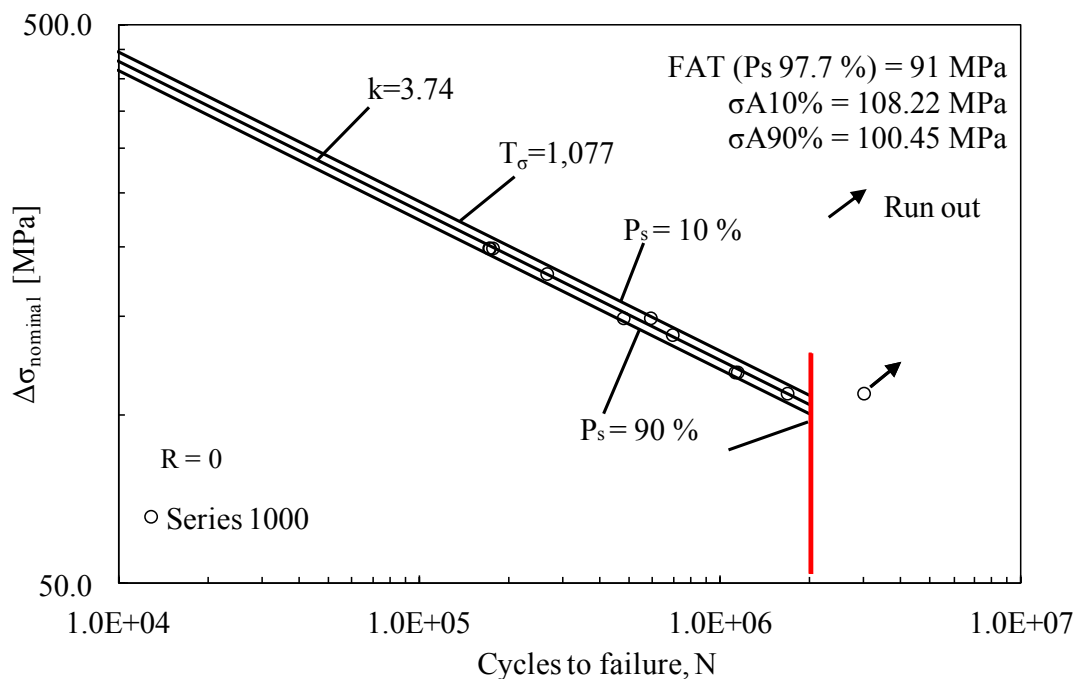


**Figure 3.20.** Fatigue data of specimens 1000 series.

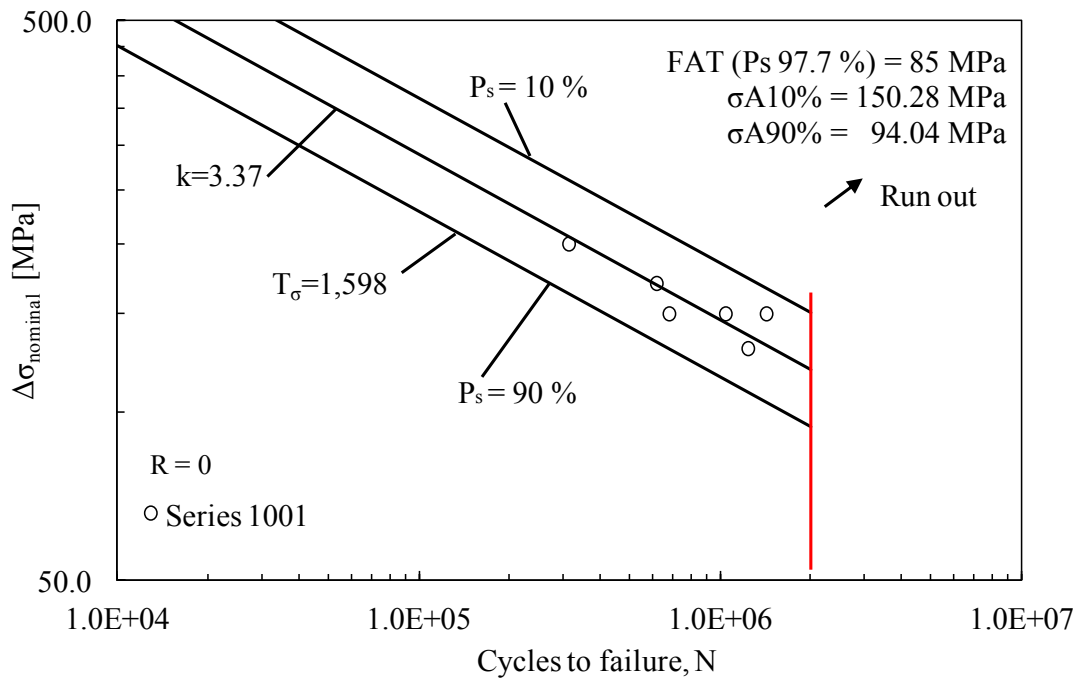


Figure 3.21. Fatigue data of specimens 1001 series.

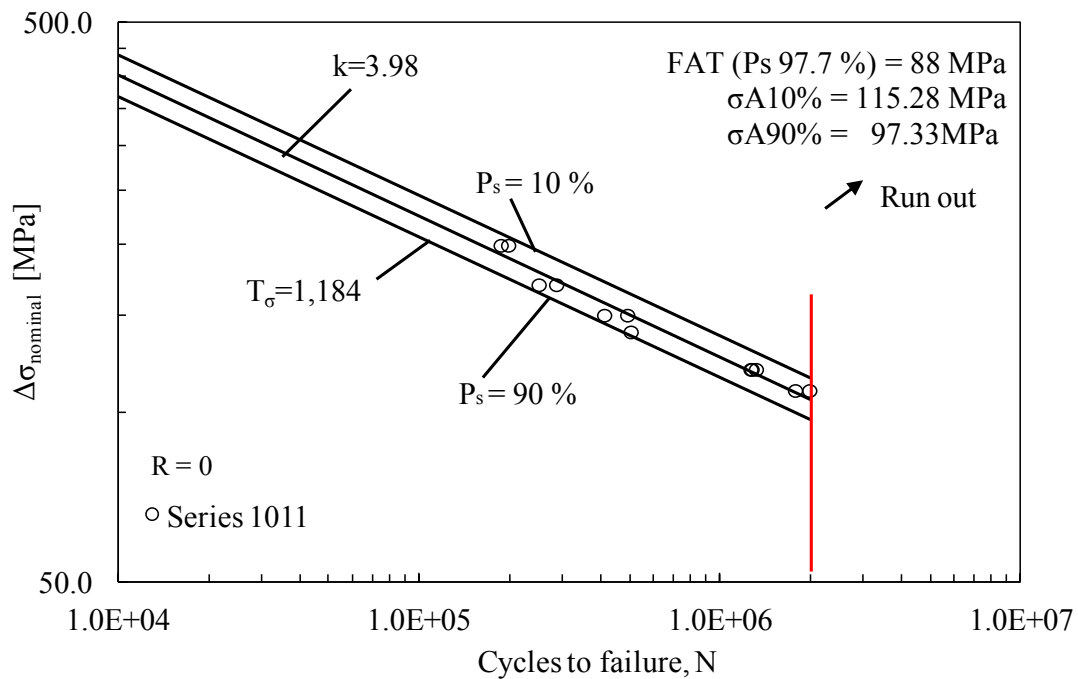
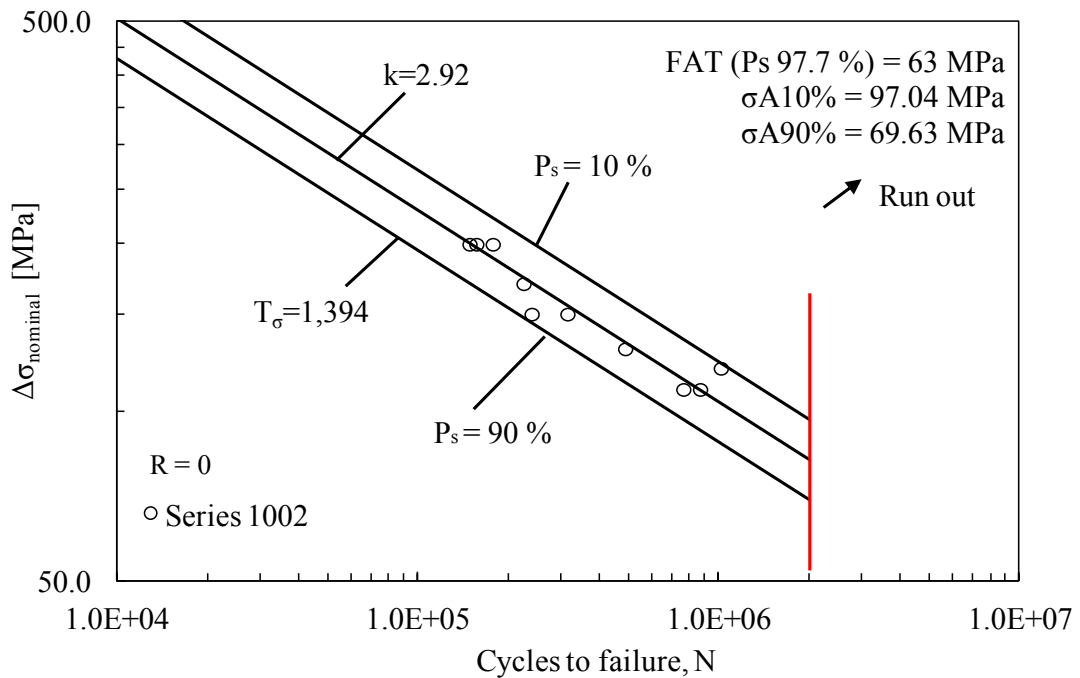


Figure 3.22. Fatigue data of specimens 1011 series.



**Figure 3.23.** Fatigue data of specimens 1002 series.

The fatigue resistance classes (FAT) at 2 million cycles and 97.7% probability of survival are summarized in Table 3.7.

**Table 3.7.** Fatigue strength classes at  $2 \cdot 10^6$  cycles and 97.7% probability of survival obtained on the four series of cover plate specimens.

Series	End weld slope		Cover plate chamfer	Fatigue class
	Ratio	Opening angle $2\alpha$		
	[-]	[°]	[-]	FAT [MPa]
1000	1:4	166	YES	91
1001	1:2	154	YES	85
1011	1:2	154	NO	88
1002	1:1	135	NO	63

### 3.4.1 Analysis of crack initiation causes

The analysis took place in two phases: a macroscopic inspection of the outer appearance of the specimens, to identify any geometric defects, and a microscopic inspection to analyze the metallurgical quality of the base material, as well as the weld bead quality.

Phase 1: the macroscopic analysis showed some faults on the geometrical symmetry. In particular, the two transverse weld toes (on the two faces of the main plate) were found to be misaligned in some cases, resulting in an eccentricity which probably could have influenced the resistance of some specimens due to a secondary bending moment. This feature was more pronounced in the specimens of the 1000 series, with a misalignment which in some cases was found to be up to 5 mm (Figure 3.24). Another defect found is a variation in the transverse weld slope near the toe (Figure 3.29). Such slope grows suddenly, in the proximity of the weld toe, probably leading to a marked increase in local stress with obvious consequences on fatigue resistance.

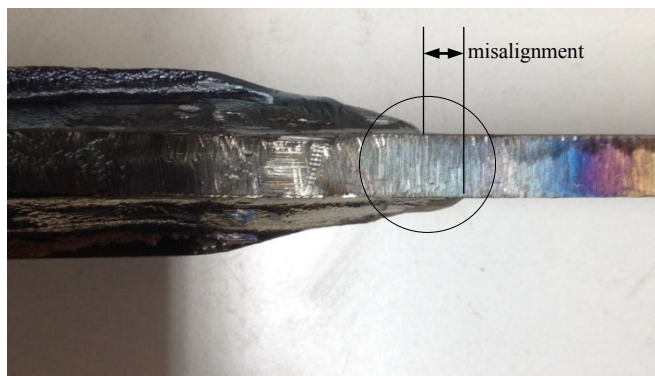


**Figure 3.24.** Picture of a specimen 1000 series. It is evident the transverse weld misalignment.

Phase 2: microscopic analysis required the creation of new specimens from those tested against fatigue (Figure 3.25). The following steps have been performed:

- i) observation of the fracture surface by means of an optical microscope, to detect the area where the crack nucleation occurred (Figure 3.25 and Figure 3.26);
- ii) at the specified point, new specimens (small work-pieces) have been obtained by cutting the broken ones through a lubricated grinding wheel (Figure 3.27);
- iii) the obtained work-pieces have been embedded in a polymeric support (phenolic resin) leaving the surface exposed to be examined and conferring greater handling to the work-pieces;
- iv) polishing of exposed surface. It has been carried out in 6 phases by using a water-cooled abrasive paper disc polisher. Discs with decreasing granulometry have been used, in detail: 180 - 600 - 1200 - 2400. Finally, two additional polishing phases with polycrystalline granule paddle discs of size 6 and 3 microns, respectively, have been performed.



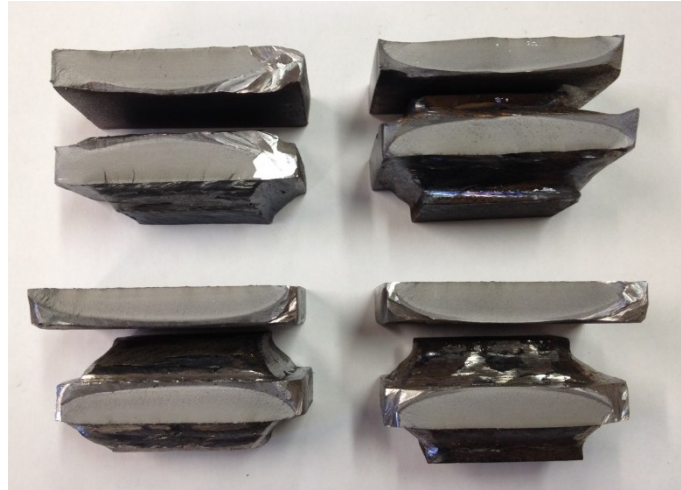


**Figure 3.25.** Specimens fracture surfaces.

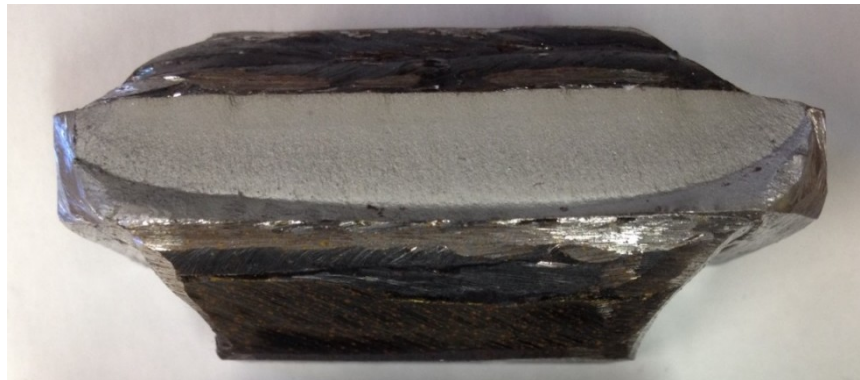


**Figure 3.26.** Detail view of the fracture surface of a specimen 1000 series. The crack propagation surface and the final brittle fractured one are clearly visible.

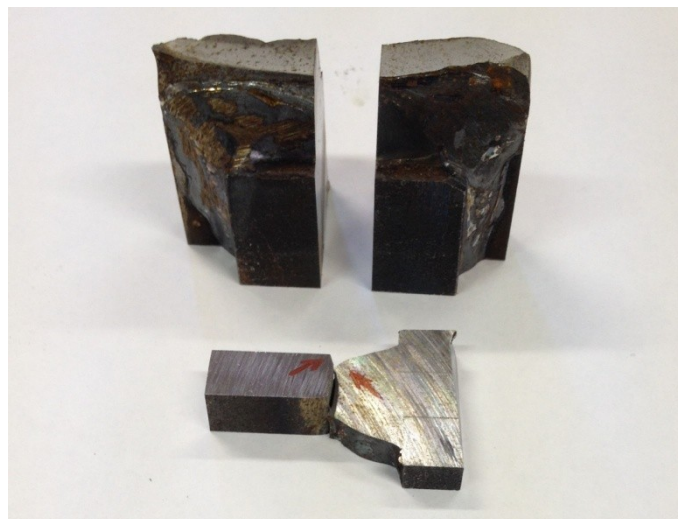


**Figure 3.27.** Work-pieces obtained from fatigue tested specimens through a lubricated grinding wheel.

Once completed, the new specimens showed a correct planarity of the surface, which was suitable for observation by electronic microscope (Figure 3.28). Four specimens have been prepared and analyzed (one for each series) (Figure 3.29).

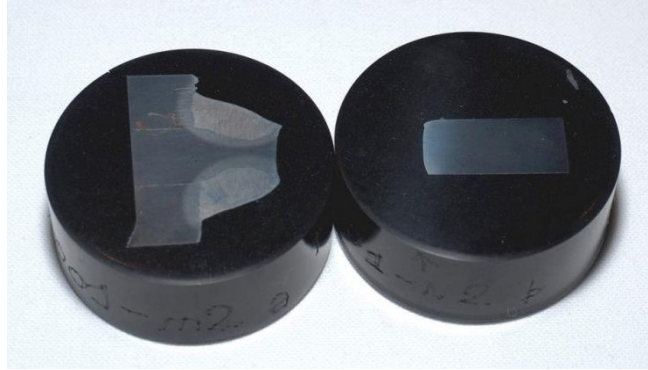


**Figure 3.28.** Work-pieces, taken from 1010 series, embedded in a polymeric support, polished and ready for observation by electronic microscope.

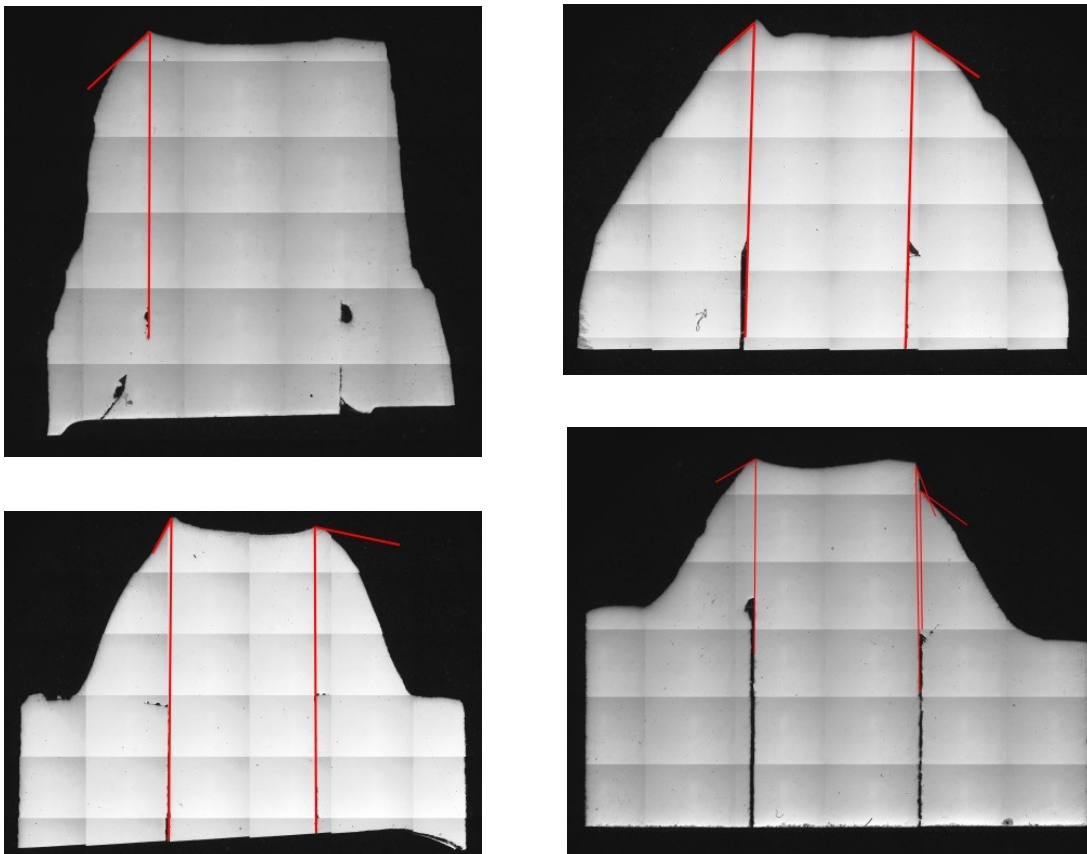


**Figure 3.29.** Images obtained by electronic microscope (x25 magnification). From the top left and clockwise, sections of 1000, 1001, 1011 and 1002 series. Red lines indicate the local weld slope in the proximity of the weld toe.

By means of the digital interface of the instrument, detailed panoramic photos of the surface of the specimens have been obtained and the transverse weld slope in the proximity of the weld toe has been measured on both faces of the plates. Such angles are listed in Table 3.8. In all the investigated specimens a strong difference between the average (design) slope and the local slope at the weld toe has been found. The extension in height of the local slope has been evaluated at most equal to 2 mm.

**Table 3.8.** Measured weld slopes in the proximity of the crack initiation point and on the opposite side.

Specimen series	Local weld slope [°]	
	Crack side	Opposite side
1000	47.05	//
1001	56.54	46.55
1011	77.91	27.87
1002	59.24	20.18

The same specimens have then been used for a metallographic analysis: through chemical etching of their surface, made with Nittel3 (3% HNO<sub>3</sub> solution in ethyl alcohol), the crystalline structure of the material has been highlighted (Figure 3.30). In general, the material did not exhibit noteworthy features, showing a proper dendrites conformation inside the beads and the heat altered zones (detail pictures in Section 3.4.3). Some shortage of fusion has been found near the weld roots but was not a reason or fatigue failure (Figure 3.31), which always happened at the toe. Finally, some cracks nucleated but not propagated have been observed (Figure 3.32).

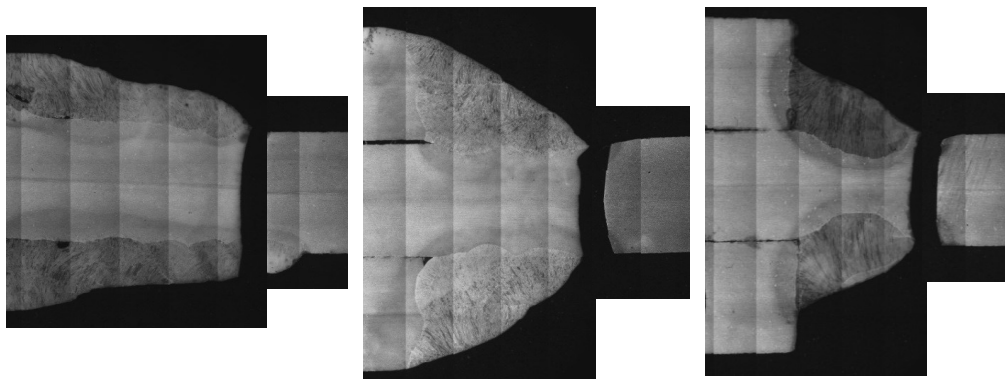


**Figure 3.30.** Images obtained by electronic microscope (x25 magnification) after chemical etching. From left to right sections of 1000, 1001 and 1011 series.

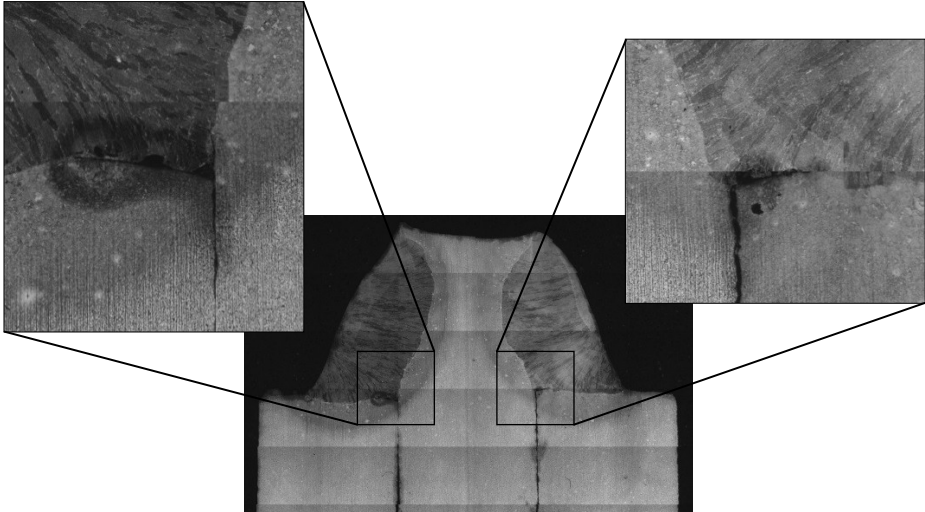


**Figure 3.31.** Example of lack of fusion at the weld root. Specimen from 1011 series (25x).

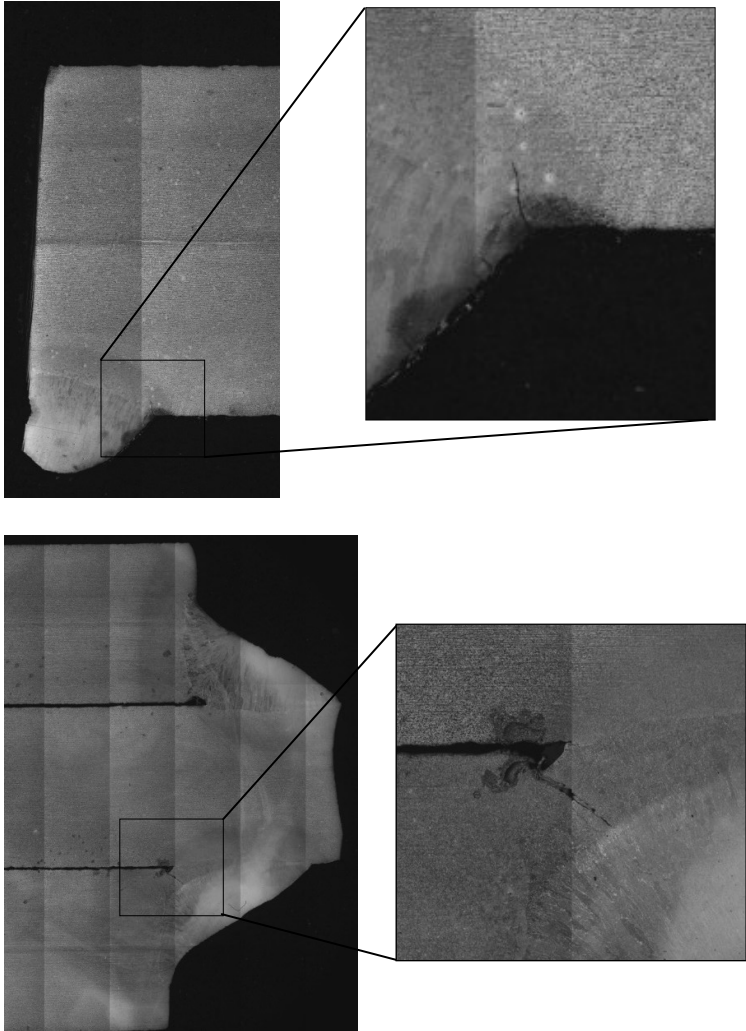


**Figure 3.32.** Example of crack nucleated but not propagated to fracture. From the top: 1000 series, crack of length 0.6 mm nucleated at the weld toe; 1002 series, crack of length 1.3 mm nucleated at the weld root.

### 3.4.2 Discussion on experimental results

According to the observed results, it first of all appears that the fatigue class (56 MPa) assigned by the Eurocode 3 to the specimen geometry 1000 series is conservative: it corresponds to about 60% of the resistance obtained here through tests. On the other hand, the results obtained also for the other tested geometries exceed the value of 56 MPa. The comparison between the 1001 and 1011 series shows that the presence of the cover plate chamfer does not give any benefit: almost the same fatigue resistance classes have been here obtained. Finally, the 1002 series, having a simple fillet weld with slope 1:1, demonstrates a significantly lower resistance, highlighting the importance of the transverse weld slope on the fatigue behavior of cover plates. At the same time, it can be seen that the complication of the geometry required by Eurocode 3 may not be fully justified, since results of the first three series are comparable.

#### 3.4.2.1 Scale effect evaluation on experimental results

It is important to notice that the considerations made here apply, in principle, to the tested specimens, which have thickness of plates equal to 10 mm. No scale effect has been up to now adopted. The fatigue class supplied by Eurocode 3 instead does not vary according to the thickness, suggesting that the scale effect is already taken into account in the proposed fatigue class.

From the experimental data it is possible to determine the fatigue classes by varying the thicknesses, applying a scale effect according to the following equation [19]:

$$\sigma_{nom,b} = \sigma_{nom,a} \left( \frac{t_a}{t_b} \right)^{1-\lambda_1} \quad (3.1)$$

where  $\lambda_1$  is the first *eigenvalue* of Williams' solution for sharp V-notches, as presented in Chapter 2,  $t$  is the main plate thickness,  $\sigma_{nom}$  is the endurable nominal stress, subscripts  $a$  and  $b$  indicate two specimens geometrically scaled to each other.

In Table 3.9 fatigue classes, as a function of the main plate thickness, evaluated by applying Equation (3.1) to classes experimentally obtained, are listed. It has been assumed that the main plate is equal to the attached plate and that both vary among 20 and 50 mm. What is to be noted is that the fatigue class associated with the geometries of the first three series is kept at a higher value than the one provided by

the Eurocode 3. However, the 1002 series shows a fatigue resistance lower than 56 MPa, already for thicknesses of 20 mm.

**Table 3.9.** Measured weld slopes in the proximity of the crack initiation point and on the opposite side.

Series	$1-\lambda_I$	Plates thickness [mm]				
		10	20	30	40	50
		FAT				
1000	0.132	91	83	79	76	74
1001	0.245	85	72	65	61	57
1011	0.245	88	74	67	63	59
1002	0.326	63	50	44	40	37

### 3.4.3 Micrographic analysis

In order to verify if defects in the base material or in the welding bead were present, 200 magnification micrographs have been made. The following five characteristic areas have been investigated (Figure 3.33):

- (1) Base material
- (2) Base material among welds
- (3) Heat altered zone (HAZ)
- (4) Transition area among HAZ and welds
- (5) Weld bead

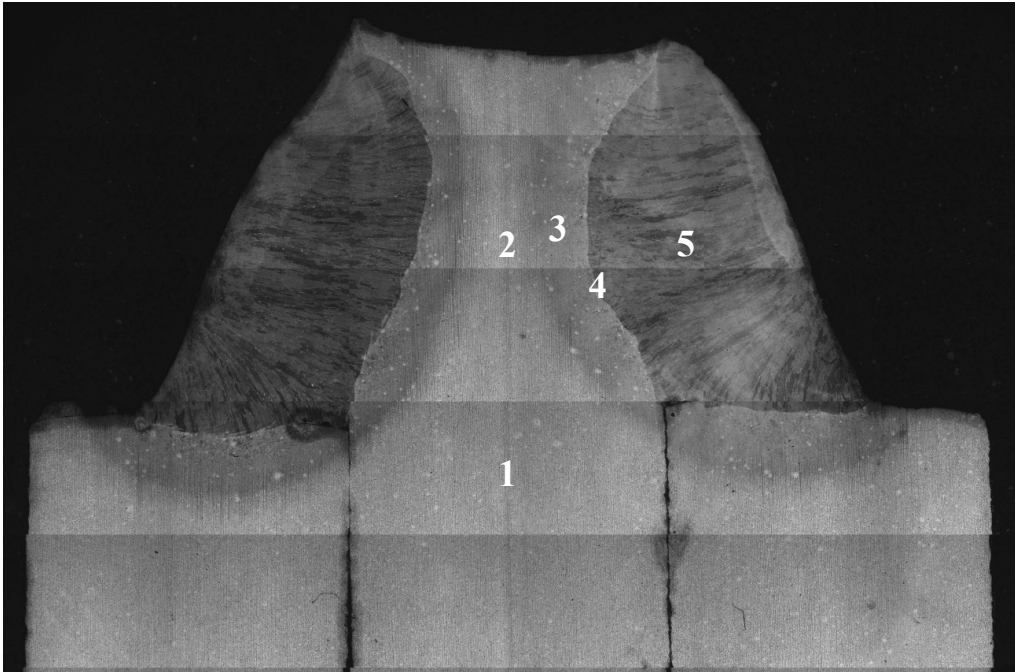


**Figure 3.33.** Position of obtained micrographs. Image at 25x, from 1011 series.



No defects, such as hot or cold cracks, glues or inclusions (solid or gaseous) have been observed. Figures 3.34 to 3.38 show in detail the aforementioned pictures.

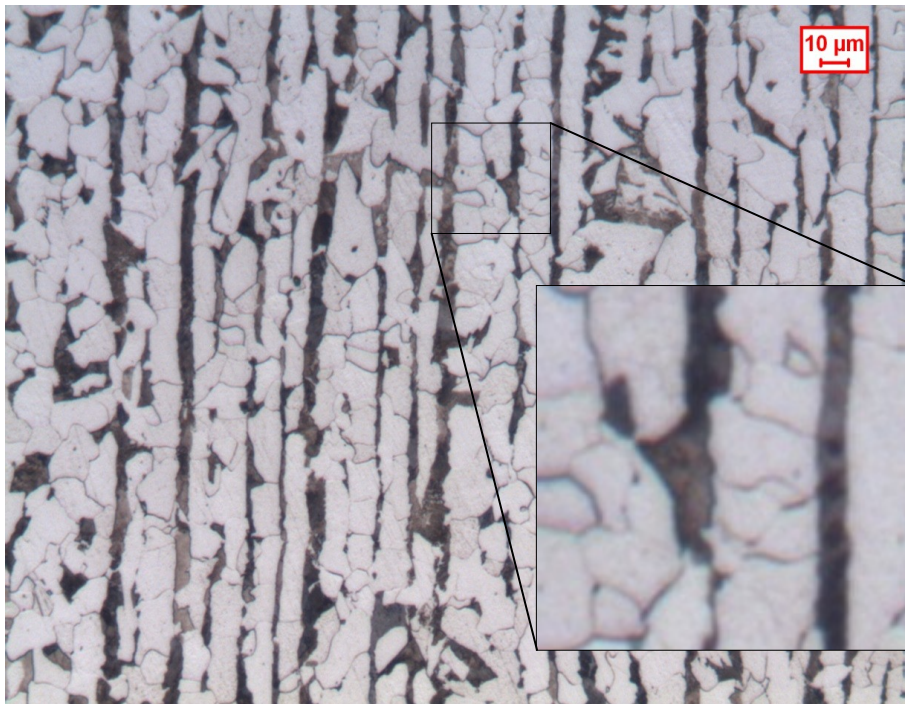


**Figure 3.34.** Micrograph of the base material at 200x. Ferritic grains and pearlitic bands are visible, which indicate the rolling direction. Sulfur compounds are circular, as expected.

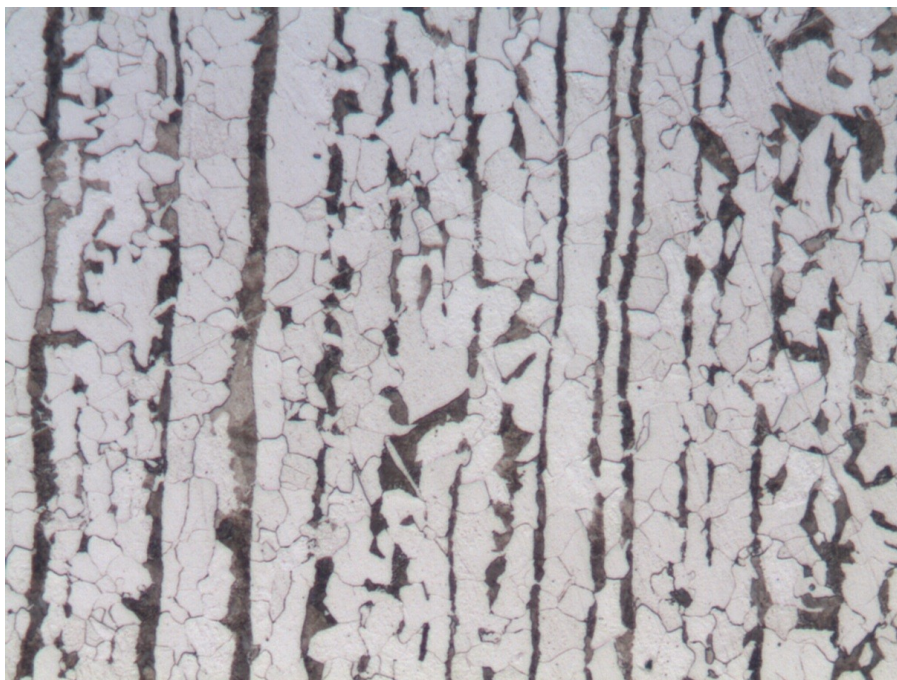


**Figure 3.35.** Micrograph of the base material among welds at 200x. A slight increase in ferritic grains is appreciable.





**Figure 3.36.** Micrograph of the interface between HAZ and base material at 200x. A dense segregation of pearlite and ferrite, due to the rapid cooling, is appreciable.

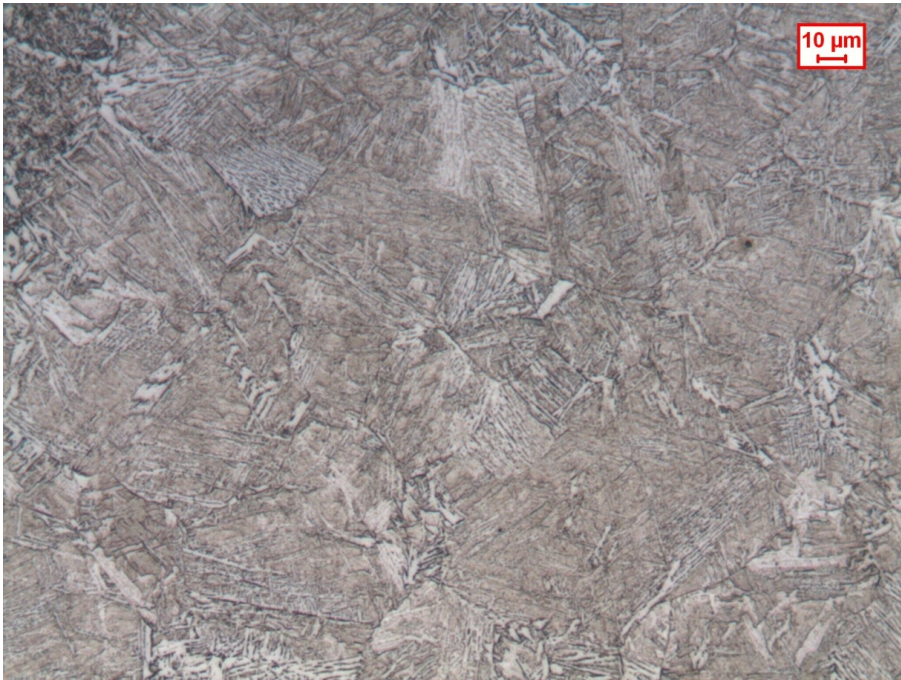


**Figure 3.37.** Micrograph of the HAZ at 200x. Pearlite has a lamellar shape, as expected.



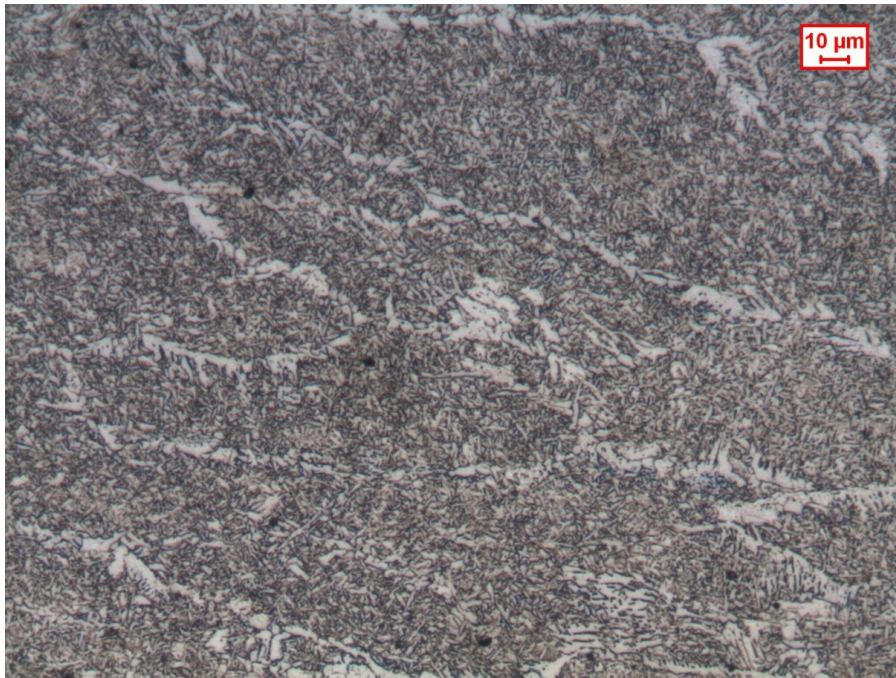


**Figure 3.38.** Micrograph of the weld bead at 200x. Some grains of ferrite rounded by martensite are visible.

### 3.4.4 Workshop drawings of tested specimens

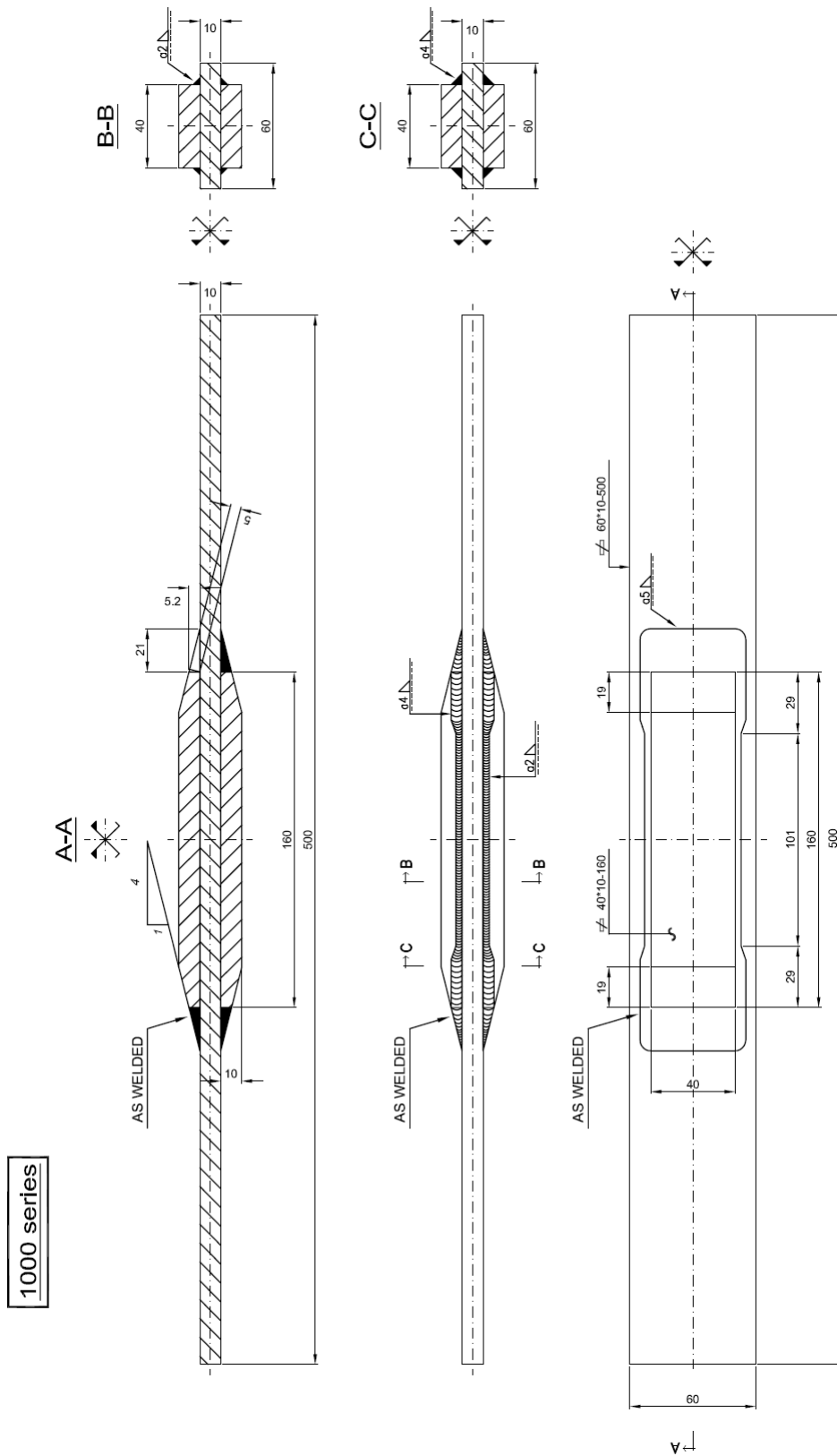


Figure 3.39. Workshop drawing of specimens 1000 series.

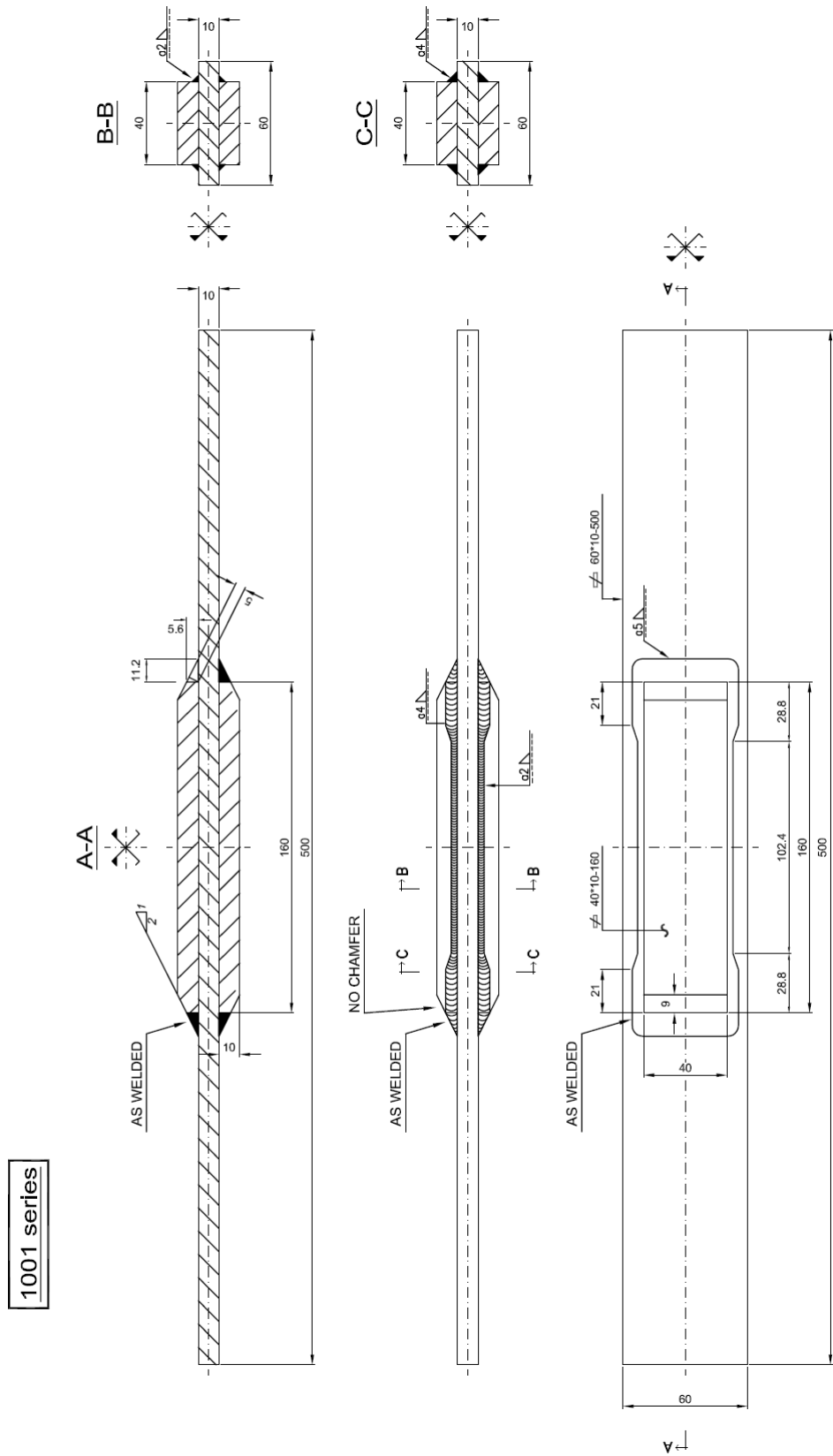


Figure 3.40. Workshop drawing of specimens 1001 series.

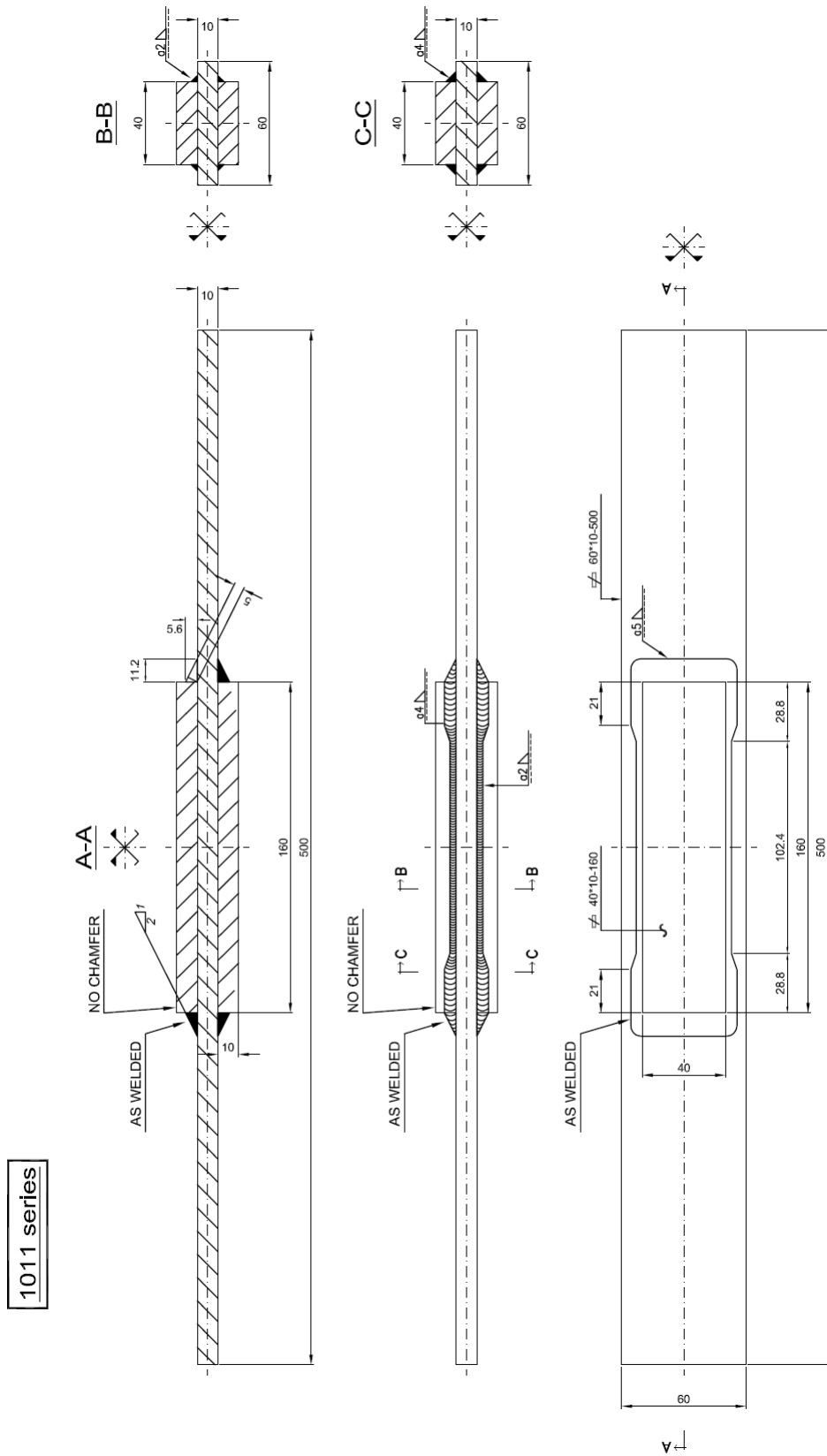


Figure 3.41. Workshop drawing of specimens 1011 series.

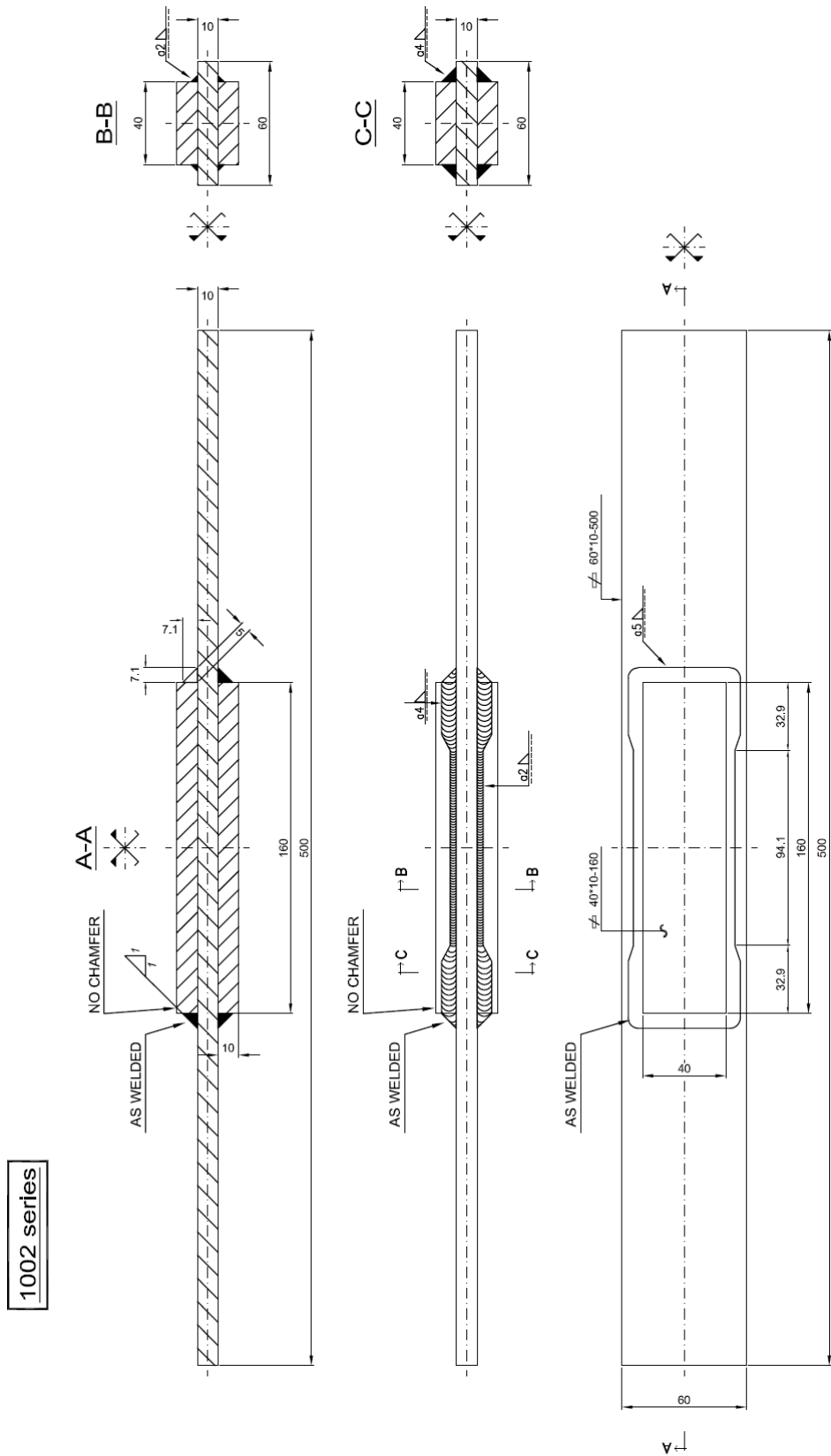
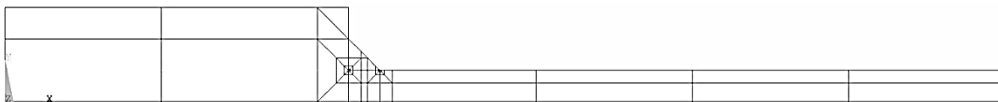


Figure 3.42. Workshop drawing of specimens 1002 series.

### 3.5 Detailed numerical analyses

The aim of the here presented numerical analyses is characterizing the effect of macroscopic defects identified in Section 3.4.1 on the specimens fatigue resistance. Particular focus has been given to the effect of the local weld slope variation at the weld toe and to the effect of the welds misalignment. The influence of the ratio between main plate thickness and attached plate thickness has been also investigated. Once proved the suitability of the plane strain condition (see Section 3.3.2.7) to assess the fatigue behavior of joints under investigation, 2D models representing the plane transverse section located at the crack initiation point have been produced. An example of model is shown in Figure 3.43.



**Figure 3.43.** Example of 2D plane strain FE model of 1002 series.

The following Table 3.10 shows the calculated SED values, at the weld toe and root, for the geometries of the 4 series of specimens. A nominal stress equal to 56 MPa has been considered.

**Table 3.10.** Computed SED values and control volume areas, as a function of specimens series.

Series	Notch opening angle $2\alpha$ [°]	SED [MJ/m <sup>3</sup> ]		Control volume areas [mm <sup>2</sup> ]	
		Toe	Root	Toe	Root
1000	166	0.01237	0.00434	0.1328	0.2456
1001	153	0.01873	0.00628	0.1413	0.2456
1011	153	0.01872	0.00597	0.1413	0.2456
1002	135	0.03131	0.01095	0.1539	0.2456

Results are fully comparable to those found in the preliminary analysis. Moreover, comparing 1001 series and 1011 series, it is possible to appreciate how, in the latter, the chamfer absence does not reduce the fatigue resistance in terms of SED at the weld toe. On the other hand, a slight increase in SED has been found at the weld root. However, the weld toe remains the critical point against fatigue, being characterized by a value of SED about three times larger than the one at the root.

### 3.5.1 Effect of plates thickness ratio

The influence of the ratio between the thickness of the attached plate  $t_c$  and the thickness of the main plate  $t$  has been investigated by keeping  $t$  equal to 10 mm and varying  $t_c$ . The range of variation chosen for the ratio  $t_c/t$  is from 0.5 to 1.5. Such range is compatible with the usual cover plates applications in steel bridges. In terms of SED computed at the weld toe, what emerged is a slight dependence of fatigue resistance on  $t_c/t$  (Figure 3.44).

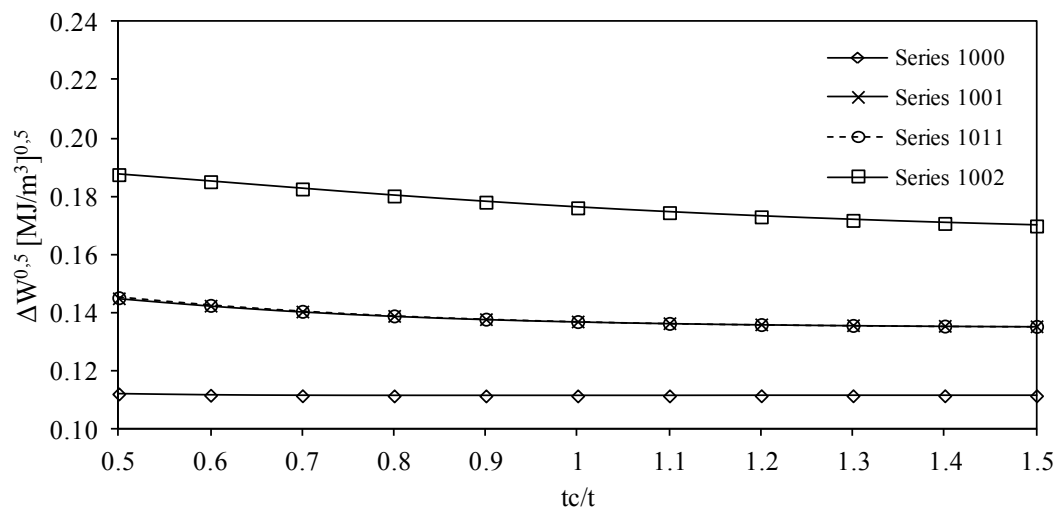


**Figure 3.44.** Trend of the square root of SED, at the weld toe, as a function of plates thickness ratio  $t_c/t$ , with  $t$  fixed to 10 mm.

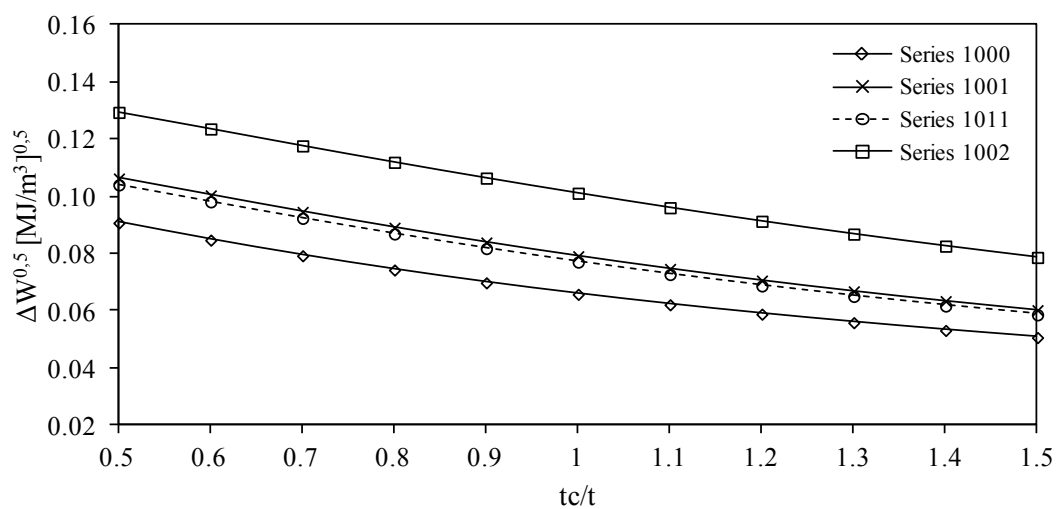


**Figure 3.45.** Trend of the square root of SED, at the weld root, as a function of plates thickness ratio  $t_c/t$ , with  $t$  fixed to 10 mm.

In detail, a substantial SED independence of  $t_c/t$  has been found with reference to 1000 series, characterized by a transverse weld slope 1:4; whereas a slight dependence of SED on  $t_c/t$  has been found with reference to 1001, 1011 and 1002 series, characterized by transverse weld slopes 1:2 to 1:1. On the other hand, a marked dependence has been always found at the weld root (Figure 3.45). Nevertheless, comparing Figures 3.44 and 3.45 it is possible to point out that SED computed at the weld root is always lower than the one computed at the weld toe. Figures 3.44 and 3.45 plot the square root of the SED, being this parameter directly comparable (proportional) to a stress value, on the contrary of SED, which depends on the square of stress.

For the sake of completeness, the same comparisons have been made for  $t$  equal to 20, 30, 40 and 50 mm. It has been observed that this parameter causes SED changes coincident with those due to the scale effect which can be estimated through Equation (3.1). Dealing with the cover plate geometry of the 1000 series there is total independence of  $t_c/t$ , thus agreeing with the unique classification provided by the Eurocode 3, which does not provide a variable fatigue class depending on  $t_c/t$  if a transverse weld slope 1:4 is assumed. Furthermore, the slight dependence of SED on  $t_c/t$ , which has been found at the weld toe with reference to 1001, 1011 and 1002 series considering  $t = 10$  mm, tends to vanish by increasing  $t$  (Figure 3.46). It is not the same at the weld root, where the dependence on  $t_c/t$  is still appreciable (Figure 3.47).

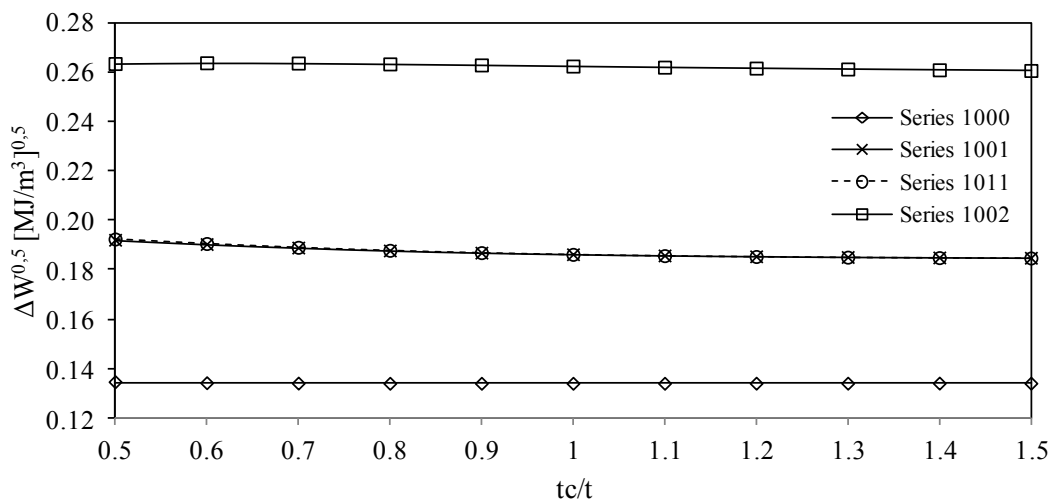


**Figure 3.46.** Trend of the square root of SED, at the weld toe, as a function of plates thickness ratio  $t_c/t$ , with  $t$  fixed to 40 mm.



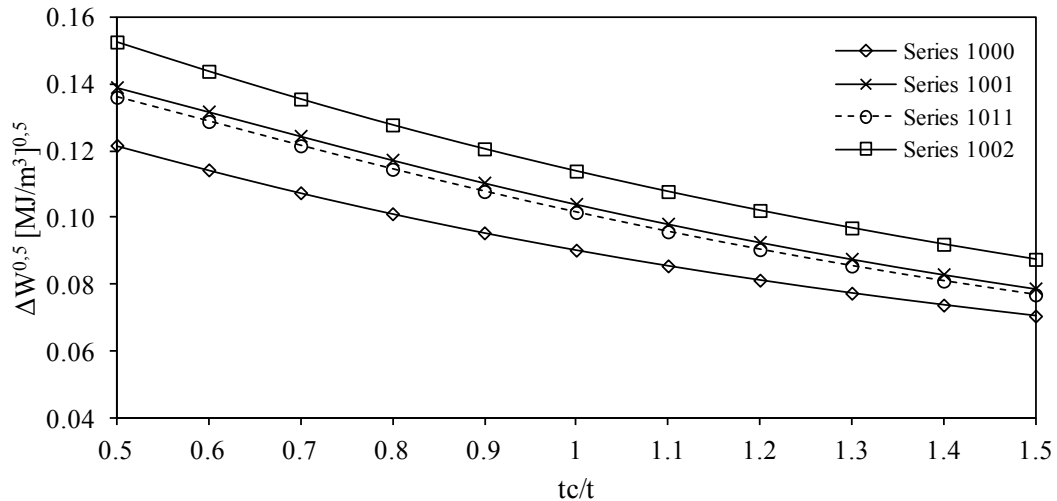


**Figure 3.47.** Trend of the square root of SED, at the weld root, as a function of plates thickness ratio  $t_c/t$ , with  $t$  fixed to 40 mm.

### 3.5.2 Effect of the local weld toe slope

To model this feature it has been assumed that the local weld slope, in the proximity of the weld toe, corresponds to  $45^\circ$  (1:1). This choice is, of course, an approximation, because the measured local weld slopes differ from specimen to specimen. In some cases, a local slope sensibly larger or lower than  $45^\circ$  has been measured; however, the assumption made here seems reasonable, with the purpose to keep the application of the SED approach simple by excluding the large number of process parameters that could affect such local slope in actual welds. Then, the effect of the height  $h$  of the affected local slope at the weld section has been investigated series by series. Figure 3.48 shows an example of the adopted finite element models.

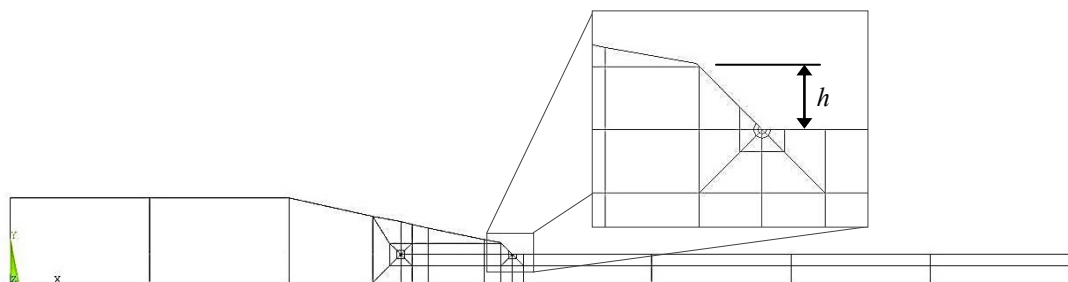


**Figure 3.48.** Example of 2D plane strain FE model of 1001 series and detail of the locally increased weld slope.

It should be noted that such local slope modification at the weld toe does not affect specimens of 1002 series, being for this series the average slope of the transverse weld equal to  $45^\circ$  and equal to the local one. Table 3.11 shows the SED values obtained by varying  $h$  in the range from 0.5 mm to 2.0 mm. Such range has been considered of interest, because comparable with the one measured on specimens.

**Table 3.11.** Computed SED values [ $\text{MJ}/\text{m}^3$ ] as a function of the height  $h$  of the local weld toe slope (assumed to be equal to  $45^\circ$ ).

$h$ [mm]	Series 1000		Series 1001		Series 1011	
	Toe	Root	Toe	Root	Toe	Root
0.50	0.01621	0.00395	0.02154	0.00591	0.02154	0.00561
1.00	0.01933	0.00358	0.02369	0.00560	0.02370	0.00532
1.50	0.02124	0.00324	0.02491	0.00535	0.02493	0.00508
2.00	0.02254	0.00294	0.02571	0.00516	0.02573	0.00490

Observing Table 3.11, a strong influence of local toe geometry on SED can be found. In detail, such influence is greater in 1000 series, indicating that as the notch opening angle  $2\alpha$  increases, the sensitivity to geometrical defects localized at the weld toe increases as well. By comparing 1001 and 1011 series, the uselessness of the cover plate chamfer is highlighted once again. Table 3.12 shows the percentage variations of SED, with respect to Table 3.10 (where no increased slope has been considered).

**Table 3.12.** Percentage SED variations with respect to Table 3.10, as a function of the height  $h$  of the local weld toe slope (assumed to be equal to  $45^\circ$ ).

$h$ [mm]	Series 1000		Series 1001		Series 1011	
	$\Delta\%$ Toe	$\Delta\%$ Root	$\Delta\%$ Toe	$\Delta\%$ Root	$\Delta\%$ Toe	$\Delta\%$ Root
0.50	31.0	-9.1	15.0	-5.9	15.1	-6.0
1.00	56.3	-17.6	26.5	-10.8	26.6	-10.9
1.50	71.7	-25.3	33.0	-14.8	33.2	-14.9
2.00	82.2	-32.2	37.3	-17.9	37.4	-17.9

### 3.5.3 Effect of transverse welds misalignment

The transverse welds misalignment causes, in principle, a secondary bending stress, which can be detrimental for fatigue resistance. The magnitude of this phenomenon

is not only dependent on the magnitude of the defect, but also on the overall dimensions of specimens and on the type of constraint applied by the testing machine. Finite element models, which reproduce the whole longitudinal section of specimens and the type of constraint at the machine grips, have been produced. Bead 1 and bead 2 have been defined, respectively, as the upper bead, considered as reference, and the lower one, which is moved forward so as to cause the misalignment (see Figure 3.49).

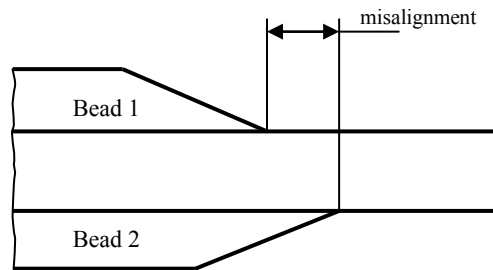


**Figure 3.49.** Definition of bead 1, bead 2 and misalignment.

In order to check the suitability of the model, the trend of stress  $\sigma_x$  through the thickness of the main plate has been investigated. Stress  $\sigma_x$  has been computed at 3 different transverse sections placed at coordinate  $x$  (reference in Figure 3.50) equal to 10 mm, 70 mm and 155 mm. Figure 3.50 shows, as an example, the 1000 series geometry with an eccentricity of 4 mm. As expected, by approaching the weld toe, through-thickness stress  $\sigma_x$  changes from pure membrane to a sum of membrane and bending stresses.

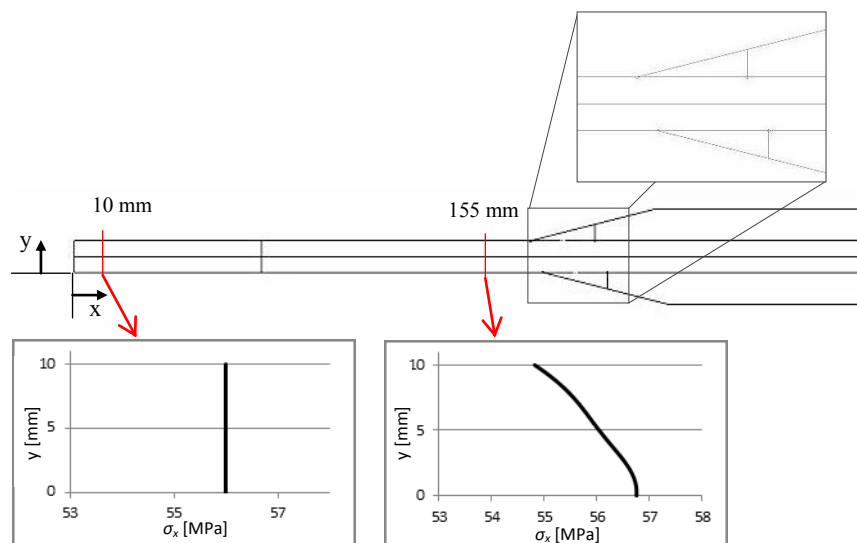


**Figure 3.50.** Through-thickness stress variation in the longitudinal direction, due to the presence of a secondary moment induced by the welds misalignment.

Table 3.13 shows the SED values obtained ranging the misalignment from 1 to 4 mm. What was observed in terms of stress has been confirmed in terms of SED at the weld toe. Dealing with the weld root, the bead 1 has shown a decreasing trend of SED with the increase of the misalignment, whereas the bead 2 has shown the opposite trend. Such behavior is much marked in the case of large opening angles, but does not represent any issue, being the SED at the weld toe of the bead 1 always the largest one. Table 3.14 shows the percentage SED variations, with respect to Table 3.10 (where no misalignment is present). The most critical points in terms of SED have been listed for each series: the weld toe of the bead 1 and the weld root of the bead 2.

**Table 3.13.** Computed SED values, both at the weld toe and at the weld root, as a function of the misalignment.

Misalignment [mm]	Series 1000 SED [MJ/m <sup>3</sup> ]				Series 1001 SED [MJ/m <sup>3</sup> ]			
	Bead 1		Bead 2		Bead 1		Bead 2	
	Toe	Root	Toe	Root	Toe	Root	Toe	Root
1,00	0.0128	0.0045	0.0120	0.0056	0.0203	0.0066	0.0176	0.0088
2,00	0.0134	0.0040	0.0117	0.0062	0.0221	0.0054	0.0166	0.0103
3,00	0.0140	0.0036	0.0115	0.0069	0.0240	0.0047	0.0159	0.0119
4,00	0.0147	0.0032	0.0114	0.0076	0.0262	0.0041	0.0154	0.0138

Misalignment [mm]	Series 1011 SED [MJ/m <sup>3</sup> ]				Series 1002 SED [MJ/m <sup>3</sup> ]			
	Bead 1		Bead 2		Bead 1		Bead 2	
	Toe	Root	Toe	Root	Toe	Root	Toe	Root
1,00	0.0203	0.0059	0.0175	0.0084	0.0360	0.0110	0.0289	0.0151
2,00	0.0221	0.0050	0.0166	0.0099	0.0403	0.0095	0.0263	0.0177
3,00	0.0241	0.0043	0.0159	0.0116	0.0449	0.0083	0.0243	0.0204
4,00	0.0263	0.0038	0.0154	0.0135	0.0497	0.0075	0.0228	0.0231

**Table 3.14.** Percentage SED variations with respect to Table 3.10, as a function of the misalignment. Labels (1) and (2) stay for bead 1 and bead 2, respectively.

Misalignment [mm]	Series 1000		Series 1001		Series 1011		Series 1002	
	Δ%	Δ%	Δ%	Δ%	Δ%	Δ%	Δ%	Δ%
	Toe (1)	Root (2)	Toe (1)	Root (2)	Toe (1)	Root (2)	Toe (1)	Root (2)
1.00	3.8	29.2	8.4	40.0	8.5	40.9	15.0	38.3
2.00	8.3	43.7	17.8	63.9	17.9	66.4	28.8	61.3
3.00	13.3	58.9	28.4	90.3	28.6	95.0	43.6	86.0
4.00	18.6	74.5	40.1	119.1	40.3	126.1	58.7	111.1

### 3.6 SED based summary of experimental results

Once the influence of geometric defects has been determined (Section 3.5.2 and Section 3.5.3), four finite element models have been created, one for each series, which represent a sort of "average" specimen for each of them. From a sample analysis on broken specimens, considering five specimens for each series, the following assumptions have been considered to be suitable to represent the "average" specimen for each series:

- Height  $h$  of the local increased slope at the weld toe: 1 mm for all series.
- Misalignment of transverse welds: 4 mm for 1000 series, 2 mm for 1001 and 1011 series, 1.5 mm for 1002 series.

In this way a representative SED value has been computed for each series, assuming a nominal stress equal to 56 MPa as loading condition. The radius of the control volume has been assumed equal to 0.28 mm, according to the SED approach for steel welded joints. Results are listed in Table 3.15 for both bead 1 and bead 2.

**Table 3.15.** Computed SED values, both at the weld toe and at the weld root, considering an "average" specimen for each series. Percentage SED variations are also provided with respect to Table 3.10. Labels (1) and (2) stay for bead 1 and bead 2, respectively.

Series	SED [MJ/mm <sup>3</sup> ]				$\Delta\%$ Toe (1)	$\Delta\%$ Root (2)
	Bead 1		Bead 2			
	Toe	Root	Toe	Root		
1000	0.0242	0.0027	0.0162	0.0060	95.6	39.1
1001	0.0285	0.0048	0.0204	0.0091	52.2	45.8
1011	0.0285	0.0044	0.0204	0.0088	52.5	48.0
1002	0.03812	0.0102	0.0275	0.0164	21.8	49.5

The SED value related to each broken specimen can be computed, series by series, from values listed in Table 3.15, through the following proportion:

$$\frac{\sqrt{\Delta\bar{W}_{FEM}}}{56MPa} = \frac{\sqrt{\Delta\bar{W}_{SPECIMEN}}}{\Delta\sigma_{SPECIMEN}} \quad (3.2)$$

in which, series by series,  $\Delta\bar{W}_{FEM}$  are the SED values computed through the "average" finite element model and listed in Table 3.15, whereas  $\Delta\bar{W}_{SPECIMEN}$  are the SED values corresponding to the nominal stress  $\Delta\sigma_{SPECIMEN}$  applied during testing.

By doing so, it has been possible to obtain a double log scale diagram  $\overline{\Delta W} - N$  (Figure 3.51), where  $N$  is the number of cycles to failure (assumed to be the crack initiation) for each specimen. It is possible to observe in Figure 3.51 that the inverse slope  $k$  is equal to 1.64 and the scatter index related to the two curves with probabilities of survival  $P_s=2.3\%$  and  $97.7\%$  has been found equal to 2.50, which returns a scatter index  $T_\sigma=1.58$  when reconverted to an equivalent local stress range. For the sake of completeness, SED range values referred to 2 million cycles are reported in the figure. Thanks to the SED approach it has been possible to summarize in a single scatter band all the fatigue data, regardless of the specimen geometry.

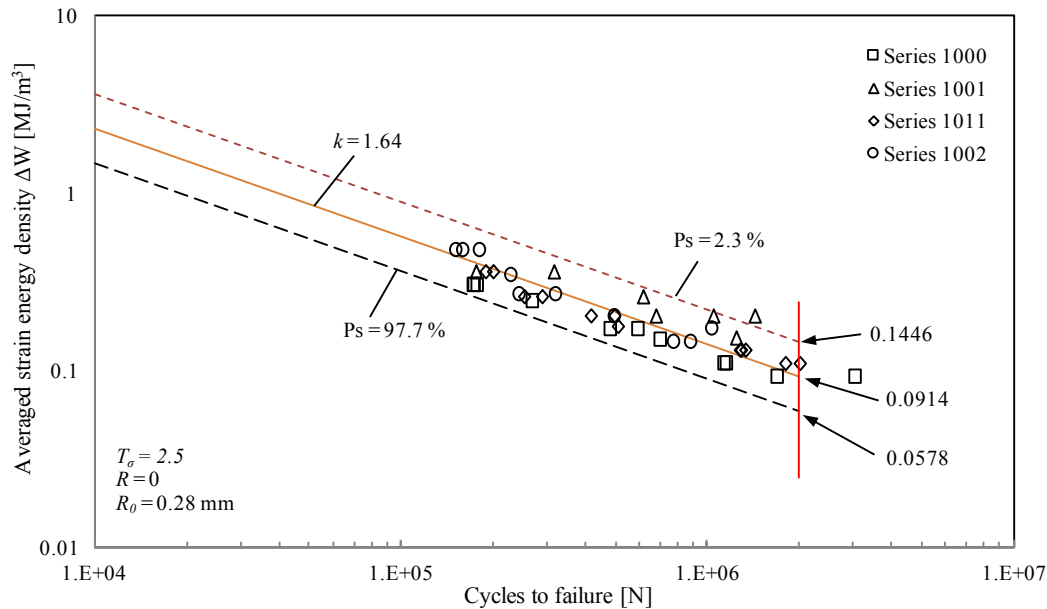


**Figure 3.51.** SED based summary of fatigue test data related to steel cover plates. Control volume radius  $R_0=0.28$  mm; loading ratio  $R=0$ ; testing condition *as welded*.

Finally, Figure 3.52 shows that all experimental data fit well inside the SED based design scatter band proposed by Lazzarin and coworkers [20] and presented in Section 2.3.2. The suitability of the SED approach and of the related design curve to perform the fatigue assessment of welded cover plates has, therefore, not been proven wrong.

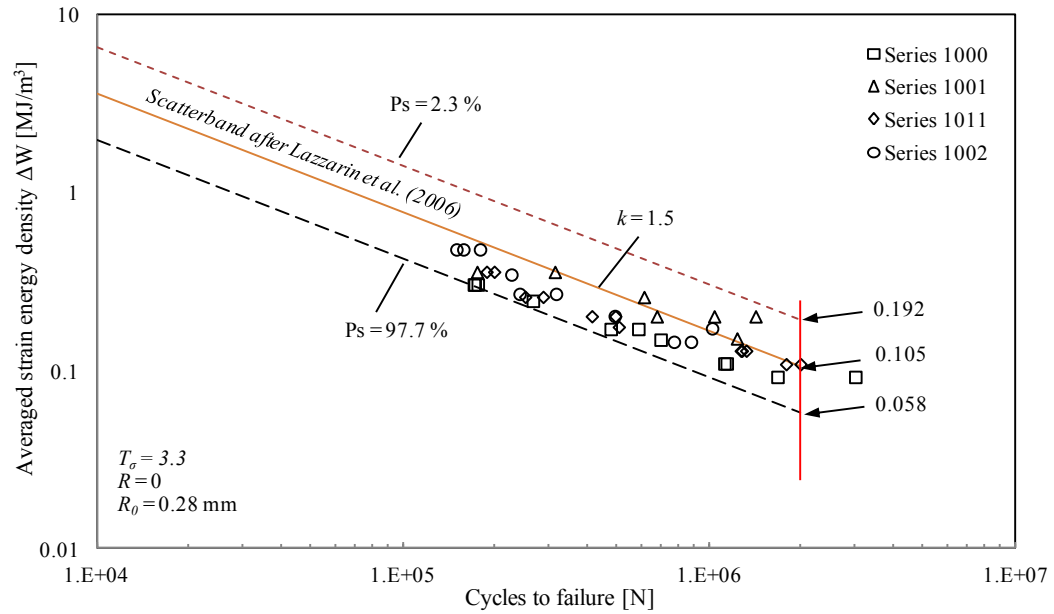


**Figure 3.52.** SED based design scatter band according to Lazzarin et al. [20]. Fatigue test data related to steel cover plates here investigated fit well inside the scatter band.

### 3.7 Discussion and conclusion

In this chapter a type of welded joint for which there is no uniform fatigue classification at standards level has been presented. Geometrical conditions imposed by standards current have been numerically investigated through the local SED approach. Four geometric variants have been selected as eligible to be experimentally tested against fatigue and the related fatigue classes at 2 million cycles and 97.7% probability of survival have been obtained. It has been observed that the solution suggested by the Eurocode 3 (which is the main normative reference in civil design of steel structures), in spite of a noticeable geometrical and machining complication, does not give appreciable advantages in terms of fatigue resistance if compared with simpler geometries (e.g. reference is made to the results related to 1000 and 1011 series of specimens). It is astonishing that the presence or not of the cover plate chamfer brings no tangible effect to the fatigue resistance of cover plates. Detailed finite element analyses have been performed on both 3D solid and 2D plane models to identify advantages and drawbacks of different geometries and mechanical processing (tapering, chamfering, etc.). Results are summarized in Figure 3.53. In detail, it has been found that the cover plate chamfer and the lateral weld reinforcement, which are Eurocode 3 and IIW requirements, have negligible effect

on fatigue resistance, while relevant is the average slope of the transverse weld. Likewise relevant is the transition slope at the weld toe (local slope). On the other hand, it is also mentioned by IIW as one of the governing parameters for fatigue failures from the weld toe [21]. If this slope differs from the average slope, the effect of the latter is compromised. This means that a prescribed weld slope must be guaranteed even at toe, otherwise the expected resistance cannot be reached. Since the weld toe shape depends on welding process parameters (welding technology, filler material, welder, etc.) and is approximately equal to 1:1, it follows that, in the absence of specific post weld treatments (grinding, dressing, etc.), the increase of resistance that standards propose with transverse end weld slope lower than 1:1 (typically 1:3 to 1:4) is not actually guaranteed.

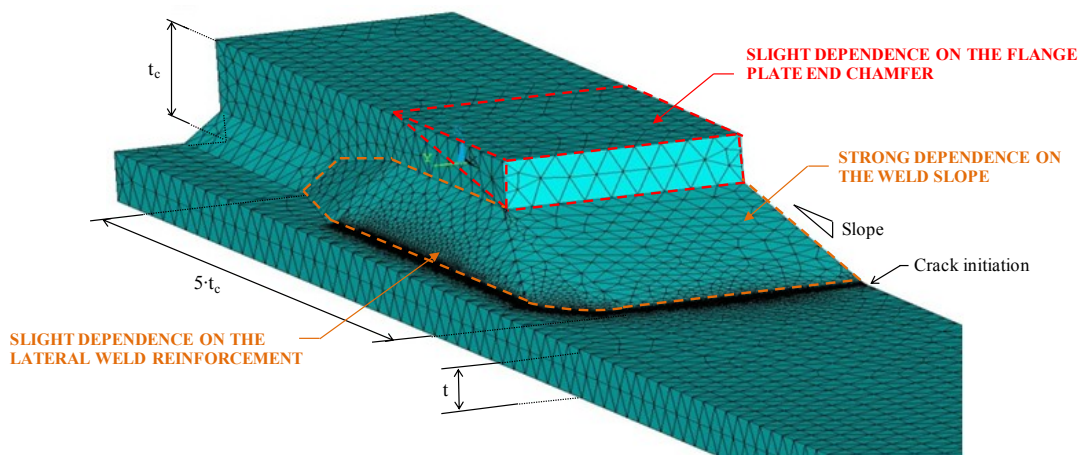


**Figure 3.53.** Summary of the main investigated parameters and of their effect on fatigue strength of welded cover plates.

Another important parameter affecting cover plates fatigue resistance turned out to be the transverse weld misalignment, due to inaccuracies in the attached plates positioning during the welding process. This defect has lower effect than the local shape of the weld toe, but numerical analyses have shown that it can increase the SED value up to 18%. Compared with the local toe shape, this defect appears to be easier to be controlled and can be avoided using proper bracket systems (templates and so on) to support the welding process.

It can be assumed that the non-uniform fatigue classification of cover plates provided by current standards is due to the geometrical variability of weld beads in *as welded* condition. Furthermore, having proved that the scale effect also plays a paramount



role on the fatigue resistance and being this parameter not taken into account by many standards, it can be supposed that norms relating different fields (civil buildings, mechanics, railways, cranes, off-shore structures, pressure vessels and so on) suggest fatigue classes which are implicitly calibrated on the thicknesses usual for the scope of the regulation. In particular, it is conceivable that regulations dealing with cranes (UNI EN 13001) and railways bogies (DVS 1612), which suggest fatigue classes almost double compared to those suggested by the Eurocode 3, are suitable for smaller thicknesses than those used in the civil field.

Finally, all experimental data have been successfully summarized in a unique scatter band in terms of SED, regardless of the specimen geometry. The scatter index related to the two curves with probabilities of survival  $P_S=2.3\%$  and  $97.7\%$ , has been found equal to 2.50, which returns a scatter index  $T_\sigma=1.58$  when reconverted to an equivalent local stress range. Then, it has been found that all experimental data fit well inside the SED based design scatter band proposed by Lazzarin and coworkers [20]. The suitability of the SED approach and of the related design curve to perform the fatigue assessment of welded cover plates has, therefore, not been proven wrong. However, the application of SED approach in this chapter has shown how time consuming it is to build three-dimensional control volumes all along a weld toe (and root) line. A proposal to overcome this drawback is presented in the next chapter.

## References

- [1] D. Radaj, Design and analysis of fatigue resistant welded structures, Woodhead Publishing, Cambridge, 1990.
- [2] A. Neumann, Schweißtechnisches Handbuch für Konstrukteure (in German), F. Vieweg, 1961.
- [3] EN 1993-1-9 Eurocode 3 - Design of steel structures - Part 1-9: Fatigue, European Committee for Standardization, Brussels, 2005.
- [4] A.F. Hobbacher, Recommendations for Fatigue Design of Welded Joints and Components, International Institute of Welding, 2008.
- [5] A.F. Hobbacher, Recommendations for Fatigue Design of Welded Joints and Components, Springer International Publishing, 2016.
- [6] L.R. Hall, J.E. Stallmeyer, The fatigue strength of flexural members, University of Illinois, Department of Civil Engineering, 1959.
- [7] J.W. Fisher, K.H. Frank, M.A. Hirt, B.M. McNamee, Effect of weldments on the fatigue strength of steel beams, TRB, 1970.
- [8] R.E. Slockbower, J.W. Fisher, Fatigue resistance of full scale cover-plated beams., (1976).
- [9] W.H. Munse, J.E. Stallmeyer, Fatigue in welded beams and girders, Highw. Res. Board Bull. (1962).
- [10] BS 7608 British Standard - Code of Practice for Fatigue Design and Assessment of Steel Structures, British Standard institution, 2014.
- [11] DVS 1612 - Design and endurance strength assessment of welded joints with steels in rail vehicle construction, German Welding Society, Brussels, 2009.
- [12] EN 13001-3-1+A1 Cranes - General Design - Part 3-1: Limit States and proof competence of steel structure, European Committee for Standardization, 2013.
- [13] DIN 15018 - Cranes - Steel structures - Verification and analyses, German Institute for Standardization, 1984.
- [14] DNVGL-RP-C203 - Fatigue design of offshore steel structures, Det Norske Veritas - Germanischer Lloyd, 2016.
- [15] EN 13445-3 Unfired pressure vessels - Part 3: Design, European Committee for Standardization, Brussels, 2014.
- [16] FKM Guideline - Analytical strength assessment of components, 6th Editio, VDMA Verlag, 2012.

- [17] P. Lazzarin, F. Berto, F.J. Gomez, M. Zappalorto, Some advantages derived from the use of the strain energy density over a control volume in fatigue strength assessments of welded joints, *Int. J. Fatigue*. 30 (2008) 1345–1357.
- [18] P. Lazzarin, F. Berto, M. Zappalorto, Rapid calculations of notch stress intensity factors based on averaged strain energy density from coarse meshes: theoretical bases and applications, *Int. J. Fatigue*. 32 (2010) 1559–1567.
- [19] P. Lazzarin, R. Zambardi, A finite-volume-energy based approach to predict the static and fatigue behavior of components with sharp V-shaped notches, *Int. J. Fract.* 112 (2001) 275–298.
- [20] P. Lazzarin, F. Berto, D. Radaj, Uniform fatigue strength of butt and fillet welded joints in terms of the local strain energy density, in: *Proc. Fatigue*, 2006.
- [21] B. Jonsson, G. Dobmann, A. Hobbacher, M.E. Kassner, G. Marquis, International Institute of Welding., *IIW guidelines on weld quality in relationship to fatigue strength*, 2016.



## **4. Rapid local Strain Energy Density evaluation through coarse free-generated meshes**

### **Highlights**

In the notch stress intensity approach to the fatigue assessment of welded joints, the weld toe and the weld root are modeled as sharp V-notches and local stress distributions in plane configurations are given on the basis of the relevant mode 1 and mode 2 notch stress intensity factors (NSIFs). Whilst the NSIF evaluation needs very fine meshes in the vicinity of the points of singularity, which is a drawback of the approach, the mean value of the elastic SED on a control volume can be accurately determined by using relatively coarse meshes. However, some meshing criteria have to be used to take advantage of this coarse mesh option: both the SED control volume and specific geometrical modules, which “guide” the free meshing algorithm, have to be introduced, which results in a time consuming pre-processing procedure, particularly in the presence of complex three-dimensional geometries.

Here, a method to compute the local SED by using the coarse mesh option and a completely free-generated mesh pattern has been formalized and its limitations of applicability have been provided. Its accuracy has been evaluated by using a large number of FE models, both bi- and three-dimensional. The method has shown robustness in terms of insensitivity to mesh pattern, mesh refinement and finite element formulation. Practical applications on three-dimensional welded geometries, highlighting pre-processing, solution and post-processing efficiency of the method have been given. For the sake of completeness and with the aim to generalize the method's applicability, some of the presented here analyses have been performed both by using Ansys® and Straus7® software. In the author's opinion, the proposed method permits to keep the advantages of SED and NSIF local approaches, by using meshes with degree of refinement equal to the one usually required to determine the hot spot stress according to the structural stress approach.



## 4.1 Introduction

Notch stress intensity factors (NSIFs) permit the quantification of local stress distributions near geometrical singularities. Nowadays, numerical methods are increasingly adopted by engineers focused on safe design of structural components against brittle fracture and fatigue [1–3] and the analysis of the local stress distributions ahead of cracks and notches is an intriguing topic. A major drawback of numerical modeling stress concentration regions is that refined or extremely refined meshes are required to obtain reliable results in terms of local stresses and strains. Cracks can be modeled by special quarter-point elements which contain the crack tip stress singularity [4,5] and permit to obtain accurate results, despite the use of relatively coarse meshes. Special singular finite elements and boundary elements have been developed to account for the appropriate singularity [6,7] and to facilitate the evaluation of the generalized stress intensity factors [8,9]. Among such special finite elements, additional and commonly used numerical techniques include degenerated asymptotic finite elements [10,11], hybrid finite elements [12,13], extended finite elements [14,15] and analytical finite elements [16]. Karihaloo and Xiao extended the hybrid crack element originally introduced by Tong et al. [17] to calculate directly not only the stress concentration factor (SIF) but also the coefficients of the higher-order terms of the crack tip asymptotic field [18]. Extensive studies have proved the versatility and accuracy of the element for pure mode 1 problems, but also for mode 2 and mixed mode cracks [19]. Special finite elements have been presented in the literature also to capture the asymptotic nature of other stress singularities, like those arising from sharp V-shaped notches [20,21]. However, they are not yet available in commercial software. Moreover, no special element exists for severe notches where the notch root is very small but different from zero.

The NSIFs have a fundamental role in static strength estimation of V-notched structural elements made of brittle or quasi-brittle materials [22–26]. This also holds true for components made of structural materials undergoing high-cycle fatigue loading [26–28]. A valuable example of application of the NSIF approach to a practical problem is the fatigue design of welded joints [29–32]. Local approaches based on NSIFs extend the concepts of linear elastic fracture mechanics (LEFM) and play the same role the SIFs have in strength evaluations of cracked components.

In plane problems, the mode 1 and mode 2 NSIFs for sharp V-notches, which quantify the intensity of the asymptotic stress distributions in the close neighborhood of the notch tip, can be expressed by means of the Gross and Mendelson definitions [33]:

$$K_1 = \sqrt{2\pi} \lim_{r \rightarrow 0} \sigma_{\theta\theta}(r, 0) r^{1-\lambda_1} \quad (4.1)$$

$$K_2 = \sqrt{2\pi} \lim_{r \rightarrow 0} \tau_{r\theta}(r, 0) r^{1-\lambda_2} \quad (4.2)$$

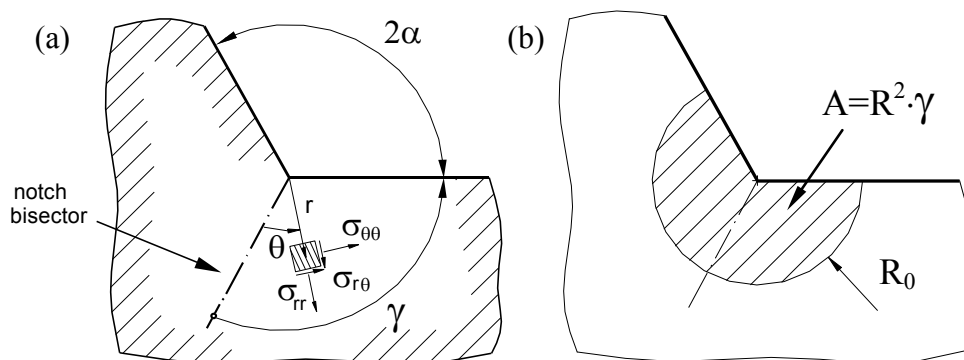


**Figure 4.1.** Polar coordinate system centered at the V-notch tip (a) and control volume (area) of radius  $R_0$  embracing the V-notch tip,  $\bar{W} = W/A$ .

where  $(r, \theta)$  is a polar coordinate system centered at the notch tip (Figure 4.1(a)),  $\sigma_{\theta\theta}$  and  $\tau_{r\theta}$  are the stress components according to the above coordinate system and  $\lambda_1$  and  $\lambda_2$  are the mode 1 and mode 2 first eigenvalues in William's equations [34], respectively. The condition  $\theta = 0$  identifies the notch bisector line. When the V-notch opening angle  $2\alpha$  is equal to zero,  $\lambda_1$  and  $\lambda_2$  are equal to 0.5, and  $K_I$  and  $K_{II}$  match the conventional stress intensity factors,  $K_I$  and  $K_{II}$ , of a crack according to LEFM.

Structural strength problems of V-notches (with arbitrary opening angle  $2\alpha$ ) subjected to mixed-mode loading can be treated using the linear elastic strain energy density averaged over a material-dependent structural volume (the SED parameter), which was idealized as a circular sector of radius  $R_0$ , as shown in Figure 4.1(b), according to Lazzarin and Zambardi [26]. The SED approach has been extensively applied in static [26,35,36] as well as fatigue [26,32,37,38] strength assessments. With reference to plane strain conditions, the SED value can be evaluated analytically as a function of the NSIFs:



$$\bar{W} = \frac{e_1}{E} \cdot \left( \frac{K_1}{R_0^{(1-\lambda_1)}} \right)^2 + \frac{e_2}{E} \cdot \left( \frac{K_2}{R_0^{(1-\lambda_2)}} \right)^2 \quad (4.3)$$

where  $E$  is the Young's modulus,  $e_1$  and  $e_2$  are two parameters which depend on the notch opening angle  $2\alpha$  and the Poisson's ratio  $\nu$  [26], as shown in Figure 2.6. Equation (4.3) is valid when the influence of the higher-order non-singular terms can be neglected inside the control volume. Therefore, taking as an example the case of short cracks or thin welded lap joints, Equation (4.3) is incomplete because the T-stress must be included in the local SED evaluation [39]. The main drawback in the practical application of Equation (4.3) combined with Equations (4.1) and (4.2) is that very refined meshes are needed to calculate the NSIFs by means of definitions (4.1) and (4.2) applied to the results of linear elastic finite element analyses. The reason is that the complete local stress distributions must be calculated accurately. The modeling procedure becomes particularly time-consuming for components that cannot be analyzed by means of two-dimensional models and instead require three-dimensional FE analyses.

That is why Lazzarin and coworkers provided evidence that it is convenient to evaluate the SED parameter directly from the results of FE analyses [40,41]. They proved that the SED parameter can be computed by summing up the strain energies  $W_{FEM,i}$  calculated for the  $i$ -th finite element located inside the control volume and subsequently by dividing by the total volume (area  $A$  in plane problems, as shown in Figure 4.1(b)), calculated as the summation of the  $i$ -th finite element volume (area):

$$\bar{W}_{FEM} = \frac{\sum_i W_{FEM,i}}{\sum_i A_i} \quad (4.4)$$

Equation (4.4) defines the so-called direct approach to evaluate the SED parameter. Additionally, it has been shown that the adopted FE meshes can be very coarse inside the control volume having radius  $R_0$  [40,41].

However, some meshing criteria have to be used to take advantage of the coarse mesh option, keeping small (at least from an engineering point of view) the committed error. It results in a modification of the geometry to be meshed, localized near the points of singularities, to introduce both the SED control volume and a specific geometrical module, which "guide" the free meshing algorithm [40,41].

If a general welded joint geometry is considered (Figure 4.2), various geometrical modules have been proved to be suitable, permitting to keep the error in the estimation of SED within about 10%, regardless of the element formulation (linear or quadratic), as compared to the one obtained with a very refined mesh (approximately 500 FE inside the control volume). Figure 4.3 shows some examples of modules for direct SED evaluation at the weld toe; other examples, involving also the weld root, are provided in the literature [41].

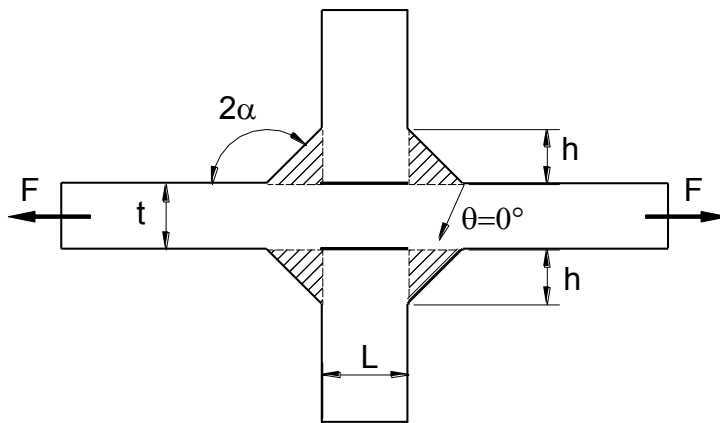


**Figure 4.2.** Geometrical parameters for transverse non-load carrying welded joints [40].

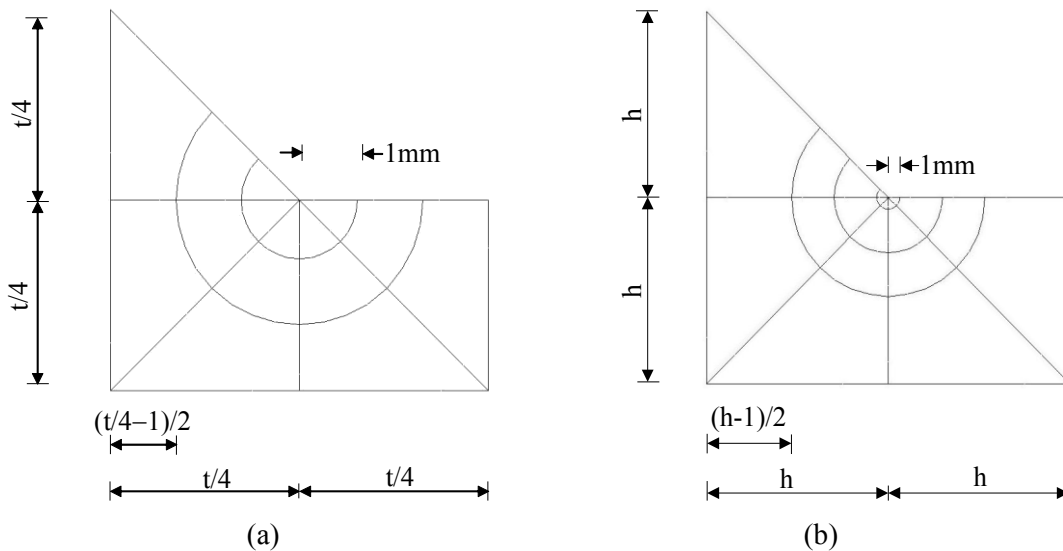


**Figure 4.3.** Examples of geometrical modules used near the weld toe for direct SED calculation in a control volume having radius equal to 1 mm: geometries with  $h > t/2$  (a); geometries with  $h < t/2$  (b) [40].

Recently, it has been shown that pure mode 1 crack problems, as well as mixed-modes (1+2) and (1+3), can be analyzed through the direct SED calculation approach, with only eight finite elements inside the control volume [42–44]. This holds true if second order elements are used and two concentric rings, consisting of eight elements each, are generated outside the control volume in the circular sector  $R_0 < r < 10 \cdot R_0$ , while a free mesh of elements having a fixed average size  $d$  is generated outside by using a free mesh generation algorithm. It has been proved that such FE meshes are as coarse as possible to keep the error in the estimation of SED within 10%, as compared to the one obtained with a very refined mesh.

The introduction of a control volume, as well as the above mentioned geometrical modules, to compute the averaged SED is generally a time consuming procedure. That is why an alternative approach, where modeling the control volume is no longer necessary and the coarse mesh option is maintained, is being extensively proposed in the literature [45–50]. The approach is referred to as the peak stress method (PSM) and the theoretical background has already been presented in Section 2.4. The PSM enables to rapidly estimate the NSIFs  $K_I$  and  $K_{II}$  from the notch tip singular, linear elastic, opening and sliding peak stresses  $\sigma_{yy,peak}$  and  $\tau_{xy,peak}$ , respectively. The peak stresses are defined as the maximum linear elastic stresses in the considered crack tip or notch tip nodal point of the mesh. A completely free-generated mesh pattern has to be employed. Typical mesh patterns near a notch tip, obtained setting an average element size  $d$ , are shown in Figure 2.10. Provided that the adopted mesh pattern has previously been calibrated on geometries for which the exact *NSIF* values are known, the PSM allows a rapid evaluation of averaged SED by using Equation (4.3), once  $K_I$  and  $K_{II}$  have been computed. However, being the PSM a stress based procedure, different stress extrapolation rules from integration points to nodes, as well as different finite element formulations and significantly different mesh patterns, with respect to the limitations provided by the calibration, may lead, in principle, to different values of the peak stresses. This behavior, which can be considered as a dependence on the adopted FE code, is an intrinsic feature of stress based methods and can be a limitation.

Within this framework, it may be wondered if it is possible to have a method which keeps both direct SED calculation and PSM advantages, which consist in a substantial insensitivity to element formulation and mesh refinement, for the former,

in the use of a completely free-generated mesh pattern, for the latter. The problem is addressed in the present chapter, whose aims are:

- i) to recall the fundamental concepts of the local strain energy density (SED) approach and the peculiarities of its numerical calculation;
- ii) to present a method to compute the local SED by using the coarse mesh option and completely free-generated mesh patterns;
- iii) to present the calibration of the proposed method, as well as its limitations in the applicability;
- iv) to show practical applications on three-dimensional welded geometries, highlighting pre-processing, solution and post-processing efficiency of the method.

For the sake of completeness and with the aim to show the robustness of the method here proposed, some of the numerical analyses here presented have been performed both by using Ansys® and Straus7® finite element software.

## 4.2 Averaged strain energy density numerical calculation

The aim of the present subsection is to recall some fundamentals of the finite element method (FEM), with the purpose to explain the numerical calculation procedure of the strain energy density.

Let us consider a generic finite element with a certain number of nodes and define  $\{d\}$  as the nodal displacements vector,  $\{f\}$  as the nodal forces vector. The displacement of a generic point within the element can be related, by interpolation, to the displacements of the nodes via proper shape functions. A displacement interpolation matrix  $[N]$ , multiplying the nodal displacement vector, expresses the field of displacements  $\{u\}$  of the generic element point:

$$\{u\} = [N]\{d\} \quad (4.5)$$

The strain in a generic point is defined as the spatial derivative of the displacement:

$$\{\varepsilon\} = \frac{\partial\{u\}}{\partial x_i} = [B]\{d\} \quad (4.6)$$

where  $[B]$  is the strain-displacement matrix.

Considering an ideal linear elastic behaviour, the stresses are related to the displacements by the generalized Hooke's law:

$$\{\sigma\} = [E]\{\varepsilon\} \quad (4.7)$$

and the strain energy density in a point of the element is:

$$W = \frac{1}{2} \{\varepsilon\}^t \{\sigma\} = \frac{1}{2} \{d\}^t [B]^t [E] [B] \{d\} \quad (4.8)$$

Since:

$$([B]\{d\})^t = \{d\}^t [B]^t \quad (4.9)$$

the strain energy totally stored in the element is:

$$E_t = \int_V W dV = \frac{1}{2} \{d\}^t \left( \int_V [B]^t [E] [B] dV \right) \{d\} = \frac{1}{2} \{d\}^t [K] \{d\} \quad (4.10)$$

where  $V$  is the volume of the element and  $[K]$  is the elemental stiffness matrix:

$$[K] = \int_V [B]^t [E] [B] dV \quad (4.11)$$

It is possible to note how the total energy stored in the element is a function of the displacements and does not involve the stresses and strains and the same is for the averaged SED:

$$\bar{W} = E_t/V \quad (4.12)$$

This represents the powerful advantage of an energetic approach, with respect to a stress based approach, leading to a substantial mesh refinement independence and to a quite good element formulation insensitivity [40,41], as practically shown in the present chapter.

### 4.3 Basic theoretical recalls on averaged SED from sharp V-notches

Let us consider a plate weakened by a sharp V-notch with a notch opening angle  $2\alpha$ . The degree of the singularity of the mode 1 and mode 2 stress fields is in agreement with Williams' solution [34]. The NSIFs quantify the intensity of the asymptotic stress distributions close to the notch tip. By using a polar coordinate system  $(r, \theta)$  having its origin located at the sharp notch tip, the NSIFs related to mode 1 and mode 2 stress distributions are defined by Equations (4.1) and (4.2). Under plane stress or plane strain conditions, considering only the leading order terms of the Williams' solution [34], the total elastic strain energy density averaged over a small sector of radius  $R_0$  is given by Equation (4.3).

#### 4.3.1 Sharp V-notches under pure loading modes

Under pure mode 1 loading or, alternatively, under pure mode 2 loading, Equation (4.3) simply gives:

$$K_1 = R_0^{1-\lambda_1} \sqrt{\frac{E \cdot \bar{W}}{e_1}} \quad (4.13)$$

$$K_2 = R_0^{1-\lambda_2} \sqrt{\frac{E \cdot \bar{W}}{e_2}} \quad (4.14)$$

where  $E$  is the Young's modulus,  $e_1$  and  $e_2$  are two parameters which depend on the notch opening angle  $2\alpha$  and the Poisson's ratio  $\nu$ , as shown in Figure 2.6.

### 4.3.2 Sharp V-notches under mixed mode loading (1+2)

In the presence of mixed mode 1 and mode 2 loading conditions, the evaluation of the NSIFs of a V-notch requires the knowledge of the SED from two concentric circles with different radii [41]. The method is based on the evaluation of the averaged SED on two different control volumes (circular sectors) centered at the notch tip and characterized by the radii  $R_a$  and  $R_b$  (Figure 4.4). Known the SED values ( $\bar{W}_a$  and  $\bar{W}_b$ ), by means of a FE analysis, it is possible to obtain a system of two equations in two unknowns ( $K_1$  and  $K_2$ ):

$$\begin{cases} \bar{W}_a = \frac{1}{E} \left[ e_1 \cdot \frac{K_1^2}{R_a^{2(1-\lambda_1)}} + e_2 \cdot \frac{K_2^2}{R_a^{2(1-\lambda_2)}} \right] = C_a \cdot K_1^2 + D_a \cdot K_2^2 \\ \bar{W}_b = \frac{1}{E} \left[ e_1 \cdot \frac{K_1^2}{R_b^{2(1-\lambda_1)}} + e_2 \cdot \frac{K_2^2}{R_b^{2(1-\lambda_2)}} \right] = C_b \cdot K_1^2 + D_b \cdot K_2^2 \end{cases} \quad (4.15)$$

where all terms have already been defined with reference to Equation (4.3).

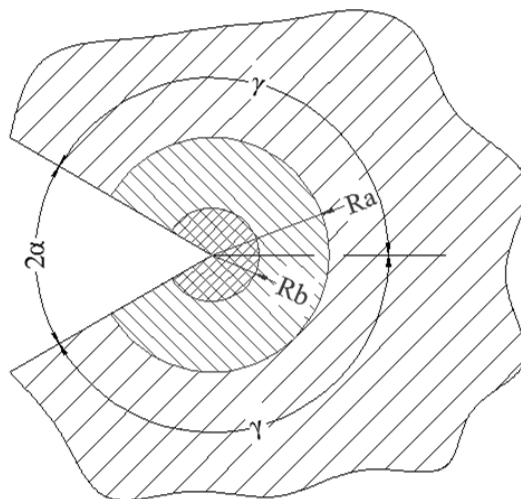


**Figure 4.4.** Schematization of two concentric SED control volumes, having different radii, used to estimate mode 1 and mode 2 contributions.

It is worth noting that this method cannot be applied to a crack subjected to mixed mode loading, since an indeterminate system of equations would be obtained, being  $\lambda_1 = \lambda_2$ . On the other hand, if an open notch is considered, the contributions of the two modes of loading are decoupled due to their different degree of singularity ( $\lambda_1 \neq \lambda_2$ ). Solving the system of equations, the values of the NSIFs can be determined:

$$K_1 = \sqrt{\frac{D_a \cdot \bar{W}_b - D_b \cdot \bar{W}_a}{D_a \cdot C_b - D_b \cdot C_a}} \quad (4.16)$$

$$K_2 = \sqrt{\frac{\bar{W}_a - C_a \cdot K_1^2}{D_a}} \quad (4.17)$$

### 4.3.3 Scale effect

Coming closer to the main topic of the chapter, it might be useful to briefly analyze the scale effect from the theoretical point of view, that is, the influence of the absolute dimensions of the component on its NSIF values.

Let us consider two plane similar geometries, scaled by a factor  $s$ , so that the absolute dimension of the latter case (denoted "b") is  $s$  times greater than the former one ("a"), the boundary conditions on forces and displacements being scaled by the same ratio. Being this the case, the NSIF values of the two similar geometries are related by the following condition [30]:

$$K_{i,b} = K_{i,a} \cdot s^{1-\lambda_i} \quad (4.18)$$

where the first index "i" is 1 or 2 according to the loading mode and the second index depends on the case considered.

When the mode 1 or the mode 2 stress distributions are absent or non singular, Equation (4.3) becomes, respectively:

$$\bar{W} = \frac{e_1}{E} \cdot \left( \frac{K_1}{R_0^{(1-\lambda_1)}} \right)^2 \quad (4.19)$$

$$\bar{W} = \frac{e_2}{E} \cdot \left( \frac{K_2}{R_0^{(1-\lambda_2)}} \right)^2 \quad (4.20)$$

By substituting Equation (4.18) in Equation (4.19) or (4.20) and considering the two scaled geometries above mentioned, the following relations exist for pure mode 1 and for pure mode 2, respectively:

$$\bar{W}_{1,b} = \bar{W}_{1,a} \cdot s^{2(1-\lambda_1)} \quad (4.21)$$

$$\bar{W}_{2,b} = \bar{W}_{2,a} \cdot s^{2(1-\lambda_2)} \quad (4.22)$$

In Equations (4.21) and (4.22) it is assumed that the control volume radius is the same for geometry “a” and “b”. The above equations show that the averaged strain energy density retains the advantages of the NSIF approach in terms of scale effect.

#### 4.4 Averaged SED evaluation by using free-generated mesh patterns

The aim of this section is to formalize a method to evaluate the strain energy density averaged over a control volume, without generating the control volume itself in the finite element model. The method is here called volume-free SED approach and it works with completely free-generated mesh patterns. Both bi- and three-dimensional conditions are taken into account.

##### 4.4.1 Plane condition

Let us consider now two identical plane geometries, denoted with “a” and “b”, having control volume radius  $R_{0,a}$  and  $R_{0,b}$ , respectively. Being this the case, the NSIF values of the two geometries are the same, whereas the SED values averaged in the respective control volumes, under pure mode 1 and pure mode 2, are related by the following equations, respectively:

$$\bar{W}_{1,b} = \bar{W}_{1,a} \cdot \left( \frac{R_{0,a}}{R_{0,b}} \right)^{2(1-\lambda_1)} \quad (4.23)$$

$$\bar{W}_{2,b} = \bar{W}_{2,a} \cdot \left( \frac{R_{0,a}}{R_{0,b}} \right)^{2(1-\lambda_2)} \quad (4.24)$$

Equations (4.23) and (4.24) have the same meaning of scale effect of Equations (4.21) and (4.22), just to think that geometries “a” and “b” have their respective control volumes characterized by radii scaled by a factor  $s$ . Being this the case, Equations (4.23) and (4.24) turn out to be Equations (4.21) and (4.22). It is worth noting by now that Equations (4.23) and (4.24) can be used with the aim to reduce the number of degrees of freedom in the finite element model, allowing the computation of SED in control volumes larger than the critical one, with respect to the overall geometry.



Let us assume that at the notch tip of the geometry “b” there is a control volume which is a circular sector having radius  $R_0$  (so that  $R_{0,b}=R_0$ ). In this chapter,  $R_0$  is assumed equal to 0.28 mm, according to SED approach for fatigue assessment of steel welded joints, but the following deductions are completely independent of such hypothesis, so that their meaning remains general. Let us imagine, now, that the control volume placed at the notch tip of the geometry “a” could have a shape other than the circular sector (e.g. it could be a square, a rectangle or it could have any desired shape, in principle). In plane condition, the area of such general control volume is designated with  $\Omega$ .

It is possible to define  $R_{0,a}$  as the radius of a circular sector control volume, which is equivalent to the general one in terms of area  $\Omega$ , through:

$$R_{0,a} = \sqrt{\frac{\Omega}{\pi} \left(1 + \frac{\alpha}{\gamma}\right)} \quad (4.25)$$

where  $\alpha$  and  $\gamma$  are in accordance with Figure 4.1(a).

Substituting Equation (4.25) in Equations (4.23) and (4.24) and remembering that it has been set  $R_{0,b}=R_0$ , it is found:

$$\bar{W}_{1,b} = \bar{W}_{1,a} \cdot \left( \frac{\sqrt{\frac{\Omega}{\pi} \left(1 + \frac{\alpha}{\gamma}\right)}}{R_0} \right)^{2(1-\lambda_1)} \quad (4.26)$$

$$\bar{W}_{2,b} = \bar{W}_{2,a} \cdot \left( \frac{\sqrt{\frac{\Omega}{\pi} \left(1 + \frac{\alpha}{\gamma}\right)}}{R_0} \right)^{2(1-\lambda_2)} \quad (4.27)$$

Being the basic idea of this chapter the removal of a fixed (even if general in shape) control volume, it is assumed that the “control volume” of the geometry “a” is simply represented by the few finite elements which share the node located at the notch tip (regardless of their shape and of their number). This means that the mesh pattern can be generated by using any free-generation meshing algorithm. Figure 4.5 shows an example of mesh pattern generated by Ansys® free meshing algorithm and used for the PSM [45].

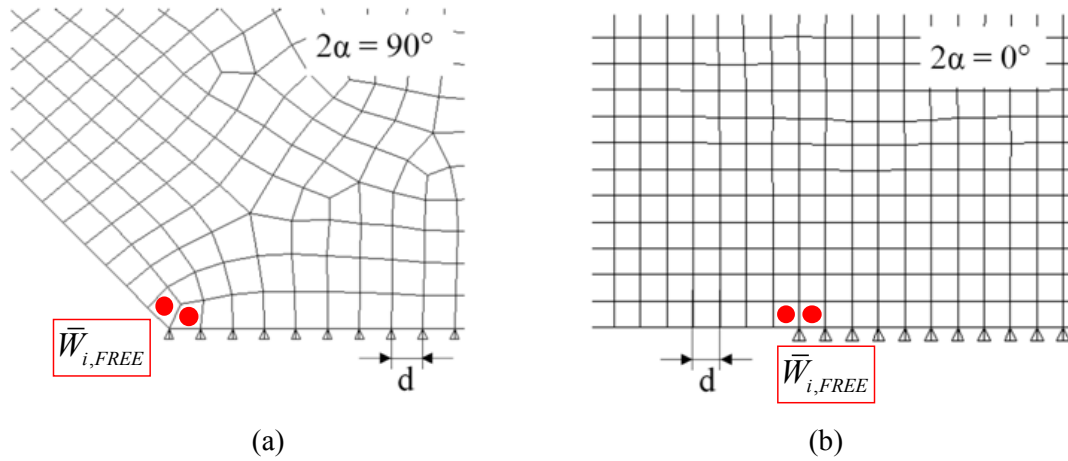


**Figure 4.5.** Example of free-generated mesh patterns close to the notch tip of an open V-notch (a) and near a crack tip (b). The strain energy density is computed and averaged on the few elements, which share the node located at the notch tip (indicated with red dots).

The volume-free averaged strain energy densities so calculated are here designated as  $\bar{W}_{1,FREE}$  and  $\bar{W}_{2,FREE}$ , under pure mode 1 and pure mode 2, respectively. So, Equations (4.26) and (4.27) can be rewritten as:

$$\bar{W}_1(R_0) = \bar{W}_{1,FREE} \cdot \left( \frac{\sqrt{\frac{\Omega}{\pi} \left( 1 + \frac{\alpha}{\gamma} \right)}}{R_0} \right)^{2(1-\lambda_1)} \quad (4.28)$$

$$\bar{W}_2(R_0) = \bar{W}_{2,FREE} \cdot \left( \frac{\sqrt{\frac{\Omega}{\pi} \left( 1 + \frac{\alpha}{\gamma} \right)}}{R_0} \right)^{2(1-\lambda_2)} \quad (4.29)$$

where  $\bar{W}_{1,FREE}$  and  $\bar{W}_{2,FREE}$  are computed by summing up the strain energies  $\bar{W}_{1,FREE,i}$  and  $\bar{W}_{2,FREE,i}$  calculated for the  $i$ -th finite element, which has a node located at the notch tip, whereas  $\Omega$  is calculated as the summation of the  $i$ -th finite element area  $\Omega_i$ .

The mode 1 and mode 2 NSIFs can be obtained *a posteriori* from SED, according to Equations (4.13) and (4.14), so the following expressions are valid:

$$K_{1,FREE} = \sqrt{\frac{E \cdot \bar{W}_{1,FREE}}{e_1} \left[ \frac{\Omega}{\pi} \left( 1 + \frac{\alpha}{\gamma} \right) \right]^{(1-\lambda_1)}} \quad (4.30)$$

$$K_{2,FREE} = \sqrt{\frac{E \cdot \bar{W}_{2,FREE}}{e_2} \left[ \frac{\Omega}{\pi} \left( 1 + \frac{\alpha}{\gamma} \right) \right]^{(1-\lambda_2)}} \quad (4.31)$$

Being, in principle, assumed that Equation (4.3) is obtained by the integration of the strain energy density over a circular area (see Section 2.3.1 and Equation (2.14) for reference), Equations (4.28) and (4.29) represent an approximate relation between strain energy densities averaged over control volumes having different shapes. That is why a limitation in their applicability must be made. Moreover, the dimension of the general control volume, with respect to the notch geometry, should not exceed the size of the zone governed by the mode 1 or mode 2 singularity, respectively.

Such limitation is here given in terms of mesh density ratio  $a/d$ , where  $d$  is the averaged mesh size set before meshing and  $a$  is half of the minimum thickness of plates involved in a welded joint otherwise  $a$  is the notch (crack) depth in notched (cracked) plates, as shown in Section 4.5.

#### 4.4.2 Three-dimensional condition

Let us consider now two identical three-dimensional geometries, having their control volumes geometrically scaled in the three dimensions by a factor  $s$ . Under the hypothesis that the stress singularity exponents  $\lambda_1$  and  $\lambda_2$  and the intensity of the local stress fields  $K_1$  and  $K_2$  do not vary along the length of the control volume and assuming that such length is equal to the control volume radius, according to the SED approach, Equations (4.28) and (4.29) become:

$$\bar{W}_1(R_0) = \bar{W}_{1,FREE} \cdot \left( \frac{\sqrt[3]{\frac{V}{\pi} \left( 1 + \frac{\alpha}{\gamma} \right)}}{R_0} \right)^{2(1-\lambda_1)} \quad (4.32)$$

$$\bar{W}_2(R_0) = \bar{W}_{2,FREE} \cdot \left( \frac{\sqrt[3]{\frac{V}{\pi} \left( 1 + \frac{\alpha}{\gamma} \right)}}{R_0} \right)^{2(1-\lambda_2)} \quad (4.33)$$

where  $\bar{W}_{1,FREE}$  and  $\bar{W}_{2,FREE}$  are computed by summing up the strain energies  $\bar{W}_{1,FREE,i}$  and  $\bar{W}_{2,FREE,i}$  calculated for the  $i$ -th finite element, which has a node located at the notch tip, whereas  $V$  is calculated as the summation of the  $i$ -th finite element volume  $V_i$ . Equations (4.30) and (4.31) are still valid in three-dimensional condition, as:

$$K_{1,FREE} = \sqrt{\frac{E \cdot \bar{W}_{1,FREE}}{e_1} \left[ \frac{V}{\pi} \left( 1 + \frac{\alpha}{\gamma} \right) \right]^{\frac{2(1-\beta_1)}{3}}} \quad (4.34)$$

$$K_{2,FREE} = \sqrt{\frac{E \cdot \bar{W}_{2,FREE}}{e_2} \left[ \frac{V}{\pi} \left( 1 + \frac{\alpha}{\gamma} \right) \right]^{\frac{2(1-\beta_2)}{3}}} \quad (4.35)$$

## 4.5 Limitation of applicability of the volume-free SED approach

To investigate the suitability of the proposed here volume-free SED approach in the estimation of the strain energy density averaged over a specific circular control volume, as well as in the estimation of NSIF values, about 60 calibration analyses have been performed under pure mode 1 loading and about 90 analyses have been performed under pure mode 2 loading, both in 2D plane strain condition.

### 4.5.1 Pure mode 1 loading

A number of two-dimensional FE models subjected to mode 1 loading have been considered to calibrate the volume-free SED method. For the sake of generality, geometries involved in the calibration consist in cracks, in pointed V-notches and in welded joints. The investigated geometries have been taken from the original calibration of the PSM performed in Ansys® software [45] under mode 1 loading and are summarized in Figure 4.6. They include cracks at the tip of a U-notch (Figure 4.6(a)); edge cracks in a finite-width plate (Figure 4.6(b)); a plate with lateral open V-notches (Figure 4.6(c)) and a full-penetration cruciform welded joint having weld reinforcement angle equal to  $135^\circ$  (Figure 4.6(d)). The material is assumed to be a structural steel having Young's modulus  $E = 206000$  MPa and Poisson's ratio  $\nu = 0.3$ . A nominal stress equal to 1 MPa has been applied to the gross section. Taking advantage of the double symmetry of the investigated geometries, only a quarter of each model has been analyzed.

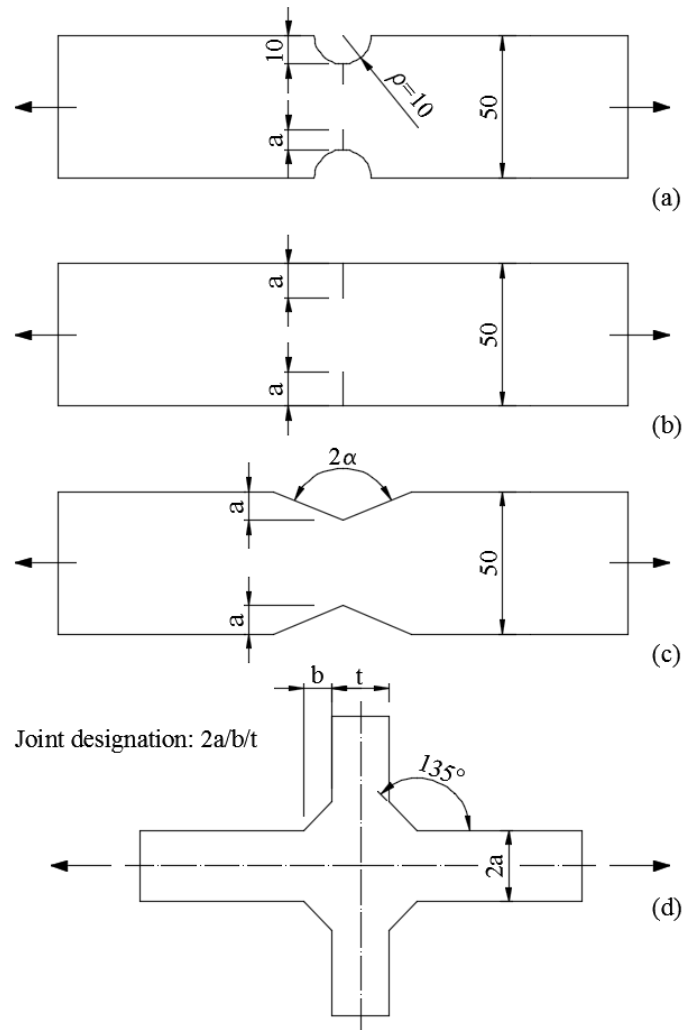


**Figure 4.6.** Plane geometries investigated to calibrate the volume-free SED approach under mode 1 loading. Dimensions are in mm.

To calculate volume-free averaged SED, linear elastic static analyses under plain strain condition have been carried out in Ansys®. Completely free mesh patterns have been generated, simply by setting the desired average finite element size  $d$ . An example of generated meshes is given in Figure 2.10, with reference to the PSM calibration [45]. Four-node quadrilateral elements, i.e. Plane182 type elements in Ansys® library, have been adopted in the FE analyses. The numerical integration scheme was set to 2x2 Gauss points (full integration scheme), which is the default option in Ansys®.

It is worth noting that, according to the considerations presented in Section 4.2, the obtained results are independent of nodal stress averaging options and extrapolation rules from integration points to nodal points. This means that, conversely to the PSM

calibration in Ansys® environment, as presented in the literature [45], and in Sysweld® environment, as presented in Chapter 9, here no limitations need to be imposed, except for the mesh density ratio  $a/d$ . In addition, the number of finite elements sharing the node located at the notch tip is not conditioned.

By varying both the notch or crack size  $a$  and the finite element size  $d$ , as reported in Table 4.1, many different mesh density ratios  $a/d$  have been considered. The exact values of mode 1 NSIFs  $K_I$  have been obtained from local stress fields computed through Ansys® software with very fine mesh patterns, where the size adopted in the FE mesh was on the order of  $10^{-5}$  mm, according to Lazzarin and Tovo [30].

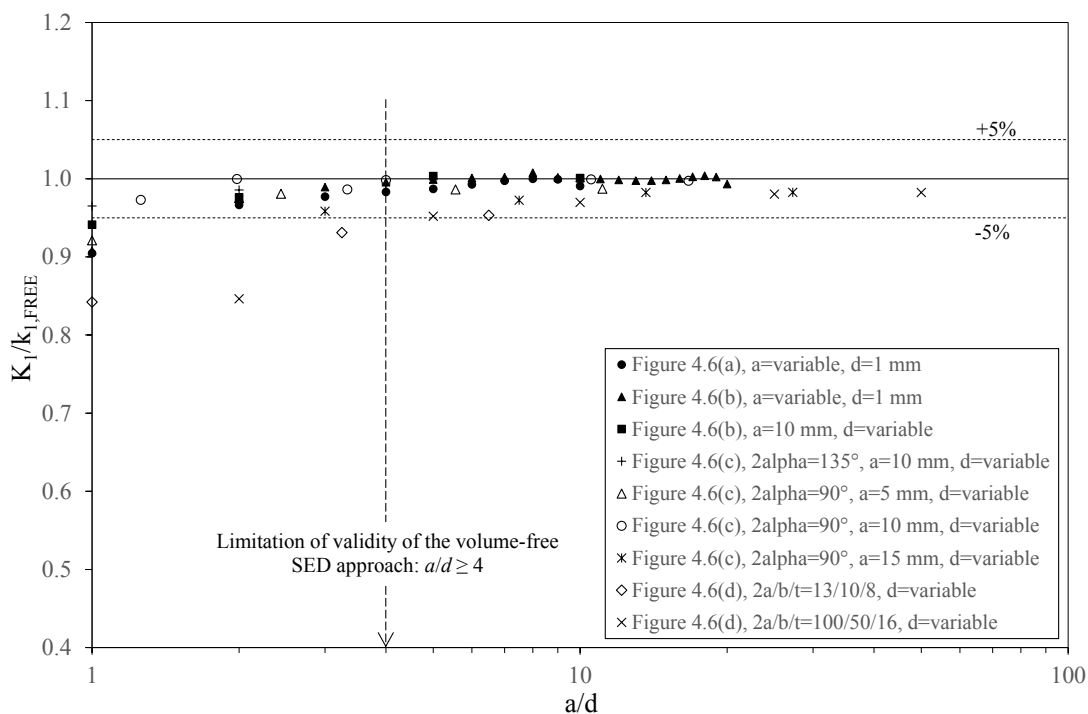


**Figure 4.7.** Ratio of the exact mode 1 NSIFs over the ones calculated from the volume-free SED, as evaluated from the 61 calibration FE analyses (see Figure 4.6 and Table 4.1).

The obtained results are shown in Figure 4.7, where the ratio of the exact mode 1 NSIFs over the ones calculated from the volume-free SED (Equation (4.30)) is plotted as a function of the mesh density ratio  $a/d$ . Figure 4.7 shows that the computed values are arranged into a narrow scatter band of  $\pm 5\%$  around the unit value, regardless of the notch geometry. The convergence is guaranteed for a mesh density ratio  $a/d \geq 4$ .

**Table 4.1.** FE analyses of 2D problems (plane strain) under mode 1 loading.

Analyzed geometries						
Figure	$a$ [mm]	$d$ [mm]	$2\alpha$ [°]	$b$ [mm]	$t$ [mm]	Number of analyses**
4.6(a)	1, 2, ..., 9, 10	1	0	-	-	10
4.6(b)	1, 2, ..., 19, 20	1	0	-	-	20
4.6(b)	10	1, 2, 5, 10	0	-	-	4
4.6(c)	10	1, 2.5, 5, 10	135	-	-	4
4.6(c)	5	0.5, 1, 2, 2.5, 5	90	-	-	5
4.6(c)	10	0.6, 1, 2.5, 3, 5, 7.5	90	-	-	6
4.6(c)	15	0.6, 1, 2, 5	90	-	-	4
4.6(d)	6.5	1, 1.64, 6.5	135	10	8	3
4.6(d)	50	1, 2, 5, 10, 25	135	50	16	5

\*\* : total number of analyses: 61

#### 4.5.2 Pure mode 2 loading

A crack (zero opening angle  $2\alpha$ ) centered in a plate having the geometry reported in Figure 4.8 and subjected to pure mode 2 loading has been considered. As for the mode 1 analyses, also this case study has been taken from the original calibration of the PSM under mode 2 loading conditions for Ansys® [45].

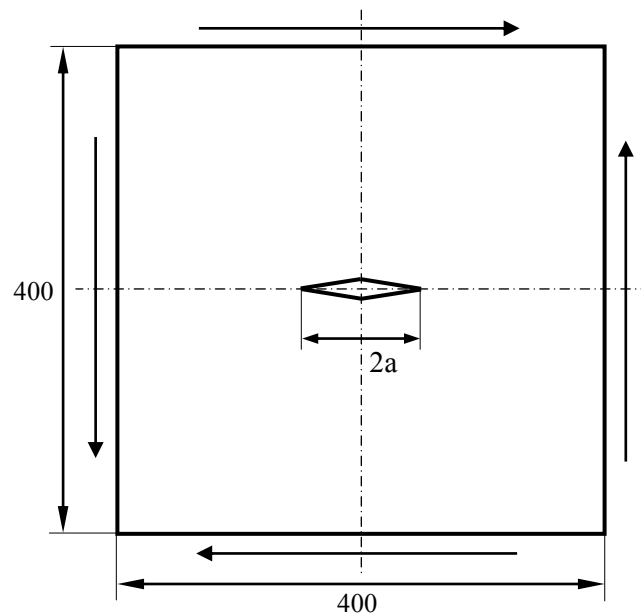


**Figure 4.8.** Plane geometry investigated to calibrate the volume-free SED approach under mode 2 loading. Dimensions are in mm.

The considered material is a structural steel with Young's modulus  $E = 206000$  MPa and Poisson's ratio  $\nu = 0.3$ . The strain energy density has been calculated by means of linear elastic analyses under plain strain condition and a free-generated pattern of four-node linear quadrilateral elements. The external load has been applied to the FE model by means of displacements  $u=1.262 \cdot 10^{-3}$  mm at the plate free edges, in the direction parallel to the edges themselves (Figure 4.8). Such displacements translate into a nominal gross shear stress equal to 1 MPa in absence of the crack.

The mesh density ratio  $a/d$  has been varied in a wide range from 1 to 200 as reported in Table 4.2.

**Table 4.2.** FE analyses of 2D problems (plane strain) under mode 2 loading.

Analyzed geometries			
$a$ [mm]	$d$ [mm]	$2\alpha$ [°]	Number of analyses **
1	0.5, 1	0	2
2	0.5, 1, 2	0	3
3	0.5, 1, 3	0	3
4	0.5, 1, 2, 4	0	4
5	0.5, 1, 5	0	3
6	0.5, 1, 2, 3	0	4
7	0.5, 1	0	2
8	0.5, 1, 2, 4	0	4
9	0.5, 1, 3	0	3
10	0.5, 1, 2, 5, 10	0	5
20	0.5, 1, 2, 4, 5, 10	0	6
30	0.5, 1, 2, 3, 5, 10, 15	0	7
40	0.5, 1, 2, 4, 5, 10, 20	0	7
50	0.5, 1, 2, 5, 10	0	5
60	0.5, 1, 2, 3, 4, 5, 10, 15, 20	0	9
70	0.5, 1, 2, 5, 10	0	5
80	0.5, 1, 2, 4, 5, 10, 20	0	7
90	0.5, 1, 2, 3, 5, 10, 15	0	7
100	0.5, 1, 2, 4, 5, 10, 20	0	7

\*\* : total number of analyses: 93



Only a quarter of the cracked plate has been analyzed by taking advantage of the double anti-symmetry boundary conditions.

The exact values of mode 2 SIFs  $K_2$  have been obtained from local stress fields computed through Ansys® software with very fine mesh patterns, where the size adopted in the FE mesh was on the order of  $10^{-5}$  mm, according to Lazzarin and Tovo [30]. The obtained results are shown in Figure 4.9 where the ratio of the exact mode 2 SIFs over the ones calculated from the volume-free SED (Equation (4.31)) is plotted as a function of the mesh density ratio  $a/d$ . Figure 4.9 shows that the computed values are arranged into a narrow scatter band of  $\pm 3\%$  around the unit value, regardless of the notch geometry. The convergence is guaranteed for a mesh density ratio  $a/d \geq 3$ .

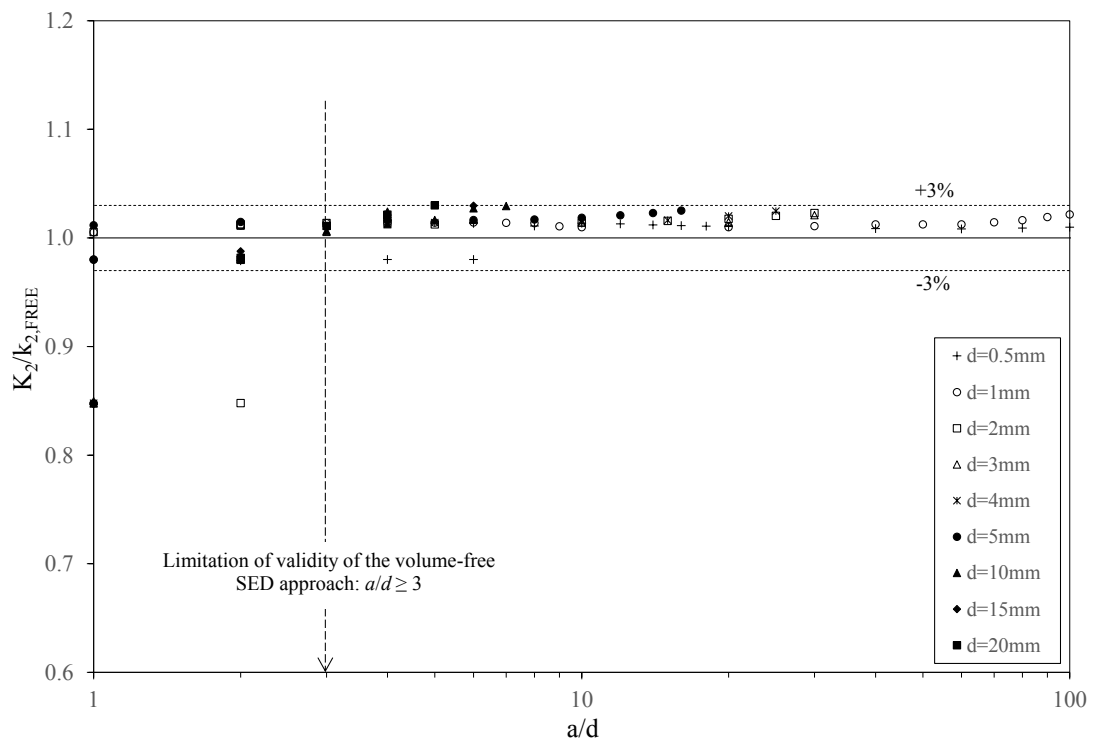


**Figure 4.9.** Ratio of the exact mode 2 NSIFs over the ones calculated from the volume-free SED, as evaluated from the 93 calibration FE analyses (see Figure 4.8 and Table 4.2).

## 4.6 Volume-free SED approach applied to 2D and 3D welded joints

### 4.6.1 Plane models

In order to show the interesting features of the volume-free SED approach, a number of different geometries related to transverse non-load-carrying fillet welded joints has been considered (reference is made to Figure 4.2). The geometrical parameters listed in Table 4.3 match those characterizing the welded joints analyzed in the literature by Maddox [51] and Gurney [52], who determined experimentally the fatigue strength properties and compared experimental data and theoretical predictions carried out on the basis of linear elastic fracture mechanics. The same set of experimental data was used by other researchers to check the NSIF approach [30,53,54], a modified structural stress approach, as formulated by Poutianen and Marquis [55] and, finally, to demonstrate some advantages related to the direct SED approach [40].

The material is assumed to be a structural steel having Young's modulus  $E = 206000$  MPa and Poisson's ratio  $\nu = 0.3$ . A nominal stress equal to 100 MPa has been applied to the gross section. Taking advantage of the double symmetry of the investigated geometries, only a quarter of each model has been analyzed. Considering plane strain conditions, both Plane182 (linear element) and Plane183 (quadratic element), as implemented in the Ansys® software (default options), have been investigated.

Some models are shown in Figure 4.10 to illustrate the simple free-generated meshes. The only parameter set before meshing is the average finite element size  $d$ , which has been chosen so that  $a/d=4$ , with  $a$  being the minimum among the half of the loaded plate thickness and the half of the attached plate thickness. Such assumption assures the coarser mesh possible according to the volume-free SED calibration presented in Section 4.5. The averaged SED has been evaluated directly from the FE models, over the few elements which shared the node located at the weld toe (notch tip), regardless of the shape and the number of the considered elements. Then, such volume-free averaged SED has been converted in the averaged SED on a circular control volume having radius  $R_0 = 0.28$  mm by means of Equation (4.28) and in mode 1 NSIF by using Equation (4.30), being the mode 2 stress distribution non-singular. In Equations (4.28) and (4.30) it has been used  $1-\lambda_1=0.326$  and  $e_1=0.118$ , being the V-notch opening angle  $2\alpha=135^\circ$  (see Chapter 1 for

reference). In parallel, all the geometries have been analyzed by using models with very fine meshes, as it is usually done when the main aim of the analyses is the direct evaluation of the NSIFs. The SED values have been calculated over the circular control volume having radius  $R_0 = 0.28$  mm according to the direct SED calculation and also exact NSIF values have been directly obtained analyzing local stress fields. The values of the strain energy density and of the NSIFs obtained by means of the volume-free approach for all the joints are reported in Tables 4.3 and 4.4 and are compared to those obtained by means of very fine meshes. By using quadratic FE the maximum error between the  $K_1$  values as determined by means of very fine meshes and those from direct SED evaluation is 5.3% (see Table 4.3, series 11), whereas the maximum error computed by using the volume-free approach is 5.7% (see Table 4.3, series 12). In all the other geometries, if the volume-free approach is used, the error is even smaller, being usually less than 3%. By using linear FE the maximum error becomes about equal to about 9% if the direct approach is used (see Table 4.4, series 2 and 3) and to 5% if the volume-free approach is used (see Table 4.4, series 12).

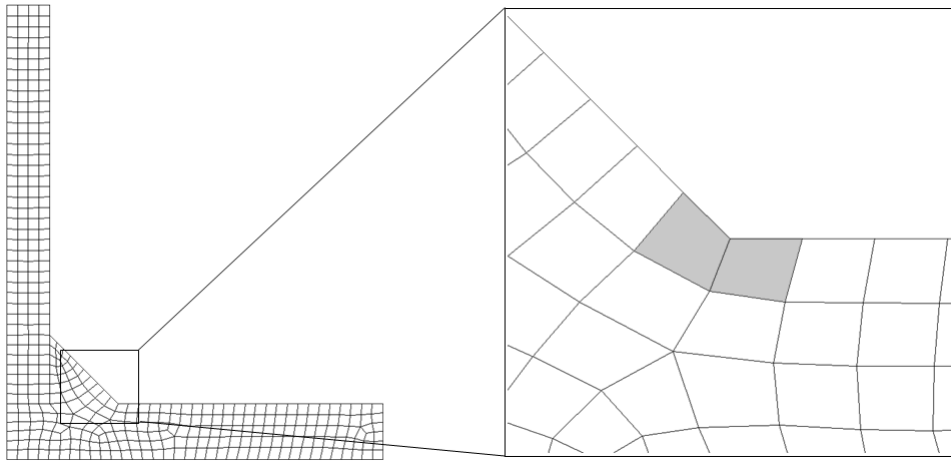
To investigate the stability of the volume-free SED calibration, all the geometries have been analyzed by varying the average element size from  $a/d=1$  to  $a/d=10$ , with steps of  $a/d$  equal to 1. For this purpose, linear finite elements have been used. The obtained results are shown in Figure 4.11, where the ratio of the exact mode 1 NSIFs over the ones calculated from the volume-free SED (Equation (4.30)) is plotted as a function of the mesh density ratio  $a/d$ . Figure 4.11 shows that the computed values are arranged into a narrow scatter band of  $\pm 5\%$  around the unit value, regardless of the weld geometry, as soon as the mesh density ratio reaches  $a/d=4$ . If mesh density ratios larger than 4 are used, the committed error always decreases (up to about 3% for  $a/d=10$ ), qualifying a really good reliability of the method. Figure 4.11 permits also to point out that, if errors larger than 5% are acceptable, depending on the design, really coarse meshes are allowed. To make an example, meshes characterized by  $a/d=2$  (which means that only 4 elements are present through the whole thickness) are suitable to estimate mode 1 NSIFs at the weld toe with a maximum error of about 10%. An example of free-generated mesh pattern characterized by  $a/d=2$  is shown in Figure 4.12 with reference to series 2. Being this the specific case, the committed error is 10%.

**Table 4.3.** Comparison between the values of the NSIFs evaluated with very fine meshes and coarse meshes, using the direct SED approach (Equation (4.13)) and the volume-free SED approach (Equation (4.30)). In the volume-free approach the coarser mesh possible has been used:  $a/d=4$ . Geometries according to Maddox [51] and Gurney [52], see Figure 4.2. The remotely applied nominal stress is 100 MPa. Parabolic elements have been used.

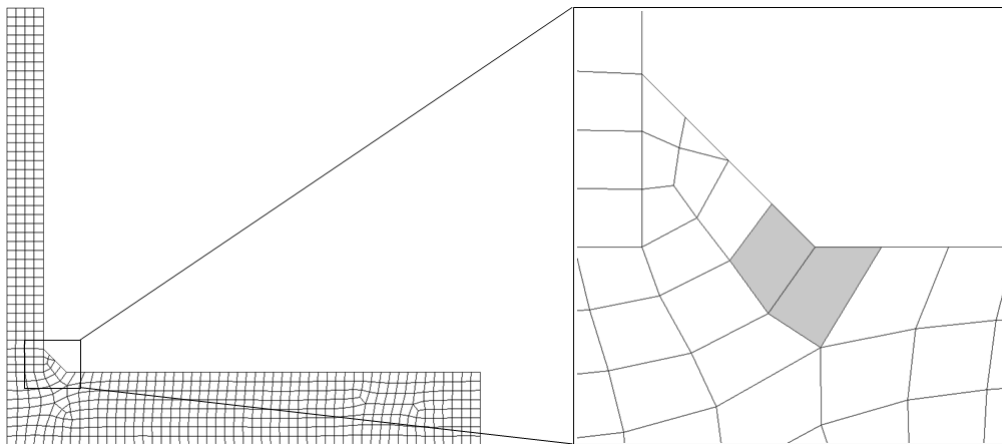
Series	t [mm]	h [mm]	L [mm]	Fine mesh $K_1$ [MPa mm <sup>0.326</sup> ]	Direct SED, $R_0 = 0.28$ mm			Volume-free SED, $R_0 = 0.28$ mm		
					$\bar{W}$ [N mm/mm <sup>3</sup> ]	$K_1$ [MPa mm <sup>0.326</sup> ]	$\Delta$ %	$\bar{W}$ [N mm/mm <sup>3</sup> ]	$K_1$ [MPa mm <sup>0.326</sup> ]	$\Delta$ %
1	13	8	10	265	0.0981	274.3	3.5	0.0949	268.5	1.3
2	50	16	50	396	0.2080	399.3	0.7	0.2149	404.1	2.0
3	100	16	50	413	0.2279	417.9	1.2	0.2295	417.6	1.1
4	13	5	3	228.8	0.0745	238.9	4.4	0.0705	231.4	1.1
5	13	10	8	267.5	0.0970	272.8	2.0	0.0970	271.4	1.4
6	25	5	3	231	0.0761	241.6	4.6	0.0714	233.0	0.9
7	25	9	32	329.5	0.1401	327.7	-0.5	0.1447	331.6	0.6
8	25	15	220	405	0.2082	399.4	-1.4	0.2151	404.2	-0.2
9	38	8	13	296.7	0.1195	302.5	2.0	0.1200	302.0	1.8
10	38	15	220	476	0.2866	469	-1.5	0.2828	463.5	-2.7
11	100	5	3	228.1	0.0752	240.2	5.3	0.0703	231.2	1.3
12	100	15	220	589.5	0.4288	573	-2.8	0.4091	557.5	-5.7

**Table 4.4.** Comparison between the values of the NSIFs evaluated with very fine meshes and coarse meshes, using the direct SED approach (Equation (4.13)) and the volume-free SED approach (Equation (4.30)). In the volume-free approach the coarser mesh possible has been used:  $a/d=4$ . Geometries according to Maddox [51] and Gurney [52], see Figure 4.2. The remotely applied nominal stress is 100 MPa. Linear elements have been used.

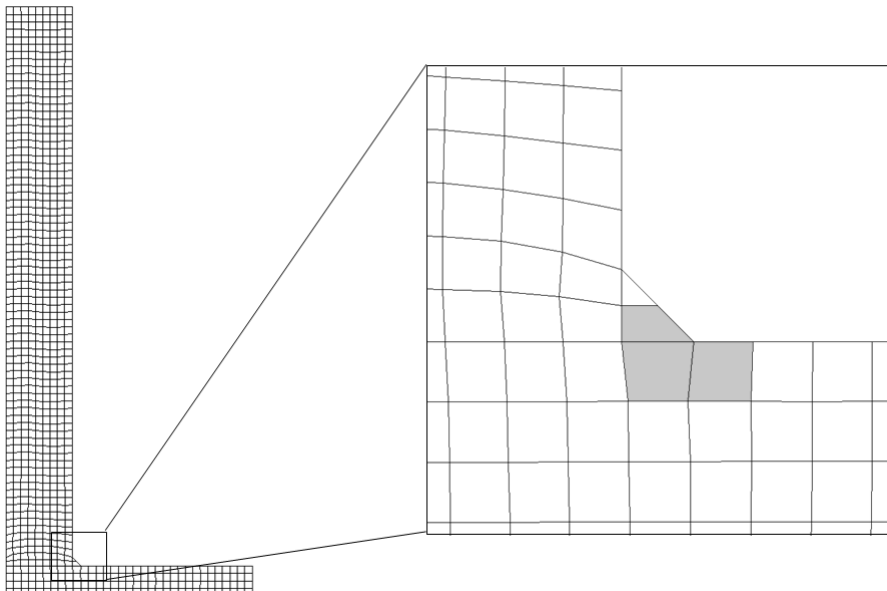
Series	t [mm]	h [mm]	L [mm]	Fine mesh $K_1$ [MPa mm <sup>0.326</sup> ]	Direct SED, $R_0 = 0.28$ mm			Volume-free SED, $R_0 = 0.28$ mm		
					$\bar{W}$ [N mm/mm <sup>3</sup> ]	$K_1$ [MPa mm <sup>0.326</sup> ]	$\Delta$ %	$\bar{W}$ [N mm/mm <sup>3</sup> ]	$K_1$ [MPa mm <sup>0.326</sup> ]	$\Delta$ %
1	13	8	10	265	0.0945	274.3	1.6	0.0988	274.0	3.3
2	50	16	50	396	0.2431	399.3	8.9	0.2266	414.9	4.6
3	100	16	50	413	0.2660	417.9	9.4	0.2382	425.4	2.9
4	13	5	3	228.8	0.0720	238.9	2.6	0.0735	236.2	3.1
5	13	10	8	267.5	0.0986	272.8	2.7	0.1008	276.8	3.4
6	25	5	3	231	0.0745	241.6	3.5	0.0745	238.0	2.9
7	25	9	32	329.5	0.1468	327.7	1.7	0.1514	339.1	2.8
8	25	15	220	405	0.2206	399.4	1.5	0.2244	412.9	1.9
9	38	8	13	296.7	0.1229	302.5	3.5	0.1259	309.3	4.1
10	38	15	220	476	0.3073	469	1.9	0.2965	474.6	-0.3
11	100	5	3	228.1	0.0743	240.2	4.5	0.0733	236.0	3.3
12	100	15	220	589.5	0.4724	573	2.0	0.4147	561.3	-5.0



Series 1: 370 elements in the entire model; 2 elements represent the “control volume”



Series 2: 576 elements in the entire model; 2 elements represent the “control volume”



Series 3: 800 elements in the entire model; 3 elements represent the “control volume”

**Figure 4.10.** Example of free-generated meshes to compute the volume-free SED. In gray are indicated the elements on which SED has been computed and averaged.

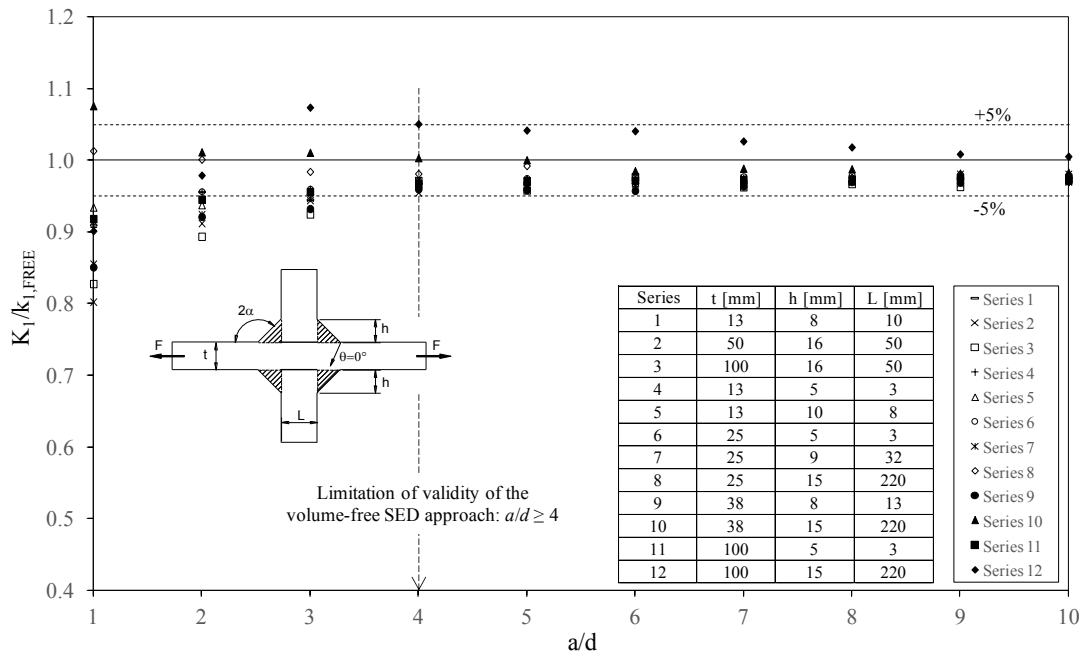
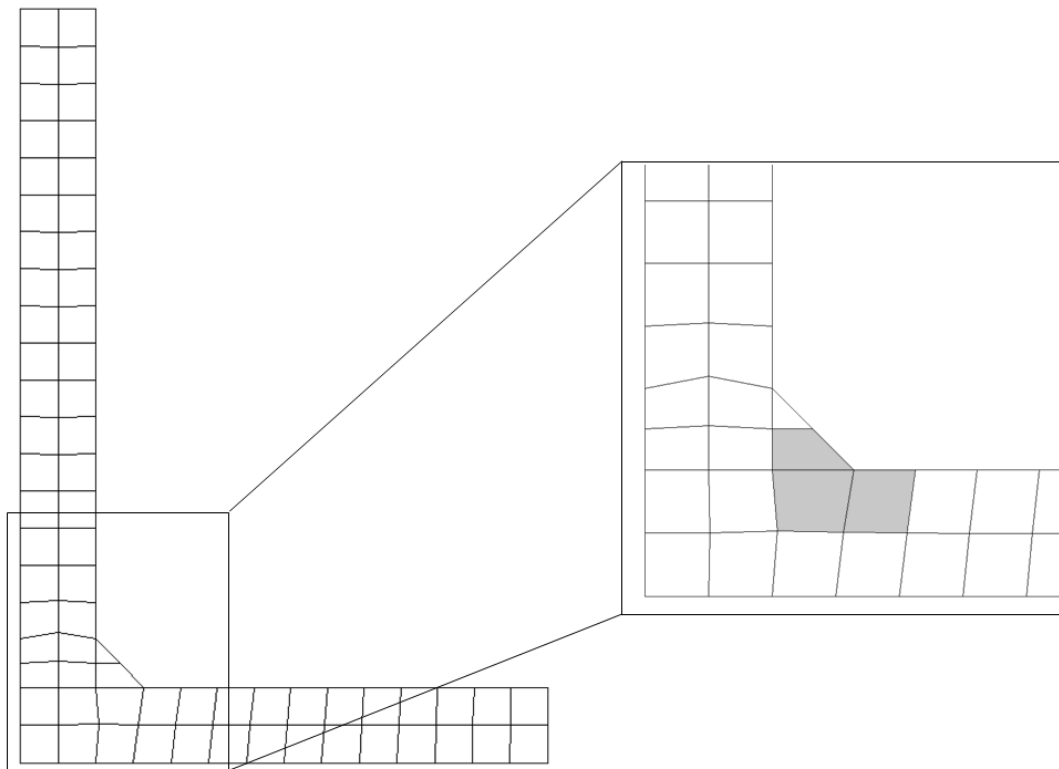


**Figure 4.11.** Ratio of the exact mode 1 NSIFs over those calculated from the volume-free SED. Linear elements have been used. A good stability of the method is shown for  $a/d \geq 4$ .



Series 2: 68 elements in the entire model; 3 elements represent the “control volume”

**Figure 4.12.** Example of extremely coarse free-generated mesh characterized by  $a/d=2$ . In gray are indicated the elements on which SED has been computed and averaged.

### 4.6.2 Three-dimensional models

The longitudinal non-load-carrying attachment represented schematically in Figure 4.13, which has been analyzed in terms of direct SED approach by Lazzarin and co-workers [40], has been reanalyzed here in terms of the volume-free SED approach. The finite element model is shown in Figure 4.14, where only a quarter of the geometry has been considered taking advantage of the symmetry conditions. It has been applied a nominal stress equal to 100 MPa, the Young's modulus and the Poisson's ratio equal to 206000 MPa and 0.3, respectively.

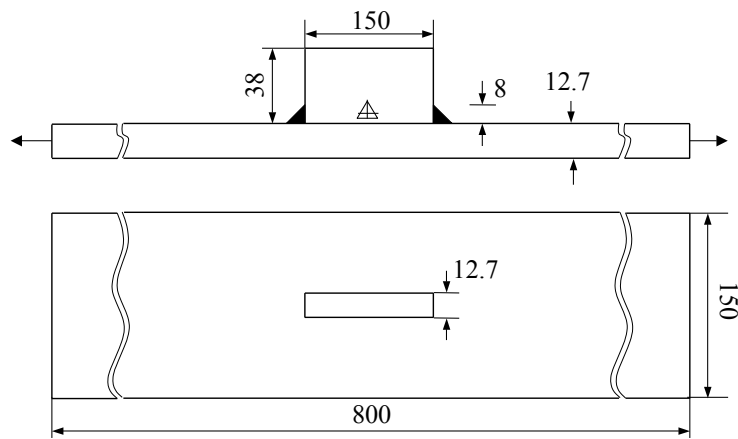


**Figure 4.13.** Geometry of the welded longitudinal attachment [40].

In principle, stress gradients can be present not only in the radial direction (according to Williams' plane solution) but also in the direction parallel to the line drawn by the V-notch tips (i.e. the weld toe direction). Then, to account for these secondary stress gradients, according to the direct SED approach, the strain energy density should be determined in a control volume (cylindrical sector) having a length approximately equal to its radius  $R_0$ , as shown in Section 3.3.1.

Results obtained by Lazzarin and co-workers [40] are here reported in Table 4.5, where very different mesh refinements are compared. Precise information about the number of FE used to model the control volume and the degrees of freedom characterizing the entire models are listed in Table 4.5. It is evident that the maximum difference between the models with very refined meshes and coarse meshes is less than 3%. All analyses have been carried out by Lazzarin and co-workers [40] using 20 node solid finite elements.



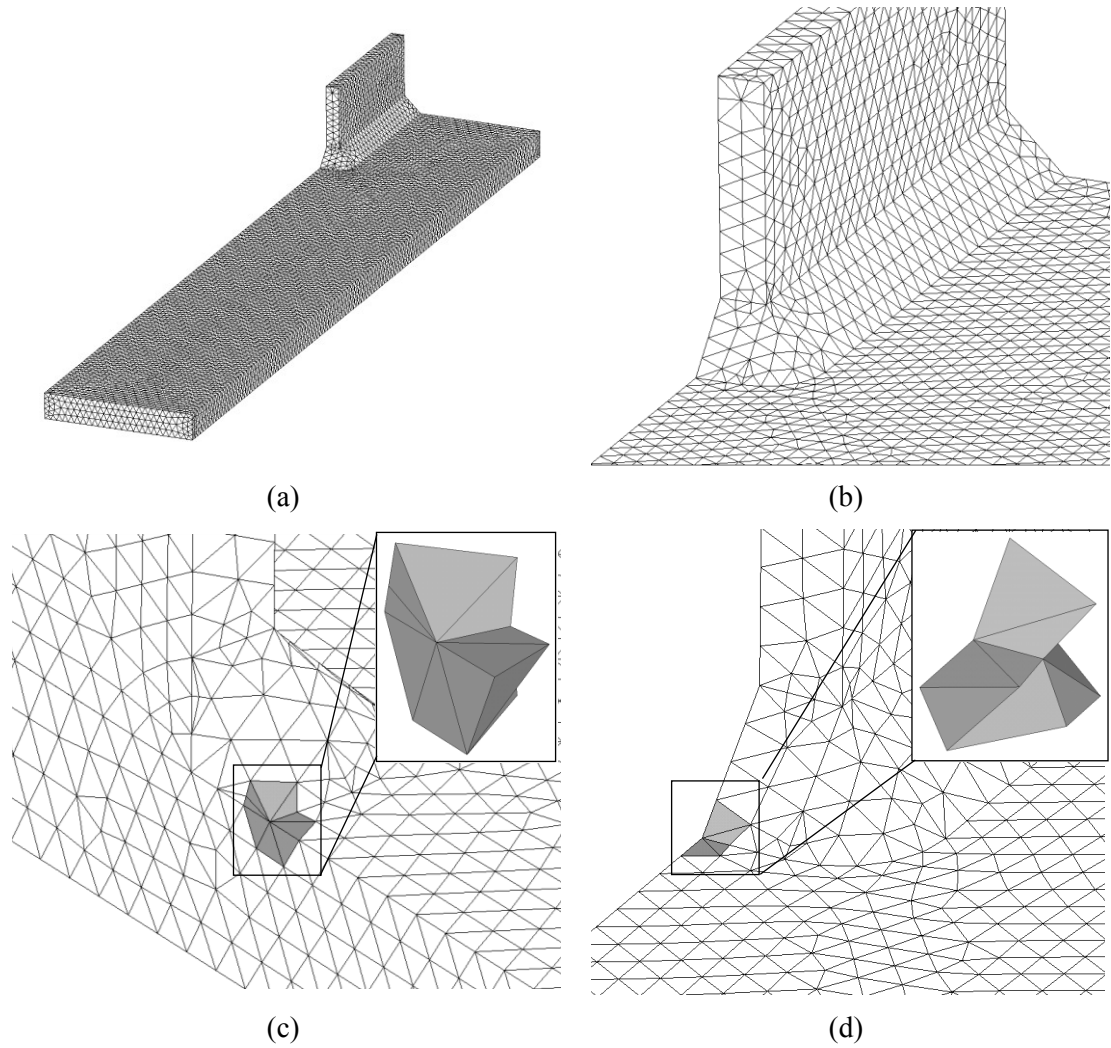


**Figure 4.14.** Longitudinal welded attachment: one quarter of the geometry. Free-generated tetrahedron mesh pattern having  $a/d=4$  (a). Detail of the mesh near the weld toe (b). Close-up views of the few elements over which SED has been computed and averaged (c-d).

**Table 4.5.** Results from 3D models having different number of elements within the control volume [40]. Direct SED computation in the control volume is considered.

$R_0$ [mm]	Elements in the volume	Degrees of freedom (complete model)	$\bar{W}$ [Nmm/mm <sup>3</sup> ]	$K_1$ [MPa mm <sup>0.326</sup> ]	$\Delta\%$
1.0	1696	$8.6 \cdot 10^5$	0.07937	373.5	0
	768	$4.6 \cdot 10^5$	0.07903	372.7	0.21
	324	$2.5 \cdot 10^5$	0.07896	372.5	0.26
	96	$1.7 \cdot 10^5$	0.07895	372.5	0.26
	24	$4.5 \cdot 10^4$	0.0779	370	0.93
	4	$1.1 \cdot 10^4$	0.07594	365.3	2.18

The values of the strain energy density and of the NSIFs obtained by means of the volume-free approach are reported in Tables 4.6 and 4.7 and are compared to those obtained by means of the direct approach (Table 4.5). By using quadratic tetrahedron finite elements (named Solid186 in Ansys® library) the maximum error between the  $K_1$  value determined from direct SED evaluation and by using the volume-free approach is 2.9% (see Table 4.6,  $a/d=4$ ). By using linear tetrahedron finite elements (named Solid285 in Ansys® library) the maximum error between the  $K_1$  value determined from direct SED evaluation and by using the volume-free approach is 2.6% (see Table 4.7,  $a/d=4$ ). NSIF values have been calculated *a posteriori* from the local strain energy density by using Equation (4.34), therefore tacitly considering realistic the hypothesis of plane strain.

**Table 4.6.** Comparison between the values of the NSIFs evaluated using the direct SED approach [40] and the volume-free SED approach (Equation (4.34)). The remotely applied nominal stress is 100 MPa.  $R_0=1$  mm is considered. Parabolic elements have been used.

	Ratio $a/d$	Elements in the volume	Degrees of freedom (whole model)	$\bar{W}$ [Nmm/mm <sup>3</sup> ]	$K_1$ [MPa mm <sup>0.326</sup> ]	$\Delta\%$
Direct SED [40]	-	1696	$8.6 \cdot 10^5$	0.07937	373.5	0
Volume-free SED	5	7	$8.1 \cdot 10^5$	0.0766	365.7	-2.1
	4	11	$4.6 \cdot 10^5$	0.0846	384.2	2.9

**Table 4.7.** Comparison between the values of the NSIFs evaluated using the direct SED approach [40] and the volume-free SED approach (Equation (4.34)). The remotely applied nominal stress is 100 MPa.  $R_0=1$  mm is considered. Linear elements have been used.

	Ratio $a/d$	Elements in the volume	Degrees of freedom (whole model)	$\bar{W}$ [Nmm/mm <sup>3</sup> ]	$K_1$ [MPa mm <sup>0.326</sup> ]	$\Delta\%$
Direct SED [40]	-	1696	$8.6 \cdot 10^5$	0.07937	373.5	0
Volume-free SED	5	7	$1.1 \cdot 10^5$	0.0785	369.9	-1.0
	4	11	$6.5 \cdot 10^4$	0.0841	383.1	2.6

## 4.7 Practical applications on cover plates by using different software

In the present section, some practical applications of the volume-free SED approach are presented, with the purpose of highlighting its advantages as compared to the direct SED computation in specific control volumes. To this end, some cover plate geometries investigated in Chapter 3 have been reanalyzed. Both plane and three-dimensional models have been adopted and further generality has been given to the approach by using two different finite element software (Ansys® and Straus7®).

### 4.7.1 Plane models

The cover plate geometry designated as 1000 series in Chapter 3 (Figure 3.39) has been reanalyzed here in terms of the volume-free SED approach, under plane strain condition. Two different finite element software have been used: Ansys® and Straus7®. Linear plane finite elements have been adopted, namely Plane182 and Quad4 in Ansys® and Straus7®, respectively. In both software default element formulation and default free meshing criteria have been set. The finite element models are shown in Figure 4.15, where only a half of the geometry has been considered taking advantage of the symmetry conditions. It has been applied a nominal stress equal to 56 MPa, the Young's modulus and the Poisson's ratio equal to 206000 MPa and 0.3, respectively.

The stress singularity, as well as the mode 1 NSIF, have been computed in Ansys® by using a very refined mesh with the smallest element having size of the order of  $10^{-5}$  mm (Figure 3.39(a)) and are shown in Figure 4.16. Afterwards, the volume-free SED approach has been used adopting free-generated meshes characterized by  $a/d=4$ . The notch opening angle  $2\alpha$  is equal to  $166^\circ$  and the related values of  $\lambda_I$  and  $e_I$  are 0.132 and 0.087, respectively. The values of the strain energy density and of the NSIFs obtained by means of the volume-free approach (in both Ansys® and Straus7®) are reported in Table 4.8 and are compared to those obtained in Chapter 3 by means of the direct approach (Table 3.9 for reference).

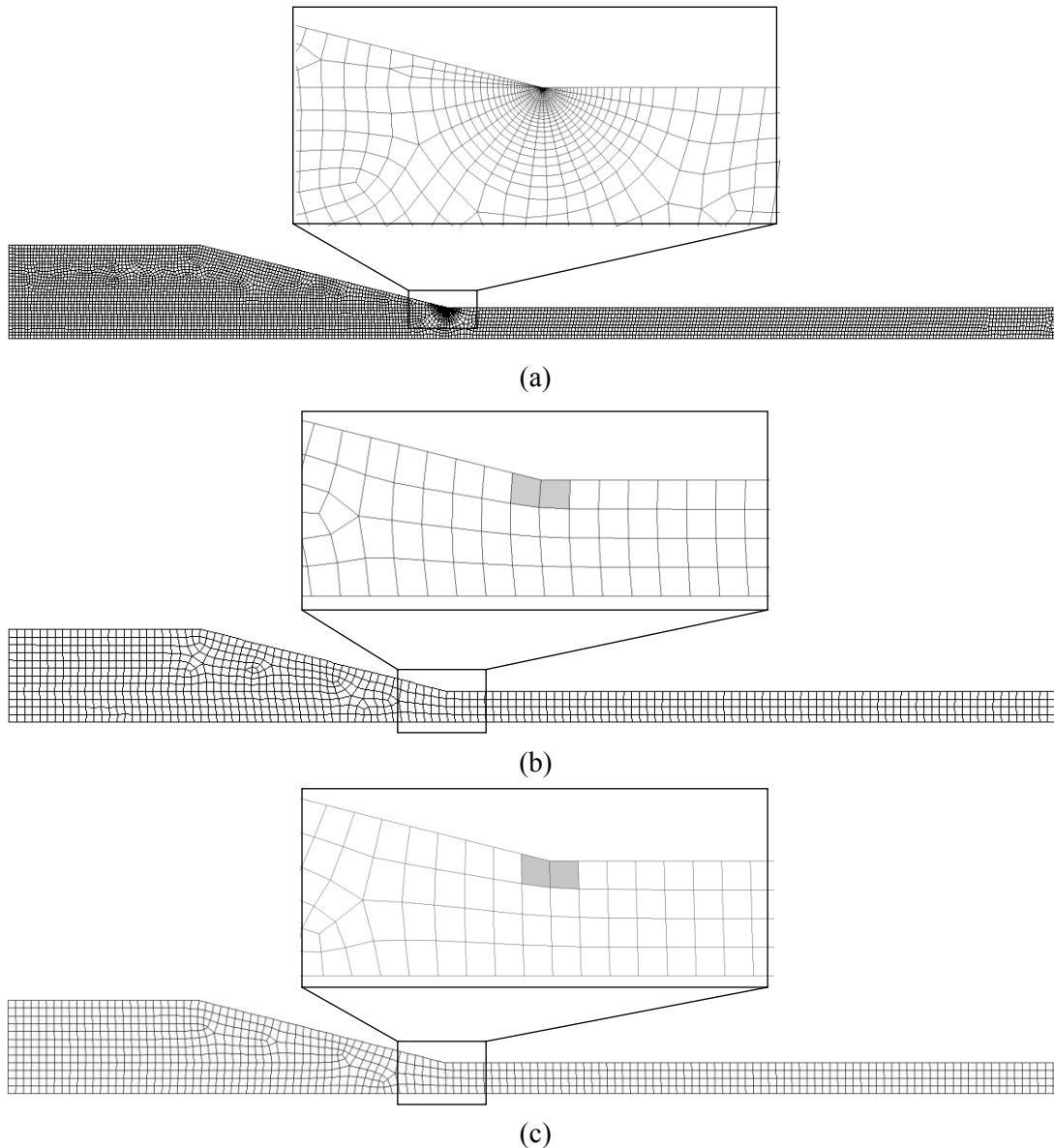


**Figure 4.15.** Cover plate geometry according to specimens series 1000 described in Chapter 3. Very refined mesh generated in Ansys® to determine  $K_I$  from local stress field (a). Coarse mesh free-generated in Ansys® to determine  $K_I$  from the volume-free SED ( $a/d=4$ ) (b). Coarse mesh free-generated in Straus7® to determine  $K_I$  from the volume-free SED (c). In gray are highlighted the elements over which SED has been calculated (b, c).

The maximum error between the  $K_I$  value accurately determined from the whole local stress field and by using the volume-free approach is 0.8% and 1.0% in Ansys® and in Straus7®, respectively (see Table 4.8). Obtained results show a robustness of the volume-free approach with respect to different software, which means with respect to different element formulations and meshing algorithms, in agreement with the considerations reported in Section 4.2.

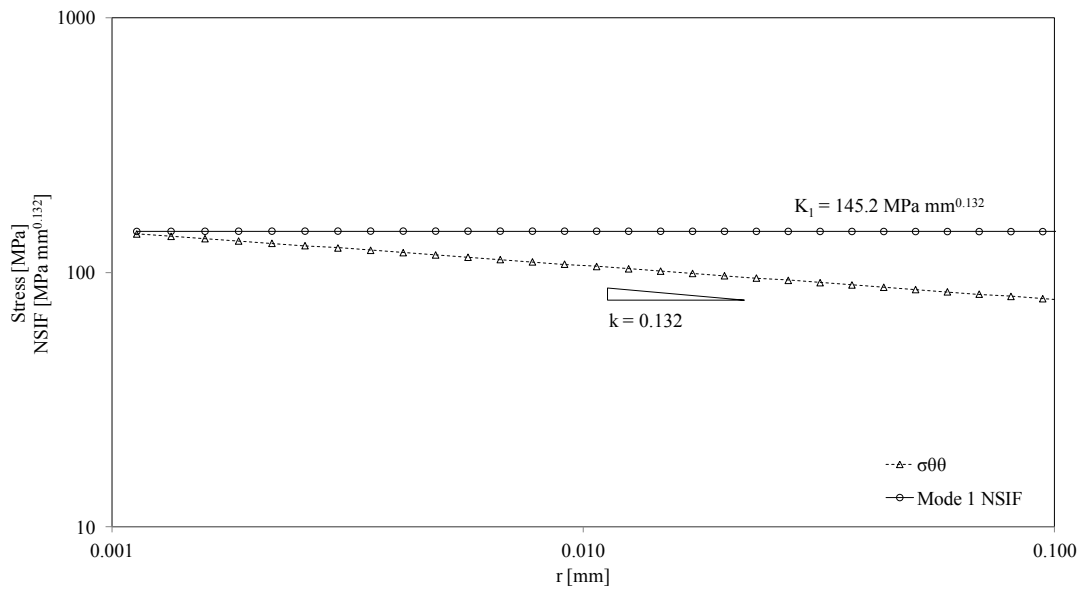


**Figure 4.16.** Log-log plot of tangential stress component  $\sigma_{\theta\theta}$ , along the notch bisector, in a cylindrical frame of reference centered at the weld toe (see Figure 4.1), as calculated in Ansys® using a very refined mesh (Figure 4.15(a)). The mode 1 NSIF is also plotted.

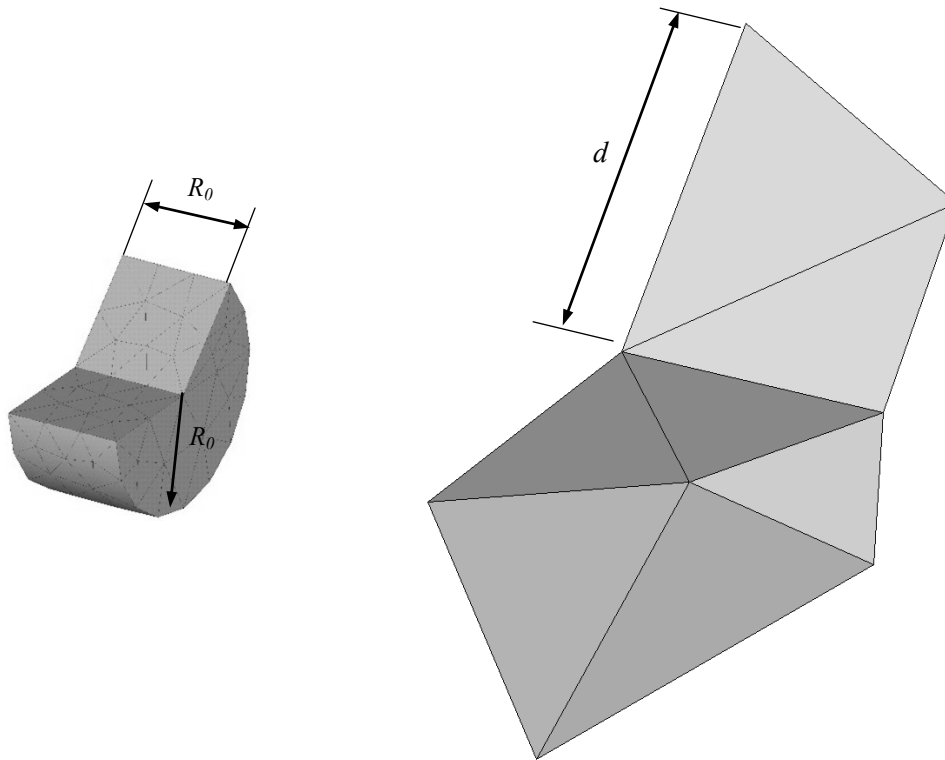
**Table 4.8.** Comparison between the values of the NSIFs calculated: from local stress, from the direct SED and from the volume-free SED, with different software. The remotely applied nominal stress is 56 MPa.  $R_0=0.28$  mm is considered. Linear elements have been used.

	Software	Ratio $a/d$	$\bar{W}$ [Nmm/mm <sup>3</sup> ]	$K_1$ [MPa mm <sup>0.326</sup> ]	$\Delta\%$
Local stress (see Figure 4.16)	Ansys®	-	-	145.2	
Direct SED (see Table 3.9)	Ansys®	-	0.01237	144.3	-0.6
Volume-free SED	Ansys®	4	0.01260	146.3	0.8
	Straus7®	4	0.01271	146.6	1.0

## 4.7.2 Three-dimensional models

### 4.7.2.1 Tapered cover plate in Straus7® environment

The tapered cover plate geometry presented in Section 3.3.1 has been reanalyzed here in terms of the volume-free SED approach in Straus7® environment. The radius  $R$  and the angle  $\beta$  characterizing the cover plate end have been assumed equal to 5 mm and  $20^\circ$ , respectively (according to Figure 3.10). Linear tetrahedron finite elements have been adopted, namely Tetra4. Default element formulation and default free meshing criteria have been set. The control volume according to the direct strain energy density computation and the few elements, which share the node located at the weld toe, according to the volume-free approach are compared in Figure 4.17.



202 elements in the control volume of radius  $R_0=0.28$  mm at the weld toe.

Free mesh generated in Ansys®.

(a)

7 elements which share the node located at the weld toe (average mesh size  $d=1$  mm).

Free mesh generated in Straus7®.

(b)

**Figure 4.17.** SED control volume according to the direct strain energy density computation (a), compared to the few elements, which share the node located at the weld toe, according to the volume-free approach by using  $a/d=5$  (b). Figures are correctly proportioned.

The volume-free SED approach has been used adopting free-generated meshes characterized by  $a/d=5$ . It has been considered a nominal stress equal to 56 MPa, the Young's modulus and the Poisson's ratio equal to 206000 MPa and 0.3, respectively. The values of the strain energy density and of the NSIFs obtained by means of the volume-free approach in Straus7® are reported in Table 4.9 and are compared to those obtained in Chapter 3 by means of the direct approach in Ansys® (Figure 3.13 for reference). Also in this case, where a three-dimensional model has been considered, the obtained results show the robustness of the volume-free approach with respect to different software.

**Table 4.9.** Comparison between the values of the NSIFs calculated from the direct SED and from the volume-free SED, with different software. The remotely applied nominal stress is 56 MPa.  $R_\sigma=0.28$  mm is considered. Linear elements have been used.

	Software	Ratio $a/d$	$\bar{W}$ [Nmm/mm <sup>3</sup> ]	$K_1$ [MPa mm <sup>0.326</sup> ]	$\Delta\%$
Direct SED (see Figure 3.13)	Ansys®	-	0.0679	227.3	0
Volume-free SED	Straus7®	5	0.0653	222.9	2.0

#### 4.7.2.2 Transverse cover plate in Ansys® environment

The transverse cover plate geometry presented in Section 3.3.2 has been reanalyzed here through the volume-free SED approach in Ansys® environment, with the aim to give a practical three-dimensional application of the method.

The finite element model is shown in Figure 4.18(a), where only a quarter of the geometry has been considered, taking advantage of the symmetry conditions. The mesh pattern has been free-generated by using the Ansys® free meshing algorithm. The average element size has been set to 1 mm, which turns in a mesh density ratio  $a/d=5 \geq 4$ . Linear tetrahedron finite elements have been adopted, namely Solid285. Default element formulation and default free meshing criteria have been set. It has been considered a nominal stress equal to 56 MPa, the Young's modulus and the Poisson's ratio equal to 206000 MPa and 0.3, respectively.

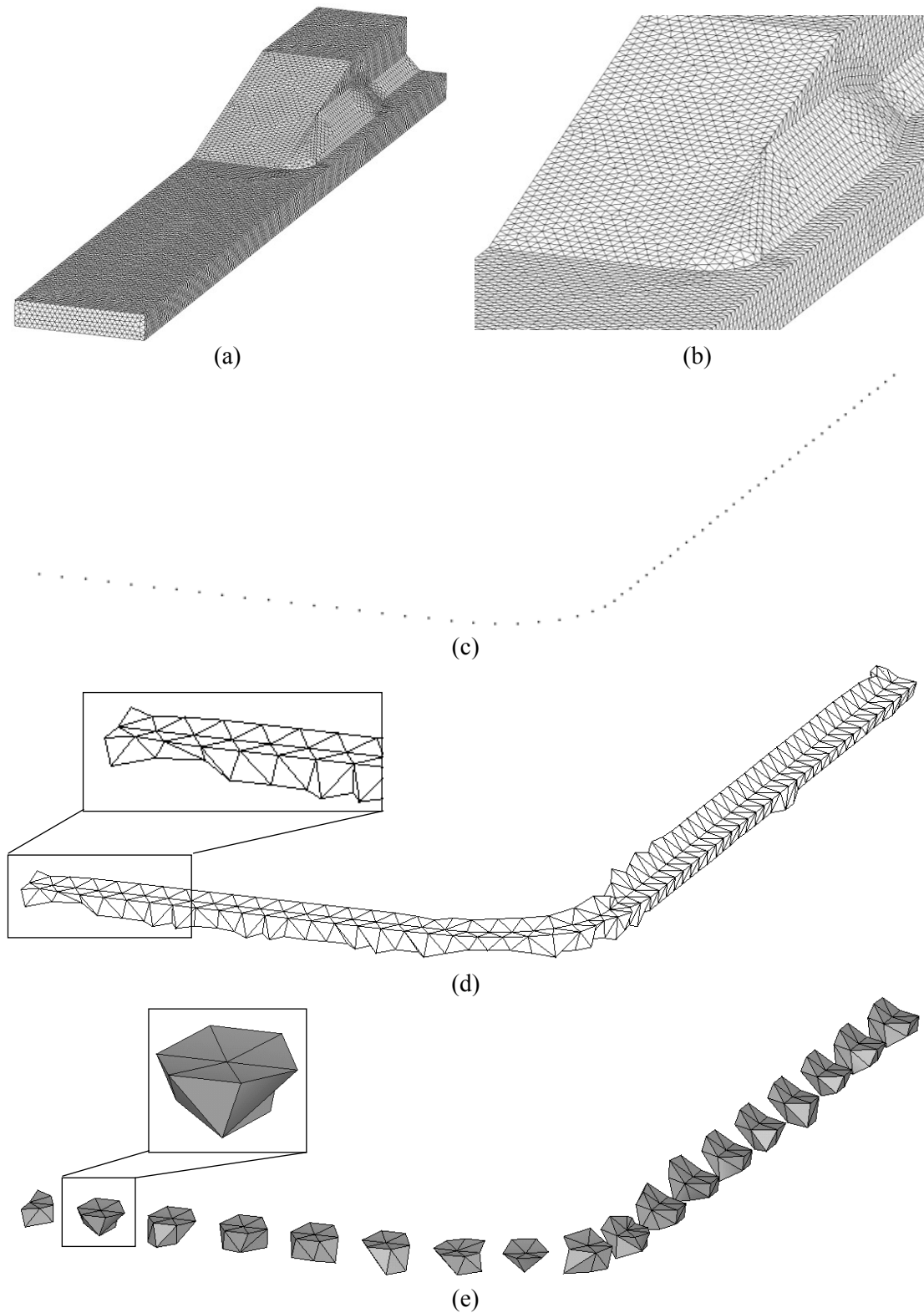


**Figure 4.18.** Transverse cover plate model. Free-generated 4-nodes tetrahedron mesh pattern having  $a/d=5$  (a). Detail of the mesh near the weld toe (b) and nodes located at the weld toe (c). Close-up views of the elements which have at least a node at the weld toe (d) and of some of the few elements over which SED has been computed and averaged (e).



The averaged strain energy density has been computed all along the weld toe line, according to the volume-free approach, simply by selecting the nodes located at the weld toe (Figure 4.18(c)) and then, node by node, selecting the elements that share it (example is given in Figure 4.18(e)). Mode 1 NSIFs along the weld toe have been calculated *a posteriori* (Equation (4.13)) from SED values computed in the control volumes (reference is made to Figure 3.15, where quadratic tetrahedron elements have been used, namely Solid186) and from the volume-free SED (Equation (4.34)). The weld shape under investigation is characterized by a notch opening angle of  $166^\circ$  along the transverse weld, which gradually decreases along the rounded corner and finally turns into  $135^\circ$  along the longitudinal weld (Figure 4.18(b)). So, in Equations (4.13) and (4.34) values of  $\lambda_I$  and  $e_I$ , both dependent on the notch opening, are needed. It has been assumed linear variation of  $\lambda_I$  and  $e_I$ , along the corner, from  $\lambda_I(166^\circ)=0.132$  and  $e_I(166^\circ)=0.087$  to  $\lambda_I(135^\circ)=0.326$  and  $e_I(135^\circ)=0.118$ .

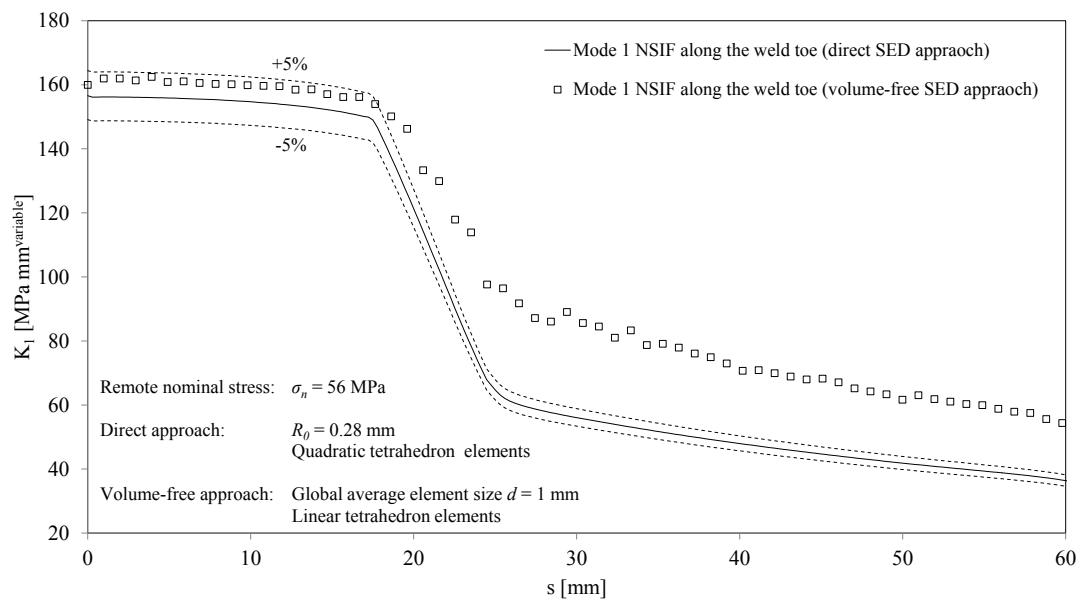


**Figure 4.19.** Comparison between trends of mode 1 NSIF along the weld toe, as calculated *a posteriori* from SED values computed in the control volumes (solid line) and from the volume-free SED (empty dots). Dashed lines represent the band  $\pm 5\%$  with respect to the solid line. In the volume-free analysis a global average element size  $d=1$  mm has been set.

The trends of the mode 1 NSIF along the weld toe, as calculated *a posteriori* from SED values directly computed in the control volumes and from the volume-free SED values are compared in Figure 4.19. Results indicate that the values of NSIF obtained

by means of the volume-free approach fit inside a band of  $\pm 5\%$ , centered on the values obtained by means of the direct approach, all along the portion of weld toe where mode 1 loading is dominant. This means that the estimate is accurate within the portion of weld toe line almost normal to the direction of the remotely applied load ( $0 \leq s \leq 17.5$  mm). Outside of such length, the estimate is quite on the safety side. Such result is a consequence of Equation (4.34), where the “size effect” is related to mode 1 eigenvalue  $\lambda_1$  only. Being fatigue failures at weld toe mostly driven by mode 1 loading, such approximation should not be considered a problem. Indeed, Figure 4.19 shows that at fatigue critical points ( $0 \leq s \leq 17.5$  mm) the estimate is accurate. The SED reference values (Figure 3.15) have been computed in control volumes with radius  $R_0 = 0.28$  mm. So, if in the volume-free model of Figure 4.18 a mesh refinement along the toe line is performed and an average element size  $d' \approx 0.28$  mm is locally reached, keeping the global element size  $d = 1$  mm, the contribution of the “size effect” in Equation (4.34) is remarkably reduced.

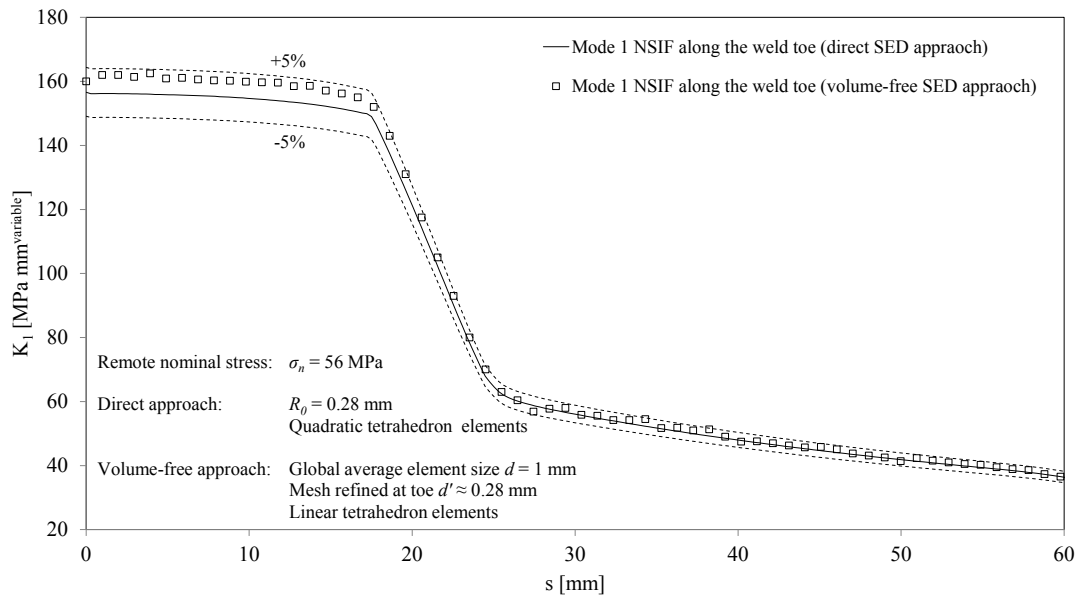


**Figure 4.20.** Comparison between trends of mode 1 NSIF along the weld toe, as calculated from SED values computed in the control volumes (solid line) and from the volume-free SED (empty dots). Dashed lines represent the band  $\pm 5\%$  with respect to the solid line. In the volume-free analysis global element size  $d = 1$  mm and refinement at weld toe has been set.

Consequently, the committed error decreases within  $\pm 5\%$  all along the weld toe (Figure 4.20). The possibility of using a globally coarse mesh ( $a/d \geq 4$ ) with a local

refinement at toe permits to accurately evaluate SED and NSIFs in 3D geometries by using a free-generated mesh of linear elements, keeping small the overall number of degrees of freedom.

#### **4.8 Discussion and conclusion**

Whilst the NSIF evaluation needs very fine meshes in the vicinity of the points of singularity, which is an important drawback of the approach, the mean value of the elastic SED on a control volume can be accurately determined by using relatively coarse meshes. However, some meshing criteria have to be used to take advantage of this coarse mesh option: both the SED control volume and specific geometrical modules, which “guide” the free meshing algorithm, have to be introduced, which results in a time consuming pre-processing procedure, particularly in the presence of complex three-dimensional geometries. That is why other methods, among which the PSM, where modeling the control volume is not necessary and the coarse mesh option is maintained, have been proposed in the literature as alternative, industrial oriented approaches. However, being the PSM a stress based procedure, different stress extrapolation rules from integration points to nodes, as well as different finite element formulations and significantly different mesh patterns, with respect to the limitations provided by calibration, may lead, in principle, to different values of the peak stresses. This means that, despite the undeniable advantages of the PSM (primarily the allowance of coarse free-generated meshes, but also the need of only one-point stress based parameter), the opportunity to use an energetic parameter, which is numerically computed from nodal displacements and therefore is mesh and element formulation insensitive, is lost.

Within this framework, the aim of the chapter was to investigate the idea of having a method which keeps both SED and PSM advantages. It has been found that the local SED, as well as the peak stress, can be conveniently computed by using a coarse and completely free-generated mesh, on the only few elements which share the node located at a notch tip, regardless of the notch opening angle. The method, here called volume-free SED approach, has been theoretically formalized and its limitations of applicability have been provided in terms of mesh density ratio  $a/d$ , where  $a$  is the notch depth (in case of crack and V-notch tips) or the half of the smallest plate thickness involved in a welded joint (in case of weld toe regions). No other rules on

meshing criteria and element formulation have been found necessary. In detail, for plane cases, a free-generated mesh composed by mixed quadrilateral and triangular elements has been found suitable, regardless of whether linear or quadratic elements are used. For three-dimensional cases, a free-generated mesh of linear tetrahedron elements has been found suitable. In both cases, the coarse mesh option is obtained taking advantage of the scale effect of the NSIF approach.

The degree of accuracy of the method has been evaluated by using a large number of FE models, both bi- and three-dimensional. It has been found that, under pure mode loadings, the mode 1 and mode 2 NSIFs can be determined *a posteriori* from the volume-free SED with a maximum difference between values obtained from very refined meshes and those from coarse meshes of about 5%. It holds true as soon as the mesh density ratio is equal or larger than 4, under mode 1 loading, and equal or larger than 3 under mode 2 loading. In all investigated cases, the method has shown insensitivity to mesh pattern, mesh refinement and finite element formulation.

In the author's opinion, undeniable advantages can be provided by the volume-free SED approach in performing the fatigue (and brittle) assessment of a welded component or notched specimen. Within the limitation of applicability presented in this chapter, the volume-free SED allows the application of both the classical SED and the NSIF approaches in a simple and efficient way. However, despite the availability of modern computational equipments (e.g. high performance computing), still appears challenging but tricky the idea to perform the fatigue assessment of large structures (e.g. bridges), characterized by thousands of welds, "simply" by "filling" the whole three-dimensional CAD model with tetrahedron elements by using a free meshing tool. Just to think that all weld beads should be explicitly represented in the CAD model, before their fatigue (and resistance) design is performed. Being design an iterative procedure from geometrical definition (CAD model) to resistance assessment (numerical model), it seems complex and time consuming the need of explicit representation of welds. Moreover, at the moment, no normative definition of SED and NSIF local approaches is available for a designer. That is why in the following Chapters 5 to 8 a different approach, fully compliant with standards and based on coarse shell element models, without weld representation, is formalized and automated.

**References**

- [1] K. Wallin, P. Karjalainen-Roikonen, P. Suikkanen, Harmonization and improvement of fracture mechanical design codes for steel constructions, *Eng. Fract. Mech.* (2017).
- [2] I. Lotsberg, Development of Fatigue Design Standards for Marine Structures, in: Vol. 9 Offshore Geotech. Torgeir Moan Honor. Symp., ASME, 2017.
- [3] M. Feldmann, B. Eichler, G. Sedlacek, W. Dahl, P. Langenberg, C. Butz, H. Leendertz, G. Hanswille, H. Amorim-Varum, Choice of steel material for bridge bearings to avoid brittle fracture, (2012).
- [4] R.D. Henshell, K.G. Shaw, Crack tip finite elements are unnecessary, *Int. J. Numer. Methods Eng.* 9 (1975) 495–507.
- [5] R.S. Barsoum, Further application of quadratic isoparametric finite elements to linear fracture mechanics of plate bending and general shells, *Int. J. Fract.* 11 (1975) 167–169.
- [6] J.E. Akin, The generation of elements with singularities, *Int. J. Numer. Methods Eng.* 10 (1976) 1249–1259.
- [7] A. Portela, M.H. Aliabadi, D.P. Rooke, Efficient boundary element analysis of sharp notched plates, *Int. J. Numer. Methods Eng.* 32 (1991) 445–470.
- [8] I. Babuška, A. Miller, The post-processing approach in the finite element method—part 1: Calculation of displacements, stresses and other higher derivatives of the displacements, *Int. J. Numer. Methods Eng.* 20 (1984) 1085–1109.
- [9] B.A. Szabò, Z. Yosibash, Numerical analysis of singularities in two dimensions. Part 2: computation of generalized flux/stress intensity factors, *Int. J. Numer. Methods Eng.* 39 (1996) 409–434.
- [10] D.M. Tracey, Finite elements for determination of crack tip elastic stress intensity factors, *Eng. Fract. Mech.* 3 (1971) 255–265.
- [11] S.L. Pu, M.A. Hussain, W.E. Lorensen, The collapsed cubic isoparametric element as a singular element for crack problems, *Int. J. Numer. Methods Eng.* 12 (1978) 1727–1742.
- [12] P.R. Heyliger, R.D. Kriz, Stress intensity factors by enriched mixed finite elements, *Int. J. Numer. Methods Eng.* 28 (1989) 1461–1473.
- [13] S.E. Benzley, Representation of singularities with isoparametric finite

- elements, *Int. J. Numer. Methods Eng.* 8 (1974) 537–545.
- [14] N. Moes, J. Dolbow, A finite element method for crack growth without remeshing, *Int. J. Numer.* 150 (1999) 131–150.
- [15] Y. Abdelaziz, A. Hamouine, A survey of the extended finite element, *Comput. Struct.* 86 (2008) 1141–1151.
- [16] D. Givoli, L. Rivkin, The DtN finite element method for elastic domains with cracks and re-entrant corners, *Comput. Struct.* 49 (1993) 633–642.
- [17] P. Tong, T.H.H. Pian, S.J. Lasry, A hybrid-element approach to crack problems in plane elasticity, *Int. J. Numer. Methods Eng.* 7 (1973) 297–308.
- [18] B.L. Karihaloo, Q.Z. Xiao, Hybrid stress elements for accurate solution of elasticity problems with traction-free segments, in: *Int. Conf. Eng. Comput. Technol.*, 2000: pp. 109–125.
- [19] Q.Z.Z. Xiao, B.L.L. Karihaloo, X.Y.Y. Liu, Direct determination of SIF and higher order terms of mixed mode cracks by a hybrid crack element, *Int. J. Fract.* 125 (2004) 207–225.
- [20] K.Y. Lin, P. Tong, Singular finite elements for the fracture analysis of V-notched plate, *Int. J. Numer. Methods Eng.* 15 (1980) 1343–1354.
- [21] A. Seweryn, Modeling of singular stress fields using finite element method, *Int. J. Solids Struct.* 39 (2002) 4787–4804.
- [22] A. Seweryn, Brittle fracture criterion for structures with sharp notches, *Eng. Fract. Mech.* 47 (1994) 673–681.
- [23] L.S. Nui, C. Chehimi, G. Pluinage, Stress field near a large blunted tip V-notch and application of the concept of the critical notch stress intensity factor (NSIF) to the fracture toughness of very brittle materials, *Eng. Fract. Mech.* 49 (1994) 325–335.
- [24] T. Fett, Failure of brittle materials near stress singularities, *Eng. Fract. Mech.* 53 (1996) 511–518.
- [25] M. Dunn, W. Suwito, Fracture initiation at sharp notches under mode I, mode II, and mild mixed mode loading, *Int. J. Fract.* 84 (1997) 367–381.
- [26] P. Lazzarin, R. Zambardi, A finite-volume-energy based approach to predict the static and fatigue behavior of components with sharp V-shaped notches, *Int. J. Fract.* 112 (2001) 275–298.
- [27] S. Kihara, A. Yoshii, A Strength Evaluation Method of a Sharply Notched

- Structure by a New Parameter, “The Equivalent Stress Intensity Factor,” *JSM Int. Journal. Ser. 1, Solid Mech. Strength Mater.* 34 (1991) 70–75.
- [28] T. Boukharouba, T. Tamine, L. Niu, C. Chehimi, G. Pluinage, The use of notch stress intensity factor as a fatigue crack initiation parameter, *Eng. Fract. Mech.* 52 (1995) 503–512.
- [29] Y. Verreman, B. Nie, Early development of fatigue cracking at manual fillet welds, *Fatigue Fract. Eng. Mater. Struct.* 19 (1996) 669–681.
- [30] P. Lazzarin, R. Tovo, A Notch Intensity Factor Approach To the Stress Analysis of Welds, *Fatigue Fract. Eng. Mater. Struct.* 21 (1998) 1089–1103.
- [31] B. Atzori, G. Meneghetti, Fatigue strength of fillet welded structural steels: Finite elements, strain gauges and reality, *Int. J. Fatigue.* 23 (2001) 713–721.
- [32] P. Livieri, P. Lazzarin, Fatigue strength of steel and aluminium welded joints based on generalised stress intensity factors and local strain energy values, *Int. J. Fract.* 133 (2005) 247–276.
- [33] B. Gross, A. Mendelson, Plane elastostatic analysis of V-notched plates, *Int. J. Fract. Mech.* 8 (1972) 267–276.
- [34] M.L. Williams, Stress singularities resulting from various boundary conditions in angular corners of plates in extension, *J. Appl. Mech.* 19 (1952) 526–528.
- [35] F. Berto, P. Lazzarin, Recent developments in brittle and quasi-brittle failure assessment of engineering materials by means of local approaches, *Mater. Sci. Eng. R.* 75 (2014) 1–48.
- [36] P. Lazzarin, A. Campagnolo, F. Berto, A comparison among some recent energy- and stress-based criteria for the fracture assessment of sharp V-notched components under mode I loading, *Theor. Appl. Fract. Mech.* 71 (2014) 21–30.
- [37] F. Berto, A. Campagnolo, P. Lazzarin, Fatigue strength of severely notched specimens made of Ti-6Al-4V under multiaxial loading, *Fatigue Fract. Eng. Mater. Struct.* 38 (2015) 503–517.
- [38] P. Gallo, F. Berto, P. Lazzarin, High temperature fatigue tests of notched specimens made of titanium Grade 2, *Theor. Appl. Fract. Mech.* 76 (2015) 27–34.
- [39] F. Berto, P. Lazzarin, Multiparametric full-field representations of the in-plane stress fields ahead of cracked components under mixed mode loading, *Int. J.*

- Fatigue. 46 (2013) 16–26.
- [40] P. Lazzarin, F. Berto, F.J. Gomez, M. Zappalorto, Some advantages derived from the use of the strain energy density over a control volume in fatigue strength assessments of welded joints, *Int. J. Fatigue*. 30 (2008) 1345–1357.
- [41] P. Lazzarin, F. Berto, M. Zappalorto, Rapid calculations of notch stress intensity factors based on averaged strain energy density from coarse meshes: theoretical bases and applications, *Int. J. Fatigue*. 32 (2010) 1559–1567.
- [42] G. Meneghetti, A. Campagnolo, F. Berto, B. Atzori, Averaged strain energy density evaluated rapidly from the singular peak stresses by FEM: cracked components under mixed-mode (I + II) loading, *Theor. Appl. Fract. Mech.* 79 (2015) 113–124.
- [43] G. Meneghetti, A. Campagnolo, F. Berto, Averaged strain energy density estimated rapidly from the singular peak stresses by FEM: Cracked bars under mixed-mode (I + III) loading, *Eng. Fract. Mech.* 167 (2016) 20–33.
- [44] A. Campagnolo, G. Meneghetti, F. Berto, Rapid finite element evaluation of the averaged strain energy density of mixed-mode (I + II) crack tip fields including the T-stress contribution, *Fatigue Fract. Eng. Mater. Struct.* 39 (2016) 982–998.
- [45] G. Meneghetti, P. Lazzarin, Significance of the elastic peak stress evaluated by FE analyses at the point of singularity of sharp V-notched components, *Fatigue Fract. Eng. Mater. Struct.* 30 (2007) 95–106.
- [46] G. Meneghetti, The use of peak stresses for fatigue strength assessments of welded lap joints and cover plates with toe and root failures, *Eng. Fract. Mech.* 89 (2012) 40–51.
- [47] G. Meneghetti, The peak stress method applied to fatigue assessments of steel and aluminium fillet-welded joints subjected to mode I loading, *Fatigue Fract. Eng. Mater. Struct.* 31 (2008) 346–369.
- [48] G. Meneghetti, B. Atzori, G. Manara, The Peak Stress Method applied to fatigue assessments of steel tubular welded joints subject to mode-I loading, *Eng. Fract. Mech.* 77 (2010) 2100–2114.
- [49] G. Meneghetti, C. Guzzella, The peak stress method to estimate the mode I notch stress intensity factor in welded joints using three-dimensional finite element models, *Eng. Fract. Mech.* 115 (2014) 154–171.



- [50] G. Meneghetti, C. Guzzella, B. Atzori, The peak stress method combined with 3D finite element models for fatigue assessment of toe and root cracking in steel welded joints subjected to axial or bending loading, in: *Fatigue Fract. Eng. Mater. Struct.*, 2014: pp. 722–739.
- [51] S.J. Maddox, *The Effect of Plate Thickness on the Fatigue Strength of Fillet Welded Joints*, (1987).
- [52] T.R. Gurney, *The fatigue strength of transverse fillet welded joints*, Abington Publishing, Cambridge, 1991.
- [53] R. Tovo, P. Lazzarin, Relationships between local and structural stress in the evaluation of the weld toe stress distribution, *Int. J. Fatigue*. 21 (1999) 1063–1078.
- [54] P. Lazzarin, P. Livieri, Notch stress intensity factors and fatigue strength of aluminium and steel welded joints, *Int. J. Fatigue*. 23 (2001) 225–232.
- [55] I. Poutiainen, G. Marquis, A fatigue assessment method based on weld stress, *Int. J. Fatigue*. 28 (2006) 1037–1046.



## 5. Local parameters and nominal stresses: a sound link for an efficient structural design

### Highlights

In this chapter the relationship between the local stress field near the weld toe or root and the nominal stress field, linearly distributed along the plate thickness, evaluated at a proper distance  $\delta$  from the weld is analyzed. An analytical relationship between  $\delta$  and the loaded plate thickness is provided and a criterion for the estimation of the averaged strain energy density (SED), both at the weld toe and at the weld root, as well as *a posteriori* the related NSIFs, as an explicit function of the nominal load components (membrane loads, shear loads and bending moments) is presented. An explicit link between the local and the nominal stress fields is therefore established. Properly fitting numerical results obtained through parametric finite element analyses, a significant set of ready-to-use abaci of welded joints' stress concentration has been produced. Such set of abaci permits the rapid estimation of both SED and NSIF values at the weld toe and at the weld root of joints having wide interest in industrial applications. The estimation can be performed through comfortable polynomial expressions, as a function of main weld geometrical parameters and the nominal loading condition, no longer needing detailed and computationally expensive numerical models. A practical application is also given at the end of the chapter. In this way, the proposed method appears suitable for performing the large number of fatigue assessments that a nowadays complex steel structure requires. In spite of this, the current lack of normative compliance of both SED and NSIF approaches can be a possible obstacle in industrial applications.



## 5.1 Introduction

The currently used methods of fatigue strength assessment of welded joints can be divided into different categories depending on the performed stress analysis: it is possible to distinguish criteria based on nominal stress, structural stress, local stress as other well-established methodologies, as discussed in Chapter 1. The main problem in applying local criteria is the degree of arbitrariness related to the definition of the exact weld shape [1]. However, several authors have shown the possibility of efficiently modeling the real weld geometry, which is randomly variable, as an ideal triangular shape [2,3]; which corresponds in most cases to an open notch having opening angle equal to  $135^\circ$ . Under this assumption it is also possible to neglect the weld toe radius [3,4], since usual welding processes produce a very small weld toe radius, as compared to other geometrical parameters. By so doing, the presence of a sharp notch in a linear elastic condition results in a singular stress distribution that can be described in bi-dimensional problems as the combination of a symmetric and a skew-symmetric stress field [5]; the intensity of the two stress fields is given by two notch stress intensity factors (NSIFs). Within this context, Lazzarin and Tovo [6] gave a formal definition of the NSIFs and successfully summarized several NSIF values, considering different welded joints, under the same scatter band. However, the NSIF approach requires the knowledge of the elastic stress field in the region very close to the notch tip. Therefore, finite element meshes must be very refined in these regions, representing a blank wall for industrial applications.

Methods to overcome this problem have been proposed in the literature. As opposed to the direct evaluation of the NSIFs, the mean value of the strain energy density (SED) on a control volume, which embraces the weld toe or the weld root, can be accurately determined by using relatively coarse meshes. It has been shown that at the weld toe (where only the mode 1 stress distribution is singular) accurate values for the Mode 1 NSIFs can be eventually determined *a posteriori* by using a simple closed form expression linking SED and NSIFs [7,8]. Thanks to another technique, called peak stress method (PSM), after a calibration process, it is possible to provide a closed-form equation useful to estimate the NSIFs from the fictitious peak stress evaluated on the point of singularity by means of a coarse mesh pattern with a constant element size [9]. However, since numerical models of complex structures

quickly become large and time consuming when the local weld geometry is modeled for fatigue assessment, hot spot and structural stress methods are often suggested to be used [10]. An example is the Dong's model [11], according to which the intensity of the structural stress distribution at the weld toe is obtained considering a combination of bending and membrane stresses on a surface normal to the applied load and located at the distance from the weld toe equal to the main plate thickness. Shear stress contribution acting on the same surface is included in the global equilibrium conditions. Dong's method and other structural stress calculations have been revisited by Doerk et al. [12] and by Poutiainen and Marquis [13]. Considering a variety of welds and practical situations, it has been pointed out that an analyst should always be aware of the limitations set by the structural or hot spot stress evaluation [12]. Poutiainen and Marquis [10] also noted that the structural stress does not always guarantee an accurate fatigue assessment because different types of welds may have different fatigue strengths even though the structural stress is the same.

Tovo and Lazzarin [14] have explicitly considered this problem. The aim was to provide a method which kept both the robustness of the NSIF approach and the computational advantages of the structural stress one. Hence, they proposed a link between NSIF values and structural stresses at a well-defined distance from the weld toe, which are usually analyzed by designers using shell models or relatively coarse solid models. Such a distance (where bending, membrane and shear internal loads can be evaluated), was chosen equal to the main plate thickness.

Similarly, the main task of this chapter is to develop a criterion for the estimation of the averaged SED, both at the weld toe and at the weld root, as well as *a posteriori* the related NSIFs, as an explicit function of the internal loads (membrane loads, shear loads and bending moments) evaluated at a proper distance analytically determined from the weld. According to this idea, SED and NSIF values could be efficiently evaluated through ready-to-use abaci, as a function of main weld geometrical parameters and the loading condition.

Within this framework, the aims of this chapter can be summarized as follows: (i) to propose a rapid method for evaluating SED and NSIF values, both at the weld toe and at the weld root; (ii) to define a significant set of abaci, which provide stress concentration effects of welded joints of usual interest, taking into account both membrane and bending loading conditions.

## 5.2 Analytical preliminaries

The degree of singularity of stress fields due to notches has been well established by Williams both for modes 1 and 2 loading [5]. He stated that for sharp open notches (zero radius) the stress field near the tip is singular and the singularity exponent is related to the opening angle  $2\alpha$ . The exponent values for the stress distributions are the eigenvalues already defined by Equation (2.4) and here reported:

$$\sin(\lambda_1 q\pi) + \lambda_1 \sin(q\pi) = 0 \quad (5.1)$$

$$\sin(\lambda_2 q\pi) - \lambda_2 \sin(q\pi) = 0 \quad (5.2)$$

where  $q$  is related to the opening angle by the expression  $2\alpha = \pi(2-q)$ .

In order to give a physical meaning to the Williams' analytical frame, Gross and Mendelson [15] extended to open notches the concept of the stress intensity factor, SIF, commonly used to describe cracks' stress fields. They introduced the notch stress intensity factors, NSIFs, which quantify the intensity of the asymptotic stress distributions close to a notch tip. By using a polar coordinate system  $(r, \theta)$  having its origin located at a sharp notch tip (Figure 5.1), the NSIFs related to modes 1 and 2 stress distribution are expressed as:

$$K_1 = \sqrt{2\pi} \lim_{r \rightarrow 0^+} r^{1-\lambda_1} \sigma_{\theta\theta}(r, \theta = 0) \quad (5.3)$$

$$K_2 = \sqrt{2\pi} \lim_{r \rightarrow 0^+} r^{1-\lambda_2} \sigma_{r\theta}(r, \theta = 0) \quad (5.4)$$

where the stress components  $\sigma_{\theta\theta}$  and  $\sigma_{r\theta}$  have to be evaluated along the notch bisector ( $\theta=0$ ).

By considering the definitions given by Equations (5.3) and (5.4), the Williams' formulae for stress components near sharp V-notches in plane strain condition are:

$$\begin{aligned} \begin{Bmatrix} \sigma_{\vartheta} \\ \sigma_r \\ \tau_{r\vartheta} \end{Bmatrix}_1 &= \frac{1}{\sqrt{2\pi}} \frac{r^{\lambda_1-1} K_1}{(1+\lambda_1) + \chi_1(1-\lambda_1)} \left[ \begin{Bmatrix} (1+\lambda_1) \cos(1-\lambda_1)\vartheta \\ (3-\lambda_1) \cos(1-\lambda_1)\vartheta \\ (1-\lambda_1) \sin(1-\lambda_1)\vartheta \end{Bmatrix} + \chi_1(1-\lambda_1) \begin{Bmatrix} \cos(1+\lambda_1)\vartheta \\ -\cos(1+\lambda_1)\vartheta \\ \sin(1+\lambda_1)\vartheta \end{Bmatrix} \right] \\ \sigma_{z,1} &= \nu(\sigma_{\vartheta,1} + \sigma_{r,1}) \\ \chi_1 &= -\frac{\sin(1-\lambda_1)q\pi/2}{\sin(1+\lambda_1)q\pi/2} \end{aligned} \quad (5.5)$$

for mode 1 loading, and

$$\begin{Bmatrix} \sigma_{\vartheta} \\ \sigma_r \\ \tau_{r\vartheta} \end{Bmatrix}_2 = \frac{1}{\sqrt{2\pi}} \frac{r^{\lambda_2-1} K_2}{(1-\lambda_2) + \chi_2(1+\lambda_2)} \begin{Bmatrix} -(1+\lambda_2)\sin(1-\lambda_2)\vartheta \\ -(3-\lambda_2)\sin(1-\lambda_2)\vartheta \\ (1-\lambda_2)\cos(1-\lambda_2)\vartheta \end{Bmatrix} + \chi_2(1+\lambda_2) \begin{Bmatrix} -\sin(1+\lambda_2)\vartheta \\ \sin(1+\lambda_2)\vartheta \\ \cos(1+\lambda_2)\vartheta \end{Bmatrix}$$

$$\sigma_{z,2} = \nu(\sigma_{\vartheta,2} + \sigma_{r,2})$$

$$\chi_2 = -\frac{\sin(1-\lambda_2)q\pi/2}{\sin(1+\lambda_2)q\pi/2}$$
(5.6)

for mode 2 loading.

In Equations (5.5) and (5.6)  $K_1$  and  $K_2$  are the two NSIFs and the subscript “1” and “2” denote the symmetric and the anti-symmetric stress components, respectively.

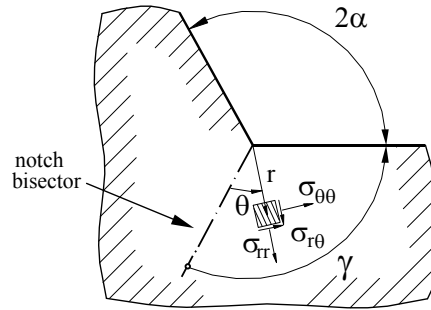


**Figure 5.1.** Frame of reference for the sharp V-notch problem according to Williams' analytical solution.

Two convenient expressions of NSIFs range for welded joints are the following [6]:

$$\Delta K_1 = k_1 \Delta \sigma_n t^{1-\lambda_1} \quad (5.7)$$

$$\Delta K_2 = k_2 \Delta \sigma_n t^{1-\lambda_2} \quad (5.8)$$

where  $\Delta \sigma_n$  is the range of the remotely applied stress (nominal stress),  $t$  is the plate thickness and  $k_i$  are non-dimensional coefficients, which depend on the overall joint geometry and on the kind of remote applied load (membrane or bending).

Equations (5.7) and (5.8) make it possible to point out a) that the scale effect is fully included in the NSIF approach, by means of the term  $t^{1-\lambda_i}$  quantifying the influence of the welded joint size, and b) that the mode 2 contribution is no longer singular when the notch opening angle is greater than  $102.6^\circ$ , since the exponent  $1-\lambda_i$  becomes negative [5]. This implies that when the opening angle  $2\alpha$  is equal to  $135^\circ$ ,



which is a typical value for fillet welded joints, the mode 1 stress distribution is singular ( $1-\lambda_1 = 0.326$ ) whereas the mode 2 distribution is not ( $1-\lambda_2 = -0.302$ ) and can be neglected at the weld toe. Conversely, at weld root the opening angle is equal to zero (crack-like) and both mode 1 and mode 2 are singular and have to be considered ( $1-\lambda_1 = 1-\lambda_2 = 0.5$ ).

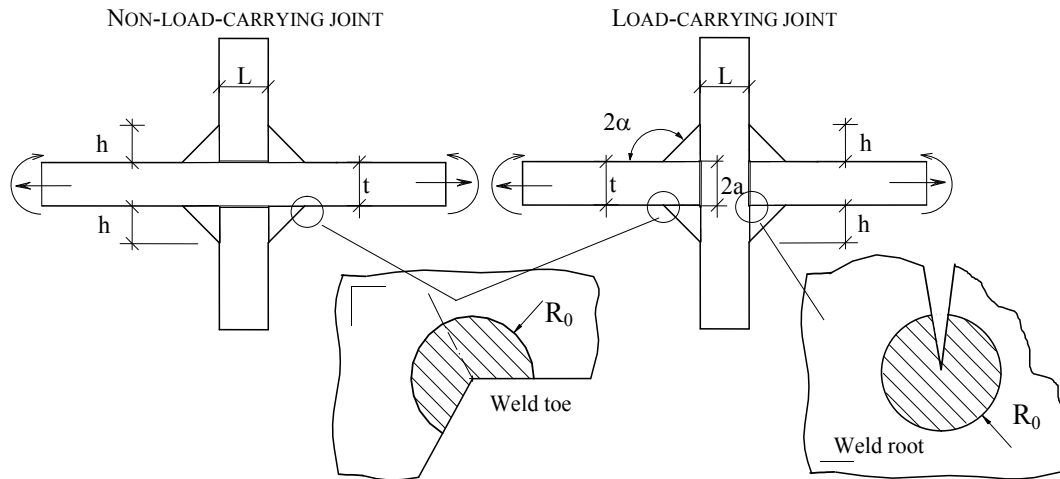


**Figure 5.2.** Joints' geometrical parameters and SED control volume at weld toes and roots.

Under plane strain condition, the total elastic strain energy density range averaged in a circular sector (centered at the weld toe) or in a full circle (centered at the weld root), as shown in Figure 5.2, is the following [16]:

$$\Delta\bar{W} = \frac{e_1}{E} \left[ \frac{\Delta K_1}{R_0^{1-\lambda_1}} \right]^2 + \frac{e_2}{E} \left[ \frac{\Delta K_2}{R_0^{1-\lambda_2}} \right]^2 \quad (5.9)$$

where  $E$  is the Young's modulus,  $R_0$  is the radius of the circular sector (control volume) and  $e_i$  are two parameters that depend on the notch opening angle  $2\alpha$  and on the Poisson's ratio  $\nu$ . A rapid calculation of  $e_i$ , with  $\nu = 0.3$ , can be carried out using expressions provided in Figure 2.6.

The control volume radius  $R_0$  has been estimated by using the fatigue strength of butt ground welded joints (in order to quantify the influence of the welding process, in the absence of any stress concentration effect) and the NSIF based fatigue strength of welded joints having a V-notch angle at the weld toe large enough to ensure the

non-singularity of mode 2 stress distribution. As a result  $R_0$  has been estimated equal to 0.28 mm for steel welded joints.

### 5.3 Some assumptions on nominal stress evaluation in welded plates

Nominal stress components should be evaluated as the stress distribution excluding the non-linear local stress due to the weld profile itself [17]. On the other hand, the intensity of the non-linear effect strongly depends on the weld profile (which in practice controls the slopes of the symmetric and anti-symmetric stress distributions) and the overall geometry of the welded components (which mainly controls the position of the stress field). Hence, the aim of this section is to investigate the relation between nominal stress components and local stress field.

Let us assume that the stress distribution in a structural element can be approximately expressed according to the shell element theory: a linear distribution of the tensile/compressive stress and a parabolic distribution of the shear stress through the plate thickness. Since the non-linear local effect is predominant close to the toe of the weld (Figure 5.3), the linear distribution can be considered valid up to a distance  $\delta$  from the weld toe.

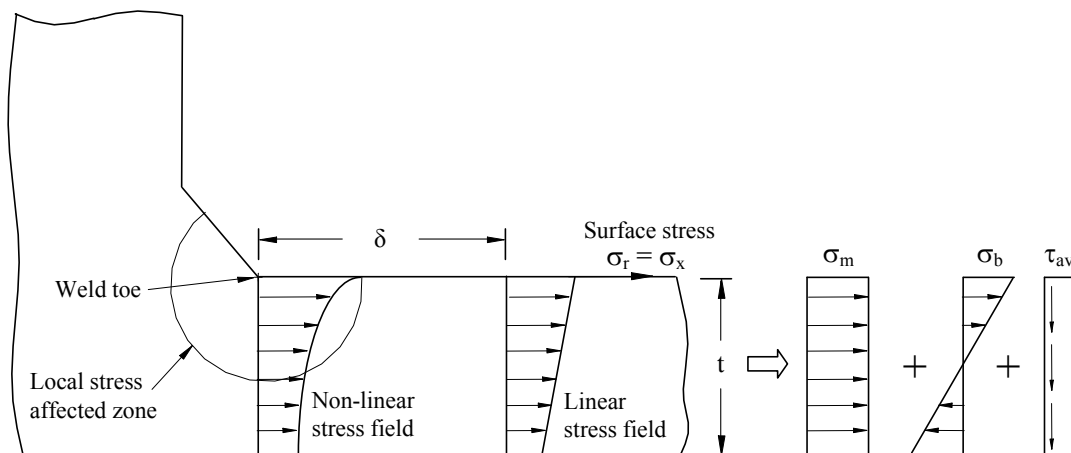


**Figure 5.3.** Schematization of stress fields near a weld toe under linear elastic hypothesis.

Now the problem is to establish a relation between the local stress field, governed by NSIF values, and a more complex stress distribution due to a general combination of

the internal generalized loads of the shell theory (membrane loading, bending moment and shear load), all defined at  $\delta$  distance from the weld.

On the basis of the previous assumptions, the internal loads cause a stress distribution approximated as linear and parabolic at each section of the welded plates. So, as well as for the internal loads, the stress condition at each section can also be completely described by the two values of tensile stress at the upper and lower surface of each plate and by the average shear stress (Figure 5.3).

It is also assumed here to consider the shear stress contribution simply as an additional (or reductive) bending stress, which increases (or reduces) the bending effect, depending on sign. This is a proper assumption, if it is considered that fatigue failures starting from weld toe are driven by mode 1 (notch opening mode), since mode 2 stresses are not singular. With this hypothesis, the following equivalent nominal stress can be calculated from the three components of stress (membrane, bending and average shear), computed at  $\delta$  distance from the weld toe:

$$\Delta\sigma_n = \Delta\sigma_m + \Delta\sigma_b + \delta \cdot \frac{6}{t} \cdot \Delta\tau_{av} \quad (5.10)$$

A qualitative  $\delta$  value equal to or greater than 1.0-1.5 times the plate thickness or the weld throat height is suggested in the literature [17–20]. Such range is justified in Section 5.5, where an analytical formulation for  $\delta$  is given.

It is useful to remember that in shell element theory the average shear stress is related to the variation of the bending moment and it is usually directly provided by the finite element code. Such a relation can be expressed as a function of stress components and, if needed, it is possible to substitute the shear stress in Equation (5.10) with the variation of the tensile stress along the main plate:

$$\Delta\tau_{av} = \frac{d(\Delta\sigma_m + \Delta\sigma_b)}{dx} \cdot \frac{t}{6} \quad (5.11)$$

As a further condition, it is assumed that the local stress fields near the points of singularity (weld toe and root) are dependent on internal loads according to Figure 5.4. It means that points of singularity (toes) representing the transition between weld and main plate are affected by loads acting on the main plate, so that loads acting on the attached plate are considered negligible; points of singularity (toes and roots) representing the transition between weld and attached plate are affected by loads acting on the attached plate, so that loads acting on the main plate are considered

negligible. Such assumption in general does not introduce appreciable errors, as shown in the practical application provided in Section 5.6.

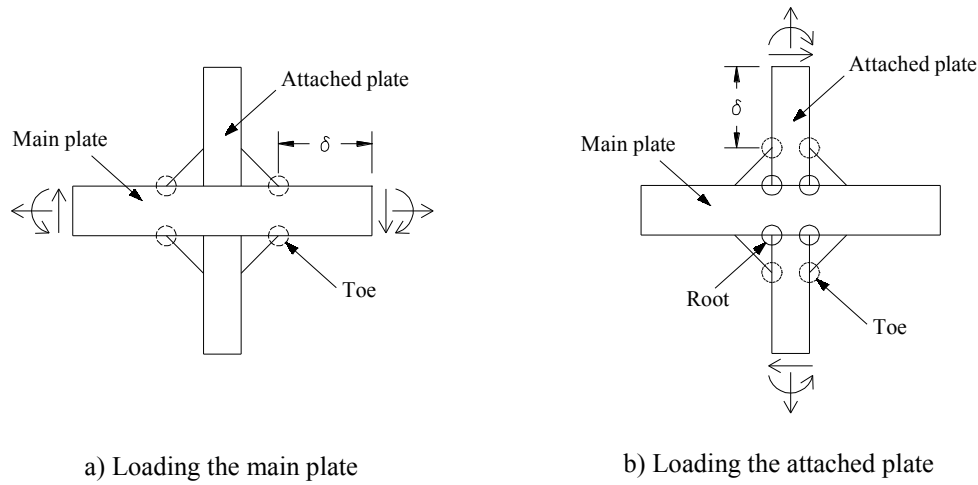


**Figure 5.4.** Assumption of local stress fields dependence on internal loads: a) areas influenced by loads acting on the main plate; b) areas influenced by loads acting on the attached plate. Dashed circles symbolize weld toe areas, where only mode 1 is singular; solid circles symbolize weld root areas, where both mode 1 and 2 are singular.

It is worth noting that the general 3D shell problem has been here simplified considering a plane section normal to the weld throat. This condition is true when the welded joint is under a plain strain condition, so that any variation of the stress components along the weld direction can be considered negligible (at least within a distance equal to or less than the main plate thickness). This can be considered true also in a three-dimensional case such as the longitudinal attachment, because at the proper distance  $\delta$  from the plates intersection the 3D effect induced on stresses by the attachment is smoothed enough.

#### 5.4 Relationship between local SED and nominal stress components

With the aim to propose a link between the local averaged SED and the nominal stress components, the following three non-dimensional parameters are defined:

$$w_1 = \sqrt{e_1 k_1^2} \quad (5.12)$$

$$w_2 = \sqrt{e_2 k_2^2} \quad (5.13)$$

$$w_{eq} = \sqrt{w_1^2 + w_2^2} \quad (5.14)$$

where  $w_1, w_2$  and  $w_{eq}$  are non-dimensional parameters, conceptually equivalent to  $k_i$  parameters, except for the further dependence on the notch opening angle and the Poisson's ratio. In the NSIF definition, such parameters are proportional to the nominal stress, thus they express the local stress concentrating capacity of a weld geometry and, once computed, can be summarized in dedicated ready-to-use abaci, as shown in Section 5.5.

By introducing Equations (5.7) and (5.8) in (5.9), and properly collecting variables, the following expression can be found:

$$\Delta\bar{W} = \frac{\Delta\sigma_n^2}{E} \left[ e_1 k_1^2 \left( \frac{t}{R_0} \right)^{2(1-\lambda_1)} + e_2 k_2^2 \left( \frac{t}{R_0} \right)^{2(1-\lambda_2)} \right] \quad (5.15)$$

Considering the above defined  $w_i$  parameters, it follows:

$$\Delta\bar{W} = \frac{\Delta\sigma_n^2}{E} \left[ w_1^2 \left( \frac{t}{R_0} \right)^{2(1-\lambda_1)} + w_2^2 \left( \frac{t}{R_0} \right)^{2(1-\lambda_2)} \right] \quad (5.16)$$

Remembering the degrees of singularity of local stress fields for the weld toe and the weld root, it is possible to obtain the following two relations (valid at toe and root, respectively):

$$\Delta\bar{W}_{toe} = \frac{\Delta\sigma_n^2 \cdot w_1^2}{E} \left( \frac{t}{R_0} \right)^{2(1-\lambda_1)} \quad (5.17)$$

$$\Delta\bar{W}_{root} = \frac{\Delta\sigma_n^2 \cdot w_{eq}^2}{E} \left( \frac{t}{R_0} \right) \quad (5.18)$$

The above relations explicitly express SED with a formulation which decouples the global joint geometry  $w_1$  and  $w_{eq}$ , the material properties  $R_0$  and  $E$ , the size effect  $t$  and the far-field loading condition  $\Delta\sigma_n$ .

A further general formulation, which permits to take into account both pure membrane and pure bending loading conditions, but also a mixed condition, is provided in the following, once defined the degree of bending (or bending ratio)  $r_b$ , which is a positive parameter that is equal to 0 under pure membrane stress and reaches the value 1 under pure bending stress:

$$r_b = \frac{\left| \Delta\sigma_b + \delta \cdot \frac{6}{t} \cdot \Delta\tau_{av} \right|}{\left| \Delta\sigma_m \right| + \left| \Delta\sigma_b + \delta \cdot \frac{6}{t} \cdot \Delta\tau_{av} \right|} \quad (5.19)$$

in which symbols are according to Figure 5.3.

By using the linear superposition principle, the parameters  $w_1$ ,  $w_2$  and  $w_{eq}$  can be expressed as:

$$w_1 = w_1(r_b) = w_{1,m} \cdot (1 - r_b) + w_{1,b} \cdot r_b \quad (5.20)$$

$$w_2 = w_2(r_b) = w_{2,m} \cdot (1 - r_b) + w_{2,b} \cdot r_b \quad (5.21)$$

$$w_{eq} = w_{eq}(r_b) = w_{eq,m} \cdot (1 - r_b) + w_{eq,b} \cdot r_b \quad (5.22)$$

where subscripts  $m$  and  $b$  indicate that the respective parameter has been computed under pure membrane or pure bending loading condition:

$$w_{1,m} = w_1(r_b = 0) \quad (5.23)$$

$$w_{1,b} = w_1(r_b = 1) \quad (5.24)$$

$$w_{eq,m} = w_{eq}(r_b = 0) \quad (5.25)$$

$$w_{eq,b} = w_{eq}(r_b = 1) \quad (5.26)$$

The above definitions permit to directly calculate SED and/or NSIF values, without performing expensive finite element computations, once the far-field loads (which could be pure membrane, pure bending or a mixed condition) and non-dimensional parameters  $w_i$  are known. Valid expressions for SED, at the weld toe and at the weld root, respectively, are as follows:

$$\Delta\bar{W}_{toe} = \Delta\bar{W}_{toe}(r_b) = \frac{[\Delta\sigma_n \cdot w_1(r_b)]^2}{E} \left( \frac{t}{R_0} \right)^{2(1-\lambda_1)} \quad (5.27)$$

$$\Delta\bar{W}_{root} = \Delta\bar{W}_{root}(r_b) = \frac{[\Delta\sigma_n \cdot w_{eq}(r_b)]^2}{E} \left( \frac{t}{R_0} \right) \quad (5.28)$$

where  $1 - \lambda_1$  varies as a function of the weld bead slope and is equal to 0.326 at weld toe for most double fillet welds (opening angle 135°).

Finally, a valid expression for the mode 1 NSIF at the weld toe is:

$$\Delta K_1 = \Delta W_1(r_b) = \frac{\Delta\sigma_n \cdot w_1(r_b)}{\sqrt{e_1}} \cdot t^{(1-\lambda_1)} \quad (5.29)$$

Equations (5.27), (5.28) and (5.29), together with Equation (3.10) represent an explicit link between the nominal stress and local approaches based on SED and NSIF for fatigue assessment of welded joints.

### 5.5 Analytical expression of the stress offset

Nominal stress components should be evaluated as the stress distribution excluding the non-linear local stress due to the weld profile itself [17]. Establishing the suitable distance  $\delta$  from the weld toe, to exclude the non-linear stress field, according to the information given by the literature [17–20], requires considerable user judgment, because no univocal formulation is provided; further important consequence is that with such definitions no automation is possible. The issue is addressed here by proposing an analytical expression, based on the notch stress intensities, for the stress offset  $\delta$ .

According to Williams' analytical frame described by Equations (5.5) and (5.6), along the free surface of a plate starting from the weld toe, as well as in every direction different from the notch bisector, the stress components are the sum of the contributions due to mode 1 and mode 2. So, the radial stress along the free edge, i.e. the stress component normal to the weld bead on the main plate surface, can be determined by summing Equations (5.5) and (5.6). By imposing  $2\alpha=135^\circ$  and  $\theta=112.5^\circ$  in Equations (5.5) and (5.6), the radial stress range distribution along the free edge starting from the weld toe can be expressed as:

$$\Delta\sigma_r = \Delta K_1 \cdot 0.423 \cdot r^{-0.326} - \Delta K_2 \cdot 0.553 \cdot r^{0.302} \quad (5.30)$$

in which  $r$  is the distance from the weld toe and the  $\Delta K_2$  value is negative.

Local stress distributions given by Equation (5.30) near the weld toe are in good agreement with numerical results, as shown by Figure 5.5.

Substituting  $\Delta K_1$  and  $\Delta K_2$  expressions given by Equations (5.7) and (5.8) in Equation (5.30) and imposing the latter equal to the nominal stress range  $\Delta\sigma_n$ , the following expression can be found:

$$0.423 \cdot k_1 \cdot \left(\frac{r}{t}\right)^{-0.326} - 0.553 \cdot k_2 \cdot \left(\frac{r}{t}\right)^{0.302} - 1 = 0 \quad (5.31)$$

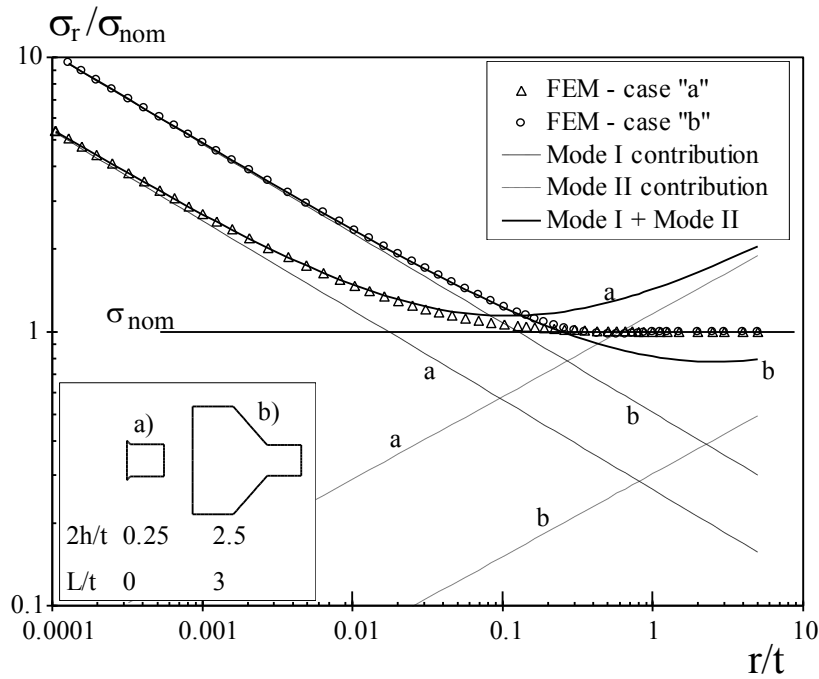


**Figure 5.5.** Contribution of mode 1 and mode 2 to the radial stress along the free edge for two different cases [6].

In Figure 5.5 the same stress distribution is plotted for the two cases having the highest and lowest  $k_2$  to  $k_1$  ratio, named case “a” and case “b” respectively. It is possible to notice that this approach accurately describes the whole stress field in the proximity of the weld toe and its range of applicability is determined either by the nominal stress value (as for case “b” in Figure 5.5) or by the intersection of the mode 1 and 2 contributions (case “a”). It can also be noted that stress distribution given by Equation (5.30) has always a minimum value and such minimum value is close to the nominal stress value. It is therefore possible to make the assumption that approximately the distance  $\delta$  from the weld toe at which the local stress becomes nominal is defined by the coordinate  $r$  at which the stress given by Equation (5.30) reaches his minimum value. Hence, imposing equal to zero the derivative of Equation (5.31) the following expression for  $\delta$  can be found:

$$\delta = \left( 0.826 \cdot \frac{k_1}{k_2} \right)^{1.589} \cdot t \quad (5.32)$$

Equation (5.32) is valid only for notch opening angle  $2\alpha=135^\circ$ , i.e. for a typical fillet welded joint. In case of different notch opening angles, coefficients and exponents in



Equation (5.30) change and as a consequence Equation (5.30) would be different too. However, the procedure here described to determine Equation (5.30) remains valid. Remembering the definitions given by Equations (5.12) and (5.13), the previous equation can also be expressed as:

$$\delta = \left( 0.801 \cdot \frac{w_1}{w_2} \right)^{1.589} \cdot t \quad (5.33)$$

In principle,  $w_1$  and  $w_2$  are dependent on the loading type (which can be pure membrane load, pure bending load or a mixed condition) as shown by Equations (5.20) and (5.21). So a further general formulation of Equation (5.33) is:

$$\delta = \left( 0.801 \cdot \frac{w_1(r_b)}{w_2(r_b)} \right)^{1.589} \cdot t \quad (5.34)$$

where  $r_b$  is the degree of bending (or bending ratio) defined by Equation (5.19).

The slopes of the symmetric and anti-symmetric local stress distributions (and therefore also the distance at which the stress field can be considered as nominal) are mainly dependent on the weld profile and the loading condition. Consistently, it has been found that  $\delta$  is not only a function of the plate thickness  $t$ , but also of the weld geometry and of the loading condition through  $w_1$  and  $w_2$  coefficients (or, analogously, through  $k_1$  and  $k_2$  coefficients). Furthermore, since the loading condition can be generally variable with  $\delta$ , Equation (5.34) should be solved with some iterations. For a cruciform non-load-carrying joint under pure membrane condition, Equation (5.34) gives  $\delta = 1.3 \cdot t$ , if a common double fillet weld with shape ratios  $2h/t = L/t = 1$  is considered (with shape ratios definition according to Figure 5.2). Such outcome is in good agreement with a distance  $\delta$  ranging from 1.0 to 1.5 times the plate thickness suggested in the literature [18–20].

For the two situations named case “a” and case “b” in Figure 5.5, Equation (5.34) reaches the two limit values equal to about 0.2 and 3.0 times the plate thickness, respectively. Such finding is in agreement with the literature [6], according to which the linear distribution can be considered valid up to a distance from the weld toe equal to or greater than the main plate thickness or the weld throat height.

With reference to a non-load-carrying cruciform joint under pure membrane condition ( $r_b=0$ ), the trend of Equation (5.34) in terms of non-dimensional  $\delta/t$  is

plotted in Figure 5.6, as a function of joint shape ratios. Once again, it can be seen that, if geometries of usual interest are considered ( $1 \leq 2h/t \leq 2$  and  $0.1 \leq L/t \leq 1.5$ ), results provided by Equation (5.34) are in perfect agreement with the literature and in particular with the value  $\delta/t \approx 1.5$  proposed by Hobbacher [18,19] and DVS recommendations [20].

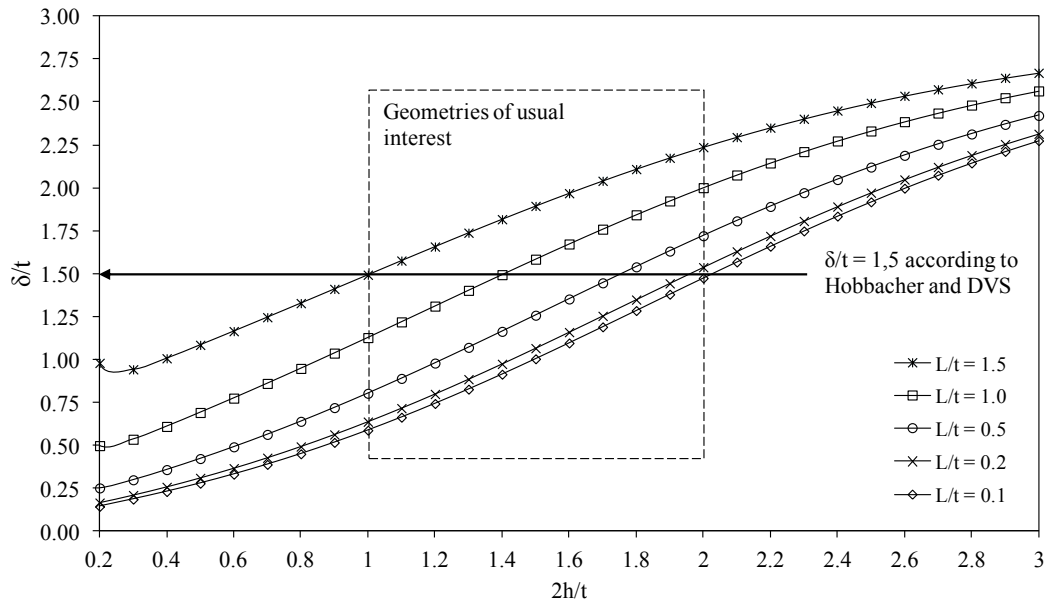


**Figure 5.6.** Trend of non-dimensional  $\delta/t$  parameter according to Equation (5.34), for a non-load-carrying cruciform joint under pure membrane condition. Range of geometries of usual industrial interest are highlighted through the dashed rectangle.

Referring to a non-load-carrying cruciform joint under pure bending condition ( $r_b = 1$ ), the trend of Equation (5.34) in terms of non-dimensional  $\delta/t$  is plotted in Figure 5.7. It can be seen that, if geometries of usual interest are considered ( $1 \leq 2h/t \leq 2$  and  $0.1 \leq L/t \leq 1.5$ ), Equation (5.34) provides  $\delta/t$  almost constant and equal to 0.85.

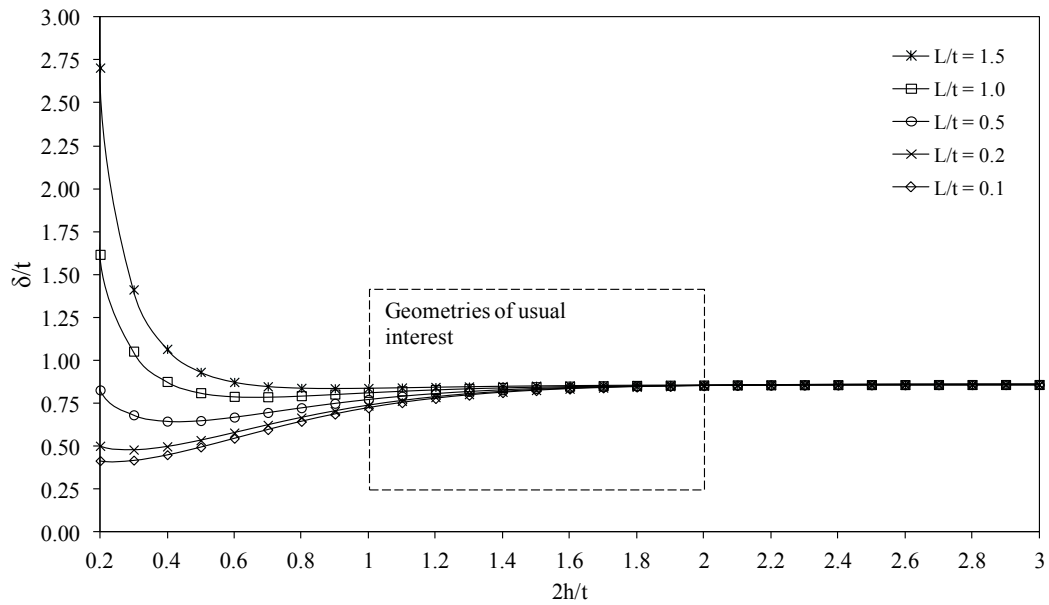


**Figure 5.7.** Trend of non-dimensional  $\delta/t$  parameter according to Equation (5.34), for a non-load-carrying cruciform joint under pure bending condition. Range of geometries of usual industrial interest are highlighted through the dashed rectangle.

## 5.5 Abaci of welded joints stress concentration

Some expressions for non-dimensional parameters  $k_1$  and  $k_2$  have already been reported in the literature for transverse non-load-carrying fillet welded joints subjected to pure tensile stress [6] or pure bending stress [21]. The reported expressions are accurate in a proper range of applicability, given in terms of shape ratios  $L/t$  and  $2h/t$  according to Figure 5.2. A limited number of real welded joint geometries has until now been investigated in the literature, mostly in order to demonstrate the general validity of the method, not to provide a comprehensive mapping of welded joints, due to the fact that computing  $k_i$  coefficients according to the procedure detailed in [6] requires the knowledge of the whole local stress fields near the points of singularity (weld toe and root) and it is therefore an extremely time consuming procedure.

Here, the described procedure is extended to the averaged local strain energy density approach, so that an overall mapping of interesting joints can be performed thanks to the computational advantages provided by SED and already discussed in Section 2.3: among all, most importantly, the insensitivity to the mesh refinement.

The parameters  $w_i$  can be calculated *a posteriori* through Equations (5.27) and (5.28), respectively, once SED has been computed by means of finite element analyses and can be mapped for all joints of interest, under pure membrane or pure bending loading condition. Then,  $w_i$  can be computed through Equations 5.20 to 5.22 for every mixed condition of membrane, bending and shear load.

### 5.5.1 Numerical analyses and data fitting

Different kinds of joints have been analyzed and their stress concentration has been mapped as a function of weld shape ratios and loading condition (pure membrane and pure bending). Investigated geometries are detailed in Sections 5.5.2 to 5.5.6. However, with general meaning, stress concentration points taken into account (toe and root) and influencing geometrical parameters ( $t$ ,  $h$ ,  $L$ , and  $\theta$ ) are depicted in Figure 5.8.

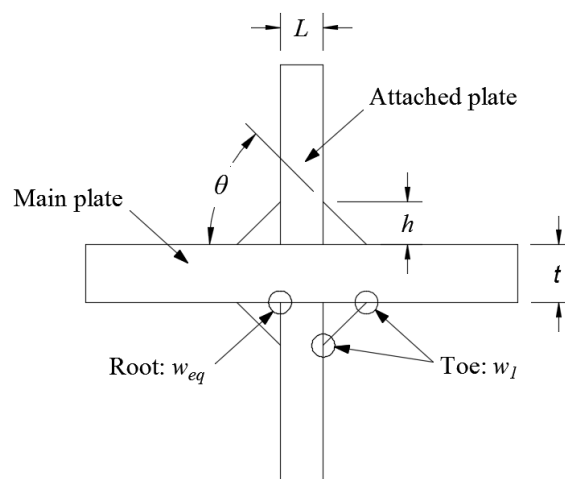


**Figure 5.8.** Definition of investigated geometrical parameters and stress concentration points (weld toe and weld root).

All finite element models have been carried out in Ansys® environment and parametric analyses have been performed using Ansys Parametric Design Language (APDL). Geometries detailed in Sections 5.5.2 to 5.5.5 have been analyzed under plane strain condition, whereas the geometries detailed in Section 5.5.7 have been analyzed in three-dimensional condition. When permitted, it has been taken advantage of the symmetry condition and a half or a quarter of the geometry has been modeled. Plane finite elements having quadratic shape functions (named Plane183 in

Ansys® library) have been used, with reference to bi-dimensional models; solid elements having quadratic shape functions (named Solid186 in Ansys® library) have been used, with reference to three-dimensional models. Linear elastic material having Young modulus equal to 206000 MPa and Poisson's ratio equal to 0.3 has been used. A circular control volume having radius  $R_0$  equal to 0.28 mm has been placed at the weld toe and at the weld root (see Figure 3.19 for reference and Figure 5.9 for meshing details in bi-dimensional condition), both modeled as sharp V-notches, according to the SED approach. The actual value of the loaded plate thickness used in the models was 40 mm, to grant a good mesh pattern regardless of the geometrical ratios. No contact elements have been introduced inside the plates gap, having assessed their effect as negligible for the purposes of the present analyses. To simulate the pure membrane condition, it has been considered a normal stress equal to 1 MPa applied to the whole nominal cross section of the loaded plate. To simulate the pure bending condition, it has been considered a normal stress equal to 2/3 MPa and to -2/3 MPa applied to the upper and lower halves of the nominal cross section, respectively. By so doing, far enough from the loaded section, a linear through-thickness stress field is reached, having upper and lower values equal to 1 MPa and to -1 MPa, respectively (Figure 5.10).

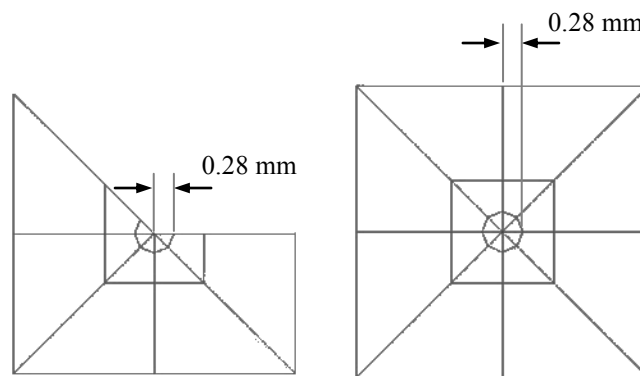


**Figure 5.9.** Detail of mesh refinement near and inside the SED control volumes having radius  $R_0=0.28$  mm. Meshing criteria according to the literature [7].

Finite element analyses only provide sparse data, whereas in practice it could be useful to have polynomial expressions interpolating such data. In order to do so, proper expressions have been used (e.g. double exponential decay), as detailed in

next sections. Fitting models have been determined by means of the least square method, using dedicated softwares (e.g. OriginPro® and MatLab®).

Within established restrictions, provided case by case in terms of weld shape ratios, the use of fitting equations given in this chapter results in a maximum error equal to 5% and most of the times lower than 2%. When it has been not possible to guarantee such reliability, the investigated geometrical ranges have been fitted considering two or more subintervals.

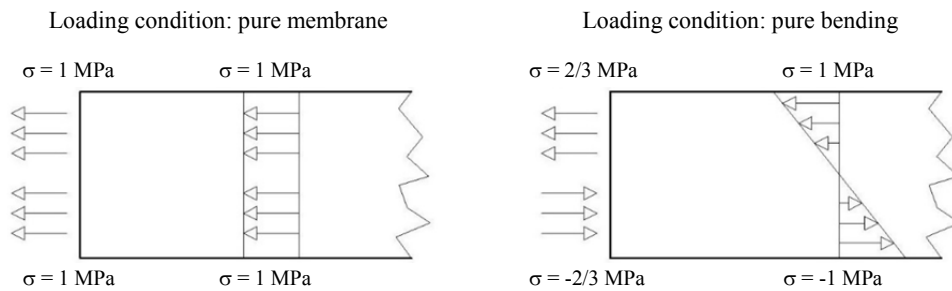


**Figure 5.10.** Boundary conditions adopted to simulate the pure membrane and pure bending loads, respectively.

### 5.5.2 Double fillet welded cruciform joint

With the aim to clearly show the mapping procedure, the double fillet welded cruciform joint is considered here. Conditions of transverse load-carrying (LC) and non-load-carrying (NLC) fillets have been analyzed, both under pure membrane loading and pure bending loading. The non-dimensional parameters  $w_1$  and  $w_{eq}$  have been calculated through Equations (5.27) and (5.28), once SED has been computed through finite element analyses. By taking symmetry into account, only one half of the joint was analyzed under plane strain hypothesis. The actual value of the main thickness used in the models was 40 mm to grant a good mesh pattern regardless of the geometrical ratios. The weld transition angle  $\theta$  has been assumed equal to  $45^\circ$  (i.e. notch opening angle  $2\alpha=135^\circ$ ). Data have been interpolated by means of proper polynomial expressions. With this purpose, a double exponential decay fitting model has been found suitable. Fitting constants have been determined through the least square method. A large amount of FE models has been produced for every condition, in order to obtain a high fidelity model. The fitting expression is:

$$w_i = A_i + B_i \cdot e^{\alpha_i (2h/t)} + C_i \cdot e^{\beta_i (2h/t) + \gamma_i (L/t)} \quad (5.35)$$

in which, according to symbols shown in Figure 5.8,  $h$  is the height of the weld bead,  $L$  is the transverse plate thickness and  $t$  is the loaded plate. This means that in NLC cases  $t$  is the main plate thickness and  $L$  the attached plate thickness, whereas in LC cases it is the opposite.

The trend of parameters  $w_l$  and  $w_{eq}$  is shown in Figures 5.11 to 5.16, in which dots represent some of the numerical results, whereas solid lines represent the fitting model. The fitting constants are given in Tables 5.1 and 5.2. Estimates are accurate when  $0.1 \leq L/t \leq 5.0$  and  $0.2 \leq 2h/t \leq 6.0$ . Within these restrictions, the use of Equation (5.35) results in a maximum error equal to 2%.

**Table 5.1.** Coefficients for  $w_l$  evaluation at weld toe of double fillet welded non-load-carrying cruciform joints.

NLC	Traction			Bending	
	$L/t \in [0.1, 1.0)$	$[1.0, 1.75]$	$(1.75, 5.0]$	$[0.1, 0.7]$	$(0.7, 5.0]$
$A_l$	0.41582	0.41609	0.41785	0.30999	0.30992
$B_l$	0.14772	0.34086	0.86318	0.15670	0.21727
$C_l$	-0.41022	-0.62170	-1.09099	-0.33375	-0.84672
$\alpha_l$	-1.62505	-2.03079	-2.35236	-2.93573	-4.64592
$\beta_l$	-1.41075	-1.77943	-2.21489	-2.94570	-5.18412
$\gamma_l$	-0.80247	-0.53332	-0.22285	-1.31398	-1.98141

**Table 5.2.** Coefficients for  $w_l$  and  $w_{eq}$  evaluation at weld toe and root of double fillet welded load-carrying cruciform joints.

LC	Traction		Bending		
	$L/t \in [0.1, 5.0]$	Toe: $w_l$	Root: $w_{eq}$	Toe: $w_l$	Root: $w_{eq}$
$A_{eq}$		0.41995	0.10419	0.31193	0.00687
$B_{eq}$		2.70387	1.01907	1.12733	0.23020
$C_{eq}$		1.61006	0.59382	-0.05575	0.48228
$\alpha_{eq}$		-7.47642	-4.10847	-3.35828	-0.89405
$\beta_{eq}$		-1.53614	-0.59169	-2.75520	-4.50230
$\gamma_{eq}$		-0.01344	-0.02771	-2.76593	-0.02193

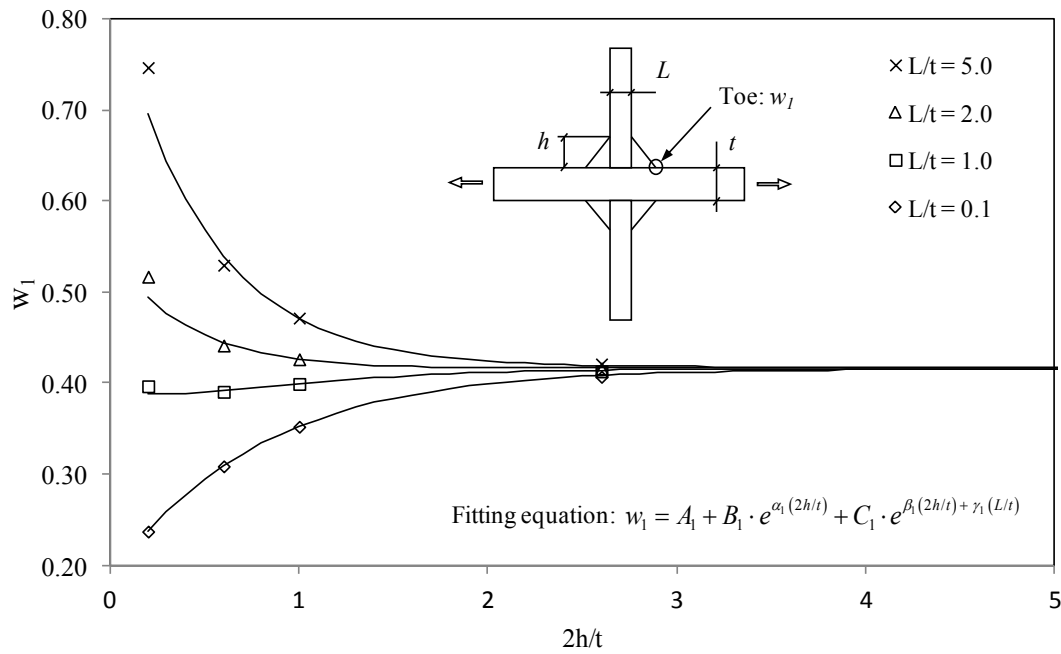


**Figure 5.11.** Curves for  $w_I$  values in non-load-carrying fillet welded cruciform joints under pure membrane loading.

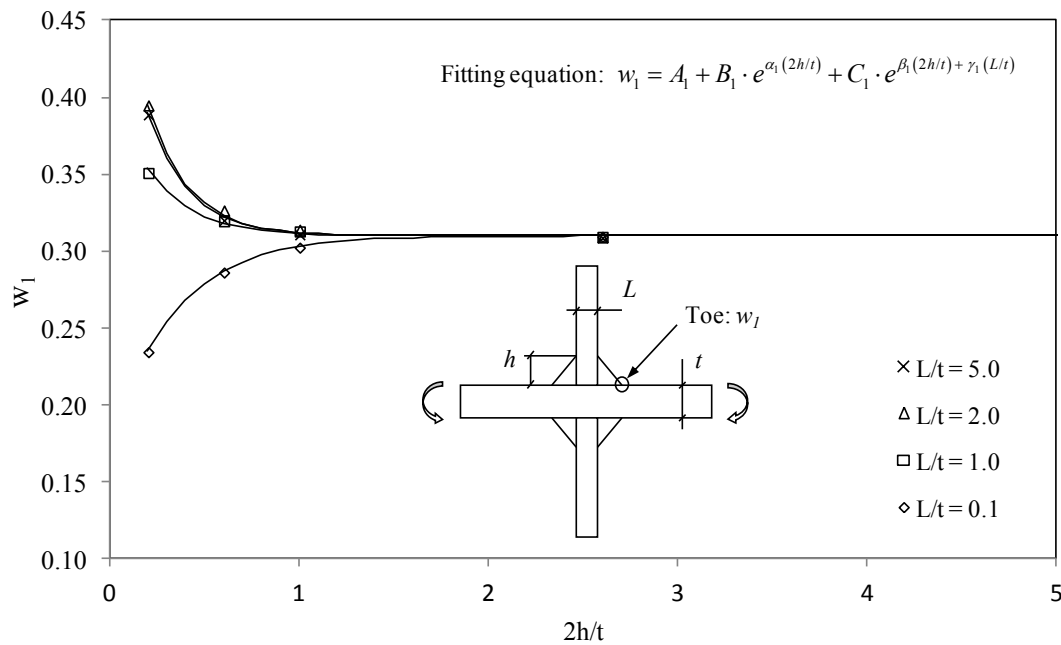


**Figure 5.12.** Curves for  $w_I$  values in non-load-carrying fillet welded cruciform joints under pure bending loading.



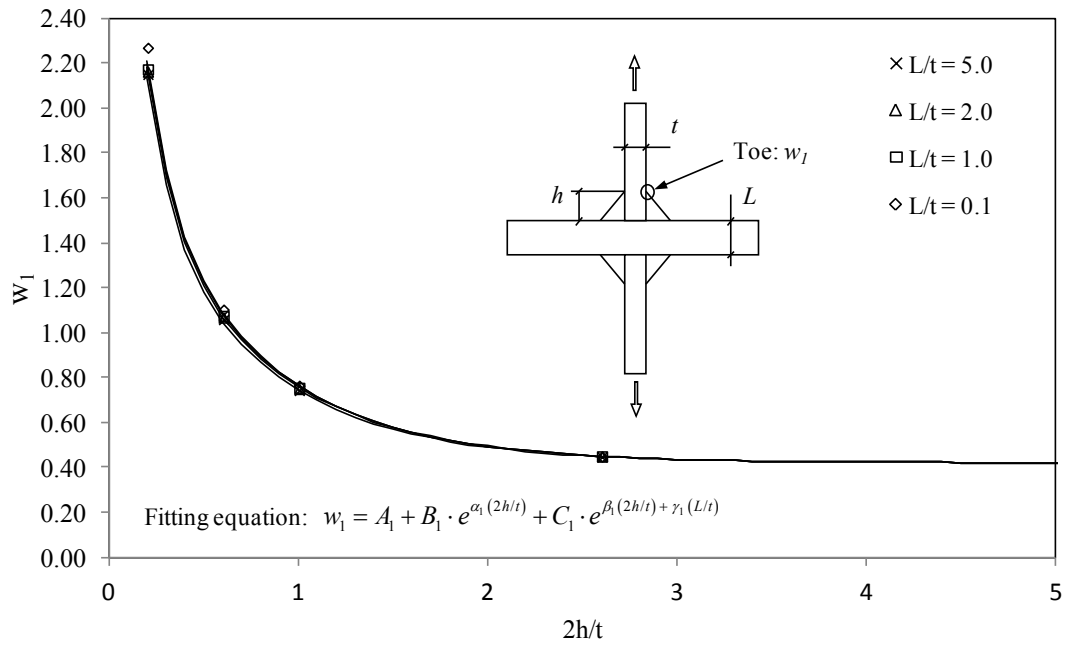


Figure 5.13. Curves for  $w_1$  values in load-carrying fillet welded cruciform joints under pure membrane loading.

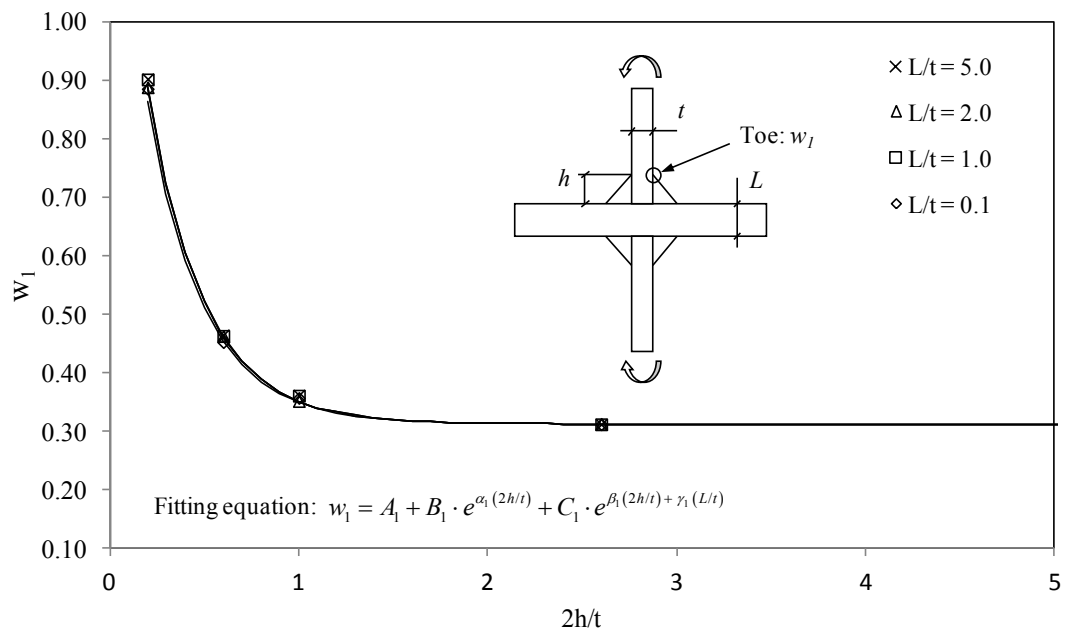
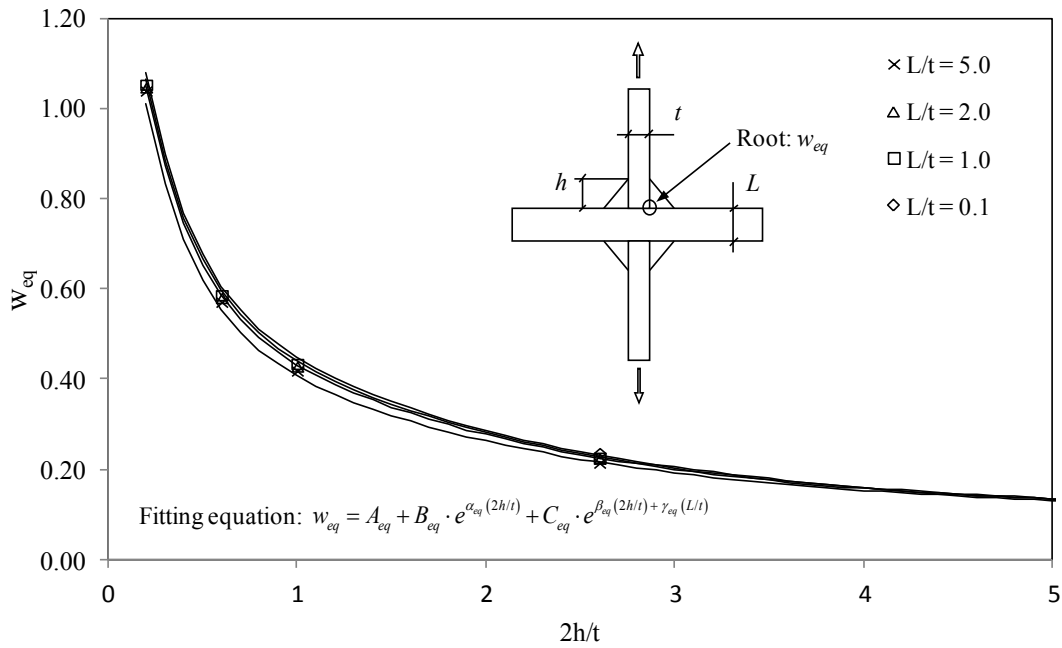
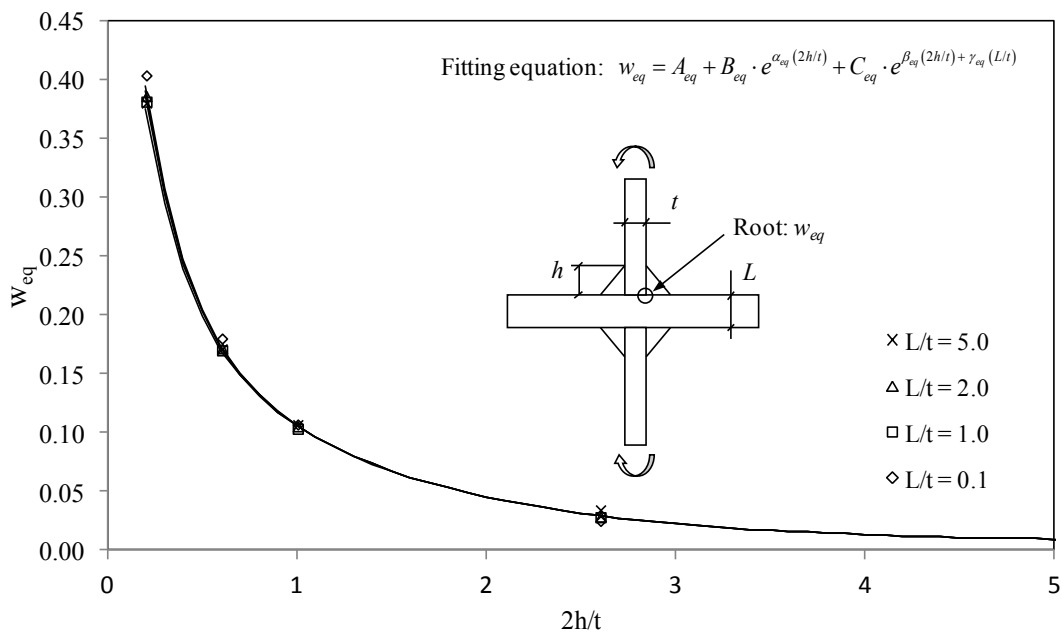


Figure 5.14. Curves for  $w_1$  values in load-carrying fillet welded cruciform joints under pure bending loading.



**Figure 5.15.** Curves for  $w_{eq}$  values in load-carrying fillet welded cruciform joints under pure membrane loading.



**Figure 5.16.** Curves for  $w_{eq}$  values in load-carrying fillet welded cruciform joints under pure bending loading.

Limited to NLC cruciform joints, also the fitting constants related to  $w_2$  are given (Table 5.3). Such  $w_2$  coefficients have been computed from SED by using two concentric control volumes having different radii, according to the procedure detailed in Section 4.3.2. In this case estimates are accurate when  $0.2 \leq L/t \leq 3.0$  and  $0.2 \leq 2h/t \leq 5.0$ . The trend of  $w_2$  is shown in Figures 5.17 and 5.18.

**Table 5.3.** Coefficients for  $w_2$  evaluation at weld toe of double fillet welded non-load-carrying cruciform joints.

NLC	Traction	Bending
$L/t \in [0.2, 3.0]$	Toe: $w_2$	Toe: $w_2$
$A_2$	0.16925	0.27253
$B_2$	-0.26553	-0.58637
$C_2$	0.90721	0.61669
$\alpha_2$	-1.95900	-5.35600
$\beta_2$	-1.12600	-2.98200
$\gamma_2$	-0.76900	-1.02600

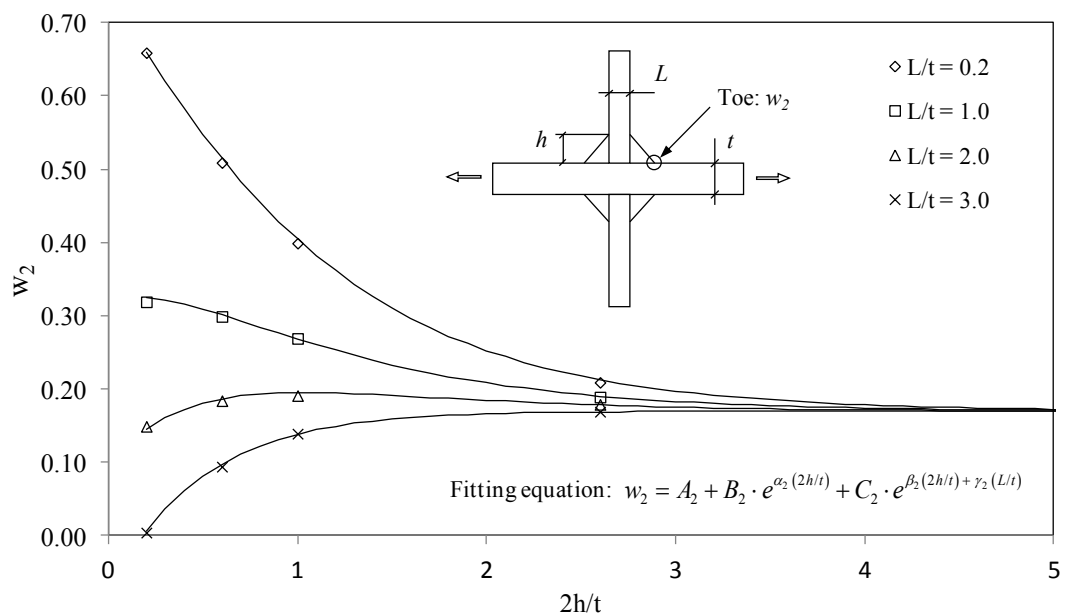


**Figure 5.17.** Curves for  $w_2$  values in non-load-carrying fillet welded cruciform joints under pure membrane loading.

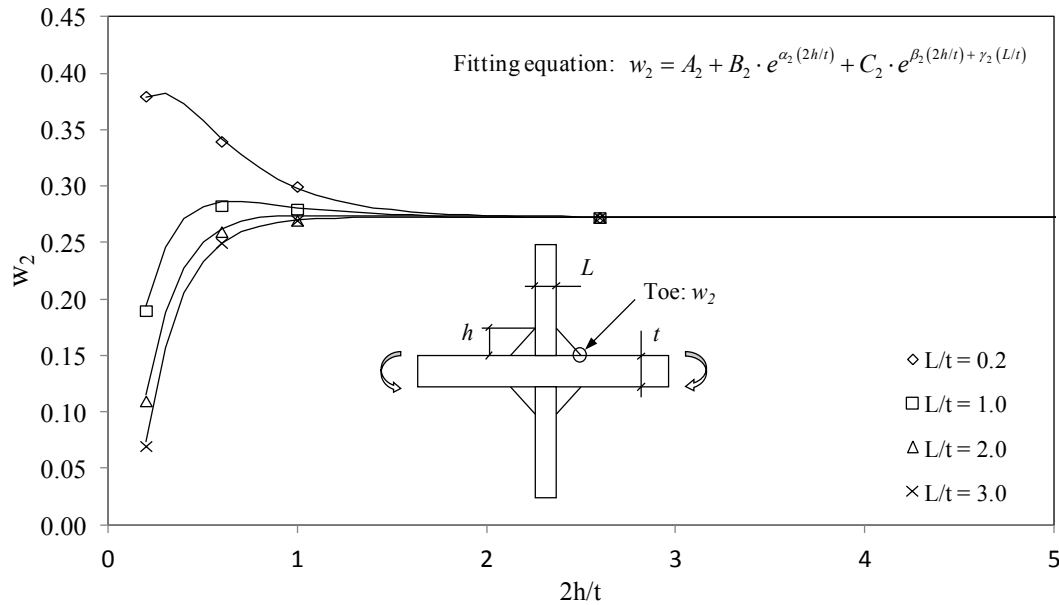


**Figure 5.18.** Curves for  $w_2$  values in non-load-carrying fillet welded cruciform joints under pure bending loading.

### 5.5.3 Double fillet welded T-joint

The double fillet welded T-joint is considered in this section. In this case, only the non-load-carrying (NLC) condition has been analyzed, because the load-carrying condition (LC) in a T-joint is not usual in industrial applications, being generally not recommended a loaded attachment without back stiffener. Both pure membrane loading and pure bending loading conditions have been considered. The non-dimensional parameter  $w_1$  has been calculated through Equation (5.27), once SED has been computed via finite element analyses. The weld transition angle  $\theta$  has been assumed equal to  $45^\circ$  (i.e. notch opening angle  $2\alpha=135^\circ$ ). Data have been interpolated by means of the following expression:

$$w_i = A_i + B_i \cdot e^{\alpha_i(h/t)} + C_i \cdot e^{\beta_i(h/t) + \gamma_i(L/t)} \quad (5.36)$$

The trend of  $w_1$  is shown in Figures 5.19 and 5.20, whereas the fitting constants are given in Table 5.4. Estimates are accurate when  $0.1 \leq L/t \leq 2.0$  and  $0.1 \leq h/t \leq 3.0$ . Within these restrictions, the use of Equation (5.36) results in a maximum error equal to 2%.

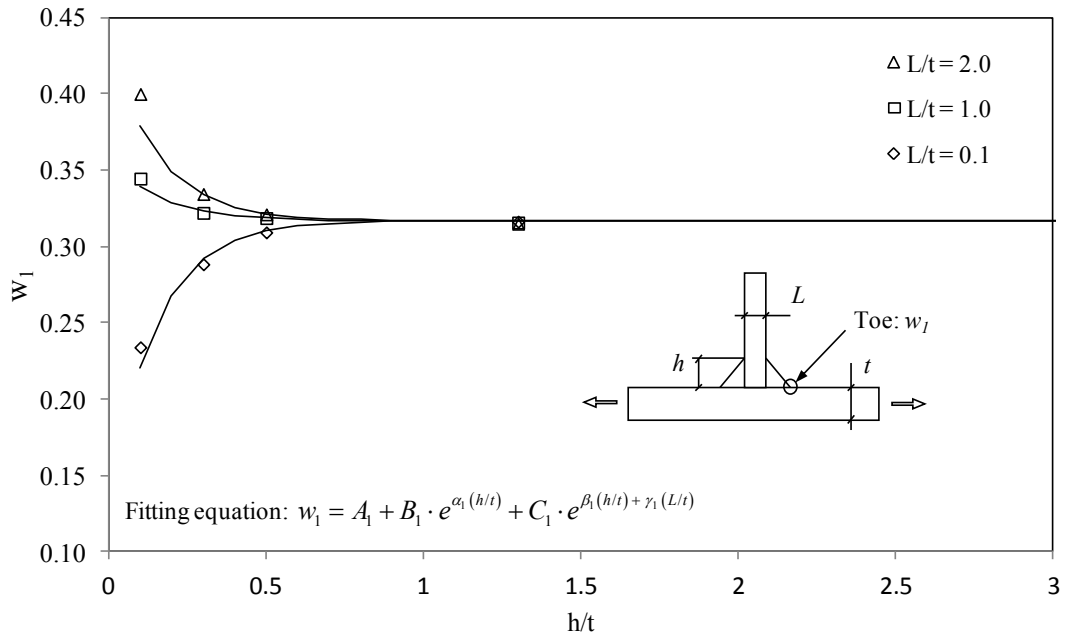


**Figure 5.19.** Curves for  $w_1$  values in non-load-carrying fillet welded T-joints under pure membrane loading.

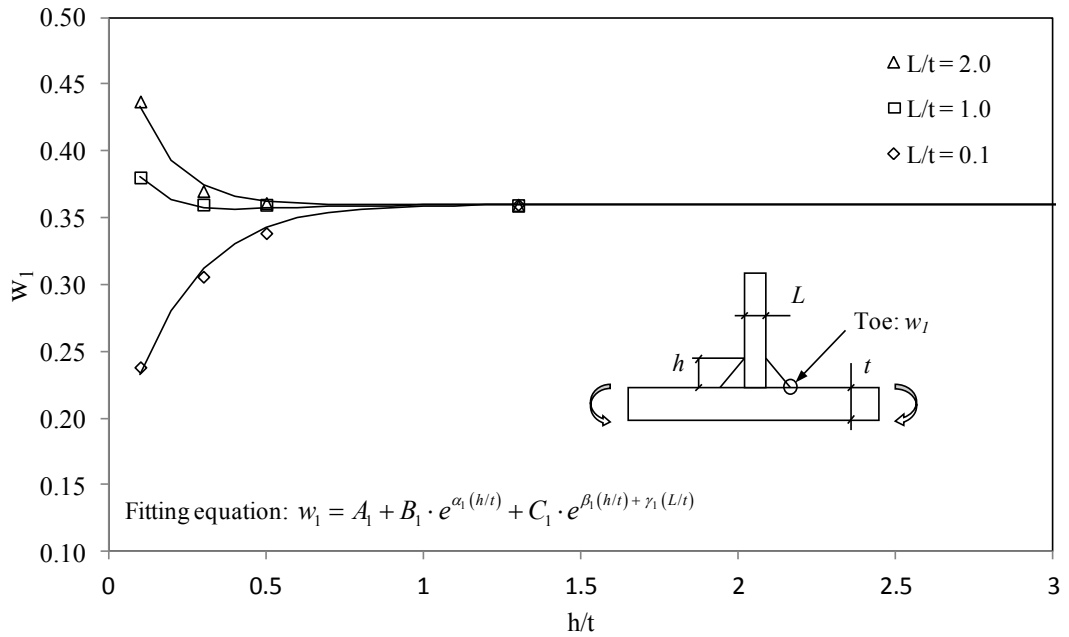


**Figure 5.20.** Curves for  $w_1$  values in non-load-carrying fillet welded T-joints under pure bending loading.

**Table 5.4.** Coefficients for  $w_I$  evaluation at weld toe of double fillet welded non-load-carrying T-joints.

NLC	Traction	Bending
$L/t \in [0.1, 2.0]$	Toe: $w_I$	Toe: $w_I$
$A_I$	0.31666	0.35976
$B_I$	0.15068	0.20490
$C_I$	-0.38509	-0.45258
$\alpha_I$	-6.55374	-7.52548
$\beta_I$	-6.66310	-5.83875
$\gamma_I$	-1.26443	-1.21313

#### 5.5.4 Full penetration welded cruciform joint

In this section the stress concentration mapping of the full penetration cruciform joint is reported. Conditions of transverse load-carrying (LC) and non-load-carrying (NLC) fillets have been analyzed, both under pure membrane loading and pure bending loading. The non-dimensional parameters  $w_I$  and  $w_{eq}$  have been calculated through Equations (5.27) and (5.28), once SED has been computed via finite element analyses. The attached plate weld chamfer has been assumed angled at  $50^\circ$  (as usual in industrial applications). Once fixed the weld chamfer, the bead height  $h$  is no more a variable, being dependent on the attachment thickness  $L$ . The weld transition angle  $\theta$  has been varied among  $40^\circ$  and  $80^\circ$  (i.e. notch opening angle  $2\alpha$  ranging from  $100^\circ$  to  $140^\circ$ ). Data have been interpolated by means of the polynomial expression provided by Equation (5.35), which has the same fitting criteria adopted for the double fillet welded cruciform joint. The trend of parameters  $w_I$  and  $w_{eq}$  is shown in Figures 5.21 to 5.24. The fitting constants are given in Tables 5.5 and 5.6.

**Table 5.5.** Coefficients for  $w_I$  evaluation at weld toe of non-load-carrying full penetration cruciform joints.

NLC	Traction
$L/t \in [0.2, 5.0]$	Toe: $w_I$
$A_I$	$2.9245 \cdot 10^{-5} \cdot \theta^2 - 5.9669 \cdot 10^{-3} \cdot \theta + 6.2494 \cdot 10^{-1}$
$B_I$	$-3.6724 \cdot 10^{-5} \cdot \theta^2 + 7.3399 \cdot 10^{-3} \cdot \theta - 5.5492 \cdot 10^{-1}$
$C_I$	$-1.3420 \cdot 10^{-3} \cdot \theta + 4.0730 \cdot 10^{-2}$
$\alpha_I$	$-9.9226 \cdot 10^{-4} \cdot \theta^2 + 1.7208 \cdot 10^{-1} \cdot \theta + 8.7066$
$\beta_I$	$-2.5515 \cdot 10^5 \cdot \theta^{-3.1526}$
NLC	Bending
$L/t \in [0.2, 5.0]$	Toe: $w_I$
$A_I$	$2.9802 \cdot 10^{-5} \cdot \theta^2 - 6.4973 \cdot 10^{-3} \cdot \theta + 5.4172 \cdot 10^{-1}$
$B_I$	$-3.9062 \cdot 10^{-5} \cdot \theta^2 + 8.2668 \cdot 10^{-3} \cdot \theta - 5.5818 \cdot 10^{-1}$
$\alpha_I$	$-1.8709 \cdot 10^{-3} \cdot \theta^2 + 3.4061 \cdot 10^{-1} \cdot \theta + 1.7964 \cdot 10$

**Table 5.6.** Coefficients for  $w_I$  evaluation at weld toe of load-carrying full penetration cruciform joints.

NLC	Traction
$L/t \in [0.2, 5.0]$	Toe: $w_I$
$A_I$	$2.3802 \cdot 10^{-5} \cdot \theta^2 - 5.6056 \cdot 10^{-3} \cdot \theta + 6.2185 \cdot 10^{-1}$
$B_I$	$-5.8738 \cdot 10^{-5} \cdot \theta^2 + 5.7657 \cdot 10^{-3} \cdot \theta - 1.6724 \cdot 10^{-1}$
$C_I$	$8.0279 \cdot 10^{-5} \cdot \theta^2 - 9.5952 \cdot 10^{-3} \cdot \theta + 2.2762 \cdot 10^{-1}$
$\alpha_I$	$-9.9284 \cdot 10^{-4} \cdot \theta^2 + 1.2711 \cdot 10^{-1} \cdot \theta - 4.4677$
$\beta_I$	$-1.0464 \cdot 10^{-3} \cdot \theta^2 + 1.3833 \cdot 10^{-1} \cdot \theta - 4.7835$
NLC	Bending
$L/t \in [0.2, 5.0]$	Toe: $w_I$
$A_I$	$4.1076 \cdot 10^{-5} \cdot \theta^2 - 7.9376 \cdot 10^{-3} \cdot \theta + 5.8511 \cdot 10^{-1}$

Where fitting constants are missing, it means that the corresponding term in Equation (5.35) has to be neglected. Estimates are accurate when  $0.2 \leq L/t \leq 5.0$  and  $35^\circ \leq \theta \leq 80^\circ$ . Within these restrictions, the use of Equation (5.35) results in a maximum error equal to 5% and most of the times lower than 2%.

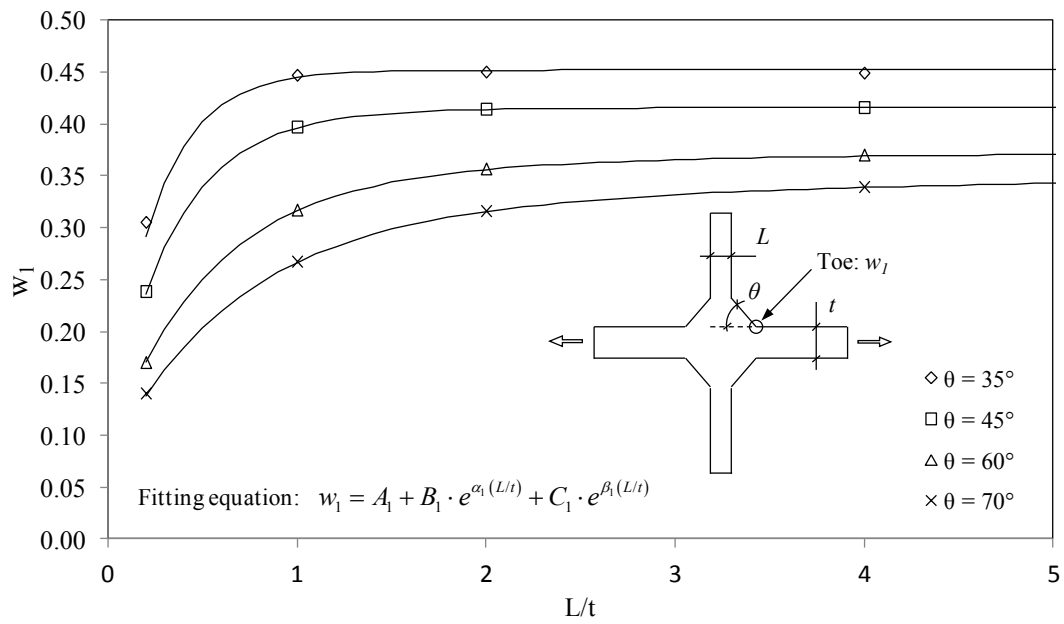


**Figure 5.21.** Curves for  $w_I$  values in non-load-carrying full penetration cruciform joints under pure membrane loading.

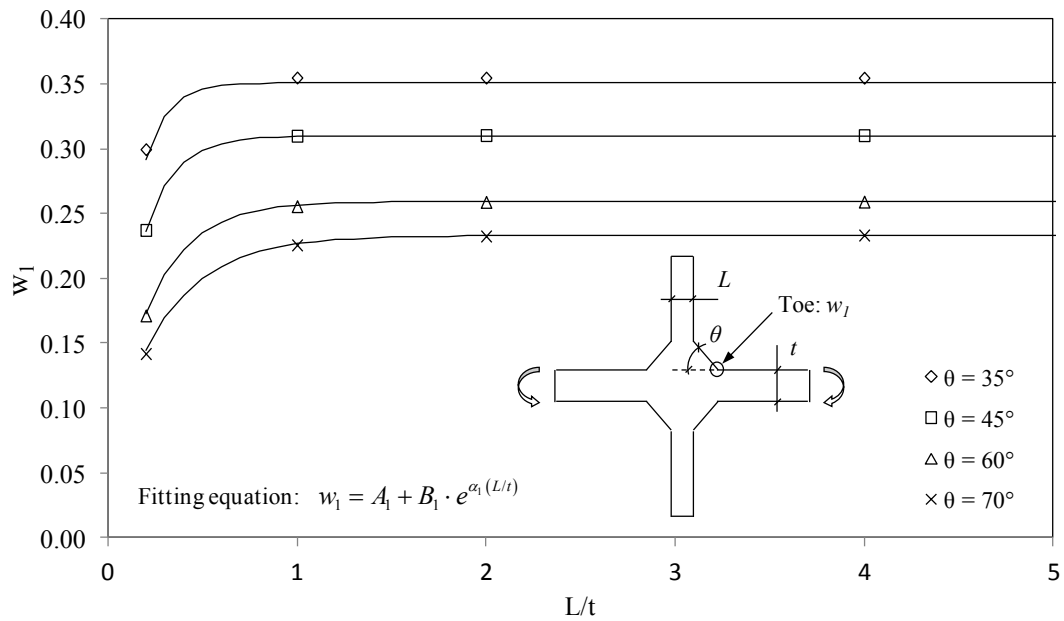


**Figure 5.22.** Curves for  $w_I$  values in non-load-carrying full penetration cruciform joints under pure bending loading.



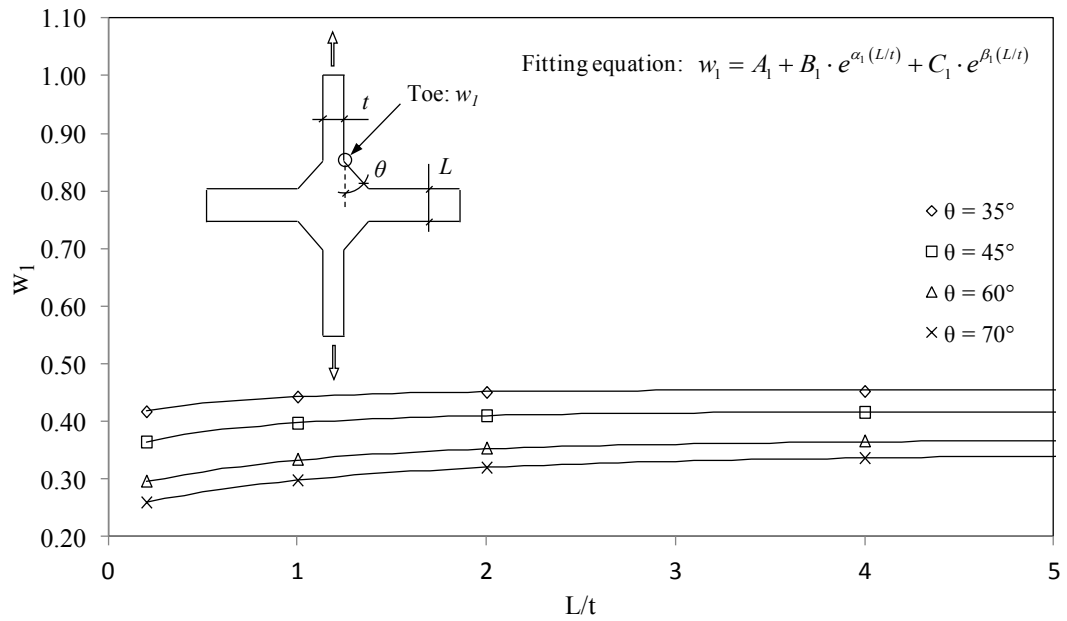


**Figure 5.23.** Curves for  $w_1$  values in load-carrying full penetration cruciform joints under pure membrane loading.

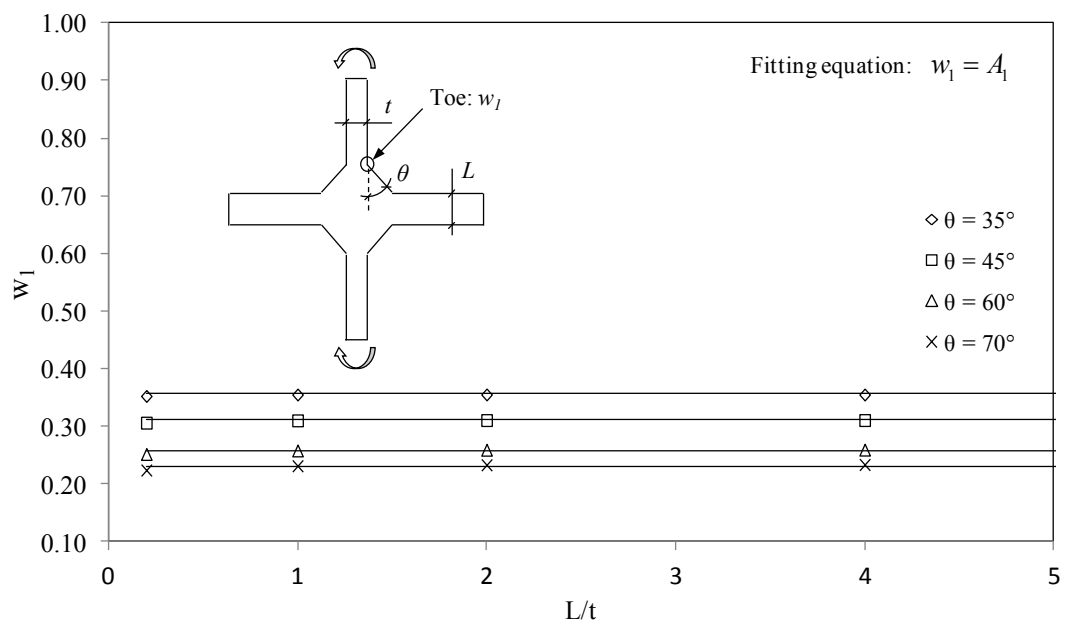


**Figure 5.24.** Curves for  $w_1$  values in load-carrying full penetration cruciform joints under pure bending loading.

### 5.5.5 Full penetration welded T-joint

In this section the stress concentration mapping of the full penetration T-joint is reported. As well as for the double fillet welded T-joint, only the non-load-carrying

(NLC) condition has been analyzed. The non-dimensional parameter  $w_1$  has been calculated through Equation (5.27), once SED has been computed using finite element analyses. The weld transition angle  $\theta$  has been varied among  $40^\circ$  and  $80^\circ$  (i.e. notch opening angle  $2\alpha$  ranging from  $100^\circ$  to  $140^\circ$ ). Data have been interpolated by means of the polynomial expression provided by Equation (5.36), which has the same fitting criteria adopted for the double fillet welded cruciform joint. The trend of  $w_1$  is shown in Figures 5.25 and 5.26. The fitting constants are given in Table 5.7. Where fitting constants are missing, it means that the corresponding term in Equation (5.35) has to be neglected. Estimates are accurate when  $0.2 \leq L/t \leq 5.0$  and  $35^\circ \leq \theta \leq 80^\circ$ . Within these restrictions, the use of Equation (5.35) results in a maximum error equal to 5% and most of the times lower than 2%.

**Table 5.7.** Coefficients for  $w_1$  evaluation at weld toe of non-load-carrying full penetration T-joints.

NLC	Traction
$L/t \in [0.2, 5.0]$	Toe: $w_1$
$A_I$	$4.4001 \cdot 10^{-5} \cdot \theta^2 - 9.0762 \cdot 10^{-3} \cdot \theta + 6.3461 \cdot 10^{-1}$
$B_I$	$-3.5957 \cdot 10^{-5} \cdot \theta^2 + 8.5628 \cdot 10^{-3} \cdot \theta - 5.9736 \cdot 10^{-1}$
$\alpha_I$	$-1.6134 \cdot 10^{-3} \cdot \theta^2 + 2.7093 \cdot 10^{-1} \cdot \theta - 1.5170 \cdot 10$
NLC	Bending
$L/t \in [0.2, 5.0]$	Toe: $w_1$
$A_I$	$3.1743 \cdot 10^{-5} \cdot \theta^2 - 6.4460 \cdot 10^{-3} \cdot \theta + 5.8662 \cdot 10^{-1}$
$B_I$	$-6.3505 \cdot 10^{-5} \cdot \theta^2 + 1.0681 \cdot 10^{-2} \cdot \theta - 6.7142 \cdot 10^{-1}$
$\alpha_I$	$-2.1675 \cdot 10^{-3} \cdot \theta^2 + 3.5159 \cdot 10^{-1} \cdot \theta - 1.6262 \cdot 10$

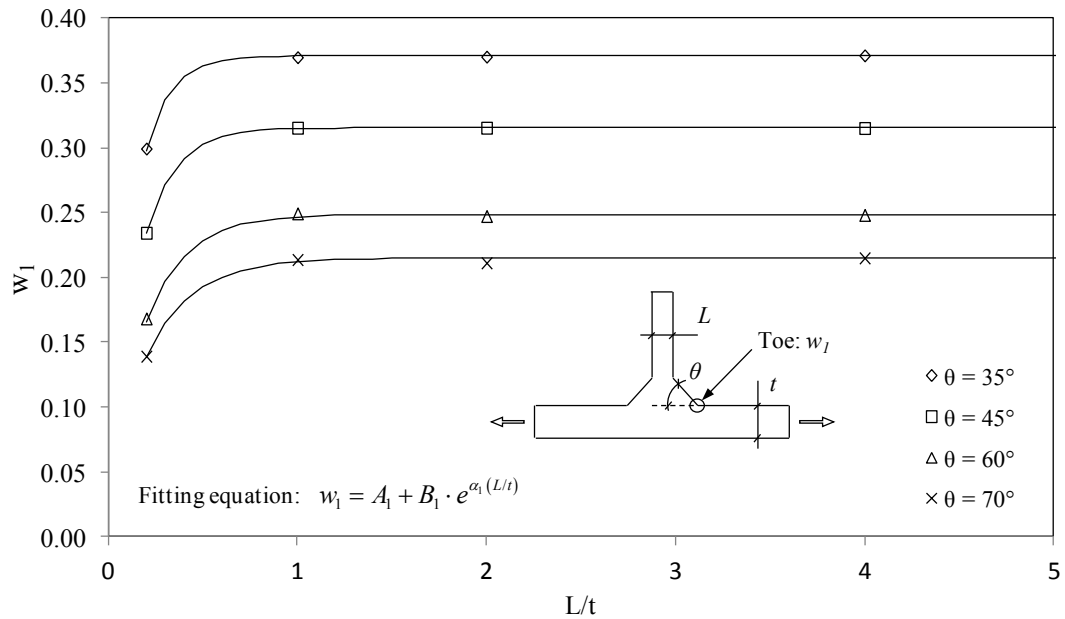


**Figure 5.25.** Curves for  $w_1$  values in non-load-carrying full penetration T-joints under pure membrane loading.

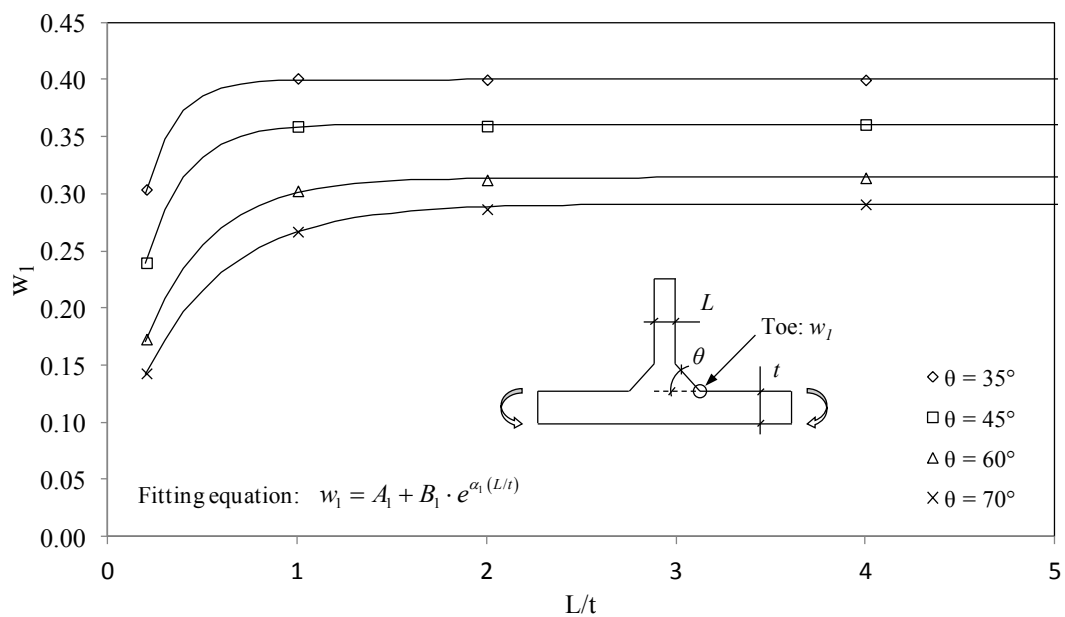


**Figure 5.26.** Curves for  $w_1$  values in non-load-carrying full penetration T-joints under pure bending loading.

### 5.5.6 Double fillet welded longitudinal attachment

The double fillet welded longitudinal attachment is reported in this section. The joint has been analyzed considering two configurations: a) symmetric attachment (cruciform shaped joint) and b) asymmetric attachment (T-shaped joint), according to Figure 5.27. Pure membrane loading and pure bending loading conditions have been considered for both configurations. The non-dimensional parameter  $w_1$  has been

calculated through Equation (5.27), once SED has been computed via finite element analyses. The weld transition angle  $\theta$  has been assumed equal to  $45^\circ$  (i.e. notch opening angle  $2\alpha=135^\circ$ ). With reference to configuration a), data have been interpolated by means of the following polynomial expression:

$$\begin{aligned}
 w_i = & p_{00} + p_{10} \left( \frac{2h}{t} \right) + p_{01} \left( \frac{L}{t} \right) + p_{20} \left( \frac{2h}{t} \right)^2 + p_{11} \left( \frac{2h}{t} \right) \left( \frac{L}{t} \right) + p_{02} \left( \frac{L}{t} \right)^2 + p_{30} \left( \frac{2h}{t} \right)^3 + \\
 & + p_{21} \left( \frac{2h}{t} \right)^2 \left( \frac{L}{t} \right) + p_{12} \left( \frac{2h}{t} \right) \left( \frac{L}{t} \right)^2 + p_{03} \left( \frac{L}{t} \right)^3 + p_{40} \left( \frac{2h}{t} \right)^4 + p_{31} \left( \frac{2h}{t} \right)^3 \left( \frac{L}{t} \right) + \\
 & + p_{22} \left( \frac{2h}{t} \right)^2 \left( \frac{L}{t} \right)^2 + p_{13} \left( \frac{2h}{t} \right) \left( \frac{L}{t} \right)^3 + p_{04} \left( \frac{L}{t} \right)^4 + p_{50} \left( \frac{2h}{t} \right)^5 + p_{41} \left( \frac{2h}{t} \right)^4 \left( \frac{L}{t} \right) + \\
 & + p_{32} \left( \frac{2h}{t} \right)^3 \left( \frac{L}{t} \right)^2 + p_{23} \left( \frac{2h}{t} \right)^2 \left( \frac{L}{t} \right)^3 + p_{14} \left( \frac{2h}{t} \right) \left( \frac{L}{t} \right)^4 + p_{05} \left( \frac{L}{t} \right)^5
 \end{aligned}
 \tag{5.37}$$

With reference to configuration b), data have been interpolated using Equation (5.37), substituting  $2h/t$  with  $h/t$ . As well as in the bi-dimensional cases presented in Sections 5.5.2 to 5.5.5, in Equation (5.37)  $h$  is the height of the weld fillet,  $L$  is the thickness of the welded longitudinal attachment and  $t$  is the thickness of the loaded plate. Other joint dimensions have been taken as dependent on  $h$  and  $L$ , so as to have negligible effect on the  $w_i$  values (Figure 5.27).

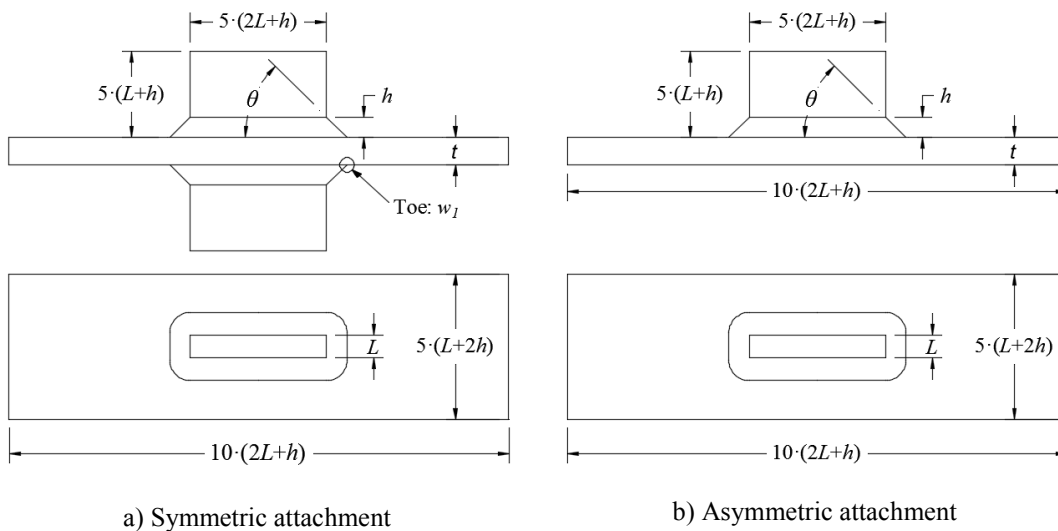


**Figure 5.27.** Geometrical definitions of the double fillet welded longitudinal attachment.

The trend of  $w_i$  is shown in Figures 5.28 and 5.29 with reference to configuration a), under pure membrane and pure bending loading, respectively. Similarly, Figures 5.30 and 5.31 show the trend of  $w_i$  with reference to configuration b). Fitting

constants are listed in Table 5.8. Estimates are accurate when  $0.2 \leq L/t \leq 4.0$  and  $0.4 \leq 2h/t \leq 8.0$ , with reference to configuration a); estimates are accurate when  $0.2 \leq L/t \leq 4.0$  and  $0.2 \leq h/t \leq 4.0$ , with reference to configuration b). Within these restrictions, the use of Equation (5.37) results in a maximum error equal to 5%.

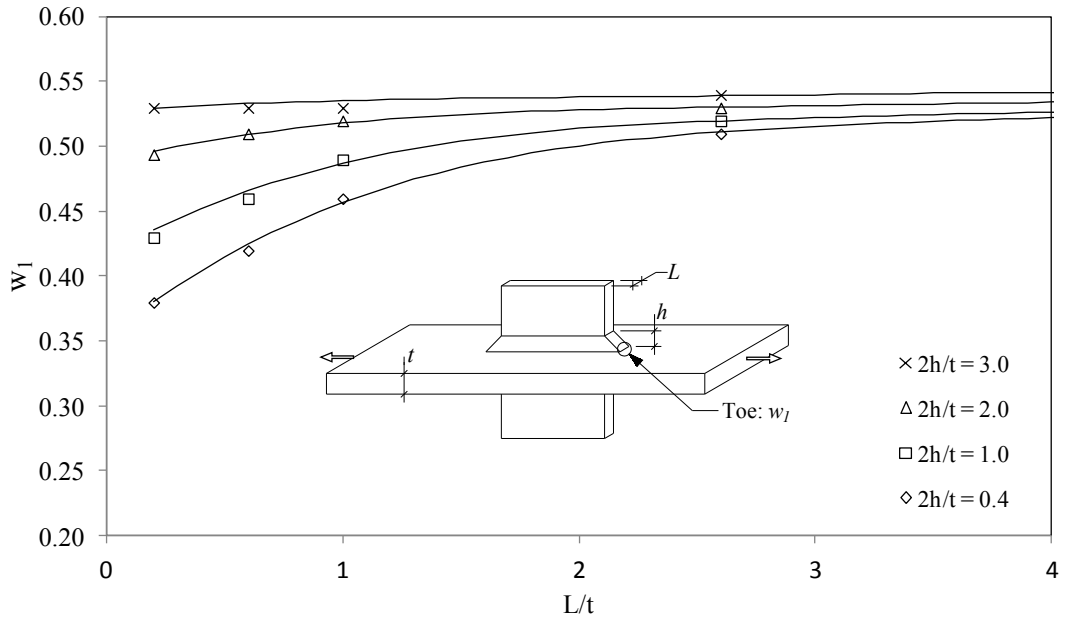


**Figure 5.28.** Curves for  $w_I$  values in non-load-carrying fillet welded symmetric longitudinal attachment under pure membrane loading.

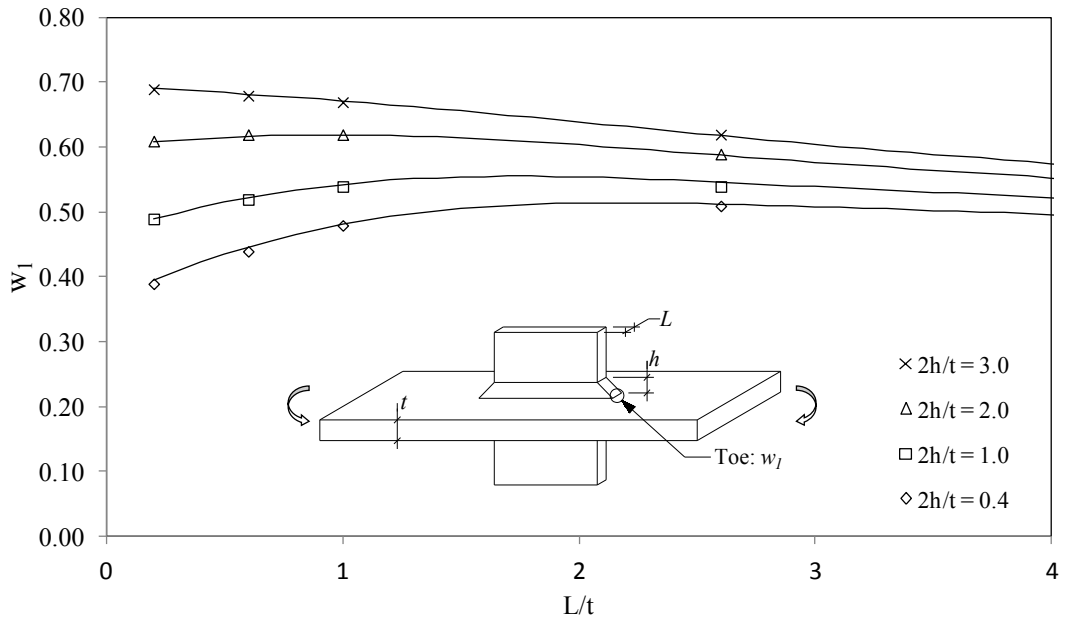


**Figure 5.29.** Curves for  $w_I$  values in non-load-carrying fillet welded symmetric longitudinal attachment under pure bending loading.

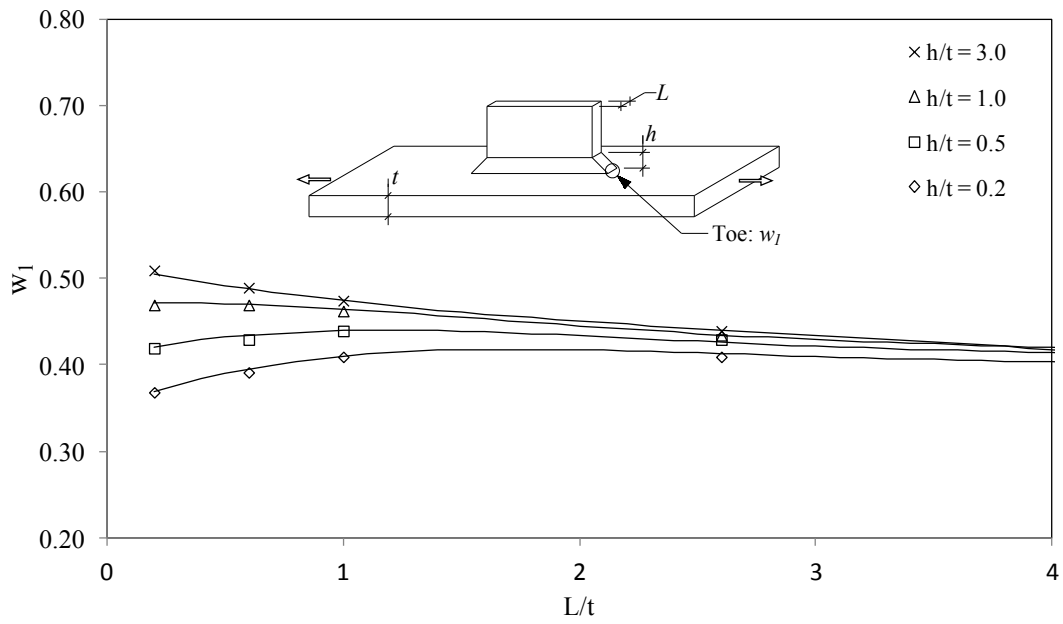


**Figure 5.30.** Curves for  $w_I$  values in non-load-carrying fillet welded asymmetric longitudinal attachment under pure membrane loading.

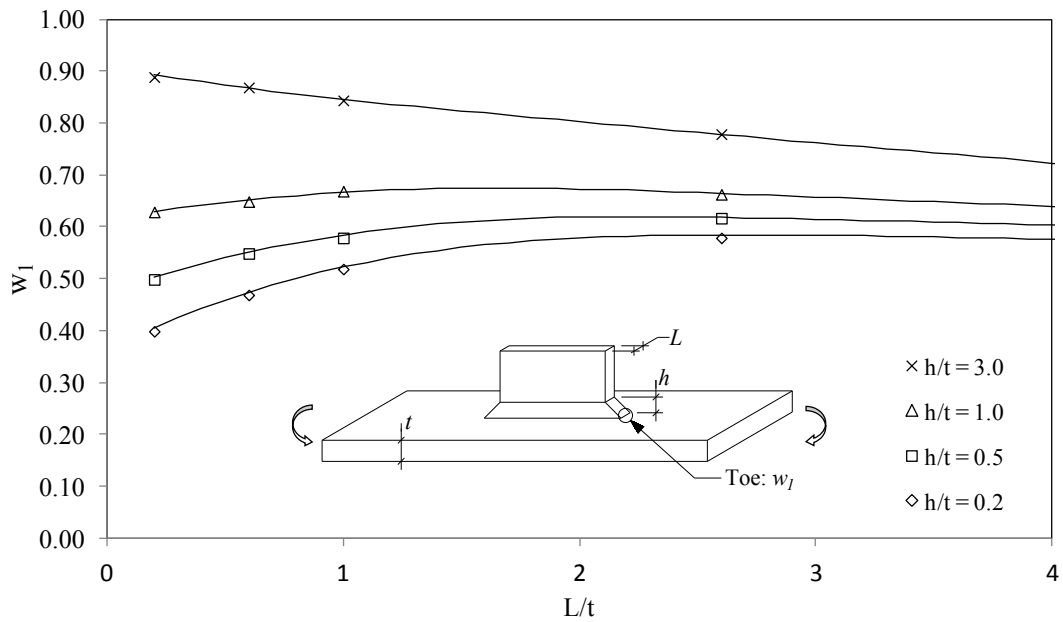


**Figure 5.31.** Curves for  $w_I$  values in non-load-carrying fillet welded asymmetric longitudinal attachment under pure bending loading.

**Table 5.8.** Coefficients for  $w_I$  evaluation at weld toe of symmetric and asymmetric non-load-carrying double fillet welded longitudinal attachments.

NLC	Symmetric longitudinal attachment		Asymmetric longitudinal attachment	
	Traction	Bending	Traction	Bending
$p_{00}$	2.970E-01	2.767E-01	2.977E-01	2.814E-01
$p_{10}$	1.527E-01	2.244E-01	2.960E-01	4.363E-01
$p_{01}$	1.827E-01	2.219E-01	1.355E-01	2.695E-01
$p_{20}$	-3.685E-02	-3.827E-02	-1.639E-01	-1.204E-01
$p_{11}$	-1.015E-01	-1.192E-01	-1.783E-01	-2.472E-01
$p_{02}$	-5.667E-02	-7.505E-02	-6.302E-02	-8.132E-02
$p_{30}$	4.653E-03	4.020E-03	4.842E-02	1.971E-02
$p_{21}$	1.875E-02	1.447E-02	5.820E-02	5.802E-02
$p_{12}$	2.692E-02	3.510E-02	5.426E-02	7.281E-02
$p_{03}$	6.171E-03	4.679E-03	1.185E-02	2.982E-03
$p_{40}$	-2.833E-04	-2.507E-04	-7.791E-03	-1.763E-03
$p_{31}$	-1.542E-03	-7.846E-04	-7.752E-03	-6.158E-03
$p_{22}$	-3.113E-03	-2.806E-03	-1.131E-02	-1.213E-02
$p_{13}$	-3.197E-03	-5.053E-03	-7.496E-03	-9.815E-03
$p_{04}$	3.601E-04	1.913E-03	-6.676E-04	2.404E-03
$p_{50}$	6.322E-06	7.206E-06	5.328E-04	6.398E-05
$p_{41}$	4.798E-05	1.468E-05	3.344E-04	2.472E-04
$p_{32}$	1.142E-04	7.766E-05	7.942E-04	6.510E-04
$p_{23}$	1.804E-04	1.901E-04	6.895E-04	8.466E-04
$p_{14}$	1.331E-04	2.824E-04	3.964E-04	4.780E-04
$p_{05}$	-8.698E-05	-2.719E-04	-2.702E-05	-3.015E-04

## 5.6 Practical application

The aim of this subsection is to practically present the link between local SED and nominal stress components and the use of the stress concentrating abaci. With this purpose, the box structure depicted in Figure 5.32 has been analyzed with Ansys® finite element code, under plane strain condition. Plane finite elements having quadratic shape functions (named Plane183 in Ansys® library) have been used. Linear elastic material having Young modulus equal to 206000 MPa and Poisson's ratio equal to 0.3 has been set. Geometrical dimensions, loading conditions and restraints have been assumed according to Figure 5.32.

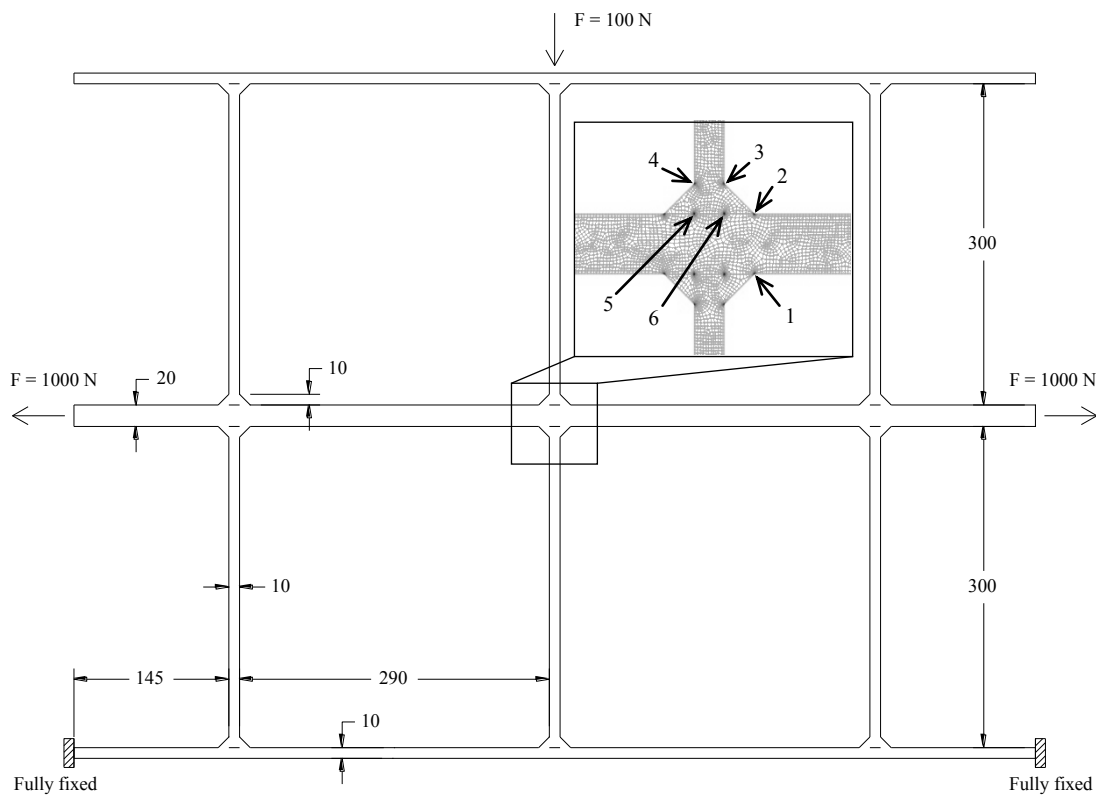


**Figure 5.32.** Box structure investigated under plane strain condition. Geometrical parameters and boundary conditions are presented in the figure. A detailed view of mesh refinement with indication of analyzed weld toes and roots is also provided.

Double fillet welded joints have been modeled as triangular shapes, producing V-notches, having opening angle equal to  $135^\circ$  and zero radius at weld toes, and crack-like notches at weld roots. The SED circular control volumes having radius  $R_0$  equal to 0.28 mm have been placed at weld toes and roots. According to Figure 5.32, the



averaged SED has been computed in control volumes indicated with numbers from 1 to 6. The obtained results are summarized in Table 5.9.

**Table 5.9.** Averaged SED computed through finite element analysis in the control volumes numbered from 1 to 6 in Figure 5.32.

	Control volume					
	1	2	3	4	5	6
SED [MJ/m <sup>3</sup> ]	$0.233 \cdot 10^0$	$0.233 \cdot 10^{-1}$	$0.952 \cdot 10^{-3}$	$0.952 \cdot 10^{-3}$	$0.149 \cdot 10^{-3}$	$0.149 \cdot 10^{-3}$

According to Table 5.9, the critical point for fatigue is the weld toe number 1, being characterized by an averaged SED of an order of magnitude larger than the one of the other 5 points of singularity. For the sake of brevity, the following analysis is limited to such point. However, the presented procedure can be analogously repeated.

Considering the weld toe number 1, reference is made to Figure 5.33. Weld shape ratios are  $2h/t=1$  and  $L/t=0.5$ . According to Equation (5.34), using values  $w_1$  and  $w_2$  from Section 5.5.2 and assuming, for this purpose and for simplicity, bending ratio  $r_b=0$ , the stress offset  $\delta$  to be adopted is equal to  $0.8 \cdot t=16$  mm. At this distance from the weld toe, stresses on the upper and lower surfaces of the plate are  $\sigma_U=-55$  MPa and  $\sigma_L=153$  MPa, respectively. Moreover, a parabolic through-thickness shear stress, having maximum value equal to  $\tau_{max}=3$  MPa, is found.

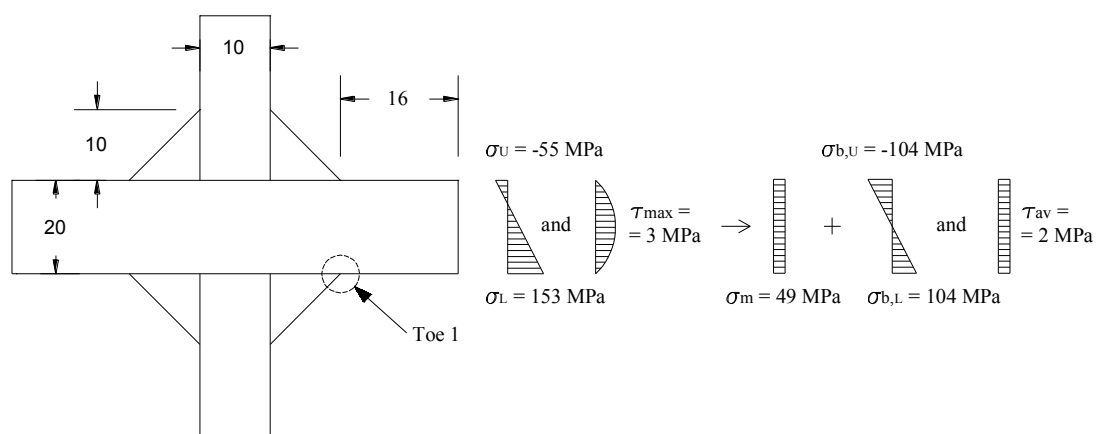


**Figure 5.33.** Nominal stress components at the distance  $\delta=16$  mm, analytically determined through Equation (5.34), from the weld toe.

Such stresses can be equivalently represented through a constant membrane stress  $\sigma_m=(\sigma_U+\sigma_L)/2=49$  MPa, an upper bending stress  $\sigma_{b,U}=\sigma_U-\sigma_m=-104$  MPa, a lower bending stress  $\sigma_{b,L}=\sigma_L-\sigma_m=104$  MPa and an average shear stress  $\tau_{av}=2/3\cdot\tau_{max}=2$  MPa. According to Equation (5.10), the nominal stress is  $\sigma_n=49+104+16\cdot6\cdot2/20=162.6$  MPa, where the sign of the shear stress is the same of the bending stress because the bending moment increases approaching the weld toe. The bending ratio, according to Equation (5.19), is  $r_b=|-104-16\cdot6\cdot2/20|/(|49|+|104+16\cdot6\cdot2/20|)=0.70$ .

By using abaci reported in Section 5.5.2, Equation (5.20) provides  $w_I=0.378\cdot(1-0.70)+0.309\cdot0.70=0.330$ . Finally, Equation (5.27) provides an averaged SED value equal to  $0.226$  MJ/m<sup>3</sup>. The averaged SED computed through the finite element model is equal to  $0.233$  MJ/m<sup>3</sup> (Table 5.9). Therefore, the error computed in the rapid estimation of SED using abaci is 3.1%, which is considered engineering acceptable.

## 5.7 Discussion and conclusion

As far as the author knows, a detailed investigation on the possibility of an efficient estimation of SED or NSIFs in a real structure, by means of finite element models, has still not been performed, demonstrating that there exist non-trivial computational issues behind the practical applicability of these local stress field parameters. Not casually, welded structures are usually analyzed by designers through shell structural models. Within this framework, this chapter has analyzed the relationships between local stress fields, near weld toes and roots, and the stress field linearly distributed along the thickness (as provided by shell element theory, by other simplified structural models or otherwise by strain gauge measurements), evaluated at a proper distance  $\delta$  from the weld toe. Such distance is usually suggested to be 1.5 times the loaded plate thickness, which is questionable. Hence, an analytical relationship between  $\delta$  and the loaded plate thickness has been here provided. The stress components computed at  $\delta$  distance, neglecting both the local stress effects caused by the weld itself and the structural stress, can be considered as nominal. Therefore, the proposed method actually establishes an explicit relation between the local and the nominal stress field.

A rapid approach, based on ready-to-use abaci, has also been proposed in order to extend the applicability of the local NSIF and SED criteria from simple welded details to real structures. So that, the proposed method seems really suitable for

performing the extremely large number of checks that fatigue assessment of a nowadays complex structure requires. However, the present lack of normative compliance of local approaches (SED and NSIF) represents an obstacle in industrial applications, especially in those fields (e.g. civil buildings) in which design is particularly influenced by norms. This is the reason why in Chapter 6 a nowadays normative compliant modified nominal stress is proposed.

Finally, it is worth noting that the presented procedure can also be viewed as a numerical mapping of the most common welded joints' fatigue behavior: a mapping which has instead been done with experimental tests in the last century, with much heavier approximations (no distinction between membrane and bending loads, no clear definition of the size effect, no structural continuity between details, etc.).

## References

- [1] D. Radaj, Review of fatigue strength assessment of non-welded and welded structures based on local parameters, *Int. J. Fatigue*. 18 (1996) 153–170.
- [2] K. Ida, T. Uemura, Stress concentration factor formulae widely used in Japan, *Fatigue Fract. Eng. Mater. Struct.* 19 (1996) 779–786.
- [3] A.F. Hobbacher, Stress intensity factors of welded joints, *Eng. Fract. Mech.* 46 (1993) 173–182.
- [4] J.-Y. Yung, F. V. Lawrence, Analytical and graphical aids for the fatigue design of weldments, *Fatigue Fract. Eng. Mater. Struct.* 8 (1985) 223–241.
- [5] M.L. Williams, Stress singularities resulting from various boundary conditions in angular corners of plates in tension, *J. Appl. Mech.* 19 (1952) 526–528.
- [6] P. Lazzarin, R. Tovo, A Notch Intensity Factor Approach To the Stress Analysis of Welds, *Fatigue Fract. Eng. Mater. Struct.* 21 (1998) 1089–1103.
- [7] P. Lazzarin, F. Berto, F.J. Gomez, M. Zappalorto, Some advantages derived from the use of the strain energy density over a control volume in fatigue strength assessments of welded joints, *Int. J. Fatigue*. 30 (2008) 1345–1357.
- [8] P. Lazzarin, F. Berto, M. Zappalorto, Rapid calculations of notch stress intensity factors based on averaged strain energy density from coarse meshes: theoretical bases and applications, *Int. J. Fatigue*. 32 (2010) 1559–1567.
- [9] G. Meneghetti, P. Lazzarin, Significance of the elastic peak stress evaluated by FE analyses at the point of singularity of sharp V-notched components, *Fatigue Fract. Eng. Mater. Struct.* 30 (2007) 95–106.
- [10] I. Poutiainen, G. Marquis, A fatigue assessment method based on weld stress, *Int. J. Fatigue*. 28 (2006) 1037–1046.
- [11] P. Dong, A structural stress definition and numerical implementation for fatigue analysis of welded joints, *Int. J. Fatigue*. 23 (2001) 865–876.
- [12] O. Doerk, W. Fricke, C. Weissenborn, Comparison of different calculation methods for structural stresses at welded joints, *Int. J. Fatigue*. 25 (2003) 359–369.
- [13] I. Poutiainen, P. Tanskanen, G. Marquis, Finite element methods for structural hot spot stress determination—a comparison of procedures, *Int. J. Fatigue*. 26 (2004) 1147–1157.
- [14] R. Tovo, P. Lazzarin, Relationships between local and structural stress in the

- evaluation of the weld toe stress distribution, *Int. J. Fatigue*. 21 (1999) 1063–1078.
- [15] B. Gross, A. Mendelson, Plane elastostatic analysis of V-notched plates, *Int. J. Fract. Mech.* 8 (1972) 267–276.
- [16] P. Lazzarin, R. Zambardi, A finite-volume-energy based approach to predict the static and fatigue behavior of components with sharp V-shaped notches, *Int. J. Fract.* 112 (2001) 275–298.
- [17] E. Niemi, *Stress determination for fatigue analysis of welded components*, Woodhead Publishing, Cambridge, 1995.
- [18] A.F. Hobbacher, The new IIW recommendations for fatigue assessment of welded joints and components - A comprehensive code recently updated, *Int. J. Fatigue*. 31 (2009) 50–58.
- [19] A.F. Hobbacher, New developments at recent update of the IIW recommendations for fatigue of welded joints and components, *Steel Constr.* 3 (2010).
- [20] DVS 1612 - Design and endurance strength assessment of welded joints with steels in rail vehicle construction, German Welding Society, Brussels, 2009.
- [21] B. Atzori, P. Lazzarin, R. Tovo, Stress field parameters to predict the fatigue strength of notched components, *J. Strain Anal. Eng. Des.* 34 (1999) 437–453.



## **6. A mathematical definition of modified nominal stress and experimental validation**

### **Highlights**

In this chapter a method, scientifically and normatively compliant, to improve the classical nominal stress approach for welded structures, which is still the most widely accepted and recognized in standards, is proposed. Finite element analyses have been carried out in order to investigate the effect of loading type on the fatigue strength of load- and non-load-carrying welded joints. It has been found that in terms of local strain energy density (SED) the fatigue strength of asymmetric joints (e.g. tee joints) is higher under tensile loading and the fatigue strength of symmetric joint (e.g. cruciform joints) is higher under bending loading. According to the results, it can be concluded that the type of loading significantly affects the fatigue behavior of welded joints. In spite of this, the current codes and recommendations do not give explicit instructions on how to consider the degree of bending in the fatigue assessment of welded joints. Here, a SED based modified nominal stress is formalized and the procedure to compute it by means of a finite element analysis is shown. The bending effect is addressed by introducing a proper coefficient obtained by linking local concepts to the classical nominal stress components. Then, the implications in fatigue design of large steel structures are discussed.





## 6.1 Introduction

Large-scale structures, characterized by thousands of welds to be checked, can be usually numerically modeled only by means of thin shell elements and really coarse meshes. Therefore, despite meshes with a degree of refinement up to three and four orders of magnitude larger than the ones used in NSIF approach and fracture mechanics are allowed adopting SED and PSM, respectively, there remains a difficult challenge to directly apply these criteria on massive fatigue investigations in large-scale structures. In this context, today a solid way to address the problem, where solid means complying with current standards and nowadays computational capabilities of design offices, can be found on the nominal approach. Therefore, the aim of this study is to propose a way, scientifically sound and normatively compliant, to improve the classical nominal stress method for welded structures, which is still the most widely accepted and recognized in standards. An efficient approach has been found by coupling local approaches (NSIF and SED) to nominal stress components. Indeed, the proposed method can be considered a modified nominal stress (with the meaning provided by the Eurocode 3[1] and by IIW recommendations [2]), having the following peculiar features: a) to grant the reliability of the classical nominal stress, which for many details still represents a touchstone, rich of all those morphological and execution differences that cannot be modeled and that only the statistics is able to capture; b) to be finite element method compatible, which means that the output of a FE model (characterized by stress gradients, both in thickness and on the surfaces of plates) should be consistent with the laboratory testing conditions; c) to require light computational effort, which means to be substantially mesh size independent; finally, d) to be fully complying with standards, in particular with the Eurocode 3 and IIW recommendations, in order to be accepted in the real industrial context.

In the following sections, previous researches concerning the issue are first discussed, then the modified nominal stress is presented and the corresponding finite element procedure is given using shell element based models. A validation of the method is provided by reanalyzing many S-N data from the literature, with reference to cruciform and T-joints subjected to membrane and bending loads. The proposed method is suitable for performing the large number of fatigue assessments which a nowadays complex structure requires.

## 6.2 Literature and normative review on the effect of loading type

Nominal stress based design curves are typically determined through fatigue tests on specimens subjected to membrane load. Bending fatigue tests are avoided, if possible, due to more complex test set-ups and utilization of results [3]. However, the influence of loading type on fatigue resistance and the often favorable "bending effect" have been already noticed in the last three decades. This phenomenon is mainly explained by two aspects: a) the growth rate of a crack initiating from the surface of a plate decreases in the presence of bending stress (i.e. the crack grows into a region with reduced stress). On this aspect it is widely accepted that when a crack propagates into a lower stressed area the stress intensity factor is also lower [4] and that stress concentration factors are not equal under pure tensile and bending loading [5,6]; b) the probability that a possible crack initiating point (for example a defect in the plate's thickness) is subjected to the maximum nominal stress decreases in the presence of bending stress [7]; conversely in the case of pure membrane load the whole thickness of a plate is loaded with the maximum nominal stress.

Recently, the issue has come up again and several studies have been published on the topic [8–10]. In principle, the conclusion has been that increasing the degree of bending improves the fatigue strength. However, tests published in the recent literature [11] offer a different point of view, indicating loss of fatigue strength in non-load-carrying T-joints bending load in as-welded condition. So, typically test results have indicated an improvement on the fatigue strength under bending loading but this benefit has not been completely confirmed and formalized yet.

The effect of loading type is included, at least as a principle, in certain standards. The Norwegian ship classification society Det Norske Veritas (DNV) has approved a reduction for bending hot spot stress component in the determination of the equivalent hot spot stress [12] through the following assumption:

$$\Delta\sigma_{e,hotspot} = \Delta\sigma_{a,hotspot} + 0.60 \cdot \Delta\sigma_{b,hotspot} \quad (6.1)$$

in which  $\Delta\sigma_{e,hotspot}$  is the equivalent hot spot stress range, whereas  $\Delta\sigma_{a,hotspot}$  and  $\Delta\sigma_{b,hotspot}$  are the membrane and the bending ones, respectively. The reduction factor on the bending stress is justified by redistribution of loads to other areas during crack growth, while the crack tip is growing into a region with reduced stress. Crack propagations in tensile and bending loading can be compared in Figure 6.1 [4].

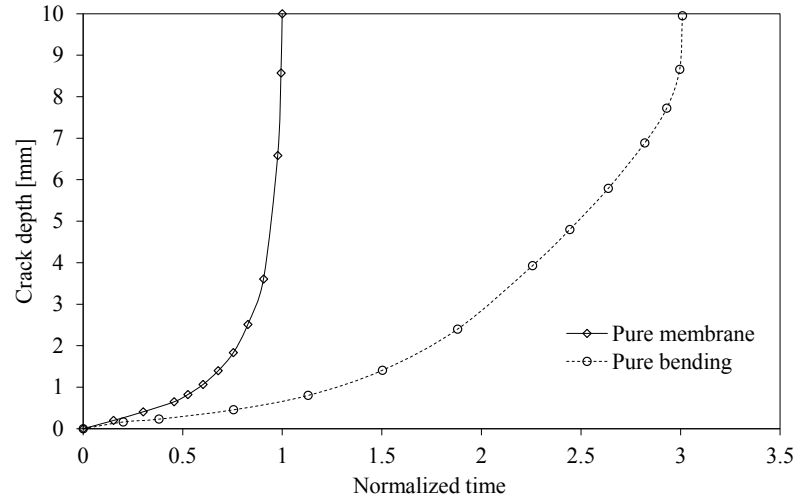


**Figure 6.1.** Qualitatively comparison of crack growth curves for the same hot spot stress with different degree of bending [4].

It should be noted that, according to DNV recommendations, it is not correct to generally reduce the bending part of the stress to 60%. This has to be restricted to cases with a pronounced stress concentration (unfortunately not quantified).

An ISO norm dedicated to crane design [13] states that in fatigue analyses the effect of the local stress can be reduced, because the fatigue strength in bending of a plate is typically 30% to 60% higher than in tension, for the same joint or detail.

Dong proposed to adopt an equivalent structural stress range parameter to evaluate the fatigue damage for results obtained from a linear elastic stress analysis, according to which the effects of the membrane and bending on S-N behavior can be inferred from fracture mechanics considerations [14–16]. He introduced the following loading type correction function:

$$I(r)^{\frac{1}{m_{ss}}} = (0.294 \cdot r^2 + 0.846 \cdot r + 24.815)^{\frac{1}{m_{ss}}} \quad (6.2)$$

in which  $I(r)$  is a dimensionless parameter derived by fracture mechanics considerations,  $m_{ss}$  is the crack propagation exponent in conventional Paris' law, assumed equal to 3.6, and  $r$  is the degree of bending (bending stress divided by total stress). The parameter  $I(r)$  is a divisor of the structural stress range and increases with the increase of the degree of bending. Such criterion has also been mentioned by Draper [17].

An ASME standard regulating the design and construction of boiler and pressure vessels [18], adopting the equivalent structural stress range parameter to evaluate the fatigue damage suggested by Dong [14], proposes the use of the following loading type correction function:

$$I(r)^{\frac{1}{m_{ss}}} = \frac{1.23 - 0.364 \cdot R_b - 0.17 \cdot R_b^2}{1.007 - 0.306 \cdot R_b - 0.178 \cdot R_b^2} \quad (6.3)$$

in which  $I(r)$  and  $m_{ss}$  have already been defined in Equation (6.2) and  $R_b$  is the degree of bending. Other formulations for  $I(r)$  parameter can be found in the literature [16].

In a superseded British standard [19], the bending effect was considered through a factor  $k_{ib}$  which took into account both the degree of bending and the plate thickness effects. The factor was based on results obtained by fracture mechanics and did not match well test results of non-load- and load-carrying fillet weld joints as well as butt welded joints. A new proposal for such factor, which agrees better with test results, has been given by Maddox [8] and is included in the latest standard version [20]:

$$k_{ib} = \left[ 1 + \Omega^{1.4} \cdot \left\{ \left( \frac{25}{t} \right)^{n_t} - 1 \right\} \right] \cdot [1 + 0.18 \cdot \Omega^{1.4}] \quad (6.4)$$

in which  $k_{ib}$  is the thickness and bending correction exponent,  $\Omega$  is the degree of bending,  $t$  is the plate thickness and  $n_t$  is the thickness correction exponent (typically equal to 0.2). The previous equation is valid for  $t < 25$  mm and transverse fillet or butt welded joints. The trend of Equations (6.2) to (6.4) is presented in Figure 6.2.

Finally, it is worth mentioning that both the Eurocode 3 [1] and the IIW recommendations [2] consider in the same way tensile and bending loads and therefore do not propose any loading type correction factor and that, nowadays, Lotsberg [21] clearly suggests that only membrane stresses have to be used together with the nominal stress approach, otherwise hot spot stress methods should be used.

As a conclusion of this brief literature and normative review, it is possible to point out that the effect of loading type is not always confirmed. In most of the studies, the fundamental impression has been that increasing the degree of bending improves the fatigue strength but further investigations are probably required. In this context, the

aim of the present work is to give an original contribution from the point of view of the local notch stress intensity based approaches.

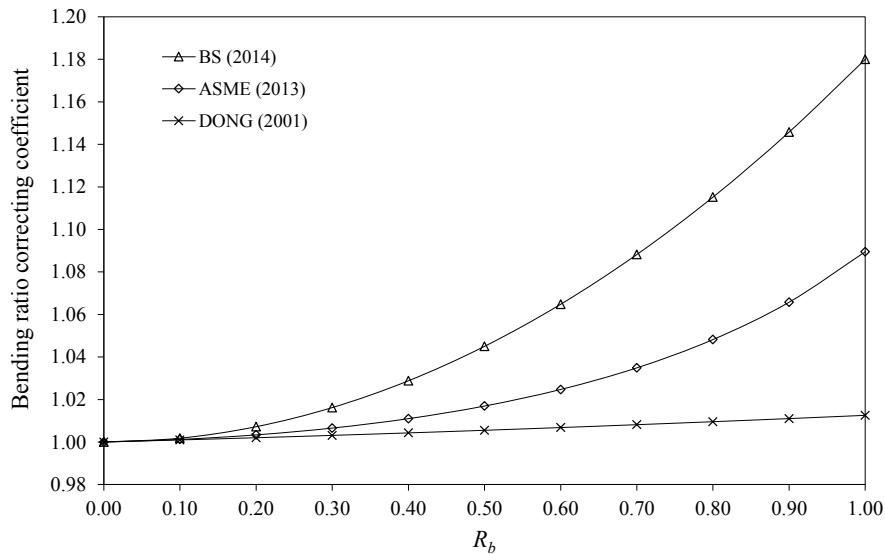


**Figure 6.2.** Trend of the bending correction according to ASME, Dong and BS. For an easy reading, curves provided by Equations (6.2) and (6.3) have been scaled so that  $I(0)=1$ ; whereas in plotting Equation (6.4) it has been assumed  $t = 25$  mm.

### 6.3 Local finite element calculation of nominal stress components

Thin shell element models are widely accepted for performing static resistance analyses of complex structures and often are the unique choice for fatigue assessments. It should be noted that the shell element solution at geometric discontinuities (e.g. weld line) reflects the solution that the corresponding shell theory is able to provide. As a consequence, local stresses at welds are forced to obey the shell theory used in the finite element model (e.g. Kirchhoff plate theory). Because of these considerations, the local stresses provided by a shell model along the plates' intersection line have to be considered numerically wrong, both for resistance and for fatigue. So, computed stresses have to be assumed reliable only up to a proper distance from plates' intersection. On this topic Draper [17] has established his point of view. He pointed out that finite elements close to the weld toe provide stresses influenced by the local stresses concentration, so, if nominal stresses are used, the corresponding calculated lives are unduly conservative and can be ignored. In addition, if nominal stresses are used, the weld beads do not need to be meshed. Quite simple meshes are therefore acceptable and both finite element and

fatigue analyses can proceed quickly. In a previous work by Niemi [22] it has been shown that, since the non-linear local effect is predominant only close to the toe of the weld, the shell solution can be considered valid up to a distance from the weld toe equal to or greater than the plate thickness or the weld throat height. In later works [23,24] and, very recently, in a DVS technical code [25] a distance (stress offset)  $\delta$  ranging from 1.0 to 1.5 times the plate thickness is suggested. The proposal to use a stress offset of about 1.5 times the plate thickness is here agreed, being also proved (see Chapter 5) to be in good agreement with the analytical dependence of such distance on the weld geometry and the loading condition, as well as on the plate thickness, given by Equation (5.34). On the other hand, the possibility to analytically quantify such  $\delta$  distance, provided by Equation (5.34), could represent a qualifying choice, giving further reliability to finite element based fatigue assessments according to the nominal stress approach (Figure 6.3). Finally, the proposed method permits to compute a finite element stress parameter, which is compatible with the nominal stress approach and has the further advantage to be substantially independent of the mesh size and element type. This is not demonstrated here, but can be considered true because the same principles of stress recovery have been adopted in the mesh-insensitive structural stress formulation according to Dong [14].

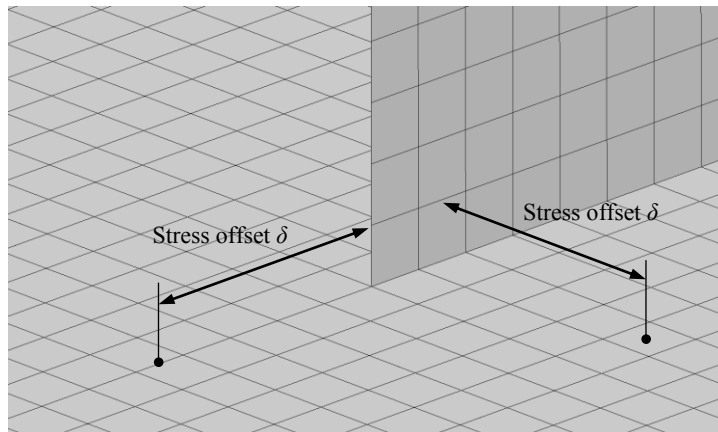


**Figure 6.3.** Example of shell finite element mesh and stress offsets to compute “local” nominal stress components. No explicit modeling of weld beads is considered.

#### 6.4 A loading type dependent modified nominal stress

As shown in Section 6.2, it is generally recognized that welded joints exhibit different fatigue strength properties under pure tensile and pure bending loads. Both

the classical hot spot and nominal stress criteria are not able to take into account the effect of this through-thickness stress gradient, because reference details are tested (in laboratory) under pure membrane load or, in rare cases, under pure bending load. According to Equations (5.27), (5.28) and (5.29), SED and NSIF values, both at the weld toe and at the weld root, are functions of the bending ratio by means of  $w_1$  and  $w_{eq}$ . This means that the bending ratio effect on the fatigue resistance of a welded joint can be fully taken into account by  $w_1$  and  $w_{eq}$  parameters.

Therefore, the following nominal stress, modified to take into consideration the bending effect, can be proposed for weld toe and weld root assessments respectively:

$$\sigma_{n,toe} = \frac{\sigma_n}{k_{b,toe}(r_b)} \quad (6.5)$$

$$\sigma_{n,root} = \frac{\sigma_n}{k_{b,root}(r_b)} \quad (6.6)$$

in which  $k_{b,toe}(r_b)$  and  $k_{b,root}(r_b)$  are nominal stress correcting coefficients, dependent on the bending ratio  $r_b$  defined by Equation (5.19). If the reference detail has been tested under pure membrane condition, the nominal stress correcting coefficients, for weld toe and for weld root assessments respectively, are defined as:

$$k_{b,toe}(r_b) = \frac{w_{1,m}}{w_1(r_b)} \quad (6.7)$$

$$k_{b,root}(r_b) = \frac{w_{eq,m}}{w_{eq}(r_b)} \quad (6.8)$$

whereas, if the reference detail has been tested under pure bending condition, as:

$$k_{b,toe}(r_b) = \frac{w_{1,b}}{w_1(r_b)} \quad (6.9)$$

$$k_{b,root}(r_b) = \frac{w_{eq,b}}{w_{eq}(r_b)} \quad (6.10)$$

Equations (6.7) to (6.10), properly fed with  $w_i$  coefficients mapped in Section 5.6 for the kind of joint of interest (e.g. load- or non-load-carrying joints, cruciform or T-joints, double-fillet or full-penetrated joints and so on), permit in principle to take into account the bending ratio effect on fatigue strength.

### 6.4.1 Application to fillet-welded non-load-carrying cruciform and T-joints

Considering the common case of a cruciform non-load-carrying joint and the related  $w_i$  coefficients mapped in Section 5.5.2, Equation (6.7) gives  $k_{b,toe}$  values ranging from 1.0 to 1.35 under pure bending condition (i.e. for  $r_b = 1$ ) (see Figure 6.4); being the values 1.0 and 1.35 reached for the limit situations of practical interest named case “a” and case “b” in Figure 5.5, respectively.

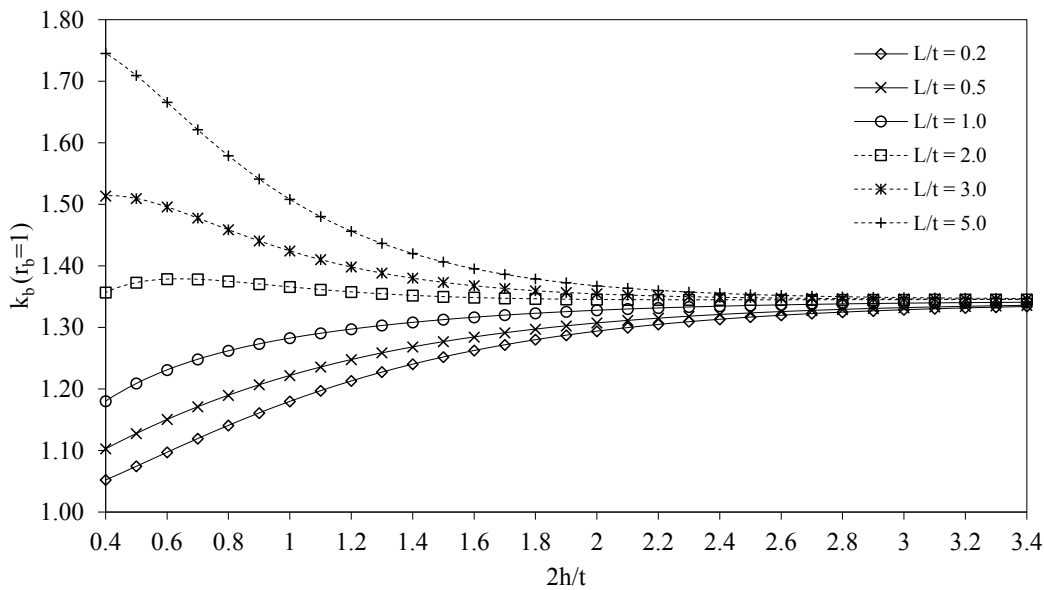


**Figure 6.4.** Load type correcting coefficient from pure membrane to pure bending condition, for non-load-carrying cruciform welded joints. Solid lines represent joints having shape ratios of usual interest in practical applications (ratio  $L/t$  up to 1). Failure at the weld toe.

It is interesting to note that, under pure bending condition, Equations (6.3) and (6.4) provide a nominal stress correcting coefficient of 1.09 and 1.18, respectively (the latter assuming plate thickness equal to 25 mm). Such correcting coefficients fit well inside the range provided by Equation (6.7) with reference to cruciform joints. Therefore, both Equations (6.3) and (6.4), not taking into account the weld shape ratios, can be imagined as a particular formulation of the approach here proposed, which fit many different geometries. However, the type of joint is neglected.

Considering then another common solution, which is a non-load-carrying T-joint, the related  $w_i$  coefficients are mapped in Section 5.5.3. Being this the case, Equation (6.7) gives  $k_{b,toe}$  values ranging from 0.88 to 0.95 under pure bending condition (i.e. for  $r_b = 1$ ) (see Figure 6.5).



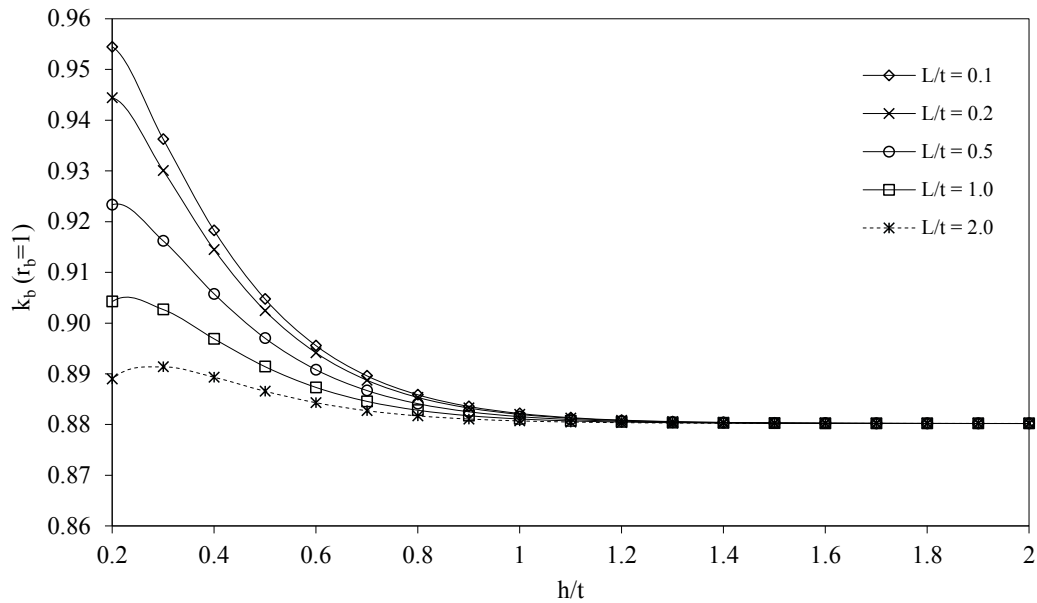


**Figure 6.5.** Load type correcting coefficient from pure membrane to pure bending condition, for non-load-carrying T-joints. Solid lines represent joints having shape ratios of usual interest in practical applications (ratio  $L/t$  up to 1). Failure at the weld toe.

#### 6.4.2 Reanalysis of data from the literature

All experimental data considered in this section are taken from the literature and refer to joints made of steel in *as-welded* condition and fatigue failures starting from the weld toe. Table 6.1 summarizes data referring to double-fillet welded cruciform joints, both load-carrying (LC) and non-load-carrying (NLC). Table 6.2 summarizes data referring to double-fillet non-load-carrying T-joints. Table 6.3 summarizes data referring to full-penetrated non-load-carrying T-joints. The loading ratio  $R$  is about 0 for all series. In each table information is given about bibliographical references, materials and geometry. The experimental fatigue strength, in terms of nominal stress  $\Delta\sigma_c$ , is given under pure traction (T) and pure bending (B) condition, together with their ratio  $\Delta\sigma_{c,B/T}$ . The inverse slope  $k$  of each S-N series is also listed, with the aim to show that, for the data here considered, no appreciable variation in terms of  $k$  can be observed by moving from pure membrane to pure bending loading. Finally, the last column gives the nominal stress correcting coefficient  $k_{b,toe}$  computed by means of Equation (6.7).

**Table 6.1.** Geometrical and fatigue strength properties of fillet-welded cruciform joints, both load- and non-load-carrying, in *as-welded* condition. Comparison of mean fatigue strengths at  $N = 5 \cdot 10^6$  cycles under pure traction and pure bending.

Series	Refs.	Material	Type	$t$ [mm]	$L/t$	$2h/t$	Load	$\Delta\sigma_{c,50\%}$ [MPa]	$k$	$\Delta\sigma_{c,B/T}$	$k_{b,10e}$
S1	Ahola et al. [26]	S960 MC	NLC	8	1.0	2.0	T	118	4.18	1.39	1.33
S2							B	166	4.39		
S3	Gustafsson [27]	Domex 550 MC	NLC	12	1.0	1.4	T	78	3.00	1.41	1.31
S4							B	110	3.00		
S5	Gustafsson [27]	Domex 550 MC	NLC	6	1.0	1.4	T	111	3.00	1.32	1.31
S6							B	147	3.00		
S7	Gurney [28]	Low C Steel	NLC	6	1.0	2.0	T	78	3.04	1.21	1.15
S8 (*)							B	94	3.13		
S9	Gurney [29]	BS4360:50D	NLC	38	0.3	0.5	T	70	3.12	1.21	1.10
S10							B	85	3.43		
S11	Andrews [30]	BS4360:43A	LC	12.5	1.0	2.1	T	90	3.94	1.67	1.55
S12							B	150	3.92		

Type of load: T - Pure traction; B - Pure bending; (\*) Series referred to a T-joint.

**Table 6.2.** Geometrical and fatigue strength properties of fillet-welded non-load-carrying T-joints in *as-welded* condition. Comparison of fatigue strengths at  $N = 5 \cdot 10^6$  cycles and 97.7% probability of survival, under pure traction and pure bending.

Series	Refs.	Material	Type	$t$ [mm]	$L/t$	$h/t$	Load	$\Delta\sigma_{c,97.7\%}$ [MPa]	$k$	$\Delta\sigma_{c,B/T}$	$k_{b,10e}$
S13	Ottesböck et al. [11]	S690	NLC	5	1.0	1.0	T	167	4.40	0.90	0.88
S14							B	150	4.10		

Type of load: T - Pure traction; B - Pure bending

**Table 6.3.** Geometrical and fatigue strength properties of full-penetrated non-load-carrying T-joints in *as-welded* condition. Comparison of mean fatigue strengths at  $N = 5 \cdot 10^6$  cycles under pure traction and pure bending.

Series	Refs.	Material	Type	$t$ [mm]	$L/t$	$h/t$	Load	$\Delta\sigma_{c,50\%}$ [MPa]	$k$	$\Delta\sigma_{c,B/T}$	$k_{b,loc}$
S15	Lindley et al. [31]	BS4360:50D	NLC	25	1.0	0.5	T	74	2.39	0.72	0.86
S16							B	53	2.42		
S17	Lindley et al. [31]	BS4360:50D	NLC	25	0.8	0.4	T	75	3.37	0.93	0.89
S18							B	70	3.66		
S19	Lindley et al. [31]	BS4360:50D	NLC	50	1.0	0.5	T	63	3.13	0.86	0.86
S20							B	54	2.96		
S21	Lindley et al. [31]	BS4360:50D	NLC	50	0.8	0.4	T	83	3.74	0.76	0.89
S22							B	63	3.10		

Type of load: T - Pure traction; B - Pure bending

### 6.4.3 Results of the investigation

According to Tables 6.1 to 6.3, in which fatigue strengths of 11 couples of series have been reported under pure membrane and pure bending loading, a good match between measured ratio  $\Delta\sigma_{c,B/T}$  and numerical prediction  $k_{b,toe}$  is shown. Percentage errors committed considering the fatigue strength under membrane loading as the one computed under bending loading, before and after applying the  $k_{b,toe}$  correcting coefficient, are summarized in Figure 6.6 and in Figure 6.7, in terms of histogram and radar chart respectively. Labels 1 to 11 represents the 11 couples of series (T and B) of Tables 6.1 to 6.3 (label 1 represents percentage errors related to S1 and S2, label 2 represent percentage errors related to S3 and S4 and so on). It is possible to point out that, before considering the bending correction, the average error computed in estimating the fatigue strength is 30%, with a peak value of 67%; after the bending correction is introduced, the average error is 7%, with a peak value of 19%.

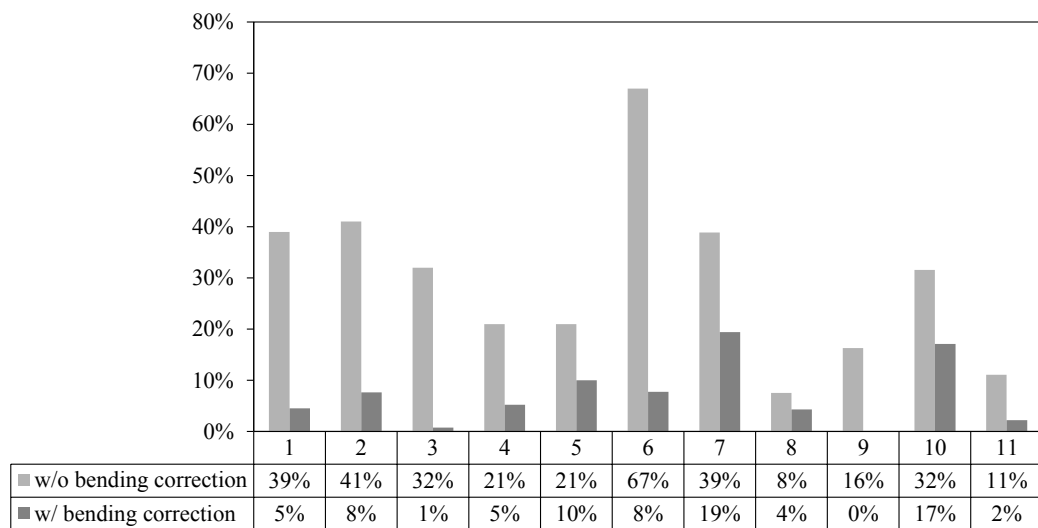


**Figure 6.6.** Percentage errors committed considering the membrane fatigue strength as the bending one, without and with applying the correcting coefficient.

Furthermore, Figure 6.7 shows that errors without correction contain (because larger) the ones with correction. This indicates that the fatigue strengths values after correction are always between the ones obtained under pure membrane load and the ones obtained under pure bending load and emphasizes the robustness of the

approach. In conclusion,  $k_{b,toe}$  appears suitable to take into account the different fatigue behavior of welded joints under pure tensile and pure bending loads.

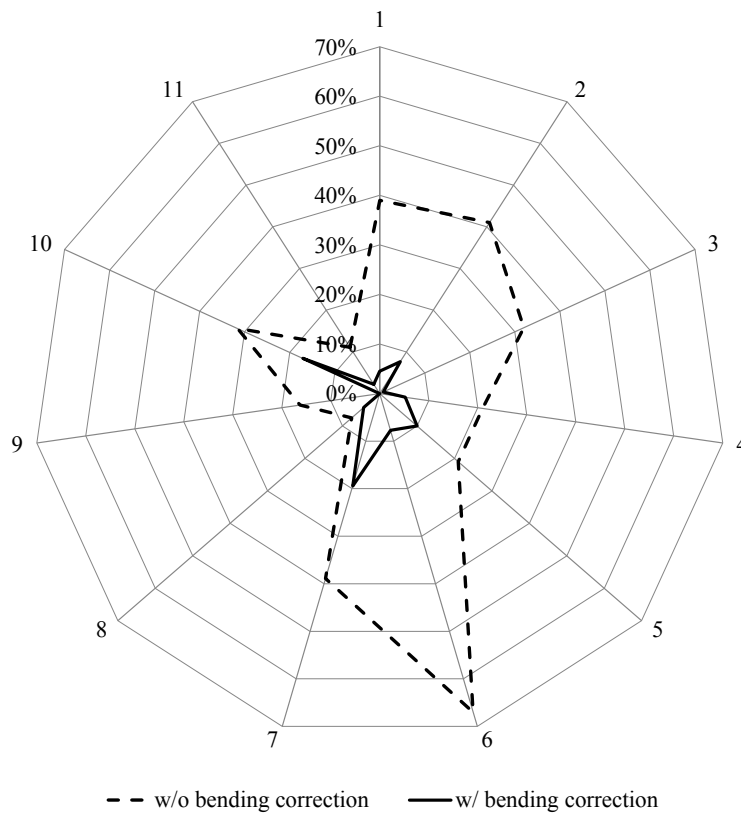


**Figure 6.7.** Radar chart of percentage errors committed considering the membrane fatigue strength as the bending one, without and with applying the correcting coefficient. Errors after correction are always smaller than before correction.

### 6.5 Open wide discussion and conclusion

In modern design offices, structures are increasingly solved with the aid of finite element models. This is a natural consequence of the structures' evolution process, which are becoming ever more complex and rarely can be wholly analyzed according to the simple elastic beam theory. Being based on empiric tests, the classical nominal stress method cannot consider all the aspects that the finite element method makes explicit. Primarily: a) the distinction between membrane and bending load; b) the number and the variety of geometries that a modern engineer faces in his everyday designing activity, which go beyond the rules of traditional steel structures composed of beams and columns. These aspects, which even for statics are tricky to be numerically considered, in fatigue produced: a) a huge quantity of critical points,

which have to be checked, not being known in advance whether they are true or false: a complete nominal stress based fatigue analysis all around a welding would require 20 checks (see Section 7.6.1), according to the Eurocode 3; b) "ghost" stresses (numerically wrong) within plates' intersections in shell models, where the finite element method should not actually be considered relevant, neither for resistance nor fatigue, but often considered "true stresses" or "good approximation of true stresses" as output of a model, or, even worse, "on the safety side". Just considering that the endurable the number of cycle and the nominal stress are usually linked by the power of 3 (which rises to 5 for shear stresses), it is clearly evident how the use of a wrong stress automatically leads to an uneconomic or even not applicable design. In this complex scenario, the standards in force are sometimes lacking in giving a real guidance. Still, most of them do not refer to any local concept, except for fracture mechanics, and, therefore, impose the use of the nominal stress method. Despite this, no recommendations exist on how to derive the nominal stress from a finite element model, so that it is left to the engineering assessment of a designer to establish which nominal stress is the suitable for fatigue checks.

The numerical solutions usually proposed by the scientific community to overcome these problems have gone, year after year, in the direction of the local and extremely refined description of the fatigue phenomenon. This is reasonable, considering the local nature of fatigue, but unpredictable effects of general cultural impoverishment and confusion have occurred, as a consequence, at the normative level and therefore in design offices. Just think, for example, of the hot spot methods, about which it is possible to find several designations, simply depending on the engineering field: civil constructions, marine, off-shore, railway, lifting equipments and cranes, mechanics, and so on. Accordingly, fatigue resulted in the designers' perception as an esoteric subject, even more than it already was, not only in the mega steel construction context but also in the ordinary steel constructions, such as bridges; or, such methods generated expensive and sight unseen software (also by renowned houses) that sell an instant solution to the problem, which appears contradictory with the huge research effort carried out in the last years, and still today, by the scientific community on the topic.

In the author's opinion, presently (and probably for many years to come), the problem of fatigue assessment of very large steel structures can only be solved on the

side of the global approaches. Just think, for example, to perform the assessment of fatigue induced by road traffic, rail traffic and wind on the Strait of Messina bridge (a project of over 130000 tons of steel), whose design is characterized by about 1 million welds. Such problem can be approached in an industrial context if the nominal stress method, properly enhanced by means of local concepts, is matched with coarse shell models, without the explicit consideration of the weld bead (because already considered in the reference S-N design curve). In this chapter, SED has been chosen as a local approach, because it requires shorter computational time as compared to other approaches. Moreover, being SED a scalar quantity, it provides stable results in a single parameter, excluding the uncertainties linked to the direction of stress components. However, it would have been possible to use other methods, such as direct NSIF computation, fracture mechanics or PSM, because interconnected by the strain energy through closed form equations. The proposed solution, here called modified nominal stress because of fully compliance with the Eurocode 3 (see the definition provided by section 6.3 in EN 1993-1-9), "brings back to the laboratory" the output of a FE calculation, where the resistance in terms of nominal stress has been statistically evaluated from simple specimens subjected to pure membrane or pure bending loading. The modified nominal stress appears suitable to perform the fatigue check of a whole structure, using a shell FE model and according to Eurocode 3 and IIW recommendations simply by means of theoretical and numerical deductions. To clarify this point, it is worth noting that the Eurocode 3 (section 6.3 in EN 1993-1-9), suggests that a stress concentration factor (e.g.  $k_b$ , for bending, in this chapter), to account for the local stress magnification in relation to a detail geometry not included in the reference  $\Delta\sigma$ -N curve, may be taken from handbooks or from appropriate finite element calculations. Nothing else than appropriate finite element calculations has been done, in principle, in this and in the previous chapters.

Certainly, the concept of a unique master curve correlating a loading parameter with the fatigue life for all welded joints, typical of many local approaches, cannot be for the moment maintained, but, as a convenience, extremely coarse meshes are allowed. On the other hand, the many S-N curves can be implemented in a software and checks can be automated once a proper nominal stress is defined.



The main findings of this chapter can be summarized in the following three points: (i) a notch stress intensity based modified nominal stress has been presented. This stress parameter is able to take into account both membrane and bending components and can be computed through shell finite element models; (ii) explicitly considering the real bending ratio of the loading condition, it is possible to provide additional reliability to the nominal stress method, in particular for those details which have been tested under pure membrane (mostly) or pure bending loads; (iii) the procedure to derive the relevant stress components, in terms of nominal stress approach, of a coarse shell finite element model has been shown, with substantial independence of the size of the mesh and from the element type and without beads representation. Furthermore, it has been mathematically found that, depending on the joint geometry, the bending effect could be positive or detrimental for fatigue resistance, which is in accordance to experimental results reported in the literature (see Section 6.4.2). Such result, in principle, questions the reliability of tests, unless full equivalence in terms of loading condition is achieved.

In conclusion, the modified nominal stress avoids the "traps" that the finite element method raises to designers in the application of the classical nominal stress method. By using local concepts derived from the linear elastic notch mechanics, or if desired from the fracture mechanics, universally accepted and proposed in current standards, it has been shown how to enhance the consistency of the well-known and stabilized nominal stress details with the output of a finite element model. However, the huge number of fatigue assessments to perform on a steel megastructure still represents a challenge, if not properly automated. This challenge is faced in Chapter 7 and a practical application on a large steel structure is presented in Chapter 8.

## References

- [1] EN 1993-1-9 Eurocode 3 - Design of steel structures - Part 1-9: Fatigue, European Committee for Standardization, Brussels, 2005.
- [2] A.F. Hobbacher, Recommendations for Fatigue Design of Welded Joints and Components, Springer International Publishing, 2016.
- [3] S.-W. Kang, W.-S. Kim, Y.-M. Paik, Fatigue strength of fillet welded steel structure under out-of-plane bending load, *Int. J. Korean Weld. Soc.* 2 (2002) 33–39.
- [4] I. Lotsberg, G. Sigurdsson, Hot Spot Stress S-N Curve for Fatigue Analysis of Plated Structures, *J. Offshore Mech. Arct. Eng.* 128 (2006) 330–336.
- [5] A.F. Hobbacher, Stress intensity factors of welded joints, *Eng. Fract. Mech.* 46 (1993) 173–182.
- [6] A. Chattopadhyay, G. Glinka, M. El-Zein, J. Qian, R. Formas, Stress analysis and fatigue of welded structures, *Weld. World.* 55 (2011) 2–21.
- [7] S. Timoshenko, History of strength of materials: with a brief account of the history of theory of elasticity and theory of structures, Courier Corporation, 1953.
- [8] S.J. Maddox, Allowance for bending in fatigue design rules for welded joints, *Int. Inst. Welding, Doc.* 13 (2015) 2515–2580.
- [9] B. Baik, K. Yamada, T. Ishikawa, Fatigue crack propagation analysis for welded joint subjected to bending, *Int. J. Fatigue.* 33 (2011) 746–758.
- [10] Z.-G. Xiao, T. Chen, X.-L. Zhao, Fatigue strength evaluation of transverse fillet welded joints subjected to bending loads, *Int. J. Fatigue.* 38 (2012) 57–64.
- [11] M. Ottersböck, M. Leitner, M. Stoschka, Effect of Loading Type on Welded and HFMI-treated T-joints, *IIW-Document.* 13 (2015) 2515–2584.
- [12] DNVGL-RP-C203 - Fatigue design of offshore steel structures, Det Norske Veritas - Germanischer Lloyd, 2016.
- [13] ISO 16881-1 - Cranes - Design calculation for rail wheels and associated trolley track supporting structure, International Organization for Standardization, 2005.
- [14] P. Dong, A structural stress definition and numerical implementation for fatigue analysis of welded joints, *Int. J. Fatigue.* 23 (2001) 865–876.

- [15] H. Kyuba, P. Dong, Equilibrium-equivalent structural stress approach to fatigue analysis of a rectangular hollow section joint, *Int. J. Fatigue*. 27 (2005) 85–94.
- [16] P. Dong, J.K. Hong, D.A. Osage, D.J. Dewees, M. Prager, The Master SN Curve Method an Implementation for Fatigue Evaluation of Welded Components in the ASME B&PV Code, Section VIII, Division 2 and API 579-1/ASME FFS-1, *Weld. Res. Counc. Bull.* (2010).
- [17] J. Draper, *Modern metal fatigue analysis*, EMAS publications, 2008.
- [18] ASME VIII - Rules for Construction of Pressure Vessels - Division 2: Alternative Rules, American Society of Mechanical Engineers, Brussels, 2013.
- [19] BS 7608 British Standard - Code of Practice for Fatigue Design and Assessment of Steel Structures, British Standard institution, 1993.
- [20] BS 7608 British Standard - Code of Practice for Fatigue Design and Assessment of Steel Structures, British Standard institution, 2014.
- [21] I. Lotsberg, Development of Fatigue Design Standards for Marine Structures, in: Vol. 9 Offshore Geotech. Torgeir Moan Honor. Symp., ASME, 2017.
- [22] E. Niemi, *Stress determination for fatigue analysis of welded components*, Woodhead Publishing, Cambridge, 1995.
- [23] A.F. Hobbacher, The new IIW recommendations for fatigue assessment of welded joints and components - A comprehensive code recently updated, *Int. J. Fatigue*. 31 (2009) 50–58.
- [24] A.F. Hobbacher, New developments at recent update of the IIW recommendations for fatigue of welded joints and components, *Steel Constr.* 3 (2010).
- [25] DVS 1612 - Design and endurance strength assessment of welded joints with steels in rail vehicle construction, German Welding Society, Brussels, 2009.
- [26] A. Ahola, T. Nykänen, T. Björk, Effect of loading type on the fatigue strength of asymmetric and symmetric transverse non-load carrying attachments, *Fatigue Fract. Eng. Mater. Struct.* (2016) 1–13.
- [27] M. Gustafsson, Thickness effect in fatigue of welded extra high strength steel joints, *Des. Anal. Welded High Strength Steel Struct.* (2002) 205–224.
- [28] T.R. Gurney, *Fatigue of thin walled joints under complex loading*, Abingdon

Publishing, 1997.

- [29] T.R. Gurney, *The fatigue strength of transverse fillet welded joints*, Abington Publishing, Cambridge, 1991.
- [30] R.M. Andrews, *The effect of misalignment on the fatigue strength of welded cruciform joints*, *Fatigue Fract. Eng. Mater. Struct.* 19 (1996) 755–768.
- [31] C. Lindley, P.H. Bateson, *Influence of attachment thickness on fatigue endurance of welded joints*, in: *Proc. Int. Conf. OFFSHORE Mech. Arct. Eng.*, 1993: p. 689.

# 7. Automatic fatigue assessment of large structures by using a dedicated post-processor

## Highlights

This chapter presents a finite element post-processor, developed to perform the almost automatic fatigue assessment of a large structure. The post-processor is compatible with Straus7® finite element solver and it is based on shell models, to be suitable for large assemblies. Results provided by a Straus7® solution are read by the post-processor, which analyzes them automatically, with respect to the fatigue strength analysis parameters. Both parent material and welds can be assessed, as well as other particular features detrimental for fatigue strength (e.g. holes, bolts and so on). The results are provided in the form of safety factors and degrees of utilization, and can be displayed graphically or in the form of text report.

Strengths of this tool are the automatic finding of weld lines in shell model assemblies, as well as the availability of dedicated menus to easily define fatigue spectra, fatigue properties (fatigue classes) and to make the design itself of the welds. Both global and local approaches are automated. In detail, local SED and NSIF approaches have been implemented, as well as the modified nominal stress and, finally, the classical nominal stress and hot spot stress approaches according to the Eurocode 3 and IIW recommendations. Recovery of nominal and hot spot stress components, through automatic offset from the weld, is available.

Some practical applications are given at the end of the chapter, considering double fillet welded joints both load- and non-load-carrying. A very good agreement between “manually” performed assessments, both through global and local approaches, and those rapidly performed by using the post-processor has been found. Further good agreement has been highlighted between expected fatigue lives estimated through the local SED approach and those estimated through the modified nominal stress, in the presence of bending stresses.



## 7.1 Introduction

In structural engineering, the fatigue strength assessment of a component is an important issue. What is more, welded steel structures are particularly susceptible to fatigue, since this type of joining introduces a discontinuity, which acts as a stress concentrator, lowering the fatigue strength of the parent material. That is why in almost every industrial field there are specific standards and guidelines dealing with the fatigue design and the related margins of safety against failure: civil constructions [1–6], mechanics [7], naval and off-shore [8–11], railway [12], lifting equipments and cranes [13,14], pressure vessels [15,16], to mention a few.

Addressing the theme of the present thesis, focused on making the fatigue assessment of large steel structures affordable, it has been considered essential developing a post-processor based on shell Finite Elements (FE) and coarse meshes. Cimolai SpA has developed such post-processor, named PostFatigue, in-house in the context of the present research work and with the collaboration of the Italian National Research Council (C.N.R.). It represents the fatigue module of the suite PostCimolai®, which includes other three modules: PostBeam (dedicated to resistance and buckling assessments of beams), PostWeld (dedicated to the static resistance analysis of welds) and PostYield (for elastoplastic assessment of plates). PostCimolai® suite is based on Straus7® finite element solver, provided by Strand7®.

Both global and local approaches have been automated in PostFatigue. In detail, local SED and NSIF approaches with the shell element based formulation presented in Chapter 5 have been implemented, as well as the modified nominal stress proposed in Chapter 6 and, finally, the classical nominal stress and hot spot stress approaches according to the Eurocode 3 and IIW recommendations. The most interesting aspects of PostFatigue are presented in this chapter. Some practical applications are also given, considering simple geometries representing double fillet welded joints both load- and non-load-carrying.

## 7.2 Assessing welds and parent material with PostFatigue

PostFatigue is a dedicated post-processor for fatigue assessment of welded joints and parent material (Figure 7.1). PostFatigue is compatible with shell based FE models realized and solved within Straus7® software. The FE stress results provided by a Straus7® solution are read by PostFatigue, which analyzes them automatically,

based on the definitions of the EN 1993-1-9 (Eurocode 3), with respect to the fatigue strength analysis parameters. The results are provided in the form of safety factors and degrees of utilization, and can be displayed graphically on the FE mesh in PostFatigue environment. Detailed output of the fatigue analysis is also supplied in the form of text report. Information about the derivation of the results is also available graphically and in the report (relevant load cases, stress amplitude and mean values, critical locations within weld seams, and so forth).

Within a single analysis run, both parent material and check lines (e.g. welds) can be assessed. Even for complex components containing different steels, a complete picture of the safety situation can be gained and visualized within one analysis run. Moreover, PostFatigue offers the possibility of assessing both proportional and non-proportional multiaxial loadings [17,18].

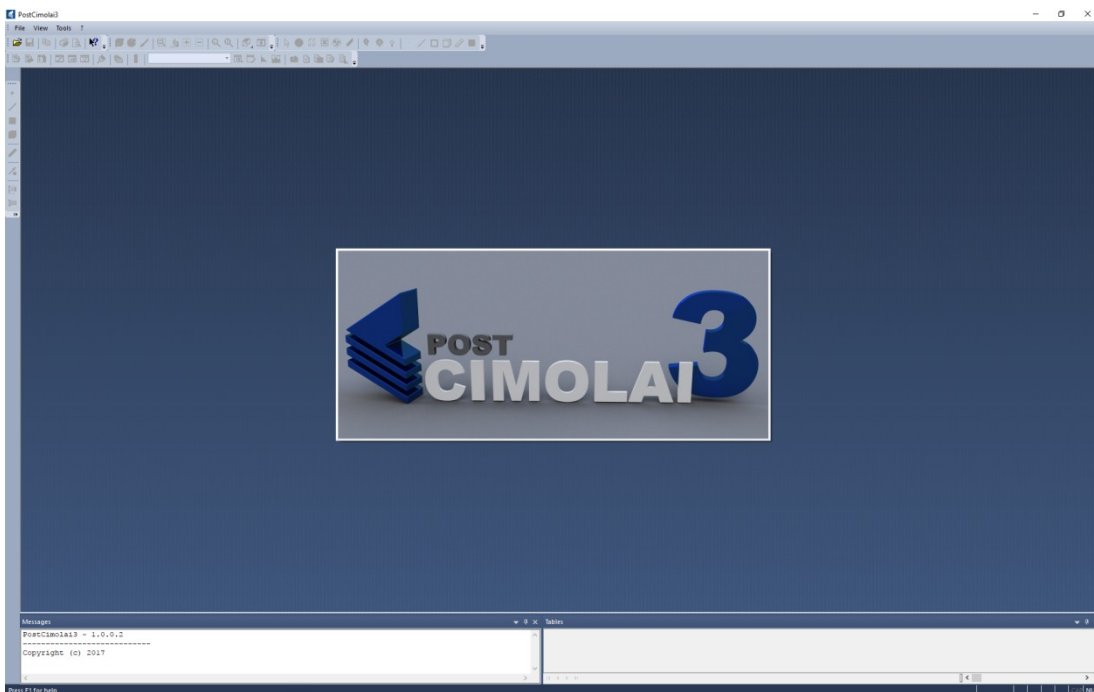


Figure 7.1. Start-up window.

### 7.2.1 Graphical user interface

PostFatigue graphical user interface (GUI) is composed of the following main components (Figure 7.2):

- The title bar, which indicates the start-up type and software version.



- The menu bar, which contains all available functions. It includes the following sub-menus: “File”, “Modify”, “View”, “Model”, “Attributes”, “Properties”, “Tools”, “Results”, “Window”, “?”.
- The viewport, which is the working area. Model and results are displayed here.
- The quick access menus, which permit a rapid access to many functions. They are placed by default under the menu bar and on the left of the viewport, but can be moved elsewhere if needed, by a simple drag and drop.
- The selection information bar, which displays the number of objects (nodes, beams, plates, check lines) currently selected.
- The message area, which displays the database, results file name and status messages.

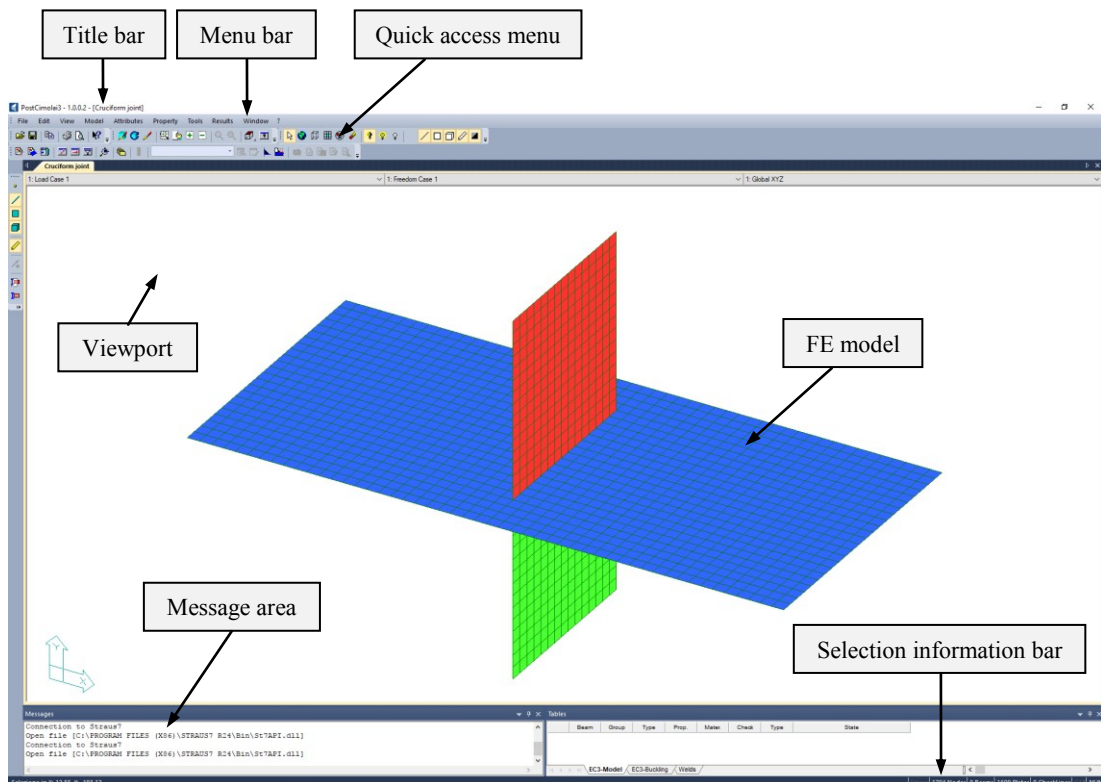


**Figure 7.2.** Graphical user interface.

The viewport provides the following options through mouse buttons:

- “Zoom in” and “zoom out” through the mouse scroll wheel.
- “Pan” by moving the cursor after pressing and holding the mouse scroll wheel.
- “Pan-zoom-rotate” through the dynamic view function named “Arcball”.

The right mouse button permits to open a menu, which gives quick access to various view options (among which the Arcball function).

Intentionally, the PostFatigue GUI is quite similar to the one of Straus7®. The purpose is to make PostFatigue user-friendly to a Straus7® user.

### 7.2.2 Workflow of fatigue assessment with PostFatigue

A fatigue strength assessment analysis through PostFatigue is characterized by the following steps:

- Mid surface geometry creation (Rhinoceros®, Spaceclaim®, ...)
- Model creation with a FE pre-processor (Straus7® environment):
  - Creation of a FE mesh
  - Definition of boundary conditions
  - Definition of load cases (different load cases are needed to define spectra load blocks in PostFatigue)
  - Definition of weld lines (the group of FE nodes identified by the intersection between shell elements having different properties automatically defines a weld line in PostFatigue)
- Running the FE analysis (Straus7® environment)
- Definition of the PostFatigue analysis (PostFatigue environment):
  - Automatic (or manual) identification of check lines
  - Definition of load spectra
- Running the PostFatigue analysis (PostFatigue environment):
  - Global screening of parent material and welds
  - Identification of critical regions
  - Detailed fatigue check (20 different checks all around a weld line)
- Report generation (PostFatigue environment)

### 7.2.3 Results cache management

Once opened the output results file of a Straus7® FE model, PostFatigue saves stress and strain information in its own cache file. If the PostFatigue session is saved, a following reopening of the model will produce the reloading of the cache file.

The option "update results" permits to clean the cache file (Figure 7.3). This option can be used to update the stress and strain information in PostFatigue whenever the Straus7® FE model is modified and re-solved.

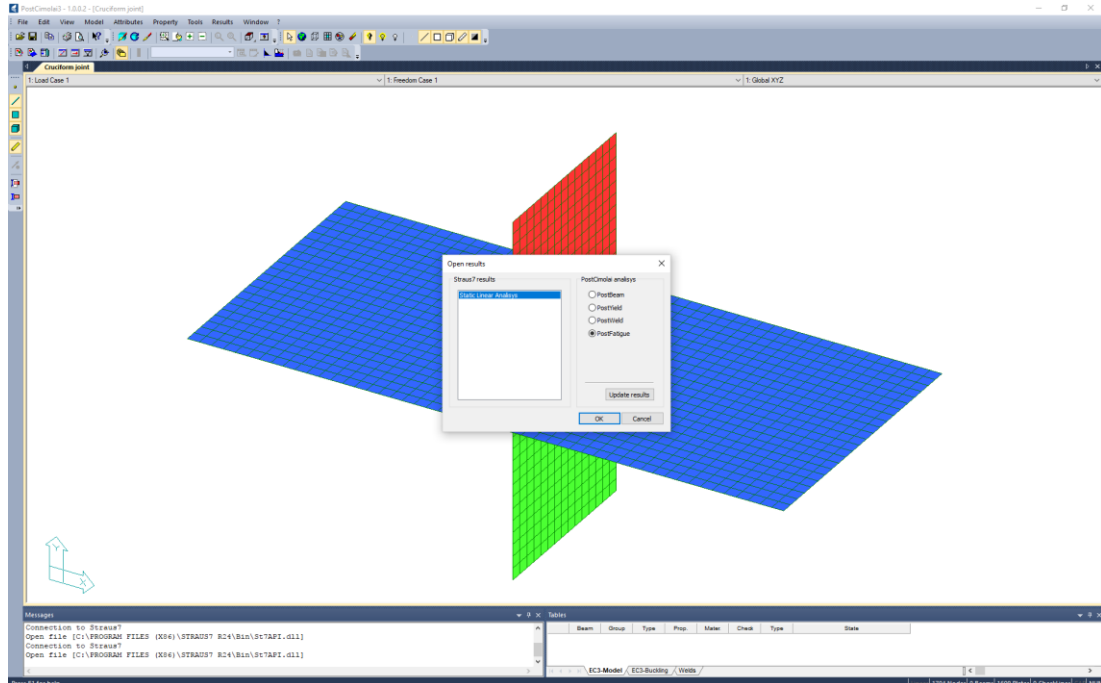


**Figure 7.3.** Management of Straus7® finite element results.

## 7.3 Model and load groups

Once opened the results from the “Results” sub-menu in the menu bar, it is possible to assign material properties to plates and to define fatigue load groups.

### 7.3.1 Material parameters

Material parameters are available in the sub-menu “Attribute” in the menu bar (Figure 7.4). It is possible to automatically assign to plates the same material properties adopted in the Straus7® FE model or other user-defined values. Material properties are available for consulting in an internal database named “Plate material catalogue” present in the sub-menu “Property” in the menu bar (Figure 7.5).

### 7.3.2 Fatigue load groups

In fatigue analyses, load groups definition is needed. This permits to PostFatigue to compute stress ranges (generally  $\Delta\sigma$  and  $\Delta\tau$ ) relevant for fatigue. Every load group is

characterized through a number of cycles (e.g. 100000 openings and closures of a gate in 10 years) and the related loading conditions (the same of the *load cases* in Straus7® environment). Every load group can be defined by one or more loading conditions as well as one or more loading combinations. The definition of fatigue load groups is available in the sub-menu “Model→Load cases→Fatigue load groups” in the menu bar (Figure 7.6).

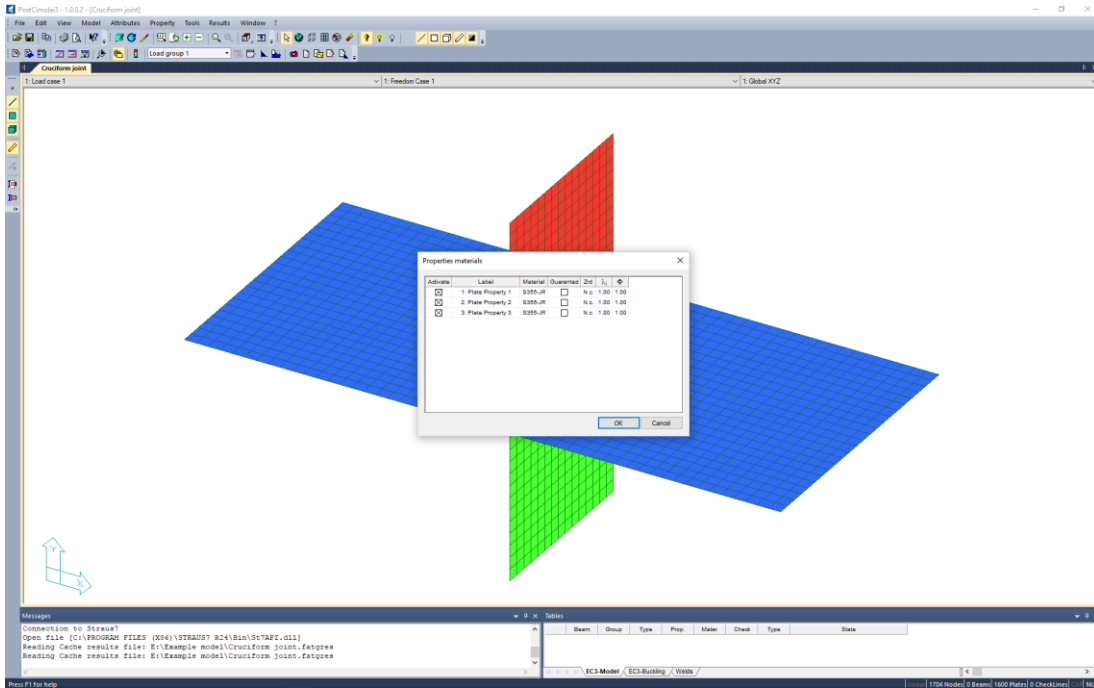


Figure 7.4. Material properties assignment dialog window.

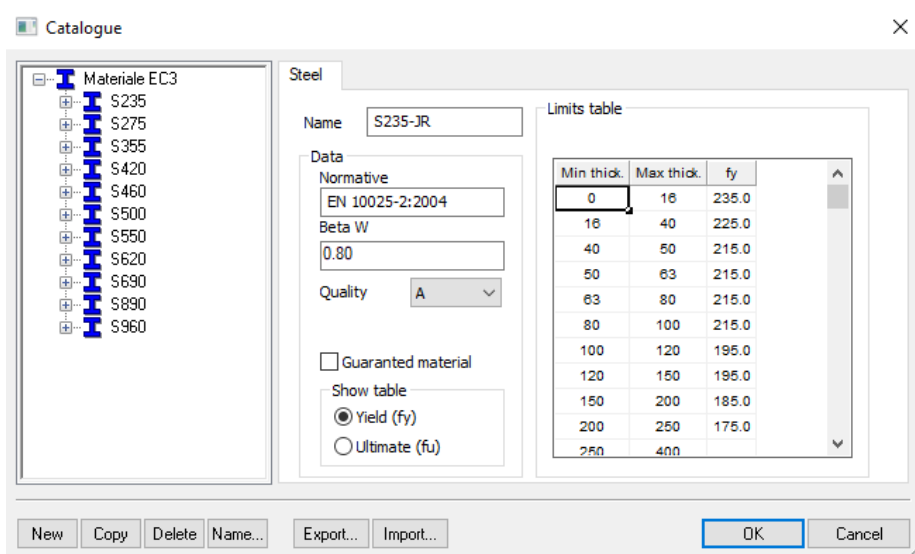
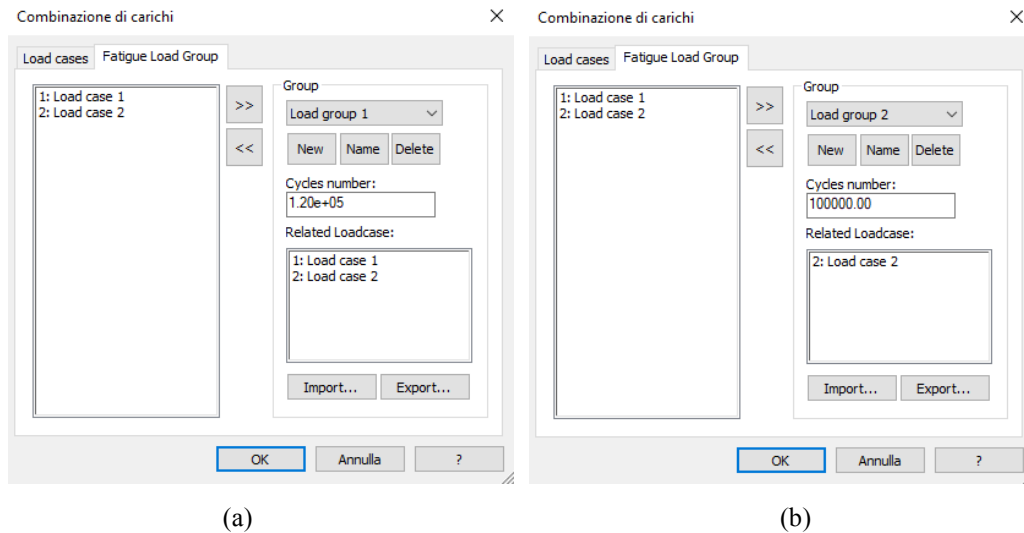


Figure 7.5. Catalogue of material properties.



**Figure 7.6.** Dialog windows for fatigue load groups and spectra definition.

Figure 7.6(a) shows that the load group 1 is characterized by a number of cycles equal to 120000 and by loading conditions “Load case 1” and “Load case 2”. In such case PostFatigue makes the vector difference of forces applied in the single load cases and computes the corresponding stress ranges. If more than two loading conditions are present in a single load group, PostFatigue finds the maximum stress ranges considering all the possible vector differences among load cases. Figure 7.6(b) shows that the load group 2 is characterized by a number of cycles equal to 100000 and by the only loading condition “Load case 2”. In such case, stresses induced by the loading condition “Load case 2” are considered by PostFatigue directly as stress ranges.

## 7.4 Normative reference

PostFatigue analysis is primarily based on EN 1993-1-9 (Eurocode 3) standard. In detail, fatigue checks implemented in PostFatigue are those related to section 8 and annex A of EN 1993-1-9. Therefore, before performing any fatigue analysis in PostFatigue, some normative parameters have to be set (Figure 7.7). Such parameters deal with safety factors to be applied both on loads and on resistance ( $\gamma_{Ff}$  and  $\gamma_{Mf}$ , respectively), according to EN 1993-1-9. Safety factors  $\gamma_{Ff}$  and  $\gamma_{Mf}$  are applied through the sub-menu “Model→Eurocode parameters” in the menu bar.

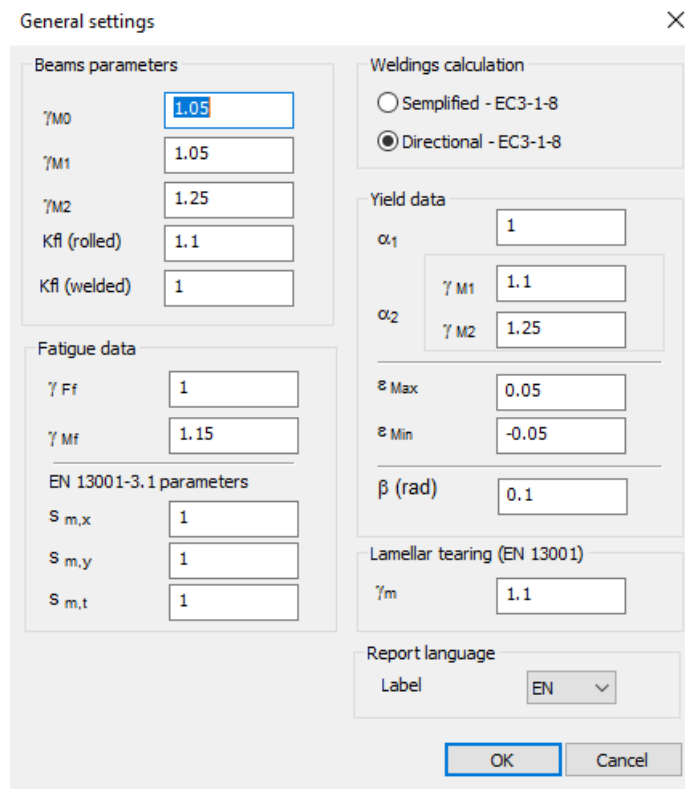


Figure 7.7. Dialog window for normative parameters definition.

## 7.5 Fatigue assessment of parent material

To perform the fatigue analysis in PostFatigue, nominal stress reference details have to be assigned. All reference details reported in table 8.1 of EN 1993-1-9 and the corresponding fatigue classes are implemented in PostFatigue database. Such details, as well as the related fatigue checks, can be assigned to the parent material.

### 7.5.1 Fatigue details

Parent material reference details can be assigned both directly, by selecting plates of interest, and by using the properties defined in the Straus7® FE model.

In the first case the reference sub-menu is “Attributes→Plates→Base material details” in the menu bar (Figure 7.8). Both reference details for normal stresses (Figure 7.9(a)) and for shear stresses (Figure 7.9(b)) can be considered.

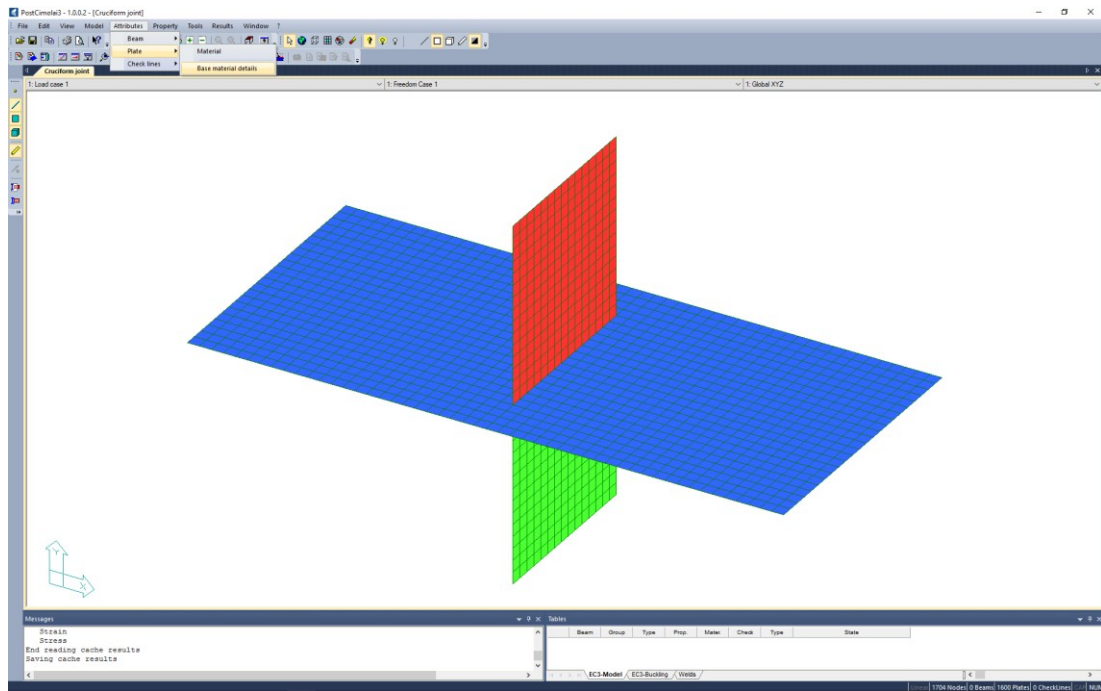


**Figure 7.8.** Menu path for assignation of base material fatigue endurable classes.

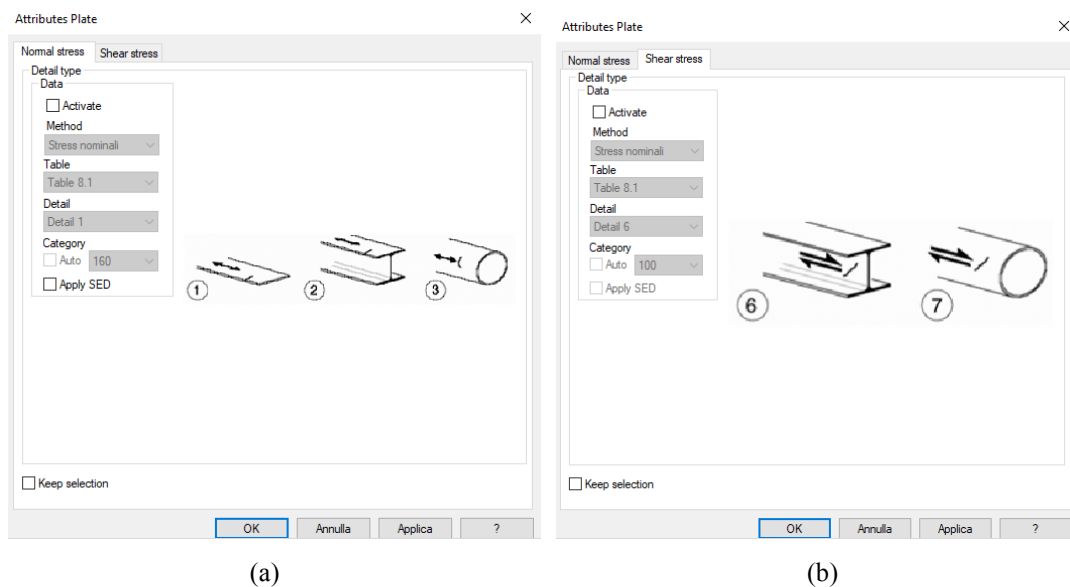


**Figure 7.9.** Dialog windows for assignation of base material endurable classes, in the presence of normal stresses (a) and shear stresses (b).

In the second and faster way, it is possible to assign a specific parent material reference detail to every different plate property defined in the Straus7® FE model. The reference sub-menu is “Tools→Assign fatigue details for plates” in the menu bar (Figure 7.10). Another useful tool is the automatic finding of plates' free edges and assignation of the corresponding reference detail. The sub-menu is “Tools→Assign

border details for plates” in the menu bar (Figure 7.11). Also in this case, both reference details for normal stresses and for shear stresses are available.

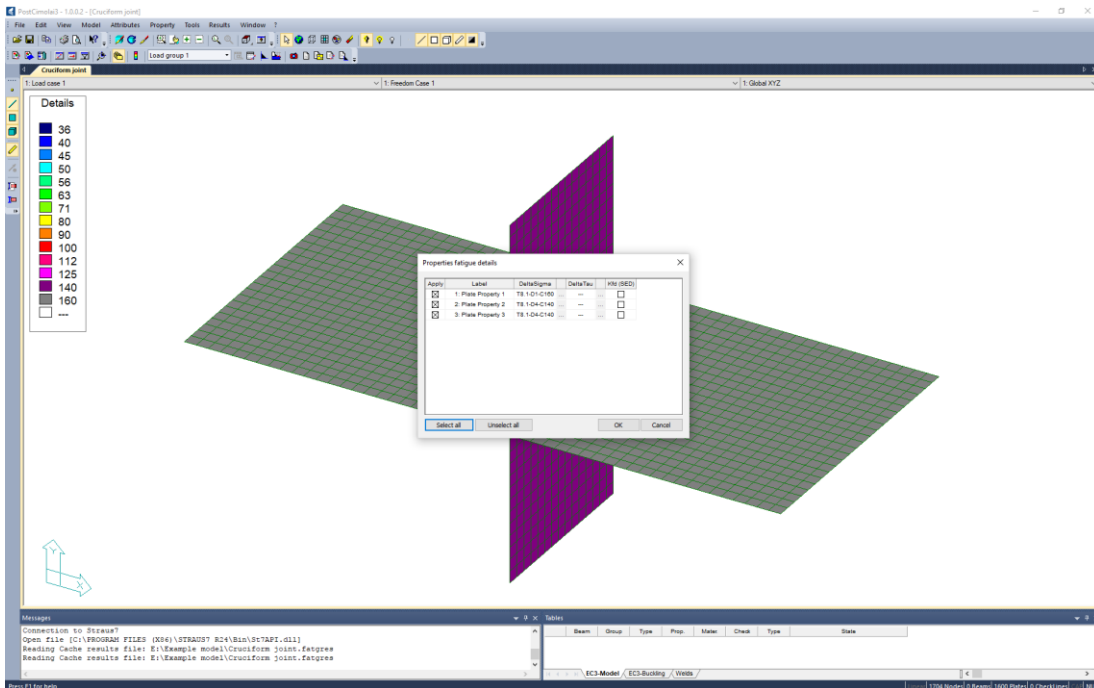


**Figure 7.10.** Dialog window for automatic fatigue class assignation to every different plate property defined in Straus7® model.

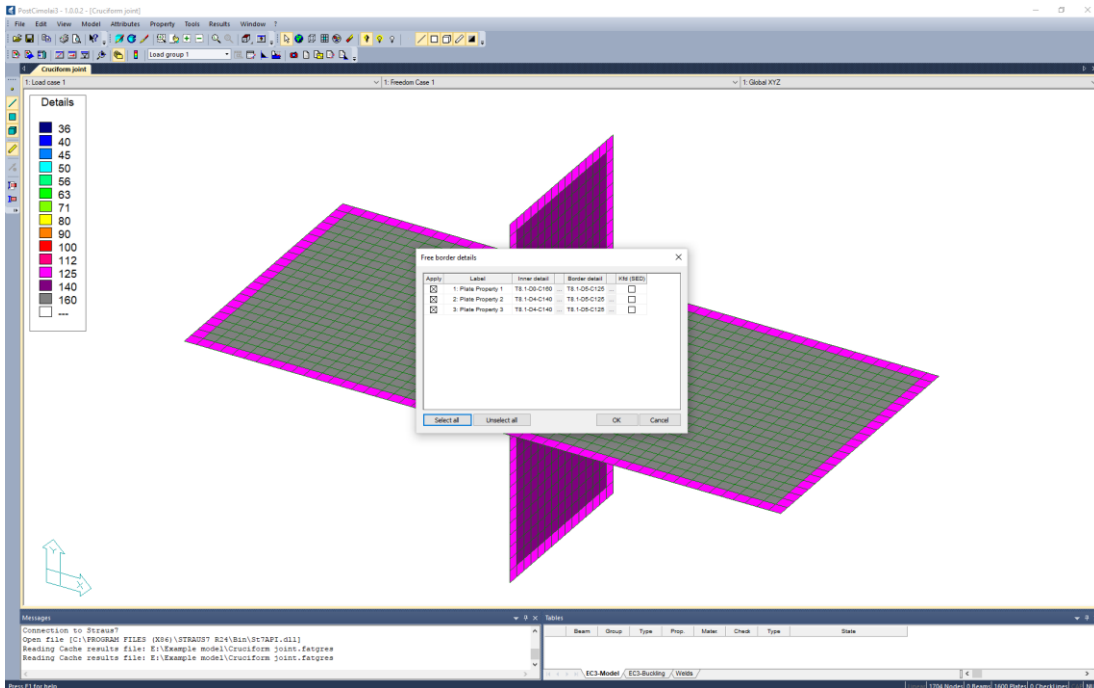


**Figure 7.11.** Dialog window for automatic fatigue class assignation to free edges.



### 7.5.2 Graphical output of stresses and parent material details

After assigning the reference fatigue details, it is possible to plot, as colored maps (contours), both the acting stress ranges for each load group and the reference details assigned to the parent material, distinguishing among normal stress based details and shear stress based details.

The reference load group to plot the acting stress ranges can be activated through “Results→Fatigue check→Current fatigue group” (Figure 7.12).

Acting stress ranges ( $\Delta\sigma$  and  $\Delta\tau$ ) can be plotted through “Results→Fatigue check→Stress” (Figure 7.13(a-d)).

Assigned details can be plotted through “Results→Fatigue check→Detail maps” (Figure 7.14).

### 7.5.3 Analysis options

Before performing the fatigue check of the parent material, some options dealing with the kind of stress components to be used in the analysis have to be set. The reference sub-menu is “Results→Fatigue check→Fatigue check options” in the menu bar (Figure 7.15).

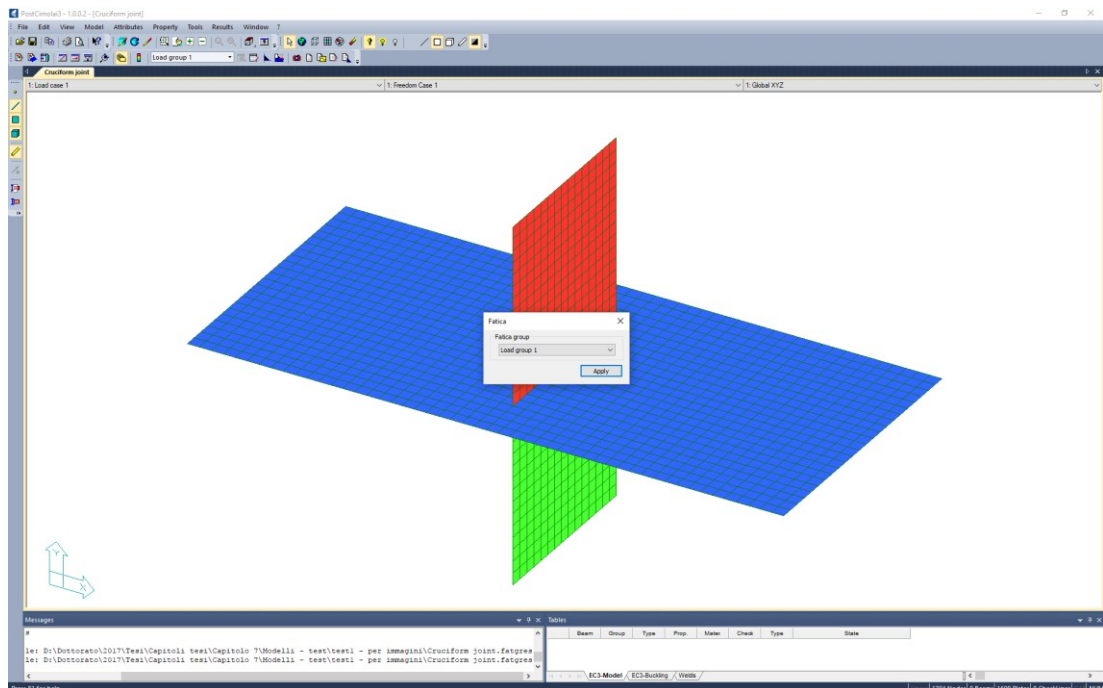


**Figure 7.12.** Dialog window to choose the desired fatigue load group for parent material fatigue assessment.

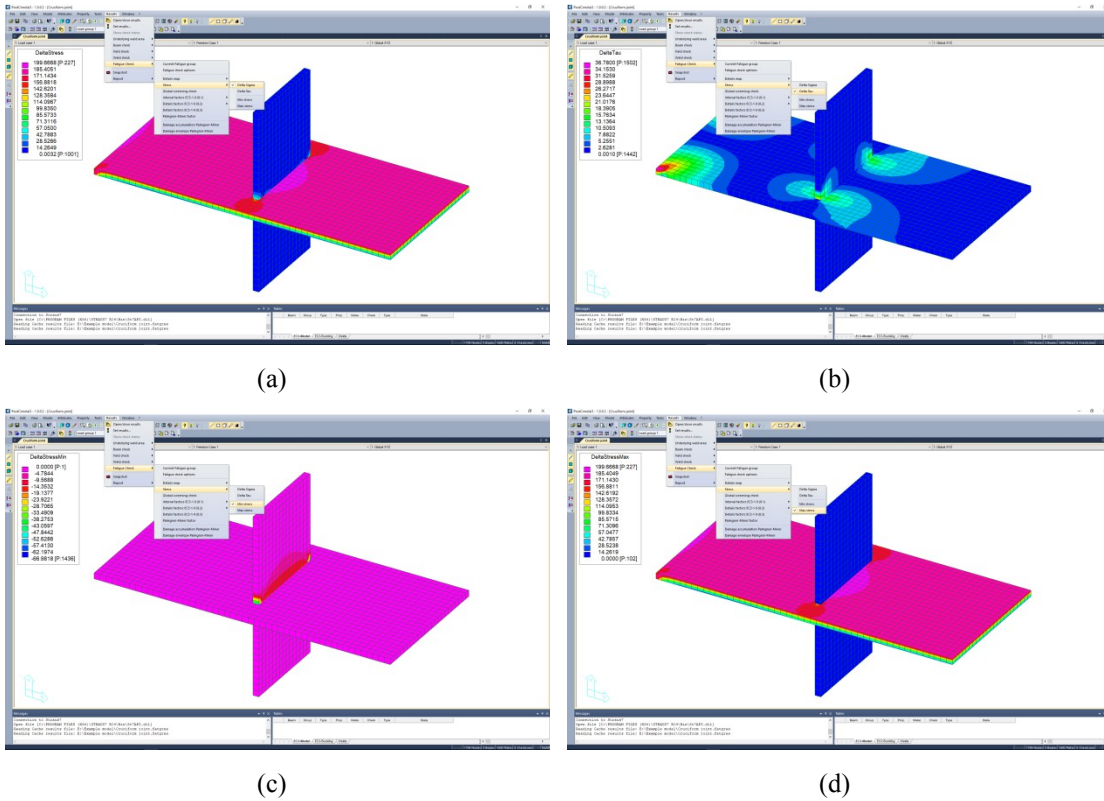


Figure 7.13. Menu paths and graphical outputs of base material stresses related to a specific fatigue load group:  $\Delta\sigma$  (a);  $\Delta\tau$  (b); minimum  $\Delta\sigma$  (c); maximum  $\Delta\sigma$  (d).

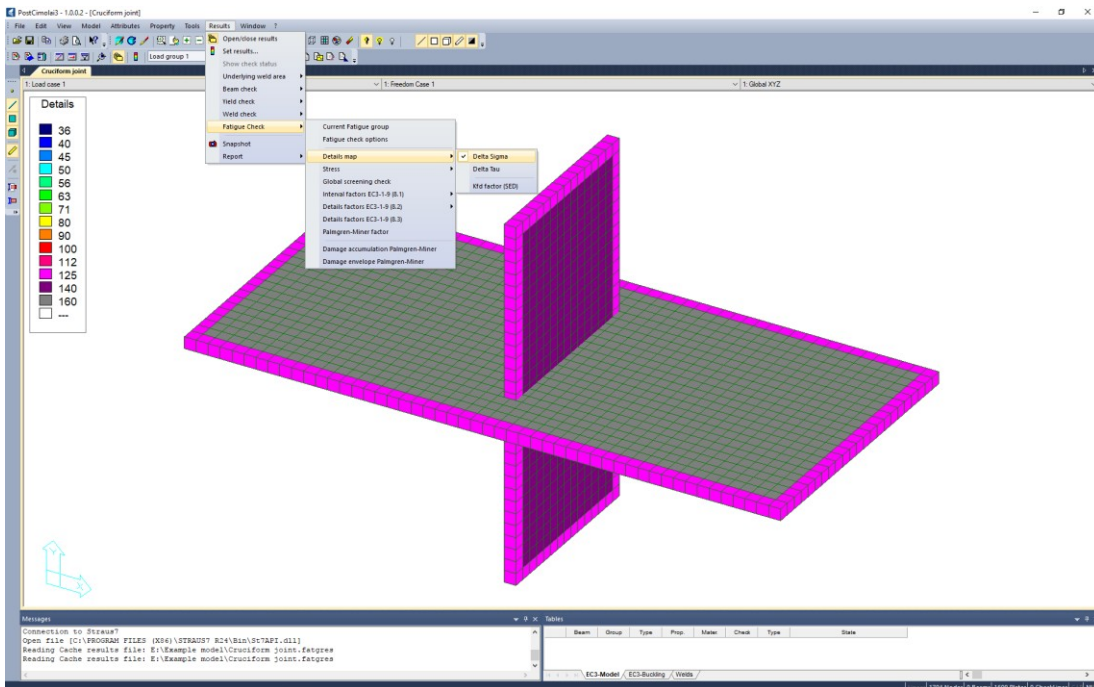
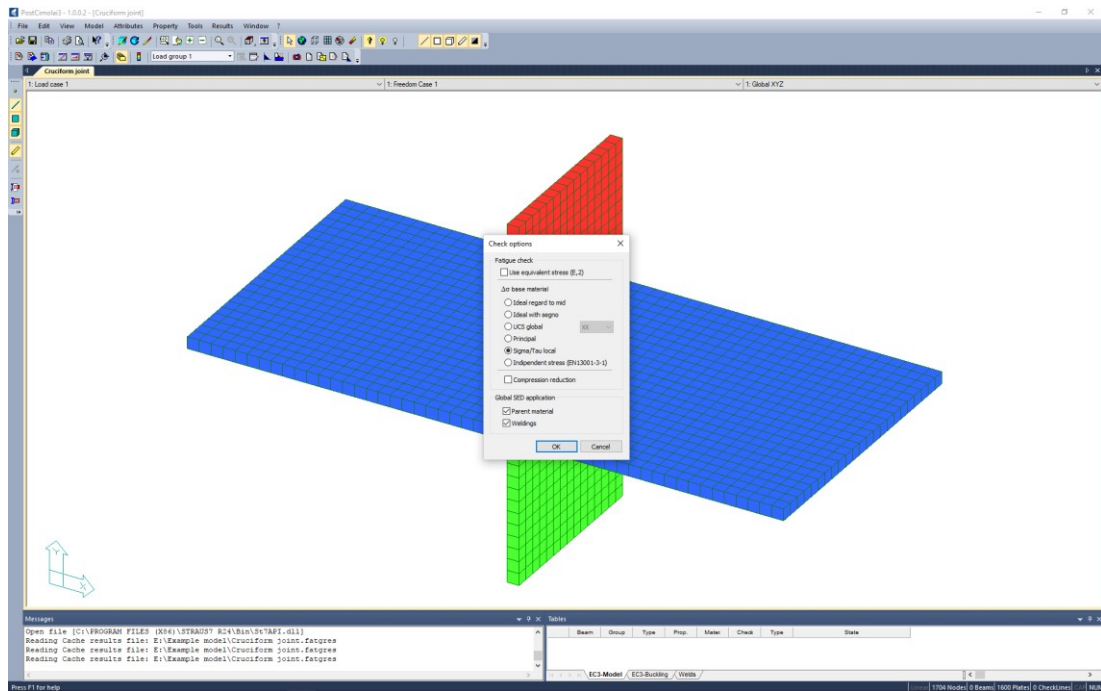


Figure 7.14. Menu path and graphical output of fatigue classes assigned to parent material and free edges.



**Figure 7.15.** Dialog window to assign fatigue assessment options.

By default, PostFatigue transforms endurable stresses (fatigue classes) defined at 2 million cycles in endurable stresses at the number of acting cycles defined through the fatigue load group. Dually, it is possible to transform stresses acting for a specified number of cycles in stresses at 2 million cycles, before performing the analysis. Furthermore, in this sheet it is possible to specify which kind of stresses have to be used in the parent material check. The following choices are available:

- Ideal regard to mid: von Mises stress ranges with reference to the mid value;
- Ideal with sign: von Mises (with the sign of the principal stress) of stress ranges with reference to the mid value;
- UCS global: stress ranges in a specified direction of the global frame of reference;
- Principal: principal stress ranges;
- Sigma/Tau local: normal and shear stress ranges in the local frame of reference (default in PostFatigue);
- Independent stresses: formulation provided in section 6.5.4 of EN 13001-3-1.

### 7.5.4 Fatigue check

The fatigue check of the parent material is performed with a graphical output (contour) in the viewport of PostFatigue. Fatigue checks available in PostFatigue are those established by section 8 and annex A of EN 1993-1-9. In detail, such checks are designed with 8.1, 8.2, 8.3 and A.2 in EN 1993-1-9. The same nomenclature has been adopted in PostFatigue (Figure 7.16(a-f)).

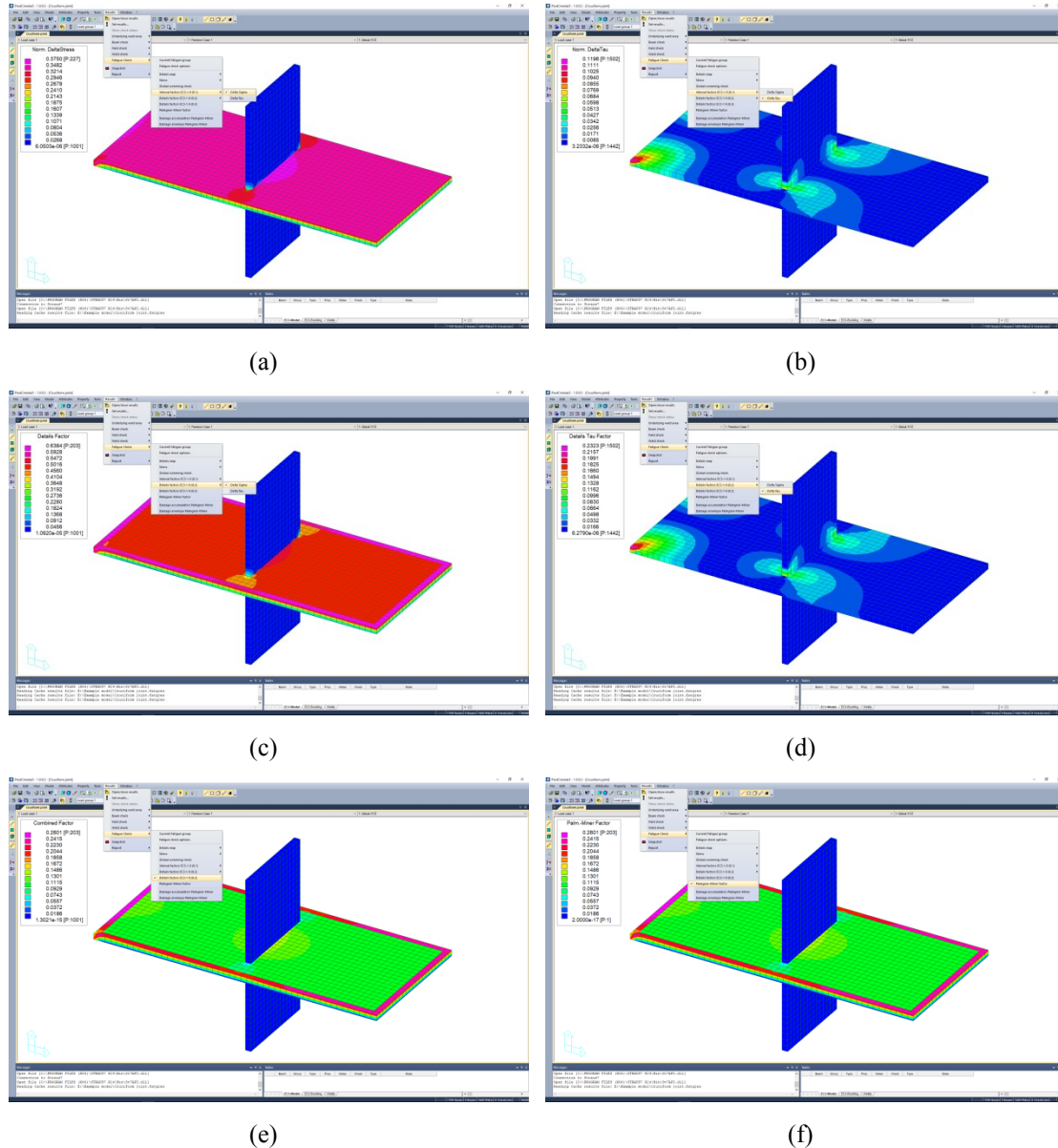


**Figure 7.16.** Menu paths and graphical outputs of parent material fatigue assessments according to EN 1993-1-9:  $\Delta\sigma$  check type 8.1 (a);  $\Delta\tau$  check type 8.1 (b);  $\Delta\sigma$  check type 8.2 (c);  $\Delta\tau$  check type 8.2 (d); combined check type 8.3 (e); damage summation (f).

## 7.6 Fatigue assessment of check lines

To perform the fatigue analysis in PostFatigue, nominal stress or hot spot stress reference details have to be assigned to any particular feature (e.g. holes, welds and so on). All reference details reported in tables 8.2 to 8.10 of EN 1993-1-9 and the corresponding fatigue classes are implemented in PostFatigue database.

### 7.6.1 Fatigue details

To perform the fatigue assessment of particular features (e.g. holes, welds and so on), the element “Check line” has been introduced in PostFatigue. To build a check line, a straight segment, having ends on two distinct nodes of the model, should be created through dedicated tools. PostFatigue then automatically recognizes stresses acting on shell elements where the segment has been drawn and performs the fatigue check.

Check lines can be created manually or automatically. The manual approach can be used to draw check lines where it is expected that a particular feature is present (e.g. a set of holes due to a bolted connection).

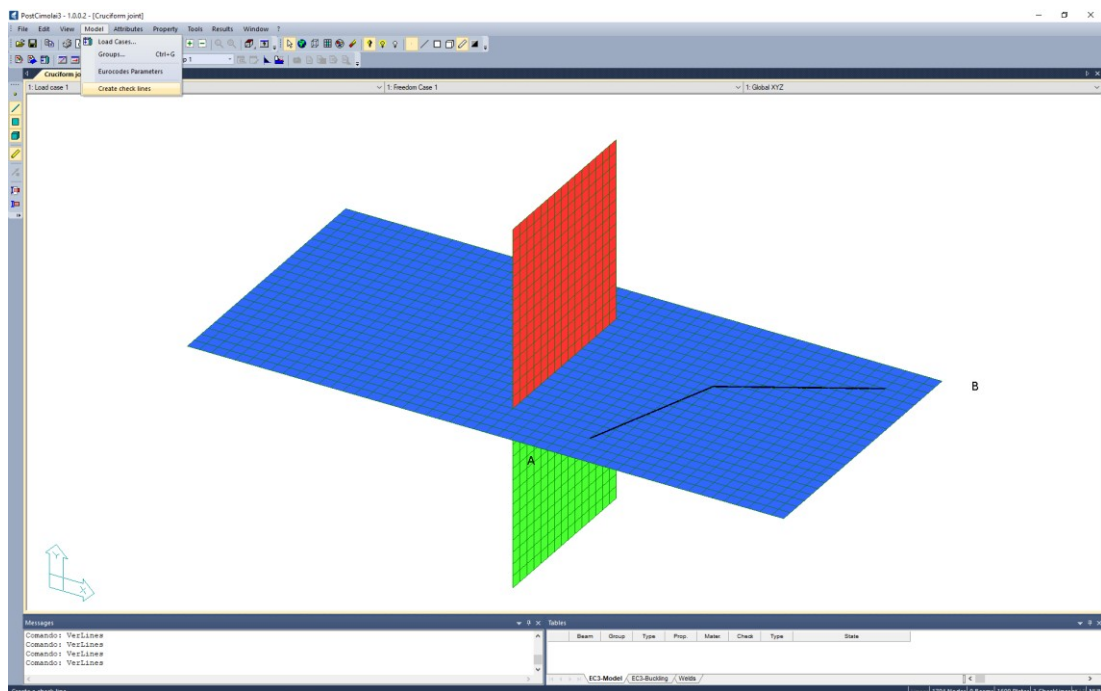


**Figure 7.17.** Menu path for manual creation of check lines and example of check line A-B.

The sub-menu to manually generate check lines is “Model→Create check lines” in the menu bar (Figure 7.17). The manual creation of check lines is particularly useful



to perform the fatigue assessment of a feature which is not explicitly modeled in Straus7®. It is the case, for example, of the fatigue check of a plate in the presence of holes which are not represented in the FE analysis.

The automatic approach can be used to find all at once the check lines represented by weld lines. The sub-menu to automatically find check lines is “Tools→Find check lines” in the menu bar (Figure 7.18).

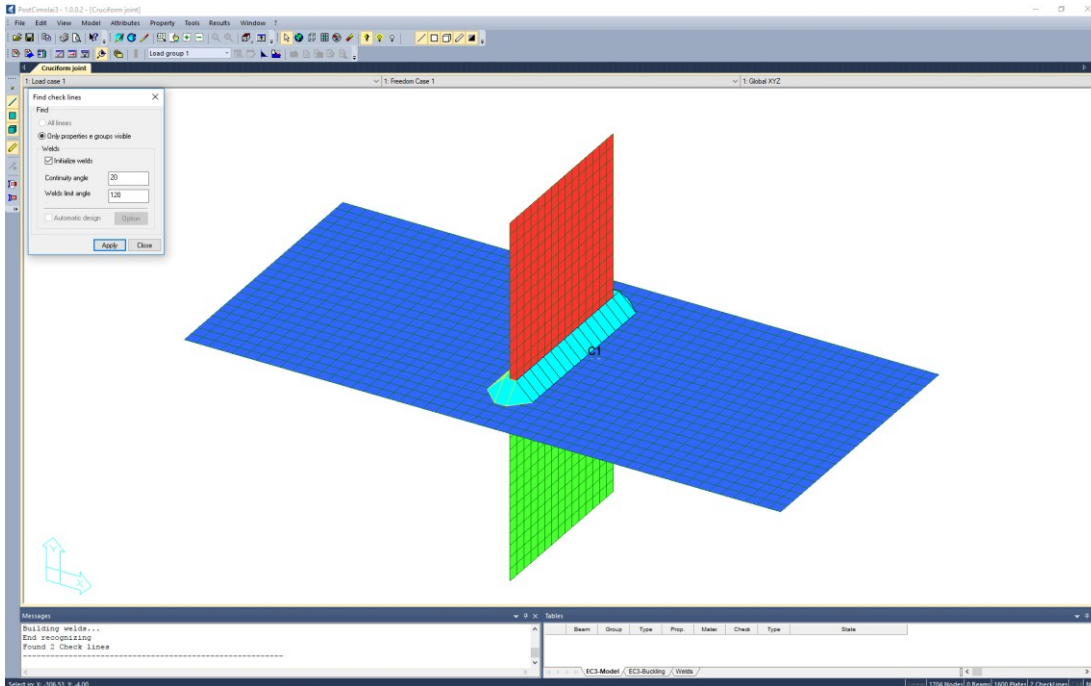


**Figure 7.18.** Dialog window for automatic finding of check lines represented by welds.

This tool works on the assumption that a group of FE nodes identified in Straus7® by the intersection between shell elements having different properties defines a weld line. Therefore, care must be taken in building the FE model in Straus7® environment, because PostFatigue automatically recognizes a weld line only in the presence of an intersection between plates having different properties.

The sub-menu “Tools→Split check lines” in the menu bar permits to split a check line into two or more parts. Such tool is useful whenever a check line is characterized by a change of reference detail along his length. It is the case, for example, of a weld whose bevel changes along the length of the weld itself. Once a check line is created, it is possible to assign the related reference details according to EN 1993-1-9. This operation can be performed manually or automatically. According to the manual

approach, one or more reference details can be chosen by the user and assigned to a check line. The sub-menu to manually assign a reference detail is “Attributes→Check lines→Fatigue details” in the menu bar (Figure 7.19).

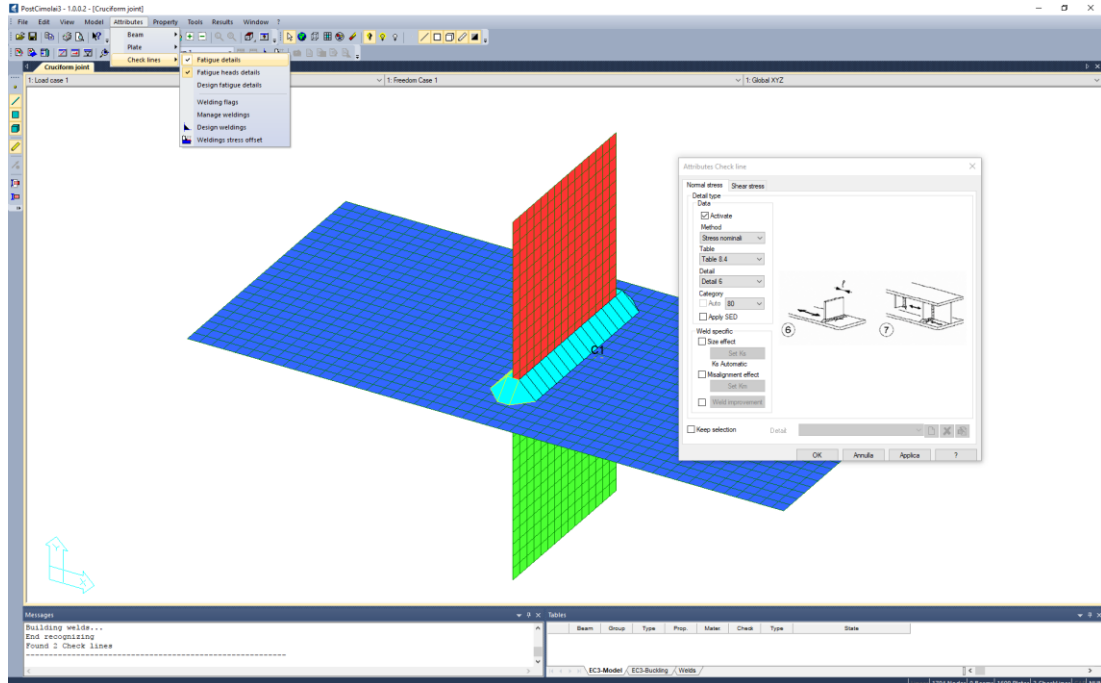


Figure 7.19. Menu path and dialog window for assignation of weld fatigue classes.

As for the parent material, both reference details for normal stresses (Figure 7.20(a)) and for shear stresses (Figure 7.20(b)) can be considered.

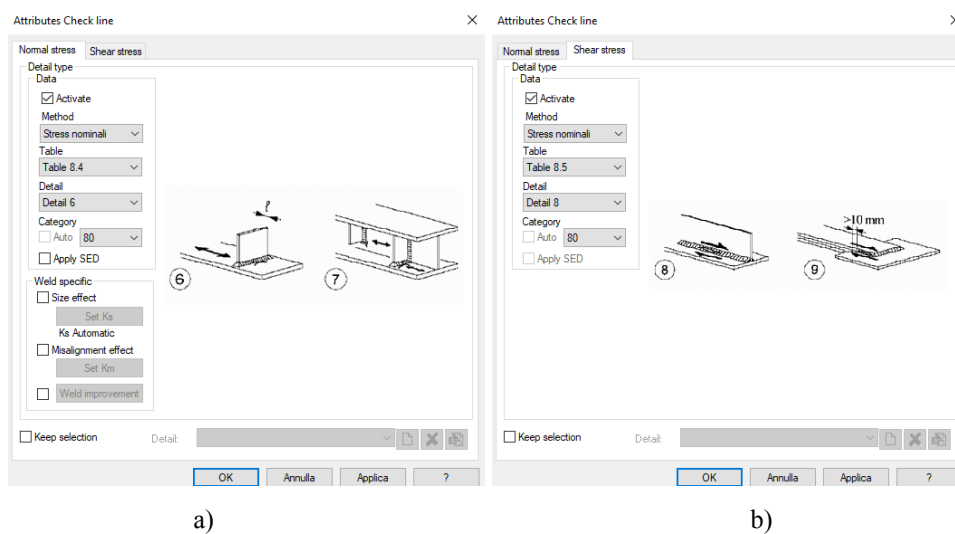
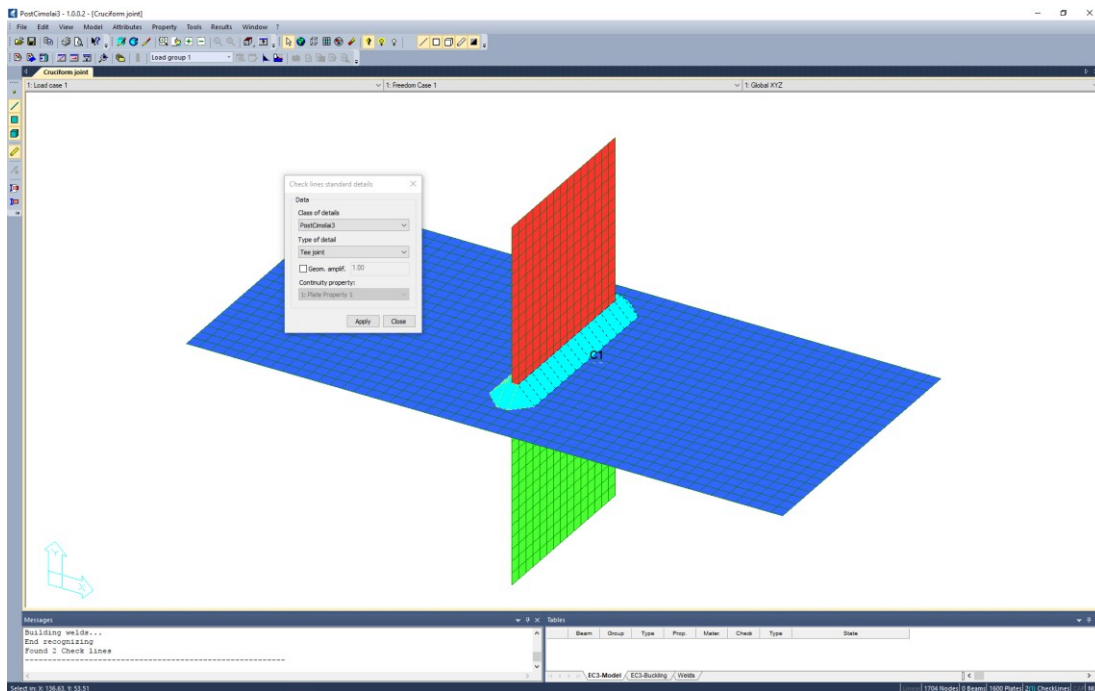


Figure 7.20. Dialog windows for assignation of weld endurable classes, in the presence of normal stresses (a) and shear stresses (b).

The automatic approach permits to assign to one or more welded junctions the related reference details all at once, according to EN 1993-1-9. It is the case, for example, of a stiffener (which can be generally considered a tee or a cruciform joint). The sub-menu to automatically assign a type of junction and the related standard details is “Tools→Assign standard details” in the menu bar (Figure 7.21).



**Figure 7.21.** Dialog window for automatic assignation of standard details as a function of the type of junction.

Through this tool, it is also possible to specify which property defines the continuous plate (if different from the default proposed value) and the geometrical amplification factor, which is described as the ratio of the summation of the weld throats over the thickness of the attached plate. The geometrical amplification factor is not needed if the weld geometry is defined through the dedicated design tool (see Section 7.6.2). Being this the case, such factor is automatically computed.

In PostFatigue three types of junctions and the related reference details are considered: tee joints, which include cruciform joints (Figures 7.22 and 7.23); corner joints (Figures 7.24 and 7.25); butt joints (Figures 7.26 and 7.27). The three mentioned joints include all most commonly used joints in the industrial context.



POINT	CHECK	DETAIL (EN 1993-1-9)
a1	throat	tab. 8.5 - det.3
a2	throat	tab. 8.5 - det.8
b	toe	tab. 8.5 - det.1
c / e	built up	tab. 8.2 - det.1-7
d	attachments	tab. 8.4 - det.6;8
f1	attachments (all around weld)	tab. 8.4 - det.1-3
f2	attachments (interrupted weld)	tab. 8.2 - det.8
g1/g2	attachments	tab. 8.4 - det.7 (stiffener) / tab. 8.9 - det.2 (stringer)
h	open stringers	tab. 8.9 - det.1

Total number of checks 10+10=20

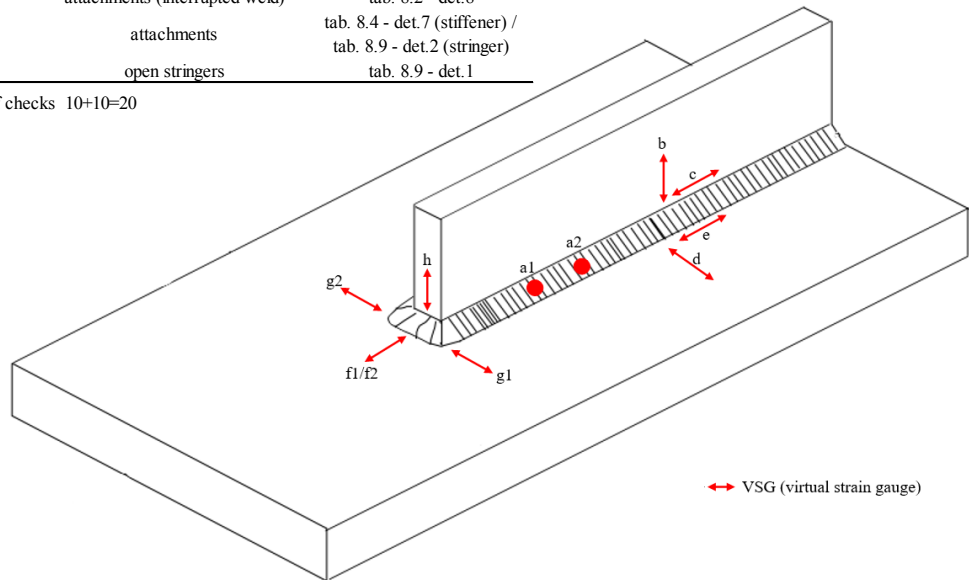


**Figure 7.22.** Standard details for double fillet and partial penetration welded tee and cruciform joints. 20 checks all around a weld are identified, according to EN 1993-1-9.

POINT	CHECK	DETAIL (EN 1993-1-9)
b (with NDT)	top flange to web junction	tab. 8.10 - det.2
b (without NDT)	top flange to web junction	tab. 8.10 - det.3
c / e	built up	tab. 8.2 - det.1-7
d	attachments	tab. 8.4 - det.6;8
f1	attachments (all around weld)	tab. 8.4 - det.1-3
f2	attachments (interrupted weld)	tab. 8.2 - det.8
g1/g2	attachments	tab. 8.4 - det.7 (stiffener) / tab. 8.9 - det.2 (stringer)
h	open stringers	tab. 8.9 - det.1

Total number of checks 8+8=16

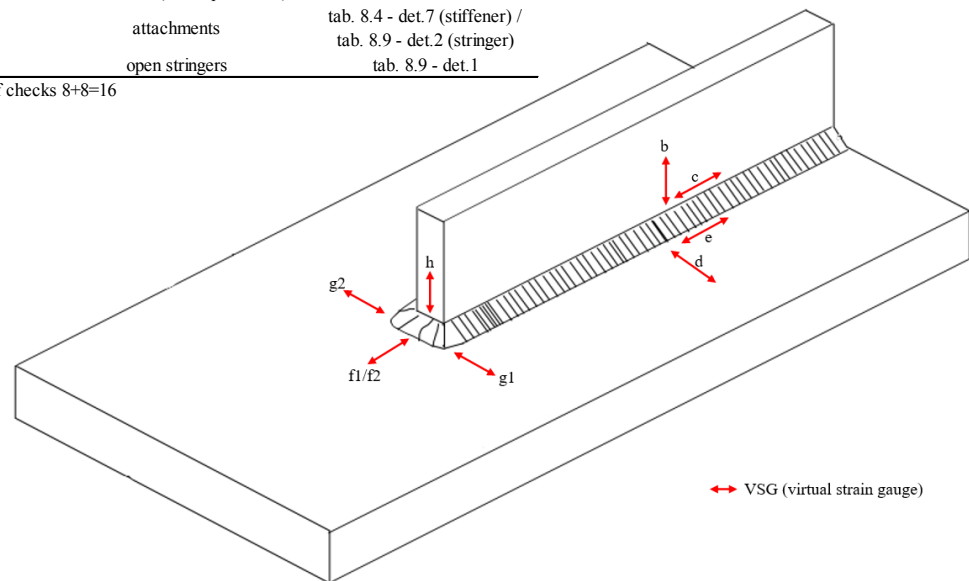


**Figure 7.23.** Standard details for full penetration welded tee and cruciform joints. 16 checks all around a weld are identified, according to EN 1993-1-9.

POINT	CHECK	DETAIL (EN 1993-1-9)
a1	throat	tab. 8.5 - det.3
a2	throat	tab. 8.5 - det.8
b	toe	tab. 8.5 - det.1
c / e	built up	tab. 8.2 - det.1-7
d	attachments	tab. 8.4 - det.6;8
f1	attachments (all around weld)	tab. 8.4 - det.1-3
f2	attachments (interrupted weld)	tab. 8.2 - det.8
g	attachments	tab. 8.4 - det.7 (stiffener) / tab. 8.9 - det.2 (stringer)
h	open stringers	tab. 8.9 - det.1

Total number of checks 7+9=16

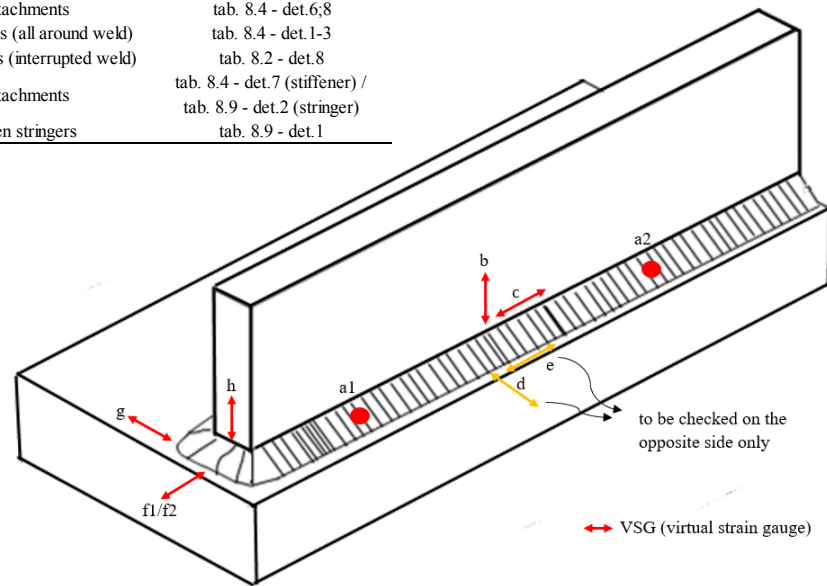


**Figure 7.24.** Standard details for double fillet and partial penetration welded corner joints.

16 checks all around a weld are identified, according to EN 1993-1-9.

POINT	CHECK	DETAIL (EN 1993-1-9)
b (with NDT)	top flange to web junction	tab. 8.10 - det.2
b (without NDT)	top flange to web junction	tab. 8.10 - det.3
c / e	built up	tab. 8.2 - det.1-7
d	attachments	tab. 8.4 - det.6;8
f1	attachments (all around weld)	tab. 8.4 - det.1-3
f2	attachments (interrupted weld)	tab. 8.2 - det.8
g	attachments	tab. 8.4 - det.7 (stiffener) / tab. 8.9 - det.2 (stringer)
h	open stringers	tab. 8.9 - det.1

Total number of checks 5+7=12

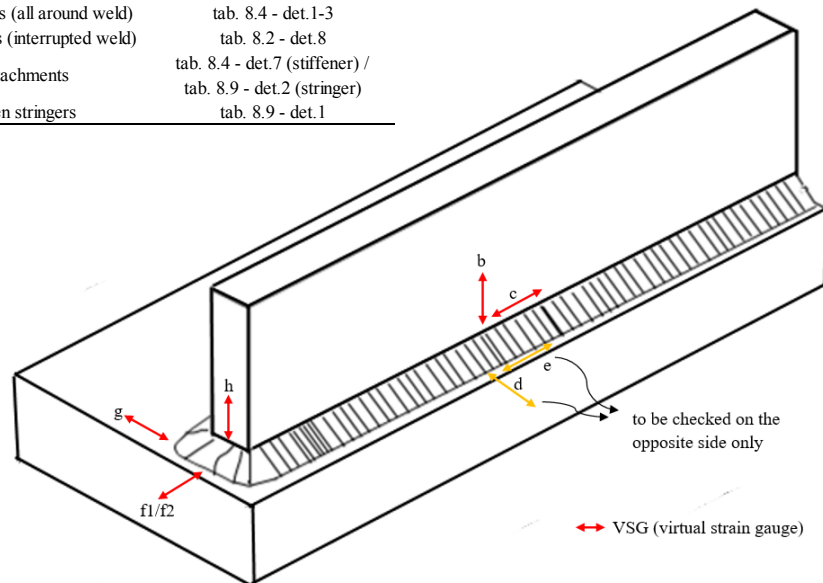


**Figure 7.25.** Standard details for full penetration welded corner joints. 12 checks all around

a weld are identified, according to EN 1993-1-9.

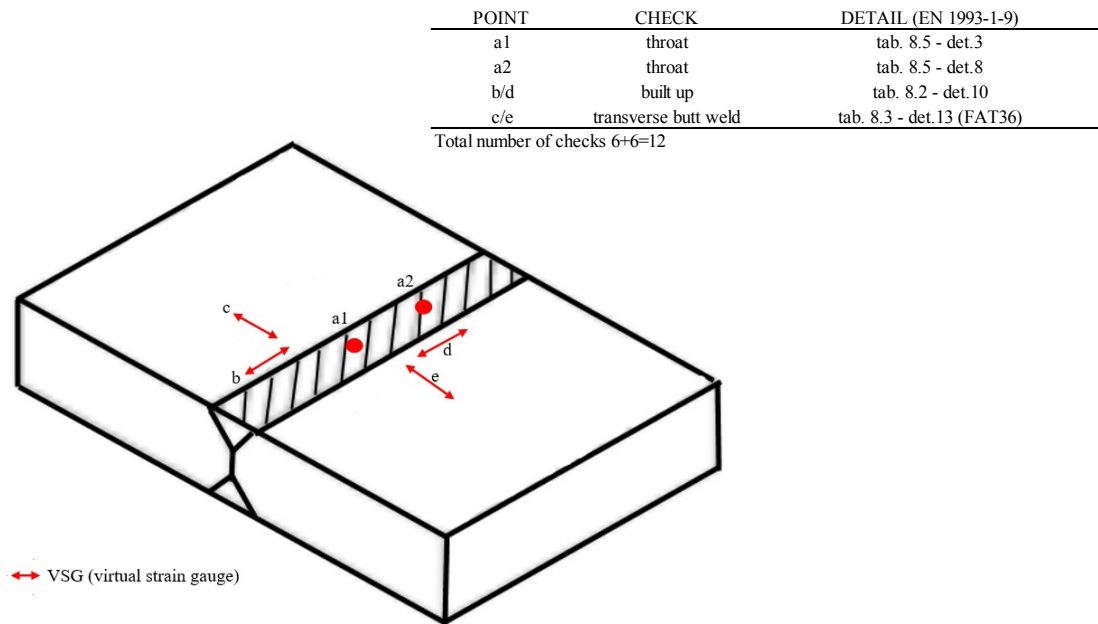


**Figure 7.26.** Standard details for partial penetration welded butt joints. 12 checks along a weld are identified, according to EN 1993-1-9.

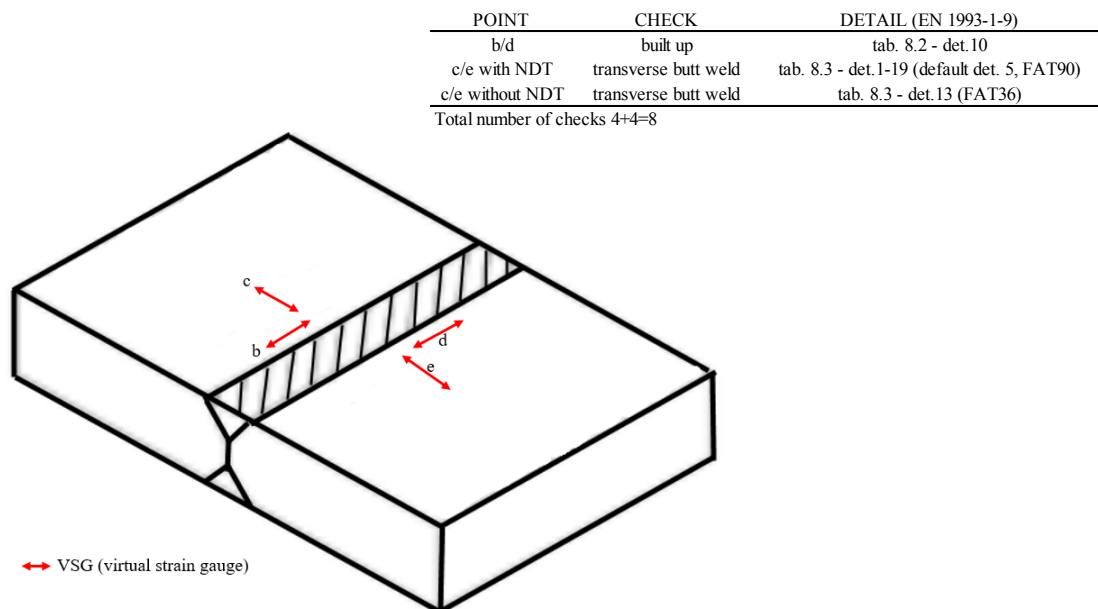


**Figure 7.27.** Standard details for full penetration welded butt joints. 8 checks along a weld are identified, according to EN 1993-1-9.

For every assigned type of joint, a series of fatigue checks is planned. Being the case of a tee junction, the number of planned fatigue checks (named a÷g) is 20 all around the weld line (Figure 7.22). For each one of these checks PostFatigue automatically assigns the reference detail according to EN 1993-1-9. Assigned details can be viewed in the window “Attribute→Check lines→Fatigue details” (Figure 7.28).

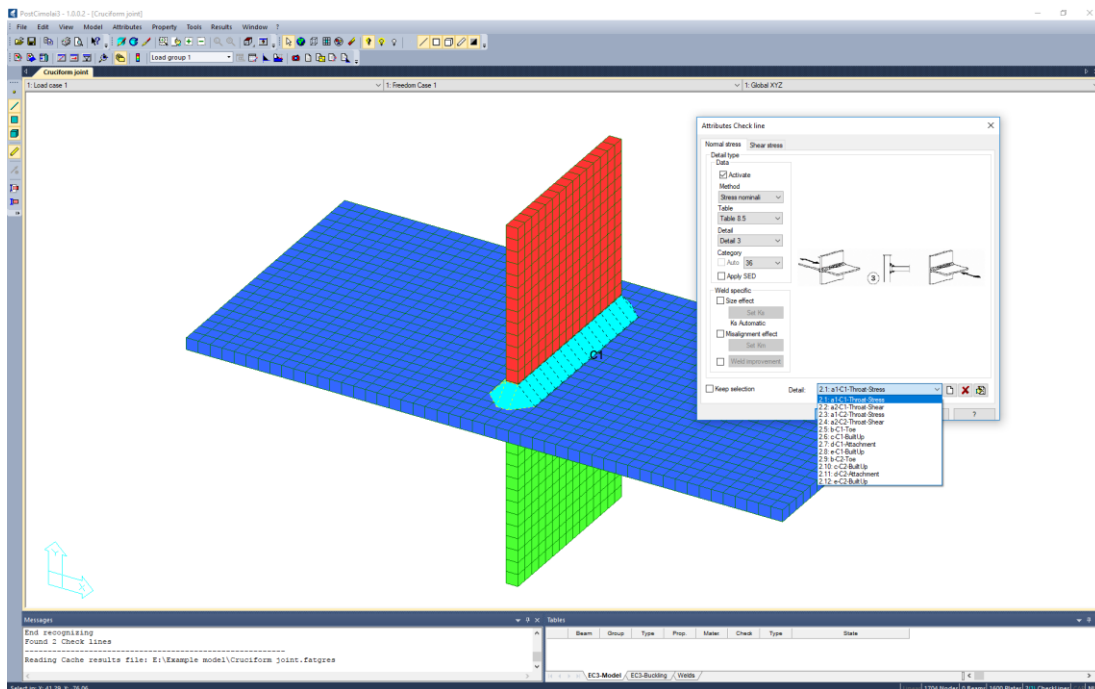


Figure 7.28. Dialog window to manage automatically assigned standard details.

Each planned check is identified by a standard name, e.g. “1-1-a-Throat stress”, in which the first number identifies the check line number 1, the second number (ranging from 1 to 10 in the case of the tee joint) states that the first check is being performed on the check line, the small letter “a” refers to the assigned type of joint and indicates the check area (e.g. the weld throat, the weld toe and so on) and the orientation of the considered stresses. Finally, the term “Throat stress” is a brief description to clarify which kind of check is being performed.

PostFatigue recovers stresses properly oriented on plates with respect to the weld line (e.g. normal or parallel to the weld bead), depending on the reference details.

If the weld geometry is defined through the dedicated design tool (see Section 7.6.2), reference details, which are dependent on the weld geometry (for example the one shown in Figure 7.20), are automatically assigned.

### 7.6.2 Weld geometry design tool

A dedicated tool to rapidly define weld geometries is available in PostFatigue. The related sub-menu is “Attributes→Check lines→Design weldings” in the menu bar (Figures 7.29 and 7.30). It is the same tool used in PostWeld, which is the module of PostCimolai® suite dedicated to perform static resistance analyses of welds according to EN 1993-1-8 [19].

The weld design dialog window permits to choose among fillet welds and custom welds (e.g. partial and full penetration welds). It is possible to change the weld throat dimension, as well as, being the case of partial and full penetration welds, the bevel shape. Symmetric and non-symmetric welds can be managed. It is also possible to decide whether there is a weld ending, which characterizes an all around weld, or not, that is an interrupted weld. If the weld ending is present, the weld throat dimension has to be specified, which, in principle, can be different from the one used on the longitudinal side.

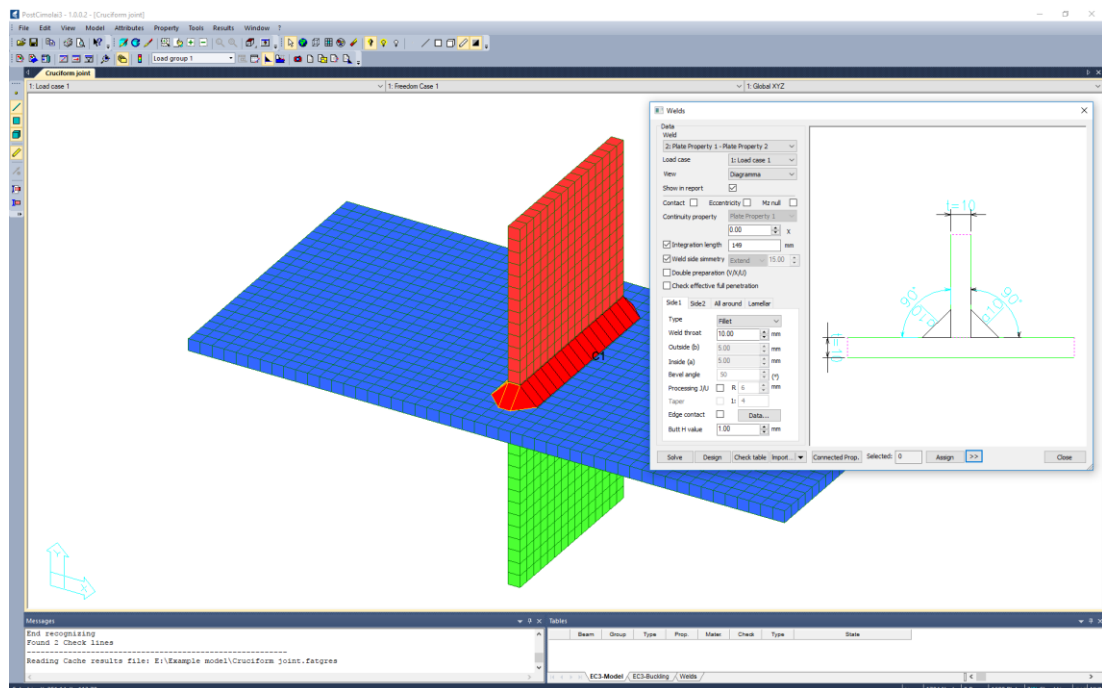
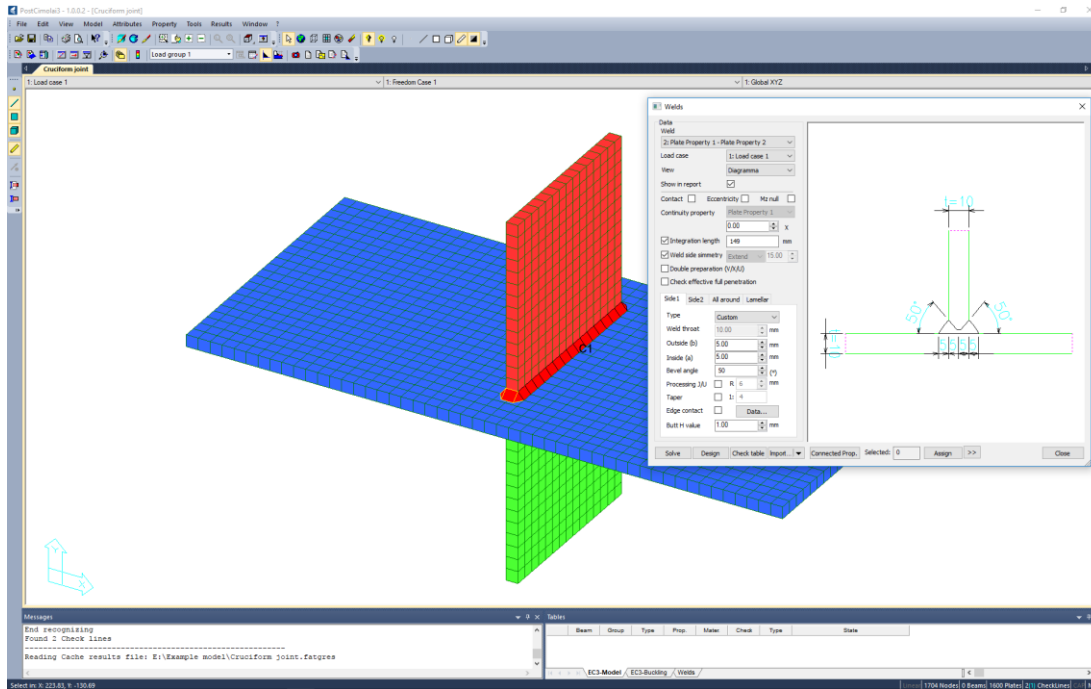


Figure 7.29. Weld design dialog window. Example of double fillet weld definition.



**Figure 7.30.** Weld design dialog window. Example of partial penetration weld definition.

Any geometrical modification of a weld performed through the weld design dialog window produces an instantaneous update of the geometry in the viewport. This permits to easily take the design under control. For example, possible structural interferences can be immediately recognized by the user.

A dimensioned section drawing of the weld is also provided in the dialog window (Figures 7.29 and 7.30), giving information about thickness of jointed plates, weld shape and throat value.

Finally, inside the dialog window it is also possible to execute a rapid resistance check of the weld, called PostWeld module, which can be useful for a pre-design, before performing the fatigue assessment.

### 7.6.3 Assessing welds with shell models

In the following subsections the principles of fatigue assessment of welded joints, basing on shell element models, is presented. Theoretical reference is made to Chapters 5 and 6.

### 7.6.3.1 Selecting a stress concept for welded structures

Different ways to extract stresses from the shell model are available in PostFatigue. The following sections describe the different options. The sub-menu to make the selection is “Attributes→Check lines→Welding stress offset” in the menu bar (Figure 7.31). The parameters named *edge offset* and *head offset* are used to define the stress concept in the direction perpendicular to the weld (edge offset) and at the ends parallel to the weld (head offset).

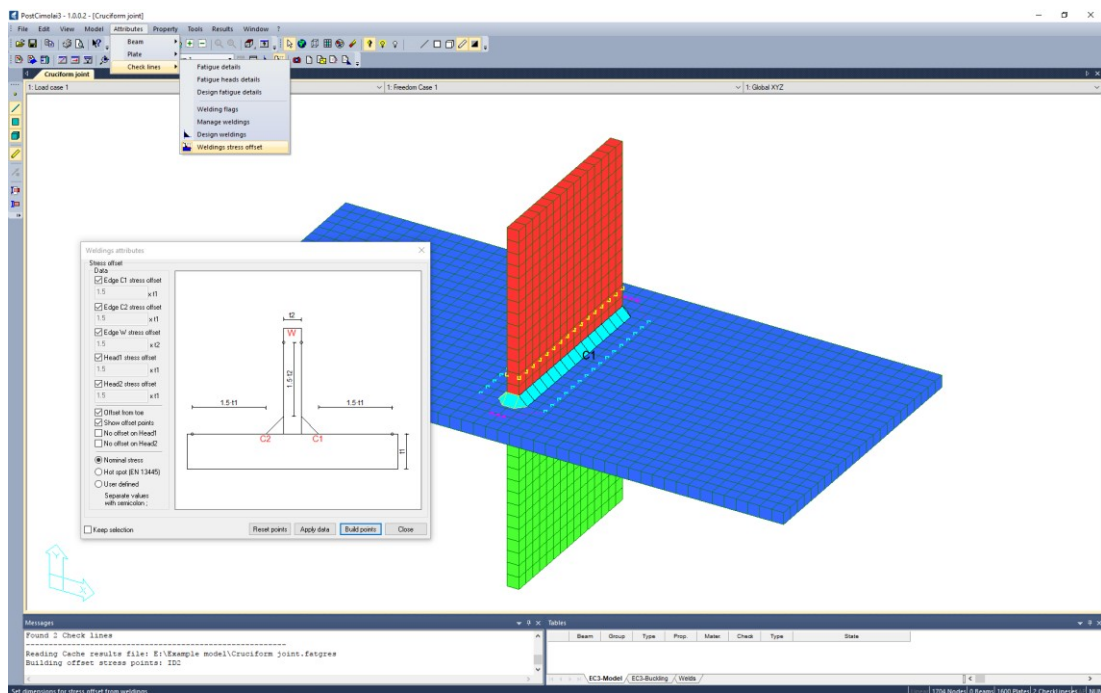


**Figure 7.31.** Menu path and dialog window for the definition of stress offsets all around a weld. Head offset, edge offset on the main plate and edge offset on the attached plate are purple, light blue and yellow dots, respectively. Stresses are automatically recovered, through nodal interpolation, no matter if reading points are located on FE nodes or not.

### 7.6.3.2 Stress taken directly at the shell intersection

This was the first assessment method implemented in PostFatigue. In this case, the user sets to zero all values related to edge offset and head offset. The stresses are taken directly at the nodes defining the weld line. In case of large changes in the stiffness or even singular points, the stresses could be heavily dependent on shell element formulation and mesh size. Taking these stresses in combination with permissible stresses for a nominal stress approach tends to give very conservative results. Therefore, this is not the suggested procedure.

### **7.6.3.3 Local nominal stress approach**

The so-called *local nominal stresses* can be evaluated by the extraction of stress values at a defined distance  $\delta$  from the weld (see Section 6.3). The extraction point can be positioned in two directions relative to the weld: edge offset means extraction points at a given distance perpendicular to the weld; head offset means extraction points aligned with weld at a given distance from the weld endings.

The distance for both variants is set by default as 1.5 times the plate thickness (as motivated by DVS code [12] and Hobbacher [20,21]), see also Figure 6.3. In addition to this simple formulation, a user-defined value can also be entered or the analytical formulation given by Equation (5.34) in Section (5.5) can be activated. The distance value can be measured from the weld toe, i.e. the plates thickness and the weld geometry are considered when the extraction points are computed, or from the plates intersection nodes. The former choice is the default in PostFatigue.

The extraction points mark the locations for the evaluation of the local nominal stress states, which will in most cases involve interpolation of stress values from the FE nodes to the extraction points. The position of the extraction points can be visualized during post-processing, see Figure 7.31. In some cases, the automatically assigned offsets might not be appropriate for the assessment, e.g. for configurations for which the reference points would fall outside of the actual structure. Then, extraction points are automatically regenerated approaching plates intersection.

For the local nominal stress assessment, the stress components are always defined with respect to the weld direction. This means that for the definition of the longitudinal and transverse directions, as well as the associated shear value, the local weld path will be considered. For the weld ends, this implies that the longitudinal direction points in the direction of the weld tangent at the end of the weld.

### **7.6.3.4 Hot spot stress approach**

The hot spot stress is evaluated by interpolation of stress values at prescribed distances from the weld and then by extrapolation to the weld toe or to plates' intersection, depending on the normative formulation. As for the local nominal stress, the extraction points can be positioned in two directions relative to the weld: edge offset means extraction points at a given distance perpendicular to the weld; head offset means extraction points aligned with weld at a given distance from the



weld endings. The default in PostFatigue is the hot spot stress approach formulation according to EN 13445 [15], being the most general formulation available in standards in force. In addition to this default formulation, other formulations provided by standards or a user-defined formulation can also be entered. The distance values can be measured from the weld toe, or from the plates' intersection nodes. For all hot spot stress concepts, stress components are defined with respect to the extrapolation directions. These directions are the transverse direction along the weld and the longitudinal direction at the end of the weld.

#### 7.6.4 Fatigue check according to nominal and hot spot stress approaches

The fatigue assessment of a check line is performed directly by double clicking with the left mouse button on the line itself. Figure 7.32 shows the related dialog window.

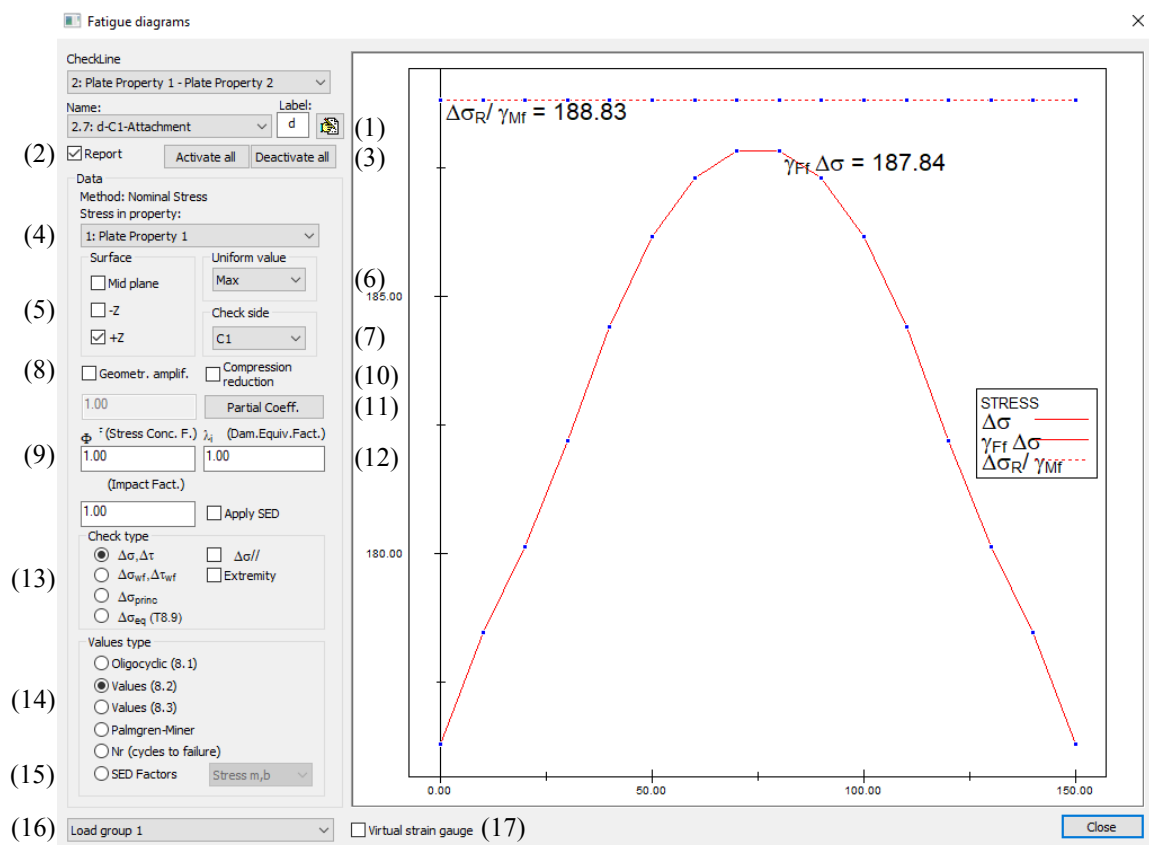


Figure 7.32. Dialog window to perform the fatigue assessment of a check line.

On the left of the dialog window (Figure 7.32), it is possible to choose among the fatigue type checks planned for the check line under consideration (see Section 7.6.1) and,

if needed, the related fatigue attributes can be modified through (1), which gives direct access to the sub-menu already presented in Figure 7.20. Here, it is also possible to specify possible size and misalignment effects, post-weld improvements (see Section 7.6.4.1), and whether or not to apply the bending ratio correction, as formalized in Section 6.4.

By using the provided tools, it is possible to decide if a single check has to be included in the report or not (2), included all or none (3).

The menu (4) allows to select the plate property on which stresses have to be calculated. Moreover, it is possible to decide if stresses have to be computed on the top, bottom or mid surface of the plate (5). Furthermore, it is possible to choose whether the maximum or the average stress along a check line has to be considered (6) (maximum is the default) and the check location (7) (which weld toe or which weld root). Default options are automatically suggested by PostFatigue, leaving the possibility to edit points (1-7) to an expert fatigue designer.

A geometrical amplification factor, which is defined as the ratio of the summation of the weld throats over the thickness of the attached plate, can be applied through (8). The geometrical amplification factor is not needed if the weld geometry is defined through the dedicated design tool (see Section 7.6.2). Being this the case, such factor is automatically computed. Any needed stress concentration factor can be inserted in (9). In (10) it is possible to activate or deactivate the stress reduction for compression, while in (11) it is possible to attribute the check line specific safety factors modifying those globally assigned (see Section 7.4). In (12) it is possible to enter a damage equivalent factor, according to EN 1993-1-9.

Since fatigue checks can be performed considering independently stress ranges  $\Delta\sigma$  and  $\Delta\tau$  (check types 8.1 and 8.2 in EN 1993-1-9) or can be performed by combining stress ranges (checks types 8.3 and A.2 in EN 1993-1-9), the mask (13) permits to set different kind of stresses to be used, as a function of fatigue check, which can be chosen through (14). Stress ranges  $\Delta\sigma$  and  $\Delta\tau$  refer to plate,  $\Delta\sigma_{wf}$  and  $\Delta\tau_{wf}$  refer to weld throats (according to definition provided by EN 1993-1-9). As well as for points (1-7), also in this case PostFatigue automatically suggests the proper kind of stress range to be used as a function of the check type. Among check types, also the local averaged SED approach is available (see Section 7.6.5) and can be chosen through (15).

The plot is updated instantly to each change and summarizes loading and endurable stress ranges (check 8.1 in EN 1993-1-9), or normalized values compared to the unit in the case of other checks. In (16) it is also possible to choose for which load group checks have to be plotted or whether to plot the overall damage summation.

Finally, through (17) virtual strain gauges can be activated and displayed on positions where, all around a weld, the related fatigue assessment is performed (see Section 7.9 for some practical demonstrations).

#### 7.6.4.1 Size, misalignment and post-weld treatments effects

Inside the dialog mask for the attributes of check lines (Figure 7.20) it is possible to specify possible size, misalignment and post-weld treatments effects.

According to EN 1993-1-9, a detrimental size effect factor has to be applied to some fatigue details in the presence of plates having thickness larger than 25 mm. In PostFatigue such factor  $k_s$  is implicitly considered, where required (e.g. transverse butt welds listed in table 8.3 of the normative). However, it is possible to control it in detail (Figure 7.33), having the possibility to decide which reference thickness has to be used (maybe different from 25 mm) and the exponent  $n$  of the  $k_s$  expression. The latter because it is known that such exponent, which is fixed to 0.2 in EN 1993-1-9, is indeed variable and related to the weld transition angle [6,8]. What is more, the exponent's dependence on the weld transition angle has also been well justified by the notch mechanics [22], according to which it corresponds to the value  $1-\lambda_I$ , where  $\lambda_I$  is the eigenvalue of Williams' analytical solution for local stress fields near sharp V-notches, which is dependent on the notch opening angle (see Section 2.2.1).

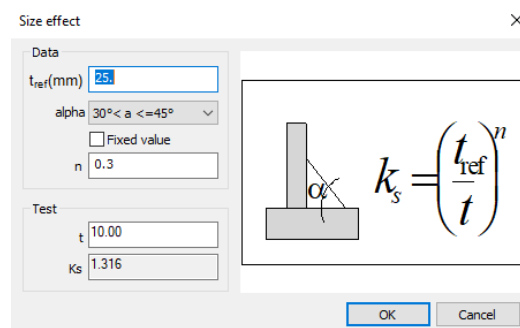


Figure 7.33. Dialog window to control the size effect on fatigue resistance.

In a similar way, the misalignment effect can be taken into account through the detrimental factor  $k_m$ . Various formulations of  $k_m$  are available in PostFatigue, both for transverse butt welds (Figure 7.34(a)) and for cruciform joints (Figure 7.34(b)), according to EN 1993-1-9 and IIW recommendations [6].

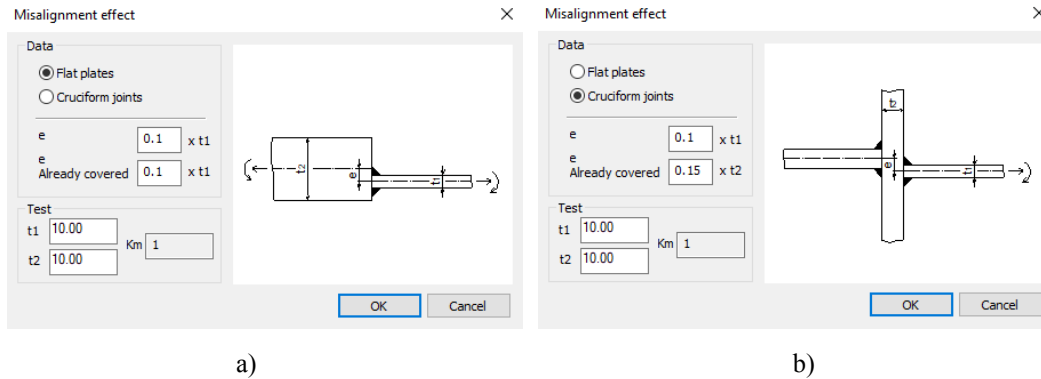


Figure 7.34. Dialog window to control the misalignment effect on fatigue resistance.

Finally, a resistance improvement factor  $k_{wi}$  is available to take into consideration the effect of potential post-weld treatments. Values of  $k_{wi}$  as a function of the post-weld treatments are provided by IIW recommendations [6]. Burr grinding and tig dressing treatments are considered (Figure 7.35(a)), as well as hammer and needle peening (Figure 7.35(b)).

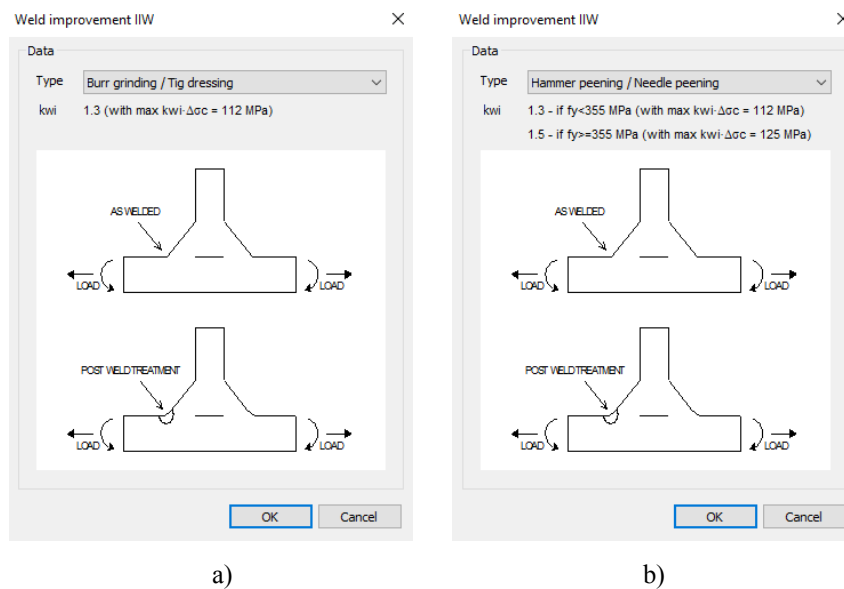
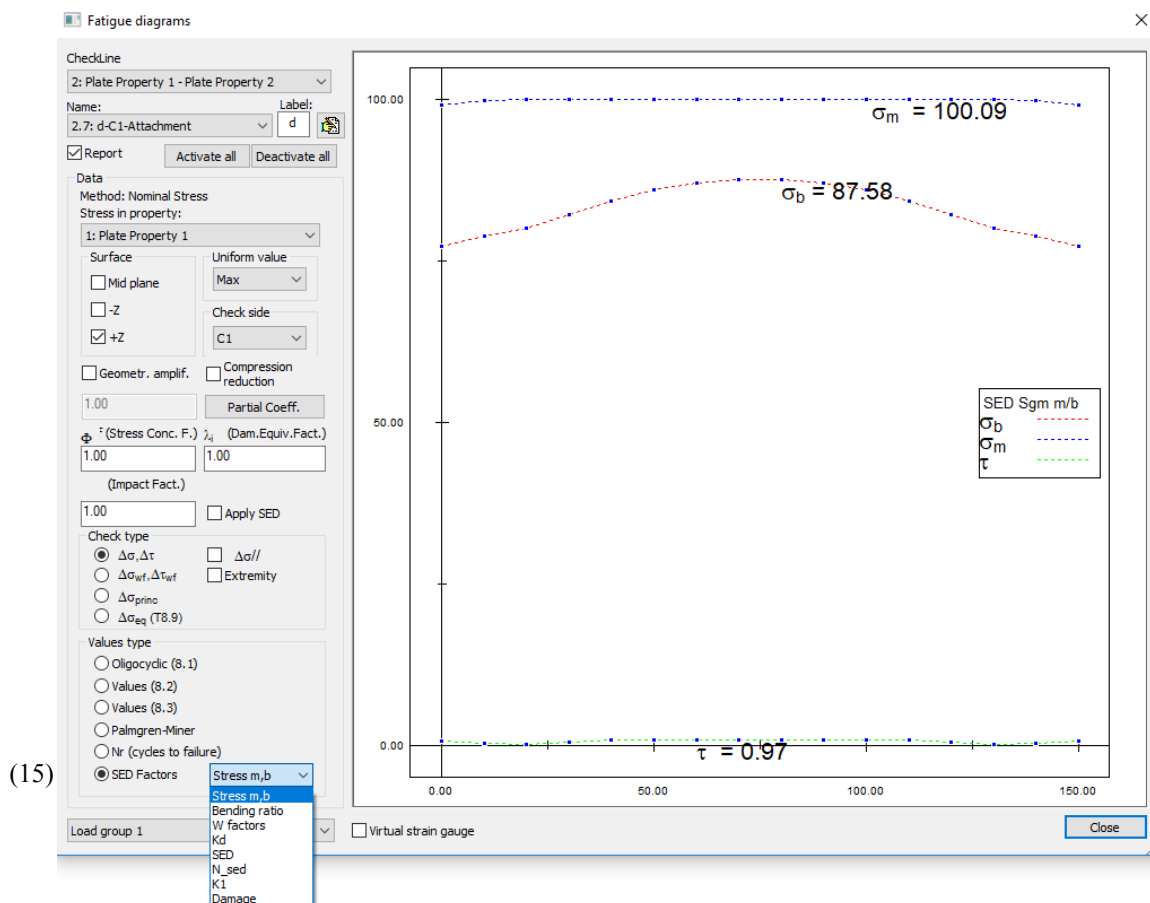


Figure 7.35. Dialog window to control the effect of post-weld treatments on fatigue resistance.

### 7.6.5 Fatigue check according to local SED approach

The local SED approach, as formulated for shell elements in Chapter 5, is available in PostFatigue. The fatigue assessment of a weld is performed directly by double clicking with the left mouse button on the weld line itself. Figure 7.36 shows the related dialog window, which is the same used according to nominal and hot spot stress based approaches (Figure 7.32).

On the bottom left of the dialog window (Figure 7.36) it is possible to enter into the SED factors menu (15), which gives access to plots representing all along the weld the trend of: membrane, bending and shear stress components; non-dimensional stress concentration factors  $w_I$  and  $w_{eq}$ ; bending correction coefficients  $k_{b,toe}$  and  $k_{b,root}$ ; local SED; endurable number of cycles according to local SED approach; mode 1 NSIF; the fatigue damage. A practical demonstration is given in Section 7.9.



**Figure 7.36.** Dialog window to perform the fatigue assessment of a check line according to the local SED approach.

## 7.7 Global fatigue screening of parent material and welds

With the purpose of performing a rapid fatigue assessment, a global fatigue screening procedure has been implemented. Such tool is available at “Results→Fatigue check→Global screening check” in the menu bar (Figure 7.37). According to this procedure, both parent material and welds are assessed all at once, assuming a fixed endurable fatigue class. By default, PostFatigue proposes the class 56 MPa for welds (36 MPa for the weld root only), which is on the safety side for most of the details according to EN 1993-1-9 and IIW recommendations [6], and 125 MPa for parent material. It is left to the designer the possibility to set a different fatigue class. The basic idea of the screening is to make a rapid check of the whole structure, leaving the detailed analysis (as described in Section 7.6.1) to the only welds which do not satisfy it. It is worth noting that also a British standard document [23] suggests the use of the class 56 MPa in global screening like procedure, for the determination of quantified service category on which both the minimum extent of welds inspection and the acceptance criteria are dependent. The global fatigue screening is performed with a graphical output (damage contour) fast to read in the viewport of PostFatigue. So, a continuously colored map gives the fatigue damage distribution (regardless of whether parent material or welds are considered).

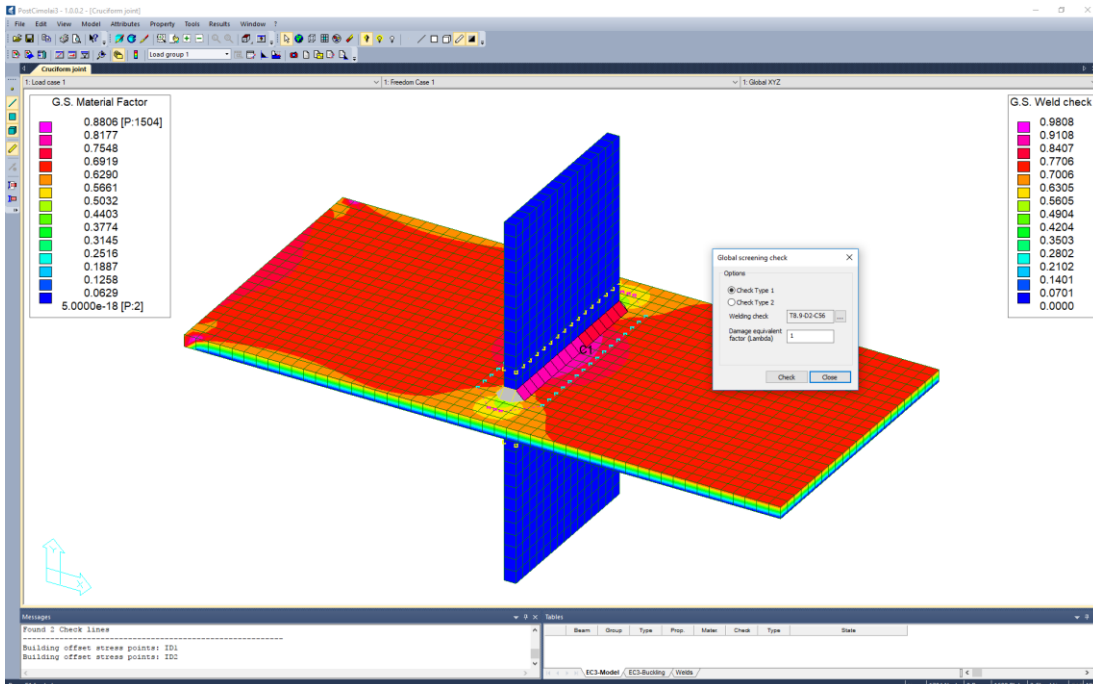


Figure 7.37. Dialog window and graphical output of the global fatigue screening tool.

PostFatigue offers the possibility of assessing both proportional and non-proportional loadings. That is why two types of checks are available for the global screening (Figure 7.37). The default one (Check Type 1) is suitable for proportional loads. Being this the case, the fatigue assessment is executed by performing two distinct biaxial checks (according to EN 1993-1-6 [2]) using the following equivalent stress ranges, respectively:

$$\Delta\sigma_{eq,\perp} = \frac{1}{2} \left( \Delta\sigma_{\perp} + \sqrt{\Delta\sigma_{\perp}^2 + 4\Delta\tau^2} \right)$$

$$\Delta\sigma_{eq,\parallel} = \frac{1}{2} \left( \Delta\sigma_{\parallel} + \sqrt{\Delta\sigma_{\parallel}^2 + 4\Delta\tau^2} \right)$$

where  $\Delta\sigma_{\perp}$ ,  $\Delta\sigma_{\parallel}$  and  $\Delta\tau$  are local stress components computed within shell elements. The other possibility (Check Type 2) is suitable for non-proportional loads. Being this the case, the fatigue assessment is executed by summation of damages due to  $\Delta\sigma_{\perp}$ ,  $\Delta\sigma_{\parallel}$  and  $\Delta\tau$  stress components independently.

## 7.8 Report generation

As a conclusion of a fatigue analysis in PostFatigue, the automatic generation of a report is available. The report generation begins with “Results→Report→Fatigue” (Figure 7.38).

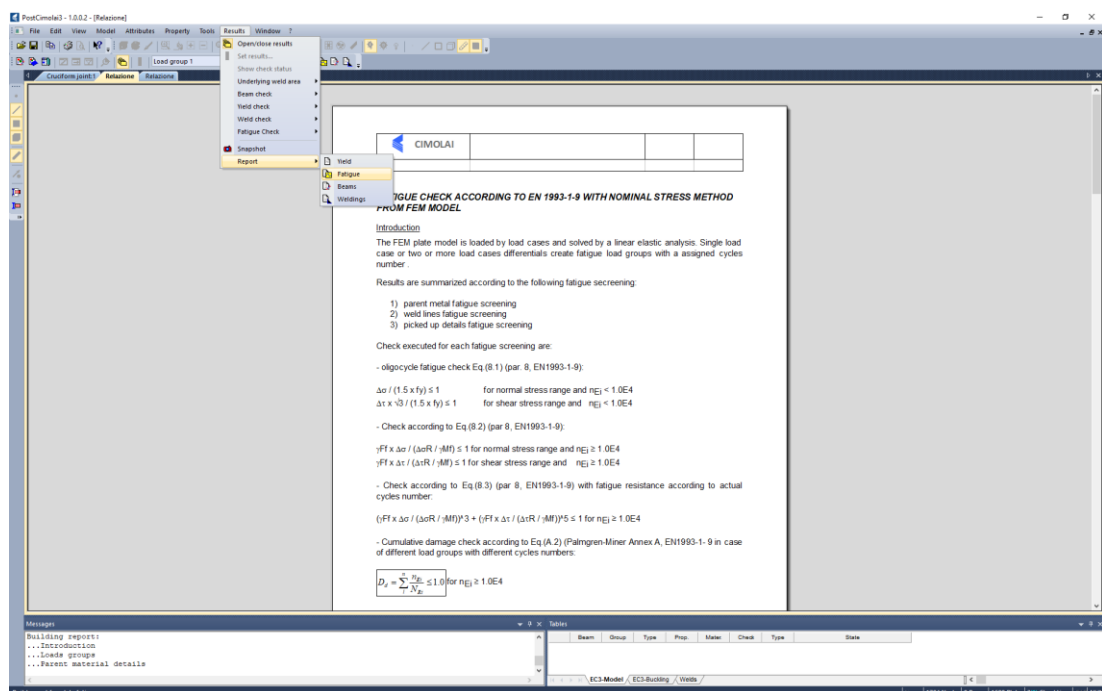


Figure 7.38. Menu path for automatic fatigue report generation.

A dialog window permits the selection of the fatigue checks to be included in the report (Figure 7.39). At the beginning of the report a description of the assessment approach is generated (Figure 7.38), then all the desired checks are reported.

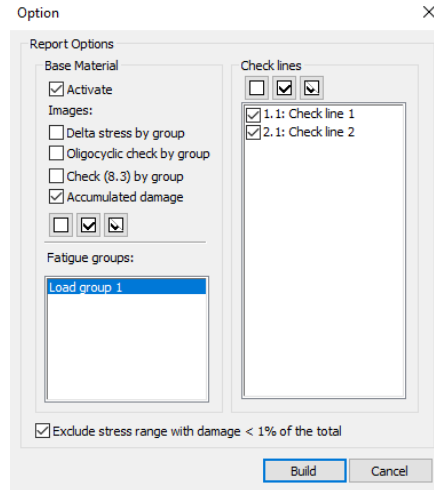


Figure 7.39. Dialog window for automatic fatigue report generation.

## 7.9 Practical applications

In this subsection, some practical applications are presented to show PostFatigue capabilities and its suitability in performing a fatigue assessment according to both global and local approaches. For this purpose, two simple case studies are considered: a symmetric non-load-carrying transverse attachment and a symmetric load-carrying cruciform joint. Analyses have been performed both “manually”, by picking stresses on the Straus7® model, and automatically through PostFatigue.

### 7.9.1 Symmetric non-load-carrying transverse attachment

As first case study, a double fillet welded transverse attachment, with fatigue failure starting from the weld toe, is considered. Geometrical dimensions, loading conditions and restraints have been assumed according to Figure 7.40. Moreover, the loaded plate thickness is 10 mm, the attached plate thickness is 10 mm and the weld throat is 3.5 mm. The weld bead is assumed as a triangular shape having transition angle, with the loaded plate, equal to 45°. The weld is not explicitly modeled in the finite element analysis. Shell finite elements having linear shape functions (named Quad4 in Straus7® library) have been used. Linear elastic material having Young modulus equal to 210000 MPa and Poisson’s ratio equal to 0.3 has been set.



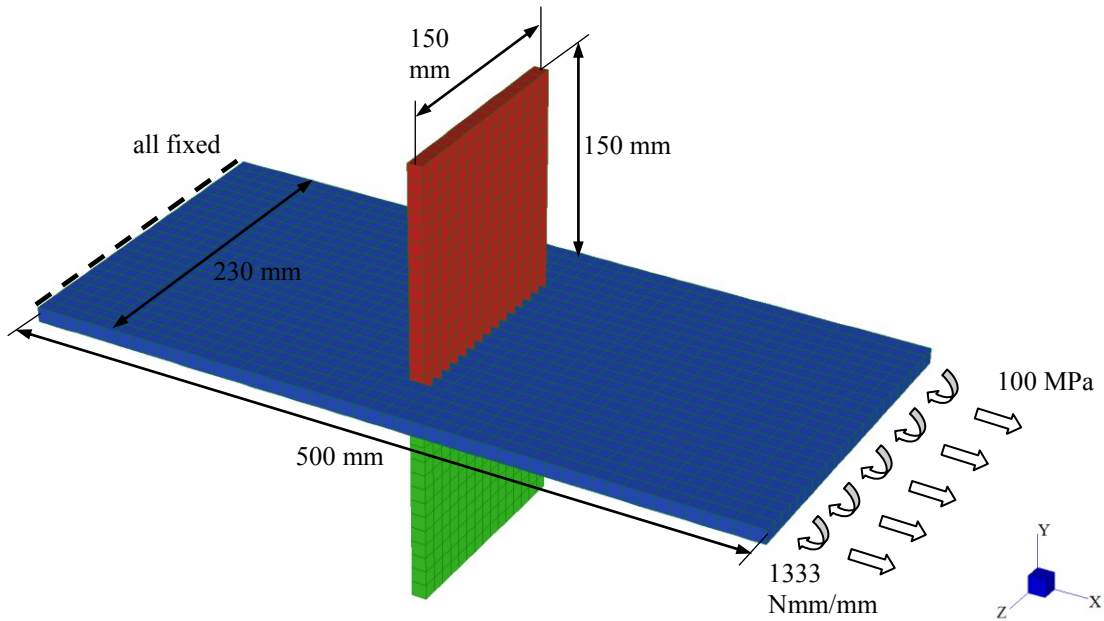


**Figure 7.40.** Symmetric double fillet welded transverse attachment: definition of geometry and boundary conditions.

**7.9.1.1 Manual assessment by picking stresses in the Straus7® model**

Figure 7.41 shows the Straus7® stress contour in direction normal to the weld bead (loading direction), as well as the stress queries in the critical locations, assuming stress offsets equal to zero and to 1.5 times the thickness of the loaded plate.

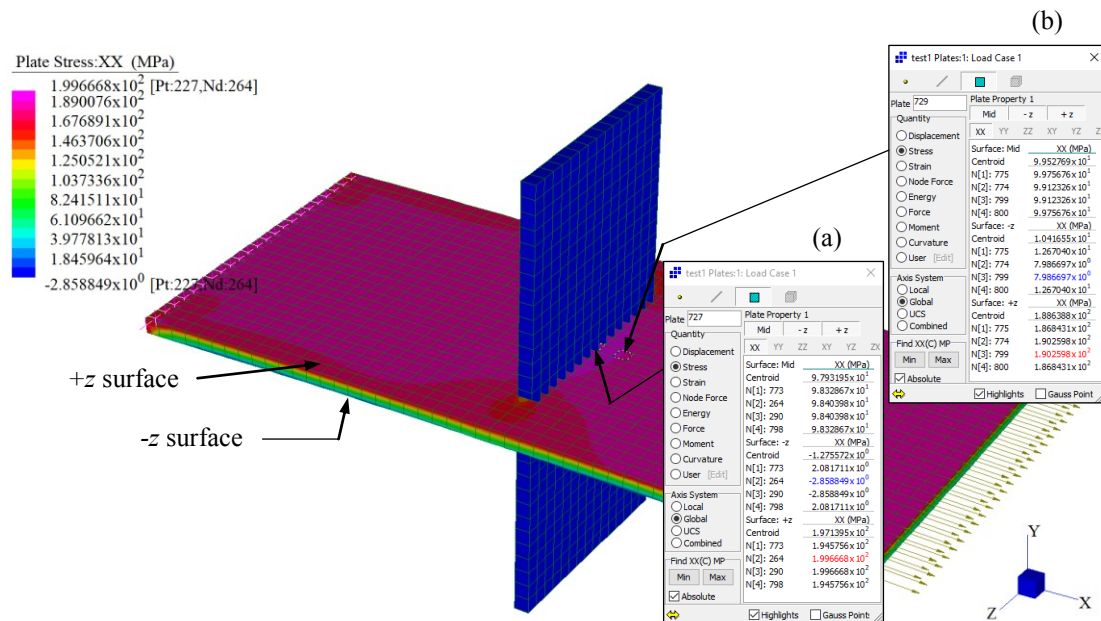


**Figure 7.41.** Stress contour  $\sigma_x$  provided by Straus7® analysis. Dialog windows show stresses picked at plates' intersection (a) and at a distance equal to 1.5 times the loaded plate thickness (b). Also +z and -z surface definitions are provided on the loaded plate.

According to Figure 7.41, stresses at plates' intersection (zero stress offset) are:

$$\sigma_m = 98 \text{ MPa}$$

$$\sigma_{+z} = 200 \text{ MPa}$$

$$\sigma_{-z} = 3 \text{ MPa}$$

whereas stresses at 1.5 times the loaded plate thickness are:

$$\sigma_m = 100 \text{ MPa}$$

$$\sigma_{+z} = 190 \text{ MPa}$$

$$\sigma_{-z} = 8 \text{ MPa}$$

The bending ratio at 1.5 times the loaded plate thickness, according to Equation (5.19), being negligible the shear contribution, is:

$$r_b = \frac{|\sigma_b|}{|\sigma_m| + |\sigma_b|} = \frac{|\sigma_{+z} - \sigma_m|}{|\sigma_m| + |\sigma_{+z} - \sigma_m|} = \frac{90}{190} = 0.47$$

Being considered the weld toe of a double fillet welded a non-load-carrying cruciform joint, coefficients for  $w_1$  evaluation are listed in Table 5.1. Weld shape ratios are  $2h/t=1$  and  $L/t=1$ . Therefore, by using Equation (5.35), it is found:

$$w_{1,m} = 0.41609 + 0.34086e^{-2.03079(1)} - 0.62170e^{-1.77943(1)-0.53332(1)} = 0.399$$

$$w_{1,b} = 0.30992 + 0.21727e^{-4.64592(1)} - 0.84672e^{-5.18412(1)-1.98141(1)} = 0.311$$

Then, according to Equation (5.20), it is found:

$$w_1 = w_1(r_b = 0.47) = w_{1,m} \cdot (1 - 0.47) + w_{1,b} \cdot 0.47 = 0.358$$

The bending correcting coefficient, computed according to Equation (6.7), is:

$$k_{b,toe} = \frac{w_{1,m}}{w_1} = \frac{0.399}{0.358} = 1.11$$

Being the joint endurable fatigue class according to EN 1993-1-9 (table 8.4, detail 6) equal to  $\Delta\sigma_c=80$  MPa (at 97.7% probability of survival), assuming  $\gamma_{Mf}=1$ , stresses computed at plates intersection and no bending correction, the fatigue life is:

$$N = \left( \frac{1}{\gamma_{Mf}} \cdot \frac{\Delta\sigma_c}{\Delta\sigma_n} \right)^3 \cdot 2 \cdot 10^6 = \left( \frac{1}{1} \cdot \frac{80}{200} \right)^3 \cdot 2 \cdot 10^6 = 128000 \text{ cycles}$$

Considering stresses computed at 1.5 times the plate thickness the fatigue life is:

$$N = \left( \frac{1}{\gamma_{Mf}} \cdot \frac{\Delta\sigma_c}{\Delta\sigma_n} \right)^3 \cdot 2 \cdot 10^6 = \left( \frac{1}{1} \cdot \frac{80}{190} \right)^3 \cdot 2 \cdot 10^6 = 149293 \text{ cycles}$$

Finally, considering stresses computed at 1.5 times the plate thickness and bending correction the fatigue life is:

$$N = \left( \frac{k_{b,toe}}{\gamma_{Mf}} \cdot \frac{\Delta\sigma_c}{\Delta\sigma_n} \right)^3 2 \cdot 10^6 = \left( \frac{1.11}{1} \cdot \frac{80}{190} \right)^3 2 \cdot 10^6 = 204178 \text{ cycles}$$

If the local SED approach is considered, the averaged strain energy density, computed according to Equation (5.27), is:

$$\begin{aligned} \Delta\bar{W} &= \Delta\bar{W}(r_b = 0.47) = \frac{\Delta\sigma_n^2}{E} \cdot w_1^2 \cdot \left( \frac{t}{R_0} \right)^{2(1-\lambda_1)} = \\ &= \frac{190^2}{210000} \cdot 0.358^2 \cdot \left( \frac{10}{0.28} \right)^{2(1-0.6736)} = 0.227 \text{ [MJ/m}^3\text{]} \end{aligned}$$

where  $\lambda_I=0.6736$ , being  $2\alpha=135^\circ$ .

The endurable number of cycles, according to the SED design master curve (Figure 2.8), is:

$$N = \left( \frac{0.02}{\Delta\bar{W}} \right)^{1.5} \cdot 10^7 = \left( \frac{0.02}{0.227} \right)^{1.5} \cdot 10^7 = 261521 \text{ cycles}$$

If the local NSIF approach is considered, the mode 1 notch stress intensity factor, computed according to Equation (5.29), is:

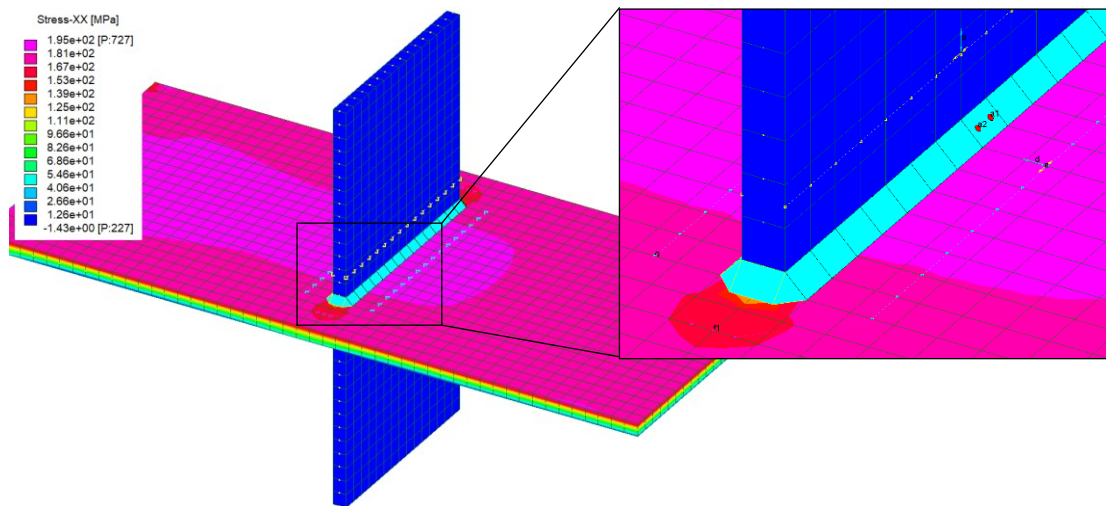
$$\begin{aligned} \Delta K_1 &= \Delta K_1(r_b = 0.47) = \frac{\Delta\sigma_n}{\sqrt{e_1}} \cdot w_1 \cdot t^{(1-\lambda_1)} = \frac{190}{\sqrt{0.118}} \cdot 0.358 \cdot 10^{(1-0.6736)} = 419.5 \\ &[\text{MPa} \cdot \text{mm}^{1-0.6736}] \end{aligned}$$

where, according to Figure 2.6, the parameter  $e_I$  is:

$$e_1 = -5.373 \cdot 10^{-6} \cdot (135)^2 + 6.151 \cdot 10^{-4} \cdot (135) + 0.1330 = 0.118$$

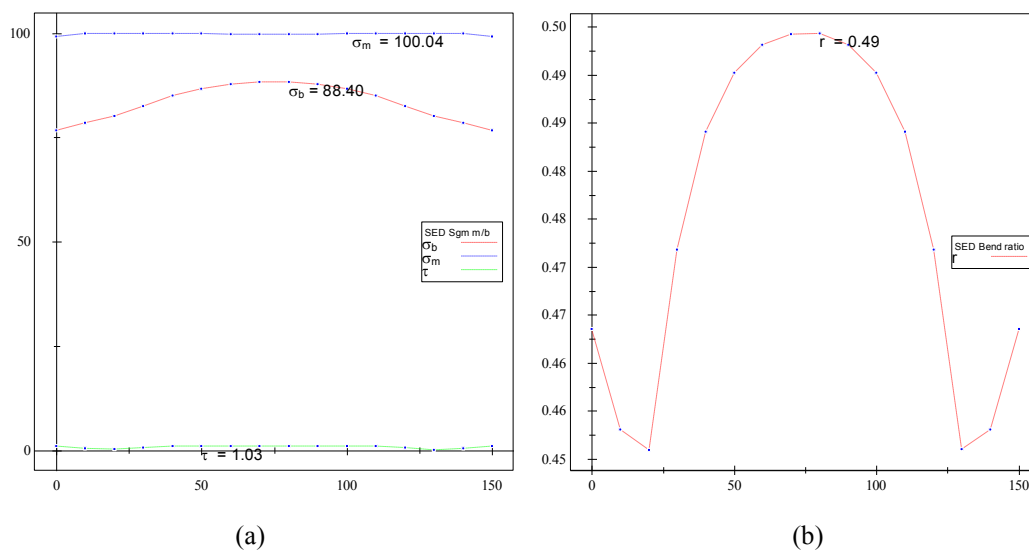
### 7.9.1.2 Automatic assessment by using PostFatigue

Figure 7.42 shows the PostFatigue stress contour in the direction normal to the weld bead (loading direction), as well as the stress offset, set to 1.5 times the thickness of the loaded plate. It is worth specifying that the weld is not explicitly modeled (i.e. its stiffness contribution is neglected, as discussed in Section 6.3); in spite of this, in PostFatigue a cosmetic representation of welds is available to give immediately the feeling of the weld geometry to the designer (Figure 7.42). Furthermore, virtual strain gauges can be activated, whose designation is related to planned fatigue checks for the weld under examination (as explained in Section 7.6.1). Such virtual strain gauges are automatically positioned by PostFatigue at the most critical points, all around a weld, with reference to the corresponding fatigue check (Figure 7.42). Virtual strain gauges are not only useful to highlight the most critical points along a weld, they are also reactive to double clicking providing quick access to the related fatigue check.



**Figure 7.42.** Stress contour  $\sigma_x$  provided by PostFatigue. The detailed view highlights the representation of the weld bead, stress offset points and virtual strain gauges automatically located, check by check, at the most critical points, all around the weld.

Figure 7.43 shows the trend of the stress components and of the bending ratio along the weld line. Figure 7.44 shows the trend of the non-dimensional stress concentration parameter  $w_l$  and of the bending correction coefficient  $k_{b,loe}$  (in PostFatigue named  $k_d$ ). Figure 7.45 shows the trend of the averaged SED and of mode 1 NSIF. All depicted parameters are computed at 1.5 times the loaded plate thickness.



**Figure 7.43.** Trend of stress components (a) and bending ratio (b) along the weld.

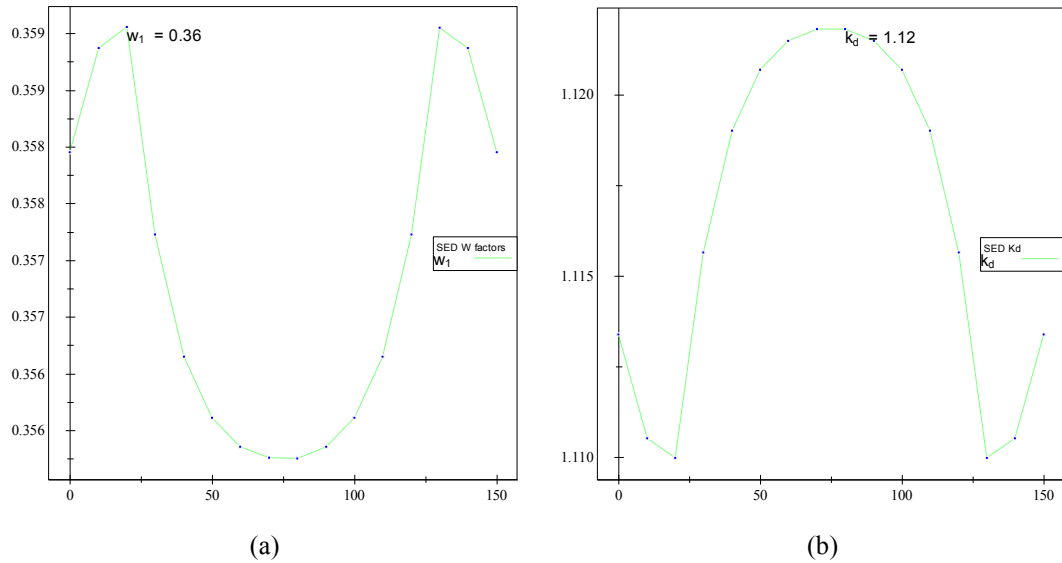


**Figure 7.44.** Trend of non-dimensional stress concentration factor  $w_I$  (a) and bending ratio correction coefficient  $k_d$  (b) along the weld.

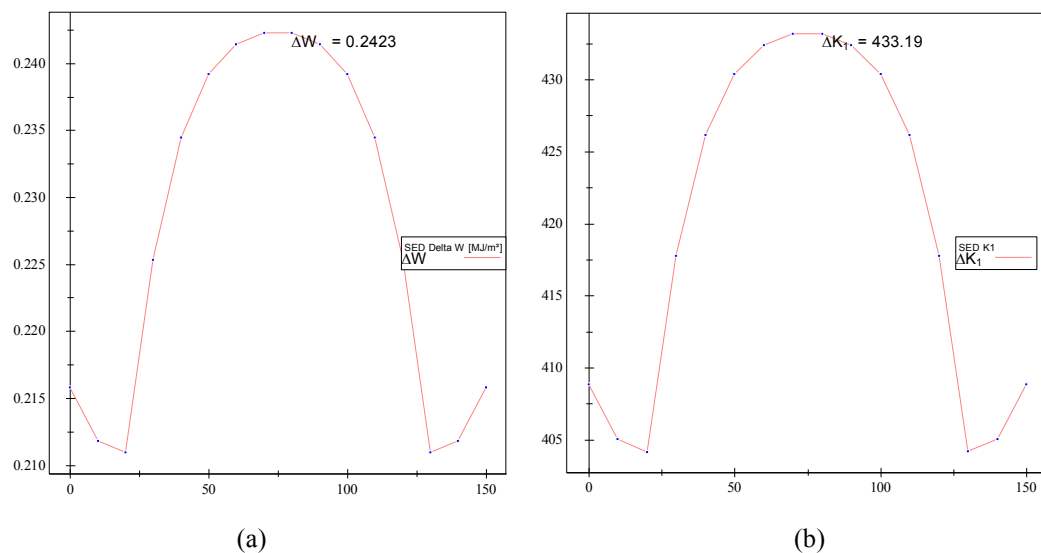


**Figure 7.45.** Trend of local SED (a) and mode 1 NSIF (b) along the weld.

Figure 7.46 shows the trend of the endurable number of cycles computed along the weld line. In detail, the plot on top left is computed assuming stresses at plates' intersection (stress offset equal to zero); the plot on top right assuming stresses at 1.5 times the thickness of the loaded plate; the plot on bottom left assuming stresses at 1.5 times the thickness of the loaded plate and applying the bending correction. Finally, the plot on bottom right represents the endurable number of cycles according to the averaged SED approach.

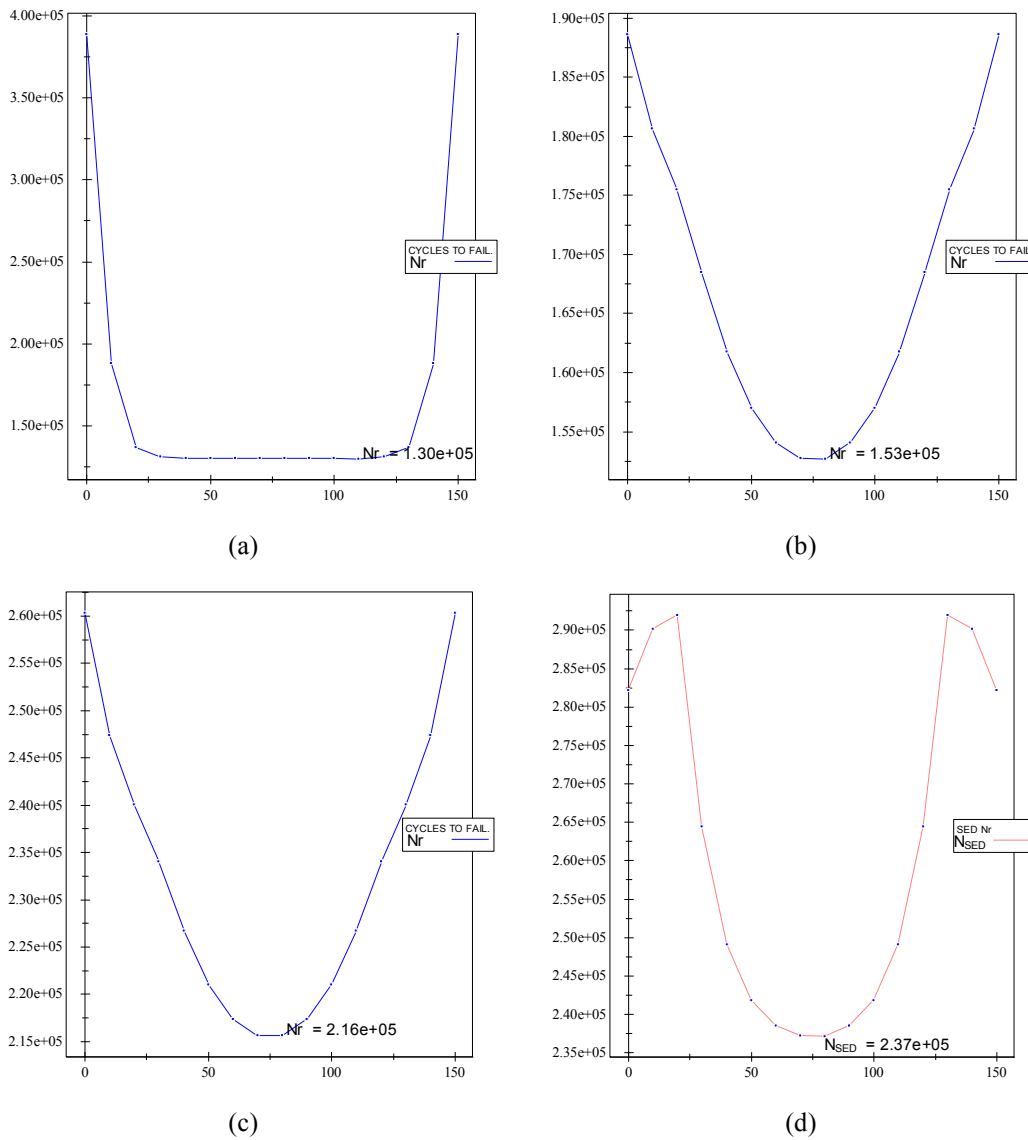


**Figure 7.46.** Trend of endurable number of cycles according to the nominal stress calculated at plates' intersection (a), to the nominal stress calculated at offset points (b), to the nominal stress calculated at offset points with bending correction (c) and to SED approach (d).

### 7.9.1.3 Comparison

Obtained results, in terms of endurable number of cycles, computed “manually” by picking stresses on the Straus7® model and automatically through PostFatigue, are summarized in Table 7.1. It is possible to observe a good agreement between values “manually” computed and the automatically obtained ones. Moreover, in Table 7.2 percentage errors committed with reference to the averaged SED assessment (assumed as a benchmark) are summarized. It is possible to notice a remarkable error reduction if the modified nominal stress (with bending correction) is used.

**Table 7.1.** Comparison between endurable number of cycles “manually” calculated and the automatically computed ones, by using PostFatigue.

	Stress offset	Endurable number of cycles		$\Delta\%$
		“Manual”	PostFatigue	
Nominal stress	no	128000	130000	1.6
	yes	149000	153000	2.7
Modified nominal stress (bending correction)	yes	204000	216000	5.9
Averaged SED	yes	261500	237000	10.1

**Table 7.2.** Percentage errors on the endurable number of cycles committed with reference to the averaged SED approach. PostFatigue estimates are considered.

	Stress offset	Error % with respect to SED approach
Nominal stress	no	82.3
	yes	54.9
Modified nominal stress (bending correction)	yes	9.7

### 7.9.2 Symmetric load-carrying cruciform joint

As second case study, a double fillet welded load-carrying cruciform joint, with fatigue failure starting from the weld root, is considered. Geometrical dimensions, loading conditions and restraints have been assumed according to Figure 7.47. Moreover, the loaded plate thickness is 10 mm, the attached plate thickness is 10 mm and the weld throat is 3.5 mm. The weld bead is assumed as a triangular shape having transition angle, with the loaded plate, equal to  $45^\circ$ . The weld is not explicitly modeled in the finite element analysis. Shell finite elements having linear shape functions (named Quad4 in Straus7® library) have been used. Linear elastic material having Young modulus equal to 210000 MPa and Poisson’s ratio equal to 0.3 has been set.

#### 7.9.1.1 Manual assessment by picking stresses in the Straus7® model

Figure 7.48 shows the Straus7® stress contour in the direction normal to the weld bead (loading direction), as well as the stress queries in the most critical locations, assuming stress offsets equal to zero and to 1.5 times the loaded plate thickness.

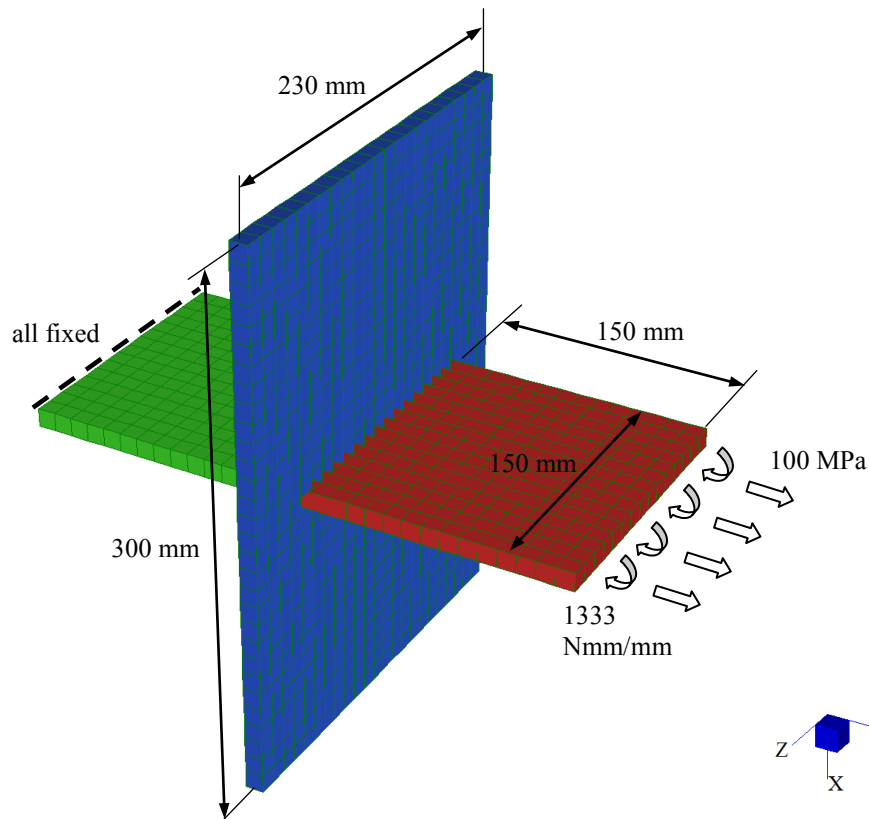


**Figure 7.47.** Symmetric load-carrying cruciform joint: definition of geometry and boundary conditions.

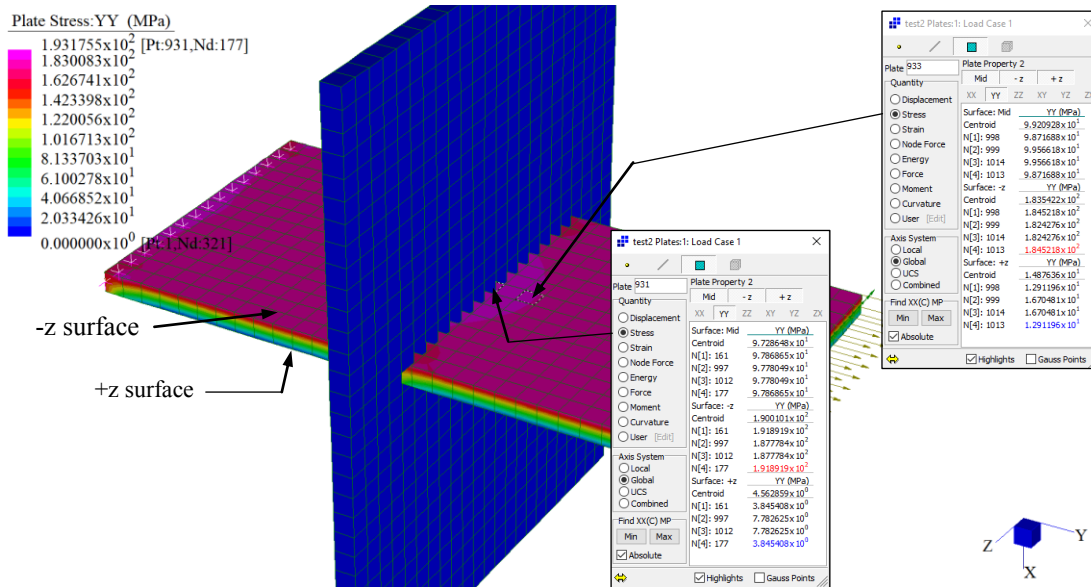


**Figure 7.48.** Stress contour  $\sigma_y$  provided by Straus7® analysis. Dialog windows show stresses picked at plates' intersection (a) and at 1.5 times the loaded plate thickness (b). Also +z and -z surface definitions are provided on the loaded plate.



According to Figure 7.48, stresses at plates' intersection (zero stress offset) are:

$$\sigma_m = 98 \text{ MPa}$$

$$\sigma_{+z} = 192 \text{ MPa}$$

$$\sigma_{-z} = 8 \text{ MPa}$$

whereas stresses at 1.5 times the loaded plate thickness are:

$$\sigma_m = 99 \text{ MPa}$$

$$\sigma_{+z} = 184 \text{ MPa}$$

$$\sigma_{-z} = 17 \text{ MPa}$$

The bending ratio at 1.5 times the loaded plate thickness, according to Equation (5.19), being negligible the shear contribution, is:

$$r_b = \frac{|\sigma_b|}{|\sigma_m| + |\sigma_b|} = \frac{|\sigma_{+z} - \sigma_m|}{|\sigma_m| + |\sigma_{+z} - \sigma_m|} = \frac{85}{184} = 0.46$$

Being considered the weld toe of a double fillet welded a non-load-carrying longitudinal attachment, coefficients for  $w_l$  evaluation are listed in Table 5.2. Weld shape ratios are  $2h/t=1$  and  $L/t=1$ . Therefore, by using Equation (5.35), it is found:

$$w_{eq,m} = 0.10419 + 1.01907e^{-4.10847(1)} + 0.59382e^{-0.59169(1)-0.02771(1)} = 0.441$$

$$w_{eq,b} = 0.00687 + 0.23020e^{-0.89405(1)} + 0.48228e^{-4.50230(1)-0.02193(1)} = 0.106$$

Then, according to Equation (5.22), it is found:

$$w_{eq} = w_{eq}(r_b = 0.46) = w_{eq,m} \cdot (1 - 0.46) + w_{eq,b} \cdot 0.46 = 0.287$$

The bending correcting coefficient, computed according to Equation (6.8), is:

$$k_{b,root} = \frac{w_{eq,m}}{w_{eq}} = \frac{0.358}{0.227} = 1.54$$

Being the joint endurable fatigue class according to EN 1993-1-9 (table 8.5, detail 3) equal to  $\Delta\sigma_c=36$  MPa (at 97.7% probability of survival), assuming  $\gamma_{Mf}=1$ , stresses computed at plates intersection and no bending correction, the fatigue life is:

$$N = \left( \frac{1}{\gamma_{Mf}} \cdot \frac{\Delta\sigma_c}{\Delta\sigma_n} \right)^3 2 \cdot 10^6 = \left( \frac{1}{1} \cdot \frac{36}{192} \right)^3 2 \cdot 10^6 = 13183 \text{ cycles}$$

Considering stresses computed at 1.5 times the plate thickness the fatigue life is:

$$N = \left( \frac{1}{\gamma_{Mf}} \cdot \frac{\Delta\sigma_c}{\Delta\sigma_n} \right)^3 2 \cdot 10^6 = \left( \frac{1}{1} \cdot \frac{36}{184} \right)^3 2 \cdot 10^6 = 14979 \text{ cycles}$$

Finally, considering stresses computed at 1.5 times the plate thickness and bending correction the fatigue life is:

$$N = \left( \frac{k_{b,root}}{\gamma_{Mf}} \cdot \frac{\Delta\sigma_c}{\Delta\sigma_n} \right)^3 2 \cdot 10^6 = \left( \frac{1.54}{1} \cdot \frac{36}{184} \right)^3 2 \cdot 10^6 = 54707 \text{ cycles}$$

If the local SED approach is considered, the averaged strain energy density, computed according to Equation (5.28), is:

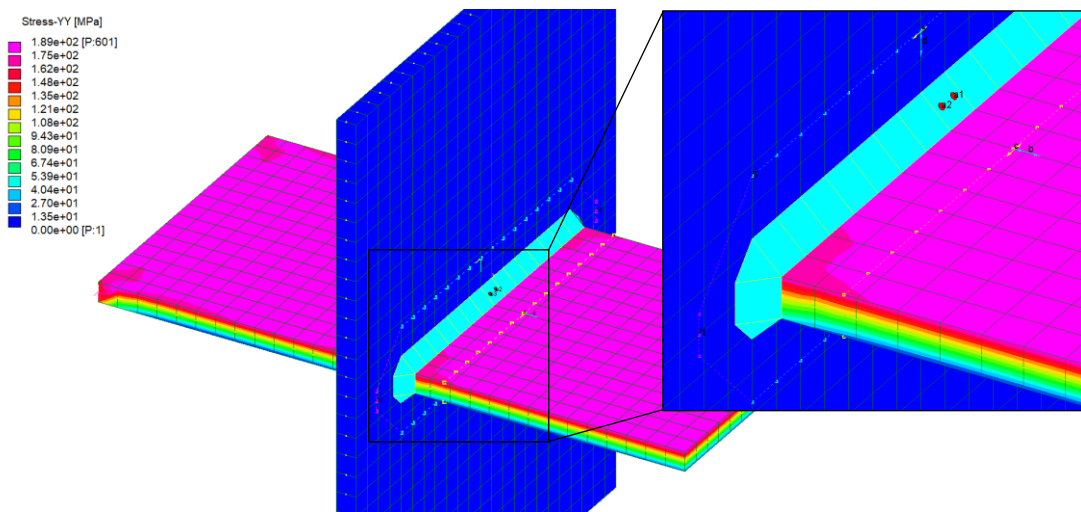
$$\Delta\bar{W} = \Delta\bar{W}(r_b = 0.46) = \frac{\Delta\sigma_n^2}{E} \cdot w_{eq}^2 \cdot \frac{t}{R_0} = \frac{184^2}{210000} \cdot 0.287^2 \cdot \frac{10}{0.28} = 0.474 [\text{MJ/m}^3]$$

The endurable number of cycles, according to the SED design master curve (Figure 2.8), is:

$$N = \left( \frac{0.02}{\Delta\bar{W}} \right)^{1.5} \cdot 10^7 = \left( \frac{0.02}{0.297} \right)^{1.5} \cdot 10^7 = 86599 \text{ cycles}$$

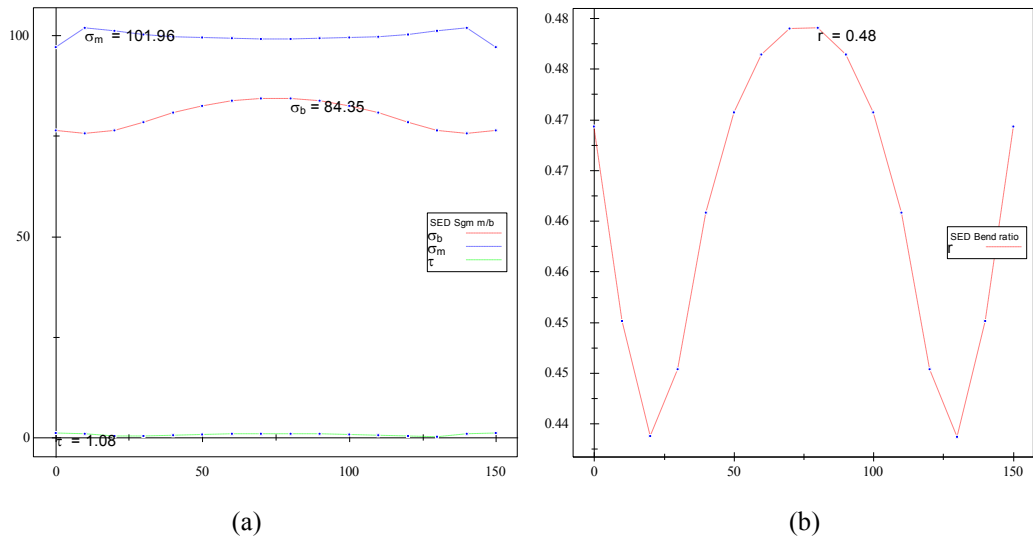
### 7.9.1.2 Automatic assessment by using PostFatigue

Figure 7.49 shows the PostFatigue stress contour in the direction normal to the weld bead (loading direction), as well as the stress offset, set to 1.5 times the thickness of the loaded plate.



**Figure 7.49.** Stress contour  $\sigma_y$  provided by PostFatigue. The detailed view highlights the representation of the weld bead, stress offset points and virtual strain gauges automatically located, check by check, at the most critical points, all around the weld.

Figure 7.50 shows the trend of the stress components and of the bending ratio along the weld line. Figure 7.51 shows the trend of the non-dimensional stress concentration parameter  $w_{eq}$  and of the bending correction coefficient  $k_{b,root}$  (in PostFatigue named  $k_{d,l+2}$ ).



**Figure 7.50.** Trend of stress components (a) and bending ratio (b) along the weld.

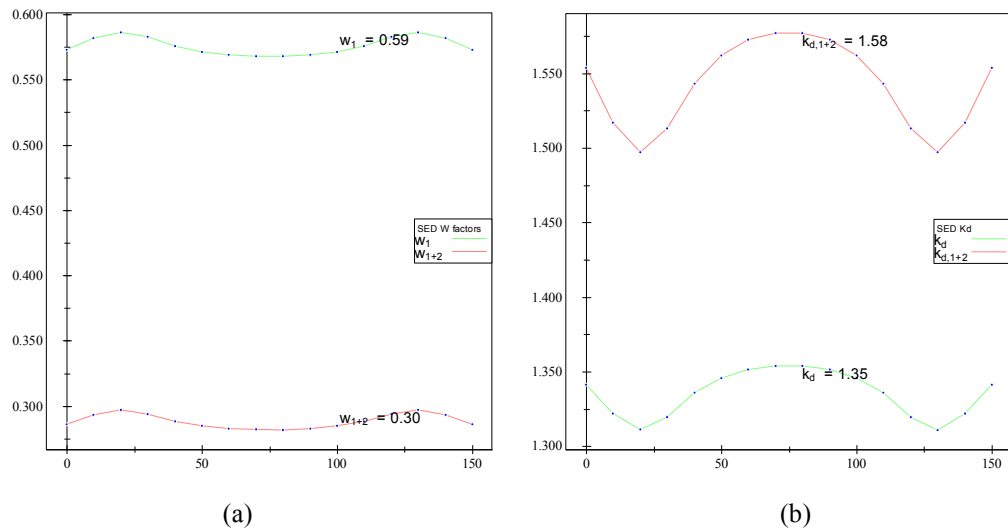


**Figure 7.51.** Trend of non-dimensional stress concentration factors  $w_I$  and  $w_{I+2}$ , at the weld toe and at the weld root, respectively (a) and trend of bending ratio correction coefficients  $k_d$  and  $k_{d,I+2}$ , at the weld toe and at the weld root, respectively (b), both along the weld.

Figure 7.52 shows the trend of the averaged SED. Figure 7.53 shows the trend of the endurable number of cycles computed along the weld line. In detail, the plot on top left is computed assuming stresses at plates' intersection (stress offset equal to zero); the plot on top right assuming stresses at 1.5 times the thickness of the loaded plate; the plot on bottom left assuming stresses at 1.5 times the thickness of the loaded plate and applying the bending correction. Finally, the plot on bottom right represents the endurable number of cycles according to the averaged SED approach.

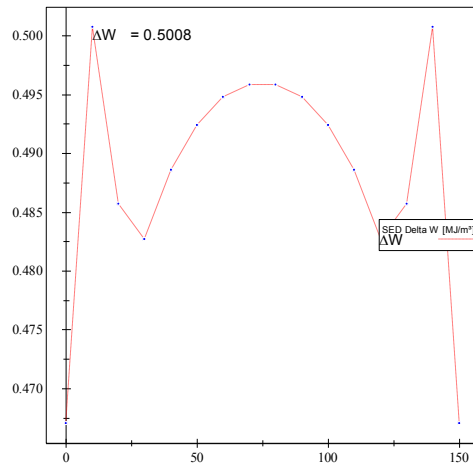
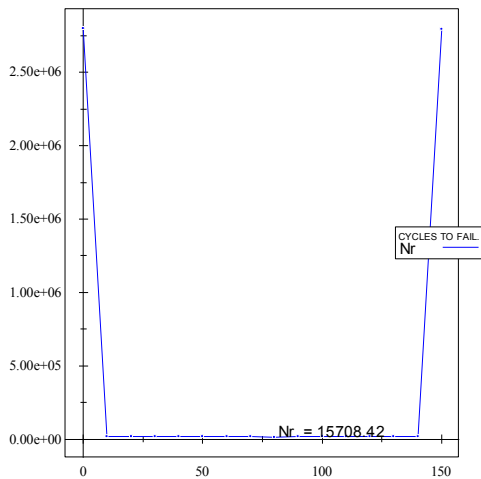
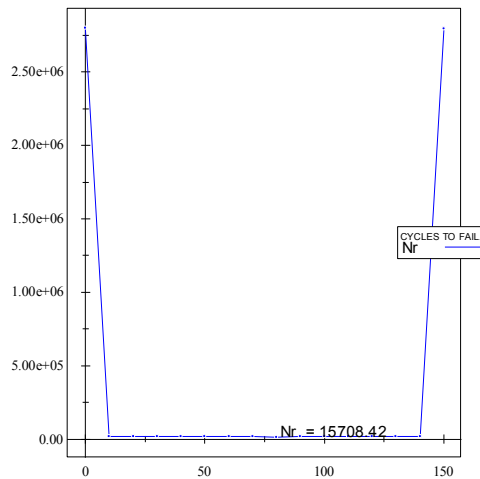


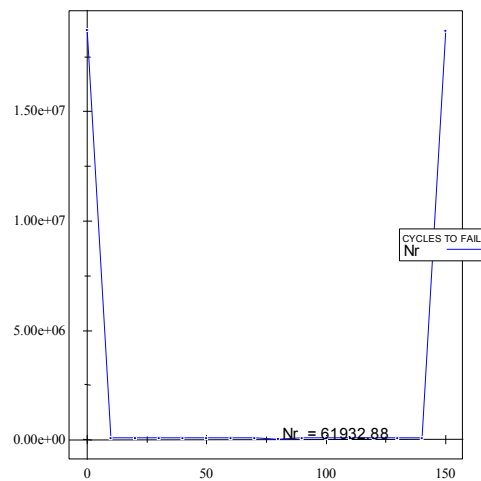
Figure 7.52. Trend of local SED along the weld.



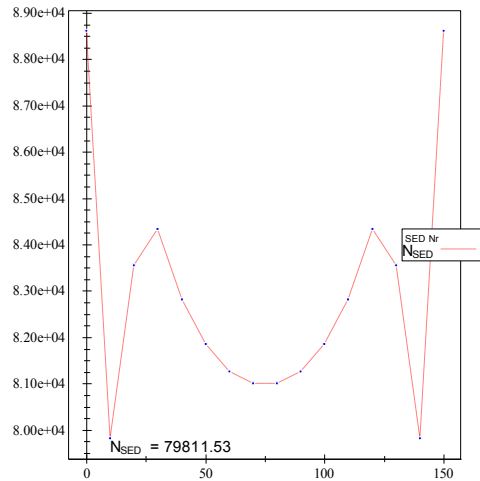
(a)



(b)



(c)



(d)

Figure 7.53. Trend of endurable number of cycles according to the nominal stress calculated at plates' intersection (a), to the nominal stress calculated at offset points (b), to the nominal stress calculated at offset points with bending correction (c) and to SED approach (d).

### 7.9.1.3 Comparison

Obtained results, in terms of endurable number of cycles, computed “manually” by picking stresses on the Straus7® model and automatically through PostFatigue, are summarized in Table 7.3. It is possible to observe a good agreement between values “manually” computed and the automatically obtained ones. Moreover, in Table 7.4 percentage errors committed with reference to the averaged SED assessment (assumed as a benchmark) are summarized. It is possible to notice a remarkable error reduction if the modified nominal stress (with bending correction) is used.

**Table 7.3.** Comparison between endurable number of cycles “manually” calculated and the automatically computed ones, by using PostFatigue.

	Stress offset	Endurable number of cycles		$\Delta\%$
		“Manual”	PostFatigue	
Nominal stress	no	13200	15700	18.9
	yes	14500	15700	8.3
Modified nominal stress (bending correction)	yes	54700	62000	13.3
Averaged SED	yes	86900	79800	10.0

**Table 7.4.** Percentage errors on the endurable number of cycles committed with reference to the averaged SED approach. PostFatigue estimates are considered.

	Stress offset	Error % with respect to SED approach
Nominal stress	no	508.3
	yes	508.9
Modified nominal stress (bending correction)	yes	28.7

## 7.10 Program specification overview

- Stand-alone graphical user interface
- Supported file formats:
  - Straus7®: .lsa
- Supported FE data:
  - Nodes
  - Elements
  - Stresses
  - Strains
- Supported element types:
  - Shell elements
  - Beam elements
- Assessment groups:
  - Welds
  - Parent material
  - General check lines
- Manipulation of stress data:
  - Superposition of basic load cases
  - Spectra blocks from load cases
  - Rainflow counting
- Available assessment concepts:
  - Weld assessment on the basis of shell elements:
    - Nominal stress method (EN 1993-1-9 and IIW recommendations)
    - Modified nominal stress method
    - Hot spot stress method (EN 1993-1-9 and EN 13445-3)
    - Strain energy density approach (SED)
    - Notch stress intensity factor approach (NSIF)
  - Parent material assessment on the basis of shell elements:
    - Nominal stress method
    - Modified nominal stress method

- Supported design codes and guidelines:
  - EN 1993-1-9 (Eurocode 3)
  - IIW recommendations
  - User-defined on the basis of S-N curves
- Post-processing capabilities:
  - Visualization of all relevant data in PostFatigue graphical user interface
  - Automated report generator
- Supported hardware platforms:
  - PC operating under Windows® (32 and 64 bit versions)

## 7.11 Discussion and conclusion

Large steel welded structures are usually made out of plates with large dimensions compared to their thickness. Consequently, according to the finite element method, shell elements can be used to capture the behavior of such structures very efficiently. However, in practical applications there can be arguments against the shell element approach. Usually, they are the following: a) the geometry of a structure is often defined as a full 3D CAD model (Figure 7.54(a)) and the effort required to generate an appropriate mid surface model (Figure 7.54(b)) could be time consuming (not casually, automated mid surface generators are spreading pre-processing tools); b) some regions of a structure can violate the assumptions of shell theory, when their thickness is large as compared to other dimensions (for example, the stiffness itself of a weld is neglected in a shell model, unless the weld bead is explicitly represented). For the above mentioned reasons many structural engineers prefer working with solid elements and volume geometries, even if, as compared to shell models, solid ones are computationally more expensive. Indeed, with most of the pre-processors available on the market the volume mesh is produced quite fast by using an automatic free-meshing algorithm based on tetrahedral elements and on the use of modern hardware (e.g. high performance computing) in combination with the continually improved solvers, allows to handle such models with acceptable computing time. Figure 7.54(c) gives an example for a tetrahedron mesh, generated with the free-meshing algorithm provided by Ansys®.

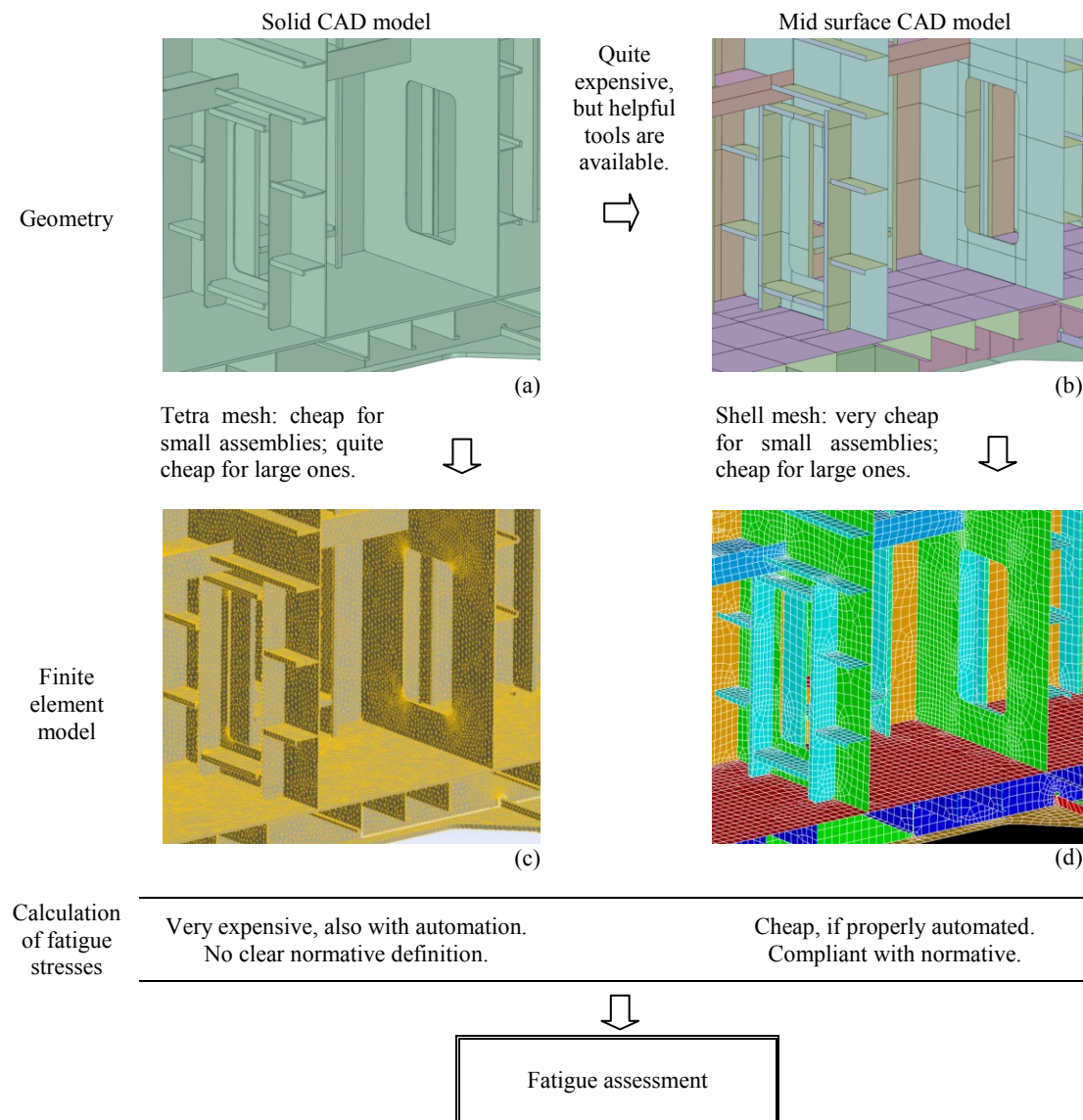


**Figure 7.54.** Workflow of fatigue assessment through solid or shell mesh models.

However, any supposed gain in efficiency (which is still questionable for extremely large assemblies) is lost when dealing with fatigue assessments. The use of solid models leads to stress results which are very difficult to be categorized and assessed. Still, most of the standards do not refer to any local concept and lead to use the nominal stress or hot spot stress methods [21], but nominal stresses or hot spot stresses are not directly available after the FE analysis and the permissible values from current fatigue standards are thus not applicable. Dealing with the nominal stress method, no recommendations exist on how to derive the nominal components from a solid finite element model; dealing with the hot spot stress method, a time



consuming pre- and post-processing work has to be done in order to perform a fatigue assessment according to typical standards (e.g. IIW recommendations). The assessment can therefore usually be limited to a small number of assessment positions, which may not capture all fatigue hot spots in the structure correctly.

On the other hand, results obtained with shell models (Figure 7.54(d)), can provide a good representation of nominal stresses (even if in principle no recommendations exist on how to obtain nominal stress components from them). For this reason, in Chapter 6 of the present thesis a way to overcome such lack of consistency of in force standards has been proposed by using the so-called *modified nominal stress*. The modified nominal stress components can be assessed fully according to typical standards, i.e. Eurocode 3, IIW recommendations and many more and the permissible stress ranges, for different weld types, can directly be compared with the calculated FE stress values, leading to compute margins of safety at each assessment position. That is why to make a fatigue assessment affordable, which is both suitable to large structures and compliant with standards in force, it has been considered a right choice developing a post-processor based on coarse shell meshes.

In this chapter the most interesting aspects of such post-processor have been presented and some practical applications have been given. A very good agreement between “manually” performed assessments, both through global and local approaches, and those rapidly performed by using the post-processor has been found. Further good agreement has been highlighted between expected fatigue lives estimated through the local SED approach and those estimated through the modified nominal stress, in the presence of bending stresses.

Here, simple welded geometries (like those usually tested in laboratory) have been considered, as benchmarks. In Chapter 8 a practical application of the post-processor on a real large welded structure, characterized by hundreds of welds, is shown.

## References

- [1] EN 1993-1-1+A1 Eurocode 3: Design of steel structures - Part 1-1: General rules and rules for buildings, European Committee for Standardization, Brussels, 2014.
- [2] EN 1993-1-6 Eurocode 3 - Design of steel structures - Part 1-6: Strength and stability of shell structures, European Committee for Standardization, Brussels, 2007.
- [3] EN 1993-1-9 Eurocode 3 - Design of steel structures - Part 1-9: Fatigue, European Committee for Standardization, Brussels, 2005.
- [4] EN 1993-2 Eurocode 3 - Design of steel structures - Part 2: Steel bridges, European Committee for Standardization, Brussels, 2006.
- [5] EN 1993-6 Eurocode 3 - Design of steel structures - Part 6: Crane supporting structures, European Committee for Standardization, Brussels, 2007.
- [6] A.F. Hobbacher, Recommendations for Fatigue Design of Welded Joints and Components, Springer International Publishing, 2016.
- [7] FKM Guideline - Analytical strength assessment of components, 6th Editio, VDMA Verlag, 2012.
- [8] DNVGL-RP-C203 - Fatigue design of offshore steel structures, Det Norske Veritas - Germanischer Lloyd, 2016.
- [9] ISO 19901-3 Petroleum and natural gas industries - Specific requirements for offshore structures - Part 3: Topsides structure, International Organization for Standardization, 2014.
- [10] IACS Common structural rules for double hull oil tankers, International Association of Classification Societies, 2012.
- [11] IACS Common structural rules for bulk carriers, International Association of Classification Societies, 2012.
- [12] DVS 1612 - Design and endurance strength assessment of welded joints with steels in rail vehicle construction, German Welding Society, Brussels, 2009.
- [13] ISO 16881-1 - Cranes - Design calculation for rail wheels and associated trolley track supporting structure, International Organization for Standardization, 2005.
- [14] EN 13001-3-1+A1 Cranes - General Design - Part 3-1: Limit States and proof competence of steel structure, European Committee for Standardization, 2013.

- [15] EN 13445-3 Unfired pressure vessels - Part 3: Design, European Committee for Standardization, Brussels, 2014.
- [16] ASME VIII - Rules for Construction of Pressure Vessels - Division 2: Alternative Rules, American Society of Mechanical Engineers, Brussels, 2013.
- [17] M. Bäckström, G. Marquis, Interaction equations for multiaxial fatigue assessment of welded structures, *Fatigue Fract. Eng. Mater. Struct.* 27 (2004) 991–1003.
- [18] C.M. Sonsino, Multiaxial fatigue assessment of welded joints--recommendations for design codes, *Int. J. Fatigue.* 31 (2009) 173–187.
- [19] EN 1993-1-8 Eurocode 3 - Design of steel structures - Part 1-8: Design of joints, European Committee for Standardization, Brussels, 2005.
- [20] A.F. Hobbacher, The new IIW recommendations for fatigue assessment of welded joints and components - A comprehensive code recently updated, *Int. J. Fatigue.* 31 (2009) 50–58.
- [21] A.F. Hobbacher, New developments at recent update of the IIW recommendations for fatigue of welded joints and components, *Steel Constr.* 3 (2010).
- [22] P. Lazzarin, R. Tovo, A Notch Intensity Factor Approach To the Stress Analysis of Welds, *Fatigue Fract. Eng. Mater. Struct.* 21 (1998) 1089–1103.
- [23] PD 6705-2+A1 Structural use of steel and aluminium. Recommendations for the execution of steel bridges to BS EN 1090-2, British Standard institution, 2013.



## **8. Fatigue assessment of a New Panama Canal lock gate: comparison of procedures**

### **Highlights**

The purpose of this chapter is to provide the reader with a clear idea of what may mean performing the fatigue assessment of a megastructure, in terms of number of analyses and data processing. To this end, a practical application, in principle not different from what a designer engineer faces every day, has been considered. The “manual”, fault susceptible and time consuming procedure, has been compared with the automatic fatigue analysis by using PostFatigue. As an example of megastructure, one of the 16 steel gates fabricated by Cimolai SpA for the New Panama Canal has been chosen. The overall dimensions of the gate are about 60 m of length, 10 m of width and 32 m of height. The weight of the gate, made out of S460 structural steel, is about 3500 t. It has been pointed out that a post-processor like PostFatigue not only speeds up the assessment procedure (e.g. limiting the detailed analysis to those few welds which do not pass the global screening) but makes the correct design of welds and parent material possible, no more justified through meaningless colored maps (stress contours). Critical points for fatigue can all be checked (locally and one by one) and the design is no longer inordinately conservative (at best) or random (in worst cases).



## 8.1 Introduction

Nowadays civil (but not only) steel structures are increasingly large, daring and optimized in weight. Such structures are not only susceptible to traditional traffic induced fatigue but also to vibration and to wind induced fatigue. Moreover, large structures are all different from each other and there is no mass production. So, with rare exceptions, the fatigue design cannot be based on large-scale experimental investigations and certainly not on full-scale testing. As a result, the proof of safety is numerically given by respecting standards, from the design to the inspection and acceptance phases. What is more, the European standards have recently reinforced the request to consider the fatigue phenomenon for the design of large steel structures. The size of the structure is now part of the concept of Consequence Class and the large size automatically leads to fatigue calculations, as discussed in Chapter 1. Then, to fulfill nowadays normative requirements, it is essential to have numerical procedures to perform massive fatigue assessments, which are supported by standards and allow time and costs associated with the design to be within budget. Within this framework, the aim of this chapter is giving to the reader the feeling of what means, nowadays, performing the fatigue assessment of a megastructure. To this end, a practical application is presented. First the “manual”, fault susceptible and time consuming procedure, which a designer engineer has to carry out, is shown. Afterwards, the fatigue analysis by using PostFatigue is presented. As an example of megastructure, one of the 16 steel gates fabricated by Cimolai SpA for the New Panama Canal (Third Set of Locks Project) has been chosen (Figure 8.1).



**Figure 8.1.** Some of the 16 lock gates at their arrival in Panama, after about 40 days of ocean traveling from Trieste (Italy).

## 8.2 The case study: a section of a New Panama Canal lock gate

Object of the analysis is a section of the buoyancy chamber of the gate called Type B. The overall dimensions of the gate are about 60 m of length, 10 m of width and 32 m of height. The weight of the gate, made out of S460 structural steel, is about 3500 t. It is worth specifying that, for reasons of confidentiality, the models and engineering solutions here presented are similar, but not the same, to those adopted in the as-built structure. Such approximation does not affect the purposes of this chapter. In Figure 8.2 the Ansys® global Finite Element (FE) model of the gate is shown, together with his overall dimensions. For the sake of brevity, in the following analyses only a portion of the whole model is considered. Such portion, whose location is indicated in Figure 8.2, is a section of the buoyancy chamber of the gate and, in terms of volume, can be considered as 1/42 of the whole gate.

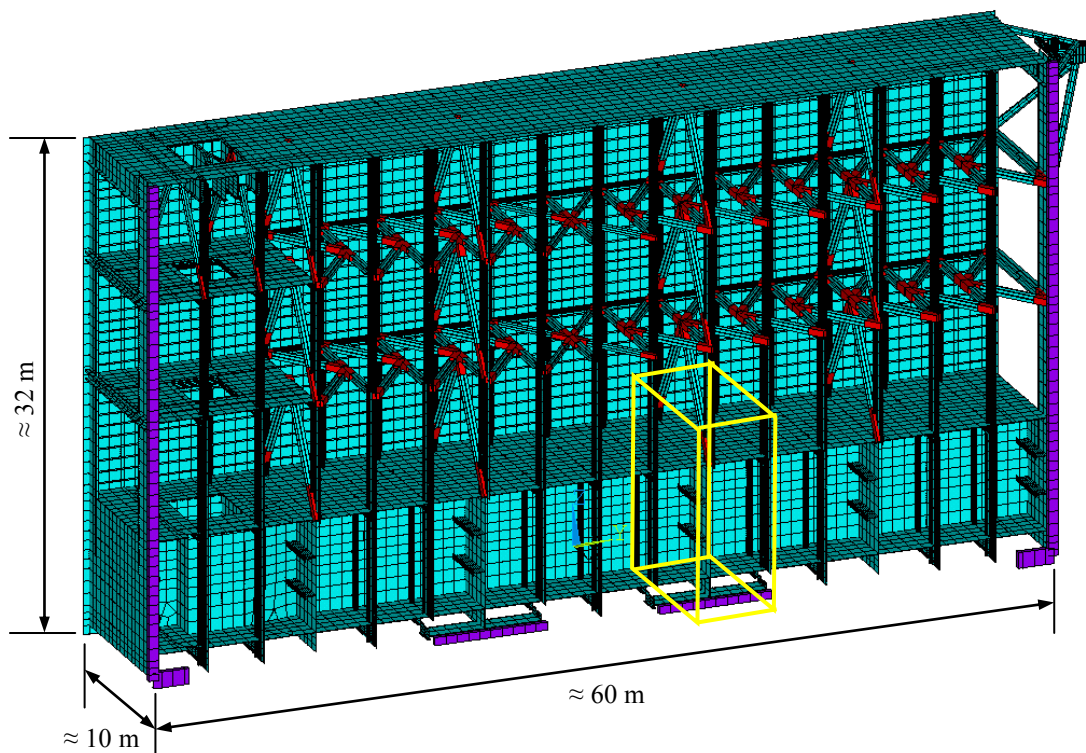


**Figure 8.2.** Global very coarse shell FE model of the gate Type B. The portion of buoyancy chamber considered in the present chapter is highlighted by a yellow box having length of 4.32 m, width of 10 m and height of 11.64 m. It is about 1/42 of the whole gate model.

The fatigue loading condition is represented by the cyclic flooding and un-flooding of the canal lock. The number of occurrences has been estimated in 125000 times



during the lifetime of the gate. In the global FE model such load has been taken into account through a proper system of hydrostatic pressures applied to the wet skins of the gate. A FE sub-model of the portion of buoyancy chamber has then been produced in Straus7® environment (Figure 8.3). As the global one, it has been meshed by using shell elements, but the degree of refinement has been improved (while remaining compatible with the dimension of the assembly). The number of degrees of freedom of the sub-model has been kept under  $5 \cdot 10^5$ . Such sub-model has been loaded applying, as boundary conditions on the cutting planes, the displacements obtained from the global model.

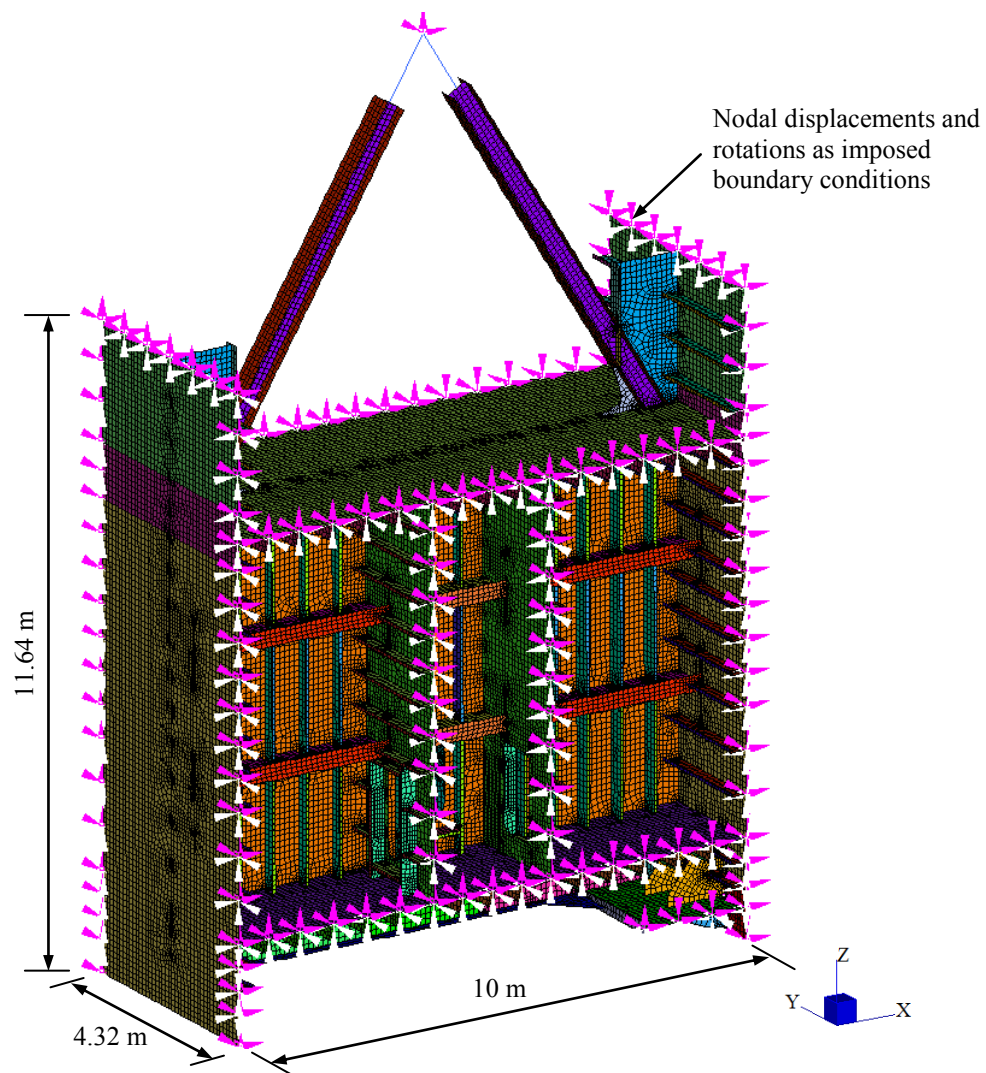


**Figure 8.3.** Coarse shell FE sub-model of the portion of buoyancy chamber under investigation. Overall dimensions and boundary conditions are also shown.

Global stress contours  $\sigma_x$ ,  $\sigma_y$  and  $\sigma_z$  are reported in Figures 8.4 to 8.6, respectively.

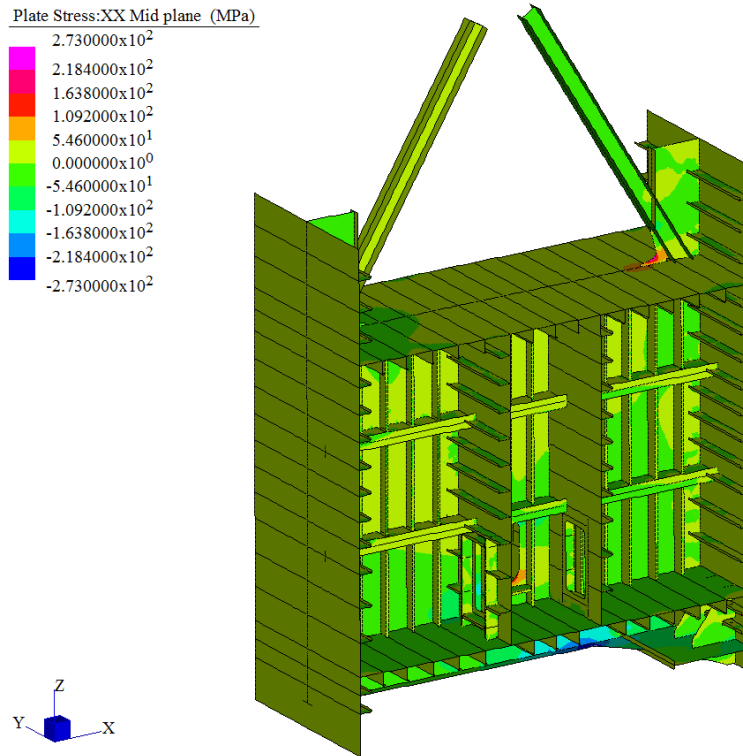


**Figure 8.4.** Global  $\sigma_x$  stress contour limited to  $\pm 273$  MPa (parent material fatigue strength at 125000 cycles, with  $\gamma_{Mf} = 1.15$  and endurable fatigue class 125 MPa at 2 million cycles).

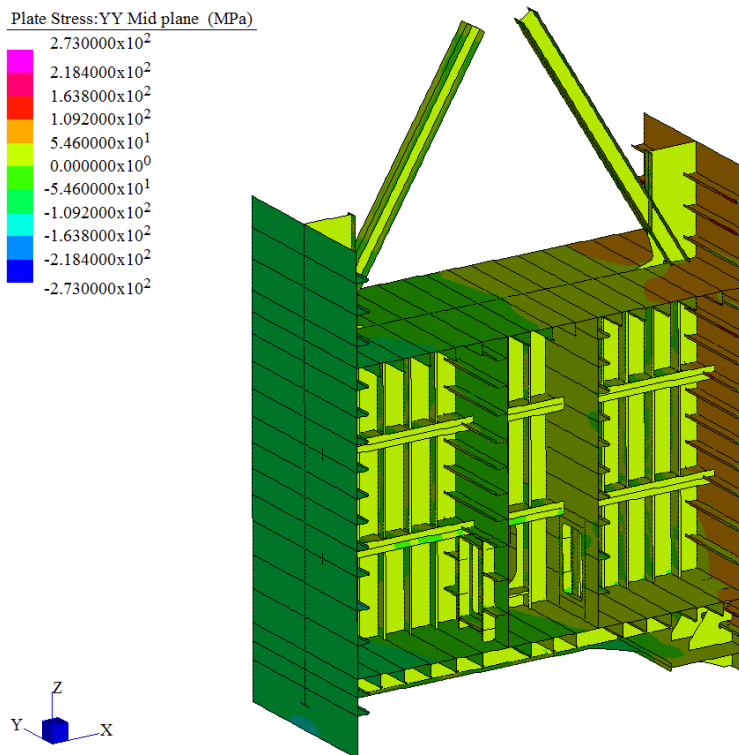


**Figure 8.5.** Global  $\sigma_y$  stress contour limited to  $\pm 273$  MPa (parent material fatigue strength at 125000 cycles, with  $\gamma_{Mf} = 1.15$  and endurable fatigue class 125 MPa at 2 million cycles).

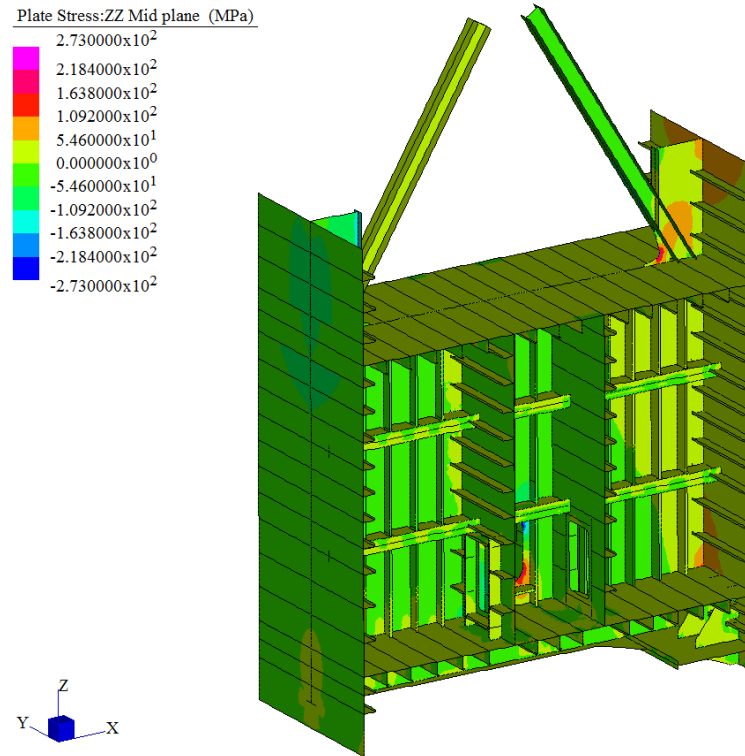


**Figure 8.6.** Global  $\sigma_z$  stress contour limited to  $\pm 273$  MPa (parent material fatigue strength at 125000 cycles, with  $\gamma_{Mf} = 1.15$  and endurable fatigue class 125 MPa at 2 million cycles).

### 8.3 “Manual” fatigue assessment procedure

#### 8.3.1 Method of analysis

The “manual” fatigue assessment is here performed according to the nominal stress method and, in particular, according to the allowable stress check (check type 8.2 in section 8 of EN 1993-1-9), according to which it must be verified:

$$\frac{\gamma_{Ff} \Delta\sigma_{E,2}}{\Delta\sigma_c / \gamma_{Mf}} \leq 1 \quad (8.1)$$

$$\frac{\gamma_{Ff} \Delta\tau_{E,2}}{\Delta\tau_c / \gamma_{Mf}} \leq 1 \quad (8.2)$$

where  $\gamma_{Ff}$  is the partial factor (here assumed equal to 1) for equivalent constant amplitude stress ranges  $\Delta\sigma_E$  and  $\Delta\tau_E$  related to 2 million cycles;  $\gamma_{Mf}$  is the partial factor (here assumed equal to 1.15) for fatigue strength ranges  $\Delta\sigma_c$  and  $\Delta\tau_c$  related to 2 million cycles.

Each weld detail is classified in an allowable fatigue stress range  $\Delta\sigma_C$  at  $2 \cdot 10^6$  cycles. This classification can be enlarged with a correction factor when the number of cycles is less than  $2 \cdot 10^6$ . Here, 125000 loading cycles are considered, thus:

$$\text{the correction factor on } \Delta\sigma_C \text{ is } \sqrt[3]{\frac{2 \cdot 10^6}{125000}} = 2.52 \quad (8.3)$$

$$\text{and the correction factor on } \Delta\tau_C \text{ is } \sqrt[5]{\frac{2 \cdot 10^6}{125000}} = 1.74 \quad (8.4)$$

The fatigue checks to be performed all around each weld (according to tables 8.2 to 8.10 of EN 1993-1-9) are summarized in Figures 7.22 to 7.27, depending on the type of joint.

Requiring the “manual” fatigue assessment of such a structure a remarkable waste of time, it can be considered legitimate to reduce, as far as possible, such number of checks (e.g. 20 all around of a double fillet or partial penetration welded joint). Here, only few checks have been performed along each weld, considering nodal stresses computed directly at plates’ intersections, therefore not distinguishing among weld sides. It follows that, with reference to a double fillet or partial penetration welded joint, the number of checks can be reduced from 20 to 5 (check types  $f_1$ , e, d,  $a_1$  and  $a_2$ , in Figure 7.22), whereas, being the case of a full penetration joint, the number of checks can be reduced from 16 to 4 (check types  $f_1$ , e, d, and b, in Figure 7.23).

The fatigue assessment of the parent material should be performed, in principle, assuming different fatigue classifications with reference to the free edges (weakened by cutting) and inner material. The former can be classified as 160 MPa and the latter as 125 MPa, according to table 8.1 of EN 1993-1-9. Also in this case, it can be considered legitimate to make a simplification by checking the whole parent material assuming endurable class 125 MPa.

The above presented approximations inevitably lead to a non-optimized (conservative) fatigue design. However, they are generally inevitable.

### 8.3.2 Designation of check lines

The portion of buoyancy chamber under investigation is characterized by 853 welds. It is worth noting that, considering that the volume such portion of model represents about 1/42 of the whole gate and assuming a uniform distribution of welds on the

volume, it can be estimated that the entire structure is composed of more than 35000 welds (in principle all to be checked for fatigue).

Limited to the portion of buoyancy chamber, an amount of about 80 welds over 853 has been identified as essential to be assessed for fatigue (Figures 8.7 to 8.12). It has been chosen only the most loaded weld for each kind of joint (grouping them in terms of geometry). To strictly perform such a reduction, in principle, the fatigue calculation should have already been done, which is a contradiction. Therefore, it has been done with a questionable degree of accuracy, “having a look” at global stress contours (e.g. those reported in Figures 8.4 to 8.6).

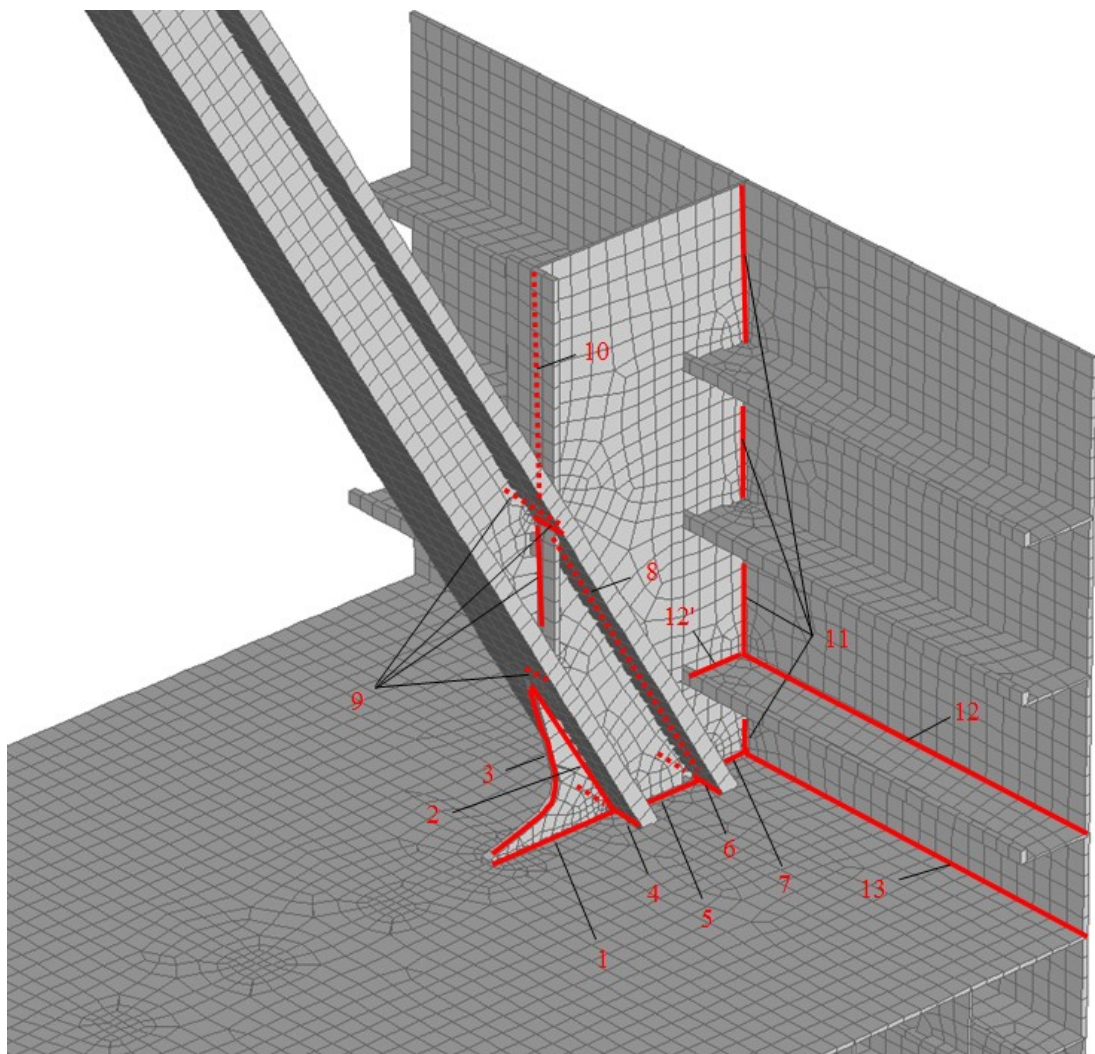


**Figure 8.7.** Top view of buoyancy chamber.



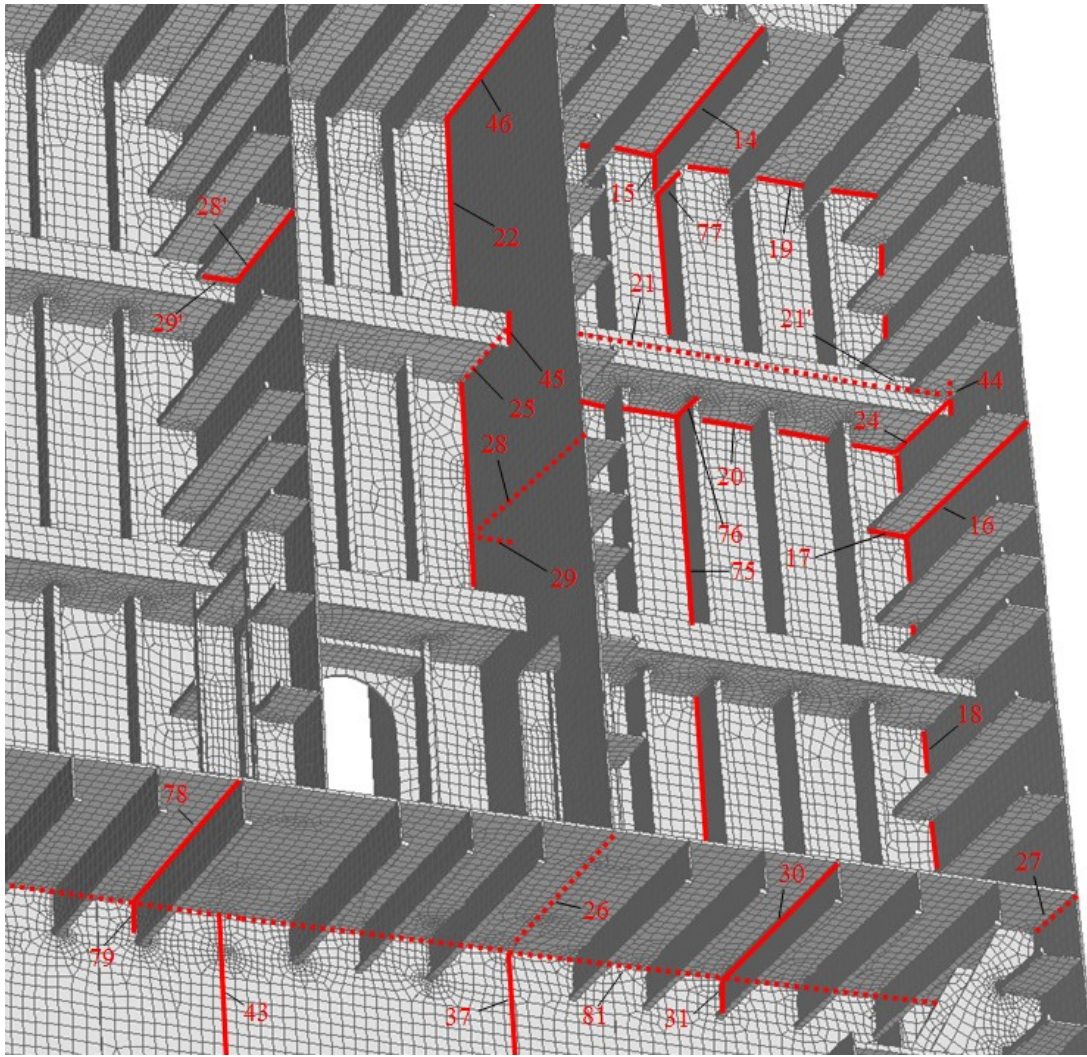


Figure 8.8. Inner view of buoyancy chamber.

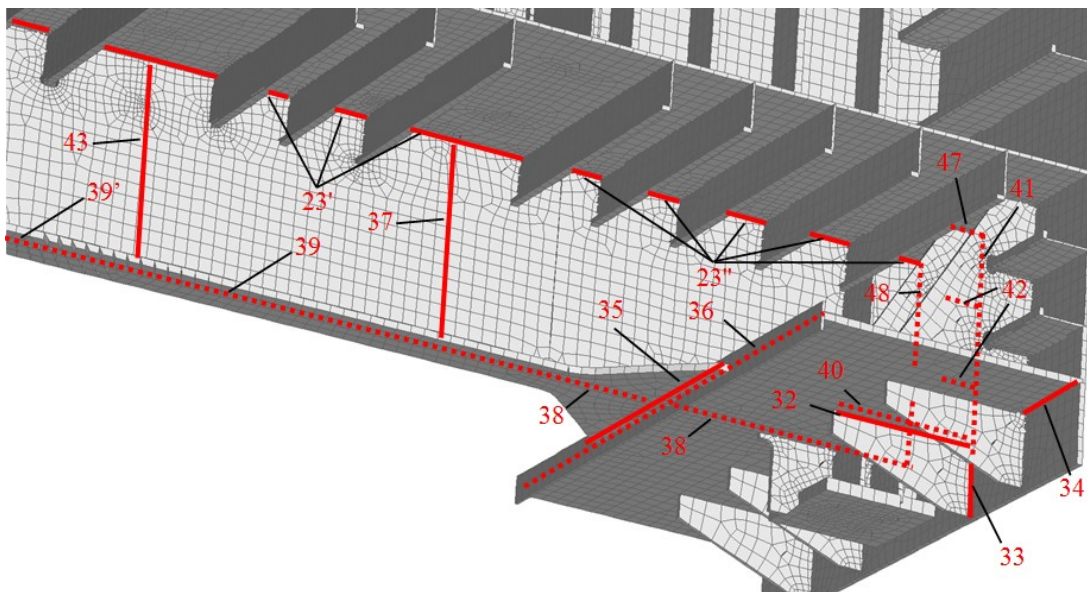
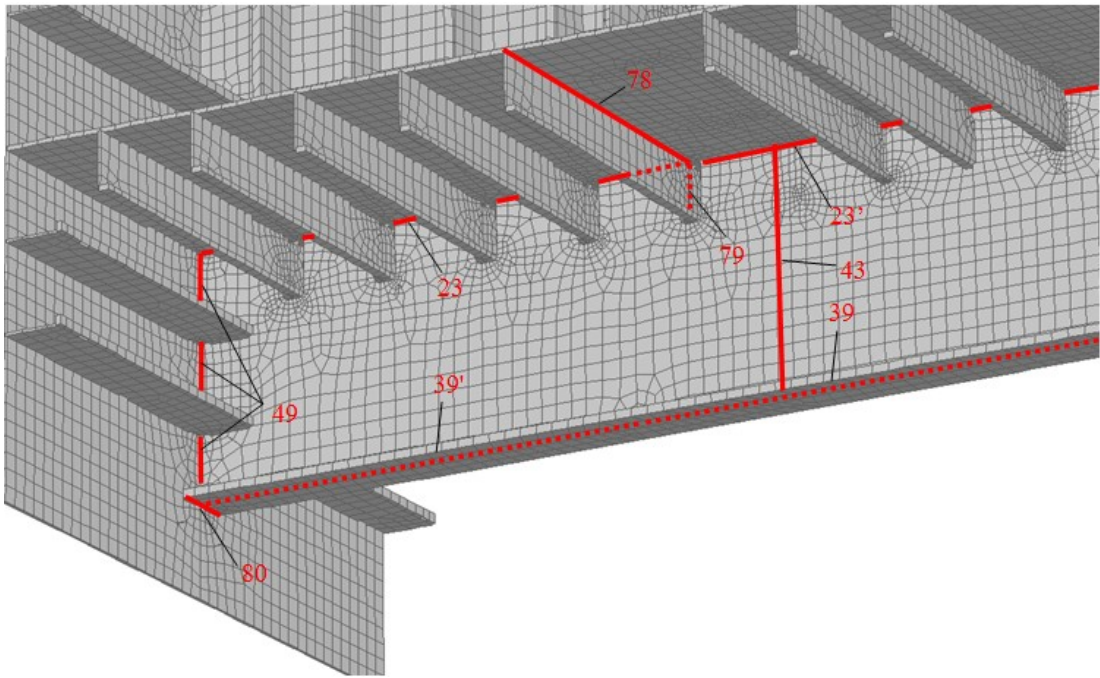
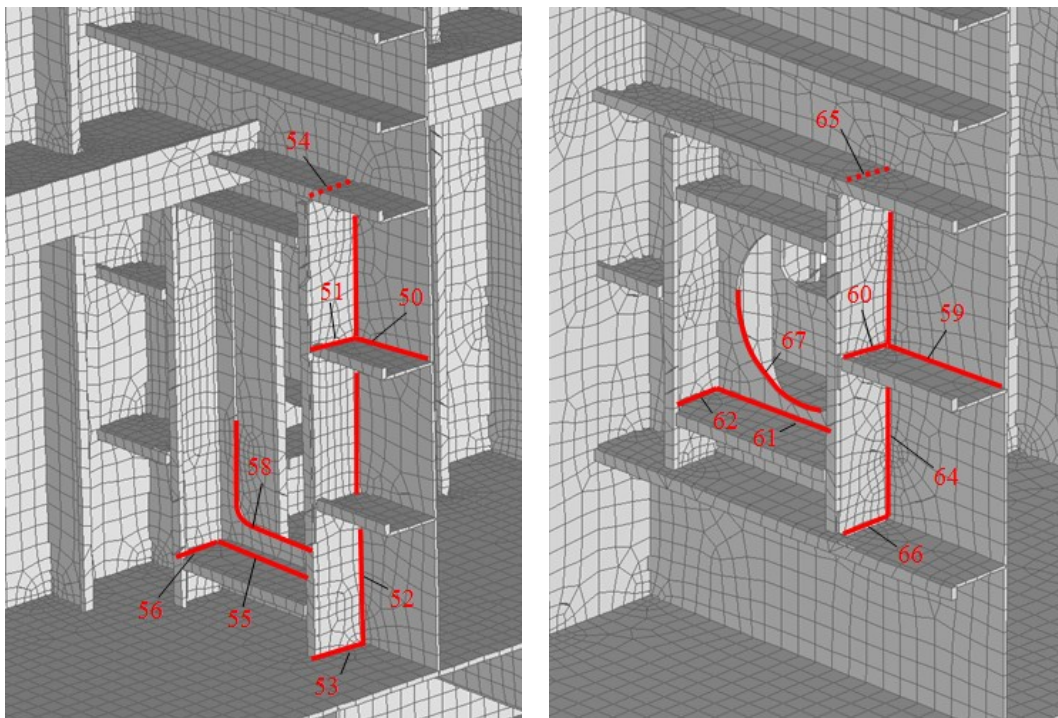


Figure 8.9. Bottom view of buoyancy chamber (lateral bearing side).



**Figure 8.10.** Bottom view of buoyancy chamber (opposite to lateral bearing side).



**Figure 8.11.** Inside views of buoyancy chamber (corridor wall openings).



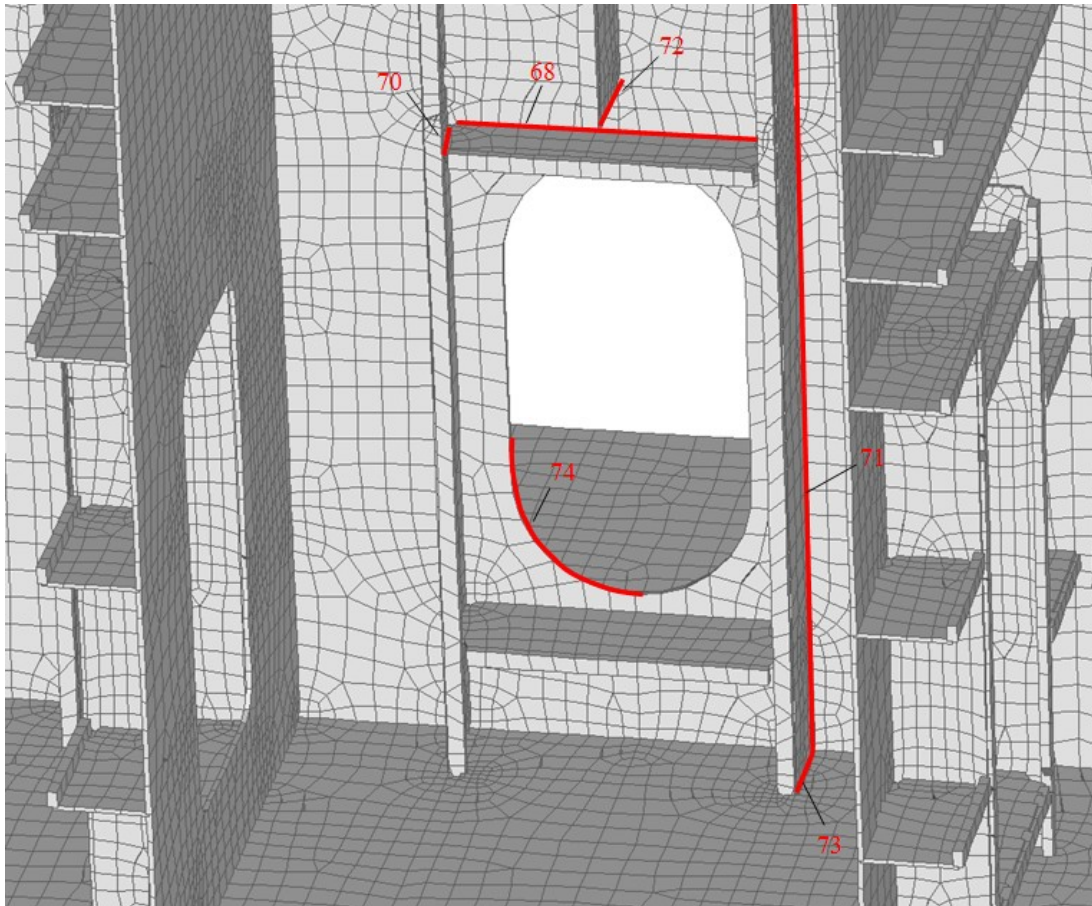


**Figure 8.12.** Inside view of buoyancy chamber (transverse bulkhead opening).

### 8.3.3 Fatigue assessment

The results of the fatigue assessment are summarized in Table 8.1, limited to some of the check lines identified in Figure 8.9. The first column reports the identifying number of the check line (with reference to Figure 8.9) and the stress component ( $\parallel$ , T and S signifying parallel, orthogonal and shear stress components, respectively) used in the check types listed in the second column (where the first two numbers indicate the reference table and the number between brackets indicates the detail number, in EN 1993-1-9). Parameters  $t$ ,  $l$  and  $L$  are related to the reference detail and determine the fatigue class. Permissible stresses have been calculated multiplying the fatigue classes by the correction factors on  $\Delta\sigma_C$  and  $\Delta\tau_C$  defined by Equations (8.3) and (8.4), respectively. Computed stresses have been obtained by the FE model directly by picking stresses at plates' intersection. Finally, the last column reports the utilization coefficient, defined by Equations (8.1) and (8.2) for normal and shear stress components, respectively.



**Table 8.1.** Summary of fatigue assessments of some check lines from Figure 8.9.

Check line nr. [-]	Reference fatigue detail (EN 1993-1-9)				Type	Weld size <i>a</i> [mm]	Fatigue class	Permissible stress		Computed stress		UC
	Tab.(det.)	<i>t</i>	<i>l</i>	<i>L</i>				$\Delta\sigma_c$	$\Delta\tau_c$	$\Delta\sigma$	$\Delta\tau$	
	[-]	[mm]	[mm]	[mm]				[-]	[mm]	[-]	[N/mm <sup>2</sup> ]	
32 //	8.4(1)	50		1000			56	123		122		0.99
32 //	8.2(5)	50					100	219		150		0.68
32 T	8.4(6)	50	38		PJP	14	80	175		63		0.36
32 T	8.5(3)	30					36	79		75		0.95
32 S	8.5(8)	30					80		121		70	0.58
33 //	8.4(1)	40		500			56	123		4		0.03
33 //	8.2(5)	40					100	219		22		0.10
33 T	8.4(6)	40	50		PJP	20	80	175		105		0.60
33 T	8.5(3)	30					36	79		73		0.92
33 S	8.5(8)	30					80		121		38	0.31
34 //	8.4(1)	40		-			56	123		42		0.34
34 //	8.2(5)	40					100	219		114		0.52
34 T	8.4(1)*	40	82		PJP	36	63	138		70		0.51
34 T	8.5(3)	50					36	79		78		0.99
34 S	8.5(8)	50					80		121		53	0.44
40 //	8.4(1)	50		1000			56	123		110		0.90
40 //	8.2(5)	50					100	219		111		0.51
40 T	8.4(6)	50	50		DFW	10	71	156		44		0.28
40 T	8.5(3)	30					36	79		54		0.68
40 S	8.5(8)	30					80		121		84	0.69
41 //	8.4(1)	18		1170			56	123		54		0.44
41 //	8.2(5)	18					100	219		38		0.17
41 T	8.4(6)	18	34		CJP	16	80	175		83		0.47
41 T	8.5(1)	30	34				80	175		152		0.87
42 //	8.4(1)	12		265			56	123		13		0.11
42 //	8.2(5)	12					100	219		17		0.08
42 T	8.4(6)	12	40		DFW	5	80	175		83		0.47
42 T	8.5(3)	30					36	79		63		0.80
42 S	8.5(8)	30					80		121		78	0.64
47 //	8.4(1)	30		260			56	123		16		0.13
47 //	8.2(5)	30					100	219		14		0.06
47 T	8.4(6)	30	40		DFW	5	80	175		56		0.32
47 T	8.5(3)	30					36	79		60		0.76
47 S	8.5(8)	30					80		121		84	0.69

// = Stress parallel to weld bead; T = Stress orthogonal to weld bead; S = Shear stress

Nomenclature:

CJP = Full penetration weld; PJP = Partial penetration weld; DFW = Double fillet weld

Weld size:

In case of double fillet welds: *a* = throat size of a single bead

In case of partial penetration weld: bead on both sides and *a* = throat size of a single bead

Note: 8.4(1)\* means that detail 8.4(1) has been used in place of detail 8.4(6) whenever *l* > 80 mm

## 8.4 Automatic fatigue assessment with PostFatigue

In this section, the basic steps of the almost automatic fatigue assessment procedure made possible by PostFatigue are presented.

Once the Straus7® model and results have been acquired in PostFatigue, fatigue load groups and Eurocode parameters have to be set, as shown in Section 7.3. A unique loading condition characterized by a number of cycles equal to 125000 has been defined, similarly to Figure 7.6(b). In such case, stresses induced by the loading condition are considered by PostFatigue directly as stress ranges. The partial safety factors  $\gamma_{Ff}$  and  $\gamma_{Mf}$  have been set to 1 and 1.15, respectively (as in Figure 7.7). The material definition, which is a linear elastic steel having Young's modulus of 210 GPa and Poisson's ratio equal to 0.3, is automatically acquired by Straus7® model. Then, the fatigue details related to the parent material have to be set according to the procedure described in Section 7.5. PostFatigue automatically recognizes the free edges by the inner material, allowing an easy and rapid differentiation among the related fatigue classes (Figure 8.13). Here, it is assumed fatigue class 125 MPa for all free edges and fatigue class 160 MPa for the inner material.

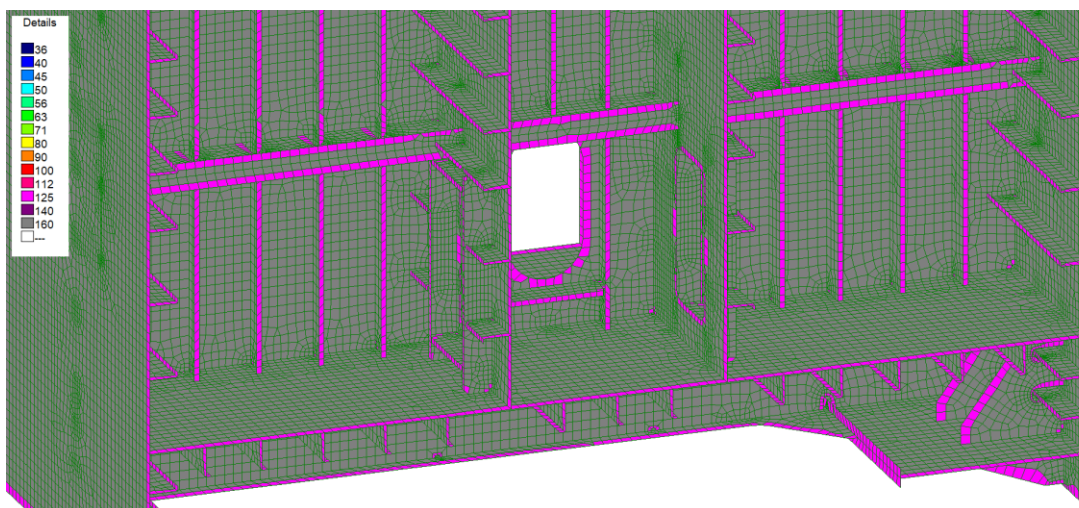


**Figure 8.13.** Inside view of buoyancy chamber. PostFatigue automatically distinguishes among free edges and inner material, permitting a fatigue class differentiation. For an easy check, assigned fatigue classes are graphically plotted on the model.

The next step in PostFatigue is the automatic finding of check lines, according to Section 7.6. As anticipated in Section 4.3.2, the post-processor has identified 853 welds (Figure 8.14 shows some of them).

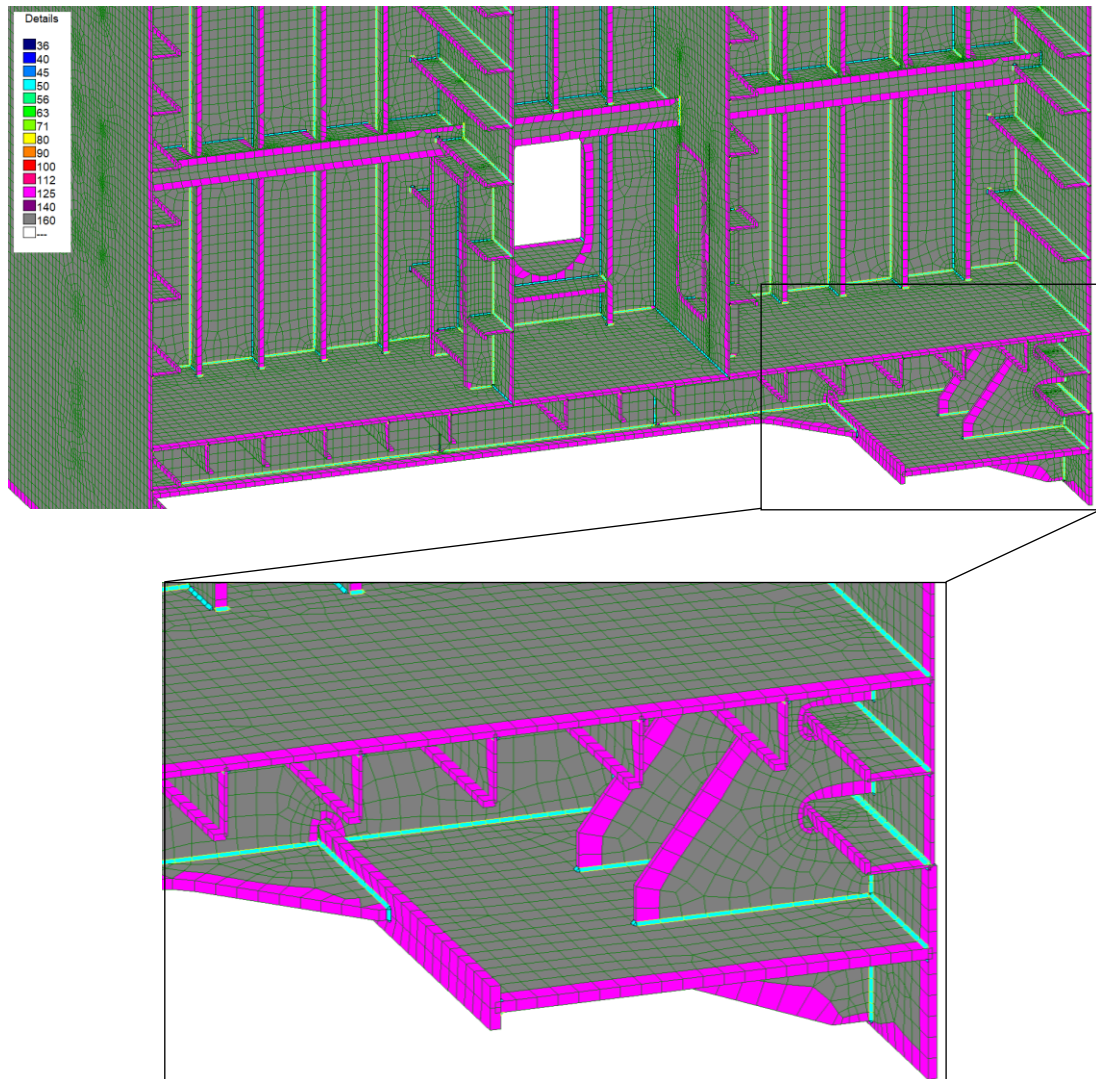


**Figure 8.14.** Inside view of buoyancy chamber. PostFatigue automatically recognizes weld lines (light blue in the figure). Fatigue classes assigned to the parent material are also shown.

Once the weld lines have been identified, it is required to define the weld geometry by using the weld design tool presented in Section 7.6.2. In this way, information about the kind of joint (e.g. partial penetration or full penetration welds), as well as the weld shape and the throat dimension, are acquired. This information, together with plate thicknesses (which are automatically acquired by Straus7® model), is used by PostFatigue to assign standard details (see Section 7.6.1), to define  $k_b$  in the modified nominal stress approach and to compute the local SED. Moreover, such information is needed to define edge and head offsets, where the nominal stress has to be computed (see Section 7.6.3). Stress offsets automatically generated are shown in Figure 8.15.

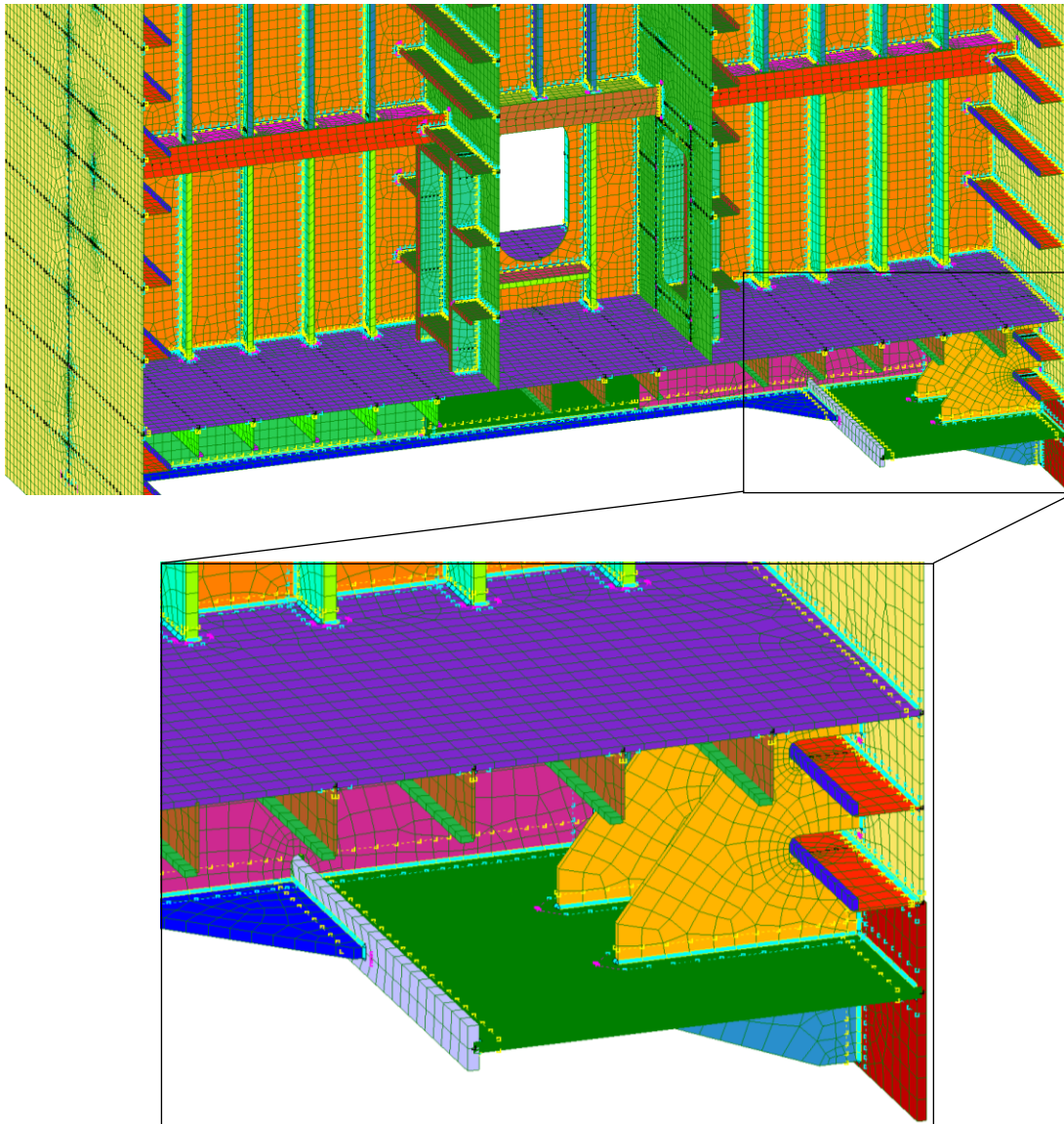


**Figure 8.15.** Inside view of buoyancy chamber. Automatic definition of head and edge offsets for nominal stress computing.

By now, it is possible to start the fatigue assessment. The fastest approach is to perform the global screening procedure, which permits to assess parent material and welds all at once, assuming a fixed endurable fatigue class (see Section 7.7). The default classes 56 MPa (36 MPa for the weld root only) and 125 MPa have been assumed for welds and parent material, respectively. The global fatigue screening output (damage contour) is shown in Figure 8.16. By so doing, a continuously colored map gives the fatigue damage distribution on the material (regardless of whether parent material or welds are considered). In Figure 8.16 the same set of welds “manually” checked in Table 8.1 has been considered.



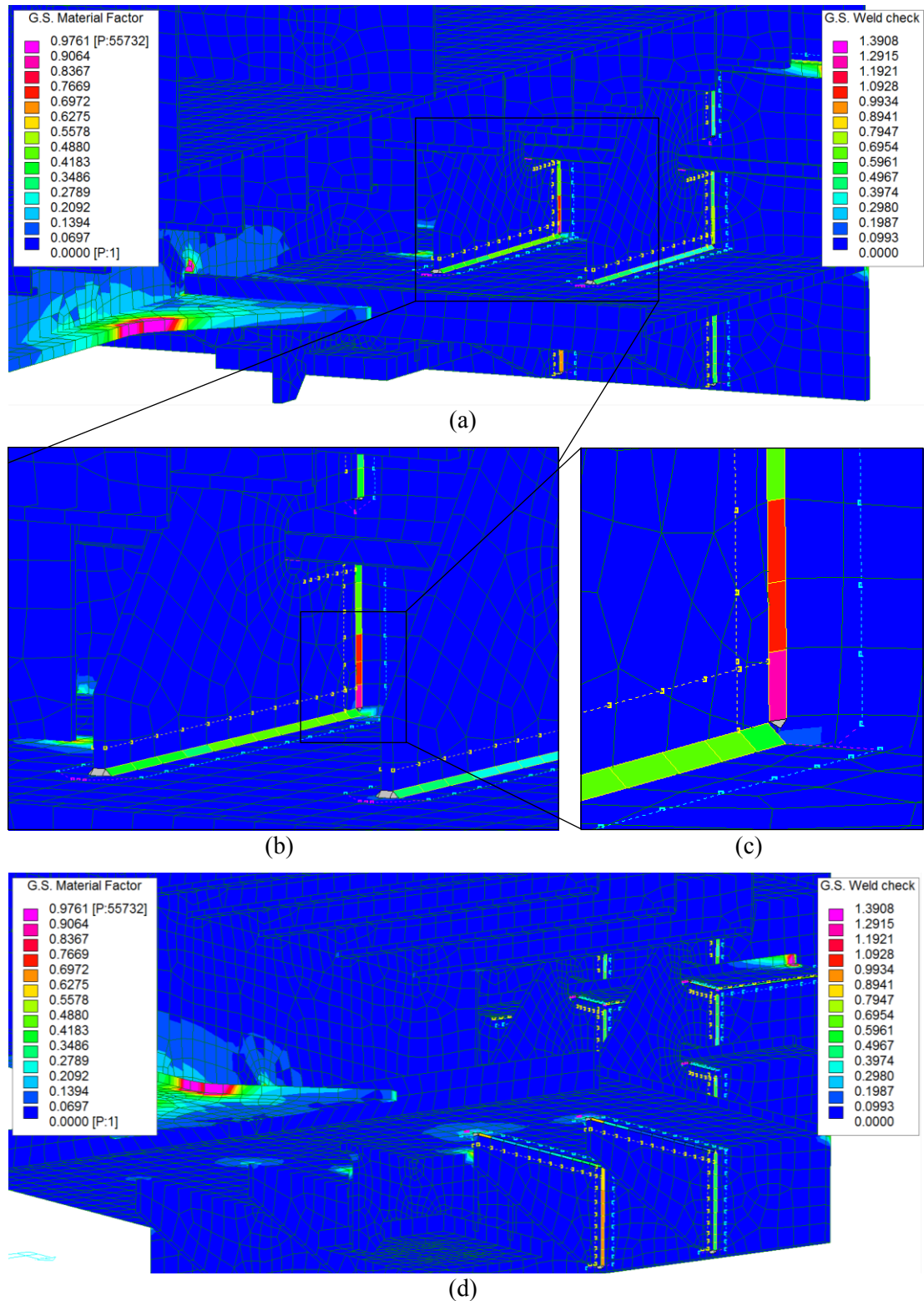


**Figure 8.16.** Automatic definition of head and edge offsets for nominal stress computing.

Figure 8.16 permits to point out that all welds and parent material (at least within the portion of model here considered) are checked in terms of global fatigue screening (being the damage contour less than 1), with the only exception of weld number 41

(according to numbering in Figure 8.9), on which the damage reaches the value 1.39 (Figure 8.16(c)). Such weld has therefore to be re-assessed by using the detailed procedure (16 checks all around the weld, being a full penetration joint), according to Section 7.6. First, the full penetration T-joint standard details have to be assigned (Figures 7.21 and 7.23), then, by using the procedure described in Section 7.6.4 and the dialog window of Figure 7.32, the detailed fatigue check is performed by using the modified nominal stress. Detailed results are summarized in Figure 8.17.

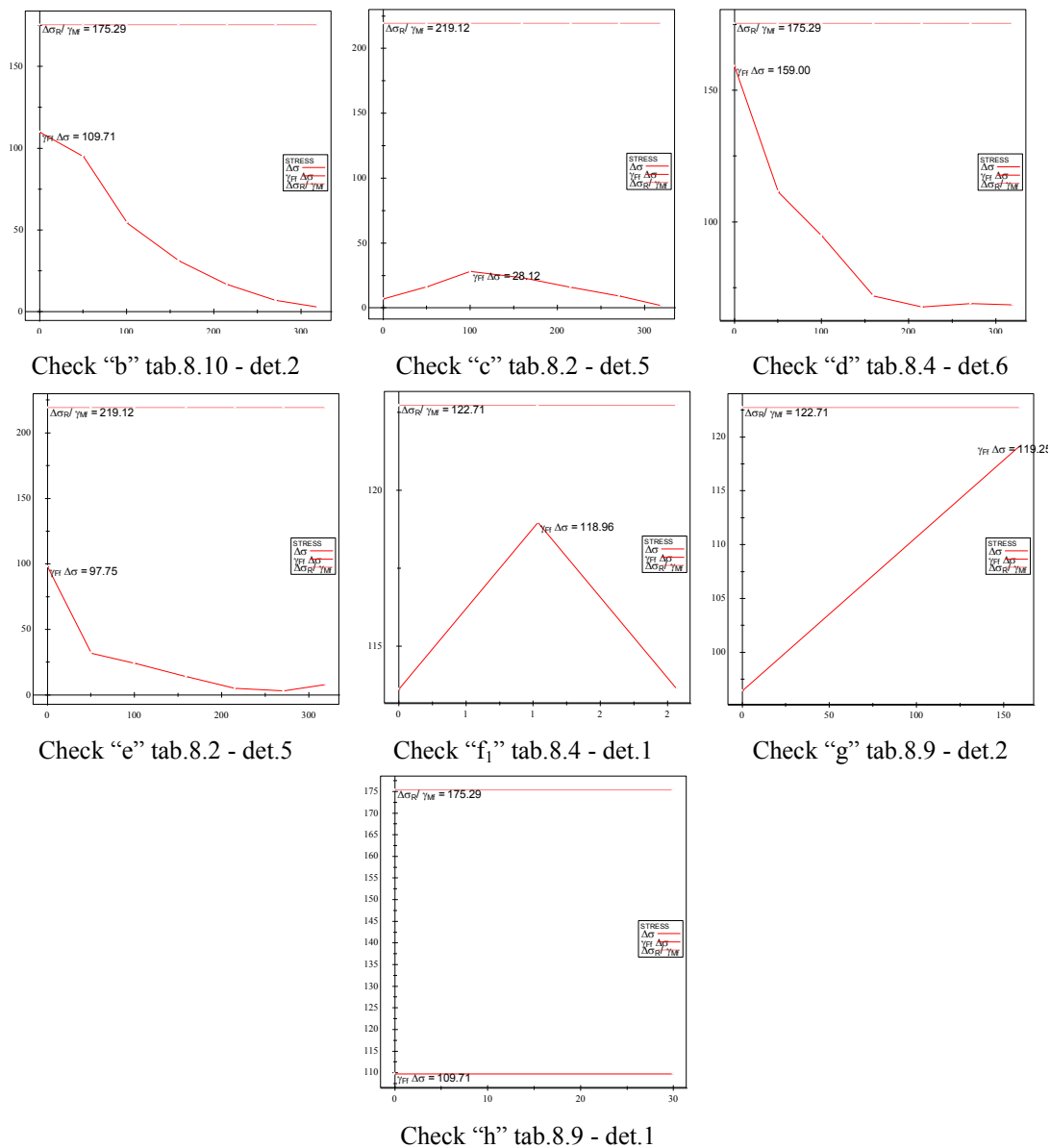


**Figure 8.17.** Trend check type 8.2 of EN 1993-1-9 along the weld number 41. Check designation "b", "c", "d", "e", "f<sub>1</sub>", "g" and "h" in accordance to Figure 7.23. Only the most loaded, among the two weld sides and the two weld ends, are here reported for brevity.

## 8.5 Discussion and conclusion

The purpose of this chapter was not to perform the complete fatigue analysis of a megastructure, which would be a repetitive and boring procedure. The aim was to provide the reader with a clear idea of what may mean performing such kind of assessment, in terms of number of analyses and data processing. To this end, a practical application, in principle not different from what a designer engineer faces every day, has been presented. The “manual”, fault susceptible and time consuming procedure has been compared with the automatic fatigue analysis by using PostFatigue. An example of large steel structure has been considered to this end.

It can be pointed out that a post-processor like PostFatigue not only speeds up the assessment procedure (e.g. limiting the detailed analysis to those few welds which do not pass the global screening), but makes the correct design of welds and parent material possible, no more justified through meaningless colored maps (stress contours). Critical points for fatigue can all be checked (locally, one by one) and the design is no longer inordinately conservative (at best) or random (in worst cases). In principle, such different designing approach makes it feasible to build structures that were not possible before. Just thinking that the endurable number of cycles and the nominal stress are usually linked by a power of 3 (which rises to 5 for shear stresses), it is clearly evident how “dangerous” the "on the safety side" principle could be, if applied to fatigue stresses. It automatically leads to a highly uneconomic design, or, even worse, leads to declare unfeasible projects without reason.

In the author’s opinion and, by now, maybe also in the reader’s one, having an automatic post-processor based on coarse shell element models and nominal stress components is today a key requirement. It is anachronistic (heritage of the past era of testing) thinking that nowadays structures (like the one here investigated) could be wholly analyzed according to the simple elastic beam theory, using the nominal stress method; but it is as anachronistic (futuristic, this time) believing that solid models and local approaches could be used on large scale. That is why to be effective, a finite element post-processor for fatigue assessment should not only eliminate the repetitive operations but also treat local FE stresses, not compatible, with the nominal stress method in a mathematically well-founded and unquestionable way. This was the guiding idea in the development of PostFatigue.





## **9. The PSM to rapidly calculate residual notch stress intensity factors in welded joints**

### **Highlights**

If the toe region of a welded joint is modeled as a sharp V-notch having zero radius, the distribution of the residual stresses in this area is singular and the degree of singularity follows the elastic-plastic solution in the close vicinity of the V-notch tip, while the singular, elastic solution might exist farther, if clamping conditions and process parameters present during welding cause reduced plasticity. It follows that the intensity of the local, linear elastic residual stress fields can be quantified by the residual notch stress intensity factors (R-NSIFs). In principle R-NSIFs can be included in NSIF based approaches for fatigue assessment of welded joints, even though this approach has not been formalized yet, so their calculation may be of great interest. The computational effort required to compute the R-NSIFs implies strong limitations of applicability in practice, due to the very refined meshes needed and to the non-linear transient nature of welding process simulations, especially in three-dimensional numerical models of large structures. The peak stress method (PSM) is a design approach which takes care of the industrial needs of rapidity and ease of use. According to the PSM, it is possible to evaluate the R-NSIFs by using the peak stress calculated at the point of singularity with coarse finite element (FE) models. While the PSM was originally calibrated by using Ansys® FE code, in the present chapter the PSM has been calibrated to rapidly estimate the R-NSIFs in Sysweld® FE environment.



## 9.1 Introduction

Structural integrity is not just an interesting research topic, but an essential requirement to guarantee public safety. There are many ways in which structural failures may occur: brittle fracture, plastic collapse, buckling and fatigue, to mention a few of them. External loads acting on a structure are usually considered in an engineering design process, but other factors may have a detrimental effect on structural strength: pre-existing microstructural features or defects and residual stresses, especially in large-scale components [1]. Unexpected failures may occur because residual stresses have critically combined with in-service stresses, or with the presence of undetected defects. Moreover, residual stresses due to welding processes could significantly affect high cycle fatigue (HCF) life of welded joints [2]: tensile residual stresses have unfavorable effects on HCF, whereas in the presence of compressive residual stresses the fatigue resistance is improved, which can be interpreted in terms of crack closure phenomenon [3–5]. Therefore, to improve structural integrity assessment procedures, it could be of interest to estimate residual stresses due to welding.

Numerical models can solve the full mathematical problem of a welding process, but a strong limitation is the large computational effort related to 3D models. A sufficiently fine mesh has to be used in order to consider the strong thermal and microstructural gradients in the heat affected zone and very short time steps are also necessary to reach the convergence because of the non-linearity of the problem. These are the reasons why 3D numerical models are still prohibitive, in particular in case of multi-pass welding and large geometries. As a consequence, the numerical models are usually 2D and only the plane perpendicular to the welding direction is considered, the out-of-plane behavior being taken into account through the generalized plane strain hypothesis. By using this approach, the residual stresses are in quite good agreement with experimental measurements [6–12].

In fatigue susceptible welded structures, cracks usually initiate and propagate from the weld toe and the weld root regions, which are stress concentration points. According to the notch stress intensity approach, the weld toe is modeled as a sharp V-notch (zero radius), as proposed in the literature in the last two decades [13–16]. The mode 1 and mode 2 notch stress intensity factors (NSIFs) quantify the magnitude of the asymptotic stress distribution according to Williams' exact solution

[17]. In case of weld-like geometries, the NSIFs quantify the intensity of the elastic stress field near the weld toe and the weld root, which take into account the overall joint geometry (both local, i.e. the weld shape effect, and global), the absolute dimensions and the loading condition. A contribution to the NSIF analysis [18] showed that near sharp V-notches thermal stresses induced by a steady thermal load have the same asymptotic nature of the stress fields induced by mechanical loads. As a consequence, new thermal-load-induced NSIFs have been defined as the natural extension of those dependent on external mechanical loads; in case of transient thermal loads, the notch stress intensity factors related to residual stresses are identified as residual notch stress intensity factors (R-NSIFs) [18,19]. In the literature [20] the R-NSIFs have been proposed to quantify the influence of residual stresses on high cycle fatigue life of butt-welded joints, where a negligible stress re-distribution due to local plasticity could be observed.

The main drawback in evaluating the R-NSIFs is that the asymptotic nature of the stress field close to the weld toe and root requires very refined finite element (FE) meshes, at least locally. The required degree of refinement is generally not easy to obtain in plane cases and very difficult in 3D cases. Additional computational effort is required by the transient and non-linear nature of the welding process simulations to compute R-NSIFs, compared to the linear elastic FE analyses to estimate the NSIFs [13,15,21] induced by external applied loads. Therefore, strong limitations of applicability in practical design situations arise.

Nisitani and Teranishi [22] showed that the linear elastic stress  $\sigma_{I,peak}$ , calculated at a crack tip through a linear elastic FE analysis characterized by a mesh pattern having a constant element size, can be used to estimate the mode I Stress Intensity Factor  $K_I$  for a crack initiating from an elliptical hole. In particular, they demonstrated that the  $K_I$  to  $\sigma_{I,peak}$  ratio depends only on the finite elements size and type, but does not depend on the crack size. As a consequence, the  $\sigma_{I,peak}$  value can be used to rapidly estimate the  $K_I$  value, assuming that both the mesh pattern and the finite element formulation have been previously calibrated on geometries for which the exact value of  $K_I$  is known. Meneghetti and Lazzarin [23] provided a theoretical justification to this approach, which was called peak stress method (PSM). Thereafter, aiming to rapidly assessing the fatigue strength of fillet welded joints, the PSM has been

extended to weld-like geometries and analytical expressions have been derived to estimate the NSIFs at the weld toe as well as the weld root [23–25].

In a recent work a preliminary investigation on the suitability of the PSM to rapidly estimate the R-NSIFs due to the welding process has been performed and a good accuracy has been found [26]. With this purpose, the weld toe region of a butt-welded joint was considered and residual stress fields were determined by means of the dedicated FE software Sysweld®. In the present chapter, the calibration of the PSM in Sysweld® environment is presented first. Mode 1 loading and generalized plane strain condition are considered. Afterwards, a practical application of the PSM to evaluate the R-NSIFs is illustrated. The obtained results are in agreement with those reported previously and support the use of the PSM to evaluate the residual notch stress intensity factors.

## 9.2. The PSM basic relations

The PSM analytical background has already been presented in Chapter 2, as well as the method's limitations and advantages. The purpose of this section is to summarize the basic PSM relationships referred to in this chapter.

In plane problems, the degree of singularity of linear elastic stress fields near sharp V-notches (having zero radius) has been given by Williams [17], both for mode 1 (opening) and mode 2 (sliding) loading, under the assumption of linear-elastic conditions. Considering a polar coordinate system  $(r, \theta)$  having its origin located at the sharp notch tip (Figure 9.1) and using only the first term of Williams' expansion series under mode 1 loading, the local stress field near the notch tip is described by:

$$\sigma_{ij}(r, \theta) = \frac{1}{\sqrt{2 \cdot \pi}} \cdot \frac{K_1}{r^{1-\lambda_i}} \cdot f_{ij}^1(\theta) \quad (i, j = r, \theta) \quad (9.1)$$

where  $f_{ij}^1(\theta)$  are angular functions, whose closed form expressions have been provided by Livieri and Lazzarin [27], and the exponent value  $\lambda_i$ , which is the degree of singularity, is defined by:

$$\sin(\lambda_1 q \pi) + \lambda_1 \sin(q \pi) = 0 \quad (9.2)$$

where  $q$  is related to the opening angle  $2\alpha$  by the expression  $2\alpha = \pi(2 - q)$ .

The mode 1 NSIF quantifies the intensity of the local stress field and it can be expressed, according to Gross and Mendelson [28], by means of:

$$K_I = \sqrt{2\pi} \lim_{r \rightarrow 0} r^{1-\lambda_I} \sigma_{\theta\theta}(r, \theta = 0) \quad (9.3)$$

where the stress components  $\sigma_{\theta\theta}$  and  $\sigma_{r\theta}$  are evaluated along the notch bisector (angular coordinate  $\theta = 0$ ). The stress singularity exponent  $\lambda_I$  refers to the notch opening angles  $2\alpha$  analyzed in the present work, which are equal to  $0^\circ$ ,  $90^\circ$  and  $135^\circ$ , and their values are 0.500, 0.544 and 0.674, respectively; as a consequence, Equation (9.1) contains a singular term ( $r^{\lambda_I-1}$ ) when  $r \rightarrow 0$ .

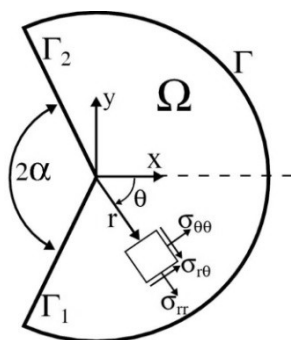


**Figure 9.1.** Domain  $\Omega$  for the sharp V-notch problem according to Williams' analytical frame.

According to the PSM, there exists an analytical expression which permits to estimate the mode 1 NSIF from the singular, linear elastic, mode 1 peak stress  $\sigma_{I,peak}$  computed at the point of singularity. In the case of welded joints, the points of singularity are both the weld toe and the weld root (see Figure 9.2). The PSM fundamental expression is [23]:

$$K_{FE}^* \cong \frac{K_I}{\sigma_{I,peak} \cdot d^{1-\lambda_I}} \quad (9.4)$$

where  $K_I$  is the exact mode 1 NSIF,  $\sigma_{I,peak}$  is the linear elastic peak stress,  $d$  is the average edge length of the finite element pattern generated by a free mesh generation algorithm, whereas the parameter  $K_{FE}^*$  is the non-dimensional mode 1 NSIF, which depends on: a) the adopted finite element formulation; b) the mesh pattern generated by the free meshing algorithm and c) nodal stress extrapolation and averaging criteria. Equation (9.4) can be applied within the limitations of applicability listed in the following section. Considering mode 1 loading, at present the PSM has been calibrated [23,29] in Ansys® FE environment for four-node quadrilateral plane elements and eight-node brick elements and sharp V-notches having opening angle

$2\alpha$  ranging from  $0^\circ$  to  $135^\circ$ . The mesh pattern generated automatically by the free mesh generation algorithm available in Ansys® was adopted [23,29], after setting the average element size  $d$  to be used. As a result, the typical mesh patterns at the notch tip are reported in Figure 2.10: four elements must share the node located at the notch tip if  $0^\circ \leq 2\alpha \leq 90^\circ$ ; two elements must share the node at the notch tip if  $90^\circ < 2\alpha \leq 135^\circ$ . If these conditions are fulfilled, the mode 1 PSM calibration constant is equal to  $K_{FE}^* = 1.38$  and, once fixed an arbitrary average finite element size  $d$  such that the mesh density ratio  $a/d$  is at least equal to 3, Equation (9.4) estimates  $K_I$  through the linear elastic peak stress  $\sigma_{I,peak}$  with a scatter band of  $\pm 3\%$ . Recently, the PSM has been calibrated also for other FE software packages different from Ansys® in case of plane FE models [30].

In the following section the PSM calibration in Sysweld® environment is presented, as well as the limitations of its applicability.

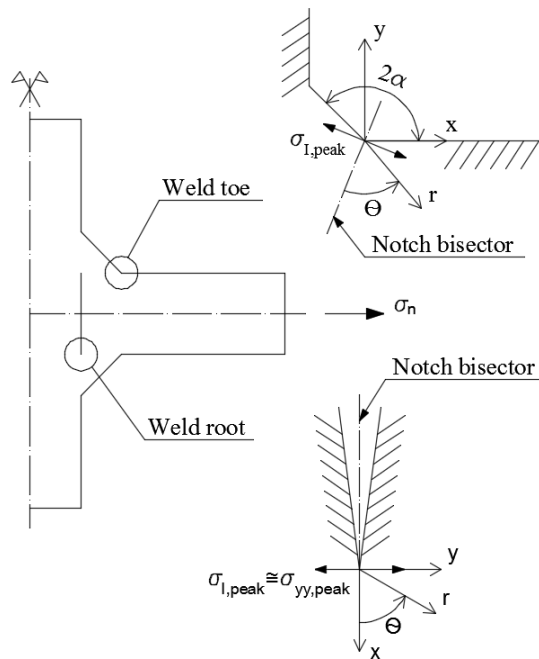


**Figure 9.2.** Schematization of weld toe and weld root as sharp V-notches having opening angles  $2\alpha=135^\circ$  and  $2\alpha=0^\circ$ , respectively. Definition of the mode 1 peak stresses  $\sigma_{I,peak}$  evaluated by means of linear elastic FE analysis.

### 9.3. Calibration of the PSM in Sysweld® environment

A number of two-dimensional FE models subjected to mode 1 loading conditions has been considered to calibrate the PSM in Sysweld® environment. For the sake of generality, geometries involved in the calibration consist in cracks, in pointed V-notches and in welded joints. The investigated geometries have been taken from the original calibration of the PSM performed in Ansys® software [23] under mode 1 loading and have already been summarized in Figure 4.6, with reference to the volume-free SED approach. It is worth to remember that they include: cracks at the tip of a U-notch (Figure 4.6(a)); edge cracks in a finite-width plate (Figure 4.6(b)); a plate with lateral open V-notches (Figure 4.6(c)) and a full-penetration cruciform welded joint having weld reinforcement angle equal to  $135^\circ$  (Figure 4.6(d)). The material is assumed to be a structural steel having Young's modulus  $E = 206000$  MPa and Poisson's ratio  $\nu = 0.3$ . A nominal stress equal to 1 MPa has been applied to the gross section. Taking advantage of the double symmetry of the investigated geometries, only a quarter of each model has been analyzed.

To calculate the peak stress values, linear elastic static analyses under generalized plane strain condition (the reason why the calibration has been performed under generalized plane strain is reported in Section 9.5) have been carried out in Sysweld® (release 12.0) and free mesh patterns according to the standard ones of PSM shown in Figure 9.3 have been used. The free mesh generation algorithm provided by Visual-Mesh (release 9.0) has been adopted after setting the desired average finite element size  $d$ . Four-node quadrilateral elements, i.e. 2004 type elements in Sysweld® library, have been chosen in the FE analyses. The numerical integration scheme was set to 2x2 Gauss points (full integration scheme), which is the default option in Sysweld®. Such choice is widely used in the literature when simulating the welding process, because it has proven to deliver results in good agreement with experimental residual stresses measurements [31–33].

By varying both the notch or crack size  $a$  and the finite element size  $d$ , many different mesh density ratios  $a/d$  have been considered. If the mesh pattern generated by the free mesh algorithm was not the standard one (Figure 9.3), the mesh would be simply re-generated after setting a slightly different FE size  $d$ . Most of the times the generated mesh fulfilled the standard requirements at the first attempt. In some cases the mesh had to be re-generated once; in ten out of the sixty-one analyses performed



(about the 15%) the mesh had to be re-generated twice. The final  $d$  value has obviously been adopted in Equation (9.4) to calculate the non-dimensional NSIF  $K_{FE}^*$ . Finally, the maximum principal stress  $\sigma_{I,peak}$  computed at the node located at the V-notch tip (Figure 9.2) has been considered. To apply the PSM correctly, nodal stress averaging must be activated, which is the default setting in Sysweld® and it consists in averaging the stress components extrapolated at FE nodes and afterwards in computing the nodal principal stresses from the nodal averaged components.

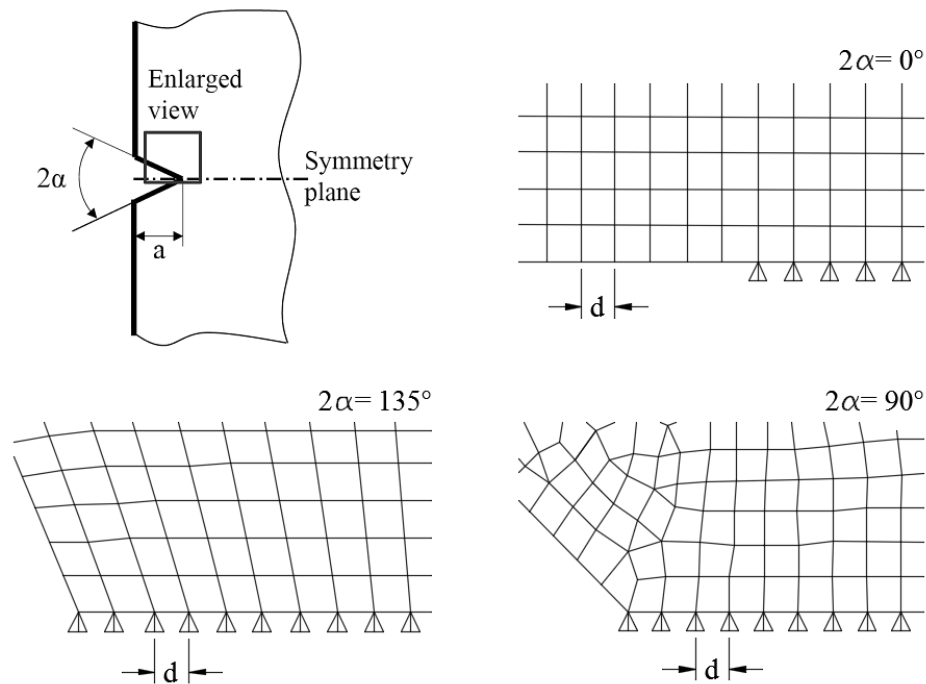


**Figure 9.3.** Standard PSM mesh patterns generated by Visual-Mesh free meshing algorithm.

The exact values of mode 1 NSIFs  $K_I$ , needed to compute  $K_{FE}^*$  according to Equation (9.4), were obtained from local stress fields computed through Ansys® software with very fine mesh patterns, where the size adopted in the FE mesh was on the order of  $10^{-5}$  mm, according to Lazzarin and Tovo [13].

The obtained results are shown in Figure 9.4 where the non-dimensional ratio  $K_{FE}^*$  defined by Equation (9.4) is plotted as a function of the mesh density ratio  $a/d$ . Figure 9.4 shows that the computed values of  $K_{FE}^*$  are arranged in two separated scatter bands, depending on the notch opening angle. More precisely, the upper scatter band with  $K_{FE}^* = 1.90 \pm 5\%$  refers to the geometries represented in Figure 4.6(a-b), having notch opening angle  $2\alpha = 0^\circ$ , while the lower scatter band with

$K_{FE}^* = 1.64 \pm 5\%$  refers to the geometries showed in Figure 4.6(c-d), having notch opening angle equal to  $90^\circ$  and  $135^\circ$ . In both cases, the convergence is guaranteed for a mesh density ratio  $a/d \geq 4$ , which is slightly different from the original calibration [23], where convergence was achieved for a mesh density ratio  $a/d > 3$ .

It is worth summarizing in the following the pre- and post-processing options under which the results shown in Figure 9.4 are valid:

- i) four-node quadrilateral elements from Sysweld® library with full integration scheme;
- ii) generalized plane strain condition;
- iii) free meshing algorithm implemented in Visual-Mesh;
- iv) nodal principal stresses calculated from averaged nodal components (default option in Sysweld®).

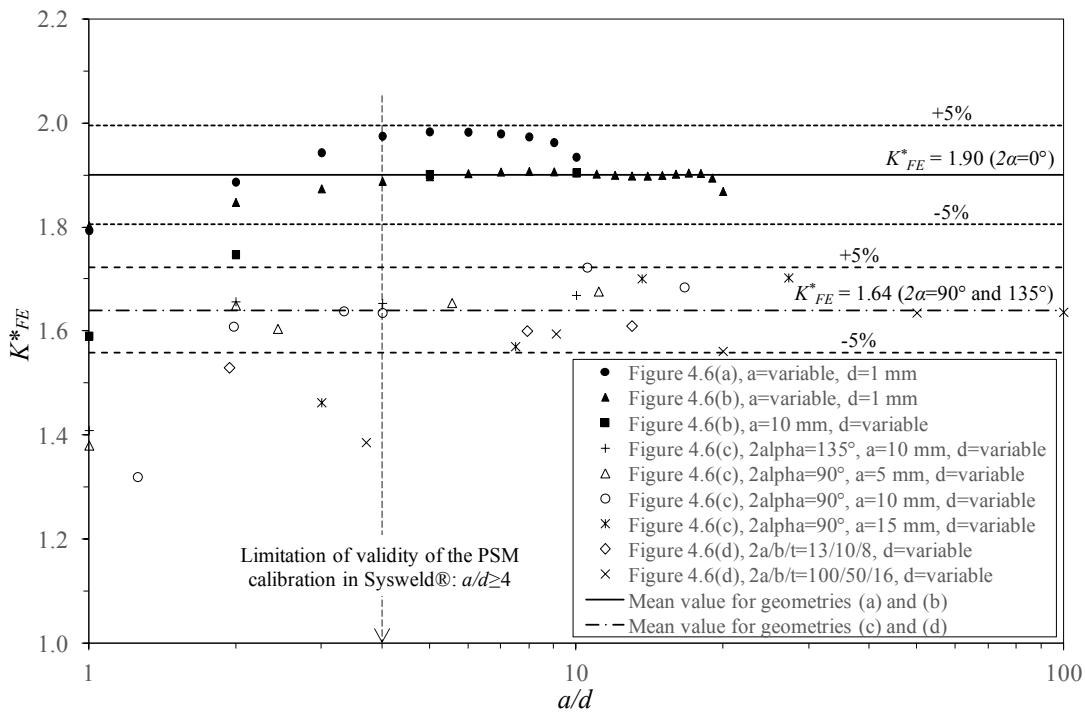


**Figure 9.4.** Non-dimensional mode 1 NSIF  $K_{FE}^*$  evaluated from the 61 calibration FE analyses (see Figure 4.6) in Sysweld® environment. Full integration scheme and stress averaging from nodal stress components are used.

## 9.4. Discussion on the PSM calibration

In the original PSM calibration performed in Ansys® environment [23], the non-dimensional NSIF  $K_{FE}^*$  was found to be equal to 1.38 under mode 1 loading condition, with a scatter of  $\pm 3\%$  for the same geometries investigated here. Conversely, different mean values of  $K_{FE}^*$  for different notch opening angles and slightly wider scatter bands have been found in the present work, as reported in Figure 9.4. This outcome is justified by the dependence of the PSM on the FE formulation of a given software package and FE analysis settings, which have previously mentioned: (i) the adopted finite element formulation; (ii) the mesh pattern generated by the free meshing algorithm and (iii) nodal stress extrapolation and averaging criteria.

Let us first mention that the nodal stress extrapolation and averaging criteria are the same in Sysweld® and in Ansys®. In summary, nodal stresses in the element are extrapolated from the integration points of finite elements and then nodal stress components are calculated by averaging the nodal stresses of the elements sharing that node. Principal stresses are eventually calculated from averaged nodal stress components. In Ansys® this method is called *average from components (AVPRIN,0 setting)*.

The reason for the differences of  $K_{FE}^*$  values between Sysweld® and Ansys® is primarily the finite element formulation (i.e. the integration scheme) of the adopted four-node quadrilateral elements and, less importantly, the mesh pattern. The original calibration of the PSM was carried out by setting the so-called *simple enhanced strain* element formulation, which is a particular 2x2 full integration scheme provided by Ansys® to avoid shear locking phenomena; however, the aforementioned integration scheme being not available in Sysweld®, the 2x2 standard full integration scheme has been adopted. It is the default setting in Sysweld®.

It could be verified that, if a different nodal principal stress evaluation method had been available in Sysweld®, then a unique scatter band could have been obtained, independently of the notch opening angle. Such different evaluation method consists in calculating first the principal stresses at the nodes of each finite element and afterwards in averaging the principal stresses at the node shared by the finite elements. In Ansys® such procedure is called *average from principals (AVPRIN,1*

setting). Several software packages make both the *average from components* technique and the *average from principals* technique available, one of them being the default setting (in Ansys® it is the *average from components* technique) and the other one being able to be activated by the FE analyst [30].

Therefore, the 61 calibration analyses have been repeated by importing in Ansys® environment the same FE meshes generated through Visual-Mesh and previously used to calibrate Sysweld®. Obviously, material elastic constants and boundary conditions have been set the same. Linear, four-node finite elements (named Plane182 in Ansys® library) with standard 2x2 full integration scheme have been used and generalized plane strain condition has been set in order to match exactly Sysweld® in the preparation of the numerical analysis. After solving the FE models in Ansys®, the *average from components* technique (*AVPRIN,0* setting) has been activated in post-processor environment with the purpose to fully match the analysis procedure performed in Sysweld®, including the nodal stress averaging option. Figure 9.5 summarizes the results and shows that the non-dimensional ratios  $K_{FE}^*$  are arranged in two separated bands, which have the same scatter and mean value of those computed with Sysweld® in previous Figure 9.4. Then, the *average from principals* technique (*AVPRIN,1* setting) has been activated in Ansys® post-processor environment and all results have been re-evaluated. By so doing, the analysis procedure performed in Ansys® matched again the one conducted in Sysweld®, the sole exception being the nodal stress averaging option. Figure 9.6 reports the results and shows that the non-dimensional ratio  $K_{FE}^*$  becomes equal to 1.55 with a scatter of  $\pm 5\%$ . The improvement achieved in the summary of all results can be appreciated by comparison with previous Figure 9.4. That said, calibrations shown in Figure 9.5 and in Figure 9.6 have not been used further, Sysweld® being the FE software which the present work is focused on.

To conclude this section, it should be mentioned that, according to the preliminary calibration performed recently [26], a constant ratio  $K_{FE}^*=1.71$  was proposed. This value falls inside the scatter band  $K_{FE}^*=1.64\pm 5\%$  suggested in this work by performing more extensive numerical investigations.

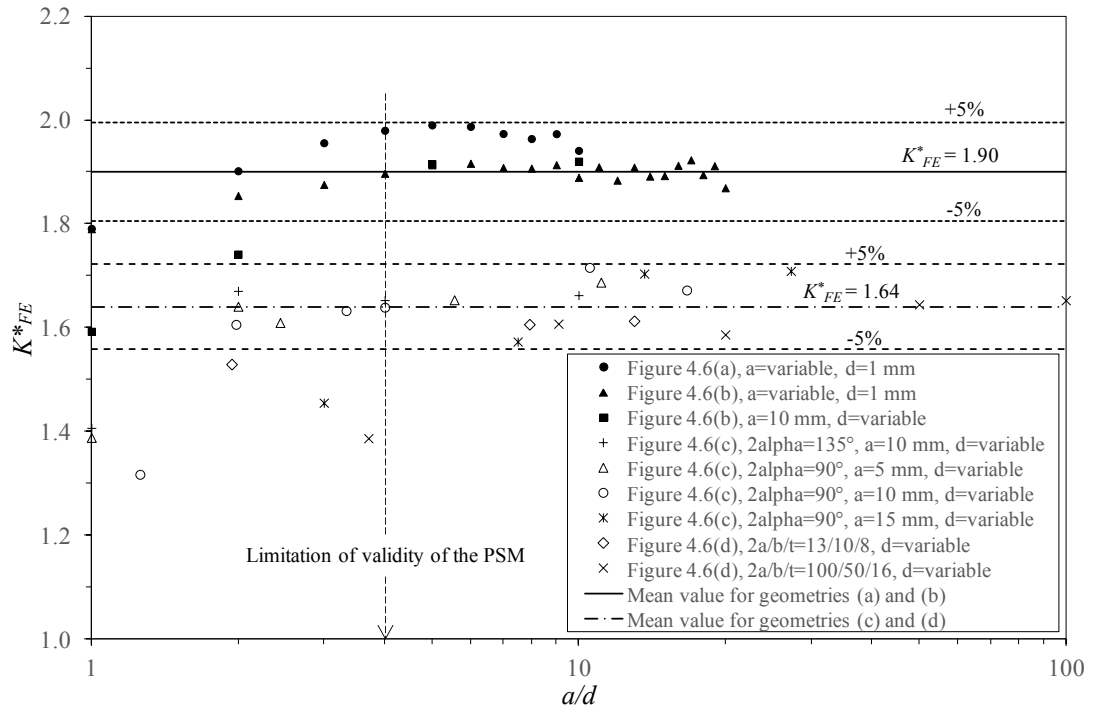


**Figure 9.5.** Non-dimensional mode 1 NSIF  $K_{FE}^*$  evaluated by using Ansys® and the same free meshes adopted in Figure 9.4. Full integration scheme and stress averaging from nodal stress components are used.

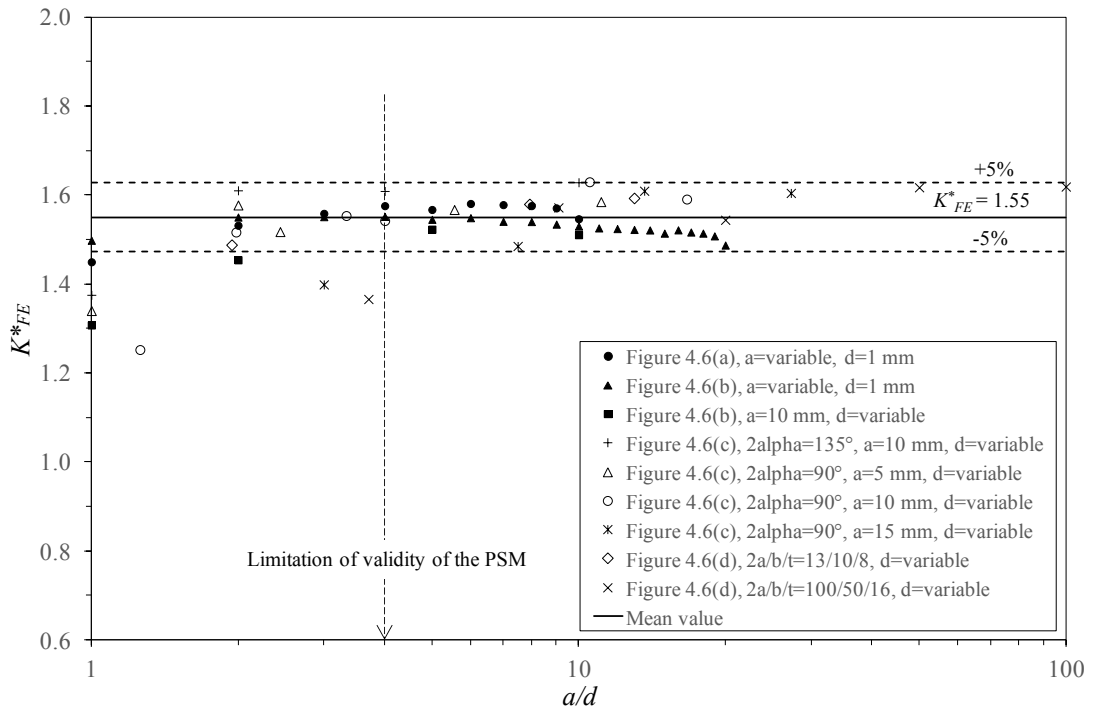


**Figure 9.6.** Non-dimensional mode 1 NSIF  $K_{FE}^*$  evaluated by using Ansys® from results reported in Figure 9.5 by activating stress averaging from nodal principal stresses.

### 9.5. Rapid R-NSIF estimation by using the PSM

To illustrate the use of the PSM to evaluate the R-NSIFs, a 6-mm-thick butt-welded joint has been analyzed using the finite element code Sysweld®, under generalized plane strain hypothesis. It was shown that this assumption better describes the out-of-plane stress values in the 2D cross-section model of the welding process [34].

The welded joint geometry and the assumed dimensions are shown in Figure 9.7. According to the NSIF based approaches, the weld toe has been modeled as a sharp V-shaped notch. The notch opening angle  $2\alpha$  has been chosen equal to  $135^\circ$ .

The adopted carbon steel has chemical composition according to the ASTM SA 516 Standard (Grade 65 resp. 70) and the corresponding thermo-mechanical and thermo-metallurgical properties have been taken from Sysweld® database. In the metallurgical analysis the following phases have been included: martensite, bainite, ferrite-pearlite. The metallurgical transformations mainly depend on thermal history, with this dependence described by Continuous Cooling Transformation (CCT) diagrams, which plot the start and the end transformation temperatures as a function of cooling rate or cooling time. In the present work the diffusion-controlled phase transformations and the displacive martensitic transformation have been modeled according to Leblond and Devaux [35] and to Koistinen and Marburger [36] kinetic laws, respectively.

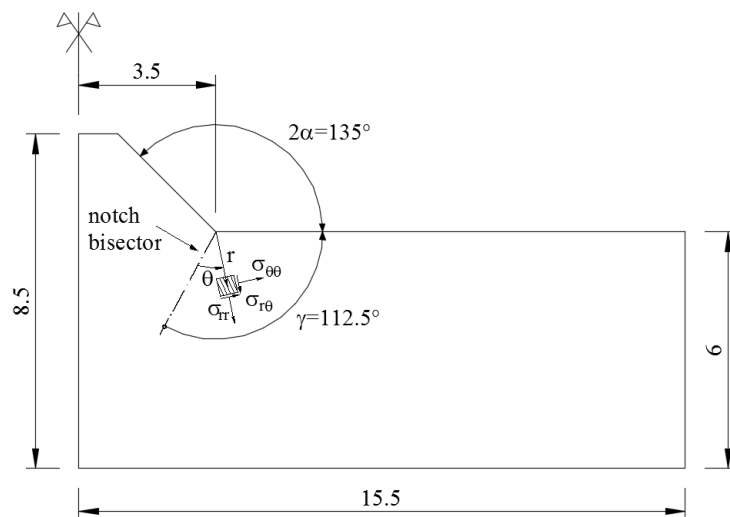


**Figure 9.7.** Schematic representation of the butt-welded joint considered in the present work and the polar coordinate system centered at the V-notch tip. Dimensions are in mm.

Radiative and convective heat losses have been applied at the boundary (external surfaces) of the plates to be joined. The former by using the Stefan-Boltzmann law, the latter by using a convective heat transfer coefficient equal to 25 W/m<sup>2</sup>K. The thermal gradient in the out-of-plane direction cannot be taken into account in a 2D cross-section model because of its intrinsic formulation. However, it is supposed that the higher the welding speed, the lower the out-of-plane thermal gradient.

The thermal energy flow into the material during the welding process represents the sole computational load modeled in the welding simulation. The amount of thermal energy flow into the material is determined by the welding parameters (including welding speed) and by the welding technology used. In this work the heat source has been modeled using a double ellipsoid power density distribution function [37] described by Equation (9.5), which has been widely used in literature for arc welding simulations [38].

$$q(x, y, t) = \frac{6\sqrt{3} f_{1,2} Q}{\pi\sqrt{\pi} a_0 b_0 c_{1,2}} e^{-\frac{3x^2}{a_0^2}} e^{-\frac{3y^2}{b_0^2}} e^{-\frac{3[v(\tau-t)]^2}{c_{1,2}^2}} \quad (9.5)$$

The double ellipsoid heat source and the meaning of the symbols used in Equation (9.5) are shown in Figure 9.8, whereas the adopted numerical values are summarized in Table 9.1.

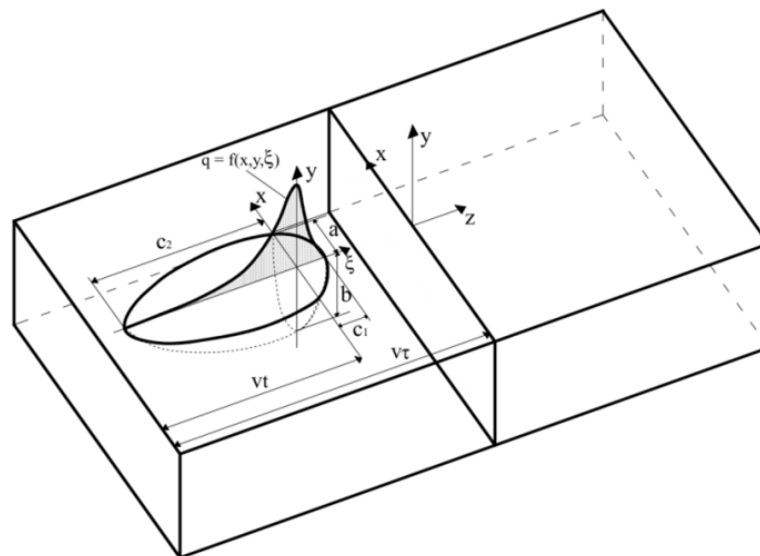


**Figure 9.8.** Double ellipsoid heat source configuration together with the power distribution function along the  $\xi$  axis of the moving coordinate system  $(x, y, \xi)$ . The transformation relating the fixed and the moving coordinate system is  $\xi = z + v(\tau - t)$ .

**Table 9.1.** Goldak's source parameters (used for the Al alloy).

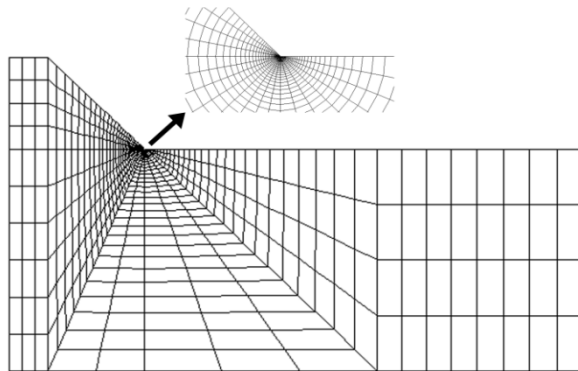
$q$	Power density [ $\text{W}/\text{m}^3$ ]	see Equation (9.5)
$Q^*$	Power input [W]	see Table 9.2
$\eta$	Efficiency	0.64
$\underline{Q}$	Absorbed power [W]	$\eta \cdot Q^*$
$a_0$		3.5
$b_0$	Molten pool dimensions [mm]	11
$c_1$		2.3
$c_2$		7.9
$f_1$	Fractions of heat deposit in the front and rear quadrants, with $f_1+f_2=2$ (subscript 1 for $\xi > 0$ ; subscript 2 for $\xi < 0$ )	0.6
$f_2$		1.4
$v$	Welding speed [mm/s]	11
$\tau$	Total time before the welding torch is over the transverse cross-section [s]	3

By taking advantage of the symmetry, only one half of the joint has been modeled. In Figure 9.9 the very refined mesh pattern used in the calculation of R-NSIF from the local stress field (Figure 9.9(a)) and two different meshes used for the PSM evaluation (Figure 9.9(b) and Figure 9.9(c)) are compared, respectively.

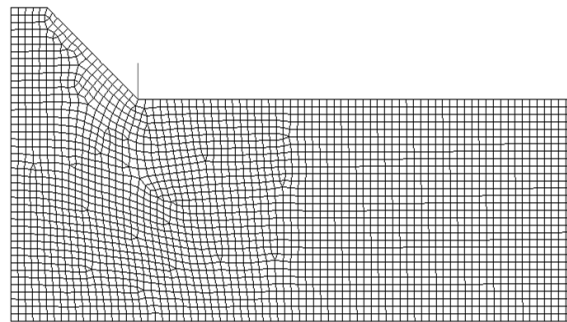
The FE model used to compute R-NSIFs from local stress fields had the minimum size of the elements at the notch tip equal to about  $5 \cdot 10^{-5}$  mm, according to Lazzarin and Tovo [13]. The FE models used to estimate R-NSIFs by means of the PSM were meshed by means of the free meshing algorithm provided by Visual-Mesh according to the PSM calibration rules. Four-node 2004 quadrilateral elements from Sysweld® library have been used and the numerical integration scheme was set to 2x2 Gauss points. Even though an average FE size  $d=6/4=1.5$  mm could have been adopted, the average finite element size  $d$  imposed to the free mesh generation algorithm was indeed much lower and equal to 0.2 mm, which translates into a mesh density ratio  $a/d$  equal to 30 (see Table 9.2). Such FE size was necessary to obtain a temperature field in agreement with that obtained with the very refined mesh pattern. More precisely, to establish the appropriate  $d$  value, a difference in nodal temperatures of few percentage points was allowed between the very refined and the PSM coarse meshes. Two different pre-processing approaches have been considered to apply the PSM. In the first case (Figure 9.9(b)), the free mesh pattern has been generated without involving any guiding line or surface division in the weld toe region, according to the PSM calibration reported in the previous section. In the second case



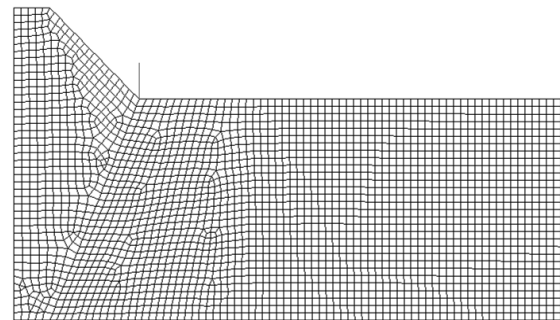
(Figure 9.9(c)), a mesh guiding line was introduced, which divides the surface to be meshed into two parts along the V-notch bisector, starting from the weld toe.



(a)



(b)



(c)

**Figure 9.9.** Finite element models: (a) very fine pattern used to compute R-NSIFs from local stress fields and detail of the notch tip refinement (order of magnitude of the smallest element equal to  $10^{-4}$  mm); (b) completely free generated mesh pattern with average element size  $d = 0.2$  mm; (c) guided free mesh pattern with average element size  $d = 0.2$  mm (a row of FE nodes is forced to be along the notch bisector line).

**Table 9.2.** Comparison between the values of the R-NSIFs evaluated with very fine meshes and coarse meshes, both using linear isoparametric elements, taking advantage of Equation (9.4) linking the peak stress and the mode 1 R-NSIF.

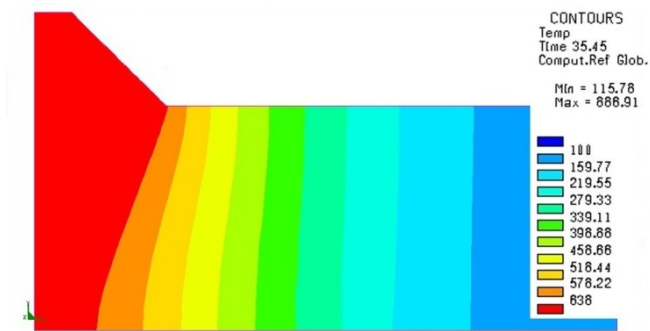
Materials	$Q^*$ (W)	$d$ (mm)	$a/d$	Fine mesh	Coarse PSM mesh		
				$K_I$ (MPa $\text{mm}^{0.326}$ )	$\sigma_{I,peak}$ (MPa)	$K_I$ (MPa $\text{mm}^{0.326}$ )	$\Delta\%$
Steel	11500	0.2	30	42.3	42.7	41.4	-2.2
Steel	11500	0.2	30	42.3	44.6	43.3	+2.4

As a consequence, a row of FE nodes is forced to be located along the V-notch bisector line. This case may be of interest and has been investigated here because it is a typical pre-processing technique in welding simulations to consider two different material models (parent material and filler material) or to simulate multi-pass welding processes. Finally, uncoupled thermo-mechanical analyses have been carried out. The molten effect has been simulated by using a function that clears the history of an element whose temperature exceeds the melting temperature. During welding the plates were supposed to be free of constraints: therefore, only the symmetry boundary condition shown in Figure 9.7 was considered.

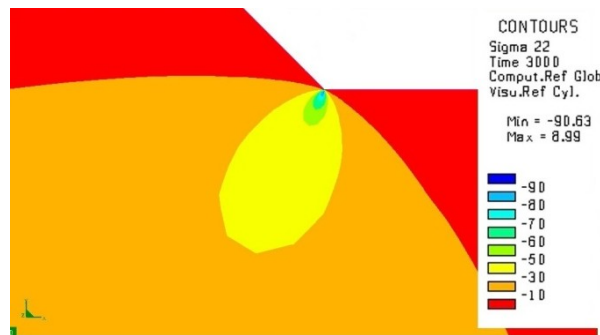
Figure 9.10(a) shows the temperature distribution when the melted zone has reached its maximum extension. In the same figure the residual stress field distributions near the toe region are reported according to a cylindrical coordinate system centered at the notch tip. The stress distribution near the weld toe is linear in a log-log plot (Figure 9.11) and its slope matches the analytical solution given by Equation (9.1). The intensity of such residual stress field has therefore been given in terms of R-NSIFs.

The results are summarized in Table 9.2. It is possible to notice a good agreement between the  $K_I$  values obtained from the local stress field computed with very fine meshes and the ones estimated by means of the coarse meshes, by using the PSM with  $K_{FE}^*=1.64$ . The investigation performed here demonstrated that the PSM can be used for a rapid R-NSIF evaluation, saving meshing and solving time. In particular, the solution time associated with the very refined meshes was about 1 minute for thermal analysis and 4 minutes for mechanical analysis, whereas the one associated

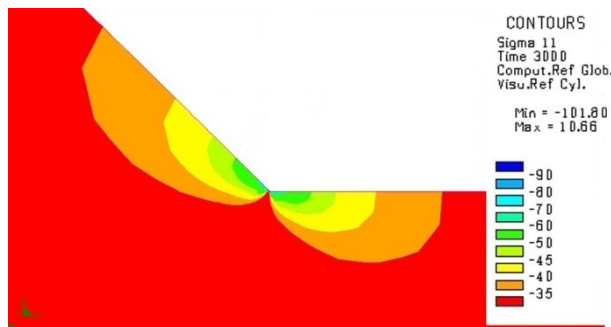
with the PSM mesh pattern was about few seconds for thermal analysis and one minute for mechanical analysis.



(a)



(b)



(c)

**Figure 9.10.** (a) Temperature distribution at the instant of maximum width of the fusion zone (in red); (b)  $\sigma_{\theta\theta}$  component of residual stress distribution near the notch tip; (c)  $\sigma_{rr}$  component of residual stress distribution near the notch tip.

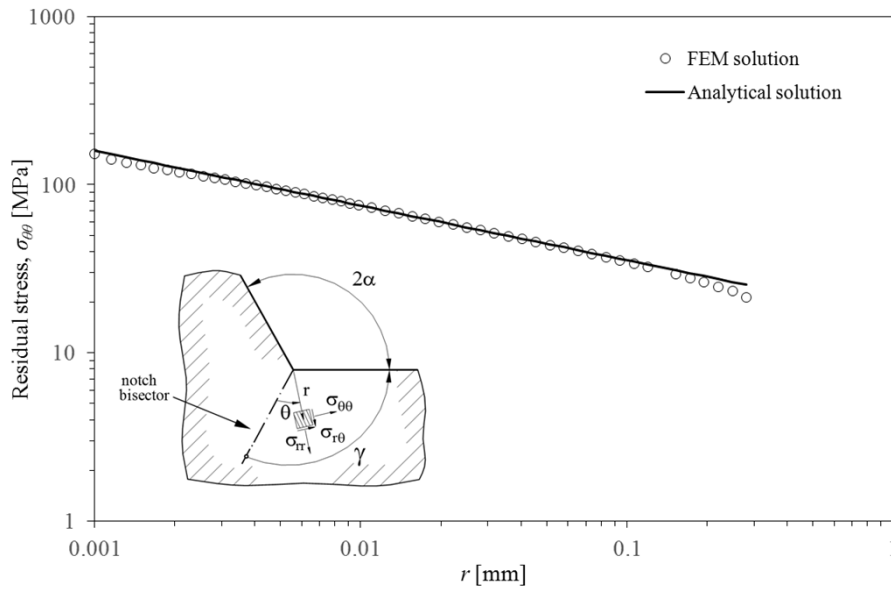


**Figure 9.11.** Asymptotic  $\sigma_{\theta\theta}$  component of the residual stress field near the notch tip along the notch bisector, i.e.  $\theta=0^\circ$ .

In summary, the following main advantages can be outlined if the R-NSIFs are estimated by means of the PSM rather than computed directly from local stress fields: a) only one nodal stress value calculated at the point of singularity is sufficient to compute the R-NSIF, the whole stress distribution along the notch bisector being no longer required; b) three orders of magnitude more coarse meshes could be employed by using the PSM, compared to the very refined meshes required to evaluate the local stress field directly. In the author's opinion, both reasons make the PSM of easy and fast applicability in industrial and research applications. Future developments are envisaged to compute R-NSIFs by using three-dimensional FE models of welding process coupled with the PSM.

## 9.6. Discussion and conclusion

The PSM has been calibrated in Sysweld® FE code, with the aim to rapidly evaluate the mode 1 residual notch stress intensity factors (R-NSIFs) in welded joints starting from welding process simulations coupled with structural stress analyses. The investigation has been conducted under the condition of reduced plasticity, in order to be able to deal with the stress singularity exponents of the asymptotic linear elastic distributions. First the calibration constant  $K_{FE}^*$  appearing in Equation (9.4) has been determined by means of approximately 60 FE analyses involving sharp V-notches

having notch opening angles between  $0^\circ$  and  $135^\circ$ . As a result,  $K_{FE}^*$  has been found equal to 1.64 in case of V-notches with opening angles ranging from  $90^\circ$  to  $135^\circ$  and equal to 1.90 in case of cracks ( $0^\circ$  notch opening angle). Provided that the mesh density ratio  $a/d$  is equal or greater than 4, all FE results fall within a scatter band of  $\pm 5\%$ , regardless of the V-notch depth. The reason why the calibration constant is different for different notch opening angles has been investigated and it has been found to depend on the element formulation combined with the principal stress averaging technique at FE nodes adopted by Sysweld®. After calibrating Equation (9.4), a practical application of the PSM to estimate the R-NSIF at the weld toe of a butt-welded joint geometry has been illustrated. The R-NSIF has been estimated in good agreement with the results of a very refined FE mesh. Thanks to the PSM, a three orders of magnitude more coarse mesh could be adopted as compared to that required to evaluate directly the asymptotic stress distribution. Moreover, in the case of the simple geometry analyzed in the present work, the analysis time of the thermal simulation was reduced by an order of magnitude and by a factor of four concerning the structural simulation. An additional factor implying time saving when adopting the PSM is that a single nodal stress value (i.e. the singular peak stress at the notch tip) is sufficient to estimate the R-NSIF, rather than a set of stress-distance data, which must be selected and processed to derive the R-NSIF from the local stress distributions. The advantages observed in the simple example analyzed in the present work seem to encourage future developments of the PSM to analyze the residual NSIFs in three-dimensional cases.

## References

- [1] B. Launert, M. Rhode, A. Kromm, H. Pasternak, T. Kannengiesser, Measurement and numerical modeling of residual stresses in welded HSLA component-like I-girders, *Weld. World*. 61 (2017) 223–229.
- [2] J. Hensel, T. Nitschke-pagel, K. Dilger, Engineering model for the quantitative consideration of residual stresses in fatigue design of welded components, *Weld. World*. (2017) 997–1002.
- [3] M. Beghini, L. Bertini, E. Vitale, Fatigue residual stress fields. Experimental results and modelling, *Fat. Fract. Eng. Mater. Struct.* 17 (1994) 1433–1444.
- [4] L. Bertini, V. Fontanari, G. Straffelini, Influence of post weld treatments on the fatigue behaviour of Al-alloy welded joints, *Science (80-. )*. 20 (1998) 749–755.
- [5] J.-Y. Yung, F. V Lawrence, Predicting the fatigue life of welds under combined bending and torsion, in: *Second Int. Conf. Biaxial, Multiaxial Fatigue Fract.*, 1985.
- [6] H.D. Hibbitt, P. V Marcal, A numerical, thermo-mechanical model for the welding and subsequent loading of a fabricated structure, *Comput. Struct.* 3 (1973) 1145–1174.
- [7] E. Friedman, Thermomechanical analysis of the welding process using the finite element method, *J. Press. Vessel Technol.* 97 (1975) 206–213.
- [8] E.F. Rybicki, D.W. Schmueser, R.W. Stonesifer, J.J. Groom, H.W. Mishler, A finite-element model for residual stresses and deflections in girth-butt welded pipes, *J. Press. Vessel Technol.* 100 (1978) 256–262.
- [9] E.F. Rybicki, R.B. Stonesifer, Computation of residual stresses due to multipass welds in piping systems, *J. Press. Vessel Technol.* 101 (1979) 149–154.
- [10] K.W. Mahin, S. MacEwen, W. Winters, Evaluation of residual stress distributions in a traveling GTA weld using finite element and experimental techniques, *Model. Control Cast. Weld. Process. IV.* (1988) 339–350.
- [11] D.H.B. Mok, R.J. Pick, Finite element study of residual stresses in a plate T-joint fatigue specimen, *Proc. Inst. Mech. Eng. Part C Mech. Eng. Sci.* 204 (1990) 127–134.
- [12] T.-L. Teng, C.-P. Fung, P.-H. Chang, W.-C. Yang, Analysis of residual

- stresses and distortions in T-joint fillet welds, *Int. J. Press. Vessel. Pip.* 78 (2001) 523–538.
- [13] P. Lazzarin, R. Tovo, A Notch Intensity Factor Approach To the Stress Analysis of Welds, *Fatigue Fract. Eng. Mater. Struct.* 21 (1998) 1089–1103.
- [14] B. Atzori, P. Lazzarin, R. Tovo, Stress field parameters to predict the fatigue strength of notched components, *J. Strain Anal. Eng. Des.* 34 (1999) 437–453.
- [15] P. Lazzarin, P. Livieri, Notch stress intensity factors and fatigue strength of aluminium and steel welded joints, *Int. J. Fatigue.* 23 (2001) 225–232.
- [16] B. Atzori, G. Meneghetti, Fatigue strength of fillet welded structural steels: finite elements, strain gauges and reality, *Int. J. Fatigue.* 23 (2001) 713–721.
- [17] M.L. Williams, Stress singularities resulting from various boundary conditions in angular corners of plates in tension, *J. Appl. Mech.* 19 (1952) 526–528.
- [18] P. Ferro, F. Berto, P. Lazzarin, Generalized stress intensity factors due to steady and transient thermal loads with applications to welded joints, *Fatigue Fract. Eng. Mater. Struct.* 29 (2006) 440–453.
- [19] P. Ferro, N. Petrone, Asymptotic thermal and residual stress distributions due to transient thermal loads, *Fatigue Fract. Eng. Mater. Struct.* 32 (2009) 936–948.
- [20] P. Ferro, The local strain energy density approach applied to pre-stressed components subjected to cyclic load, *Fatigue Fract. Eng. Mater. Struct.* 37 (2014) 1268–1280.
- [21] P. Lazzarin, G. Meneghetti, F. Berto, M. Zappalorto, Practical Application of the N-SIF Approach in Fatigue Strength Assessment of Welded Joints, *Weld. World.* 53 (2009) 76–89.
- [22] H. Nisitani, T. Teranishi, KI of a circumferential crack emanating from an ellipsoidal cavity obtained by the crack tip stress method in FEM, *Eng. Fract. Mech.* 71 (2004) 579–585.
- [23] G. Meneghetti, P. Lazzarin, Significance of the elastic peak stress evaluated by FE analyses at the point of singularity of sharp V-notched components, *Fatigue Fract. Eng. Mater. Struct.* 30 (2007) 95–106.
- [24] G. Meneghetti, The peak stress method applied to fatigue assessments of steel and aluminium fillet-welded joints subjected to mode I loading, *Fatigue Fract. Eng. Mater. Struct.* 31 (2008) 346–369.

- [25] G. Meneghetti, P. Lazzarin, The Peak Stress Method for Fatigue Strength Assessment of welded joints with weld toe or weld root failures, *Weld. World*. 55 (2011) 22–29.
- [26] P. Ferro, M. Colussi, G. Meneghetti, F. Berto, M. Lachin, S.A. Castiglione, On the use of the Peak Stress Method for the calculation of Residual Notch Stress Intensity Factors: a preliminary investigation, *Procedia Struct. Integr.* 3 (2017) 191–200.
- [27] P. Livieri, P. Lazzarin, Fatigue strength of steel and aluminium welded joints based on generalised stress intensity factors and local strain energy values, *Int. J. Fract.* 133 (2005) 247–276.
- [28] B. Gross, A. Mendelson, Plane elastostatic analysis of V-notched plates, *Int. J. Fract. Mech.* 8 (1972) 267–276.
- [29] G. Meneghetti, The use of peak stresses for fatigue strength assessments of welded lap joints and cover plates with toe and root failures, *Eng. Fract. Mech.* 89 (2012) 40–51.
- [30] G. Meneghetti, A. et al. Campagnolo, Rapid Evaluation of notch stress intensity factors in welded joints using the peak stress method: comparison of commercial finite element codes for a range of mesh patterns, *IIW-Document XIII-2696-17*. (2017).
- [31] P. Ferro, A. Zambon, F. Bonollo, Investigation of electron beam welding in wrought Inconel 706 – experimental and numerical analysis, *Mater. Sci. Eng. A*. (2005) 94–105.
- [32] P. Ferro, H. Porzner, A. Tiziani, F. Bonollo, The influence of phase transformations on residual stresses induced by the welding process - 3D and 2D numerical models, *Model. Simul. Mater. Sci. Eng.* (2006) 117–136.
- [33] F. Ferro, Un modello bidimensionale per lo studio delle tensioni indotte dal processo di saldatura, in: *Atti Convegno Naz. XIV ADM – XXXIII AIAS (In Ital., 2004*.
- [34] Z. Feng, *Processes and Mechanisms of Welding Residual Stress and Distortion*, Woodhead Publishing, 2005.
- [35] J.B. Leblond, J. Devaux, A new kinetic model for anisothermal metallurgical transformations in steels including effect of austenite grain size, *Acta Metall.* 32 (1984) 137–146.



- [36] D.P. Koistinen, R.E. Marburger, A general equation prescribing extent of austenite-martensite transformation in pure iron-carbon alloys and carbon steels, *Acta Metall.* 7 (1959) 59–68.
- [37] J. Goldak, A. Chakravarti, M. Bibby, A new finite element model for welding heat sources, *Metall. Trans. B.* 15 (1984) 299–305.
- [38] P. Ferro, F. Bonollo, A. Tiziani, Methodologies and experimental validations of welding process numerical simulation, *Int. J. Comput. Mater. Sci. Surf. Eng.* 3 (2010) 114–132.



## 10. Overall concluding remarks

The prediction of fatigue strength and service life of welded joints is an ambitious task, for which global and local approaches are available and have been investigated in this Ph.D. thesis. Global approaches, which comprise the nominal stress and the hot spot stress methods, are generally recognized by the national and international design codes and are under permanent amendment. Local approaches, which include the here considered notch stress intensity and strain energy density based approaches, are less suited to standardization. However, they are useful for the design development in industry in respect of satisfactory reliability, higher strength and longer life. Additionally, they are important as a means of assessing strength and life of structural elements without reference to the global approach. This must take place if global approach data are not available (e.g. in cases of unconventional design and service conditions).

Global approaches, especially the widespread nominal stress approach, are often considered superior to local approaches in respect of formal simplicity and statistical validation. But such aspects are bound to the condition that the structural member and the reference test specimens correspond, in respect of all essential influencing parameters. Such a correspondence is rather the exception than the rule, particularly in terms of loading condition. Local approaches can be important means to reach such correspondence, in a theoretically-founded way, becoming an indispensable supplement to global approaches.

Within this framework, the present Ph.D. thesis, focused on making the fatigue assessment of large steel structures possible, has both the purposes of originally contributing to local approaches for fatigue assessment and developing a method fully compliant with current standards, in order to be spent nowadays in the industrial context.

Dealing with local approaches, the principal drawback of local SED numerical computation, consisting in the need of a circular control volume centered on a notch tip (i.e. at the weld toe and at the weld root in case of welded joints), within which the strain energy density has to be averaged, has been overcome by using coarse meshes completely free-generated. The method and its limitations of applicability

have been formalized, finding robustness in terms of insensitivity to mesh pattern, mesh refinement and FE formulation.

Then, a link between local stress fields, near weld toes and roots, and the nominal stress components evaluated at a proper distance from the weld has been theoretically established. Such link permits to estimate SED values, both at the weld toe and at the weld root, as well as *a posteriori* the related NSIFs, as an explicit function of the nominal load components (membrane loads, shear loads and bending moments). It is also suitable of automation, to perform the large number of fatigue assessments that a nowadays complex steel structure requires.

Being aware that the current lack of normative compliance of both SED and NSIF approaches are an obstacle in industrial applications, a way to improve the classical nominal stress approach for welded structures, which is still the most widely accepted and recognized in standards, has then been proposed. The methodological problem of the *modified nominal stress* definition has been overcome through an original, finite element based approach, which takes into account both membrane and bending effects. Very good agreement has been found between fatigue lives experimentally estimated and those calculated through the modified nominal stress, in the presence of bending stresses.

Finally, the procedure to automate the fatigue assessment of welded megastructures has been presented and a finite element based post-processor has been developed. In detail, local SED and NSIF approaches have been implemented, as well as the modified nominal stress and the classical nominal stress and hot spot stress approaches. All approaches have been rethought to work with coarse shell element models, reaching the suitability for large assemblies. A very good agreement between “manually” performed assessments, both through global and local approaches, and those rapidly performed by using the post-processor has been highlighted.

In conclusion, the potentialities of the considered local approaches, and in particular of the SED one, in the fatigue assessment of structural components, characterized by different geometries and subjected to complex loadings, have been shown. What is more, the effectiveness of local approaches matched with global approaches, in particular of the nominal stress one, in the fatigue assessment of welded structures has been proved both theoretically and experimentally.

## Bibliography

*For a better reading, numbered references have been included at the end of each Chapter. Below, the complete list of references is reported in alphabetical order.*

### Literature

- Abdelaziz Y, Hamouine A (2008). A survey of the extended finite element. *Computers and Structures*, 86, 1141–1151.
- Ahola A, Nykänen T, Björk T (2016). Effect of loading type on the fatigue strength of asymmetric and symmetric transverse non-load carrying attachments. *Fatigue Fract. Eng. Mater. Struct.*, 1–13.
- Akin JE (1976). The generation of elements with singularities. *Int. J. Numer. Methods Eng.*, 10, 1249–1259.
- Andrews RM (1996). The effect of misalignment on the fatigue strength of welded cruciform joints. *Fatigue Fract. Eng. Mater. Struct.*, 19, 755–768.
- Atzori B, Lazzarin P, Tovo R (1999). From a local stress approach to fracture mechanics : a comprehensive. *Fatigue Fract. Eng. Mater. Struct.*, 22, 369–381.
- Atzori B, Lazzarin P, Tovo R (1997). Stress distributions for v-shaped notches under tensile and bending loads. *Fatigue Fract. Eng. Mater. Struct.*, 20, 1083–1092.
- Atzori B, Lazzarin P, Tovo R (1999). Stress field parameters to predict the fatigue strength of notched components. *J. Strain Anal. Eng. Des.*, 34, 437–453.
- Atzori B, Meneghetti G (2001). Fatigue strength of fillet welded structural steels: finite elements, strain gauges and reality. *Int. J. Fatigue*, 23, 713–721.
- Babuška I, Miller A (1984). The post-processing approach in the finite element method—part 1: Calculation of displacements, stresses and other higher derivatives of the displacements. *Int. J. Numer. Methods Eng.*, 20, 1085–1109.
- 1Bäckström M, Marquis G (2004). Interaction equations for multiaxial fatigue assessment of welded structures. *Fatigue Fract. Eng. Mater. Struct.*, 27, 991–1003.
- Baik B, Yamada K, Ishikawa T (2011). Fatigue crack propagation analysis for welded joint subjected to bending. *Int. J. Fatigue*, 33, 746–758.

- Bampton MCC, Craig RR (1968). Coupling of substructures for dynamic analyses. *AIAA J.*, 6, 1313–1319.
- Barsoum RS (1975). Further application of quadratic isoparametric finite elements to linear fracture mechanics of plate bending and general shells. *Int. J. Fract.*, 11, 167–169.
- Bazant Z (2005). *Scaling of structural strength*. Oxford: Elsevier.
- Beghini M, Bertini L, Vitale E (1994). Fatigue residual stress fields. Experimental results and modelling. *Fat. Fract. Eng. Mater. Struct.*, 17, 1433–1444.
- Beltrami E (1885). Sulle condizioni di resistenza dei corpi elastici (in Italian). *Rend. del Reg. Ist. Lomb.*, XVIII, 704–714.
- Benzley SE (1974). Representation of singularities with isoparametric finite elements. *Int. J. Numer. Methods Eng.*, 8, 537–545.
- Bertini L, Fontanari V, Straffelini G (1998). Influence of post weld treatments on the fatigue behaviour of Al-alloy welded joints. *Science (80-.)*, 20, 749–755.
- Berto F, Campagnolo A, Lazzarin P (2015). Fatigue strength of severely notched specimens made of Ti-6Al-4V under multiaxial loading. *Fatigue Fract. Eng. Mater. Struct.*, 38, 503–517.
- Berto F, Lazzarin P, Ayatollahi MR (2013). Brittle fracture of sharp and blunt V-notches in isostatic graphite under pure compression loading. *Carbon N. Y.*, 63, 101–116.
- Berto F, Lazzarin P (2009). The volume-based Strain Energy Density approach applied to static and fatigue strength assessments of notched and welded structures. *Procedia Eng.*, 1, 155–158.
- Berto F, Lazzarin P (2014). Recent developments in brittle and quasi-brittle failure assessment of engineering materials by means of local approaches. *Mater. Sci. Eng. R*, 75, 1–48.
- Berto F, Lazzarin P (2009). A review of the volume-based strain energy density approach applied to V-notches and welded structures. *Theor. Appl. Fract. Mech.*, 52, 183–194.
- Boukharouba T, Tamine T, Niu L, Chehimi C, Pluvinage G (1995). The use of notch stress intensity factor as a fatigue crack initiation parameter. *Eng. Fract. Mech.*, 52, 503–512.

- Boukharouba T, Tamine T, Niu L, Chehimi C, Pluvinage G (1995). The use of notch stress intensity factor as a fatigue crack initiation parameter. *Eng. Fract. Mech.*, 52, 503–512.
- Campagnolo A, Meneghetti G, Berto F (2016). Rapid finite element evaluation of the averaged strain energy density of mixed-mode (I + II) crack tip fields including the T-stress contribution. *Fatigue Fract. Eng. Mater. Struct.*, 39, 982–998.
- Catanzano A, Colussi L, Romaro C, Romaro G (2003). Sollevamento con un'unica manovra a 40 metri di altezza, di una copertura di circa 3 ettari di area e del peso di 8500 tonnellate (in Italian). In: *III Settimana delle costruzioni in acciaio*. Collegio dei Tecnici dell'Acciaio.
- Chattopadhyay A, Glinka G, El-Zein M, Qian J, Formas R (2011). Stress analysis and fatigue of welded structures. *Weld. World*, 55, 2–21.
- Davidenkov NN, Shevandin E, Wittmann F (1947). The Influence of Size on the Brittle Strength of Steel. *J. Appl. Mech.*, 14, A63–A67.
- Doerk O, Fricke W, Weissenborn C (2003). Comparison of different calculation methods for structural stresses at welded joints. *Int. J. Fatigue*, 25, 359–369.
- Dong P (2001). A structural stress definition and numerical implementation for fatigue analysis of welded joints. *Int. J. Fatigue*, 23, 865–876.
- Dong P, Hong JK, Osage DA, Dewees DJ, Prager M (2010). The Master SN Curve Method an Implementation for Fatigue Evaluation of Welded Components in the ASME B&PV Code, Section VIII, Division 2 and API 579-1/ASME FFS-1. *Weld. Res. Counc. Bull.*.
- Dowling NE (2012). *Mechanical behavior of materials: engineering methods for deformation, fracture, and fatigue*. Pearson.
- Draper J (2008). *Modern metal fatigue analysis*. EMAS publications.
- Dunn M, Suwito W (1997). Fracture initiation at sharp notches under mode I, mode II, and mild mixed mode loading. *Int. J. Fract.*, 84, 367–381.
- Fatemi A, Shamsaei N (2010). Multiaxial fatigue modeling and some simple approximations. In: *ICMFF9*.
- Feldmann M, Eichler B, Sedlacek G, Dahl W, Langenberg P, Butz C, Leendertz H, Hanswille G, Amorim-Varum H (2012). Choice of steel material for bridge bearings to avoid brittle fracture.

- Feng Z (2005). *Processes and Mechanisms of Welding Residual Stress and Distortion*. Woodhead Publishing.
- Ferro F (2004). Un modello bidimensionale per lo studio delle tensioni indotte dal processo di saldatura. In: *Atti Convegno Nazionale XIV ADM – XXXIII AIAS (In italian)*.
- Ferro P (2014). The local strain energy density approach applied to pre-stressed components subjected to cyclic load. *Fatigue Fract. Eng. Mater. Struct.*, 37, 1268–1280.
- Ferro P, Berto F, Lazzarin P (2006). Generalized stress intensity factors due to steady and transient thermal loads with applications to welded joints. *Fatigue Fract. Eng. Mater. Struct.*, 29, 440–453.
- Ferro P, Colussi M, Meneghetti G, Berto F, Lachin M, Castiglione SA (2017). On the use of the Peak Stress Method for the calculation of Residual Notch Stress Intensity Factors: a preliminary investigation. *Procedia Struct. Integr.*, 3, 191–200.
- Ferro P, Petrone N (2009). Asymptotic thermal and residual stress distributions due to transient thermal loads. *Fatigue Fract. Eng. Mater. Struct.*, 32, 936–948.
- Ferro P, Porzner H, Tiziani A, Bonollo F (2006). The influence of phase transformations on residual stresses induced by the welding process - 3D and 2D numerical models. *Model. Simul. Mater. Sci. Eng.*, 117–136.
- Ferro P, Zambon A, Bonollo F (2005). Investigation of electron beam welding in wrought Inconel 706 – experimental and numerical analysis. *Mater. Sci. Eng. A*, 94–105.
- Ferro P, Bonollo F, Tiziani A (2010). Methodologies and experimental validations of welding process numerical simulation. *Int. J. Comput. Mater. Sci. Surf. Eng.*, 3, 114–132.
- Fett T (1996). Failure of brittle materials near stress singularities. *Eng. Fract. Mech.*, 53, 511–518.
- Fisher JW, Frank KH, Hirt MA, McNamee BM (1970). *Effect of weldments on the fatigue strength of steel beams*. TRB.
- Fricke W (2013). IIW guideline for the assessment of weld root fatigue. *Weld. World*, 57, 753–791.



- Fricke W (2003). Fatigue analysis of welded joints: State of development. *Mar. Struct.*, 16, 185–200.
- Friedman E (1975). Thermomechanical analysis of the welding process using the finite element method. *J. Press. Vessel Technol.*, 97, 206–213.
- Frost NE, Marsh KJ, Pook LP (1974). *Metal fatigue*. Courier Corporation.
- Gallo P, Berto F, Lazzarin P (2015). High temperature fatigue tests of notched specimens made of titanium Grade 2. *Theor. Appl. Fract. Mech.*, 76, 27–34.
- Givoli D, Rivkin L (1993). The DtN finite element method for elastic domains with cracks and re-entrant corners. *Comput. Struct.*, 49, 633–642.
- Glinka G (1985). Energy density approach to calculation of inelastic strain-stress near notches and cracks. *Eng. Fract. Mech.*, 22, 485–508.
- Goldak J, Chakravarti A, Bibby M (1984). A new finite element model for welding heat sources. *Metall. Trans. B*, 15, 299–305.
- Gómez, F.J., Elices, M., Berto, F., Lazzarin P (2009). Fracture of U-notched specimens under mixed mode: Experimental results and numerical predictions. *Eng. Fract. Mech.*, 76, 236–249.
- Gómez, F.J., Elices, M., Berto, F., Lazzarin P (2009). Fracture of V-notched specimens under mixed mode (I + II) loading in brittle materials. *Int. J. Fract.*, 159, 121.
- Gross B, Mendelson A (1972). Plane elastostatic analysis of V-notched plates. *Int. J. Fract. Mech.*, 8, 267–276.
- Gumbel EJ (1958). Statistics of extremes. 1958. *Columbia Univ. Press. New York*.
- Gurney TR (1991). *The fatigue strength of transverse fillet welded joints*. Cambridge: Abington Publishing.
- Gurney TR (1997). *Fatigue of thin walled joints under complex loading*. Abingdon Publishing.
- Gustafsson M (2002). Thickness effect in fatigue of welded extra high strength steel joints. *Des. Anal. Welded High Strength Steel Struct.*, 205–224.
- Haibach E (2002). Service fatigue strength-methods and data for structural analysis. *Springer Verlag, Berlin*.
- Haibach E, Matschke C (1982). The concept of uniform scatter bands for analyzing SN curves of unnotched and notched specimens in structural steel. In: *Low-Cycle Fatigue and Life Prediction*. ASTM International.

- Hall LR, Stallmeyer JE (1959). *The fatigue strength of flexural members*. University of Illinois, Department of Civil Engineering.
- Hensel J, Nitschke-pagel T, Dilger K (2017). Engineering model for the quantitative consideration of residual stresses in fatigue design of welded components. *Weld. World*, 997–1002.
- Henshell RD, Shaw KG (1975). Crack tip finite elements are unnecessary. *Int. J. Numer. Methods Eng.*, 9, 495–507.
- Heyliger PR, Kriz RD (1989). Stress intensity factors by enriched mixed finite elements. *Int. J. Numer. Methods Eng.*, 28, 1461–1473.
- Hibbitt HD, Marcal P V (1973). A numerical, thermo-mechanical model for the welding and subsequent loading of a fabricated structure. *Comput. Struct.*, 3, 1145–1174.
- Hobbacher AF (1993). Stress intensity factors of welded joints. *Eng. Fract. Mech.*, 46, 173–182.
- Hobbacher AF (2016). *Recommendations for Fatigue Design of Welded Joints and Components*. Springer International Publishing.
- Hobbacher AF (2008). *Recommendations for Fatigue Design of Welded Joints and Components*. International Institute of Welding.
- Hobbacher AF (2010). New developments at recent update of the IIW recommendations for fatigue of welded joints and components. *Steel Constr.*, 3.
- Hobbacher AF (2009). The new IIW recommendations for fatigue assessment of welded joints and components - A comprehensive code recently updated. *Int. J. Fatigue*, 31, 50–58.
- Ida K, Uemura T (1996). Stress concentration factor formulae widely used in Japan. *Fatigue Fract. Eng. Mater. Struct.*, 19, 779–786.
- Jonsson B, Dobmann G, Hobbacher A, Kassner ME, Marquis G, International Institute of Welding. (2016). *IIW guidelines on weld quality in relationship to fatigue strength*.
- Kang S-W, Kim W-S, Paik Y-M (2002). Fatigue strength of fillet welded steel structure under out-of-plane bending load. *Int. J. Korean Weld. Soc.*, 2, 33–39.
- Karihaloo BL, Xiao QZ (2000). Hybrid stress elements for accurate solution of elasticity problems with traction-free segments. In: *International conference on engineering computational technology*, pp. 109–125.

- Kihara S, Yoshii A (1991). A Strength Evaluation Method of a Sharply Notched Structure by a New Parameter, 'The Equivalent Stress Intensity Factor'. *JSME Int. journal. Ser. 1, Solid Mech. strength Mater.*, 34, 70–75.
- Kihl DP, Sarkani S (1997). Thickness effects on the fatigue strength of welded steel cruciforms. *Int. J. Fatigue*, 19, 311–316.
- Koistinen DP, Marburger RE (1959). A general equation prescribing extent of austenite-martensite transformation in pure iron-carbon alloys and carbon steels. *Acta Metall.*, 7, 59–68.
- Kyuba H, Dong P (2005). Equilibrium-equivalent structural stress approach to fatigue analysis of a rectangular hollow section joint. *Int. J. Fatigue*, 27, 85–94.
- Launert B, Rhode M, Kromm A, Pasternak H, Kannengiesser T (2017). Measurement and numerical modeling of residual stresses in welded HSLA component-like I-girders. *Weld. World*, 61, 223–229.
- Lazzarin P., Berto F (2005). Some Expressions for the Strain Energy in a Finite Volume Surrounding the Root of Blunt V-notches. *Int. J. Fract.*, 135, 161–185.
- Lazzarin P, Berto F, Gomez FJ, Zappalorto M (2008). Some advantages derived from the use of the strain energy density over a control volume in fatigue strength assessments of welded joints. *Int. J. Fatigue*, 30, 1345–1357.
- Lazzarin P, Campagnolo A, Berto F (2014). A comparison among some recent energy- and stress-based criteria for the fracture assessment of sharp V-notched components under mode I loading. *Theor. Appl. Fract. Mech.*, 71, 21–30.
- Lazzarin P, Lassen T, Livieri P (2003). A notch stress intensity approach applied to fatigue life predictions of welded joints with different local toe geometry. *Fatigue Fract. Eng. Mater. Struct.*, 26, 49–58.
- Lazzarin P, Berto F (2005). From Neuber's elementary volume to Kitagawa and Atzori's diagrams: an interpretation based on local energy. *Int. J. Fract.*, 135, L33--L38.
- Lazzarin P, Berto F, Radaj D (2006). Uniform fatigue strength of butt and fillet welded joints in terms of the local strain energy density. In: *Proc. Fatigue*.
- Lazzarin P, Livieri P (2001). Notch stress intensity factors and fatigue strength of aluminium and steel welded joints. *Int. J. Fatigue*, 23, 225–232.

- Lazzarin P, Livieri P, Berto F, Zappalorto M (2008). Local strain energy density and fatigue strength of welded joints under uniaxial and multiaxial loading. *Eng. Fract. Mech.*, 75, 1875–1889.
- Lazzarin P, Sonsino CM, Zambardi R (2004). A notch stress intensity approach to assess the multiaxial fatigue strength of welded tube-to-flange joints subjected to combined loadings. *Fatigue Fract. Eng. Mater. Struct.*, 27, 127–140.
- Lazzarin P, Tovo R (1996). A unified approach to the evaluation of linear elastic stress fields in the neighborhood of cracks and notches. *Int. J. Fract.*, 78, 3–19.
- Lazzarin P, Tovo R (1998). A Notch Intensity Factor Approach To the Stress Analysis of Welds. *Fatigue Fract. Eng. Mater. Struct.*, 21, 1089–1103.
- Lazzarin P, Tovo R, Filippi S (1998). Elastic stress distributions in finite size plates with edge notches. *Int. J. Fract.*, 91, 269–282.
- Lazzarin P, Zambardi R (2002). The Equivalent Strain Energy Density approach reformulated and applied to sharp V-shaped notches under localized and generalized plasticity. *Fatigue Fract. Eng. Mater. Struct.*, 25, 917–928.
- Lazzarin P, Zambardi R (2001). A finite-volume-energy based approach to predict the static and fatigue behavior of components with sharp V-shaped notches. *Int. J. Fract.*, 112, 275–298.
- Lazzarin P, Berto F, Zappalorto M (2010). Rapid calculations of notch stress intensity factors based on averaged strain energy density from coarse meshes: Theoretical bases and applications. *Int. J. Fatigue*, 32, 1559–1567.
- Leblond JB, Devaux J (1984). A new kinetic model for anisothermal metallurgical transformations in steels including effect of austenite grain size. *Acta Metall.*, 32, 137–146.
- Lin KY, Tong P (1980). Singular finite elements for the fracture analysis of V-notched plate. *Int. J. Numer. Methods Eng.*, 15, 1343–1354.
- Lindley C, Bateson PH (1993). Influence of attachment thickness on fatigue endurance of welded joints. In: *Proceedings of the International Conference on Offshore mechanics and Artic Engineering*, p. 689.
- Livieri P, Lazzarin P (2005). Fatigue strength of steel and aluminium welded joints based on generalised stress intensity factors and local strain energy values. *Int. J. Fract.*, 133, 247–276.

- Lotsberg I, Sigurdsson G (2006). Hot Spot Stress S-N Curve for Fatigue Analysis of Plated Structures. *J. Offshore Mech. Arct. Eng.*, 128, 330–336.
- Lotsberg I (2017). Development of Fatigue Design Standards for Marine Structures. In: *Volume 9: Offshore Geotechnics; Torgeir Moan Honoring Symposium*. ASME.
- Lotsberg I (2016). *Fatigue design of marine structures*. Cambridge University Press.
- Maddox SJ (2015). Allowance for bending in fatigue design rules for welded joints. *Int. Inst. welding, Doc*, 13, 2515–2580.
- Maddox SJ (1987). The Effect of Plate Thickness on the Fatigue Strength of Fillet Welded Joints.
- Mahin KW, MacEwen S, Winters W (1988). Evaluation of residual stress distributions in a traveling GTA weld using finite element and experimental techniques. *Model. Control Cast. Weld. Process. IV*, 339–350.
- Marquis G (2007). Current Trends in Multiaxial Fatigue Research and Assessment. In: *ICMFF9*.
- Meneghetti G, Campagnolo A et al. (2017). Rapid Evaluation of notch stress intensity factors in welded joints using the peak stress method: comparison of commercial finite element codes for a range of mesh patterns. *IIW-document XIII-2696-17*.
- Meneghetti G, Campagnolo A, Berto F (2016). Averaged strain energy density estimated rapidly from the singular peak stresses by FEM: Cracked bars under mixed-mode (I + III) loading. *Eng. Fract. Mech.*, 167, 20–33.
- Meneghetti G, Campagnolo A, Berto F, Atzori B (2015). Averaged strain energy density evaluated rapidly from the singular peak stresses by FEM: cracked components under mixed-mode (I + II) loading. *Theor. Appl. Fract. Mech.*, 79, 113–124.
- Meneghetti G, Guzzella C, Atzori B (2014). The peak stress method combined with 3D finite element models for fatigue assessment of toe and root cracking in steel welded joints subjected to axial or bending loading. In: *Fatigue and Fracture of Engineering Materials and Structures*, pp. 722–739.
- Meneghetti G, Lazzarin P (2011). The Peak Stress Method for Fatigue Strength Assessment of welded joints with weld toe or weld root failures. *Weld. World*, 55, 22–29.

- Meneghetti G, Lazzarin P (2007). Significance of the elastic peak stress evaluated by FE analyses at the point of singularity of sharp V-notched components. *Fatigue Fract. Eng. Mater. Struct.*, 30, 95–106.
- Meneghetti G (2013). The peak stress method for fatigue strength assessment of tube-to-flange welded joints under torsion loading. *Weld. World*, 57, 265–275.
- Meneghetti G (2008). The peak stress method applied to fatigue assessments of steel and aluminium fillet-welded joints subjected to mode I loading. *Fatigue Fract. Eng. Mater. Struct.*, 31, 346–369.
- Meneghetti G (2012). The use of peak stresses for fatigue strength assessments of welded lap joints and cover plates with toe and root failures. *Eng. Fract. Mech.*, 89, 40–51.
- Meneghetti G, Atzori B, Manara G (2010). The Peak Stress Method applied to fatigue assessments of steel tubular welded joints subject to mode-I loading. *Eng. Fract. Mech.*, 77, 2100–2114.
- Meneghetti G, Guzzella C (2014). The peak stress method to estimate the mode I notch stress intensity factor in welded joints using three-dimensional finite element models. *Eng. Fract. Mech.*, 115, 154–171.
- Moes N, Dolbow J (1999). A finite element method for crack growth without remeshing. *Int. J. Numer.*, 150, 131–150.
- Mok DHB, Pick RJ (1990). Finite element study of residual stresses in a plate T-joint fatigue specimen. *Proc. Inst. Mech. Eng. Part C Mech. Eng. Sci.*, 204, 127–134.
- Munse WH, Stallmeyer JE (1962). Fatigue in welded beams and girders. *Highw. Res. Board Bull.*.
- Neuber H (1985). *Kerbspannungslehre (in German), 3rd Edition*. Berlin: Springer Verlag.
- Neuber H (1958). *Kerbspannungslehre (in German), 2nd Edition*. Berlin: Springer Verlag.
- Neumann A (1961). *Schweißtechnisches Handbuch für Konstrukteure (in German)*. F. Vieweg.
- Niemi E (1995). *Stress determination for fatigue analysis of welded components*. Cambridge: Woodhead Publishing.

- Niemi E, Fricke W, Maddox SJ (2006). *Fatigue analysis of welded components: Designer's guide to the structural hot-spot stress approach*. Cambridge: Woodhead Publishing.
- Niemi E, Tanskanen P (2000). Hot spot stress determination for welded edge gussets. *Weld. World*, 44, 31–37.
- Nisitani H, Teranishi T (2004). KI of a circumferential crack emanating from an ellipsoidal cavity obtained by the crack tip stress method in FEM. *Eng. Fract. Mech.*, 71, 579–585.
- Nui LS, Chehimi C, Pluvinage G (1994). Stress field near a large blunted tip V-notch and application of the concept of the critical notch stress intensity factor (NSIF) to the fracture toughness of very brittle materials. *Eng. Fract. Mech.*, 49, 325–335.
- Nussbaumer A, Borges L, Davaine L (2012). *Fatigue Design of Steel and Composite Structures: Eurocode 3: Design of Steel Structures, Part 1-9 Fatigue; Eurocode 4: Design of Composite Steel and Concrete Structures*. John Wiley & Sons.
- Ottersböck M, Leitner M, Stoschka M (2015). Effect of Loading Type on Welded and HFMI-treated T-joints. *IIW-document*, 13, 2515–2584.
- Pook LP (1983). The role of crack growth in metal fatigue. *Met. Soc. 1 Carl. House Terrace, London SW 1 Y 5 DB, England, 1983*.
- Popper K (2005). *The logic of scientific discovery*. Routledge.
- Portela A, Aliabadi MH, Rooke DP (1991). Efficient boundary element analysis of sharp notched plates. *Int. J. Numer. Methods Eng.*, 32, 445–470.
- Poutiainen I, Marquis G (2006). A fatigue assessment method based on weld stress. *Int. J. Fatigue*, 28, 1037–1046.
- Poutiainen I, Tanskanen P, Marquis G (2004). Finite element methods for structural hot spot stress determination—a comparison of procedures. *Int. J. Fatigue*, 26, 1147–1157.
- Pu SL, Hussain MA, Lorensen WE (1978). The collapsed cubic isoparametric element as a singular element for crack problems. *Int. J. Numer. Methods Eng.*, 12, 1727–1742.
- Qian J, Hasebe N (1997). Property of eigenvalues and eigenfunctions for an interface V-notch in antiplane elasticity. *Eng. Fract. Mech.*, 56, 729–734.

- Radaj D (2014). State-of-the-art review on extended stress intensity factor concepts. *Fatigue Fract. Eng. Mater. Struct.*, 37, 1–28.
- Radaj D (2015). State-of-the-art review on the local strain energy density concept and its relation to the J-integral and peak stress method. *Fatigue Fract. Eng. Mater. Struct.*, 38, 2–28.
- Radaj D (1996). Review of fatigue strength assessment of non-welded and welded structures based on local parameters. *Int. J. Fatigue*, 18, 153–170.
- Radaj D (1990). *Design and analysis of fatigue resistant welded structures*. Cambridge: Woodhead Publishing.
- Radaj D, Sonsino CM (1998). *Fatigue assessment of welded joints by local approaches*. Woodhead Publishing.
- Radaj D, Sonsino CM, Fricke W (2006). *Fatigue assessment of welded joints by local approaches*. Cambridge: Woodhead Publishing.
- Rybicki EF, Schmueser DW, Stonesifer RW, Groom JJ, Mishler HW (1978). A finite-element model for residual stresses and deflections in girth-butt welded pipes. *J. Press. Vessel Technol.*, 100, 256–262.
- Rybicki EF, Stonesifer RB (1979). Computation of residual stresses due to multipass welds in piping systems. *J. Press. Vessel Technol.*, 101, 149–154.
- Sakane M, Zhang S, Kim T (2011). Notch effect on multiaxial low cycle fatigue. *Int. J. Fatigue*, 33, 959–968.
- Schütz W (1996). A history of fatigue. *Eng. Fract. Mech.*, 54, 263–300.
- Seweryn A (1994). Brittle fracture criterion for structures with sharp notches. *Eng. Fract. Mech.*, 47, 673–681.
- Seweryn A (2002). Modeling of singular stress fields using finite element method. *Int. J. Solids Struct.*, 39, 4787–4804.
- Slockbower RE, Fisher JW (1976). Fatigue resistance of full scale cover-plated beams.
- Sonsino CM (2009). Multiaxial fatigue assessment of welded joints--recommendations for design codes. *Int. J. Fatigue*, 31, 173–187.
- Stephens RI, Fatemi A, Stephens RR, Fuchs HO (2000). *Metal fatigue in engineering*. John Wiley & Sons.



- Szabò BA, Yosibash Z (1996). Numerical analysis of singularities in two dimensions. Part 2: computation of generalized flux/stress intensity factors. *Int. J. Numer. Methods Eng.*, 39, 409–434.
- Taylor D, Barrett N, Lucano G (2002). Some new methods for predicting fatigue in welded joints. *Int. J. Fatigue*, 24, 509–518.
- Teng T-L, Fung C-P, Chang P-H, Yang W-C (2001). Analysis of residual stresses and distortions in T-joint fillet welds. *Int. J. Press. Vessel. Pip.*, 78, 523–538.
- Timoshenko S (1953). *History of strength of materials: with a brief account of the history of theory of elasticity and theory of structures*. Courier Corporation.
- Tong P, Pian THH, Lasry SJ (1973). A hybrid-element approach to crack problems in plane elasticity. *Int. J. Numer. Methods Eng.*, 7, 297–308.
- Topping BH V., International Conference on Computational Structures Technology (5th : 2000 : Leuven B, International Conference on Engineering Computational Technology (2nd : 2000 : Leuven B (2000). *Computational mechanics for the twenty-first century*. Saxe-Coburg Publications.
- Torabi, A.R., Berto F (2013). Fracture Assessment of Blunt V-Notched Graphite Specimens by Means of the Strain Energy Density. *Strength Mater.*, 45, 635–647.
- Tovo R, Lazzarin P (1999). Relationships between local and structural stress in the evaluation of the weld toe stress distribution. *Int. J. Fatigue*, 21, 1063–1078.
- Tracey DM (1971). Finite elements for determination of crack tip elastic stress intensity factors. *Eng. Fract. Mech.*, 3, 255–265.
- Verreman Y, Nie B (1997). Short crack fatigue propagation at fillet welds. In: *Proc Int Conf on Performance of Dynamically Loaded Welded Structures*. New York, WRC, pp. 240–253.
- Verreman Y, Nie B (1996). Early development of fatigue cracking at manual fillet welds. *Fatigue Fract. Eng. Mater. Struct.*, 19, 669–681.
- Weinberg S (1992). *Dreams of a final theory*. Vintage.
- Williams ML (1952). Stress singularities resulting from various boundary conditions in angular corners of plates in tension. *J. Appl. Mech.*, 19, 526–528.
- Withers PJ (2007). Residual stress and its role in failure. *Reports Prog. Phys.*, 70, 2211–2264.

- Xiao QZZ, Karihaloo BLL, Liu XYY (2004). Direct determination of SIF and higher order terms of mixed mode cracks by a hybrid crack element. *Int. J. Fract.*, 125, 207–225.
- Xiao Z-G, Chen T, Zhao X-L (2012). Fatigue strength evaluation of transverse fillet welded joints subjected to bending loads. *Int. J. Fatigue*, 38, 57–64.
- Yosibash Z, Bussiba AR, Gilad I (2004). Failure criteria for brittle elastic materials. *Int. J. Fract.*, 125, 307–333.
- Yung J-Y, Lawrence F V (1985). Analytical and graphical aids for the fatigue design of weldments. *Fatigue Fract. Eng. Mater. Struct.*, 8, 223–241.
- Yung J, Lawrence F (2013). Predicting the fatigue life of welds under combined bending and torsion. *ICBMFF2*.
- Zhu XK, Chao YJ (2002). Effects of temperature-dependent material properties on welding simulation. *Comput. Struct.*, 80, 967–976.

## Standards

- ASME VIII - Rules for Construction of Pressure Vessels - Division 2: Alternative Rules*. Brussels: American Society of Mechanical Engineers, 2013.
- BS 7608 British Standard - Code of Practice for Fatigue Design and Assessment of Steel Structures*. British Standard institution, 1993.
- BS 7608 British Standard - Code of Practice for Fatigue Design and Assessment of Steel Structures*. British Standard institution, 2014.
- DIN 15018 - Cranes - Steel structures - Verification and analyses*. German Institute for Standardization, 1984.
- DNVGL-RP-C203 - Fatigue design of offshore steel structures*. Det Norske Veritas - Germanischer Lloyd, 2016.
- DVS 1612 - Design and endurance strength assessment of welded joints with steels in rail vehicle construction*. Brussels: German Welding Society, 2009.
- EN 1993-1-1+A1 Eurocode 3: Design of steel structures - Part 1-1: General rules and rules for buildings*. Brussels: European Committee for Standardization, 2014.

- EN 1993-1-6 Eurocode 3 - Design of steel structures - Part 1-6: Strength and stability of shell structures.* Brussels: European Committee for Standardization, 2007.
- EN 1993-1-8 Eurocode 3 - Design of steel structures - Part 1-8: Design of joints.* Brussels: European Committee for Standardization, 2005.
- EN 1993-1-9 Eurocode 3 - Design of steel structures - Part 1-9: Fatigue.* Brussels: European Committee for Standardization, 2005.
- EN 1993-2 Eurocode 3 - Design of steel structures - Part 2: Steel bridges.* Brussels: European Committee for Standardization, 2006.
- EN 1993-6 Eurocode 3 - Design of steel structures - Part 6: Crane supporting structures.* Brussels: European Committee for Standardization, 2007.
- EN 13445-3 Unfired pressure vessels - Part 3: Design.* Brussels: European Committee for Standardization, 2014.
- EN 13001-3-1+A1 Cranes - General Design - Part 3-1: Limit States and proof competence of steel structure.* European Committee for Standardization, 2013.
- FKM Guideline - Analytical strength assessment of components.* 6th Editio. VDMA Verlag, 2012.
- IACS Common structural rules for bulk carriers.* International Association of Classification Societies, 2012.
- IACS Common structural rules for double hull oil tankers.* International Association of Classification Societies, 2012.
- ISO 16881-1 Cranes - Design calculation for rail wheels and associated trolley track supporting structure - Part 1: General.* International Organization for Standardization, 2005.
- ISO 19901-3 Petroleum and natural gas industries - Specific requirements for offshore structures - Part 3: Topsides structure.* International Organization for Standardization, 2014.
- PD 6705-2+A1 Structural use of steel and aluminium. Recommendations for the execution of steel bridges to BS EN 1090-2.* British Standard institution, 2013.
- prEN 1990-2:2016 Execution of steel structures and aluminium structures - Part 2: Technical requirements for steel structures.* European Committee for Standardization, 2016.



## **Acknowledgments**

I would like to express a deep gratitude to Prof. Filippo Berto, my academic supervisor, for his continuous support, for his remarkable knowledge and especially for his friendship.

I am particularly grateful to Cimolai SpA that supported this research. A special thank is reserved to Eng. Alessandro Catanzano. His knowledge on the topic and his industrial experience have been a continuous source of valuable advice.

I would like to express a very great appreciation to Prof. Paolo Ferro, to Prof. Giovanni Meneghetti and to Prof. Dario Croccolo. Their expertise and their advice represented important contributions to this work.

I wish to thank Prof. Stefano Secchi and Eng. Alessandro Corazzin for their estimable technical support on this project.

I would like to offer a special thank to Prof. Paolo Lazzarin for his unforgettable and contagious passion for research and teaching. He was a mentor and if I had never met him, I probably would never have started this work.

Grateful thanks are extended to my colleagues and to my friends for all exciting discussions and technical advice.

Finally, I wish to thank my parents, my brother and my wife for their support and encouragement throughout my study.